Ph.D. Dissertation of Engineering

Isogeometric Configuration Design Sensitivity Analysis of Geometrically Exact Nonlinear Structures

기하학적으로 정밀한 비선형 구조물의 아이소-지오메트릭 형상 설계 민감도 해석

February 2019

Seoul National University

Department of Naval Architecture and Ocean Engineering

Myung-Jin Choi

기하학적으로 정밀한 비선형 구조물의 아이소-지오메트릭 형상 설계 민감도 해석

지도 교수 조 선 호

이 논문을 공학박사 학위논문으로 제출함
2018년 12월

서울대학교 대학원
조선해양공학과
최 명 진

최명진의 공학박사 학위논문을 인준함
2018년 12월

위 원 장 홍 석 윤 (인)

부위원장 조 선 호 (인)

위 원 노 명 일 (인)

위 원 이 재 욱 (인)

위 원 구 본 용 (인)

Isogeometric Configuration Design Sensitivity Analysis of Geometrically Exact Nonlinear Structures

Thesis supervisor: Prof. Seonho Cho

Submitting a Ph.D. Dissertation of Engineering

December 2018

Seoul National University

Department of Naval Architecture and Ocean Engineering

Myung-Jin Choi

Confirming the Ph.D. Dissertation written by
Myung-Jin Choi

December 2018

Chair	Suk-Yoon Hong	(Seal)
Vice Chair	Seonho Cho	(Seal)
Examiner	Myung-Il Roh	(Seal)
Examiner	Jaewook Lee	(Seal)
Examiner	Bonyong Koo	(Seal)

To my parents and brother

Abstract

In this thesis, a continuum-based analytical adjoint configuration design sensitivity analysis (DSA) method is developed for gradient-based optimal design of curved built-up structures undergoing finite deformations. First, we investigate basic invariance property of linearized strain measures of a planar Timoshenko beam model which is combined with the selective reduced integration and $\bar{B}$ projection method to alleviate shear and membrane locking. For a nonlinear structural analysis, geometrically exact beam and shell structural models are basically employed. A planar Kirchhoff beam problem is solved using the rotation-free discretization capability of isogeometric analysis (IGA) due to higher order continuity of NURBS basis function whose superior per-DOF(degree-of-freedom) accuracy over the conventional finite element analysis using Hermite basis function is verified. Various inter-patch continuity conditions including rotation continuity are enforced using Lagrage multiplier and penalty methods. This formulation is combined with a phenomenological constitutive model of shape memory polymer (SMP), and shape programming and recovery processes of SMP structures are simulated. Furthermore, for shear-deformable structures, a multiplicative update of finite rotations by an exponential map of a skew-symmetric matrix is employed. A procedure of explicit parameterization of local orthonormal frames in a C^1-continuous spatial curve is presented using the smallest rotation method within the IGA framework. In the configuration DSA, the material derivative is applied to a variational equation, and an orientation design variation of curved structure is identified as a change of embedded local orthonormal frames. In a shell model, we use a regularized variational equation with a drilling rotational DOF. The material derivative of the orthogonal transformation matrix can be evaluated at final equilibrium configuration, which enables to compute design sensitivity using the tangent stiffness at the equilibrium without further iterations. A design optimization method for a constrained structure in a curved domain is also developed, which focuses on a lattice structure design on a specified surface. We define a lattice structure and its design variables on a rectangular plane, and utilize a concept of free-form deformation and a global curve interpolation to obtain an analytical expression for the control net of the structure on curved surface. The material derivative of the analytical expression eventually leads to precise design velocity field. Using this method, the number of design variables is reduced and design parameterization becomes more straightforward. In demonstrative examples, we verify the developed analytical adjoint DSA method in beam and shell structural problems undergoing finite deformations with various kinematic and force boundary conditions. The method is also applied to practical optimal design problems of curved built-up structures. For example, we extremize auxeticity of lattice structures, and experimentally verify nearly constant negative Poisson's ratio during large tensile and compressive deformations by using the 3-D printing and optical deformation measurement technologies. Also, we architect phononic band gap structures

having significantly large band gap for mitigating noise in low audible frequency ranges.

Keywords: Isogeometric analysis; Geometrically exact beam and shell models; Finite deformation; Adjoint sensitivity; Built-up structure; Configuration design optimization; Design velocity field
Student Number: 2012-21076

Published content and contribution

The following published articles are included as a part of the thesis with permission.

[1] Myung-Jin Choi, Minho Yoon, and Seonho Cho. Isogeometric configuration design sensitivity analysis of finite deformation curved beam structures using Jaumann strain formulation. *ComputerMethods in AppliedMechanics and Engineering*, 309:41–73, 2016.

[2] Myung-Jin Choi and Seonho Cho. Elimination of self-straining in isogeometric formulations of curved timoshenko beams in curvilinear coordinates. *Computer Methods in Applied Mechanics and Engineering*, 309:680–692, 2016.

[3] Myung-Jin Choi and Seonho Cho. Constrained isogeometric design optimization of lattice structures on curved surfaces: computation of design velocity field. *Structural and Multidisciplinary Optimization*, 58(1):1–18, 2018.

[4] Myung-Jin Choi and Seonho Cho. Isogeometric configuration design optimization of shape memory polymer curved beam structures for extremal negative poisson's ratio. *Structural and Multidisciplinary Optimization*, 58(5):1861–1883, 2018.

List of Figures

List of Tables

Contents

Chapter 1

Introduction

1.1 Motivation

Flexible built-up structures with various configurations have been widely used for mechanical systems such as ship hull with stiffeners, offshore platform support structure, automotive and aircraft body structures, and so on. Along with the advancements of manufacturing technology, these structures have become much more prominent with increasing flexibility of design. To reduce computational costs, those built-up structures are often described by beam or shell models in the deformation analysis process. Therefore, there has been significant academic endeavor to improve the efficiency and accuracy of numerical deformation analysis methods using the beam and shell structural models for their various engineering applications. However, these flexible structures may undergo large deformations, which makes it challenging to simulate their deformations and obtain appropriate design. Even though significant amount of research efforts has been reported for the deformation analysis of beam and shell structures, the importance of analytical design sensitivity analysis (DSA) has not been fully explored, in spite of its significance in what-if study and gradient-based optimal design.

1.1.1 Development of fundamentals in gradient-based optimal design

This thesis contributes to develop fundamentals of gradient-based design optimization of finite deformation curved built-up structures in the following two perspectives.

1.1.1.1 Continuum-based analytical DSA of finite deformation beam and shell structures

Design sensitivity information deals with the effect of change of design variables on the structural deformations, which plays a significant role in the convergence of design optimization process

and what-if study. Although the finite difference method (FDM) may be an easiest way to compute design sensitivity, it has serious drawbacks from the viewpoint of accuracy and computational costs. The accuracy of finite difference sensitivity strongly depends on the perturbation amount, and huge amount of computational costs is required especially if an iterative solution procedure is utilized in the deformation analysis. The discrete-analytical DSA method involves the analytical differentiation of discretized governing equation with respect to design variables. However, as mentioned in [55], since the finite element matrices are constructed using numerical integration, the explicit expression of finite element matrices in terms of design variables may not be available, and this discrete differentiation may not be achieved easily for general cases. Also, since the finite element matrix equation is an approximated one to the original continuum problem, it is theoretically dangerous to directly differentiate the finite element matrices [55]. In discrete DSA approach, the semi-analytical method, which utilizes finite difference for calculating the design derivative of finite element matrices, is a popular choice due to its simple implementation. However, this could lead to significant inaccuracy of sensitivity especially if large rotation is involved in deformation [83]. The continuum-based method directly differentiates the variational equation before discretization, which is more efficient than the discrete method [55, 25].

1.1.1.2 Design velocity computation for constrained structures on curved surfaces

Lattice structures embedded in curved domains have been utilized in myriad critical devices, including medical stents, non-pneumatic wheel frames, and ship hull curved block stiffeners, curved roof stiffeners in buildings. Especially for the medical stents, various unit cell configurations have been suggested to improve their structural performances like auxetic cellular designs for increasing the resistance to kinking and buckling [51]. These lattice structures are embedded in curved surfaces such that the medical stents and non-pneumatic wheel frames maintain cylindrical and circular shapes, respectively. For a given material point $\mathbf{x}$ and design $\mathbf{u}$, a general design optimization problem seeks for minimum objective function $\psi(\mathbf{x},\mathbf{u})$ subjected to inequality constraints $C_i(\mathbf{x},\mathbf{u}) \leq 0$ and equality constraints $D_j(\mathbf{x},\mathbf{u}) = 0$. In optimal design process of lattice structures, the designs of curved surfaces where the lattice structures are embedded usually pre-determined, and the design change of the embedded lattice structure should maintain their position on the curved surfaces. This restriction leads to the nonlinear equality constraints $D_j(\mathbf{x},\mathbf{u}) = 0$ in configuration design. In many cases, a spatial lattice structure is designed in a way that a planar pattern is mapped into complex shaped curved surfaces. Thus, if we can define the design variables in the planar pattern, two significant advantages can be attained: First, design parameterization is much more straightforward and easier than dealing with complex shaped spatial structure, and the number of design variables are reduced, since design variables are defined in planar (2-D) domain, not in spatial (3-D) domain. Second, it enables to avoid handling huge number of equality constraints $D_j(\mathbf{x},\mathbf{u}) = 0$, usually more than the number of design variables.

1.1.2 Configuration design optimization of curved built-up structures

We apply the developed DSA method to the following engineering applications.

1.1.2.1 Design of lattice structures with enhanced mechanical properties

Various shapes and topologies of lattice structures have been architected to achieve specified target artificial mechanical properties. In this research, we aims at tailoring two kinds of mechanical properties; negative Poisson's ratio and phononic band gap. First, the Poisson's ratio of a material describes the deformation in an orthogonal direction to tensile or compressive loading. The majority of materials show a positive Poisson's ratio, which is approximately 0.5 for rubber and 0.3 for steel. However, negative Poisson's ratio, or auxetic materials exhibit expansion (contraction) instead of contraction (expansion) under tension (compression). This seemingly unphysical behavior has been widely studied due to its desirable effects to enhance a variety of mechanical properties like energy absorption, shear modulus [96], indentation resistance [28], crashworthiness [95], and sound absorption [19]. Second, acoustic metamaterials with periodic arrangements of components have a significant dynamic property of band gap, which represents a certain frequency ranges where elastic wave or sound propagation through a material is prohibited. Due to its immense potential for novel applications like vibration and noise mitigations, and waveguides, there have been extensive research attentions to maximize the band gap property by architecting constituent material properties or structural geometries.

1.1.2.2 Design of compliant mechanisms

A compliant mechanism is a flexible mechanism that transforms or transfers a force or motion through elastic deformations of the components. As it accomplishes specified tasks through deflections of members instead of movements of joints, the number of required components is much less than that of rigid mechanisms. This results in the considerable reduction of structural weight, fabrication costs, and the ease of miniaturization, which might be a significant factor of their wide utilization in various applications including microelectromechanical systems (MEMS). The fact that the flexible parts of mechanism undergo large deformation complicates the deformation analysis and design process, which requires more systematic design procedures rather than conventional trial and error approaches.

1.1.2.3 Design of shape memory structures

Shape memory materials can recover their original shapes from programmed temporary ones when an appropriate stimulus like heat and light is applied. Since this kind of smart materials is able to react to environmental changes in a programmed sequence, it has been utilized in a myriad range of engineering applications such as pipe-coupling mechanism, airbags, space structures, deployable biomedical devices, and self-assembling structures. Mao et al. [72] fabricated SMP based self-assembly structures using 3-D printing technology, and realized thermal-activated sequential self-folding by controlling the glass transition temperature of hinges. The shape memory effect also can be used to implement tunable effective mechanical properties. Li et al. [65] designed a cellular structure made of bi-material strips, which changes its configuration by heating due to different thermal expansion coefficients of the strips. This enables to tune the Poisson's ratio of the structure by controlling temperature. This kind of control

of mechanical property would be realized by changing structural geometry using a shape memory effect.

1.2 Isogeometric analysis of geometrically exact nonlinear structures

1.2.1 Literature survey

1.2.1.1 Rotation-free discretization

To resolve the discrepancy between the finite element model and the computer-aided design (CAD) model, Hughes et al. [46] developed the isogeometric analysis (IGA) method, which is an analysis framework employing the same basis function as used in the CAD system in order to bridge the gap between CAD and computer-aided engineering (CAE) like finite element analysis (FEA). Due to higher order continuity of the NURBS basis functions, the IGA has a superior capability of rotation-free discretization over conventional FEA in problems of high-order partial differential equations (PDEs). The variational formulation under Kirchhoff assumption (zero transverse shear strain) involves the second order derivatives of displacement field, which requires C^1-continuous basis functions, where using only the displacement degree of freedom (DOF) in the IGA considerably reduces the total number of DOFs in comparison to the FEA employing additional DOFs, associated with rotation, to have C^1-continuity. Kiendl et al. [54] applied the IGA to deformation analysis of Kirchhoff shell model. Raknes et al. [93] presented the IGA for cable structures undergoing large deformation, with considering bending deformation confined in an osculating plane as well as membrane deformation. Bauer et al. [7] suggested an IGA formulation of spatial Kirchhoff beam undergoing large deformation considering torsion. Maurin et al. [76] performed the IGA for static and dynamic deformation analyses of planar Kirchhoff beam based on the GEBT considering single patch models. However, due to C^0-continuity between NURBS patches, there is a difficulty of using multiple patches in Kirchhoff beam or shell analysis since it requires C^1-continuous displacement field. To overcome this difficulty, there have been many attempts to impose continuity condition at the multi-patch interface. Due to absence of rotational DOF, an additional rotational continuity condition at multi-patch junction is required. Kiendl et al. [52] suggested a bending strip method imposing G^1-continuity by penalizing additional bending stiffness at the interface. Greco and Cuomo [40] employed the rotational DOFs and modified the B-spline basis functions to possess strong G^1-continuity. Benson et al. [11] also imposed strong G^1-continuity through selectively adding the rotational DOFs to the rotation-free thin shell element. Duong et al. [36] imposed various rotation continuity conditions using penalty and Lagrange multiplier methods. If a shear deformable beam model having rotational DOFs is considered, rotation continuity can be straightforwardly satisfied by a typical element assembly process.

1.2.1.2 Deformation analysis of shear-deformable beam and shell structures

Recently, in the context of isogeometric collocation method, several works on the finite deformation analysis of beam structures are reported including [73] for a geometrically exact shear-deformable beam model and its extension to mixed collocation method to alleviate shear locking troubles in [74]. Weeger et al. [113] also simulated three-dimensional beam structures considering spatially varying material parameters and cross-section radius. In order to alleviate the shear and membrane locking troubles, Bouclier et al. [15] extended the selective reduced integration (SRI) and $\bar{B}$ projection methods to the IGA context. This is further developed in terms of SRI by Adam et al. [1], to higher order basis function. Also, Beirão da Veiga et al. [31] and Auricchio et al. [4] developed locking-free mixed formulations respectively for straight planar and spatial curved Timoshenko beams in the context of isogeometric collocation method. For the finite deformation analysis of shear-deformable shell structures, many research works are recently reported within the isogeometric analysis context. Benson et al. [10] implemented for linear and nonlinear deformation analyses of Reissner-Mindlin shell structures based on a degenerated solid element where a small rotational stiffness is added to avoid singularity associated with the drilling rotational DOF. Hosseini et al. [43] used a higher order interpolation using B-spline element in discretization along thickness-direction. Oesterle et al. [82] presented a hierarchic shell model using a nonlinear Kirchhoff-Love shell model with enrichment by two extra shear rotation or displacement variables. In this formulation, shear rotation is assumed to be small but total rotation can be large. Dornisch et al. [35] solved a system of linear equations to determine initial local orthonormal basis system at integration points, and calculate current director through a orthogonal transformation of a interpolated initial exact director. This work was extended in Dornishch and Klinkel [34] to treat a multiple patch model with sharp interface through employing an automatic classification algorithm to determine control point whether on smooth or non-smooth region. Also, in Dornishch et al. [33], it was shown that using a multiplicative rotation update instead of an additive update procedure makes a variation of the current director vector have much simpler expressions.

1.2.2 Research objectives

We investigate strain invariance property in a planar linear Timoshenko beam problem formulated in a curvilinear coordinate system. An invariant formulation is combined with SRI and $\bar{B}$ projection methods to avoid shear and membrane locking. For planar Kirchhoff beam structures, we verify the advantages of rotation-free discretization of IGA method in terms of per-DOF accuracy, compared with FEA using Hermite interpolation. For the geometrically exact shear-deformable beam and shell models, we employ a multiplicative update procedure of finite rotation using an exponential map of a skew symmetric matrix, presented in [102]. We consider various force and kinematic boundary conditions including non-conservative problems due to pressure load. For a spatial beam structure, we employ the smallest rotation (SR) method to determine initial orthonormal frame. This method was utilized for curve framing in FEA context

by Meier et al. [78]. We present a procedure of determine reference orthonormal frame for each knot span of NURBS curves within the IGA framework. If a tangent vector and a reference orthonormal frame are given at a curve point, the SR method determines an orthonormal frame at the given point through a mapping such that the first base vector of the given reference frame rotates onto the given tangent vector with minimum rotation angle. Especially if a curve is embedded in a curved surface, it is shown that convected basis of the surface can be effectively used to construct the reference orthonormal frame at an arbitrary point of a curve.
We also investigate an elastic wave propagation in infinitely periodic lattice structure. Using the Bloch theorem, the computational domain is reduced to a single unit cell, and a consistent linearization of the nonlinear problems yield a generalized Hermitian eigenvalue problem. This problem is solved for wave dispersion relations using the inverse method for various lattice topologies. Thus, our research objectives in terms of deformation analysis can be summarized as

- **Invariant locking-free formulation of a planar linear Timoshenko beam problem,**
- **Verification of superior per-DOF accuracy of IGA in planar Kirchhoff beam problems,**
- **Explicit parameterization of initial orthonormal frame for spatial beams using the SR method,**
- **IGA of finite deformation shear-deformable curved beam and shell built-up structures,**
- **Calculation of dispersion relation for infinite lattice using the Bloch theorem.**

1.3 Isogeometric design optimization of finite deformation built-up structures

1.3.1 Literature survey

In plane elasticity, isogeometric shape DSA and optimization were presented for linear [22] and geometrically nonlinear [56] deformations, where the following advantages of isogeometric approach are emphasized: *First*, it considers exact higher order geometric information such as normal vector and curvature, which provides more accurate sensitivity than the conventional FEA-based one. *Second*, it significantly simplifies the design modification during the design optimization process without communicating with CAD systems. An isogeometric configuration DSA method was developed for Mindlin plate problems [63]. In the plate design component under the assumption of small design perturbations, the design variation is represented by the tangential design velocity for the shape variation and by the out-of-plane design velocity for the orientation variation. Nagy et al. [80] performed the shape and sizing design optimization of planar Kirchhoff beams considering infinitesimal deformation. In their work, a discrete-analytic approach is used for the DSA, where single patch models are considered and the shape design includes the orientation variation.

1.3.1.1 Configuration design sensitivity analysis

Extending the design sensitivity analysis (DSA) of built-up structures consisting of straight design components, this research focuses on the design of curved geometry, which refers to a configuration design associated with the change of integral domain of curved structures. In Twu and Choi [106], a straight beam design is decomposed into a shape (length) change, and an orientation change by rigid body rotation, and their combination is termed *configuration design*. Cho and Choi [21] employed this concept of configuration design in transient dynamic and path-dependent problems, where Euler angles are utilized to represent orientation design variations. Kim et al. [55] generalized this method to curved structures using the material derivatives by identifying an orientation design change as a change of pointwise local coordinate system. This formulation has significance in perspective of unifying the procedures of configuration DSA of beams/shells and shape DSA of solid elasticity problems into a material derivative process without decomposing shape and orientation design variations. On the other hand, sizing design parameters of beam structures include material properties like Young's modulus, and cross-section geometry like thickness, area, and so one. Nagy et al. [80] defined the sizing design variables of cross-section thickness of planar beams at control points within IGA framework. Recently, Weeger et al. [112] reported an analytical adjoint DSA method for 3-D curved beam structures within the context of isogeometric collocation method. However, the accuracy of analytic design sensitivity for a design change in clamped boundary region was not satisfactory. Also, their another contribution so called *inconsistent analytic DSA method* which neglects the design dependence of initial orthonormal frame may not yield accurate sensitivity values if orientation design change becomes significant.

On the optimal design of linear shell structures, several works have been reported within the IGA framework. Nagy et al. [81] presented a comprehensive works on optimizing the form and the material anisotropy distribution of a shell structure where control point coordinates as well as weights were used as design variables that control shell mid-surface geometry, and a discrete analytical DSA approach was used. Kiendl et al. [53] presented an isogeometric shape optimization for Kirchhoff shell structures using a discrete semi-analytical DSA approach. Ha [41] presented a continuum-based analytical configuration DSA formulation for shell structures in generalized curvilinear coordinate system. Ahn et al. [2] performed optimal configuration design of nanoscale thin-walled structures using continuum-based shell theory incorporating surface effect. Hirschler et al. [42] utilized a solid-shell model in shape optimization where a smooth sizing design variations can be represented by changing the distance between the control points of the surfaces. They used a discrete semi-analytic DSA approach.

1.3.1.2 Determination of initial orthonormal frame

One of the existing difficulties in the configuration DSA of three-dimensional beams might be a parameterization of initial orthonormal frame, associated with initial cross-section orientation. For a C^1-continuous curve, among three orthonormal base vectors, unit tangent vector only can be uniquely determined, and the others are generally not unique due to a rotational degree-of-

freedom (DOF) about the tangent vector. The Frenet frame is a very useful tool for a spatial curve framing. It determines normal vector fields by a derivative of tangent vector with respect to an arc-length parameter, divided by its magnitude, and a binormal vector simply by the cross product of the tangent and normal vectors. However, this method has a main drawback that the normal and binormal vectors are not able to be defined at those points having vanishing curvature. On the other hand, the Bishop frame [14] is well defined even for a straight curve segment. Due to its implicit definition, Weeger et al. [112] solved a nonlinear equation to determine initial quaternion control coefficients. It requires a heuristic in determination of a user-defined boundary condition for the nonlinear equation. The quaternion interpolation using NURBS basis function may not be necessarily orthonormal at an arbitrary point except the collocation points, which may result in inaccurate representation of beam geometry. As an alternative, we employ the smallest rotation (SR) method which was utilized for curve framing in FEA context by [78]. If a tangent vector and a reference orthonormal frame are given at a curve point, the SR method determines an orthonormal frame at the given point through a mapping such that the first base vector of the given reference frame rotates onto the given tangent vector with minimum rotation angle. In the later section, we present a procedure of determine reference orthonormal frame for each knot span of NURBS curves within the IGA framework. Especially if a curve is embedded in a curved surface, it is shown that convected basis of the surface can be effectively used to construct the reference orthonormal frame at an arbitrary point of a curve.

1.3.1.3 Computation of design velocity on curved surface

Design velocity field is defined as a rate of mapping between original and perturbed designs, and its computation is a crucial step in configuration DSA as well as the update of finite element mesh during design optimization process. Braibant and Fleury [16] suggested to use B-spline curves to define design variables instead of finite element nodal coordinates to avoid drawbacks such as too many design variables and undesirable designs due to irregular boundary. Zhang and Belegundu [116] utilized a deformation field from a fictitious load to determine a domain design velocity field. Choi and Chang [24] suggested a combination of isoparametric mapping and boundary displacement methods as an ideal choice for the design velocity field computation. Kuci et al. [58] utilized the finite difference of nodal positions to identify the design velocity field at design boundary, and employed a Laplacian smoothing, equivalent to the boundary displacement method [24], or an element layer method for generating a domain design velocity field. The element layer method interpolates the priorly determined boundary nodal velocity vectors using shape functions in finite elements adjacent to the design boundary only. Cho and Ha [22] showed that, in the IGA framework, a smooth design velocity field can be easily obtained by the perturbation of control point combined with NURBS basis function.

In this thesis, we are particularly interested in structural design on curved domains. Bauer et al. [8] utilized a nested parameterization to model this kind of embedded structural entities. Parametric coordinates of an embedded curve are described by a corresponding NURBS curve in parametric space of a super element, and the control net of the super element expresses the

embedded curve geometry, which enables to model the embedded curve geometry exactly on the super element. A similar concept appears in the free-form deformation (FFD) method, which illustrates a deformation of embedded object due to a deformation of surrounding pliable solid, which would be effectively utilized to obtain an analytical expression of control net of the curve together with a global curve interpolation strategy. It would be significantly advatageous if design variables and corresponding design velocity fields are given in a planar rectangular domain; however, since an analysis model is constructed in a specified curved domain, it is essential to identify the mapping relation between the design velocity fields of the lattice structures in those planar and curved domains for the configuration DSA, which is one of the main objectives of this thesis.

1.3.2 Research objectives

In perspective of DSA, we develop a configuration DSA method that accommodates large displacements and rotations in three-dimensional space. This research is considered as a generalization of the conventional configuration DSA of built-up structures with straight design components to general curved structures. Geometrically exact beam and shell models are employed in deformation analyses, and we basically use the material derivative of their varational equation for DSA formulations. We present direct differentiation method (DDM) and adjoint variable method (AVM) for DSA which are respectively advantageous if the number of performance measures are larger than that of design variables, and vice versa. We further discuss the symmetry property of tangent operator in adjoint equation for non-conservative problems. Moreover, we present design velocity computation and optimization method for constrained structures on curved domains. Thus, the research objectives in perspectives of DSA and optimization can be stated as

- **Continuum-based analytical configuration DSA method for curved beam and shell buil-up structures undergoing finite deformations,**
- **Design velocity computation and optimization of a constrained structural design on curved domain.**

1.4 Applications

1.4.1 Auxetic structures

Ever since a reentrant honeycomb structure with NPR is suggested by the seminal work of Lakes [59], there have been considerable investigations for developing structural geometry representing auxetic behaviors. For a stable isotropic material, the Poisson's ratio ranges between -1 and 0.5, where the lower bound value -1 and the upper bound value 0.5, respectively, represent perfect dilatational and incompressible materials. Many lattice structural geometries having Poisson's ratio -1 have been reported, for example, chiral honeycombs exhibiting auxetic behaviors under the major deformation mechanism of flexure of ligaments due to cylinder rotations [92], which was extended to a three-dimensional structure in [39]. Also, a class of two-dimensional lattice

models having omnidirectional negative Poisson's ratio arbitrarily close to -1 was proposed in [17], and extended to three-dimensional cubic lattice structure in [18]. There have been several theoretical studies on the unboundedness of Poisson's ratio of anisotropic structures. Ting and Chen [104] investigated that Poisson's ratio for anisotropic elastic materials can have an arbitrarily large magnitude along specific directions. In Cabras and Brun [18], Poisson's ratios outside of the isotropic range of $-1 \leq \nu \leq 1/2$ occurs at small strains. Lethbridge et al. [64] investigated the relationship between elastic anisotropy and extreme Poisson's ratio in single-crystals. However, to the best of our knowledge, lattice structural design having nearly constant Poisson's ratio lower than -1 in a large deformation range and its experimental verification has not yet been reported.

Mathematical optimization methods are often exploited to achieve extremal Poisson's ratio. Materials have been tailored by mathematical optimization method to achieve target performances. Sigmund [99] presented an inverse homogenization method to design periodic microstructures of a material to obtain prescribed constitutive properties. Shwerdtfeger et al. [97] performed the design optimization of mesoscale elastic metallic NPR structures, using the topology optimization starting from the known re-entrant honeycomb structure, and utilized the selective electron beam melting (SEBM) system for manufacturing. Under large deformations, Poisson's ratio strongly depends on the amount of strains. The optimization objective can be mathematically defined as minimizing deviations between actual and prescribed values of Poisson's ratio over a range of discrete, applied nominal strain values. Using this optimization formulation, Wang et al. [107] performed topology optimization to tailor nearly strain-independent Poisson's ratio under finite tensile deformations, based on the method of solid isotropic material with penalization (SIMP). Clausen et al. [27] further elaborated this work by direct ink writing (DIW) 3D printing of optimal designs and experimental verification of the numerically predicted behaviors. They additionally performed shape optimizations using a concept of super-ellipse, from the conceptual design by the topology optimization, for fine tuning of design objectives. Within the IGA framework, several works of auxetic structural designs have been reported. In order to mitigate stress concentration effect of star-shaped auxetic structure, Wang et al. [110] designed petal-shaped planar auxetic structures with smooth connections using a shape design optimization approach, which represented in-plane isotropy and low negative Poisson's ratio.

In this reserach, we present a systematic synthesis of lattice structures achieving extremal negative Poisson's ratio in both of tensile and compressive loadings, using a gradient-based mathematical optimization method. This is combined with 3-D printing to digitally fabricate the designs and validate against the numerically predicted behavior. Specifically, we create new designs having Poisson's ratio -1.5 and -2 that display a nearly constant Poisson's ratio over large deformations of up to 10% applied nominal tensile strain and about 4% of compressive strain. To ensure manufacturability under capability (resolution limit) of printing machine, several geometric constraints are imposed: first, maximum curvature of the ligaments is restricted at selected discrete points, and second, minimum distance between selected ligaments is restricted.

Thus, our research object in this application is summarized as

- **Synthesize of two- and three-dimensional auxetic structures having Poisson's ratio -2 in both of finite tensile and compressive loadings using mathematical optimization**
- **Experimental validation of two-dimensional auxetic structures fabricated by 3-D printing**

1.4.2 Phononic band-gap structures

The fundamental mechanisms of band gap formations have been classified into Bragg scattering or local resonance of structural elements. In the Bragg-type one, destructive interferences of wave reflections due to structural periodicity account for decays of waves in a certain frequency. However, since a wavelength, in a periodic lattice, is scaled with unit cell size, low frequency band gap requires to significantly increase overall structural dimension, which is impractical. Thus, for the low frequency band gaps, locally resonating units have been successfully exploited to dissipate energy of wave propagation around their resonance frequency. Liu et al. [70] fabricated locally resonant structures, so called sonic crystals, composed of hard spherical inclusion coated with a soft cladding and a stiff matrix, with much lower frequency of band gap formation than Bragg-type ones due to localized vibrational motion of the inclusions. Bacigalupo et al. [5] combined anti-chiral lattice structure with inertial resonators, and designed the number, arrangements and material properties of the resonators to improve band gap properties using a nonlinear optimization algorithm. Matlack et al. [75] embedded steel cubes as local resonators in a polycarbonate beam lattice, and altered geometrical parameters of the lattice like the number of constituent beams, cross-section-thickness of beams, unit cell size, and resonator filling fraction, which shows a variety of band gap formations due to different local resonant modes. Jensen [50] studied in-plane wave propagation in 1-D and 2-D mass-spring models. This study showed that complete band gaps exist for certain distributions of stiffness and mass and demonstrated how band gaps can be created at low frequency ranges by introducing a local resonator into periodic structures. Instead of introducing local resonators, it has been shown that single material systems can have band gaps by local resonances. Krödel et al. [57] locally increased wall thickness of hollow trusses, and showed that additional masses at truss junction points lead to broader band gaps at low frequencies due to amplification of microscopic rotatory inertia. Wang et al. [108] demonstrated band gap properties in beam lattices due to local resonances, and investigated effects of lattice topologies and joint conditions. They correlate band gap properties with the average connectivity of a beam network, so called the coordination number. Warmuth et al. [111] fabricated a three-dimensional cellular structure made of a single phase titanium alloy having low frequency band gap using selected electron beam melting, and experimentally verified the band gap property.

Our objective in the present study is to architect two- and three-dimensional lattice structures with enhanced band gap properties using a gradient-based optimization algorithm. We basically control beam neutral axis geometry and cross-section thickness for a given lattice topology.

Various lattice topologies of two-dimensional structures have been suggested through parametric studies on configuration designs, including self-similar fractal [66], star [79], zig-zag [115], and chiral [118] shaped structures. Also, introduction of undulated lattice geometries in the ligaments have turned out to generate band gap properties. Trainity et al. [105] showed that wave propagation properties of lattice structures are significantly affected by the specific pattern of undulation due to the coupling of longitudinal and flexural modes. Chen et al. [20] also presented that low frequency band gaps can be generated within a square lattice by introducing sinusoidal undulations. There also have been researches exploiting mathematical optimization methods to obtain phononic crystal structures having large band gap sizes. Sigmund and Jensen [101] performed a topology optimization, based on the solid isotropic material penalization (SIMP) method, to design periodic structures exhibiting band gap properties. Lu et al. [71] synthesized a three-dimensional phononic crystal structure using a SIMP based topology optimization of two-phase material, where very large size of band gaps are generated at high frequency levels. Li et al. [16] attained low frequency level band gaps by embedding inclusions in a base material through the bi-directional evolutionary structural optimization (BESO) process. In Wormser et al. [114], a two-dimensional design, obtained by combination of shape and topology optimization, is manually interpreted into a three-dimensional structure having enhanced band gap property. Diaz et al. [32] studied optimal mass distributions of plane grid structures to create and maximize band gaps, also identified the influence of the skew angle of ligaments on the band gap distribution. In this research, we calculate wave dispersion relations in infinite periodic lattices using the Bloch theorem which reduces the maximization problem to that of a single unit cell, and also utilize the IGA using higher order B-spline basis functions for spatial discretization of given eigenvalue problem. We basically employ several lattice topologies and slenderness ratios without band gap or with slight band gaps from previous literatures as initial designs, and then their geometries are controlled by an optimization algorithm using the adjoint sensitivity. Thus, our research objectives in this application is summarized as

- **Synthesize of ligament configuration and sizing design in two- and three-dimensional phononic band gap structures having extremal band gap sizes at low audible frequency range ($20 \sim 20,000$Hz)**
- **Verification of architected unit cell design by harmonic response analysis of finite unit cell assembly**

1.4.3 Compliant mechanisms

Three kinds of approaches to the systematic design of compliant mechanisms have appeared in literatures. *First*, a pseudo-rigid-body mechanism describes the deflection of flexible members using rigid links connected by pin joints and torsional springs that have equivalent force-deflection characteristics [77]. Then, traditional rigid mechanism design approaches can be employed for the pseudo-rigid-body models. This is often preferred during the early phases of design process since many designs can be quickly evaluated. *Second*, using the solid isotropic

material with penalization (SIMP) model, a topology optimization method is utilized to find optimal material distribution in a specified domain. Sigmund [100] presented continuum-type topology optimization for the design of compliant mechanism, considering the stiffness of the workpiece. Also, it was demonstrated that the maximum stress level in compliant mechanisms can be controlled by constraining the displacement at the input port. This work was extended, by Pedersen et al. [88], to design large displacement compliant mechanisms based on nonlinear finite element analysis (FEA). *Third*, especially in designing path generating mechanisms, a topology optimization using beam elements can be performed using heuristic algorithms combined with nonlinear FEA. Zhao et al. [117] synthesized path generating compliant mechanisms using two-objective genetic algorithm to find a group of viable designs that trade off minimizing the average and peak distance between target and actual paths. The aforementioned methodologies can be utilized in conceptual design steps, and further refinement can be efficiently made through configuration and sizing design optimizations using gradient-based algorithms. *In this research, the initial design of compliant mechanisms refers to the known topology optimization results in literatures. Then, to further improve the performances and satisfy the specified design objectives, we perform a gradient-based configuration design optimization combined with nonlinear deformation analysis of beam structures. Through this procedure, starting from the conceptual design results, we can find more sophisticated configuration and sizing designs that show much better performances.*

1.4.4 Shape memory structures

Various design optimization examples using shape memory materials are found in literatures. A self-folding sheet by combining shape memory alloy (SMA) wires and compliant passive layers was modeled in Peraza-Hernandez et al. [89], where the effect of SMA mesh configurations on folding performances was investigated. They optimized the power input and geometric parameters to achieve the tightest fold under stress and temperature constraints. Wang and Brigham [109] synthesized morphing structures with maximal efficiency and accuracy in shape changes by an optimization method to determine the location, magnitude, and sequence of thermal activation. Salehi et al. [94] investigated the effect of several configuration design parameters of micro-actuators to have a maximum actuation force during shape recovery process using the regression analysis of characteristic curves. Langelaar and Van Keulen [62] performed the configuration design optimization of SMA shell structures using a semi-analytical DSA approach. Also, Langelaar et al. [61] performed an adjoint DSA for the topology optimization of SMA thermal actuators using the approach of element connectivity parameterization. In this research, we investigate shape memory polymer (SMP) structures undergoing large deformations and their design optimizations. In contrast to shape memory alloys, the SMP has several advantages such as large elastic deformation, low cost for shape programming, and potential biocompatibility. In the design of SMP-based devices, the constitutive modeling is critical to accurately predict the deformations during shape programming and recovery processes. In

developing constitutive models for SMPs, two general approaches have mainly been adopted: micro-modeling and macro-modeling. The former is useful for understanding the micro-scale features and fundamental phenomena, although not easily applicable to a structural scale. On the other hand, the latter phenomenologically describes the material behavior and is generally appropriate for numerical methods like finite element method in an efficient manner. Several phenomenological constitutive models have been proposed in recent years. Liu et al. [69] developed a linear elastic and rate-independent constitutive model based on the results of uniaxial experiments. They suggested an empirical formula of frozen volume fraction as a function of temperature by fitting free strain recovery response. Bergman and Yang [12] employed this phenomenological model to geometrically nonlinear problems. However, they did not deal with the shape recovery process. Baghani et al. [6] developed a small strain constitutive model for the SMPs under time-dependent multiaxial thermomechanical loading conditions. The constitutive model is based on an additive decomposition of the strain into six parts considering viscoelastic behavior. In the constitutive model, the evolution laws for internal variables are derived for both cooling and heating thermomechanical loadings. In this research, the linear elastic and rate-independent SMP constitutive model developed by Liu et al. [69] is employed. In this application, we particularly aim at the followings.

- **Large deformation analysis of SMP-based structures**
- **Analytical DSA method considering the thermomechanical process of SMP where the stored strain sensitivity consistently follows the integration algorithm of stored strain evolution.**

Chapter 2

Isogeomtric analysis of geometrically exact nonlinear structures

2.1 B-splines and NURBS

This section briefly introduces geometric modeling by B-spline and NURBS (Non-uniform rational B-spline) and their desirable properties for basis functions in analysis.

2.1.1 Basis functions

In the isogeometric analysis (IGA), the response field is approximated in terms of the same basis functions like B-spline and NURBS as used to express the geometry in CAD; thus it has several advantages over the conventional finite element analysis (FEA) such as easy refinements and geometrical exactness. A *knot* represents a coordinate in the parameteric space, and we term a *set of knots*, written in one-dimensional space

$$\Xi = \{\xi_1, \xi_2, \cdots, \xi_{n+p+1}\}, \tag{2.1}$$

where $\xi_i \in \mathbf{R}^1$ is the i^{th} knot, and p and n are the order of basis function and the number of basis functions which comprises the B-spline, respectively. The B-spline basis functions are constructed by a recursive formula as

$$N_i^0(\xi) = \begin{cases} 1 & \text{if } \xi_i \le \xi < \xi_{i+1} \\ 0 & \text{otherwise} \end{cases}, (p = 0) \tag{2.2}$$

and

$$N_i^p(\xi) = \frac{\xi - \xi_i}{\xi_{i+p} - \xi_i} N_i^{p-1}(\xi) + \frac{\xi_{i+p+1} - \xi}{\xi_{i+p+1} - \xi_{i+1}} N_{i+1}^{p-1}(\xi), \ (p = 1, 2, 3, \ldots). \tag{2.3}$$

By a projective transformation of B-spline entities in $\mathbf{R}^{d+1}$, a desired geometric object in $\mathbf{R}^d$ can be constructed. Especially, conic sections like circles and ellipses in $\mathbf{R}^2$ can be exactly represented by projective transformaitons of quadratic B-spline curves in $\mathbf{R}^3$. From the projective (weighted) control points $\{\mathbf{B}_i^w\}$ in $\mathbf{R}^{d+1}$, the control points in $\mathbf{R}^d$ are obtained by

$$(\mathbf{B}_i)_j = \left(\mathbf{B}_i^w\right)_j / w_i, \ j = 1 \sim d, \tag{2.4}$$

and

$$w_i = \left(\mathbf{B}_i^w\right)_{d+1}, \tag{2.5}$$

where w_i is called the i^{th} weight and $(\bullet)_j$ denotes the j^{th} component of the vector $(\bullet)$. From the B-spline basis function $N_i^p(\xi)$ and the corresponding weight w_i, the univariate NURBS basis function $W_i^p(\xi)$ is given by

$$W_i^p(\xi) = \frac{N_i^p(\xi) w_i}{\sum_{j=1}^{n} N_j^p(\xi) w_j}. \tag{2.6}$$

If weights are equal, NURBS becomes B-spline. NURBS possesses the following crucial properties for analysis.

(**1**) **Partition of unity**: $\sum_{i=1}^{n} W_i^p(\xi) = 1, \ \forall \xi$.

(**2**) **Compact support**: The local support of each $W_i^p(\xi)$ is compact and included in the interval $[\xi_i, \ \xi_{i+p+1}]$.

(**3**) **Non-negativity**: $W_i^p(\xi) \geq 0, \ \forall \xi$.

(**4**) **Variational diminishing**

It is noted that due to the third property in the above, all of the coefficients of a mass matrix calculated from NURBS basis functions are non-negative. The fourth property is advantageus to represent sharp layers, and more discussions of the variational diminishing property in NURBS can be found in [46, 68].

2.1.2 Geometric modeling

A curve geometry is described from the linear combination of NURBS basis functions and corresponding control points as

$$\mathbf{C}(\xi) = \sum_{i=1}^{n} W_i(\xi) \mathbf{B}_i, \tag{2.7}$$

where the superscipt denoting the order of basis function is omitted for brevity. Similarly, a NURBS surface is obtained as,

$$\mathbf{S}(\xi, \eta) = \sum_{i=1}^{n} \sum_{j=1}^{m} W_{ij}(\xi, \eta) \mathbf{B}_{ij}, \tag{2.8}$$

where the bivariate NURBS basis function is given by

$$W_{ij}(\xi,\eta) = \frac{N_i^p(\xi)N_j^q(\eta)\,w_{ij}}{\sum_{k=1}^{n}\sum_{\ell=1}^{m} N_k^p(\xi)N_\ell^q(\eta)\,w_{k\ell}}. \tag{2.9}$$

$\mathbf{B}_{ij}$ and w_{ij} are a bidirectional control net and the weights. p and q denote the order of the basis functions in the directions of ξ and η parametric coordinates, respectively. For the brevity of expression, Eq. (2.8) can be rewritten as

$$\mathbf{S}(\xi,\eta) = \sum_{N=1}^{n} \tilde{W}_N(\xi,\eta)\tilde{\mathbf{B}}_N, \tag{2.10}$$

where n denotes the total number of control points. NURBS geometry has the following crucial properties.

(**1**) **High order continuity**: $(p-k)$ continuous differentiability for order p and knot multiplicity k.

(**2**) **Affine covariance**: Affine transformation is obtained by applying the transformation to the control points.

The high order continuity of NURBS basis is significantly advantageous in discretization of variational equation from high order partial differential equation (PDE) like Kirchhoff beam problem, since it enables a *rotation-free* discretization in contrast to the cubic Hermite interpolation of FEA adopting additional DOF to have C^1-continuity. This will be investigated in section 2.3. Also, the affine covariance property is useful in the proof of invariance of approximated strain measures with respect to rigid body rotation (patch test), which will be shown in section 2.2.

For a one-dimensional model, a half-open interval $[\xi_i,\xi_{i+1})$ is called the i^{th} knot span. In the analysis context, the non-zero knot span, *i.e.*, a span between two distinct knot values is somtimes called the *element*, and the number of elements in a curve will then mean the number of non-zero knot spans in the set of knots. This definition is extended to each parametric coordinate direction of multi-dimensional geometries.

2.1.3 Mesh refinement

The basis function is refined for purpose of analysis without alterning an object geometrically or parametrically.

2.1.3.1 h-refinement: knot insertion

The analogue of h-refinement in FEA is *knot insertion*. Given a set of knots $\Xi = \{\xi_1,\xi_2,\dots\xi_{n+p+1}\}$, let $\tilde{\Xi} = \{\xi_1,\xi_2,\dots,\xi_k,\tilde{\xi},\xi_{k+1},\dots,\xi_{n+p+2}\}$ be a new knot vector where a knot $\tilde{\xi}$ is inserted. From the original control points $\{\mathbf{B}_1,\mathbf{B}_2,\dots,\mathbf{B}_n\}$, the new $(n+1)$ control points $\{\tilde{\mathbf{B}}_1,\tilde{\mathbf{B}}_2,\dots,\tilde{\mathbf{B}}_{n+1}\}$ are obtained

by

$$\tilde{\mathbf{B}}_i = \alpha_i \mathbf{B}_i + (1-\alpha_i)\mathbf{B}_{i-1}, \tag{2.11}$$

where

$$\alpha_i = \begin{cases} 1, & i \le k-p \\ \frac{\tilde{\xi}-\xi_i}{\xi_{i+p}-\xi_i}, & k-p+1 \le i \le k \\ 0, & k+1 \le i \end{cases} . \tag{2.12}$$

A simple example of knot refinement is presented in Fig. 2.1. The original cubic B-spline curve consists of a given set of knots $\Xi = \{0,0,0,0,1,1,1,1\}$ and four control points. If a new knot $\tilde{\xi} = 0.5$ is inserted, a refined curve shown on the right, is obtained without changing the original entity geometrically or parameterically, but the basis functions and control points are altered.

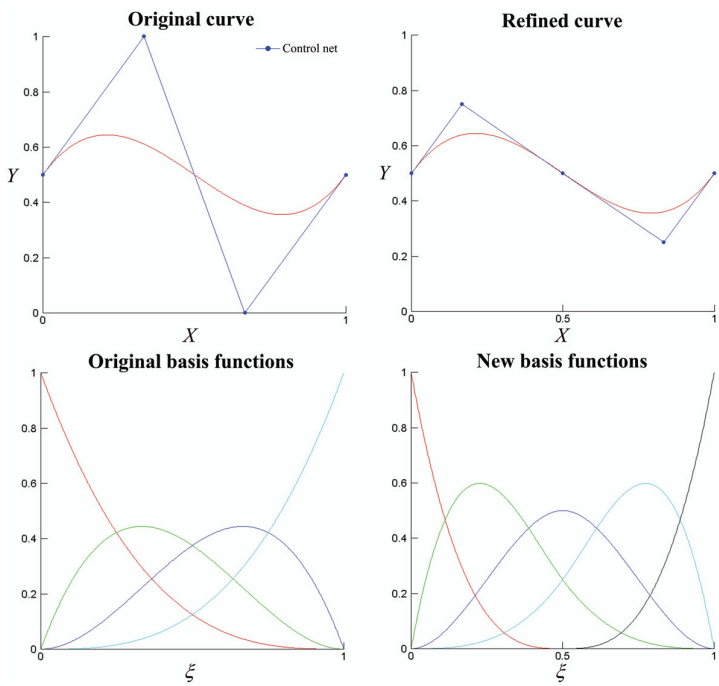

Figure 2.1: An example of knot insertion

2.1.3.2 *p*-refinement: order elevation

The analogue of *p*-refinement in FEA is *order elevation* which is referred to as *degree elevation* in CAD community. The order of NURBS may be increased without alterning the geometry or parmeterization. The process of order elevation is outlined as follows:

(1) Subdivision the entity into Bézier segments by knot insertion

(2) Order elevation of each individual segement

(3) Removal of the unnecessary knots

We omit the details of processes of the knot removal and order elevation of a Bézier segment for the sake of brevity. More details can be found in [91]. An example of order elevation is illustrated in Fig. 2.2. The original curve and cubic basis functions, shown on the left, are the same ones as in the previous example. The order elevated curve, shown on the right, is geometrically and parametrically identical to the original curve, but the control points and basis functions are changed.

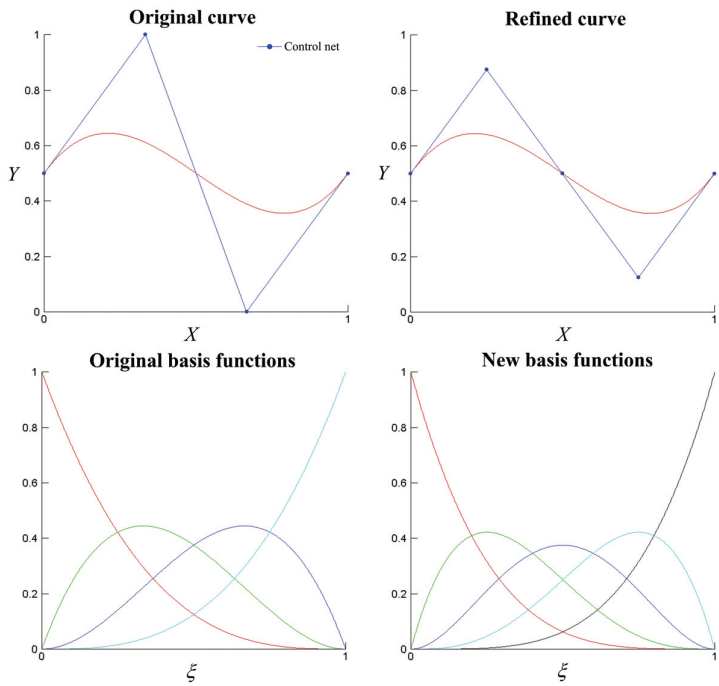

Figure 2.2: An example of order elevation

2.1.3.3 k-refinement

It is significant to note that the processes of knot insertion and order elevation are not commutative. For a curve of order p, if a unique knot value, $\bar{\xi}$, is inserted between two distinct knots, then the continuity of the basis functions at $\bar{\xi}$ becomes C^{p-1}. If the degree is subsequently elevated to q by following the aforementioned process, the multiplicity of every distinct knot values is increased so that the original curve continuity is preserved, meaning that the order elevated basis still has C^{p-1}-continuity at $\bar{\xi}$. Interestingly, if we reversed the sequence of those two operations, the basis would have C^{q-1} continuity at $\bar{\xi}$. The results shown in Figs. 2.3 and 2.4 are compared to illustrate the non-conmmutativity of knot insertion and order elevation. As a base case, we consider linear B-spline basis functions, shown in Fig. 2.3a, with a set of knots $\Xi = \{0,0,1,1\}$. Then, a subsequent insertion of a knot $\bar{\xi} = 0.5$ yields basis functions shown in Fig. 2.3b, and a subsequent order elevation gives the quadratic basis functions illustrated in Fig. 2.3c, where a C^0-continuity between two knot spans is apparently shown. On the other hand, if we make the order elevation first, new basis functions are obtained as shown in Fig. 2.4a. Then,

an insertion of new knot $\bar{\xi} = 0.5$ results in basis functions shown in Fig. 2.4b, where the basis functions have C^1 inter-element continuity, in contrast to the C^0 continuity in the previous case. The former case shown in Fig. 2.3 is the classical p-refinement approach, and the latter approach depicted in Fig. 2.4 is called as *k-refinement* which has no analogue in FEA. More discussions on the k-refinement strategy can be found in [46].

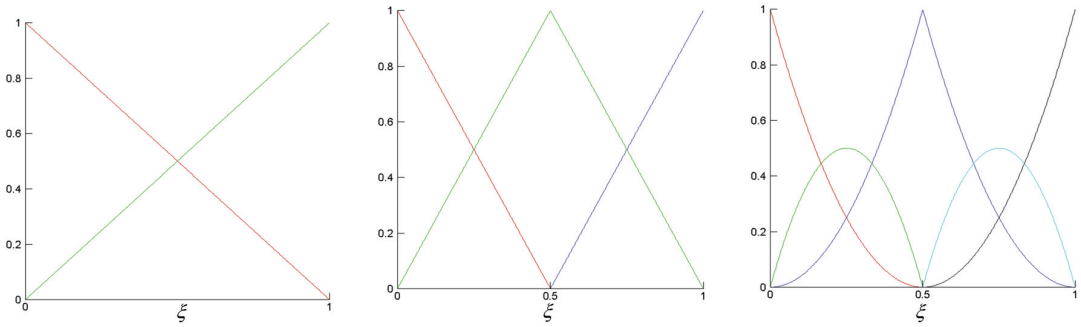

(a) Original basis functions (b) Step 1: knot insertion (c) Step 2: order elevation

Figure 2.3: An example of knot insertion followed by order elevation

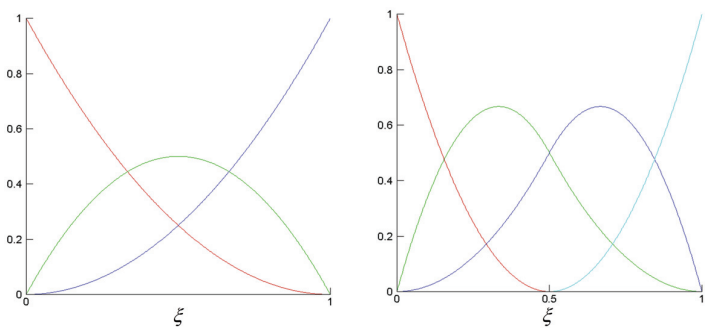

(a) Step 1: order elevation (b) Step 2: knot insertion

Figure 2.4: An example of order elevation followed by knot insertion (k-refinement)

2.2 Basic invariance properties of strain measures

In this section, we study basic invariance properties of strain measures discretized by NURBS basis functions. In several recent works, the local displacement field in curvilinear coordinate system is discretized to obtain the approximated membrane and shear strains. However, these approximated strain measures generally fail to pass the patch test of rigid body motions, which is called as self-straining [3]. Especially as the initial curvature variation of the beam increases, this self-straining triggers severe numerical instabilities. Armero and Valverde [3] showed that, in a finite element context for the curved Kirchhoff beam analysis using Hermite basis functions, the classical elements which interpolate the axial and the transversal displacement components separately do not represent the rigid body motions exactly. We consider shear deformable beams within the isogeometric analysis framework using NURBS basis functions. In the followings, we prove the invariance of the strain measures in continuum form. We then investigate self-straining

of the approximated strain measures, and a method to eliminate self-straining is discussed together with locking-free formulations.

2.2.1 Self-straining in curved structural models

2.2.1.1 Invariance of strain measures in continuum form

The global displacement vector $\hat{\mathbf{z}}$ is expressed in curvilinear frame as

$$\hat{\mathbf{z}} = z_1 \mathbf{j}_1 + z_2 \mathbf{j}_2, \tag{2.13}$$

where $\mathbf{j}_1$ and $\mathbf{j}_2$ are the unit tangential and normal vectors, respectively. The following strain measures can be derived, from the equilibrium equations and the principle of virtual work [3], as

$$\left.\begin{aligned} \varepsilon_m &= z_{1,s} - k z_2 \\ \gamma_s &= k z_1 + z_{2,s} - \theta_b \\ \omega_b &= \theta_{b,s} \end{aligned}\right\}, \tag{2.14}$$

where ε_m, γ_s, and ω_b are the membrane, shear, and bending strain measures, respectively. $(\bullet)_{,s}$ denotes a differentiation with respect to the arc-length coordinate s. k and θ_b represent the initial curvature and the rotation angle of cross-section, respectively. Combining the Frenet-Serret formulas ($\mathbf{j}_{1,s} = k\mathbf{j}_2$, $\mathbf{j}_{2,s} = -k\mathbf{j}_1$) with the derivative of Eq. (2.13) with respect to s, Eq. (2.14) can be rewritten as

$$\left.\begin{aligned} \varepsilon_m &= \hat{\mathbf{z}}_{,s} \cdot \mathbf{j}_1 \\ \gamma_s &= \hat{\mathbf{z}}_{,s} \cdot \mathbf{j}_2 - \theta_b \\ \omega_b &= \theta_{b,s} \end{aligned}\right\}. \tag{2.15}$$

To prove the invariance of Eq. (2.15), take a rigid body translation given by an arbitrary constant vector $\hat{\mathbf{z}} = \mathbf{c}_T \in \mathbf{R}^2$ and a rotation angle $\theta_b = c_R = 0$. Then, for all $\mathbf{c}_T \in \mathbf{R}^2$, Eq. (2.15) satisfies the following:

$$\left.\begin{aligned} \varepsilon_m &= \mathbf{c}_{T,s} \cdot \mathbf{j}_1 = 0 \\ \gamma_s &= \mathbf{c}_{T,s} \cdot \mathbf{j}_2 - c_R = 0 \\ \omega_b &= c_{R,s} = 0 \end{aligned}\right\}. \tag{2.16}$$

Next, consider an infinitesimal rigid body rotation $\theta_b = c_R$ expressed by the constant rotation angle and the associated displacement vector as

$$\hat{\mathbf{z}} = (\mathbf{X} - \mathbf{X}_{ref}) \times \boldsymbol{\theta} = c_R \tilde{\mathbf{I}} (\mathbf{X} - \mathbf{X}_{ref}), \text{ where } \tilde{\mathbf{I}} \equiv \begin{bmatrix} 0 & -1 \\ 1 & 0 \end{bmatrix}. \tag{2.17}$$

$\boldsymbol{\theta} \equiv [0, 0, c_R]^T$ denotes the infinitesimal rotation vector. $\mathbf{X}, \mathbf{X}_{ref} \in \mathbf{R}^2$ represent the position vectors of a point on the neutral axis and a reference point, respectively. Substituting Eq. (2.17) into Eq.

(2.15) leads to

$$\left.\begin{aligned} \varepsilon_m &= \theta_b \tilde{\mathbf{I}}\mathbf{X}_{,s} \cdot \mathbf{j}_1 = \theta_b \mathbf{j}_2 \cdot \mathbf{j}_1 = 0 \\ \gamma_s &= \theta_b \tilde{\mathbf{I}}\mathbf{X}_{,s} \cdot \mathbf{j}_2 - \theta_b = 0 \\ \omega_b &= c_{R,s} = 0 \end{aligned}\right\}, \tag{2.18}$$

for all $c_R \in \mathbf{R}$ and $\mathbf{X}_{ref} \in \mathbf{R}^2$, since $\mathbf{X}_{,s} = \mathbf{j}_1$ due to the arc-length parameterization and the orthonormal vectors $\mathbf{j}_1$ and $\mathbf{j}_2$ are related by $\mathbf{j}_2 = \tilde{\mathbf{I}}\mathbf{j}_1$.

Observation 1. The strain measures in Eqs. (2.14) and (2.15) are equivalent to each other and invariant. However, after the approximation using the NURBS basis functions, it depends on the discretization manner whether the approximated strain measures are still invariant or not.

2.2.1.2 Non-invariance of strain measures in discrete form

Bouclier *et al.* [15] and Adam *et al.* [1] discretized the displacement component vector and the rotation as follows:

$$\mathbf{z}^h = \sum_{I=1}^{n} W_I(\xi)\mathbf{y}_I \tag{2.19}$$

and

$$\theta_b^h = \sum_{I=1}^{n} W_I(\xi)\theta_{bI}, \tag{2.20}$$

where W_I and ξ are the I-th NURBS basis function and the parametric coordinate, respectively. $\mathbf{y}_I$ and θ_{bI} are the response coefficients corresponding to the I-th control point. n is the total number of the NURBS basis functions. Using Eqs. (2.19) and (2.20), the strain fields in Eq. (2.14) are approximated as

$$\varepsilon_m^h = \sum_{I=1}^{n} (W_{I,s} y_{1I} - k W_I y_{2I}), \tag{2.21}$$

$$\gamma_s^h = \sum_{I=1}^{n} (k W_I y_{1I} + W_{I,s} y_{2I} - W_I \theta_{bI}), \tag{2.22}$$

and

$$\omega_b^h = \sum_{I=1}^{n} W_{I,s} \theta_{bI}, \tag{2.23}$$

where $W_{I,s} = W_{I,\xi}/J_{cb}$, $J_{cb} \equiv s_{,\xi} = \left\|\mathbf{X}_{,\xi}\right\|$, and $\mathbf{X}$ represents the neutral axis curve. The rotation coefficient θ_{bI} represents the rotation of control net, which is related to the rotation of physical domain by the affine covariance property of NURBS basis function [91]. In contrast, the displacement component coefficient $\mathbf{y}_I = [y_{1I}, y_{2I}]^T$ has no physical significance so that it needs to be expressed by the global displacement vector, which requires constructing the following two linear systems of n equations due to the non-interpolatory characteristic of the NURBS basis

function.

$$\left.\begin{aligned} z_1^h(\bar{\xi}_i) &= \sum_{I=1}^{n} W_I(\bar{\xi}_i) y_{1I} = \sum_{I=1}^{n} A_{iI} y_{1I} \\ z_2^h(\bar{\xi}_i) &= \sum_{I=1}^{n} W_I(\bar{\xi}_i) y_{2I} = \sum_{I=1}^{n} A_{iI} y_{2I} \end{aligned}\right\}, \tag{2.24}$$

where $A_{iI} \equiv W_I(\bar{\xi}_i)$ are the components of collocation matrix and the positions of the collocation points $\bar{\xi}_i$ (i=1∼n) are determined, by the Greville abscissae, as

$$\bar{\xi}_i = \frac{1}{p}(\xi_{i+1} + \xi_{i+2} + \cdots + \xi_{i+p}), \tag{2.25}$$

where p is the degree of NURBS basis functions. Using Eq. (2.24) and the relation of Eq. (2.13), the displacement coefficients can be expressed as

$$\left.\begin{aligned} y_{1I} &= \sum_{i=1}^{n} A_{Ii}^{-1} z_1^h(\bar{\xi}_i) = \sum_{i=1}^{n} A_{Ii}^{-1} \mathbf{j}_1{}^T(\bar{\xi}_i) \hat{\mathbf{z}}^h(\bar{\xi}_i) \\ y_{2I} &= \sum_{i=1}^{n} A_{Ii}^{-1} z_2^h(\bar{\xi}_i) = \sum_{i=1}^{n} A_{Ii}^{-1} \mathbf{j}_2{}^T(\bar{\xi}_i) \hat{\mathbf{z}}^h(\bar{\xi}_i) \end{aligned}\right\}, \tag{2.26}$$

where A_{Ii}^{-1} are the components of inverse matrix. Substituting Eq. (2.26) into Eqs. (2.21) and (2.22), we have the followings:

$$\varepsilon_m^h = \sum_{I=1}^{n} \sum_{i=1}^{n} \left\{ W_{I,s} A_{Ii}^{-1} \mathbf{j}_1{}^T(\bar{\xi}_i) - k W_I A_{Ii}^{-1} \mathbf{j}_2{}^T(\bar{\xi}_i) \right\} \hat{\mathbf{z}}^h(\bar{\xi}_i) \tag{2.27}$$

and

$$\gamma_s^h = \sum_{I=1}^{n} \sum_{i=1}^{n} \left\{ k W_I A_{Ii}^{-1} \mathbf{j}_1{}^T(\bar{\xi}_i) + W_{I,s} A_{Ii}^{-1} \mathbf{j}_2{}^T(\bar{\xi}_i) \right\} \hat{\mathbf{z}}^h(\bar{\xi}_i) - \sum_{i=1}^{n} W_I \theta_{bI}. \tag{2.28}$$

To investigate the non-invariance of the approximated strain measures, consider the rigid body translation as

$$\left.\begin{aligned} \hat{\mathbf{z}}^h(\bar{\xi}_i) &= \mathbf{c}_T \\ \theta_{bI} = \theta_b^h &= c_R = 0 \end{aligned}\right\} \quad (i, I = 1 \sim n), \tag{2.29}$$

where the relation $\theta_{bI} = \theta_b^h$ is obtained from the affine covariance property of the NURBS basis function. Substituting Eq. (2.29) into Eqs. (2.27),(2.28), and (2.23) yield the followings:

$$\varepsilon_m^h = \mathbf{c}_T{}^T \sum_{I=1}^{n} \sum_{i=1}^{n} \left\{ W_{I,s} A_{Ii}^{-1} \mathbf{j}_1(\bar{\xi}_i) - k W_I A_{Ii}^{-1} \mathbf{j}_2(\bar{\xi}_i) \right\} \equiv \mathbf{c}_T{}^T \mathbf{a}, \tag{2.30}$$

$$\gamma_s^h = \mathbf{c}_T{}^T \sum_{I=1}^{n} \sum_{i=1}^{n} \left\{ k W_I A_{Ii}^{-1} \mathbf{j}_1(\bar{\xi}_i) + W_{I,s} A_{Ii}^{-1} \mathbf{j}_2(\bar{\xi}_i) \right\} = \mathbf{c}_T{}^T (\tilde{\mathbf{I}}\mathbf{a}), \tag{2.31}$$

and $\omega_b^h = 0$. The vector function $\mathbf{a} = \mathbf{a}(\xi)$ generally does not vanish. However, if the initial geometry is circular or straight, it can be proved that the vector function vanishes. First, for a circular

geometry, the unit tangential and normal vectors are expressed as:

$$\left.\begin{aligned}\mathbf{j}_2 &= (\mathbf{X}_c - \mathbf{X})/R = k(\mathbf{X}_c - \mathbf{X}) \\ \mathbf{j}_1 &= -\tilde{\mathbf{I}}\mathbf{j}_2 = -k\tilde{\mathbf{I}}(\mathbf{X}_c - \mathbf{X})\end{aligned}\right\}, \tag{2.32}$$

where $\mathbf{X}_c$ and R denote the center position and radius of a circle, respectively, and the relation $k = 1/R$ is used. Substituting Eq. (2.32) into the expression of the vector $\mathbf{a}$ in Eq. (2.30), and using the partition of unity of NURBS basis functions, the vector $\mathbf{a}$ is rewritten as

$$\begin{aligned}\mathbf{a} &= -k\sum_{I=1}^{n}\sum_{i=1}^{n}\left[-W_{I,s}A_{Ii}^{-1}\tilde{\mathbf{I}}\mathbf{X}(\bar{\xi}_i) + kW_I A_{Ii}^{-1}\left\{\mathbf{X}_c - \mathbf{X}(\bar{\xi}_i)\right\}\right] - k\tilde{\mathbf{I}}\mathbf{X}_c\sum_{I=1}^{n}W_{I,s} \\ &= -k\sum_{I=1}^{n}\left\{-W_{I,s}\tilde{\mathbf{I}}\mathbf{B}_I + kW_I(\mathbf{X}_c - \mathbf{B}_I)\right\},\end{aligned} \tag{2.33}$$

where $\mathbf{B}_I$ denotes the position of I-th control point. Then, using the relation $\mathbf{X}_{,s} = \sum_{I=1}^{n} W_{I,s}\mathbf{B}_I = \mathbf{j}_1$ and Eq. (2.32), we have the following:

$$\mathbf{a} = -k\left\{-\tilde{\mathbf{I}}\mathbf{j}_1 + k(\mathbf{X}_c - \mathbf{X})\right\} = -k(-\tilde{\mathbf{I}}\mathbf{j}_1 + \mathbf{j}_2) = \mathbf{0}. \tag{2.34}$$

Thus, $\varepsilon_m^h = \gamma_s^h = \omega_b^h = 0$ for any $\mathbf{c}_T \in \mathbf{R}^2$, if the initial geometry is circular. Second, if the initial geometry is straight ($k = 0$), $\mathbf{j}_1$ is a constant vector so that we have the following:

$$\mathbf{a} = \sum_{I=1}^{n} W_{I,s}\left(\sum_{i=1}^{n} A_{Ii}^{-1}\mathbf{j}_1\right) = \sum_{I=1}^{n} W_{I,s}\mathbf{c} = \mathbf{0}, \tag{2.35}$$

due to the partition of unity of NURBS basis functions, where $\mathbf{c} \in \mathbf{R}^2$ is a constant vector. Thus, $\varepsilon_m^h = \gamma_s^h = \omega_b^h = 0$ for any $\mathbf{c}_T \in \mathbf{R}^2$, if the initial geometry is straight.

We only present the proof of vanishing shear strain if the initial geometry is circular or straight for the infinitesimal rigid body rotation of Eq. (2.17) and $\theta_{bI} = \theta_b^h = c_R$. Similar procedures can be straightforwardly applied to show the invariance of the membrane strain. First, for a circular geometry, substituting Eq. (2.17) into Eq. (2.28), and using the expression of $\tilde{\mathbf{I}}\mathbf{a}$ of Eq. (2.31) and the relation $\tilde{\mathbf{I}}^T = \tilde{\mathbf{I}}^{-1}$, we have the following:

$$\begin{aligned}\gamma_s^h &= c_R\sum_{I=1}^{n}\sum_{i=1}^{n}\left\{kW_I A_{Ii}^{-1}\mathbf{j}_1{}^T(\bar{\xi}_i) + W_{I,s}A_{Ii}^{-1}\mathbf{j}_2{}^T(\bar{\xi}_i)\right\}\tilde{\mathbf{I}}\left\{\mathbf{X}(\bar{\xi}_i) - \mathbf{X}_{ref}\right\} - c_R\sum_{i=1}^{n}W_I \\ &= -c_R\sum_{I=1}^{n}\sum_{i=1}^{n}\left\{W_I A_{Ii}^{-1}\mathbf{j}_1{}^T(\bar{\xi}_i) + W_{I,s}A_{Ii}^{-1}\mathbf{j}_2{}^T(\bar{\xi}_i)/k\right\}\tilde{\mathbf{I}}k\left\{\mathbf{X}_c - \mathbf{X}(\bar{\xi}_i)\right\} + \mathbf{a}^T(\mathbf{X}_c - \mathbf{X}_{ref}) - c_R.\end{aligned} \tag{2.36}$$

Then, using Eqs. (2.32) and (2.35), the shear strain of Eq. (2.36) can be shown to vanish, as follows:

$$\gamma_s^h = c_R\sum_{I=1}^{n}\sum_{i=1}^{n}\left\{W_I A_{Ii}^{-1}\mathbf{j}_1{}^T(\bar{\xi}_i) + W_{I,s}A_{Ii}^{-1}\mathbf{j}_2{}^T(\bar{\xi}_i)/k\right\}\mathbf{j}_1(\bar{\xi}_i) - c_R = c_R\sum_{I=1}^{n}W_I - c_R = 0. \tag{2.37}$$

Second, for straight geometry, $k = 0$ and $\mathbf{j}_2$ is a constant vector. Substituting Eq. (2.17) into (2.28),

and using the relations $\mathbf{X}_{,s} = \sum_{I=1}^{n} W_{I,s}\mathbf{B}_I = \mathbf{j}_1$ and $\mathbf{j}_2 = \tilde{\mathbf{I}}\mathbf{j}_1$, we obtain the following:

$$\begin{aligned}\gamma_s^h &= c_R \mathbf{j}_2{}^T \tilde{\mathbf{I}} \sum_{I=1}^{n}\sum_{i=1}^{n} W_{I,s} A_{Ii}^{-1} \mathbf{X}(\bar{\xi}_i) - c_R \mathbf{j}_2{}^T \tilde{\mathbf{I}} \sum_{I=1}^{n} W_{I,s} \left(\sum_{i=1}^{n} A_{Ii}^{-1} \mathbf{X}_{ref} \right) - c_R \\ &= c_R \mathbf{j}_2{}^T \tilde{\mathbf{I}} \sum_{I=1}^{n} W_{I,s}\mathbf{B}_I - c_R \mathbf{j}_2{}^T \tilde{\mathbf{I}} \mathbf{X}_{ref} \sum_{I=1}^{n} W_{I,s} - c_R \\ &= c_R \mathbf{j}_2{}^T \mathbf{j}_2 - c_R = 0, \end{aligned} \tag{2.38}$$

for all $c_R \in \mathbf{R}$ and $\mathbf{X}_{ref} \in \mathbf{R}^2$. Therefore, the following observation is given.

Observation 2. The discretization of Eqs. (2.19) and (2.20) lead to the non-invariance of the approximated membrane strain of Eq. (2.21) and the shear strain of Eq. (2.22). However, in case the initial geometry is circular or straight, the strain measures remain invariant as well. Also, self-straining can be reduced through h-refinement as the initial curvature variation of elements decreases. The approximated bending strain is always invariant, regardless of the initial geometry.

Hereafter, the discretization using Eqs. (2.19) and (2.20) is denominated as "*Discretization* #1 (D#1)".

2.2.2 Locking-free invariant formulation

Membrane and shear locking mean the inability to represent the "inextensible bending" and "shearless bending," respectively. Bouclier *et al.* [15] and Adam *et al.* [1] suggested locking-free isogeometric formulations of curved Timoshenko beams in curvilinear coordinates. However, the self-straning trouble prevents those locking-free formulations from being utilized for arbitrarily curved beams. In the following, we demonstrate a formulation to have invariance in diecretized strain measures, and combine it with the $\bar{B}$ projection method developed in [15]. Invesigation of the selective reduced integration (SRI) in [15, 1] is performed thorugh numerical examples in section 4.1.1.

2.2.2.1 Invariant discretization using the global displacement field

We prove that the discretization of the global displacement vector instead of Eq. (2.19) can eliminate self-straining of the membrane and shear strain measures. The global displacement is discretized as

$$\hat{\mathbf{z}}^h = \sum_{I=1}^{n} W_I \hat{\mathbf{y}}_I, \tag{2.39}$$

where $\hat{\mathbf{y}}_I$ is the displacement coefficient corresponding to I-th control point. The approximated membrane and shear strain measures of Eq. (2.15) can be rewritten, using Eqs. (2.20) and (2.39),

as

$$\left.\begin{aligned} \varepsilon_m^h &= \sum_{I=1}^{n} (W_{I,s}\hat{\mathbf{y}}_I)\cdot\mathbf{j}_1 \\ \gamma_s^h &= \sum_{I=1}^{n} \left\{(W_{I,s}\hat{\mathbf{y}}_I)\cdot\mathbf{j}_2 - W_I\theta_{bI}\right\} \end{aligned}\right\}. \tag{2.40}$$

To verify the invariance of the strain measures of Eq. (2.40), consider the rigid body translation expressed by $\hat{\mathbf{z}} = \mathbf{c}_T$ and the rotation angle $c_R = 0$. By the affine covariance property of NURBS basis function, $\hat{\mathbf{y}}_I = \mathbf{c}_T$ and $\theta_{bI} = c_R = 0$. Then, Eq. (2.40) is rewritten as

$$\left.\begin{aligned} \varepsilon_m^h &= (\mathbf{c}_T\cdot\mathbf{j}_1)\sum_{I=1}^{n} W_{I,s} = 0 \\ \gamma_s^h &= (\mathbf{c}_T\cdot\mathbf{j}_2)\sum_{I=1}^{n} W_{I,s} = 0 \end{aligned}\right\}, \tag{2.41}$$

for all $\mathbf{c}_T \in \mathbf{R}^2$ due to the partition of unity of NURBS basis function. Next, we consider the infinitesimal rigid body rotation expressed by a constant angle $c_R \in \mathbf{R}$. The affine covariance property of NURBS basis function enables to represent the rigid body rotation of physical domain as $\hat{\mathbf{y}}_I = c_R\tilde{\mathbf{I}}(\mathbf{B}_I - \mathbf{X}_{ref})$ and $\theta_{bI} = c_R$. Substituting into (2.40) gives

$$\begin{aligned} \varepsilon_m &= \sum_{I=1}^{n} \left\{W_{I,s}c_R\tilde{\mathbf{I}}(\mathbf{B}_I - \mathbf{X}_{ref})\right\}\cdot\mathbf{j}_1 \\ &= c_R\tilde{\mathbf{I}}\sum_{I=1}^{n}(W_{I,s}\mathbf{B}_I\cdot\mathbf{j}_1) - (c_R\tilde{\mathbf{I}}\mathbf{X}_{ref}\cdot\mathbf{j}_1)\sum_{I=1}^{n} W_{I,s} \\ &= c_R\tilde{\mathbf{I}}\mathbf{j}_1\cdot\mathbf{j}_1 = 0 \end{aligned} \tag{2.42}$$

and

$$\begin{aligned} \gamma_s &= \sum_{I=1}^{n} \left\{W_{I,s}c_R\tilde{\mathbf{I}}(\mathbf{B}_I - \mathbf{X}_{ref})\right\}\cdot\mathbf{j}_2 - c_R \\ &= \sum_{I=1}^{n} W_{I,s}c_R\tilde{\mathbf{I}}\mathbf{B}_I\cdot\mathbf{j}_2 - (c_R\tilde{\mathbf{I}}\mathbf{X}_{ref}\cdot\mathbf{j}_2)\sum_{I=1}^{n} W_{I,s} - c_R \\ &= c_R\tilde{\mathbf{I}}\mathbf{j}_1\cdot\mathbf{j}_2 - c_R = 0, \end{aligned} \tag{2.43}$$

for all $c_R \in \mathbf{R}$, where $\mathbf{X}_{,s} = \sum_{I=1}^{n} W_{I,s}\mathbf{B}_I = \mathbf{j}_1$ and $\mathbf{j}_2 = \tilde{\mathbf{I}}\mathbf{j}_1$ are used.

Observation 3. The approximated membrane and shear strain measures in Eq. (2.40) are invariant regardless of the initial geometry.

Hereafter, the discretization using Eqs. (2.20) and (2.39) is denominated as "*Discretization* #2 (D#2)".

2.2.2.2 Locking-free invariant formulation

The proposed invariant formulation (D#2) is combined with the $\bar{B}$ projection method for NURBS basis functions whereas the formulation D#1 is used in Bouclier *et al.* [15]. Basically, in the $\bar{B}$ projection method, the approximated strain field described in the space Q_p of p-th order NURBS basis functions is linearly projected onto the space Q_{p-1} of (p-1)-th order. The detailed description of selecting the number of basis functions and the set of knots in the space Q_{p-1} can be found in Bouclier et al. [15]. The strain field in the space Q_p is projected onto the space Q_{p-1} as

$$\left.\begin{aligned} \tilde{\varepsilon}_m^h &= \sum_{I=1}^{\tilde{n}} \tilde{W}_I \tilde{\varepsilon}_{mI}^h \\ \tilde{\gamma}_s^h &= \sum_{I=1}^{\tilde{n}} \tilde{W}_I \tilde{\gamma}_{sI}^h \end{aligned}\right\}, \tag{2.44}$$

where $\tilde{n}$ denotes the number of basis functions in the lower order space. $\tilde{W}_I$ is the corresponding lower order basis function. Then, the equivalence between the original and the projected strain fields is weakly expressed, for all $v \in Q_{p-1}$, as

$$\left.\begin{aligned} \int_\Omega v\varepsilon_m^h d\Omega &= \int_\Omega v \sum_{I=1}^{\tilde{n}} \tilde{W}_I \tilde{\varepsilon}_{mI}^h d\Omega \\ \int_\Omega v\gamma_s^h d\Omega &= \int_\Omega v \sum_{I=1}^{\tilde{n}} \tilde{W}_I \tilde{\gamma}_{sI}^h d\Omega \end{aligned}\right\}. \tag{2.45}$$

The test function $v \in Q_{p-1}$ can be expressed by the lower order basis functions $\tilde{W}_I$ so that

$$\left.\begin{aligned} \int_\Omega \varepsilon_m^h \sum_{K=1}^{\tilde{n}} \tilde{W}_K v_K d\Omega &= \int_\Omega \sum_{I,J=1}^{\tilde{n}} \tilde{W}_I \tilde{W}_J \tilde{\varepsilon}_{mI}^h v_J d\Omega \\ \int_\Omega \gamma_s^h \sum_{K=1}^{\tilde{n}} \tilde{W}_K v_K d\Omega &= \int_\Omega \sum_{I,J=1}^{\tilde{n}} \tilde{W}_I \tilde{W}_J \tilde{\gamma}_{sI}^h v_J d\Omega \end{aligned}\right\}. \tag{2.46}$$

Then, defining $\tilde{M}_{IJ} = \int_\Omega \tilde{W}_I \tilde{W}_J d\Omega$, the coefficients of the projected strain field are obtained as

$$\left.\begin{aligned} \tilde{\varepsilon}_{mI}^h &= \sum_{J=1}^{\tilde{n}} \tilde{M}_{IJ}^{-1} \int_\Omega \tilde{W}_J \varepsilon_m^h d\Omega \\ \tilde{\gamma}_{sI}^h &= \sum_{J=1}^{\tilde{n}} \tilde{M}_{IJ}^{-1} \int_\Omega \tilde{W}_J \gamma_s^h d\Omega \end{aligned}\right\}. \tag{2.47}$$

In the proposed invariant formulation (D#2) using Eqs. (2.40) and (2.44), $\tilde{\varepsilon}_m^h$ and $\tilde{\gamma}_s^h$ are derived as

$$\left.\begin{aligned} \tilde{\varepsilon}_m^h &= \sum_{I,J=1}^{\tilde{n}} \sum_{K=1}^{n} \tilde{W}_I \tilde{M}_{IJ}^{-1} \int_\Omega \tilde{W}_J (W_{K,s} \hat{\mathbf{y}}_K) \cdot \mathbf{j}_1 d\Omega \\ \tilde{\gamma}_s^h &= \sum_{I,J=1}^{\tilde{n}} \sum_{K=1}^{n} \tilde{W}_I \tilde{M}_{IJ}^{-1} \int_\Omega \tilde{W}_J \left\{ (W_{K,s} \hat{\mathbf{y}}_K) \cdot \mathbf{j}_2 - W_K \theta_{bK} \right\} d\Omega \end{aligned}\right\}. \tag{2.48}$$

Also, by the formulation D#1, as in reference [15], they can be derived as

$$\left.\begin{aligned}\tilde{\varepsilon}_m^h &= \sum_{I,J=1}^{\tilde{n}} \sum_{K=1}^{n} \tilde{W}_I \tilde{M}_{IJ}^{-1} \int_\Omega \tilde{W}_J (W_{K,s} y_{1K} - k W_K y_{2K}) d\Omega \\ \tilde{\gamma}_s^h &= \sum_{I,J=1}^{\tilde{n}} \sum_{K=1}^{n} \tilde{W}_I \tilde{M}_{IJ}^{-1} \int_\Omega \tilde{W}_J (k W_K y_{1K} + W_{K,s} y_{2K} - W_K \theta_{bK}) d\Omega\end{aligned}\right\}. \tag{2.49}$$

2.3 Geometrically exact Kirchhoff beam structures

2.3.1 Basic kinematics

In this section, the kinematics of curved Kirchhoff beam based on the geometrically exact beam theory (GEBT) will be briefly reviewed. For more details of the displacement-based formulation based on the GEBT and the derivations of kinematic quantities, interested readers may refer to [84].

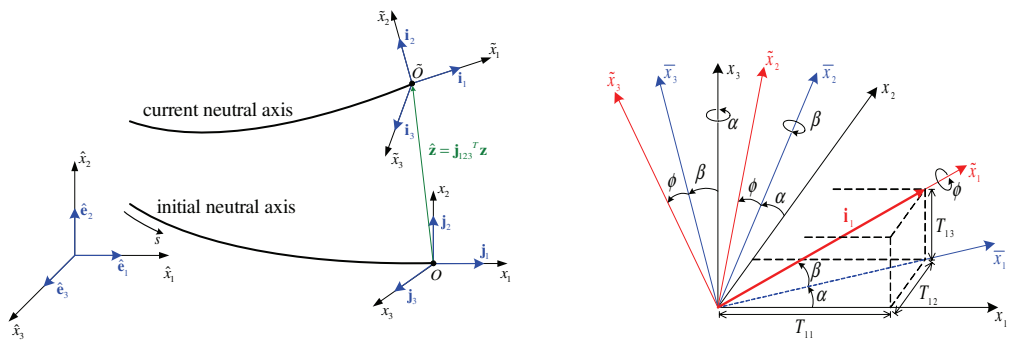

(a) Coordinate systems (b) Relation of two local frames

Figure 2.5: Kinematics of curved beams

Figure 2.5a shows a curved beam undergoing large deformation in three-dimensional space. Three coordinate systems are employed for describing the deformation of initially curved beam. *First*, $\hat{x}_1 - \hat{x}_2 - \hat{x}_3$ frame is a global rectangular Cartesian coordinate system whose base vectors are $\{\hat{\mathbf{e}}_1, \hat{\mathbf{e}}_2, \hat{\mathbf{e}}_3\}$. *Second*, $x_1 - x_2 - x_3$ frame is a local orthogonal curvilinear coordinate system in initial configuration, and the x_1 axis represents the tangential direction of initial neutral axis. $\{\mathbf{j}_1, \mathbf{j}_2, \mathbf{j}_3\}$ are the orthonormal base vectors of $x_1 - x_2 - x_3$ frame. *Third*, $\tilde{x}_1 - \tilde{x}_2 - \tilde{x}_3$ frame is a local orthogonal curvilinear coordinate system in current configuration, and the $\tilde{x}_1$ axis represents the tangential direction of current neutral axis. $\{\mathbf{i}_1, \mathbf{i}_2, \mathbf{i}_3\}$ are the orthonormal base vectors of $\tilde{x}_1 - \tilde{x}_2 - \tilde{x}_3$ frame. Under the assumption of Kirchhoff beam, the base vector $\mathbf{i}_1$ is normal to the current cross-section. Note that the arc-length parameterization is used for the initial neutral axis. $s \in [0, L] \subset R^1$ denotes the arc-length coordinate, where L is the beam length in initial configuration. In Figure 2.5a, the displacement vector of point O, $\hat{\mathbf{z}} = \hat{\mathbf{z}}(s)$, represents the following rigid body translation of $\tilde{x}_1 - \tilde{x}_2 - \tilde{x}_3$ frame.

$$\mathbf{r}_{\tilde{O}} = \mathbf{r}_O + \hat{\mathbf{z}} = \mathbf{r}_O + \mathbf{j}_{123}{}^T\mathbf{z}, \tag{2.50}$$

where $\mathbf{r}_O$ and $\mathbf{r}_{\tilde{O}}$ represent the position vectors at O and $\tilde{O}$ on the neutral axis of initial and current configurations, respectively. $\mathbf{j}_{123} \equiv [\mathbf{j}_1, \mathbf{j}_2, \mathbf{j}_3]^T$ and $\mathbf{z} = \mathbf{z}(s)$ denotes a displacement component vector that represents the displacement measured in $x_1 - x_2 - x_3$ frame. The tangential derivatives of the initial base vector $\mathbf{j}_i$ (i=1,2,3) is expressed as [86]

$$\mathbf{j}_{123,s} = \mathbf{\Omega}_0 \mathbf{j}_{123}, \tag{2.51}$$

where

$$\mathbf{\Omega}_0 = \mathbf{\Omega}_0(s) \equiv \begin{bmatrix} 0 & k_3 & -k_2 \\ -k_3 & 0 & k_1 \\ k_2 & -k_1 & 0 \end{bmatrix}, \tag{2.52}$$

and, k_1 is the initial twisting curvature with respect to the x_1 axis, and k_2 and k_3 are initial bending curvatures with respect to x_2 and x_3 axes, respectively. $(\bullet)_{,s}$ denotes a differentiation with respect to the arc-length coordinate s, which is the tangential derivative. Taking the tangential derivative of Eq. (2.50), the tangential vector $\mathbf{r}_{\tilde{O},s} = \left\|\mathbf{r}_{\tilde{O},s}\right\| \mathbf{i}_1$ in the current configuration whose corresponding initial one is $\mathbf{r}_{O,s} = \mathbf{j}_1 = \mathbf{j}_{123}{}^T \hat{\mathbf{e}}_1$ can be expressed, using Eq. (2.51) and the fact that $\mathbf{\Omega}_0$ is skew-symmetric, as

$$\begin{aligned} \mathbf{r}_{\tilde{O},s} &= \mathbf{r}_{O,s} + \hat{\mathbf{z}}_{,s} \\ &= \mathbf{j}_{123}{}^T([1,0,0]^T + \mathbf{z}_{,s} - \mathbf{\Omega}_0 \mathbf{z}) \equiv \mathbf{j}_{123}{}^T \mathbf{E} \end{aligned} \tag{2.53}$$

where $\mathbf{E} = \mathbf{E}(s, \mathbf{z})$ is the component vector of the current tangential vector $\mathbf{r}_{\tilde{O},s}$ in $x_1 - x_2 - x_3$ frame whose components are obtained by substituting Eq. (2.52) into Eq. (2.53), as

$$\left.\begin{aligned} E_1(s,\mathbf{z}) &= 1 + z_{1,s} - z_2 k_3 + z_3 k_2 \\ E_2(s,\mathbf{z}) &= z_{2,s} + z_1 k_3 - z_3 k_1 \\ E_3(s,\mathbf{z}) &= z_{3,s} - z_1 k_2 + z_2 k_1 \end{aligned}\right\}. \tag{2.54}$$

Stretching

The axial strain $e = e(s, \mathbf{z})$ at the neutral axis is expressed, using Eq. (2.53), as

$$e \equiv \left\|\mathbf{r}_{\tilde{O},s}\right\| - 1 = \|\mathbf{E}\| - 1. \tag{2.55}$$

Employing $\tilde{s}$ as an arc-length coordinate of the current configuration such that $\mathbf{r}_{\tilde{O},\tilde{s}} = \mathbf{i}_1$ and $\left\|\mathbf{r}_{\tilde{O},\tilde{s}}\right\| = 1$, we have the relation $\mathbf{r}_{\tilde{O},s} = \mathbf{r}_{\tilde{O},\tilde{s}}(d\tilde{s}/ds)$ by the chain rule of differentiation. Therefore, an infinitesimal length of the neutral axis in the current configuration ($d\tilde{s}$) is expressed by that of the initial configuration (ds), using the relation $\left\|\mathbf{r}_{\tilde{O},s}\right\| = 1 + e$ obtained from Eq. (2.55), as

$$d\tilde{s} = \left(\left\|\mathbf{r}_{\tilde{O},s}\right\| / \left\|\mathbf{r}_{\tilde{O},\tilde{s}}\right\|\right) ds = (1+e)\, ds. \tag{2.56}$$

Rigid body rotation

Since the sets of base vectors $\{\mathbf{j}_1, \mathbf{j}_2, \mathbf{j}_3\}$ and $\{\mathbf{i}_1, \mathbf{i}_2, \mathbf{i}_3\}$ are orthonormal, there exists the proper orthogonal transformation $\mathbf{T}$ such that

$$\mathbf{i}_{123} = \mathbf{T}\mathbf{j}_{123} = \begin{bmatrix} \cos\theta & \sin\theta & 0 \\ -\sin\theta & \cos\theta & 0 \\ 0 & 0 & 1 \end{bmatrix} \mathbf{j}_{123}, \tag{2.57}$$

where $\mathbf{i}_{123} \equiv [\mathbf{i}_1, \mathbf{i}_2, \mathbf{i}_3]^T$, and $\theta \in \mathbf{R}^1$ is a rotation angle about x_3 axis. From the relation of Eq. (2.57), the following is obtained.

$$\mathbf{i}_1 = {\mathbf{j}_{123}}^T \mathbf{T}_1, \text{ where } \mathbf{T}_1 \equiv [T_{11}, T_{12}, T_{13}]^T. \tag{2.58}$$

Pai [85] described the rotational transformation of Eq. (2.57) by three consecutive rotations; two Euler angles (α,β) for bending and one Euler angle (ϕ) for torsion. As shown in 2.5b, the angle α about the x_3 axis rotates the axes x_1 and x_2 to $\bar{x}_1$ and $\bar{x}_2$; the angle β about the $\bar{x}_2$ axis rotates the axes $\bar{x}_1$ and x_3 to $\tilde{x}_1$ and $\bar{x}_3$; and the angle ϕ about the $\tilde{x}_1$ axis rotates the axes $\bar{x}_2$ and $\bar{x}_3$ to $\tilde{x}_2$ and $\tilde{x}_3$. Using the relation of $\mathbf{r}_{\tilde{O},\tilde{s}} = \mathbf{i}_1$ and the chain rule of differentiation, we have $\mathbf{i}_1 = \mathbf{r}_{\tilde{O},s}(ds/d\tilde{s})$, which is rewritten, using the relations of Eqs. (2.53) and (2.56), as

$$\mathbf{i}_1 = {\mathbf{j}_{123}}^T \left(\frac{1}{1+e} \mathbf{E} \right). \tag{2.59}$$

From Eqs. (2.58) and (2.59), $\mathbf{T}_1 = \mathbf{T}_1(s, \mathbf{z})$ is expressed, using Eq. (2.55) and $\|\mathbf{T}_1\| = \|\mathbf{E}\| / (1+e) = 1$, as

$$\mathbf{T}_1(s, \mathbf{z}) = \frac{1}{1 + e(s, \mathbf{z})} \mathbf{E}(s, \mathbf{z}). \tag{2.60}$$

From 2.5b, and using Eq. (2.58) and the fact that $\|\mathbf{T}_1\| = 1$, we have the following [85].

$$\left.\begin{aligned} \mathbf{i}_{\bar{2}} &= -\sin\alpha \mathbf{j}_1 + \cos\alpha \mathbf{j}_2 = \frac{-T_{12}}{\sqrt{1-{T_{13}}^2}} \mathbf{j}_1 + \frac{T_{11}}{\sqrt{1-{T_{13}}^2}} \mathbf{j}_2 \\ \mathbf{i}_{\bar{3}} &= \mathbf{i}_1 \times \mathbf{i}_{\bar{2}} = -\frac{T_{11}T_{13}}{\sqrt{1-{T_{13}}^2}} \mathbf{j}_1 - \frac{T_{12}T_{13}}{\sqrt{1-{T_{13}}^2}} \mathbf{j}_2 + \sqrt{1-{T_{13}}^2} \mathbf{j}_3 \end{aligned}\right\}, \tag{2.61}$$

where $\mathbf{i}_{\bar{2}}$ and $\mathbf{i}_{\bar{3}}$ are respectively the unit vectors along the $\bar{x}_2$ and $\bar{x}_3$ axes. Then, using Eqs. (2.58) and (2.61), the transformation $\mathbf{T}$ can be exactly described by the displacement component $\mathbf{z}$ and the torsional angle ϕ as [85]

$$\begin{aligned} \mathbf{T} &= \mathbf{T}(s, \mathbf{z}, \phi) \\ &= \begin{bmatrix} 1 & 0 & 0 \\ 0 & \cos\phi & \sin\phi \\ 0 & -\sin\phi & \cos\phi \end{bmatrix} \begin{bmatrix} T_{11} & T_{12} & T_{13} \\ -T_{12}/\sqrt{1-{T_{13}}^2} & T_{11}/\sqrt{1-{T_{13}}^2} & 0 \\ -T_{11}T_{13}/\sqrt{1-{T_{13}}^2} & -T_{12}T_{13}/\sqrt{1-{T_{13}}^2} & \sqrt{1-{T_{13}}^2} \end{bmatrix}. \end{aligned} \tag{2.62}$$

Differentiating Eq. (2.57) with respect to the arc-length coordinate s and using Eqs. (2.51) and (2.57) again with the relation $\mathbf{T}^{-1} = \mathbf{T}^T$, the following is obtained [86].

$$\mathbf{i}_{123,s} = (\mathbf{T}_{,s}\mathbf{T}^T + \mathbf{T}\boldsymbol{\Omega}_0\mathbf{T}^T)\mathbf{i}_{123} \equiv \begin{bmatrix} 0 & \rho_3 & -\rho_2 \\ -\rho_3 & 0 & \rho_1 \\ \rho_2 & -\rho_1 & 0 \end{bmatrix} \mathbf{i}_{123}, \tag{2.63}$$

where ρ_1 is the current twisting curvature with respect to the $\tilde{x}_1$ axis, and ρ_2 and ρ_3 are the current bending curvatures with respect to $\tilde{x}_2$ and $\tilde{x}_3$ axes, respectively. Note that the current curvatures are not geometric curvatures. In this research, we consider plane $(\hat{x}_1 - \hat{x}_2)$ problems, and the aforementioned kinematic description is reduced to the plane case. Eqs. (2.52) and (2.54) are rewritten, using $z_3 = k_1 = k_2 = 0$, $k \equiv k_3$, as

$$\boldsymbol{\Omega}_0 = \boldsymbol{\Omega}_0(s) \equiv \begin{bmatrix} 0 & k & 0 \\ -k & 0 & 0 \\ 0 & 0 & 0 \end{bmatrix}, \tag{2.64}$$

and

$$\left.\begin{aligned} E_1(s,\mathbf{z}) &= 1 + z_{1,s} - z_2 k \\ E_2(s,\mathbf{z}) &= z_{2,s} + z_1 k \\ E_3(s,\mathbf{z}) &= 0 \end{aligned}\right\}. \tag{2.65}$$

Using $\phi = T_{13} = 0$, Eq. (2.62) is rewritten as

$$\mathbf{T} = \mathbf{T}(s,\mathbf{z}) = \begin{bmatrix} T_{11} & T_{12} & 0 \\ -T_{12} & T_{11} & 0 \\ 0 & 0 & 1 \end{bmatrix}, \tag{2.66}$$

and $\mathbf{T}_1 = [T_{11}, T_{12}, 0]^T$. Also, Eq. (2.63) is rewritten, using $\rho_1 = \rho_2 = 0$ and $\rho \equiv \rho_3$, as

$$\mathbf{i}_{123,s} = (\mathbf{T}_{,s}\mathbf{T}^T + \mathbf{T}\boldsymbol{\Omega}_0\mathbf{T}^T)\mathbf{i}_{123} = \begin{bmatrix} 0 & \rho & 0 \\ -\rho & 0 & 0 \\ 0 & 0 & 0 \end{bmatrix} \mathbf{i}_{123}. \tag{2.67}$$

Substituting Eqs. (2.64) and (2.66) into Eq. (2.67), and using the fact that $\|\mathbf{T}_1\| = 1$ yields

$$\rho = -{\mathbf{T}_{1,s}}^T \tilde{\mathbf{T}}_1 + k, \tag{2.68}$$

where $\tilde{\mathbf{T}}_1 \equiv [T_{12}, -T_{11}, 0]^T$. Substituting Eq. (2.60) into Eq. (2.68) and using Eq. (2.60) again, followed by using the relation ${\mathbf{T}_1}^T \tilde{\mathbf{T}}_1 = 0$, the current curvature (2.68) is rewritten as

$$\rho = -\frac{1}{1+e}{\tilde{\mathbf{T}}_1}^T \mathbf{E}_{,s} + k. \tag{2.69}$$

The Jaumann strain $\mathbf{B} = B_{IJ}\mathbf{j}_I \otimes \mathbf{j}_J$ (I, J=1,2,3) considering the Kirchhoff beam assumption can be derived, using the polar decomposition [87] or the concept of local displacement [86]. For the plane cases, the only non-zero component is given by

$$B_{11} = \varepsilon_m - x_2\omega_b, \tag{2.70}$$

where $\varepsilon_m = \varepsilon_m(s,\mathbf{z}) \equiv e$ is a membrane strain and $\omega_b = \omega_b(s,\mathbf{z})$ is a bending strain defined, using Eq. (2.69), as

$$\omega_b \equiv \rho - k = -\frac{1}{1+\varepsilon_m}\tilde{\mathbf{T}}_1{}^T\mathbf{E}_{,s}. \tag{2.71}$$

Using $\|\mathbf{E}\|^2 = (1+\varepsilon_m)^2$ from Eq. (2.55) and the relation of Eq. (2.60), the virtual membrane strain $\widehat{\varepsilon}_m(s,\mathbf{z};\bar{\mathbf{z}})$ is derived as

$$\widehat{\varepsilon}_m(s,\mathbf{z};\bar{\mathbf{z}}) = \delta\mathbf{E}^T\mathbf{E}/(1+\varepsilon_m) = \widehat{\mathbf{E}}(s,\bar{\mathbf{z}})^T\mathbf{T}_1, \tag{2.72}$$

where $\delta(\bullet)$, $\widehat{(\bullet)}$, and $\overline{(\bullet)}$ denote the first variation and $\widehat{\mathbf{E}}(s,\bar{\mathbf{z}})$ is derived, by taking the first variation of $\mathbf{E}$ in Eq. (2.53), as

$$\widehat{\mathbf{E}}(s,\bar{\mathbf{z}}) = \bar{\mathbf{z}}_{,s} - \mathbf{\Omega}_0\bar{\mathbf{z}}. \tag{2.73}$$

The virtual bending strain $\widehat{\omega}_b(s,\mathbf{z};\bar{\mathbf{z}})$ is derived, by taking the first variation of Eq. (2.71) and using Eq. (A.7), as

$$\begin{aligned}\widehat{\omega}_b(s,\mathbf{z};\bar{\mathbf{z}}) &= -\delta\left(\frac{1}{1+\varepsilon_m}\tilde{\mathbf{T}}_1{}^T\right)\mathbf{E}_{,s} - \frac{1}{1+\varepsilon_m}\tilde{\mathbf{T}}_1{}^T\delta\mathbf{E}_{,s}\\ &= \widehat{\mathbf{E}}(s,\bar{\mathbf{z}})^T\mathbf{D}_2\mathbf{E}_{,s} - \frac{1}{1+\varepsilon_m}\{\widehat{\mathbf{E}}(s,\bar{\mathbf{z}})\}_{,s}^T\tilde{\mathbf{T}}_1.\end{aligned} \tag{2.74}$$

The virtual Jaumann strain is obtained by taking the first variation of Eq. (2.70), as

$$\bar{B}_{11} = \bar{\varepsilon}_m - x_2\bar{\omega}_b, \tag{2.75}$$

where $\bar{B}_{11} \equiv \delta B_{11}$, $\bar{\varepsilon}_m \equiv \widehat{\varepsilon}_m(s,\mathbf{z};\bar{\mathbf{z}})$, and $\bar{\omega}_b \equiv \widehat{\omega}_b(s,\mathbf{z};\bar{\mathbf{z}})$. The Jaumann stress $\mathbf{J} = J_{IJ}\mathbf{j}_I \otimes \mathbf{j}_J$ (I, J=1,2,3) is obtained, using a linear constitutive relation and the fact that $J_{11} = EB_{11}$ is the only non-zero component. E denotes the Young's modulus obtained directly from experiments using engineering stress and strain measures. As shown in [49], the resultant force and moment are also linearly proportional to the membrane and bending strains, respectively, regardless of magnitude of the strain for the linear constitutive relation.

2.3.2 Variational formulation

Based on the total Lagrangian formulation and the principle of virtual work, the strain energy form $a(\mathbf{z},\bar{\mathbf{z}})$ is defined as

$$a(\mathbf{z},\bar{\mathbf{z}}) \equiv \int_\Omega\int_A J_{11}\bar{B}_{11}\,dA\,ds = \int_\Omega \left\{EA\varepsilon_m(s,\mathbf{z})\widehat{\varepsilon}_m(s,\mathbf{z};\bar{\mathbf{z}}) + EI\omega_b(s,\mathbf{z})\widehat{\omega}_b(s,\mathbf{z};\bar{\mathbf{z}})\right\}ds, \tag{2.76}$$

where the variational and the trial solution spaces are defined, respectively, as

$$\bar{Z} = \{\bar{\mathbf{z}} \in H^2(0,L) : \bar{\mathbf{z}} = \bar{\mathbf{z}}_{,s} = \mathbf{0} \text{ on } \Gamma_D\} \tag{2.77}$$

and

$$Z = \{\mathbf{z} \in H^2(0,L) : \mathbf{z} \text{ and } \mathbf{z}_{,s} \text{ are prescribed on } \Gamma_D\}. \tag{2.78}$$

E, A, and I denote the Young's modulus, a cross-sectional area, and the second moment of inertia, respectively. $\Omega = [0,L] \subset \mathbf{R}^1$ represents the parametric domain of arc-length coordinate s.

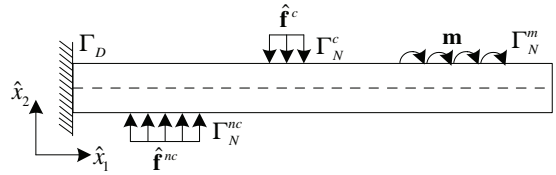

Figure 2.6: Cantilever beam

Figure 2.6 shows an elastic cantilever beam problem subjected to general loadings, where Γ_D is the boundary of kinematic boundary conditions. The boundaries of Γ_N^c, Γ_N^{nc}, and Γ_N^m are subjected to the distributed loadings of a conservative force ($\hat{\mathbf{f}}^c$), a non-conservative force ($\hat{\mathbf{f}}^{nc}$), and a moment ($\mathbf{m}$), respectively. Given a conservative physical force vector $\hat{\mathbf{f}}^c = \hat{\mathbf{f}}^c(s) = \mathbf{j}_{123}{}^T\mathbf{f}^c$, the force component vector $\mathbf{f}^c$ in $x_1 - x_2 - x_3$ frame can be expressed as

$$\mathbf{f}^c = \mathbf{j}_{123}\hat{\mathbf{f}}^c. \tag{2.79}$$

Also, given a non-conservative physical force vector $\hat{\mathbf{f}}^{nc} = \hat{\mathbf{f}}^{nc}(s,\mathbf{z})$, the force component vector $\mathbf{f}^{nc}$ in $x_1 - x_2 - x_3$ frame is obtained, using Eq. (2.57), as

$$\mathbf{f}^{nc} = \mathbf{j}_{123}\hat{\mathbf{f}}^{nc} = \mathbf{j}_{123}\mathbf{i}_{123}{}^T\tilde{\mathbf{f}} = \mathbf{T}^T\tilde{\mathbf{f}}, \tag{2.80}$$

where $\tilde{\mathbf{f}}$ denotes the force component vector in $\tilde{x}_1 - \tilde{x}_2 - \tilde{x}_3$ frame. We consider a moment loading condition, which could be converted to equivalent deformation dependent load. Pai et al. [86, 84] derived the expression of the virtual rotation under the assumption of small virtual rotation, which can be reduced to the plane case as

$$\delta\mathbf{i}_{123} = \begin{bmatrix} 0 & \bar{\theta} & 0 \\ -\bar{\theta} & 0 & 0 \\ 0 & 0 & 0 \end{bmatrix} \mathbf{i}_{123} \equiv \boldsymbol{\Theta}(\bar{\theta})\mathbf{i}_{123}, \tag{2.81}$$

where $\bar{\theta} \equiv \widehat{\theta}(s,\mathbf{z};\bar{\mathbf{z}})$ is the virtual rotation with respect to $\tilde{x}_3$ axis derived as

$$\bar{\theta} = \delta\mathbf{i}_1{}^T\mathbf{i}_2 = -\delta\mathbf{T}_1{}^T\tilde{\mathbf{T}}_1 = -\frac{1}{1+\varepsilon_m}\widehat{\mathbf{E}}(\bar{\mathbf{z}})^T\tilde{\mathbf{T}}_1, \tag{2.82}$$

where the second equality is obtained by taking the first variation of Eq. (A.4) and using the relations $\mathbf{i}_2 = -\mathbf{j}_{123}{}^T\tilde{\mathbf{T}}_1$ and $\mathbf{j}_{123}\mathbf{j}_{123}{}^T = \mathbf{I}$. The third equality is derived by using Eq. (A.4) and the relation $\mathbf{T}_1{}^T\tilde{\mathbf{T}}_1 = 0$. Using Eq. (2.82), the equivalent load vectors $\mathbf{f}_1^{eq} = \mathbf{f}_1^{eq}(s,\mathbf{z})$ and $\mathbf{f}_2^{eq} = \mathbf{f}_2^{eq}(s,\mathbf{z})$ are derived as

$$m\bar{\theta} = \bar{\mathbf{z}}^T\left(\frac{mk}{1+\varepsilon_m}\mathbf{T}_1\right) + \bar{\mathbf{z}}_{,s}{}^T\left(-\frac{m}{1+\varepsilon_m}\tilde{\mathbf{T}}_1\right) \equiv \bar{\mathbf{z}}^T\mathbf{f}_1^{eq} + \bar{\mathbf{z}}_{,s}^T\mathbf{f}_2^{eq}, \tag{2.83}$$

where $m = m(s)$ is the magnitude of bending moment with respect to $\tilde{x}_3$ axis. Then, we have the load form considering all of the aforementioned loading conditions as

$$\ell(\mathbf{z},\bar{\mathbf{z}}) \equiv \int_\Omega \left\{\bar{\mathbf{z}}^T\mathbf{f}^c(s) + \bar{\mathbf{z}}^T\mathbf{f}^{nc}(s,\mathbf{z}) + \bar{\mathbf{z}}^T\mathbf{f}_1^{eq}(s,\mathbf{z}) + \bar{\mathbf{z}}_{,s}^T\mathbf{f}_2^{eq}(s,\mathbf{z})\right\} ds. \tag{2.84}$$

Hence, the equilibrium of a deformable body can be expressed as: Find $\mathbf{z} \in Z$ such that

$$a(\mathbf{z},\bar{\mathbf{z}}) = \ell(\mathbf{z},\bar{\mathbf{z}}), \quad \forall \bar{\mathbf{z}} \in \bar{Z}. \tag{2.85}$$

2.3.2.1 Linearization

An incremental-iterative scheme is employed to solve the equation (2.85) which is nonlinear with respect to the response $\mathbf{z}$. The external load is applied incrementally and the solution of each load step (n+1) is found based on the equilibrium at the previous load step (n). Using the Newton-Raphson iterative method, the following steps are repeated until the specified convergence criterion is satisfied. The Newton-Raphson iterative scheme to obtain the solution ${}^{n+1}\mathbf{z}$ at the configuration (n+1) is stated as: For a given ${}^{n+1}\mathbf{z}^{(i-1)}$, find $\Delta\mathbf{z}^{(i)} \in \bar{Z}$ such that

$$a^*({}^{n+1}\mathbf{z}^{(i-1)}; \Delta\mathbf{z}^{(i)}, \bar{\mathbf{z}}) = \ell^*({}^{n+1}\mathbf{z}^{(i-1)}; \bar{\mathbf{z}}), \quad \forall \bar{\mathbf{z}} \in \bar{Z}, \tag{2.86}$$

where the solution is updated as

$${}^{n+1}\mathbf{z}^{(i)} = {}^{n+1}\mathbf{z}^{(i-1)} + \Delta\mathbf{z}^{(i)}, \quad {}^{n+1}\mathbf{z}^{(0)} = {}^{n}\mathbf{z}. \tag{2.87}$$

The linearized strain energy and load forms in Eq. (2.86) are derived in the following procedure.

At the current configuration (n+1), the equilibrium equation is written by

$$\begin{aligned}&\int_\Omega \left\{EA\varepsilon_m({}^{n+1}\mathbf{z})\widehat{\varepsilon}_m({}^{n+1}\mathbf{z};\bar{\mathbf{z}}) + EI\omega_b({}^{n+1}\mathbf{z})\widehat{\omega}_b({}^{n+1}\mathbf{z};\bar{\mathbf{z}})\right\} ds \\ &= \int_\Omega \left[\bar{\mathbf{z}}^T\left\{\mathbf{f}^c + \mathbf{f}^{nc}({}^{n+1}\mathbf{z}) + \mathbf{f}_1^{eq}({}^{n+1}\mathbf{z})\right\} + \bar{\mathbf{z}}_{,s}^T\mathbf{f}_2^{eq}({}^{n+1}\mathbf{z})\right] ds.\end{aligned} \tag{2.88}$$

Under the reference frame of $x_1 - x_2 - x_3$ and using the increment $\Delta(\bullet)$, the displacement component vector at the configuration (n+1) can be decomposed into

$${}^{n+1}\mathbf{z} = {}^{n}\mathbf{z} + \Delta\mathbf{z}. \tag{2.89}$$

The membrane and bending strains are decomposed into

$$\left.\begin{aligned}\varepsilon_m({}^{n+1}\mathbf{z}) &= \varepsilon_m({}^{n}\mathbf{z}) + \widehat{\varepsilon}_m({}^{n}\mathbf{z};\Delta\mathbf{z}) + H_m\\ \omega_b({}^{n+1}\mathbf{z}) &= \omega_b({}^{n}\mathbf{z}) + \widehat{\omega}_b({}^{n}\mathbf{z};\Delta\mathbf{z}) + H_b\end{aligned}\right\}, \tag{2.90}$$

and the virtual membrane and bending strains are also decomposed into

$$\left.\begin{aligned}\widehat{\varepsilon}_m({}^{n+1}\mathbf{z};\bar{\mathbf{z}}) &= \widehat{\varepsilon}_m({}^{n}\mathbf{z};\bar{\mathbf{z}}) + \widehat{\eta}_m({}^{n}\mathbf{z};\Delta\mathbf{z},\bar{\mathbf{z}}) + \widehat{H}_m\\ \widehat{\omega}_b({}^{n+1}\mathbf{z};\bar{\mathbf{z}}) &= \widehat{\omega}_b({}^{n}\mathbf{z};\bar{\mathbf{z}}) + \widehat{\eta}_b({}^{n}\mathbf{z};\Delta\mathbf{z},\bar{\mathbf{z}}) + \widehat{H}_b\end{aligned}\right\}, \tag{2.91}$$

where H_m, H_b, $\widehat{H}_m$, and $\widehat{H}_b$ represent the nonlinear terms of the increment $\Delta\mathbf{z}$. The increments of the virtual membrane strain is derived, following the differentiation process of (A.2) for $\Delta\mathbf{T}_1$, as

$$\Delta\widehat{\varepsilon}_m(\mathbf{z};\bar{\mathbf{z}}) = \widehat{\mathbf{E}}(\bar{\mathbf{z}})^T\Delta\mathbf{T}_1 = \widehat{\mathbf{E}}(\bar{\mathbf{z}})^T\boldsymbol{\Gamma}\widehat{\mathbf{E}}(\Delta\mathbf{z}) \equiv \widehat{\eta}_m({}^{n}\mathbf{z};\Delta\mathbf{z},\bar{\mathbf{z}}). \tag{2.92}$$

Note that $\widehat{\eta}_m({}^{n}\mathbf{z};\Delta\mathbf{z},\bar{\mathbf{z}})$ is symmetric in its arguments $\Delta\mathbf{z}$ and $\bar{\mathbf{z}}$ since $\boldsymbol{\Gamma}$ of (A.2) is symmetric. Also, the increments of virtual bending strain is derived as (A.1)

$$\widehat{\eta}_b({}^{n}\mathbf{z};\Delta\mathbf{z},\bar{\mathbf{z}}) \equiv \widehat{\mathbf{E}}(\bar{\mathbf{z}})^T\mathbf{D}_1\widehat{\mathbf{E}}(\Delta\mathbf{z}) + \widehat{\mathbf{E}}(\bar{\mathbf{z}})^T\mathbf{D}_2\{\widehat{\mathbf{E}}(\Delta\mathbf{z})\}_{,s} + \{\widehat{\mathbf{E}}(\bar{\mathbf{z}})\}_{,s}^T\mathbf{D}_2\widehat{\mathbf{E}}(\Delta\mathbf{z}). \tag{2.93}$$

Note that $\widehat{\eta}_b({}^{n}\mathbf{z};\Delta\mathbf{z},\bar{\mathbf{z}})$ is also symmetric since $\mathbf{D}_1$ of (A.12) and $\mathbf{D}_2$ of (A.7) are symmetric.
We consider the linearization of the deformation dependent load component vectors. Using ${}^{n}\mathbf{z}$ and $\Delta\mathbf{z}$, the force component vectors are decomposed into

$$\left.\begin{aligned}\mathbf{f}^{nc}({}^{n+1}\mathbf{z}) &= \mathbf{f}^{nc}({}^{n}\mathbf{z}) + \widehat{\mathbf{f}}^{nc}({}^{n}\mathbf{z};\Delta\mathbf{z}) + \mathbf{H}_f\\ \mathbf{f}_i^{eq}({}^{n+1}\mathbf{z}) &= \mathbf{f}_i^{eq}({}^{n}\mathbf{z}) + \widehat{\mathbf{f}}_i^{eq}({}^{n}\mathbf{z};\Delta\mathbf{z}) + \mathbf{H}_i^{eq},\ i=1,2\end{aligned}\right\} \tag{2.94}$$

where $\mathbf{H}_f$ and $\mathbf{H}_i^{eq}$ (i=1,2) denote nonlinear terms in terms of the increment $\Delta\mathbf{z}$. The incremental form of $\mathbf{f}^{nc}$ is derived, using the relation $\Delta\mathbf{T} = [\Delta\mathbf{T}_1, -\Delta\tilde{\mathbf{T}}_1, \mathbf{0}]^T$ and following the differentiation process of Eqs. (A.2) and (A.4) for $\Delta\mathbf{T}_1$ and $\Delta\tilde{\mathbf{T}}_1$, respectively, as

$$\Delta\mathbf{f}^{nc} = \Delta\mathbf{T}^T\tilde{\mathbf{f}} = (\tilde{f}_1\mathbf{I} - \tilde{f}_2\check{\mathbf{I}})\boldsymbol{\Gamma}\widehat{\mathbf{E}}(\Delta\mathbf{z}) \equiv \widehat{\mathbf{f}}^{nc}({}^{n}\mathbf{z};\Delta\mathbf{z}), \tag{2.95}$$

where $\tilde{\mathbf{f}} = [\tilde{f}_1, \tilde{f}_2, 0]^T$. Following the differentiation process of Eqs. (A.8) and (A.7) for $\Delta\{\mathbf{T}_1/(1+\varepsilon_m)\}$ and $\Delta\{\tilde{\mathbf{T}}_1/(1+\varepsilon_m)\}$, respectively, the incremental forms of the equivalent load vectors are derived as

$$\Delta\mathbf{f}_1^{eq} = mk\Delta\left(\frac{1}{1+\varepsilon_m}\mathbf{T}_1\right) = mk\tilde{\mathbf{I}}\mathbf{D}_2\widehat{\mathbf{E}}(\Delta\mathbf{z}) \equiv \widehat{\mathbf{f}}_1^{eq}({}^{n}\mathbf{z};\Delta\mathbf{z}), \tag{2.96}$$

and

$$\Delta\mathbf{f}_2^{eq} = -m\Delta\left(\frac{1}{1+\varepsilon_m}\tilde{\mathbf{T}}_1\right) = m\mathbf{D}_2\widehat{\mathbf{E}}(\Delta\mathbf{z}) \equiv \widehat{\mathbf{f}}_2^{eq}({}^{n}\mathbf{z};\Delta\mathbf{z}). \tag{2.97}$$

Substituting Eqs. (2.90), (2.91), and (2.94) into Eq. (2.88) and dropping the nonlinear terms yield the linearized variational equation at the previous configuration (n) to find the solution ${}^{n+1}\mathbf{z}$ at

the next configuration (n+1), which can be stated as: For a given ${}^n\mathbf{z}$, find $\Delta\mathbf{z} \in \bar{Z}$ such that

$$a^*({}^n\mathbf{z}; \Delta\mathbf{z}, \bar{\mathbf{z}}) = \ell^*({}^n\mathbf{z}; \bar{\mathbf{z}}), \quad \forall \bar{\mathbf{z}} \in \bar{Z}, \tag{2.98}$$

where the linearized strain energy form and load form are defined, respectively, as

$$\begin{aligned} a^*({}^n\mathbf{z}; \Delta\mathbf{z}, \bar{\mathbf{z}}) \equiv & \int_\Omega \left\{ EA\widehat{\varepsilon}_m({}^n\mathbf{z}; \Delta\mathbf{z})\widehat{\varepsilon}_m({}^n\mathbf{z}; \bar{\mathbf{z}}) + EA\varepsilon_m({}^n\mathbf{z})\widehat{\eta}_m({}^n\mathbf{z}; \Delta\mathbf{z}, \bar{\mathbf{z}}) \right\} ds \\ & + \int_\Omega \left\{ EI\widehat{\omega}_b({}^n\mathbf{z}; \Delta\mathbf{z})\widehat{\omega}_b({}^n\mathbf{z}; \bar{\mathbf{z}}) + EI\omega_b({}^n\mathbf{z})\widehat{\eta}_b({}^n\mathbf{z}; \Delta\mathbf{z}, \bar{\mathbf{z}}) \right\} ds \\ & - \int_\Omega \left\{ \bar{\mathbf{z}}^T \widehat{\mathbf{f}}^{nc}({}^n\mathbf{z}; \Delta\mathbf{z}) + \bar{\mathbf{z}}^T \widehat{\mathbf{f}}_1^{eq}({}^n\mathbf{z}; \Delta\mathbf{z}) + \bar{\mathbf{z}}_{,s}^T \widehat{\mathbf{f}}_2^{eq}({}^n\mathbf{z}; \Delta\mathbf{z}) \right\} ds, \end{aligned} \tag{2.99}$$

and

$$\begin{aligned} \ell^*({}^n\mathbf{z}; \bar{\mathbf{z}}) \equiv & \int_\Omega \left\{ \bar{\mathbf{z}}^T \mathbf{f}^c + \bar{\mathbf{z}}^T \mathbf{f}^{nc}({}^n\mathbf{z}) + \bar{\mathbf{z}}^T \mathbf{f}_1^{eq}({}^n\mathbf{z}) + \bar{\mathbf{z}}_{,s}^T \mathbf{f}_2^{eq}({}^n\mathbf{z}) \right\} ds \\ & - \int_\Omega \left\{ EA\varepsilon_m({}^n\mathbf{z})\widehat{\varepsilon}_m({}^n\mathbf{z}; \bar{\mathbf{z}}) + EI\omega_b({}^n\mathbf{z})\widehat{\omega}_b({}^n\mathbf{z}; \bar{\mathbf{z}}) \right\} ds. \end{aligned} \tag{2.100}$$

The last term in Eq. (2.99) represents the load stiffness due to the non-conservative load, which makes $a^*({}^n\mathbf{z}; \Delta\mathbf{z}, \bar{\mathbf{z}})$ non-symmetric in its arguments $\Delta\mathbf{z}$ and $\bar{\mathbf{z}}$.

2.3.3 Isogeometric discretization

The increment of approximated displacement component vector and the virtual displacement component vector at configuration (n) are respectively expressed, using the isoparametric mapping, as

$$\Delta\mathbf{z}^h(\xi) = \sum_{I=1}^{CP} \mathbf{N}_I(\xi)\Delta\mathbf{y}_I = \left(\mathop{\mathbf{A}}_{I=1}^{CP} \mathbf{N}_I \right) \Delta\mathbf{y} \equiv \mathbf{N}\Delta\mathbf{y} \tag{2.101}$$

and

$$\bar{\mathbf{z}}^h(\xi) = \sum_{I=1}^{CP} \mathbf{N}_I(\xi)\bar{\mathbf{y}}_I = \left(\mathop{\mathbf{A}}_{I=1}^{CP} \mathbf{N}_I \right) \bar{\mathbf{y}} \equiv \mathbf{N}\bar{\mathbf{y}}, \tag{2.102}$$

where $\mathbf{N}_I = \mathbf{N}_I(\xi) \equiv W_I\mathbf{I}$, $\mathbf{N} = \mathbf{N}(\xi) = [\mathbf{N}_1, \ldots, \mathbf{N}_{CP}]$ by the Boolean operation $\mathbf{A}$ for matrix assembly, and the NURBS basis functions are not interpolatory. Here, $\mathbf{I}$ denotes the 3×3 identity matrix. Also, $\Delta\mathbf{y}_I \equiv [\Delta y_{1I}, \Delta y_{2I}, \Delta y_{3I}]^T$ and $\bar{\mathbf{y}}_I \equiv [\bar{y}_{1I}, \bar{y}_{2I}, \bar{y}_{3I}]^T$ are the coefficients of the increment of displacement component and the virtual displacement component vectors, respectively. $\Delta\mathbf{y} \equiv [\Delta\mathbf{y}_1{}^T, \ldots, \Delta\mathbf{y}_{CP}{}^T]^T$ and $\bar{\mathbf{y}} \equiv [\bar{\mathbf{y}}_1{}^T, \ldots, \bar{\mathbf{y}}_{CP}{}^T]^T$ are the assembled global coefficient vectors, respectively. In Figure 2.7, $\Omega = [0, L] \subset \mathbf{R}^1$ and $\Xi \subset \mathbf{R}^1$ represent the parametric domains of arc-length coordinate s and NURBS parametric coordinate ξ, respectively. The Jacobian of mapping between the physical domain ${}^0\bar{\Omega}$ and the parametric domain Ω is unity due to arc-length parameterization. The mapping relation between two parametric domains is given by

$$s(\hat{\mathbf{x}}(\xi)) = \int_0^{\xi_0 = \xi} \left\| {}^0\hat{\mathbf{x}}(\xi_0)_{,\xi_0} \right\| d\xi_0, \tag{2.103}$$

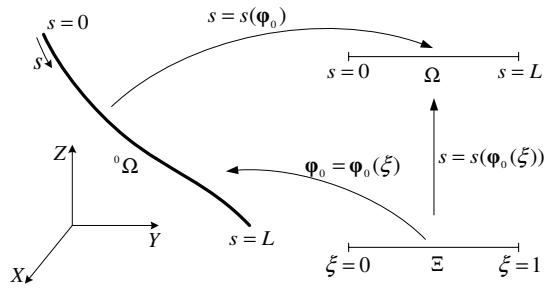

Figure 2.7: Mapping relations of physical and parametric domains

and the Jacobian of the mapping is

$$J_{cb} \equiv s_{,\xi} = \left\| {}^0\hat{\mathbf{x}}_{,\xi} \right\|. \tag{2.104}$$

$\widehat{\mathbf{E}}(\Delta\mathbf{z})$, obtained by replacing $\bar{\mathbf{z}}$ with $\Delta\mathbf{z}$ in Eq. (2.73) and using Eq. (2.102), is discretized as

$$\widehat{\mathbf{E}}(\Delta\mathbf{z}) = (\mathbf{N}_{I,s} - \boldsymbol{\Omega}_0\mathbf{N}_I)\Delta\mathbf{y}_I \equiv \mathbf{B}_{1I}\Delta\mathbf{y}_I. \tag{2.105}$$

Hereafter, the repeated indices I and J imply summations, and $I, J = 1 \sim CP$. Taking the tangential derivative of Eq. (2.105), $\{\widehat{\mathbf{E}}(\Delta\mathbf{z})\}_{,s}$ is discretized as

$$\{\widehat{\mathbf{E}}(\Delta\mathbf{z})\}_{,s} = (\mathbf{N}_{I,ss} - \boldsymbol{\Omega}_0\mathbf{N}_{I,s} - \boldsymbol{\Omega}_{0,s}\mathbf{N}_I)\Delta\mathbf{y}_I \equiv \mathbf{B}_{2I}\Delta\mathbf{y}_I, \tag{2.106}$$

where the first and second order derivatives of NURBS basis functions with respect to the arc-length coordinate s are respectively derived as $W_{I,s} = W_{I,\xi}/J_{cb}$ and $W_{I,ss} = (1/J_{cb})_{,s}W_{1,\xi} + W_{1,\xi\xi}/{J_{cb}}^2$. The discretized forms of the incremental strains are obtained, using Eqs. (2.72), (2.74), (2.105), and (2.106), as

$$\left.\begin{aligned} \widehat{\varepsilon}_m({}^n\mathbf{z};\Delta\mathbf{z}) &= {\mathbf{T}_1}^T\mathbf{B}_{1I}\Delta\mathbf{y}_I \equiv \mathbf{G}_I^m\Delta\mathbf{y}_I \\ \widehat{\omega}_b({}^n\mathbf{z};\Delta\mathbf{z}) &= ({\mathbf{E}_{,s}}^T\mathbf{D}_2\mathbf{B}_{1I} - \frac{1}{1+\varepsilon_m}{\tilde{\mathbf{T}}_1}^T\mathbf{B}_{2I})\Delta\mathbf{y}_I \equiv \mathbf{G}_I^b\Delta\mathbf{y}_I \end{aligned}\right\}. \tag{2.107}$$

Also, the incremental virtual strains are discretized, using Eqs. (2.92), (2.93), (2.105), and (2.106), as

$$\left.\begin{aligned} \widehat{\eta}_m({}^n\mathbf{z};\Delta\mathbf{z},\bar{\mathbf{z}}) &= \bar{\mathbf{y}}_I{}^T{\mathbf{B}_{1I}}^T\boldsymbol{\Gamma}\mathbf{B}_{1J}\Delta\mathbf{y}_J \equiv \bar{\mathbf{y}}_I{}^T\mathbf{K}_{IJ}^m\Delta\mathbf{y}_J \\ \widehat{\eta}_b({}^n\mathbf{z};\Delta\mathbf{z},\bar{\mathbf{z}}) &= \bar{\mathbf{y}}_I{}^T\{{\mathbf{B}_{1I}}^T\mathbf{D}_1\mathbf{B}_{1J} + \mathbf{B}_{1I}\mathbf{D}_2\mathbf{B}_{2J} + \mathbf{B}_{2I}\mathbf{D}_2\mathbf{B}_{1J}\}\Delta\mathbf{y}_J \equiv \bar{\mathbf{y}}_I{}^T\mathbf{K}_{IJ}^b\Delta\mathbf{y}_J \end{aligned}\right\}. \tag{2.108}$$

The incremental form of the load vector components are discretized, using Eqs. (2.95)-(2.97), and (2.105), as

$$\left.\begin{aligned} \widehat{\mathbf{f}}^{nc}({}^n\mathbf{z};\Delta\mathbf{z}) &= (\tilde{f}_1\mathbf{I} - \tilde{f}_2\tilde{\mathbf{I}})\boldsymbol{\Gamma}\mathbf{B}_{1I}\Delta\mathbf{y}_I \equiv \mathbf{F}_I^{nc}\Delta\mathbf{y}_I \\ \widehat{\mathbf{f}}_1^{eq}({}^n\mathbf{z};\Delta\mathbf{z}) &= mk\tilde{\mathbf{I}}\mathbf{D}_2\mathbf{B}_{1I}\Delta\mathbf{y}_I \equiv \mathbf{F}_{1I}^{eq}\Delta\mathbf{y}_I \\ \widehat{\mathbf{f}}_2^{eq}({}^n\mathbf{z};\Delta\mathbf{z}) &= m\mathbf{D}_2\mathbf{B}_{1I}\Delta\mathbf{y}_I \equiv \mathbf{F}_{2I}^{eq}\Delta\mathbf{y}_I \end{aligned}\right\}. \tag{2.109}$$

Finally, the linearized strain energy form of Eq. (2.99) is rewritten in discrete form as

$$\begin{aligned} a^*({}^n\mathbf{z};\Delta\mathbf{z},\bar{\mathbf{z}}) &= \bar{\mathbf{y}}^T\left[\mathop{\mathbf{A}}_{J=1}^{CP}\mathop{\mathbf{A}}_{I=1}^{CP}\int_\Omega\left\{EA\varepsilon_m({}^n\mathbf{z})\mathbf{K}_{IJ}^m + EA\mathbf{G}_I^{mT}\mathbf{G}_J^m\right\}ds\right]\Delta\mathbf{y} \\ &+\bar{\mathbf{y}}^T\left[\mathop{\mathbf{A}}_{J=1}^{CP}\mathop{\mathbf{A}}_{I=1}^{CP}\int_\Omega\left\{EI\omega_b({}^n\mathbf{z})\mathbf{K}_{IJ}^b + EI\mathbf{G}_I^{bT}\mathbf{G}_J^b\right\}ds\right]\Delta\mathbf{y} \\ &-\bar{\mathbf{y}}^T\left[\mathop{\mathbf{A}}_{J=1}^{CP}\mathop{\mathbf{A}}_{I=1}^{CP}\int_\Omega\left\{\mathbf{N}_I{}^T\mathbf{F}_J^{nc} + \mathbf{N}_I{}^T\mathbf{F}_{1J}^{eq} + \mathbf{N}_{I,s}{}^T\mathbf{F}_{2J}^{eq}\right\}ds\right]\Delta\mathbf{y} \\ &\equiv \bar{\mathbf{y}}^T\mathbf{K}\Delta\mathbf{y}, \end{aligned} \tag{2.110}$$

and the load form of Eq. (2.100) is

$$\begin{aligned} \ell^*({}^n\mathbf{z};\bar{\mathbf{z}}) &= \bar{\mathbf{y}}^T\left[\mathop{\mathbf{A}}_{I=1}^{CP}\int_\Omega\left\{\mathbf{N}_I^T\mathbf{f}^c + \mathbf{N}_I^T\mathbf{f}^{nc}({}^n\mathbf{z}) + \mathbf{N}_I^T\mathbf{f}_1^{eq}({}^n\mathbf{z}) + \mathbf{N}_{I,s}^T\mathbf{f}_2^{eq}({}^n\mathbf{z})\right\}ds\right] \\ &-\bar{\mathbf{y}}^T\left[\mathop{\mathbf{A}}_{I=1}^{CP}\int_\Omega\left\{EA\varepsilon_m({}^n\mathbf{z})\mathbf{G}_I^{mT} + EI\omega_b({}^n\mathbf{z})\mathbf{G}_I^{bT}\right\}ds\right] \\ &\equiv \bar{\mathbf{y}}^T\mathbf{F}, \end{aligned} \tag{2.111}$$

where **A**, **K**, and **F** are the Boolean operator for the matrix assembly, the global tangent stiffness matrix, and the global load vector, respectively.

2.3.4 Invariant formulation

In the following, we present a discretization of global displacement field to avoid self-straining trouble due to the investigation in section 2.2. Here we denote the global displacement by $\mathbf{z}$ instead of $\hat{z}$ for brevity. The vector $\mathbf{E}$ in Eq. (2.53) can be rewritten in terms of the global displacement as

$$\mathbf{E}(\mathbf{z}) = \mathbf{j}_{123}\mathbf{z}_{,s} + [1,0,0]^T. \tag{2.112}$$

Also, Eq. (2.73) can be rewritten in terms of the global virtual displacement as

$$\overset{\frown}{\mathbf{E}}(\bar{\mathbf{z}}) = \mathbf{j}_{123}\bar{\mathbf{z}}_{,s}. \tag{2.113}$$

Considering a non-conservative force vector $\mathbf{f}^{nc} = \mathbf{f}^{nc}(s,\mathbf{z})$ whose component vector in $\tilde{x}_1 - \tilde{x}_2 - \tilde{x}_3$ frame is $\tilde{\mathbf{f}}$, then using Eq. (2.57), we have the following.

$$\mathbf{f}^{nc} = \mathbf{i}_{123}{}^T\tilde{\mathbf{f}} = \mathbf{j}_{123}{}^T\mathbf{T}^T\tilde{\mathbf{f}}. \tag{2.114}$$

Eq. (2.83) also can be rewritten as

$$m\bar{\theta} = \bar{\mathbf{z}}_{,s}{}^T\left(-\frac{m}{1+\varepsilon_m}\mathbf{j}_{123}{}^T\tilde{\mathbf{T}}_1\right) \equiv \bar{\mathbf{z}}_{,s}{}^T\mathbf{f}^{eq}, \tag{2.115}$$

where $m = m(s)$ is the magnitude of bending moment with respect to $\tilde{x}_3$ axis. Also, the load form of Eq. (2.84) is rewritten as

$$\ell(\mathbf{z},\bar{\mathbf{z}}) \equiv \int_\Omega \left\{\bar{\mathbf{z}}^T\mathbf{f}^c + \bar{\mathbf{z}}^T\mathbf{f}^{nc}(\mathbf{z}) + \bar{\mathbf{z}}_{,s}^T\mathbf{f}^{eq}(\mathbf{z})\right\} ds, \tag{2.116}$$

where $\mathbf{f}^c \equiv \mathbf{f}^c(s)$ denotes a conservative distributed force vector. The equilibrium equation of a deformable body can be expressed as

$$a(\mathbf{z},\bar{\mathbf{z}}) = \ell(\mathbf{z},\bar{\mathbf{z}}), \ \ \forall \bar{\mathbf{z}} \in \bar{Z}. \tag{2.117}$$

where the variational space is defined as

$$\bar{Z} = \{\bar{\mathbf{z}} \in H^2(0,L) : \bar{\mathbf{z}} = \mathbf{0} \ \text{ on } \ \Gamma_D\}. \tag{2.118}$$

For a clamped boundary condition, the rotational constraint $\theta = 0$ is enforced by penalization and Lagrange multiplier methods, which is later explained in section 2.3.5.1. The linearized problem of Eq. (2.86) is also rewritten in terms of the global displacement as

$$a^*({}^n\mathbf{z};\Delta\mathbf{z},\bar{\mathbf{z}}) = \ell^*({}^n\mathbf{z};\bar{\mathbf{z}}), \ \ \forall \bar{\mathbf{z}} \in \bar{Z}, \tag{2.119}$$

where the linearized strain energy form and load form are defined, respectively, as

$$\begin{aligned} a^*({}^n\mathbf{z};\Delta\mathbf{z},\bar{\mathbf{z}}) \equiv & \int_\Omega \left\{EA\widehat{\varepsilon}_m({}^n\mathbf{z};\Delta\mathbf{z})\widehat{\varepsilon}_m({}^n\mathbf{z};\bar{\mathbf{z}}) + EA\varepsilon_m({}^n\mathbf{z})\widehat{\eta}_m({}^n\mathbf{z};\Delta\mathbf{z},\bar{\mathbf{z}})\right\} ds \\ & + \int_\Omega \left\{EI\widehat{\omega}_b({}^n\mathbf{z};\Delta\mathbf{z})\widehat{\omega}_b({}^n\mathbf{z};\bar{\mathbf{z}}) + EI\omega_b({}^n\mathbf{z})\widehat{\eta}_b({}^n\mathbf{z};\Delta\mathbf{z},\bar{\mathbf{z}})\right\} ds \\ & - \int_\Omega \left\{\bar{\mathbf{z}}^T\widehat{\mathbf{f}}^{nc}({}^n\mathbf{z};\Delta\mathbf{z}) + \widehat{\mathbf{E}}(\bar{\mathbf{z}})^T\widehat{\mathbf{f}}^{eq}({}^n\mathbf{z};\Delta\mathbf{z})\right\} ds, \end{aligned} \tag{2.120}$$

and

$$\begin{aligned} \ell^*({}^n\mathbf{z};\bar{\mathbf{z}}) \equiv & \int_\Omega \left\{\bar{\mathbf{z}}^T\mathbf{f}^c + \bar{\mathbf{z}}^T\mathbf{f}^{nc}({}^n\mathbf{z}) + \bar{\mathbf{z}}_{,s}^T\mathbf{f}^{eq}({}^n\mathbf{z})\right\} ds \\ & - \int_\Omega \left\{EA\varepsilon_m({}^n\mathbf{z})\widehat{\varepsilon}_m({}^n\mathbf{z};\bar{\mathbf{z}}) + EI\omega_b({}^n\mathbf{z})\widehat{\omega}_b({}^n\mathbf{z};\bar{\mathbf{z}})\right\} ds. \end{aligned} \tag{2.121}$$

The linearization of $\mathbf{f}^{eq}$ yields a load stiffness expression as

$$\bar{\mathbf{z}}_{,s}{}^T\Delta\mathbf{f}^{eq} = \widehat{\mathbf{E}}(\bar{\mathbf{z}})^T(m\mathbf{D}_2)\widehat{\mathbf{E}}(\Delta\mathbf{z}) \equiv \widehat{\mathbf{E}}(\bar{\mathbf{z}})^T\widehat{\mathbf{f}}^{eq}({}^n\mathbf{z};\Delta\mathbf{z}). \tag{2.122}$$

The linearization of $\mathbf{f}^{nc}$ of Eq. (2.114) is obtained as

$$\Delta\mathbf{f}^{nc} = \mathbf{j}_{123}{}^T(\tilde{f}_1\mathbf{I} - \tilde{f}_2\tilde{\mathbf{I}})\mathbf{\Gamma}\widehat{E}(\Delta\mathbf{z}) \equiv \widehat{\mathbf{f}}^{nc}({}^n\mathbf{z};\Delta\mathbf{z}). \tag{2.123}$$

The load stiffness operator from Eq. (2.123) is not symmetric, thus, Eq. (2.120) is not symmetric for $\Delta\mathbf{z}$ and $\bar{\mathbf{z}}$. In contrast to the discretization in section 2.3.3, the global displacement field is

discretized in order to express rigid body motions exactly in linearized problems during iterative solution process. The approximated incremental global displacement vector and the virtual displacement vector are respectively expressed, using the isoparametric mapping, as

$$\Delta \mathbf{z}^h(\xi) = \sum_{I=1}^{n} W_I(\xi) \Delta \mathbf{y}_I, \tag{2.124}$$

and

$$\bar{\mathbf{z}}^h(\xi) = \sum_{I=1}^{n} W_I(\xi) \bar{\mathbf{y}}_I, \tag{2.125}$$

where $\Delta \mathbf{y}_I \equiv [\Delta y_{1I}, \Delta y_{2I}, \Delta y_{3I}]^T$ and $\bar{\mathbf{y}}_I \equiv [\bar{y}_{1I}, \bar{y}_{2I}, \bar{y}_{3I}]^T$ are the coefficients of the incremental displacement and virtual displacement vectors, respectively. Then, $\widehat{\mathbf{E}}(\bar{\mathbf{z}})$ of 2.113 is discretized by substituting Eq. (2.125)into Eq. (2.113), as

$$\widehat{\mathbf{E}}(\bar{\mathbf{z}}) = \mathbf{j}_{123} \sum_{I=1}^{n} W_{I,s} \bar{\mathbf{y}}_I. \tag{2.126}$$

2.3.5 Inter-patch continuity condition

2.3.5.1 Constarint for displacement continuity

Consider the inter-patch continuity condition at junction in case of joining two patches (patch #1 and #2) without loss of generality, as shown in Fig. 2.8. $(\bullet)^*$ and $(\tilde{\bullet})$ denote the evaluated quantities at junction and patch 2, respectively. Two conditions of junction continuity are imposed for multi-patch models, where the local displacement field discretization is utilized. Here we denote the local and global displacement vectors respectively by $\mathbf{z}$ and $\tilde{z}$, and the isogeometric discretization expressions of Eqs. (2.101) and (2.102) are utilized. *First*, C^0-continuity condition of physical displacement is considered due to the discontinuity of base vectors at junction for initially G^0-continuous model. This continuity should be satisfied for both FEA and IGA models. *Second*, C^1-continuity of displacement component vector at junction is imposed for initially G^2-continuous model with C^0-continuous displacement field, which is proven to be sufficient and necessary for continuous rigid body rotation and membrane strain (A.3). The C^1-continuity implies that the function is continuously differentiable with respect to arc-length coordinate *s*.

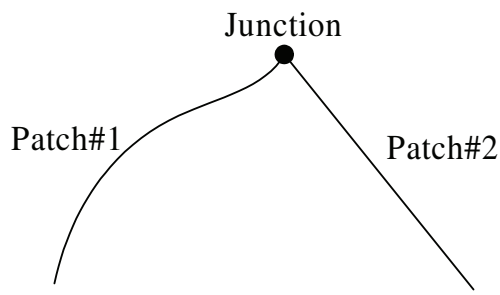

Figure 2.8: Illustration of a multi-patch junction

Case #1: continuous displacement

Using a Lagrange multiplier $\boldsymbol{\lambda}^*$ at junction, the virtual work due to the C^0-continuity condition (${}^{n+1}\hat{\mathbf{z}}^* = {}^{n+1}\underset{\sim}{\hat{\mathbf{z}}}^*$) at the current configuration (n+1) can be written, using the relation ${}^{n+1}\hat{\mathbf{z}} = \mathbf{j}_{123}{}^{T\,n+1}\mathbf{z}$, as

$$\begin{aligned}
&\bar{\boldsymbol{\lambda}}^{*\,T}(\mathbf{j}_{123}{}^{*\,T\,n+1}\mathbf{z}^* - \underset{\sim}{\mathbf{j}}_{123}{}^{*\,T\,n+1}\underset{\sim}{\mathbf{z}}^*) + {}^{n+1}\boldsymbol{\lambda}^{*\,T}(\mathbf{j}_{123}{}^{*\,T}\bar{\mathbf{z}}^* - \underset{\sim}{\mathbf{j}}_{123}{}^{*\,T}\underset{\sim}{\bar{\mathbf{z}}}^*) \\
&= \bar{\boldsymbol{\lambda}}^{*\,T}(\mathbf{j}_{123}{}^{*\,T\,n+1}\mathbf{z}^* - \underset{\sim}{\mathbf{j}}_{123}{}^{*\,T\,n+1}\underset{\sim}{\mathbf{z}}^*) + (\bar{\mathbf{z}}^{*\,T}\mathbf{j}_{123}{}^* - \underset{\sim}{\bar{\mathbf{z}}}^{*\,T}\underset{\sim}{\mathbf{j}}_{123}{}^*)^{n+1}\boldsymbol{\lambda}^* \\
&\equiv b({}^{n+1}\mathbf{d}, \bar{\mathbf{d}}),
\end{aligned} \tag{2.127}$$

where $\mathbf{d} \equiv (\mathbf{z}; \underset{\sim}{\mathbf{z}}; \boldsymbol{\lambda}^*)$, $\bar{\mathbf{d}} = (\bar{\mathbf{z}}; \underset{\sim}{\bar{\mathbf{z}}}; \bar{\boldsymbol{\lambda}}^*)$. The Lagrange multiplier ${}^{n+1}\boldsymbol{\lambda}^*$ is decomposed into

$${}^{n+1}\boldsymbol{\lambda}^* = {}^{n}\boldsymbol{\lambda}^* + \Delta\boldsymbol{\lambda}^*. \tag{2.128}$$

Using Eqs. (2.89) and (2.128), the energy form of Eq. (2.127) is rewritten as

$$b({}^{n+1}\mathbf{d}, \bar{\mathbf{d}}) = b({}^{n}\mathbf{d}, \bar{\mathbf{d}}) + b^*(\Delta\mathbf{d}, \bar{\mathbf{d}}). \tag{2.129}$$

The strain energy form $b({}^{n}\mathbf{d}, \bar{\mathbf{d}})$ and the linearized strain energy form $b^*(\Delta\mathbf{d}, \bar{\mathbf{d}})$ are discretized as

$$\begin{aligned}
b({}^{n}\mathbf{d}, \bar{\mathbf{d}}) &= \bar{\boldsymbol{\lambda}}^{*\,T}(\mathbf{j}_{123}{}^{*\,T\,n}\mathbf{z}^* - \underset{\sim}{\mathbf{j}}_{123}{}^{*\,T\,n}\underset{\sim}{\mathbf{z}}^*) + (\bar{\mathbf{z}}^{*\,T}\mathbf{j}_{123}{}^* - \underset{\sim}{\bar{\mathbf{z}}}^{*\,T}\underset{\sim}{\mathbf{j}}_{123}{}^*)^{n}\boldsymbol{\lambda}^* \\
&= \bar{\boldsymbol{\lambda}}^{*\,T}(\mathbf{j}_{123}{}^{*\,T\,n}\mathbf{z}^* - \underset{\sim}{\mathbf{j}}_{123}{}^{*\,T\,n}\underset{\sim}{\mathbf{z}}^*) + \bar{\mathbf{y}}^T(\mathbf{N}^{*\,T}\mathbf{j}_{123}{}^{*\,n}\boldsymbol{\lambda}^*) + \underset{\sim}{\bar{\mathbf{y}}}^T(-\underset{\sim}{\mathbf{N}}^{*\,T}\underset{\sim}{\mathbf{j}}_{123}{}^{*\,n}\boldsymbol{\lambda}^*) \\
&\equiv \bar{\boldsymbol{\lambda}}^{*\,T}\mathbf{Q}_3 + \bar{\mathbf{y}}^T\mathbf{Q}_1 + \underset{\sim}{\bar{\mathbf{y}}}^T\mathbf{Q}_2,
\end{aligned} \tag{2.130}$$

and

$$\begin{aligned}
b^*(\Delta\mathbf{d}, \bar{\mathbf{d}}) &= \bar{\boldsymbol{\lambda}}^{*\,T}(\mathbf{j}_{123}{}^{*\,T}\Delta\mathbf{z}^* - \underset{\sim}{\mathbf{j}}_{123}{}^{*\,T}\Delta\underset{\sim}{\mathbf{z}}^*) + (\bar{\mathbf{z}}^{*\,T}\mathbf{j}_{123}{}^* - \underset{\sim}{\bar{\mathbf{z}}}^{*\,T}\underset{\sim}{\mathbf{j}}_{123}{}^*)\Delta\boldsymbol{\lambda}^* \\
&= \bar{\boldsymbol{\lambda}}^{*\,T}(\mathbf{j}_{123}{}^{*\,T}\mathbf{N}^*)\Delta\mathbf{y} + \bar{\boldsymbol{\lambda}}^{*\,T}(-\underset{\sim}{\mathbf{j}}_{123}{}^{*\,T}\underset{\sim}{\mathbf{N}}^*)\Delta\underset{\sim}{\mathbf{y}} + \bar{\mathbf{y}}^T(\mathbf{N}^{*\,T}\mathbf{j}_{123}{}^*)\Delta\boldsymbol{\lambda}^* + \underset{\sim}{\bar{\mathbf{y}}}^T(-\underset{\sim}{\mathbf{N}}^{*\,T}\underset{\sim}{\mathbf{j}}_{123}{}^*)\Delta\boldsymbol{\lambda}^* \\
&\equiv \bar{\boldsymbol{\lambda}}^{*\,T}\mathbf{C}_1\Delta\mathbf{y} + \bar{\boldsymbol{\lambda}}^{*\,T}\mathbf{C}_2\Delta\underset{\sim}{\mathbf{y}} + \bar{\mathbf{y}}^T\mathbf{C}_1{}^T\Delta\boldsymbol{\lambda}^* + \underset{\sim}{\bar{\mathbf{y}}}^T\mathbf{C}_2{}^T\Delta\boldsymbol{\lambda}^*.
\end{aligned} \tag{2.131}$$

Case #2: continuous first order tangential derivative of local displacement

Employing a Lagrange multiplier $\boldsymbol{\lambda}^*$ at the junction, the virtual work due to the C^1-continuity condition (${}^{n+1}\mathbf{z}^*_{,s} = {}^{n+1}\underset{\sim}{\mathbf{z}}^*_{,\underset{\sim}{s}}$) at the current configuration (n+1) can be written as

$$\bar{\boldsymbol{\lambda}}^{*\,T}({}^{n+1}\mathbf{z}^*_{,s} - {}^{n+1}\underset{\sim}{\mathbf{z}}^*_{,\underset{\sim}{s}}) + (\bar{\mathbf{z}}^*_{,s} - \underset{\sim}{\bar{\mathbf{z}}}^*_{,\underset{\sim}{s}})^{T\,n+1}\boldsymbol{\lambda}^* \equiv b({}^{n+1}\mathbf{d}, \bar{\mathbf{d}}). \tag{2.132}$$

Likewise, the strain energy form (2.132) is decomposed into

$$b({}^{n+1}\mathbf{d}, \bar{\mathbf{d}}) \equiv b({}^{n}\mathbf{d}, \bar{\mathbf{d}}) + b^*(\Delta\mathbf{d}, \bar{\mathbf{d}}). \tag{2.133}$$

The strain energy form $b(^n\mathbf{d},\bar{\mathbf{d}})$ and the linearized strain energy form $b^*(\Delta\mathbf{d},\bar{\mathbf{d}})$ are discretized as

$$\begin{aligned} b(^n\mathbf{d},\bar{\mathbf{d}}) &= \bar{\boldsymbol{\lambda}}^{*T}(^n\mathbf{z}^*_{,s} - {}^n\underset{\sim}{\mathbf{z}}^*_{,\underset{\sim}{s}}) + (\bar{\mathbf{z}}^*_{,s} - \bar{\underset{\sim}{\mathbf{z}}}^*_{,\underset{\sim}{s}})^{T\,n}\boldsymbol{\lambda}^* \\ &= \bar{\boldsymbol{\lambda}}^{*T}(^n\mathbf{z}^*_{,s} - {}^n\underset{\sim}{\mathbf{z}}^*_{,\underset{\sim}{s}}) + \bar{\mathbf{y}}^T(\mathbf{N}_{,s}{}^{*T\,n}\boldsymbol{\lambda}^*) - \bar{\underset{\sim}{\mathbf{y}}}^T(\underset{\sim}{\mathbf{N}}_{,\underset{\sim}{s}}{}^{*T\,n}\boldsymbol{\lambda}^*) \equiv \bar{\boldsymbol{\lambda}}^{*T}\mathbf{Q}_3 + \bar{\mathbf{y}}^T\mathbf{Q}_1 + \bar{\underset{\sim}{\mathbf{y}}}^T\mathbf{Q}_2 \end{aligned} \tag{2.134}$$

and

$$\begin{aligned} b^*(\Delta\mathbf{d},\bar{\mathbf{d}}) &= \bar{\boldsymbol{\lambda}}^{*T}(\Delta\mathbf{z}^*_{,s} - \Delta\underset{\sim}{\mathbf{z}}^*_{,\underset{\sim}{s}}) + (\bar{\mathbf{z}}^*_{,s} - \bar{\underset{\sim}{\mathbf{z}}}^*_{,\underset{\sim}{s}})^T\Delta\boldsymbol{\lambda}^* \\ &= \bar{\boldsymbol{\lambda}}^{*T}\mathbf{N}^*_{,s}\Delta\mathbf{y} + \bar{\boldsymbol{\lambda}}^{*T}(-\underset{\sim}{\mathbf{N}}^*_{,\underset{\sim}{s}})\Delta\underset{\sim}{\mathbf{y}} + \bar{\mathbf{y}}^T\mathbf{N}_{,s}{}^{*T}\Delta\boldsymbol{\lambda}^* + \bar{\underset{\sim}{\mathbf{y}}}^T(-\underset{\sim}{\mathbf{N}}_{,\underset{\sim}{s}}{}^{*T})\Delta\boldsymbol{\lambda}^* \\ &\equiv \bar{\boldsymbol{\lambda}}^{*T}\mathbf{C}_1\Delta\mathbf{y} + \bar{\boldsymbol{\lambda}}^{*T}\mathbf{C}_2\Delta\underset{\sim}{\mathbf{y}} + \bar{\mathbf{y}}^T\mathbf{C}_1{}^T\Delta\boldsymbol{\lambda}^* + \bar{\underset{\sim}{\mathbf{y}}}^T\mathbf{C}_2{}^T\Delta\boldsymbol{\lambda}^*. \end{aligned} \tag{2.135}$$

Considering the above two cases the junction continuity, the linearized variational equation (2.98) can be rewritten as follows : For a given $^n\mathbf{d} = (^n\mathbf{z};{}^n\underset{\sim}{\mathbf{z}};{}^n\boldsymbol{\lambda}^*)$, find $\Delta\mathbf{d} = (\Delta\mathbf{z};\Delta\underset{\sim}{\mathbf{z}};\Delta\boldsymbol{\lambda}^*) \in \bar{W}$ such that

$$a^*(^n\mathbf{z};\Delta\mathbf{z},\bar{\mathbf{z}}) + \underset{\sim}{a}^*(^n\underset{\sim}{\mathbf{z}};\Delta\underset{\sim}{\mathbf{z}},\bar{\underset{\sim}{\mathbf{z}}}) + b^*(\Delta\mathbf{d},\bar{\mathbf{d}}) = \ell^*(^n\mathbf{z};\bar{\mathbf{z}}) + \underset{\sim}{\ell}^*(^n\underset{\sim}{\mathbf{z}};\bar{\underset{\sim}{\mathbf{z}}}) - b(^n\mathbf{d},\bar{\mathbf{d}}),\ \ \forall\bar{\mathbf{d}} \in \bar{W}, \tag{2.136}$$

where the variational space is defined as

$$\bar{W} = \{\bar{\mathbf{d}} = (\bar{\mathbf{z}};\bar{\underset{\sim}{\mathbf{z}}};\bar{\boldsymbol{\lambda}}^*)\,\Big|\,(\bar{\mathbf{z}};\bar{\underset{\sim}{\mathbf{z}}}) \in \bar{Z}\times\bar{\underset{\sim}{Z}},\ \bar{\boldsymbol{\lambda}}^* \in R^3\}. \tag{2.137}$$

Finally, after applying kinematic boundary conditions, the linearized variational equation (2.136) can be expressed as the following augmented matrix form.

$$\left[\begin{array}{cc|c} \mathbf{K}^r & \mathbf{0} & \mathbf{C}_1^T \\ \mathbf{0} & \underset{\sim}{\mathbf{K}}^r & \mathbf{C}_2^T \\ \hline \mathbf{C}_1 & \mathbf{C}_2 & \mathbf{0} \end{array}\right]\left\{\begin{array}{c} \Delta\mathbf{y} \\ \Delta\underset{\sim}{\mathbf{y}} \\ \Delta\boldsymbol{\lambda}^* \end{array}\right\} = \left\{\begin{array}{c} \mathbf{F} \\ \underset{\sim}{\mathbf{F}} \\ \mathbf{0} \end{array}\right\} - \left\{\begin{array}{c} \mathbf{Q}_1 \\ \mathbf{Q}_2 \\ \mathbf{Q}_3 \end{array}\right\}, \tag{2.138}$$

where $\mathbf{K}^r$ represents a reduced global stiffness matrix with kinematic boundary conditions imposed.

2.3.5.2 Constraint for rotation continuity

We consider the rotational continuity condition at multi-patch junction. Two kinds of numerical methods are employed for the imposition of constraint condition; Lagrange multiplier and penalty methods. Here we denote the global displacement field by $\mathbf{z}$ instead of $\hat{z}$ for brevity.

Lagrange multiplier method

The energy functional suggested in Duong et al. [36] for a rotational continuity condition at edge in thin shell formulation can be rewritten for planar beam problems to enforce the continuity of rotation angle $\theta = \underset{\sim}{\theta}$,

$$\Pi_L = \lambda_L\left\{1 - \cos(\theta - \underset{\sim}{\theta}) + \sin(\theta - \underset{\sim}{\theta})\right\}, \tag{2.139}$$

where λ_L denotes the Lagrange multiplier. Taking the first variation of Eq. (2.139) yields the following.

$$\begin{aligned}\delta\Pi_L &= \bar{\lambda}_L\left\{1-\cos(\theta-\underset{\sim}{\theta})+\sin(\theta-\underset{\sim}{\theta})\right\}\\ &\quad+\lambda_L(\bar{\theta}-\bar{\underset{\sim}{\theta}})\left\{\sin(\theta-\underset{\sim}{\theta})+\cos(\theta-\underset{\sim}{\theta})\right\}\\ &\equiv b(^{n+1}\mathbf{d},\bar{\mathbf{d}}),\end{aligned} \tag{2.140}$$

where $^{n+1}\mathbf{d}\equiv(^{n+1}\mathbf{z},^{n+1}\underset{\sim}{\mathbf{z}},\lambda_L)$ and $\bar{\mathbf{d}}\equiv(^{n+1}\bar{\mathbf{z}},^{n+1}\bar{\underset{\sim}{\mathbf{z}}},\bar{\lambda}_L)$, and $\bar{\lambda}_L)$ represents the virtual Lagrange multiplier. The increment of the virtual rotation angle is derived, through a linearization of Eq. (2.82), using Eq. (A.7), as

$$\Delta\bar{\theta}=\widehat{\mathbf{E}}(\bar{\mathbf{z}})^T\mathbf{D}_2\widehat{\mathbf{E}}(\Delta\mathbf{z})\equiv\widehat{\eta}_\theta(\mathbf{z};\Delta^{n+1}\mathbf{z},\bar{\mathbf{z}}). \tag{2.141}$$

The Lagrange multiplier $^{n+1}\lambda_L$ is decomposed into

$$^{n+1}\lambda_L={}^n\lambda_L+\Delta\lambda_L. \tag{2.142}$$

Then, using Eqs. (2.141) and (2.142), the linearized energy form is obtained as

$$\begin{aligned}b^*(\mathbf{d};\Delta\mathbf{d},\bar{\mathbf{d}}) &= (\tilde{\mathbf{T}}_1+\mathbf{T}_1)^T\underset{\sim}{\mathbf{T}}_1\left\{\begin{array}{l}\bar{\lambda}_L\widehat{\theta}(\mathbf{z};\Delta\mathbf{z})-\bar{\lambda}_L\widehat{\underset{\sim}{\theta}}(\underset{\sim}{\mathbf{z}};\Delta\underset{\sim}{\mathbf{z}})\\ +\widehat{\theta}(\mathbf{z};\bar{\mathbf{z}})\Delta\lambda_L-\widehat{\underset{\sim}{\theta}}(\underset{\sim}{\mathbf{z}};\bar{\underset{\sim}{\mathbf{z}}})\Delta\lambda_L\\ +\lambda_L\widehat{\eta}_\theta(\mathbf{z};\Delta\mathbf{z},\bar{\mathbf{z}})-\lambda_L\widehat{\underset{\sim}{\eta}}_\theta(\underset{\sim}{\mathbf{z}};\Delta\underset{\sim}{\mathbf{z}},\bar{\underset{\sim}{\mathbf{z}}})\end{array}\right\}\\ &\quad+\lambda_L(\mathbf{T}_1-\tilde{\mathbf{T}}_1)^T\underset{\sim}{\mathbf{T}}_1\left\{\begin{array}{l}\widehat{\theta}(\mathbf{z};\bar{\mathbf{z}})\widehat{\theta}(\mathbf{z};\Delta\mathbf{z})-\widehat{\theta}(\mathbf{z};\bar{\mathbf{z}})\widehat{\underset{\sim}{\theta}}(\underset{\sim}{\mathbf{z}};\Delta\underset{\sim}{\mathbf{z}})\\ -\widehat{\underset{\sim}{\theta}}(\underset{\sim}{\mathbf{z}};\bar{\underset{\sim}{\mathbf{z}}})\widehat{\theta}(\mathbf{z};\Delta\mathbf{z})+\widehat{\underset{\sim}{\theta}}(\underset{\sim}{\mathbf{z}};\bar{\underset{\sim}{\mathbf{z}}})\widehat{\underset{\sim}{\theta}}(\underset{\sim}{\mathbf{z}};\Delta\underset{\sim}{\mathbf{z}})\end{array}\right\},\end{aligned} \tag{2.143}$$

where the linearized rotation angle $\widehat{\theta}$ is defined in Eq. (2.82) where the expression of $\widehat{\mathbf{E}}(\bar{\mathbf{z}})$ is replated by Eq. (2.113).

Penalty method

In plane problems, it should be clear that the continuity of the transformation matrix of Eq. (2.57), *i.e.*, $\mathbf{T}=\underset{\sim}{\mathbf{T}}$ is sufficient and necessary for the following condition,

$$\mathbf{T}_1^d\equiv\mathbf{T}_1-\underset{\sim}{\mathbf{T}}_1=\mathbf{0}, \tag{2.144}$$

The penalization energy of the condition (2.144) can be expressed as

$$\Pi_p=\frac{1}{2}k_p{\mathbf{T}_1^d}^T\mathbf{T}_1^d, \tag{2.145}$$

where k_p is a penalty parameter. Taking the first variation of Eq. (2.145) and using Eq. (A.2), we obtain the following penalization energy form.

$$b(\mathbf{d},\bar{\mathbf{d}})\equiv k_p\left\{\widehat{\mathbf{E}}(\bar{\mathbf{z}})^T\mathbf{\Gamma}-\widehat{\underset{\sim}{\mathbf{E}}}(\bar{\underset{\sim}{\mathbf{z}}})^T\underset{\sim}{\mathbf{\Gamma}}\right\}\mathbf{T}_1^d, \tag{2.146}$$

where $\mathbf{d} \equiv (\mathbf{z}; \underset{\sim}{\mathbf{z}})$ and $\bar{\mathbf{d}} \equiv (\bar{\mathbf{z}}; \underset{\sim}{\bar{\mathbf{z}}})$. Then, the linearization of Eq. (2.146) using Eq. (A.16) yields the linearized penalization energy form, as follows.

$$
\begin{aligned}
b^*(\mathbf{d}; \Delta\mathbf{d}, \bar{\mathbf{d}}) \equiv & -k_p \widehat{\mathbf{E}}(\bar{\mathbf{z}})^T \left[\frac{1}{1+\varepsilon_m} \left\{ \mathrm{sym}\left(\boldsymbol{\Gamma} \mathbf{T}_1^{\mathrm{d}} \mathbf{T}_1{}^{\mathrm{T}} \right) + \boldsymbol{\Gamma} \mathbf{T}_1{}^{\mathrm{T}} \mathbf{T}_1^{\mathrm{d}} \right\} - \boldsymbol{\Gamma}\boldsymbol{\Gamma} \right] \widehat{\mathbf{E}}(\Delta\mathbf{z}) \\
& + k_p \widehat{\underset{\sim}{\mathbf{E}}}(\bar{\underset{\sim}{\mathbf{z}}})^T \left[\frac{1}{1+\underset{\sim}{\varepsilon}_m} \left\{ \mathrm{sym}\left(\underset{\sim}{\boldsymbol{\Gamma}} \underset{\sim}{\mathbf{T}}_1^{\mathrm{d}} \underset{\sim}{\mathbf{T}}_1{}^{\mathrm{T}} \right) + \underset{\sim}{\boldsymbol{\Gamma}} \underset{\sim}{\mathbf{T}}_1{}^{\mathrm{T}} \mathbf{T}_1^{\mathrm{d}} \right\} + \underset{\sim}{\boldsymbol{\Gamma}}\underset{\sim}{\boldsymbol{\Gamma}} \right] \widehat{\underset{\sim}{\mathbf{E}}}(\Delta\underset{\sim}{\mathbf{z}}) \\
& - k_p \left[\widehat{\mathbf{E}}(\bar{\mathbf{z}})^T \boldsymbol{\Gamma} \underset{\sim}{\boldsymbol{\Gamma}} \widehat{\underset{\sim}{\mathbf{E}}}(\Delta\underset{\sim}{\mathbf{z}}) + \widehat{\underset{\sim}{\mathbf{E}}}(\bar{\underset{\sim}{\mathbf{z}}})^T \underset{\sim}{\boldsymbol{\Gamma}} \boldsymbol{\Gamma} \widehat{\mathbf{E}}(\Delta\mathbf{z}) \right],
\end{aligned}
\tag{2.147}
$$

where $\Delta\mathbf{d} \equiv (\Delta\mathbf{z}; \Delta\underset{\sim}{\mathbf{z}})$, and it is noted that this form is symmetric for $\Delta\mathbf{d}$ and $\bar{\mathbf{d}}$ due to the symmetry of $\boldsymbol{\Gamma}$ of Eq. (A.4).

Considering the rotational continuity condition, the linearized variational equation Eq. (2.119) can be rewritten as follows : For a given ${}^n\mathbf{d}$, find $\Delta\mathbf{d} \in \bar{W}$ such that

$$
\begin{aligned}
& a^*({}^n\mathbf{z}; \Delta\mathbf{z}, \bar{\mathbf{z}}) + \underset{\sim}{a}^*({}^n\underset{\sim}{\mathbf{z}}; \Delta\underset{\sim}{\mathbf{z}}, \bar{\underset{\sim}{\mathbf{z}}}) + b^*(\mathbf{d}; \Delta\mathbf{d}, \bar{\mathbf{d}}) \\
& = \ell^*({}^n\mathbf{z}; \bar{\mathbf{z}}) + \underset{\sim}{\ell}^*({}^n\underset{\sim}{\mathbf{z}}; \bar{\underset{\sim}{\mathbf{z}}}) - b({}^n\mathbf{d}, \bar{\mathbf{d}}), \quad \forall \bar{\mathbf{d}} \in \bar{W}.
\end{aligned}
\tag{2.148}
$$

It is note that the expressions of the linearized energy form $b^*({}^n\mathbf{d}; \Delta\mathbf{d}, \bar{\mathbf{d}})$ and the energy form $b({}^n\mathbf{d}, \bar{\mathbf{d}})$ are chosen as Eqs. (2.146) and (2.147) for the penalty method, and Eqs. (2.140) and (2.143) for the Lagrange multiplier method. Also, the variational spaces are defined as

$$
\bar{W} = \{ \bar{\mathbf{d}} = (\bar{\mathbf{z}}; \bar{\underset{\sim}{\mathbf{z}}}) \,\big|\, (\bar{\mathbf{z}}; \bar{\underset{\sim}{\mathbf{z}}}) \in \bar{Z} \times \bar{\underset{\sim}{Z}} \},
\tag{2.149}
$$

and

$$
\bar{W} = \left\{ \bar{\mathbf{d}} = (\bar{\mathbf{z}}; \bar{\underset{\sim}{\mathbf{z}}}; \bar{\lambda}_L) \,\big|\, (\bar{\mathbf{z}}; \bar{\underset{\sim}{\mathbf{z}}}) \in \bar{Z} \times \bar{\underset{\sim}{Z}}, \ \bar{\lambda}_L \in \mathbf{R}^1 \right\}.
\tag{2.150}
$$

2.3.6 Constitutive model of shape memory polymer

Here we investigate the large deformation analysis of shape memory polymer (SMP)-based structures. The linear elastic and rate-independent SMP constitutive model developed by Liu *et al.* [69] is adopted. Note that an expression of stored strain evolution during the shape recovery process in this research, not presented in [69], refers to Baghani *et al.* [6].

Fig. 2.9 shows a stress-strain-temperature diagram illustrating the shape memory effect from a macroscopic point of view. The thermomechanical cycle, comprised of four steps, starts at a strain- and stress-free state while the temperature is T_h (high temperature) (point A). At this point, a mechanical loading is applied and the material in rubbery phase can undergo large elastic deformation due to low stiffness (step #1). During this pre-deformation process, the structure is fully in active phase and no strain storage or release occurs. From point B, the external loading is held fixed and the temperature decreases to T_ℓ (point C). The rubbery polymer, meanwhile, turns into a glassy polymer, and the strain storage occurs (step #2). Subsequently, the material is unloaded, *i.e.*, the applied mechanical loading is removed (step #3). Due to the much higher

stiffness of the glassy phase in comparison to the rubbery phase, a spring-back occurs with slight strain change (point D). Finally, the temperature increases up to T_h (step #4). It is observed that the strain will be released and the original permanent shape can be recovered (point A). As illustrated in Fig. 2.9b, the strain is drastically released in the vicinity of the glass transition temperature $T = T_g$ of the SMP material.

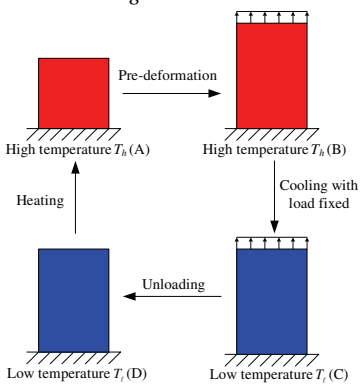

(a) Shape memory and recovery process

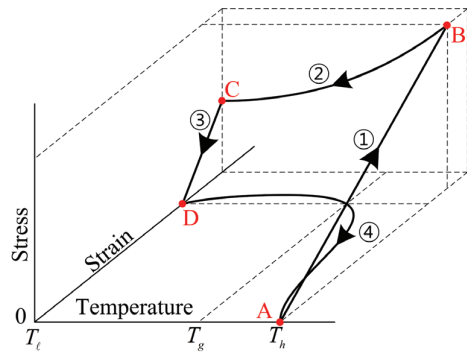

(b) Stress-strain-temperature diagram

Figure 2.9: Illustration of shape memory and recovery cycle

Since the Jaumann strain component B_{11} of Eq. (2.70) represents a stretching of material fiber, the constitutive model for uniaxial deformation developed in [69] can be consistently employed. Under the small strain assumption, total Jaumann strain is additively decomposed into three parts; elastic strain (B^e_{11}), stored strain (B^s_{11}), and thermal strain (ε^{th}), as follows.

$$\begin{aligned} B_{11} &= B^e_{11} + B^s_{11} + \varepsilon^{th} \\ &= \phi_f B^f_{11} + (1-\phi_f) B^a_{11} + B^s_{11} + \varepsilon^{th}, \end{aligned} \tag{2.151}$$

where the elastic strain is further decomposed into elastic strains in active (B^a_{11}) and frozen (B^f_{11}) phases. $\phi_f(T)$ denotes the frozen volume fraction function, which is assumed to depend only on temperature, and not to be affected by the strain and stress state of the material. The stored strain has been introduced to identify the strain storage and release mechanisms. It is assumed that the polymer model is a mixture of two kinds of extreme phases: the "active phase" and the "frozen phase". In the active phase, the polymer exists in fully rubbery state. In contrast, the frozen phase is the major phase of a glassy state polymer. By changing the ratio of these two material phases, the glass transition and shape memory behavior during the thermomechanical cycle can be captured. In Liu et al. [69], an empirical formula of the frozen volume fraction function is obtained by fitting the uniaxial free strain recovery curve of the pre-compressed sample, as

$$\phi_f(T) = 1 - \frac{1}{1 + c_f (T_h - T)^n}. \tag{2.152}$$

Also, by fitting the unconstrained uniaxial thermal strain curve, given in [69], the following

empirical formula of the thermal strain is obtained [6].

$$\varepsilon^{th} = a_1(T - T_h) + a_2(T^2 - T_h^2). \tag{2.153}$$

Table 2.1 shows the selected material parameter values, which are experimentally obtained by Liu *et al.* [69]. E^a and E^f are the Young's modulus in active and frozen phases, respectively.

Table 2.1: Values of material parameters

Material parameters	Values	Units
E_a,E_f	8.8, 813	MPa
T_ℓ,T_g,T_h	273, 343, 358	K
n	4	-
c_f	2.76×10^{-5}	$1/K^4$
a_1,a_2	-3.14×10^{-4}, 0.7×10^{-6}	-

The expressions of the stored strain evolutions in the four steps of thermomechanical process can be combined into [6].

$$B_{11}^s = k_1\int_0^{\phi_f} B_{11}^a d\phi_f + k_2\int_0^{\phi_f} B_{11}^s/\phi_f d\phi_f. \tag{2.154}$$

The indices k_1 and k_2 identify the heating, cooling, and isothermal processes, as

$$\begin{cases} k_1 = 1,\ k_2 = 0;\ \ \dot{T} < 0 \\ k_1 = 0,\ k_2 = 1;\ \ \dot{T} > 0 \\ k_1 = 0,\ k_2 = 0;\ \ \dot{T} = 0 \end{cases}, \tag{2.155}$$

where $\dot{T}$ denotes the time derivative of temperature. Taking the first order differentiation of Eq. (2.154) with respect to the temperature, and applying the implicit Euler method yields

$$\begin{aligned} {}^{n+1}B_{11}^s &= {}^{n}B_{11}^s + {}^{n+1}B_{11,T}^s\Delta T \\ &= {}^{n}B_{11}^s + \left(\begin{array}{l} k_1\,{}^{n+1}B_{11}^a \\ +k_2\,{}^{n+1}B_{11}^s/{}^{n+1}\phi_f \end{array}\right){}^{n+1}\phi_{f,T}\Delta T, \end{aligned} \tag{2.156}$$

where $(\bullet)_{,T}$ denotes the differentiation with respect to temperature, and the notations ${}^{n}(\bullet)$ and ${}^{n+1}(\bullet)$ indicate quantities evaluated at the previous and the current temperature steps, respectively. ΔT denotes a temperature increment. Rearranging the terms of Eq. (2.156), the stored strain at current temperature (n+1) can be expressed as

$${}^{n+1}B_{11}^s = k_3({}^{n}B_{11}^s + k_1\,{}^{n+1}B_{11}^a\,{}^{n+1}\phi_{f,T}\Delta T), \tag{2.157}$$

where $k_3 \equiv (1 - k_2\,{}^{n+1}\phi_{f,T}/{}^{n+1}\phi_f\Delta T)^{-1}$. From the expression of the Jaumann strain component

B_{11} of Eq. (2.70), Eq. (2.157) can be rewritten for each strain component, as

$$\left.\begin{aligned} {}^{n+1}\varepsilon_m^s &= k_3({}^n\varepsilon_m^s + k_1{}^{n+1}\varepsilon_m^{a\,n+1}\phi_{f,T}\Delta T) \\ {}^{n+1}\omega_b^s &= k_3({}^n\omega_b^s + k_1{}^{n+1}\omega_b^{a\,n+1}\phi_{f,T}\Delta T) \end{aligned}\right\}. \tag{2.158}$$

Assume that the corresponding stresses in the active and frozen phases are equal [69],

$${}^{n+1}J_{11} = E^{a\,n+1}B_{11}^a = E^{f\,n+1}B_{11}^f, \tag{2.159}$$

from which we have

$${}^{n+1}B_{11}^f = E^a E^{f^{-1}\,n+1}B_{11}^a. \tag{2.160}$$

Combining Eq. (2.160) with Eqs. (2.151) and (2.154) yields

$${}^{n+1}B_{11}^a = C^a({}^{n+1}B_{11} - k_3{}^nB_{11}^s - {}^{n+1}\varepsilon^{th}), \tag{2.161}$$

where C^a is defined as

$$C^a \equiv \left({}^{n+1}\phi_a + {}^{n+1}\phi_f E_a E_f{}^{-1} + k_3 k_1{}^{n+1}\phi_{f,T}\Delta T\right)^{-1}. \tag{2.162}$$

Eq. (2.161) can be rewritten for each strain component, as

$$\left.\begin{aligned} {}^{n+1}\varepsilon_m^a &= C^a({}^{n+1}\varepsilon_m - k_3{}^n\varepsilon_m^s - {}^{n+1}\varepsilon^{th}) \\ {}^{n+1}\omega_b^a &= C^a({}^{n+1}\omega_b - k_3{}^n\omega_b^s) \end{aligned}\right\}. \tag{2.163}$$

Then, substituting Eq. (2.161) into Eq. (2.159), the Jaumann stress is expressed as

$${}^{n+1}J_{11} = E^t({}^{n+1}B_{11} - k_3{}^nB_{11}^s - {}^{n+1}\varepsilon^{th}), \tag{2.164}$$

and the resultant force ${}^{n+1}N \equiv N({}^{n+1}\mathbf{z})$ and moment ${}^{n+1}M \equiv M({}^{n+1}\mathbf{z})$ can be obtained as

$$\left.\begin{aligned} {}^{n+1}N &= E^t A({}^{n+1}\varepsilon_m - k_3{}^n\varepsilon_m^s - {}^{n+1}\varepsilon^{th}) \\ {}^{n+1}M &= E^t I({}^{n+1}\omega_b - k_3{}^n\omega_b^s) \end{aligned}\right\}, \tag{2.165}$$

where $E^t \equiv E^a C^a$ is the tangent modulus. A and I are the cross-sectional area and the second moment of inertia, respectively.

2.3.6.1 Variational formulation for analysis of SMP thermomechanical process

Since a temperature increment can be interpreted as an equivalent static mechanical load increment, both the mechanical load and temperature increments are considered as quasi-static loadings. Also, in this section, for a mechanical loading condition, here we consider *displacement loadings* only. It is noted that the global displacement vector is represented by $\mathbf{z}$. The trial solution space is defined as

$$Z = \{\mathbf{z} \in H^2(0,L) : \mathbf{z} = \mathbf{z}_0 \text{ on } \Gamma_D\}, \tag{2.166}$$

where Γ_D is the boundary of the kinematic boundary conditions, and $\mathbf{z}_0$ denotes the prescribed displacement vector. Considering non-homogeneous displacement boundary conditions, the displacement at $(n+1)$ configuration can be decomposed into [23]

$$^{n+1}\mathbf{z} = {}^{n+1}\mathbf{w} + {}^{n+1}\mathbf{y} = {}^{n}\mathbf{z} + \Delta\mathbf{w} + \Delta\mathbf{y}, \tag{2.167}$$

where $^{n+1}\mathbf{w}$ and $^{n+1}\mathbf{y}$ are appropriate functions that satisfy nonhomogeneous and homogeneous displacement boundary conditions, respectively, and the notation $\Delta(\bullet)$ represents increment, that is, $\Delta(\bullet) = {}^{n+1}(\bullet) - {}^{n}(\bullet)$. We note again that the temperature increment also can be interpreted as an equivalent static loading. Thus, the superscript n is used to denote the mechanical load increment number in both pre-deformation (step #1) and unloading (step #3) processes, and the temperature increment number in both cooling (step #2) and heating (step #4) processes.

Considering the junction continuity condition, the linearized form of the variational equation of Eq. (2.117) can be written, as: For a given $^{n}\mathbf{d} = ({}^{n}\mathbf{z} + \Delta\mathbf{w}, {}^{n}\underset{\sim}{\mathbf{z}} + \Delta\underset{\sim}{\mathbf{w}}) \in W$, find $\Delta\mathbf{d} = (\Delta\mathbf{y}, \Delta\underset{\sim}{\mathbf{y}}) \in \bar{W}$ such that

$$\begin{aligned} &a^*({}^{n}\mathbf{z} + \Delta\mathbf{w}; \Delta\mathbf{y}, \bar{\mathbf{z}}) + \underset{\sim}{a}^*({}^{n}\underset{\sim}{\mathbf{z}} + \Delta\underset{\sim}{\mathbf{w}}; \Delta\underset{\sim}{\mathbf{y}}, \underset{\sim}{\bar{\mathbf{z}}}) + b^*({}^{n}\mathbf{d}; \Delta\mathbf{d}, \bar{\mathbf{d}}) \\ &= \ell^*({}^{n}\mathbf{z} + \Delta\mathbf{w}; \bar{\mathbf{z}}) + \underset{\sim}{\ell}^*({}^{n}\underset{\sim}{\mathbf{z}} + \Delta\underset{\sim}{\mathbf{w}}; \underset{\sim}{\bar{\mathbf{z}}}) - b({}^{n}\mathbf{d}, \bar{\mathbf{d}}), \quad \forall \bar{\mathbf{d}} \in \bar{W}, \end{aligned}$$

where the linearized strain energy form is written as

$$\begin{aligned} a^*({}^{n}\mathbf{z} + \Delta\mathbf{w}; \Delta\mathbf{y}, \bar{\mathbf{z}}) \equiv &\int_\Omega \left[\begin{array}{l} E^t A \widehat{\varepsilon}_m({}^{n}\mathbf{z} + \Delta\mathbf{w}; \Delta\mathbf{y}) \widehat{\varepsilon}_m({}^{n}\mathbf{z} + \Delta\mathbf{w}; \bar{\mathbf{z}}) \\ + N({}^{n}\mathbf{z} + \Delta\mathbf{w}) \widehat{\eta}_m({}^{n}\mathbf{z} + \Delta\mathbf{w}; \Delta\mathbf{y}, \bar{\mathbf{z}}) \end{array} \right] ds \\ &+ \int_\Omega \left[\begin{array}{l} E^t I \widehat{\omega}_b({}^{n}\mathbf{z} + \Delta\mathbf{w}; \Delta\mathbf{y}) \widehat{\omega}_b({}^{n}\mathbf{z} + \Delta\mathbf{w}; \bar{\mathbf{z}}) \\ + M({}^{n}\mathbf{z} + \Delta\mathbf{w}) \widehat{\eta}_b({}^{n}\mathbf{z} + \Delta\mathbf{w}; \Delta\mathbf{y}, \bar{\mathbf{z}}) \end{array} \right] ds. \end{aligned} \tag{2.168}$$

The residual is written as

$$\ell^*({}^{n}\mathbf{z} + \Delta\mathbf{w}; \bar{\mathbf{z}}) \equiv -\int_\Omega \left\{ \begin{array}{l} N({}^{n}\mathbf{z} + \Delta\mathbf{w}) \widehat{\varepsilon}_m({}^{n}\mathbf{z} + \Delta\mathbf{w}; \bar{\mathbf{z}}) \\ + M({}^{n}\mathbf{z} + \Delta\mathbf{w}) \widehat{\omega}_b({}^{n}\mathbf{z} + \Delta\mathbf{w}; \bar{\mathbf{z}}) \end{array} \right\} ds. \tag{2.169}$$

The force and momentum resultants are respectively obtained, from Eq. (2.165), as

$$N({}^{n}\mathbf{z} + \Delta\mathbf{w}) = E^t A \left\{ \begin{array}{l} \varepsilon_m({}^{n}\mathbf{z} + \Delta\mathbf{w}) - k_3 {}^{n}\varepsilon_m^s - {}^{n+1}\varepsilon^{th} \end{array} \right\}, \tag{2.170}$$

and

$$M({}^{n}\mathbf{z} + \Delta\mathbf{w}) = E^t I \left\{ \omega_b({}^{n}\mathbf{z} + \Delta\mathbf{w}) - k_3 {}^{n}\omega_b^s \right\}. \tag{2.171}$$

The trial solution space is defined by a product set of Eq. (2.166) for two joining patches as

$$W = \left\{ \mathbf{d} = (\mathbf{z}; \underset{\sim}{\mathbf{z}}) \,|\, (\mathbf{z}; \underset{\sim}{\mathbf{z}}) \in Z \times \underset{\sim}{Z} \right\}, \tag{2.172}$$

and the variational space is also defined by a product set of Eq. (2.118) as

$$\bar{W} = \left\{ \bar{\mathbf{d}} = (\bar{\mathbf{z}}; \underset{\sim}{\bar{\mathbf{z}}}) \,\middle|\, (\bar{\mathbf{z}}; \underset{\sim}{\bar{\mathbf{z}}}) \in \bar{Z} \times \underset{\sim}{\bar{Z}} \right\}. \tag{2.173}$$

Table 2.2: Update procedure of stored strain

(i) Calculate total strains from the solution ${}^{n+1}\mathbf{z}$ at the configuration (n+1).
(ii) Compute active strains by evaluating Eq. (2.163) using the stored strain at configuration (n) and the thermal strain at configuration (n+1).
(iii) Update stored strains at configuration (n+1) using Eq. (2.158), and save the stored strain at every Gauss integration point.

We note again that the superscript n indicates the load increment number in pre-deformation (step #1) and unloading (step #3) processes, and the temperature increment number in heating (step #2) and cooling (step #4) processes. Table 2 explains the update procedure of stored strain. As noted in Table 2.2, in our implementation, the stored strain at every Gauss integration point is saved at each temperature step, and then utilized to evaluate the active strain and the stored strain at the current temperature step.

Specifically, in the pre-deformation process (step #1) at high temperature $T = T_h$, the stored strain and thermal strain do not appear, so that ${}^{n}\varepsilon^{s}_{m} = {}^{n}\omega^{s}_{b} = {}^{n+1}\varepsilon^{th} = 0$ in Eqs. (2.170) and (2.171). Also, during both of the cooling (step #2) and heating (step #4) processes, the increment of the prescribed displacement is $\Delta\mathbf{w} = \mathbf{0}$, since the prescribed displacement $\mathbf{w}$ is fixed during the cooling process and subsequently removed by the unloading (step #3) process.

2.3.6.2 Effective Poisson's ratio calculation during shape recovery

The Poisson's ratio of structures could vary with configuration changes during the shape recovery process. One of our objectives is to design lattice structure that exhibits a desired Poisson's ratio in a specified temperature range. To calculate the Poisson's ratio for equilibrium configuration at each temperature step during the shape recovery process, it is necessary to perform an additional nonlinear structural analysis to measure the amount of lateral expansion due to the compressive displacement loading. Although the Poisson's ratio can have a strong dependence to the applied strain amount [107], we enforce only small displacement loading in the additional nonlinear analysis, such that 10% of the prescribed displacement in the pre-deformation process occurs.

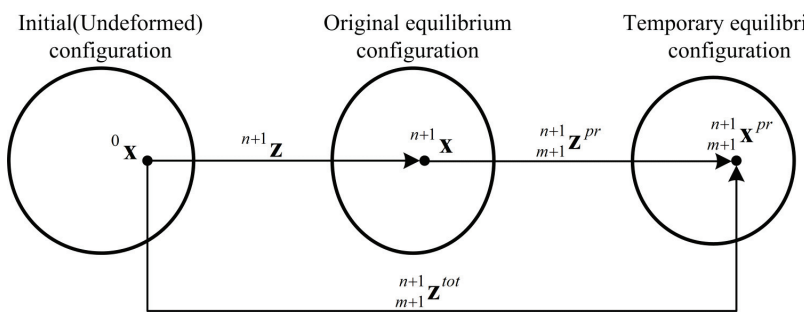

Figure 2.10: Nonlinear analysis process for Poisson's ratio calculation

Fig. 2.10 shows a schematic illustration of the additional nonlinear analysis process. An equilibrium configuration at temperature step (n+1) during shape recovery of which Poisson's

ratio is to be calculated is called "*original equilibrium configuration*". Also, an equilibrium configuration at load step (m+1) in the additional nonlinear analysis is called "*temporary equilibrium configuration*" or shortly "*temporary configuration*". At the temporary equilibrium configuration, the total displacement can be decomposed into

$$ {}^{n+1}_{m+1}\mathbf{z}^{tot} \equiv {}^{n+1}_{m+1}\mathbf{x}^{pr} - {}^{0}\mathbf{x} = {}^{n+1}\mathbf{z} + {}^{n+1}_{m+1}\mathbf{z}^{pr}, \tag{2.174} $$

where ${}^{0}\mathbf{x}$, ${}^{n+1}\mathbf{x}$, and ${}^{n+1}_{m+1}\mathbf{x}^{pr}$ denote initial, original equilibrium and temporary equilibrium configurations, respectively. ${}^{n+1}\mathbf{z} \equiv {}^{n+1}\mathbf{x} - {}^{0}\mathbf{x}$ is the displacement at the original equilibrium configuration from the undeformed one. Also, ${}^{n+1}_{m+1}\mathbf{z}^{pr} \equiv {}^{n+1}_{m+1}\mathbf{x}^{pr} - {}^{n+1}\mathbf{x}$ denotes the displacement at the temporary configuration from the original equilibrium configuration, which can be decomposed into

$$ \begin{aligned} {}^{n+1}_{m+1}\mathbf{z}^{pr} &= {}^{m+1}\mathbf{w}^{pr} + {}^{m+1}\mathbf{y}^{pr} \\ &= {}^{n+1}_{m}\mathbf{z}^{pr} + \Delta\mathbf{w}^{pr} + \Delta\mathbf{y}^{pr}, \end{aligned} \tag{2.175} $$

where ${}^{m+1}\mathbf{w}^{pr}$ and ${}^{m+1}\mathbf{y}^{pr}$ denote appropriate functions that satisfy the nonhomogeneous and homogeneous boundary conditions, respectively. m is the load increment number in the additional nonlinear analysis. Similar with Eq. (2.168), the Newton-Raphson iterative scheme to find the solution ${}^{m+1}\mathbf{y}^{pr}$ at the next configuration (m+1) can be stated as: For a given ${}^{n+1}_{m}\mathbf{d}^{tot} = ({}^{n+1}_{m}\mathbf{z}^{tot} + \Delta\mathbf{w}^{pr}; {}^{n+1}_{m}\underset{\sim}{\mathbf{z}}^{tot} + \Delta\underset{\sim}{\mathbf{w}}^{pr}) \in W$, find $\Delta\mathbf{d}^{pr} = (\Delta\mathbf{y}^{pr}, \Delta\underset{\sim}{\mathbf{y}}^{pr}) \in \bar{W}$ such that

$$ \begin{aligned} &a^*({}^{n+1}_{m}\mathbf{z}^{tot} + \Delta\mathbf{w}^{pr}; \Delta\mathbf{y}^{pr}, \bar{\mathbf{z}}) + \underset{\sim}{a}{}^*({}^{n+1}_{m}\underset{\sim}{\mathbf{z}}^{tot} + \Delta\underset{\sim}{\mathbf{w}}^{pr}; \Delta\underset{\sim}{\mathbf{y}}^{pr}, \bar{\underset{\sim}{\mathbf{z}}}) + b^*({}^{n+1}_{m}\mathbf{d}^{tot}, \Delta\mathbf{d}^{pr}, \bar{\mathbf{d}}) \\ &= \ell^*({}^{n+1}_{m}\mathbf{z}^{tot} + \Delta\mathbf{w}^{pr}; \bar{\mathbf{z}}) + \underset{\sim}{\ell}{}^*({}^{n+1}_{m}\underset{\sim}{\mathbf{z}}^{tot} + \Delta\underset{\sim}{\mathbf{w}}^{pr}; \bar{\underset{\sim}{\mathbf{z}}}) - b({}^{n+1}_{m}\mathbf{d}^{tot}, \bar{\mathbf{d}}), \quad \forall \bar{\mathbf{d}} \in \bar{W}. \end{aligned} \tag{2.176} $$

The displacement ${}^{m+1}\mathbf{y}^{pr}$ obtained by the additional nonlinear analysis is utilized to determine current positions of selected void centers from which the Poisson's ratio can be calculated [13]. A detailed procedure to calculate the Poisson's ratio using the obtained solution ${}^{m+1}\mathbf{y}^{pr}$ can be found in Appendix F.1. We note that a single load step is used for the displacement loading in the additional nonlinear analysis. On the other hand, in the examples of purely elastic materials, the displacements at each of the load steps from the undeformed configuration are utilized to calculate the position changes of void centers. That is, for purely elastic materials, the Poisson's ratio is determined within the original nonlinear analysis process and no additional nonlinear analysis is performed.

2.4 Geometrically exact shear-deformable beam structures

2.4.1 Basic kinematics

Fig. 2.11 explains the kinematics of the spatial curved beams and three coordinate systems employed. For a given arc-length parameter $s \in \Omega \equiv [0, L] \subset \mathbf{R}^1$, where L denotes an initial (undeformed) length of beam neutral axis, an initial configuration of the beam neutral axis

by a spatial curve $\boldsymbol{\varphi}_0(s) \in \mathbf{R}^3$ in the three-dimensional space $\mathbf{R}^3$ with a global Cartesian base vectors $\{\mathbf{e}_1, \mathbf{e}_2, \mathbf{e}_3\}$ such that $\mathbf{e}_1 \equiv [1,0,0]^T$, $\mathbf{e}_2 \equiv [0,1,0]^T$, and $\mathbf{e}_3 \equiv [0,0,1]^T$. Initial cross-section orientation is defined by an orthonormal frame whose base vectors are $\mathbf{j}_1(s), \mathbf{j}_2(s), \mathbf{j}_3(s) \in \mathbf{R}^3$ with the base vector $\mathbf{j}_1$ defined as a unit tangent vector such that $\mathbf{j}_1 \equiv \boldsymbol{\varphi}_{0,s}$ where $(\bullet)_{,s}$ denotes the differentiation with respect to the arc-length parameter s, which is termed tangential derivative. The initial orthonormal frame is related to the global basis through an orthogonal transformation $\boldsymbol{\Lambda}_0(s) \in SO(3)$, as

$$\mathbf{j}_I(s) = \boldsymbol{\Lambda}_0(s)\mathbf{e}_I, I = 1,2,3. \tag{2.177}$$

$SO(3)$ denotes the special orthogonal rotation group defined as

$$SO(3) \equiv \left\{ \mathbf{T} \in \mathbf{R}^{3\times 3} \middle| \mathbf{T}^T = \mathbf{T}^{-1} \text{ and } \det\mathbf{T} = 1 \right\}, \tag{2.178}$$

where $\det(\bullet)$ denotes the matrix determinant.

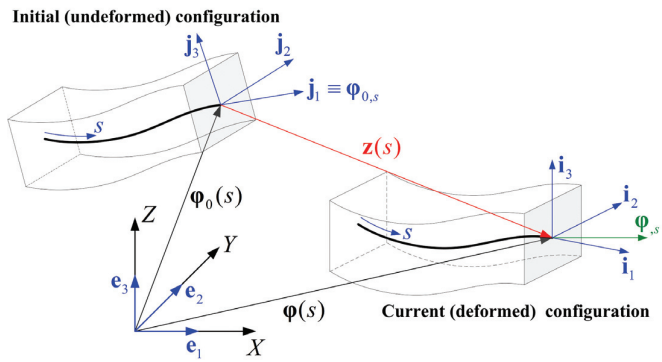

Figure 2.11: Kinematics of a spatial curved beam

A neutral axis in current (deformed) configuration is defined as a spatial curve $\boldsymbol{\varphi}(s) \in \mathbf{R}^3$, and a cross-section orientation is defined by an orthonormal frame, so called moving frame, whose base vectors are denoted as $\mathbf{i}_1(s), \mathbf{i}_2(s), \mathbf{i}_3(s) \in \mathbf{R}^3$. It is noted that, $\mathbf{i}_1(s)$ is always normal to a cross-section passing through $\boldsymbol{\varphi}(s)$, however, not necessarily tangent to the neutral axis due to shear deformations. Assuming a rigid body motion of a cross-section, the moving frame is related to the global frame through an orthogonal transformation $\boldsymbol{\Lambda} \in SO(3)$, and subsequently to the initial orthonormal frame by Eq. (2.177), as

$$\mathbf{i}_I(s) = \boldsymbol{\Lambda}(s)\mathbf{e}_I = \boldsymbol{\Lambda}(s)\boldsymbol{\Lambda}_0(s)^T\mathbf{j}_I(s) \equiv \boldsymbol{\Lambda}_L(s)\mathbf{j}_I(s), I = 1,2,3, \tag{2.179}$$

where $\boldsymbol{\Lambda}_L \in SO(3)$. For an undeformed state, it is satisfied that $\boldsymbol{\Lambda}_L = \mathbf{I}$ and $\boldsymbol{\Lambda} = \boldsymbol{\Lambda}_0$ where $\mathbf{I}$ denotes the 3×3 identity matrix. A kinematic description of admissible beam configurations is given as

$$\mathbf{x} = \boldsymbol{\varphi}(s) + \sum_{\Gamma=2}^{3} \xi^\Gamma \mathbf{i}_\Gamma(s), \tag{2.180}$$

where $[\xi^2, \xi^3]^T \in \Omega_A \subset \mathbf{R}^2$ denotes a position of material point from the neutral axis in the domain of cross-section. Evaluation of Eq. (2.180) at an undeformed state gives

$$\mathbf{x}_0 = \boldsymbol{\varphi}_0(s) + \sum_{\Gamma=2}^{3} \xi^\Gamma \mathbf{j}_\Gamma(s). \tag{2.181}$$

The neutral axis position in the current configuration is related to the initial one through the displacement field $\mathbf{z}(s) \in \mathbf{R}^3$ as

$$\mathbf{z}(s) \equiv \boldsymbol{\varphi}(s) - \boldsymbol{\varphi}_0(s). \tag{2.182}$$

We define a notation $\boldsymbol{\eta}(s) \equiv (\mathbf{z}(s), \boldsymbol{\Lambda}(s))$ which fully describes all possible deformations at each material point on the neutral axis using the displacement and the rigid body rotation of cross-section.

2.4.2 Variational formulation

An admissible perturbed solution $\boldsymbol{\eta}_\varepsilon(s) \equiv (\mathbf{z}_\varepsilon(s), \boldsymbol{\Lambda}_\varepsilon(s))$, $\forall \varepsilon \in \mathbf{R}^1$ is obtained by

$$\mathbf{z}_\varepsilon(s) = \mathbf{z}(s) + \varepsilon\delta\mathbf{z}(s), \tag{2.183}$$

and

$$\boldsymbol{\Lambda}_\varepsilon(s) = \exp\left[\varepsilon\delta\hat{\boldsymbol{\Theta}}(s)\right]\boldsymbol{\Lambda}(s), \tag{2.184}$$

where the perturbation of the orthogonal transformation matrix is defined through an exponential map of a skew-symmetric matrix $\delta\hat{\boldsymbol{\Theta}}(s) \in so(3)$. Here and hereafter, the symbol $\widehat{(\bullet)}$ represents a skew-symmetric matrix, associated with a dual vector $(\bullet) \in \mathbf{R}^3$ such that $\widehat{(\bullet)}\,\mathbf{a} = (\bullet) \times \mathbf{a}$, $\forall \mathbf{a} \in \mathbf{R}^3$. Also, $so(3)$ defines a set of all 3×3 skew-symmetric matrices, that is,

$$so(3) \equiv \left\{\mathbf{A} \in \mathbf{R}^{3\times 3} \middle| \mathbf{A}^T = -\mathbf{A}\right\}. \tag{2.185}$$

The first variation of current neutral axis position is obtained from Eqs. (2.182) and (2.183), as

$$\delta\boldsymbol{\varphi}(s) \equiv \frac{d}{d\varepsilon}\boldsymbol{\varphi}_\varepsilon(s)\Big|_{\varepsilon=0} = \bar{\mathbf{z}}(s), \tag{2.186}$$

and the first variation of the finite rotation is derived by taking the directional derivative of Eq. (2.184) as [102]

$$\delta\boldsymbol{\Lambda}(s) \equiv \frac{d}{d\varepsilon}\boldsymbol{\Lambda}_\varepsilon(s)|_{\varepsilon=0} = \hat{\bar{\boldsymbol{\Theta}}}(s)\boldsymbol{\Lambda}(s) \tag{2.187}$$

which can be interpreted as an infinitesimal rotation $\hat{\bar{\boldsymbol{\Theta}}}(s) \in so(3)$ is superposed onto a finite rotation $\boldsymbol{\Lambda}(s) \in SO(3)$. It is note that $\bar{\mathbf{z}} \equiv \delta\mathbf{z}$ and $\hat{\bar{\boldsymbol{\Theta}}} \equiv \delta\hat{\boldsymbol{\Theta}}$, where $\overline{(\bullet)} \equiv \delta(\bullet)$ denotes the first variation or the virtual quantity. Hereafter, the argument of (s) will be often omitted for convenience. By employing the kinematics of Eq. (2.180), the equations of motion of three-dimensional solids are

reduced to the following static linear and angular momentum balance equations for beams [102]

$$\left.\begin{array}{c} \mathbf{n}_{,s}+\mathbf{n}_{ext}=\mathbf{0} \\ \mathbf{m}_{,s}+\boldsymbol{\varphi}_{,s}\times\mathbf{n}+\mathbf{m}_{ext}=\mathbf{0} \end{array}\right\}, \tag{2.188}$$

where $\mathbf{n}=\mathbf{n}(s)$ and $\mathbf{m}=\mathbf{m}(s)$ respectively denote the spatial internal force and moment acting over the cross-section at $s\in\Omega$, and are respectively related to the material forms $\mathbf{N}=\mathbf{N}(s)$ and $\mathbf{M}=\mathbf{M}(s)$ via a push-forward operation as

$$\left\{\begin{array}{c}\mathbf{n}\\ \mathbf{m}\end{array}\right\}=\boldsymbol{\Pi}\mathbf{R},\ \text{where},\ \boldsymbol{\Pi}\equiv\left[\begin{array}{cc}\boldsymbol{\Lambda} & \mathbf{0}_{3\times3}\\ \mathbf{0}_{3\times3} & \boldsymbol{\Lambda}\end{array}\right]\ \text{and}\ \mathbf{R}\equiv\left\{\begin{array}{c}\mathbf{N}\\ \mathbf{M}\end{array}\right\}. \tag{2.189}$$

$\mathbf{n}_{ext}=\mathbf{n}_{ext}(s)$ and $\mathbf{m}_{ext}=\mathbf{m}_{ext}(s)$ represent distributed external force and moment, respectively, and $\mathbf{0}_{3\times3}\in\mathbf{R}^{3\times3}$ denotes the 3×3 null matrix. A variational space is defined as

$$\bar{Z}\equiv\left\{(\bar{\mathbf{z}}(s),\bar{\boldsymbol{\Theta}}(s))\in H^1(0,L)\times H^1(0,L)\,\middle|\,\bar{\mathbf{z}}(0)=\bar{\mathbf{z}}(L)=\bar{\boldsymbol{\Theta}}(0)=\bar{\boldsymbol{\Theta}}(L)=\mathbf{0}\right\}. \tag{2.190}$$

A variational equation is given as [102]

$$a(\boldsymbol{\eta},\bar{\boldsymbol{\eta}})=\ell(\bar{\boldsymbol{\eta}}),\ \ \forall\bar{\boldsymbol{\eta}}\equiv(\bar{\mathbf{z}},\bar{\boldsymbol{\Theta}})\in\bar{Z}, \tag{2.191}$$

where the strain energy and load forms are respectively defined by

$$a(\boldsymbol{\eta},\bar{\boldsymbol{\eta}})\equiv\int_\Omega\left\{\widehat{\boldsymbol{\Gamma}}(\boldsymbol{\eta};\bar{\boldsymbol{\eta}})^T\mathbf{N}+\widehat{\boldsymbol{\Omega}}(\boldsymbol{\Lambda};\bar{\boldsymbol{\Theta}})^T\mathbf{M}\right\}ds, \tag{2.192}$$

and

$$\ell(\bar{\boldsymbol{\eta}})\equiv\int_\Omega\left\{\begin{array}{c}\bar{\mathbf{z}}\\ \bar{\boldsymbol{\Theta}}\end{array}\right\}^T\left\{\begin{array}{c}\mathbf{n}_{ext}\\ \mathbf{m}_{ext}\end{array}\right\}ds. \tag{2.193}$$

$\widehat{\boldsymbol{\Gamma}}(\boldsymbol{\eta};\bar{\boldsymbol{\eta}})\equiv\bar{\boldsymbol{\Gamma}}$ and $\widehat{\boldsymbol{\Omega}}(\boldsymbol{\Lambda};\bar{\boldsymbol{\Theta}})\equiv\bar{\boldsymbol{\Omega}}$ are the first variations of material form energy-conjugate strain measures that can be written in a compact form as [102]

$$\left\{\begin{array}{c}\widehat{\boldsymbol{\Gamma}}(\boldsymbol{\eta};\bar{\boldsymbol{\eta}})\\ \widehat{\boldsymbol{\Omega}}(\boldsymbol{\Lambda};\bar{\boldsymbol{\Theta}})\end{array}\right\}=\boldsymbol{\Pi}^T\boldsymbol{\Xi}^T\left\{\begin{array}{c}\bar{\mathbf{z}}\\ \bar{\boldsymbol{\Theta}}\end{array}\right\},\ \text{where}\ \boldsymbol{\Xi}\equiv\left[\begin{array}{cc}\frac{d}{ds}\mathbf{I} & \mathbf{0}_{3\times3}\\ -[\boldsymbol{\varphi}_{,s}\times] & \frac{d}{ds}\mathbf{I}\end{array}\right], \tag{2.194}$$

where the notation $[(\bullet)\times]$ denotes a skew symmetric matrix associated with a dual vector $(\bullet)\in\mathbf{R}^3$. Through an anti-derivative process, the following material form strain measures can be obtained [78]

$$\left.\begin{array}{c}\boldsymbol{\Gamma}=\boldsymbol{\Lambda}^T\boldsymbol{\varphi}_{,s}-[1,0,0]^T\\ \hat{\boldsymbol{\Omega}}=\boldsymbol{\Lambda}^T\boldsymbol{\Lambda}_{,s}-\boldsymbol{\Lambda}_0{}^T\boldsymbol{\Lambda}_{0,s}\end{array}\right\}, \tag{2.195}$$

which is a nonlinear strain-configuration relationship, and $\boldsymbol{\Gamma}$ represents an axial-shear strain, and $\boldsymbol{\Omega}$ represents a bending-torsional strain. In this paper, a linear elastic constitutive relation

is employed as

$$\left\{ \begin{array}{c} \mathbf{N} \\ \mathbf{M} \end{array} \right\} = \left[\begin{array}{cc} \mathbf{C}_F & \mathbf{0}_{3\times3} \\ \mathbf{0}_{3\times3} & \mathbf{C}_M \end{array} \right] \left\{ \begin{array}{c} \boldsymbol{\Gamma} \\ \boldsymbol{\Omega} \end{array} \right\} \text{ and } \mathbf{C} \equiv \left[\begin{array}{cc} \mathbf{C}_F & \mathbf{0}_{3\times3} \\ \mathbf{0}_{3\times3} & \mathbf{C}_M \end{array} \right], \tag{2.196}$$

where the material constitutive tensors $\mathbf{C}_F$ and $\mathbf{C}_M$ are defined as [78]

$$\left\{ \begin{array}{l} \mathbf{C}_F = diag[EA, GA_2, GA_3] \\ \mathbf{C}_M = diag[GI_p, EI_2, EI_3] \end{array} \right. . \tag{2.197}$$

Here, $diag[a,b,c]$ defines a diagonal matrix of components a, b, and c, and the subscript $\mathbf{e}_i$ represents the basis that the tensors $\mathbf{C}_F$ and $\mathbf{C}_M$ refer to. E and G respectively denote the Young's modulus and the shear modulus. A, A_2 and A_3 denote the cross-sectional area, and two reduced cross-sectional areas, respectively. I_2 and I_3 are the two principal moments of inertia and I_p denotes the polar moment of inertia.

2.4.2.1 Pressure load problems

For a non-conservative problem, we consider a pressure load with a constant force magnitude per deformed unit arc-length of a neutral axis, whose direction is always normal to the deformed neutral axis. As the unit vector $\mathbf{i}_1$ is generally not tangent to the deformed neutral axis, it requires a new orthonormal frame $\{\mathbf{a}_1, \mathbf{a}_2, \mathbf{a}_3\}$ such that $\mathbf{a}_1$ is always tangent to neutral axis. We utilize the following expressions given in [102].

$$\mathbf{a}_1 \equiv \frac{\boldsymbol{\varphi}_{,s}}{\left\|\boldsymbol{\varphi}_{,s}\right\|}, \ \mathbf{a}_2 \equiv \frac{\mathbf{P}_{\mathbf{a}_1}\mathbf{i}_2}{\left\|\mathbf{P}_{\mathbf{a}_1}\mathbf{i}_2\right\|}, \text{ and } \mathbf{a}_3 \equiv \mathbf{a}_1 \times \mathbf{a}_2, \tag{2.198}$$

where, for brief notations, we introduce an operator $\mathbf{P}_{(\bullet)} \equiv \mathbf{I} - (\bullet) \otimes (\bullet)$ that projects a given vector $\mathbf{a} \in \mathbf{R}^3$ onto a surface normal to $(\bullet) \in \mathbf{R}^3$, so that $\mathbf{P}_{(\bullet)}\mathbf{a} \perp (\bullet)$. A pressure load vector can be resolved into the basis of Eq. (2.198) and the corresponding scalar components as

$$\tilde{\mathbf{n}}^p = \tilde{n}_2^p \mathbf{a}_2 + \tilde{n}_3^p \mathbf{a}_3. \tag{2.199}$$

Let $\tilde{s}$ denote an arc-length parameter of current neutral axis, then a current differential arc-length is related to initial one by $d\tilde{s} = \left\|\boldsymbol{\varphi}_{,s}\right\| ds$. Thus, a pressure load form can be expressed as

$$\ell_p(\boldsymbol{\eta}, \bar{\boldsymbol{\eta}}) \equiv \int_\Omega \bar{\mathbf{z}}^T \mathbf{n}^p \, ds, \tag{2.200}$$

where $\mathbf{n}^p \equiv \tilde{\mathbf{n}}^p \left\|\boldsymbol{\varphi}_{,s}\right\|$. Then, the variational equation of Eq. (2.191) is rewritten with the pressure load as

$$a(\boldsymbol{\eta}, \bar{\boldsymbol{\eta}}) = \ell(\bar{\boldsymbol{\eta}}) + \ell_p(\boldsymbol{\eta}, \bar{\boldsymbol{\eta}}), \ \ \forall \bar{\boldsymbol{\eta}} \in \bar{Z}. \tag{2.201}$$

2.4.3 Linearization and configuration update process

An incremental-iterative scheme is employed to solve Eq. (2.201) which has the geometrical nonlinearity due to the nonlinear strain-configuration relationship of Eq. (2.195) and the force nonlinearity due to the pressure load. An external load is applied incrementally and a solution of each load step $(n+1)$ is found based on the equilibrium at the previous load step (n). Using the Newton-Raphson method, the following steps are repeated until a specified convergence criterion is satisfied. The iterative scheme to find a solution ${}^{n+1}\boldsymbol{\eta} \equiv ({}^{n+1}\mathbf{z}, {}^{n+1}\boldsymbol{\Lambda})$ at the configuration $(n+1)$ is stated as: For a given ${}^{n+1}\boldsymbol{\eta}^{(i-1)}$, find $\Delta\boldsymbol{\eta}^{(i)} \equiv (\Delta\mathbf{z}^{(i)}, \Delta\boldsymbol{\Theta}^{(i)}) \in \bar{Z}$ such that

$$a^*({}^{n+1}\boldsymbol{\eta}^{(i-1)}; \Delta\boldsymbol{\eta}^{(i)}, \bar{\boldsymbol{\eta}}) = \ell^*({}^{n+1}\boldsymbol{\eta}^{(i-1)}; \bar{\boldsymbol{\eta}}), \ \ \forall \bar{\boldsymbol{\eta}} \in \bar{Z}, \tag{2.202}$$

where the left and right-hand sides respectively denote the tangent stiffness and residual. For an obtained solution increment $\Delta\boldsymbol{\eta}^{(i)}$, a configuration updated is made by

$$\left.\begin{aligned} {}^{n+1}\mathbf{z}^{(i)} &= {}^{n+1}\mathbf{z}^{(i-1)} + \Delta\mathbf{z}^{(i)}\ , \ {}^{n+1}\mathbf{z}^{(0)} = {}^{n}\mathbf{z} \\ {}^{n+1}\boldsymbol{\Lambda}^{(i)} &= \exp\left(\Delta\hat{\boldsymbol{\Theta}}^{(i)}\right) {}^{n+1}\boldsymbol{\Lambda}^{(i-1)}\ , \ {}^{n+1}\boldsymbol{\Lambda}^{(0)} = {}^{n}\boldsymbol{\Lambda} \end{aligned}\right\}. \tag{2.203}$$

Through a consistent linearization process by directional derivatives in the direction of $\Delta\boldsymbol{\eta} \equiv (\Delta\mathbf{z}, \Delta\boldsymbol{\Theta})$, the following tangent operator was derived in [102].

$$\begin{aligned} a^*({}^{n}\boldsymbol{\eta}; \Delta\boldsymbol{\eta}, \bar{\boldsymbol{\eta}}) \equiv & \int_\Omega \left(\begin{Bmatrix} \bar{\mathbf{z}} \\ \bar{\boldsymbol{\Theta}} \end{Bmatrix}^T \boldsymbol{\Xi}\boldsymbol{\Pi}\mathbf{C}\boldsymbol{\Pi}^T\boldsymbol{\Xi}^T \begin{Bmatrix} \Delta\mathbf{z} \\ \Delta\boldsymbol{\Theta} \end{Bmatrix} \right) ds + \int_\Omega \left(\begin{Bmatrix} \bar{\mathbf{z}} \\ \bar{\boldsymbol{\Theta}} \end{Bmatrix}^T \boldsymbol{\Psi}\mathbf{B}\boldsymbol{\Psi}^T \begin{Bmatrix} \Delta\mathbf{z} \\ \Delta\boldsymbol{\Theta} \end{Bmatrix} \right) ds \\ & - \ell_p^*({}^{n}\boldsymbol{\eta}; \boldsymbol{\delta\eta}, \bar{\boldsymbol{\eta}}), \end{aligned} \tag{2.204}$$

where the first and second terms on the right hand side represent the material and geometric tangent stiffness operators, respectively, and the third term represents the load stiffness operator due to the pressure load whose detailed expression will be given in the next section. The following matrix operators were defined for a compact notation.

$$\boldsymbol{\Psi} \equiv \begin{bmatrix} \frac{d}{ds}\mathbf{I} & \mathbf{0}_{3\times3} & \mathbf{0}_{3\times3} \\ \mathbf{0}_{3\times3} & \frac{d}{ds}\mathbf{I} & \mathbf{I} \end{bmatrix} \ \text{and} \ \mathbf{B} \equiv \begin{bmatrix} \mathbf{0}_{3\times3} & \mathbf{0}_{3\times3} & [-\mathbf{n}\times] \\ \mathbf{0}_{3\times3} & \mathbf{0}_{3\times3} & [-\mathbf{m}\times] \\ [\mathbf{n}\times] & \mathbf{0}_{3\times3} & [\mathbf{n}\otimes\boldsymbol{\varphi}_{,s} - (\mathbf{n}\cdot\boldsymbol{\varphi}_{,s})\mathbf{I}] \end{bmatrix}. \tag{2.205}$$

The symmetry of material stiffness is obvious, while the geometric stiffness turned out to be symmetric only at equilibrium configuration even under conservative loads [102]. The load stiffness operator is generally asymmetric. The residual of Eq. (2.202) is defined as

$$\ell^*({}^{n}\boldsymbol{\eta}; \bar{\boldsymbol{\eta}}) \equiv \ell(\bar{\boldsymbol{\eta}}) + \ell_p({}^{n}\boldsymbol{\eta}, \bar{\boldsymbol{\eta}}) - a({}^{n}\boldsymbol{\eta}, \bar{\boldsymbol{\eta}}). \tag{2.206}$$

In the update of rotation field in Eq. (2.203), the rotation at each integration point in the previous iteration step should be kept, which requires additional storages. In [102], four quaternion parameters were utilized in order to minimize the secondary storage costs and avoid the

singularity of exponential map. Details of the configuration update procedure for rotation and bending-torsional strain can be found in [102].

2.4.3.1 Linearization of pressure load vector

We present the load stiffness operator for the pressure load form of Eq. (2.200). Hereafter, a notation $D(\bullet)\cdot(*)$ represents a directional derivative of $(\bullet)$ in the direction of $(*)$. In B.1, we derive directional derivative expressions of base vectors $\mathbf{a_1}$, $\mathbf{a_2}$, and $\mathbf{a_3}$. Using Eqs. (B.1), (B.3), and (B.4), we obtain

$$\begin{aligned} D\mathbf{n}^p \cdot \Delta\boldsymbol{\eta} &\equiv \frac{d}{d\varepsilon}\mathbf{n}_\varepsilon^p\big|_{\varepsilon=0} \\ &= \left(\tilde{n}_2^p \mathbf{T}_{2\varphi}^p + \tilde{n}_3^p \mathbf{T}_{3\varphi}^p + \tilde{\mathbf{n}}^p \otimes \mathbf{a}_1\right)\Delta\mathbf{z}_{,s} + \left(\tilde{n}_2^p \mathbf{T}_{2\Theta}^p + \tilde{n}_3^p \mathbf{T}_{3\Theta}^p\right)\Delta\boldsymbol{\Theta}, \end{aligned} \tag{2.207}$$

where $D\left\|\boldsymbol{\varphi}_{,s}\right\|\cdot\Delta\mathbf{z} = \mathbf{a}_1\cdot\Delta\mathbf{z}_{,s}$ is utilized. Finally, we obtain a load stiffness expression as

$$\ell_p^*(\boldsymbol{\eta};\Delta\boldsymbol{\eta},\bar{\mathbf{z}}) \equiv D\left\{\ell_p(\boldsymbol{\eta};\bar{\boldsymbol{\eta}})\right\}\cdot\Delta\boldsymbol{\eta} = \int_\Omega \begin{Bmatrix} \bar{\mathbf{z}} \\ \bar{\Theta} \end{Bmatrix}^T \mathbf{T}^p \begin{Bmatrix} \Delta\mathbf{z}_{,s} \\ \Delta\boldsymbol{\Theta} \end{Bmatrix} ds, \tag{2.208}$$

where the following matrix $\mathbf{T}^p$ is defined for a compact notation as

$$\mathbf{T}^p \equiv \begin{bmatrix} \left(\tilde{n}_2^p \mathbf{T}_{2\varphi}^p + \tilde{n}_3^p \mathbf{T}_{3\varphi}^p + \tilde{\mathbf{n}}^p \otimes \mathbf{a}_1\right) & \tilde{n}_2^p \mathbf{T}_{2\Theta}^p + \tilde{n}_3^p \mathbf{T}_{3\Theta}^p \\ \mathbf{0}_{3\times3} & \mathbf{0}_{3\times3} \end{bmatrix}. \tag{2.209}$$

2.4.4 Isogeometric discretization

Fig. 2.7 illustrates mapping relations of a physical domain of beam neutral axis and parametric domains of arc-length parameter (Ω) and NURBS curve parametric coordinate (Ξ). The Jacobian of the mapping between physical domain ${}^0\Omega$ and parametric domain Ω is unity due to arc-length parameterization. The mapping relation between two parametric domains is given by [10]

$$s(\boldsymbol{\varphi}_0(\xi)) = \int_0^{\xi_0=\xi} \left\|\boldsymbol{\varphi}_0(\xi_0)_{,\xi_0}\right\| d\xi_0 \equiv s(\xi), \tag{2.210}$$

whose Jacobian is defined as

$$J_c \equiv s_{,\xi} = \left\|\boldsymbol{\varphi}_{0,\xi}\right\|. \tag{2.211}$$

Using an isogeometric discretization dividing a parametric domain Ξ into ne knot spans such that $\Xi = \bigcup_{e=1}^{ne}\Xi_e$, the variation of the neutral axis displacement and the infinitesimal rotation vectors are approximated by the NURBS basis function, as

$$\bar{\mathbf{z}}^h = \sum_{N=1}^{n} W_N(\xi)\bar{\mathbf{y}}_N \text{ and } \bar{\boldsymbol{\Theta}}^h = \sum_{N=1}^{n} W_N(\xi)\bar{\boldsymbol{\Theta}}_N, \tag{2.212}$$

where $\bar{\mathbf{y}}_N$ and $\bar{\boldsymbol{\Theta}}_N$ are the coefficients associated with N-th control point. In the same way, the increment of the neutral axis displacement and the incremental rotation vectors are approximated as

$$\Delta\mathbf{z}^h = \sum_{N=1}^{n} W_N(\xi)\Delta\mathbf{y}_N \text{ and } \Delta\boldsymbol{\Theta}^h = \sum_{N=1}^{n} W_N(\xi)\Delta\boldsymbol{\Theta}_N, \tag{2.213}$$

where $\Delta\mathbf{y}_N$ and $\Delta\boldsymbol{\Theta}_N$ are the N-th coefficients. Hereafter, the argument ξ will be often omitted for convenience. By substituting Eqs. (2.212) into Eqs. (2.192), (2.193) and (2.200), and through a global element assembly procedure denoted by an operator $\mathbf{A}_{e=1}^{ne}$ over whole knot spans, we have the discretization expression of Eq. (2.206) as

$$\ell^*(\boldsymbol{\eta}^h;\bar{\boldsymbol{\eta}}^h) = \mathbf{A}_{e=1}^{ne}\left[\bar{\mathbf{d}}_N{}^T\left\{\int_{\Xi_e} W_N\left(\mathbf{r}_{ext} + \begin{Bmatrix}\mathbf{n}^p\\ \mathbf{0}\end{Bmatrix}\right)J_c d\xi - \int_{\Xi_e}\Xi_N^h\boldsymbol{\Pi}\mathbf{R}J_c d\xi\right\}\right] \equiv \bar{\mathbf{d}}^T(\mathbf{F}-\mathbf{P}), \tag{2.214}$$

where $\bar{\mathbf{d}}_N \equiv [\bar{\mathbf{y}}_N{}^T, \bar{\boldsymbol{\Theta}}_N{}^T]^T$, and $N = 1{\sim}n$ is a repeated index and n denotes the number of control points having local supports in the knot span Ξ_e. $\mathbf{F}$, $\mathbf{P}$, and $\bar{\mathbf{d}}$ defines assembled global external and internal load vectors, and virtual response coefficients, respectively. Substituting Eqs. (2.212) and (2.213) into Eqs. (2.204) and (2.208), we also have

$$\begin{aligned} a^*({}^n\boldsymbol{\eta}^h;\bar{\boldsymbol{\eta}}^h,\Delta\boldsymbol{\eta}^h) &= \mathbf{A}_{e=1}^{ne}\left[\bar{\mathbf{d}}_N{}^T\left\{\int_{\Xi_e}\left(\Xi_N^h\boldsymbol{\Pi}\mathbf{C}\boldsymbol{\Pi}^T\Xi_M^h{}^T + \boldsymbol{\Psi}_N^h\mathbf{B}\boldsymbol{\Psi}_M^h{}^T - \mathbf{T}^p\Xi_{pM}^h\right)J_c d\xi\right\}\Delta\mathbf{d}_M\right] \\ &\equiv \bar{\mathbf{d}}^T\mathbf{K}_T\Delta\mathbf{d}, \end{aligned} \tag{2.215}$$

where $\Delta\mathbf{d}_N \equiv [\Delta\mathbf{y}_N{}^T, \Delta\boldsymbol{\Theta}_N{}^T]^T$, and $N, M = 1{\sim}n$ are repeated indices, and $\Delta\mathbf{d}$ denotes a global assembly of incremental response coefficients, and the following discretized matrix operators are utilized.

$$\begin{aligned} &\Xi_N^h \equiv \begin{bmatrix} W_{N,s}\mathbf{I} & \mathbf{0}_{3\times3} \\ -W_N[\boldsymbol{\varphi}_{,s}\times] & W_{N,s}\mathbf{I}\end{bmatrix},\ \Xi_{pN}^h \equiv \begin{bmatrix} W_{N,s}\mathbf{I} & \mathbf{0}_{3\times3} \\ \mathbf{0}_{3\times3} & W_N\mathbf{I}\end{bmatrix} \\ &\text{,and } \boldsymbol{\Psi}_N^h \equiv \begin{bmatrix} W_{N,s}\mathbf{I} & \mathbf{0}_{3\times3} & \mathbf{0}_{3\times3} \\ \mathbf{0}_{3\times3} & W_{N,s}\mathbf{I} & \mathbf{I}\end{bmatrix}, \end{aligned} \tag{2.216}$$

where it is noted that $W_{N,s}$ denotes the differentiation of NURBS basis function with respect to the arc-length coordinate, derived as $W_{N,s} = W_{I,\xi}/J_c$. In Eq. (2.215), $\mathbf{K}_T$ denotes an assembled global tangent stiffness matrix, and it is generally asymmetric due to the load stiffness. If conservative load considered only, it becomes symmetric only at equilibrium configurations [102]. It should be noted that $\Delta\boldsymbol{\Theta}^h$ of Eq. (2.213) represents a rotation increment vector and the NURBS basis function satisfies kronecker-delta property at patch boundary; thus, a rotation continuity condition at multi-patch junction can be automatically satisfied by a typical element assembly procedure.

2.5 Geometrically exact shear-deformable shell structures

2.5.1 Basic kinematics

The three-dimensional shell body is parameterized using a curvilinear coordinate system. The in-plane coordinates are denoted by ξ^α ($\alpha = 1,2$), and a coordinate in shell thickness direction is defined by $\xi^3 \in [-h/2, h/2]$ where h represents the thickness. Fig. 2.12 illustrates the kinematics of a shell structure undergoing large deformation in three-dimensional space. $\boldsymbol{\varphi}_0 \in \mathbf{R}^3$ and $\boldsymbol{\varphi} \in \mathbf{R}^3$ respectively denotes material point positions on initial and current shell neutral surfaces. A covariant basis on the initial neutral surface is defined by

$$\mathbf{G}_1 \equiv \boldsymbol{\varphi}_{0,\xi^1},\ \mathbf{G}_2 \equiv \boldsymbol{\varphi}_{0,\xi^2},\ \text{and}\ \mathbf{G}_3 \equiv (\mathbf{G}_1 \times \mathbf{G}_2)/\left\|\mathbf{G}_1 \times \mathbf{G}_2\right\|. \tag{2.217}$$

A covariant basis on the current neutral surface is also defined by

$$\mathbf{g}_1(\xi^1,\xi^2) \equiv \boldsymbol{\varphi}_{,\xi^1},\ \mathbf{g}_2(\xi^1,\xi^2) \equiv \boldsymbol{\varphi}_{,\xi^2},\ \text{and}\ \mathbf{g}_3(\xi^1,\xi^2) \equiv (\mathbf{g}_1 \times \mathbf{g}_2)/\left\|\mathbf{g}_1 \times \mathbf{g}_2\right\|. \tag{2.218}$$

Furthermore, three Cartesian coordinate systems are employed. *First*, $X-Y-Z$ frame is a global Cartesian coordinate system whose base vectors are $\{\mathbf{e}_1, \mathbf{e}_2, \mathbf{e}_3\}$. *Second*, a local Cartesian (orthonormal) frame in the initial (undeformed) configuration is defined by the base vectors $\{\mathbf{j}_1, \mathbf{j}_2, \mathbf{j}_3\}$ on the neutral surface. At a given material point on the initial neutral surface, $\mathbf{j}_1$ and $\mathbf{j}_2$ constitutes the tangent plane, and $\mathbf{j}_3 \equiv \mathbf{G}_3$ aligned to the thickness direction, which is called as *initial director*. *Third*, a local Cartesian frame in the current (deformed) configuration is defined by the base vectors $\{\mathbf{i}_1, \mathbf{i}_2, \mathbf{i}_3\}$ where $\mathbf{i}_3$ is always aligned to current shell thickness direction, and is called as *current director*. We note that $\mathbf{i}_3$ is not necessarily normal to the deformed neutral surface, due to the shear deformations. Thus, being by construction orthogonal to $\mathbf{i}_3$, the base vectors $\mathbf{i}_1$ and $\mathbf{i}_2$ are not necessarily tangent to the deformed neutral surface. We calculate the initial local Cartesian basis $\{\mathbf{j}_1, \mathbf{j}_2, \mathbf{j}_3\}$ using the method presented in [45] which is summarized in Appendix C.1.

A position vector $\mathbf{x}$ of an arbitrary material point of the shell body in the initial and current configuration is described respectively as

$$\mathbf{x}_0 = \boldsymbol{\varphi}_0 + \xi^3 \mathbf{j}_3. \tag{2.219}$$

and

$$\mathbf{x} = \boldsymbol{\varphi} + \xi^3 \mathbf{i}_3. \tag{2.220}$$

The current neutral surface position is related to the undeformed one by a displacement field $\mathbf{z} \equiv \mathbf{z}(\xi^1,\xi^2) \in \mathbf{R}^3$, defined as

$$\mathbf{z} \equiv \boldsymbol{\varphi} - \boldsymbol{\varphi}_0. \tag{2.221}$$

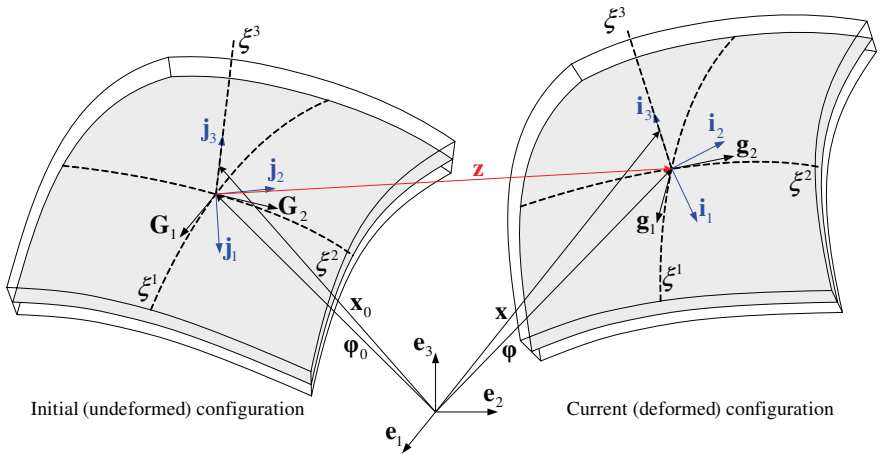

Figure 2.12: Shell kinemtaics

The initial local Cartesian basis is related to the global Cartesian basis by an orthogonal transformation $\mathbf{\Lambda}_0 \in SO(3)$, as

$$\mathbf{j}_I = \mathbf{\Lambda}_0 \mathbf{e}_I, I = 1,2,3. \tag{2.222}$$

The current local Cartesian basis is related to the initial local Cartesian basis through an orthogonal transformation tensor $\mathbf{\Lambda}_L \in SO(3)$ as

$$\mathbf{i}_I = \mathbf{\Lambda}_L \mathbf{j}_I = \mathbf{\Lambda}_L \mathbf{\Lambda}_0 \mathbf{e}_I. \tag{2.223}$$

Let $s^\alpha (\alpha = 1,2)$ denote the surface local Cartesian coordinates with the base vectors $\{\mathbf{j}_1, \mathbf{j}_2, \mathbf{j}_3\}$ in the initial configuration. Hereafter, we use the symbol $(\bullet)_{,\alpha}$ to denote the partial derivative with respect to s_α. As we are often confronted with the differentiation with respect to the local Cartesian coordinates s_1 and s_2, the following transformation for the partial differentiation is derived [48]. As we are often confronted with the differentiation with respect to the local Cartesian coordinates s^1 and s^2, the following transformation for the partial differentiation is derived [48].

$$\begin{Bmatrix} \frac{\partial}{\partial \xi^1} \\ \frac{\partial}{\partial \xi^2} \end{Bmatrix} = \begin{bmatrix} \mathbf{G}_1 \cdot \mathbf{j}_1 & \mathbf{G}_1 \cdot \mathbf{j}_2 \\ \mathbf{G}_2 \cdot \mathbf{j}_1 & \mathbf{G}_2 \cdot \mathbf{j}_2 \end{bmatrix} \begin{Bmatrix} \frac{\partial}{\partial s_1} \\ \frac{\partial}{\partial s_2} \end{Bmatrix} \equiv \mathbf{J} \begin{Bmatrix} \frac{\partial}{\partial s_1} \\ \frac{\partial}{\partial s_2} \end{Bmatrix}, \tag{2.224}$$

where $\mathbf{J}$ is assumed to be invertible due to the one-to-one correspondence between the parametric and physical domains of initial neutral surface. After introducing index notations $J_{\alpha\beta}$ and $J^{-1}_{\alpha\beta}$ $(\alpha, \beta = 1,2)$, respectively for the matrix components of $\mathbf{J}$ and its inverse $\mathbf{J}^{-1}$, and denoting the differentiation with respect to s^α as $(\bullet)_{,\alpha}$, the transformation relation can be rewritten as

$$(\bullet)_{,\alpha} = J^{-1}_{\alpha\beta} (\bullet)_{,\xi^\beta}. \tag{2.225}$$

We define a notation $\boldsymbol{\eta} \equiv \left(\mathbf{z}(\xi^1, \xi^2), \mathbf{\Lambda}_L(\xi^1, \xi^2)\right)$ which fully describes all admissible deformations at each material point on the mid-surface using the displacement and the rigid body rotation of shell director.

2.5.2 Variational formulation

An admissible perturbed solution $\boldsymbol{\eta}_\varepsilon \equiv (\mathbf{z}_\varepsilon, \boldsymbol{\Lambda}_{L\varepsilon})\ \forall \varepsilon \in \mathbf{R}^1$ is obtained by

$$\mathbf{z}_\varepsilon(\xi^1,\xi^2) = \mathbf{z}(\xi^1,\xi^2) + \varepsilon\delta\mathbf{z}(\xi^1,\xi^2) \tag{2.226}$$

and

$$\boldsymbol{\Lambda}_{L\varepsilon}(\xi^1,\xi^2) = \exp\left[\varepsilon\delta\hat{\boldsymbol{\Theta}}(\xi^1,\xi^2)\right]\boldsymbol{\Lambda}_L(\xi^1,\xi^2) \tag{2.227}$$

where the perturbation of the orthogonal transformation matrix is defined through an exponential map of a skew-symmetric matrix $\delta\hat{\boldsymbol{\Theta}} \in so(3)$. The first variation of the current neutral surface position is obtained from Eqs. (2.221) and (2.226), as

$$\delta\boldsymbol{\varphi}(\xi^1,\xi^2) \equiv \frac{d}{d\varepsilon}\boldsymbol{\varphi}_\varepsilon(\xi^1,\xi^2)\big|_{\varepsilon=0} = \bar{\mathbf{z}}(\xi^1,\xi^2), \tag{2.228}$$

and the first variation of the finite rotation is derived by taking the directional derivative of Eq. (2.227) as [102]

$$\delta\boldsymbol{\Lambda}_L(\xi^1,\xi^2) = \frac{d}{d\varepsilon}\boldsymbol{\Lambda}_{L\varepsilon}(\xi^1,\xi^2)\big|_{\varepsilon=0} = \hat{\bar{\boldsymbol{\Theta}}}(\xi^1,\xi^2)\boldsymbol{\Lambda}_L(\xi^1,\xi^2), \tag{2.229}$$

where $\overline{(\bullet)} \equiv \delta(\bullet)$ denotes the first variation or the virtual quantity, *i.e.*, $\bar{\mathbf{z}} \equiv \delta\mathbf{z}$ and $\hat{\bar{\boldsymbol{\Theta}}} \equiv \delta\hat{\boldsymbol{\Theta}}$. Eq. (2.229) can be interpreted as an infinitesimal rotation $\hat{\bar{\boldsymbol{\Theta}}} \in so(3)$ is superposed onto a finite rotation $\boldsymbol{\Lambda}_L \in SO(3)$. A variational space is defined as

$$\bar{Z} \equiv \left\{ \left(\bar{\mathbf{z}}, \bar{\boldsymbol{\Theta}}\right) \in H^1(\bar{A}) \times H^1(\bar{A}) \,\middle|\, \bar{\mathbf{z}} = \mathbf{0} \text{ and } \bar{\boldsymbol{\Theta}} = \mathbf{0} \text{ at } \partial\bar{A} \right\}, \tag{2.230}$$

where $\bar{A} \subset \mathbf{R}^2$ defines a domain of parametric coordinates ξ^1 and ξ^2 so that $(\xi^1,\xi^2) \in \bar{A}$, and its boundary is represented by $\partial\bar{A}$. Let $\mathbf{n}^\alpha$ and $\mathbf{m}^\alpha$ denote, respectively, the spatial form resultant force and moment, and $\mathbf{m}_{ext}$ and $\mathbf{n}_{ext}$ respectively represent the distributed external force and momentum resultants. The spatial form vectors are related to material forms $\mathbf{N}^\alpha$ and $\mathbf{M}^\alpha$ through a push-forward operation as

$$\left\{ \begin{array}{c} \mathbf{n}^\alpha \\ \mathbf{m}^\alpha \end{array} \right\} = \boldsymbol{\Pi}_L \left\{ \begin{array}{c} \mathbf{N}^\alpha \\ \mathbf{M}^\alpha \end{array} \right\},\ (\alpha = 1,2),\ \text{where } \boldsymbol{\Pi}_L \equiv \left[\begin{array}{cc} \boldsymbol{\Lambda}_L & \mathbf{0} \\ \mathbf{0} & \boldsymbol{\Lambda}_L \end{array} \right]. \tag{2.231}$$

A variational equation is given by [47]

$$a(\boldsymbol{\eta};\bar{\boldsymbol{\eta}}) = \ell(\bar{\boldsymbol{\eta}}),\ \ \forall\bar{\boldsymbol{\eta}} \equiv (\bar{\mathbf{z}},\bar{\boldsymbol{\Theta}}) \in \bar{Z}, \tag{2.232}$$

where the strain energy form is obtained as

$$a(\boldsymbol{\eta},\bar{\boldsymbol{\eta}}) \equiv \int_{\Omega_A} \left[\left\{ \begin{array}{c} \bar{\mathbf{E}}_\alpha \\ \bar{\mathbf{K}}_\alpha \end{array} \right\} \cdot \left\{ \begin{array}{c} \mathbf{N}^\alpha \\ \mathbf{M}^\alpha \end{array} \right\} \right] d\Omega_A, \tag{2.233}$$

and the load form is

$$\ell(\bar{\boldsymbol{\eta}}) \equiv \int_{\Omega_A} \left(\bar{\mathbf{z}} \cdot \mathbf{n}_{ext} + \bar{\boldsymbol{\Theta}} \times \mathbf{m}_{ext}\right) d\Omega_A, \tag{2.234}$$

and Ω_A denotes a physical domain of initial neutral surface. From the principle of virtual work and energy-conjugate relations, the first variations of material form strain measures are obtained by

$$\left\{ \begin{array}{c} \bar{\mathbf{E}}_\alpha \\ \bar{\mathbf{K}}_\alpha \end{array} \right\} \equiv \left\{ \begin{array}{c} \boldsymbol{\Lambda}_L{}^T(\bar{\mathbf{z}}_{,\alpha} - \bar{\boldsymbol{\Theta}} \times \boldsymbol{\varphi}_{,\alpha}) \\ \boldsymbol{\Lambda}_L{}^T \bar{\boldsymbol{\Theta}}_{,\alpha} \end{array} \right\} = \boldsymbol{\Pi}_L{}^T \boldsymbol{\Xi}_\alpha{}^T \bar{\boldsymbol{\eta}}, \text{ where } \boldsymbol{\Xi}_\alpha \equiv \left[\begin{array}{cc} (\bullet)_{,\alpha}\mathbf{I} & \mathbf{0}_{3\times 3} \\ -\left[\boldsymbol{\varphi}_{,\alpha}\times\right] & (\bullet)_{,\alpha}\mathbf{I} \end{array} \right], \tag{2.235}$$

where symbol $[(\bullet)\times]$ denotes a skew-symmetric whose dual vector is $(\bullet) \in \mathbf{R}^3$. Through an anti-derivative process, the material form strains can be retrieved, as follows [48].

$$\left. \begin{array}{c} \mathbf{E}_\alpha \equiv \boldsymbol{\Lambda}_L{}^T \boldsymbol{\varphi}_{,\alpha} - \mathbf{j}_\alpha \\ \hat{\mathbf{K}}_\alpha \equiv \boldsymbol{\Lambda}_L{}^T \boldsymbol{\Lambda}_{L,\alpha} \end{array} \right\}. \tag{2.236}$$

For notational conveniences in the constitutive relations, the component form expressions are introduced. The component of the material form strain measures in the initial local Cartesian frame are obtained by $E_{I\alpha} \equiv \mathbf{E}_\alpha \cdot \mathbf{j}_I$ and $K_{I\alpha} \equiv \mathbf{K}_\alpha \cdot \mathbf{j}_I$, then we have [48]

$$E_{\beta\alpha} = \mathbf{E}_\alpha \cdot \mathbf{j}_\beta, \;\; K_{\beta\alpha} = \mathbf{K}_\alpha \cdot \mathbf{j}_\beta, \text{ and } E_{3\alpha} = \mathbf{E}_\alpha \cdot \mathbf{j}_3 \equiv \Gamma_\alpha, \tag{2.237}$$

which, respectively, define the membrane, bending, and shear strain components. Similarly, the force and momentum resultant components are obtained by $N^{I\alpha} \equiv \mathbf{N}^\alpha \cdot \mathbf{j}_I$ and $M^{I\alpha} \equiv \mathbf{M}^\alpha \cdot \mathbf{j}_I$, then we have

$$N^{\beta\alpha} = \mathbf{N}^\alpha \cdot \mathbf{j}_\beta, \; M^{\beta\alpha} = \mathbf{M}^\alpha \cdot \mathbf{j}_\beta, \text{ and } N^{3\alpha} = \mathbf{N}^\alpha \cdot \mathbf{j}_3 \equiv Q^\alpha, \tag{2.238}$$

which, respectively, define the membrane force, bending moment, shear force components. In [48], it was verified that $M^{3\alpha} = 0$ from the basic shell kinematic description of Eq. (2.220), so that the associated work-conjugate component $K_{3\alpha} = \mathbf{K}_\alpha \cdot \mathbf{j}_3$ does not contribute to the strain energy, thus, in the below, the constitutive relation for the moment component $M^{3\alpha}$ is not provided. It is assumed that only the symmetric part of the stress resultant contributes to the strain energy, then the isotropic linear elastic constitutive equations for the stress resultants are [48]

$$N^{(\alpha\beta)} = C_N^{\alpha\beta\gamma\lambda} E_{(\gamma\lambda)}, \; C_N^{\alpha\beta\gamma\lambda} = \frac{Eh}{1-\nu^2}\left\{\nu\delta_{\alpha\gamma}\delta_{\beta\lambda} + (1-\nu)\delta_{\alpha\beta}\delta_{\gamma\lambda}\right\}, \tag{2.239}$$

and

$$\tilde{M}^{(\alpha\beta)} = C_M^{\alpha\beta\gamma\lambda} \tilde{K}_{(\gamma\lambda)}, \; C_M^{\alpha\beta\gamma\lambda} = \frac{Eh^3}{12(1-\nu^2)}\left\{\nu\delta_{\alpha\gamma}\delta_{\beta\lambda} + (1-\nu)\delta_{\alpha\beta}\delta_{\gamma\lambda}\right\}, \tag{2.240}$$

where $\delta_{\alpha\beta}$ denotes the kronecker-delta symbol for the indices α and β, and the bending moment and curvature components are renumbered for convenience as

$$\tilde{M}^{\alpha\gamma} = e_{\alpha\beta} M^{\beta\gamma}, \; \tilde{K}_{\alpha\gamma} = e_{\alpha\beta} K_{\beta\gamma} \text{ where } e_{\alpha\beta} = \left[\begin{array}{cc} 0 & -1 \\ 1 & 0 \end{array} \right], \tag{2.241}$$

and $e_{\alpha\beta}$ represents the two-dimensional alternator tensor, and the Greek repeated indices belong to $\{1,2\}$. Also, we assume linear elastic constitutive relation for the shear stress and strain as well [48]

$$Q^{\alpha} = C_Q^{\alpha\beta}\Gamma_{\beta},\ C_Q^{\alpha\beta} = \frac{Eh}{2(1+\nu)}\delta_{\alpha\beta} \equiv Gh\delta_{\alpha\beta}, \tag{2.242}$$

where E, G, and ν respectively denote the Young's modulus, shear modulus, and Poisson's ratio. The membrane strain is decomposed into the symmetric and skew-symmetric parts as

$$E_{\alpha\beta} = \frac{1}{2}\left(E_{\alpha\beta} + E_{\beta\alpha}\right) + \frac{1}{2}\left(E_{\alpha\beta} - E_{\beta\alpha}\right) \equiv E_{(\alpha\beta)} + E_{[\alpha\beta]}. \tag{2.243}$$

The bending strain component was shown to be symmetric so that [48]

$$\tilde{K}_{\alpha\beta} = \frac{1}{2}\left(\tilde{K}_{\alpha\beta} + \tilde{K}_{\beta\alpha}\right) \equiv \tilde{K}_{(\alpha\beta)}. \tag{2.244}$$

For a stabilization against drilling rotation DOFs, a regularized form of the internal virtual work is given as [48]

$$\begin{aligned} a^{\gamma}(\boldsymbol{\eta},\tilde{\boldsymbol{\eta}}) &\equiv \int_{\Omega_A}\left(\delta E_{(\alpha\beta)}C_N^{\alpha\beta\gamma\lambda}E_{(\gamma\lambda)} + \delta\tilde{K}_{(\alpha\beta)}C_M^{\alpha\beta\gamma\lambda}\tilde{K}_{(\gamma\lambda)} + \delta\Gamma_{\alpha}C_Q^{\alpha\beta}\Gamma_{\beta} + \delta E_{[\alpha\beta]}\gamma E_{[\alpha\beta]}\right)d\Omega_A \\ &= \int_{\Omega_A}\left\{\begin{array}{c}\bar{\mathbf{E}}_{\alpha}\\ \bar{\mathbf{K}}_{\alpha}\end{array}\right\}\cdot\left\{\begin{array}{c}\mathbf{N}_{\gamma}^{\alpha}\\ \mathbf{M}_{Q}^{\alpha}\end{array}\right\}d\Omega_A, \end{aligned} \tag{2.245}$$

where γ denotes a regularization parameter, and $\mathbf{N}_{\gamma}^{\alpha} \equiv \left(\mathbf{C}_N^{\alpha\beta} + \mathbf{C}_{\gamma}^{\alpha\beta} + \mathbf{C}_Q^{\alpha\beta}\right)\mathbf{E}_{\beta}$ and $\mathbf{M}_Q^{\alpha} \equiv \mathbf{C}_M^{\alpha\beta}\mathbf{K}_{\beta}$ are respectively material form regularized internal force resultant and momentum resultant, and they are rewritten in a compact form for convenience as

$$\mathbf{R}_{\gamma}^{\alpha} \equiv \left\{\begin{array}{c}\mathbf{N}_{\gamma}^{\alpha}\\ \mathbf{M}_{Q}^{\alpha}\end{array}\right\} = \mathbf{C}^{\alpha\beta}\left\{\begin{array}{c}\mathbf{E}_{\beta}\\ \mathbf{K}_{\beta}\end{array}\right\},\ \text{and}\ \mathbf{C}^{\alpha\beta} \equiv \left[\begin{array}{cc}\left(\mathbf{C}_N^{\alpha\beta} + \mathbf{C}_{\gamma}^{\alpha\beta} + \mathbf{C}_Q^{\alpha\beta}\right) & \mathbf{0}_{3\times3}\\ \mathbf{0}_{3\times3} & \mathbf{C}_M^{\alpha\beta}\end{array}\right]. \tag{2.246}$$

For future use, we define the spatial form regularized internal force resultant and momentum resultant by the push-forward operation as

$$\mathbf{n}_{\gamma}^{\alpha} \equiv \boldsymbol{\Lambda}\boldsymbol{N}_{\gamma}^{\alpha},\ \text{and}\ \mathbf{m}_{Q}^{\alpha} \equiv \boldsymbol{\Lambda}\boldsymbol{M}_{Q}^{\alpha}. \tag{2.247}$$

Detailed expressions of the constitutive matrices $\mathbf{C}_N^{\alpha\beta}$, $\mathbf{C}_{\gamma}^{\alpha\beta}$, and $\mathbf{C}_Q^{\alpha\beta}$ can be found in Appendix C.1. Then, the variational equation of Eq. (2.232) is rewritten in a regularized form as

$$a^{\gamma}(\boldsymbol{\eta};\tilde{\boldsymbol{\eta}}) = \ell(\tilde{\boldsymbol{\eta}}),\ \forall\tilde{\boldsymbol{\eta}} \equiv (\tilde{\mathbf{z}},\tilde{\boldsymbol{\Theta}}) \in \bar{Z}. \tag{2.248}$$

In this work, the regularization parameter γ is chosen as equal to the shear modulus, *i.e.*, $\gamma \equiv G$ [48].

2.5.3 Linearization and configuration update procedure

We employ an incremental-iterative scheme to solve Eq. (2.248) which is nonlinear with respect to the response $\boldsymbol{\eta} \equiv (\mathbf{z}, \boldsymbol{\Lambda}_L)$. The external load is applied incrementally and the solution of each load step $(n+1)$ is found based on the equilibrium at the previous load step (n). Using the Newton-Raphson iterative method, the following steps are repeated until the specified convergence criterion is satisfied. The Newton-Raphson iterative scheme to obtain the solution ${}^{n+1}\boldsymbol{\eta} \equiv ({}^{n+1}\mathbf{z}, {}^{n+1}\boldsymbol{\Lambda}_L)$ at the configuration $(n+1)$ is stated as: For a given ${}^{n+1}\boldsymbol{\eta}^{(i-1)}$, find $\Delta\boldsymbol{\eta}^{(i)} \equiv (\Delta\mathbf{z}^{(i)}, \Delta\boldsymbol{\Theta}^{(i)}) \in \bar{Z}$ such that

$$a^{\gamma *}({}^{n+1}\boldsymbol{\eta}^{(i-1)}; \Delta\boldsymbol{\eta}^{(i)}, \bar{\boldsymbol{\eta}}) = \ell^{*}({}^{n+1}\boldsymbol{\eta}^{(i-1)}; \bar{\boldsymbol{\eta}}), \tag{2.249}$$

where the neutral surface position is updated by an incremental displacement as

$${}^{n+1}\mathbf{z}^{(i)} = {}^{n+1}\mathbf{z}^{(i-1)} + \Delta\mathbf{z}^{(i)}\ ,\ {}^{n+1}\mathbf{z}^{(0)} = {}^{n}\mathbf{z}^{(0)}, \tag{2.250}$$

and the orthogonal transformation tensor is updated by a multiplicative manner as

$${}^{n+1}\boldsymbol{\Lambda}_L^{(i)} = \exp\left(\Delta\boldsymbol{\Theta}^{(i)}\right) {}^{n+1}\boldsymbol{\Lambda}_L^{(i-1)}\ ,\ {}^{n+1}\boldsymbol{\Lambda}_L^{(0)} = {}^{n}\boldsymbol{\Lambda}_L^{(0)}, \tag{2.251}$$

which is an algorithmic counterpart of Eq. (2.227). The configuration update procedure presented in [102] is employed as in the previous section 2.4.

The linearization of the virtual strains and multiplying the regularized resultant force and moments yields, after some algebraic manipulations, the following.

$$\left.\begin{aligned} \Delta\bar{\mathbf{E}}_\alpha \cdot \mathbf{N}_\gamma^\alpha &= -\bar{\mathbf{z}}_{,\alpha} \cdot \left(\mathbf{n}_\gamma^\alpha \times \Delta\boldsymbol{\Theta}\right) + \bar{\boldsymbol{\Theta}} \cdot \left[\mathbf{n}_\gamma^\alpha \times \Delta\mathbf{z}_{,\alpha} + \left\{\left(\mathbf{n}_\gamma^\alpha \otimes \boldsymbol{\varphi}_{,\alpha}\right) - \left(\mathbf{n}_\gamma^\alpha \cdot \boldsymbol{\varphi}_{,\alpha}\right)\mathbf{I}\right\}\Delta\boldsymbol{\Theta}\right] \\ \Delta\bar{\mathbf{K}}_\alpha \cdot \mathbf{M}_Q^\alpha &= -\bar{\boldsymbol{\Theta}}_{,\alpha} \cdot \left(\mathbf{m}_Q^\alpha \times \Delta\boldsymbol{\Theta}\right) \end{aligned}\right\}, \tag{2.252}$$

which can be rewritten in a compact form as

$$\Delta\bar{\mathbf{E}}_\alpha \cdot \mathbf{N}_\gamma^\alpha + \Delta\bar{\mathbf{K}}_\alpha \cdot \mathbf{M}_Q^\alpha = \left(\boldsymbol{\Psi}_\alpha{}^T \left\{ \begin{array}{c} \bar{\mathbf{z}} \\ \bar{\boldsymbol{\Theta}} \end{array} \right\}\right) \cdot \left(\mathbf{B}_\alpha \boldsymbol{\Psi}_\alpha{}^T \left\{ \begin{array}{c} \Delta\mathbf{z} \\ \Delta\boldsymbol{\Theta} \end{array} \right\}\right), \tag{2.253}$$

where the matrix operators are defined as

$$\boldsymbol{\Psi}_\alpha \equiv \left[\begin{array}{ccc} (\bullet)_{,\alpha} & \mathbf{0}_{3\times3} & \mathbf{0}_{3\times3} \\ \mathbf{0}_{3\times3} & (\bullet)_{,\alpha} & \mathbf{I} \end{array} \right], \text{ and } \mathbf{B}_\alpha \equiv \left[\begin{array}{ccc} \mathbf{0}_{3\times3} & \mathbf{0}_{3\times3} & -\left[\mathbf{n}_\gamma^\alpha \times\right] \\ \mathbf{0}_{3\times3} & \mathbf{0}_{3\times3} & -\left[\mathbf{m}_Q^\alpha \times\right] \\ \left[\mathbf{n}_\gamma^\alpha \times\right] & \mathbf{0}_{3\times3} & \left\{\left(\mathbf{n}_\gamma^\alpha \otimes \boldsymbol{\varphi}_{,\alpha}\right) - \left(\mathbf{n}_\gamma^\alpha \cdot \boldsymbol{\varphi}_{,\alpha}\right)\mathbf{I}\right\} \end{array} \right]. \tag{2.254}$$

Also, by using the constitutive relation of Eq. (2.246) and Eq. (2.235), we have

$$\bar{\mathbf{E}}_\alpha \cdot \left(\mathbf{C}_N^{\alpha\beta} + \mathbf{C}_\gamma^{\alpha\beta} + \mathbf{C}_Q^{\alpha\beta}\right)\Delta\mathbf{E}_\beta + \bar{\mathbf{K}}_\alpha \cdot \mathbf{C}_M^{\alpha\beta}\Delta\mathbf{K}_\beta = \left(\boldsymbol{\Xi}_\alpha{}^T \bar{\boldsymbol{\eta}}\right) \cdot \left(\boldsymbol{\Pi}\mathbf{C}^{\alpha\beta}\boldsymbol{\Pi}^T \boldsymbol{\Xi}_\beta{}^T \left\{ \begin{array}{c} \Delta\mathbf{z} \\ \Delta\boldsymbol{\Theta} \end{array} \right\}\right). \tag{2.255}$$

Using Eqs. (2.255) and (2.253), the linearized strain energy form in Eq. (2.249) is derived as

$$a^{\gamma*}(\boldsymbol{\eta};\bar{\boldsymbol{\eta}},\Delta\boldsymbol{\eta}) = \int_{\Omega_A}\left\{\left({\boldsymbol{\Xi}_\alpha}^T\left\{\begin{array}{c}\bar{\mathbf{z}}\\ \bar{\boldsymbol{\Theta}}\end{array}\right\}\right)\cdot\left(\boldsymbol{\Pi}\mathbf{C}^{\alpha\beta}\boldsymbol{\Pi}^T{\boldsymbol{\Xi}_\beta}^T\left\{\begin{array}{c}\Delta\mathbf{z}\\ \Delta\boldsymbol{\Theta}\end{array}\right\}\right)\right\}d\Omega_A$$
$$+\int_{\Omega_A}\left\{\left({\boldsymbol{\Psi}_\alpha}^T\left\{\begin{array}{c}\bar{\mathbf{z}}\\ \bar{\boldsymbol{\Theta}}\end{array}\right\}\right)\cdot\left(\mathbf{B}_\alpha{\boldsymbol{\Psi}_\alpha}^T\left\{\begin{array}{c}\Delta\mathbf{z}\\ \Delta\boldsymbol{\Theta}\end{array}\right\}\right)\right\}d\Omega_A, \tag{2.256}$$

where the first and second integral terms respectively represent the material and geometric tangent stiffness parts. The residual in Eq. (2.249) is obtained by

$$\ell^*({}^n\boldsymbol{\eta};\bar{\boldsymbol{\eta}}) \equiv \ell(\bar{\boldsymbol{\eta}}) - a({}^n\boldsymbol{\eta},\bar{\boldsymbol{\eta}}). \tag{2.257}$$

2.5.4 Isogeometric discretization

The initial neutral surface configuration is expressed by using the NURBS basis function as

$$\boldsymbol{\varphi}_0 = \sum_{N=1}^{n}\tilde{W}_N(\xi^1,\xi^2)\tilde{\mathbf{B}}_N. \tag{2.258}$$

We define the following surface convected basis in the initial configuration. A differential surface area element $d\Omega_A$ of physical domain is related to that of the NURBS parametric domain $d\Xi_A$ through

$$d\Omega_A = \tilde{J}d\Xi_A, \tag{2.259}$$

and the initial surface Jacobian is

$$\tilde{J} \equiv \|\mathbf{G}_1\times\mathbf{G}_2\|. \tag{2.260}$$

Consider an isogeometric discretization $\Xi_A = \bigcup_{e=1}^{ne}\Xi_{Ae}$, where $\Xi_{Ae}\subset\Xi_A$ denotes the e-th knot element mapped into a surface segment of the physical domain Ω_A, and ne denotes the total number of knot elements. The variation of the displacement and the rotation vectors are approximated by the NURBS basis function, as

$$\bar{\mathbf{z}}^h = \sum_{N=1}^{n}\tilde{W}_N(\xi^1,\xi^2)\bar{\mathbf{y}}_N \text{ and } \bar{\boldsymbol{\Theta}}^h = \sum_{N=1}^{n}\tilde{W}_N(\xi^1,\xi^2)\bar{\boldsymbol{\Theta}}_N, \tag{2.261}$$

where $\bar{\mathbf{y}}_N$ and $\bar{\boldsymbol{\Theta}}_N$ are the coefficients, associated with N-th control point. In the same way, the incremental displacement and rotation vectors are approximated, as

$$\Delta\mathbf{z}^h = \sum_{N=1}^{n}\tilde{W}_N(\xi^1,\xi^2)\Delta\mathbf{y}_N \text{ and } \Delta\boldsymbol{\Theta}^h(\xi,\eta) = \sum_{N=1}^{n}\tilde{W}_N(\xi^1,\xi^2)\Delta\boldsymbol{\Theta}_N, \tag{2.262}$$

where $\Delta\mathbf{y}_N$ and $\Delta\boldsymbol{\Theta}_N$ are the N-th coefficients of the corresponding increments. For brevity of notations, we often omit the arguments ξ and η of NURBS basis functions for convenience. For convenience, we define $W_{N,\alpha}$ ($\alpha = 1,2$) which is calculated from Eq. (2.225), as

$$W_{N,\alpha} \equiv J^{-1}_{\alpha\beta} W_{N,\xi^\beta}, \tag{2.263}$$

which can be rewritten as

$$\left\{ \begin{array}{c} W_{N,1} \\ W_{N,2} \end{array} \right\} \equiv \mathbf{J}^{-1} \left\{ \begin{array}{c} W_{N,\xi^1} \\ W_{N,\xi^2} \end{array} \right\}. \tag{2.264}$$

Substituting Eq. (2.261) into Eqs. (2.245) and (2.234), and using Eq. (2.259) gives the following discretization expression of Eq. (2.257).

$$\ell^*({}^n\boldsymbol{\eta}^h; \bar{\boldsymbol{\eta}}^h) = \mathbf{A}_{e=1}^{ne} \left[\bar{\mathbf{d}}_N{}^T \left\{ \int_{\Xi_{Ae}} \left(W_N \left\{ \begin{array}{c} \mathbf{n}_{ext} \\ \mathbf{m}_{ext} \end{array} \right\} - \Xi^h_{\alpha N} \boldsymbol{\Pi} \mathbf{R}^\alpha_\gamma \right) \tilde{J} d\xi^1 d\xi^2 \right\} \right] \equiv \bar{\mathbf{d}}^T \mathbf{P}. \tag{2.265}$$

where $\bar{\mathbf{d}}_N \equiv \left[\bar{\mathbf{y}}_N{}^T, \bar{\boldsymbol{\Theta}}_N{}^T \right]^T$, and n denotes the control points belongs to the local support of knot span Ξ_{Ae}, and ne denotes the total number of knot elements, and

$$\Xi^h_{\alpha N} \equiv \left[\begin{array}{cc} W_{N,\alpha}\mathbf{I} & \mathbf{0}_{3\times 3} \\ -W_N[\boldsymbol{\varphi}_{,\alpha}\times] & W_{N,\alpha}\mathbf{I} \end{array} \right], \ \alpha = 1,2, \tag{2.266}$$

and $\mathbf{P}$ denotes the assembled global internal force vector. Substitution of Eqs. (2.261) and (2.262) into Eq. (2.256) yields the following discretized linearized strain energy form.

$$\begin{aligned} a^{\gamma*}({}^n\boldsymbol{\eta}^h; \bar{\boldsymbol{\eta}}^h, \Delta\boldsymbol{\eta}^h) &= \mathbf{A}_{e=1}^{ne} \left[\bar{\mathbf{d}}_N{}^T \left\{ \int_{\Xi_{Ae}} \left(\Xi^h_{\alpha N} \boldsymbol{\Pi} \mathbf{C}^{\alpha\beta} \boldsymbol{\Pi}^T \Xi^h_{\beta M}{}^T + \boldsymbol{\Psi}^h_{\alpha N} \mathbf{B}_\alpha \boldsymbol{\Psi}^h_{\alpha M}{}^T \right) d\xi^1 d\xi^2 \right\} \Delta\mathbf{d}_M \right] \\ &\equiv \bar{\mathbf{d}}^T \mathbf{K}_T \Delta\mathbf{d} \end{aligned} \tag{2.267}$$

where $\Delta\mathbf{d}_N \equiv \left[\Delta\mathbf{y}_N{}^T, \Delta\boldsymbol{\Theta}_N{}^T \right]^T$, and $\Delta\mathbf{d}$ denotes a global assembly of incremental response coefficients, and $\mathbf{K}_T$ denotes the consistent tangent stiffness matrix. The discretized matrix operators in the above are defined by

$$\boldsymbol{\Psi}^h_{\alpha N} \equiv \left[\begin{array}{ccc} W_{N,\alpha}\mathbf{I} & \mathbf{0}_{3\times 3} & \mathbf{0}_{3\times 3} \\ \mathbf{0}_{3\times 3} & W_{N,\alpha}\mathbf{I} & \mathbf{I} \end{array} \right]. \tag{2.268}$$

2.6 Elastic wave propagation in periodic structures

We investigate a plane wave propagations in infinite periodic lattice structure using unit cell and the Bloch periodic boundary condition.

2.6.1 Bloch theorem

Wave propagation in periodic structures is investigated using the Bloch theorem, which enables to reduce the computation domain to a single unit cell by taking advantage of periodic boundary conditions. An infinite periodic material is described by a periodic arrangement of a primitive unit cell through the lattice base vectors $\mathbf{b}_i (i = 1,2,3)$, so that the position of any point $\mathbf{p}$ within the lattice is related to the corresponding position in the unit cell $\mathbf{r}_0$ as

$$\mathbf{r}_p = \mathbf{r}_0 + n_1\mathbf{b}_1 + n_2\mathbf{b}_2 + n_3\mathbf{b}_3, \tag{2.269}$$

where $n_i (i = 1,2,3)$ are integers. The Bloch theorem connects a response at any point $\mathbf{p}$ in the lattice to that of the corresponding point in the unit cell through

$$\left.\begin{aligned} \mathbf{z}(\mathbf{r}_p, t) &= \mathbf{z}(\mathbf{r}_0, t)e^{\mathbf{k}\cdot(\mathbf{r}_p-\mathbf{r}_0)} = \mathbf{z}(\mathbf{r}_0, t)e^{n_1\mu_1+n_2\mu_2+n_3\mu_3} \\ \boldsymbol{\theta}(\mathbf{r}_p, t) &= \boldsymbol{\theta}(\mathbf{r}_0, t)e^{\mathbf{k}\cdot(\mathbf{r}_p-\mathbf{r}_0)} = \boldsymbol{\theta}(\mathbf{r}_0, t)e^{n_1\mu_1+n_2\mu_2+n_3\mu_3} \end{aligned}\right\}, \tag{2.270}$$

where $\mathbf{z}(\mathbf{r}_p, t)$ and $\boldsymbol{\theta}(\mathbf{r}_p, t)$ denote the infinitesimal displacement and rotation vectors at the position $\mathbf{r}_p$ and time t, respectively, and $\mathbf{k}$ denotes the wave vector, and the propagation constant components $\mu_i = \mathbf{k}\cdot\mathbf{b}_i$ $(i = 1,2,3)$ are complex numbers such that their real and imaginary parts respectively represent the attenuation and phase constants. In this paper, we assume a purely propagating wave, thus, $\mathrm{Re}(\mu_i) = 0$, for $i = 1,2,3$. We define a notation $\mu \equiv [\mu_1, \mu_2, \mu_3]^T$ for convenience. To fulfill the periodicity of structural responses, from Eq. (2.270), the wave vector is defined in reciprocal lattice bases $\mathbf{b}_i^* (i = 1,2,3)$, defined in a way that satisfy the relation $\mathbf{b}_i \cdot \mathbf{b}_j^* = 2\pi\delta_{ij}$ where δ_{ij} denotes the kronecker-delta symbol, as [9]

$$\mathbf{b}_1^* = 2\pi\frac{\mathbf{b}_2 \times \mathbf{b}_3}{\mathbf{b}_1 \cdot (\mathbf{b}_2 \times \mathbf{b}_3)},\ \mathbf{b}_2^* = 2\pi\frac{\mathbf{b}_3 \times \mathbf{b}_1}{\mathbf{b}_1 \cdot (\mathbf{b}_2 \times \mathbf{b}_3)},\ \text{and}\ \mathbf{b}_3^* = 2\pi\frac{\mathbf{b}_1 \times \mathbf{b}_2}{\mathbf{b}_1 \cdot (\mathbf{b}_2 \times \mathbf{b}_3)}. \tag{2.271}$$

2.6.1.1 Genearlized Hermitian eigenvalue problem

A beam neutral axis is arc-length parameterized, and let s denote the arc-length coordinate. Assuming time-harmonic solutions, we have

$$\left.\begin{aligned} \mathbf{z}(s, t) &= \mathbf{z}(s)e^{-i\omega t} \\ \boldsymbol{\theta}(s, t) &= \boldsymbol{\theta}(s)e^{-i\omega t} \end{aligned}\right\}, \tag{2.272}$$

where $i^2 = -1$, and ω denotes the angular frequency. We define response amplitudes $\mathbf{z} \equiv \mathbf{z}(s)$ and $\boldsymbol{\theta} \equiv \boldsymbol{\theta}(s)$ for convenience, and they respectively represent the infinitesimal displacement and rotation vectors. Using Eq. (2.272) and the principle of virtual work, we have the following variational equation.

$$a(\boldsymbol{\eta}, \bar{\boldsymbol{\eta}}) = \omega^2 d(\boldsymbol{\eta}, \bar{\boldsymbol{\eta}}),\ \forall \bar{\boldsymbol{\eta}} \in \bar{Z}, \tag{2.273}$$

where $\boldsymbol{\eta} \equiv (\mathbf{z}, \boldsymbol{\theta})$, and $\bar{\boldsymbol{\eta}}$ denotes the corresponding virtual one, and $\bar{Z}$ denotes the kinematically admissible space of virtual responses. Here and hereafter the $\overline{(\bullet)}$ represents a virtual quantity or the first variation. The strain energy and kinetic energy bilinear forms are respectively obtained as

$$a(\boldsymbol{\eta}, \bar{\boldsymbol{\eta}}) \equiv \int_{\Omega} \left(\bar{\boldsymbol{\Gamma}}_{lin}{}^{T} \mathbf{C}_F \boldsymbol{\Gamma}_{lin} + \bar{\boldsymbol{\Omega}}_{lin}{}^{T} \mathbf{C}_M \boldsymbol{\Omega}_{lin} \right) ds, \tag{2.274}$$

and

$$d(\boldsymbol{\eta}, \bar{\boldsymbol{\eta}}) \equiv \int_{\Omega} \left(\bar{\mathbf{z}}^{T} \rho A \mathbf{z} + \bar{\boldsymbol{\theta}} \mathbf{I}_\rho \boldsymbol{\theta} \right) ds, \tag{2.275}$$

where ρ and $\mathbf{I}_\rho \equiv \rho \cdot diag[I_p, I_2, I_3]$ respectively denote the mass density and inertia tensor. For an infinitesimal deformation shear-deformable beam model, the following linearized strain measures can be obtained by evaluating Eq. (2.194) at undeformed configuration as

$$\left.\begin{array}{c} \boldsymbol{\Gamma}_{lin} \equiv \boldsymbol{\Gamma}_{lin}(\mathbf{z}, \boldsymbol{\theta}) = \boldsymbol{\Lambda}_0{}^{T} (\mathbf{z}_{,s} + \mathbf{j}_1 \times \boldsymbol{\theta}) \\ \boldsymbol{\Omega}_{lin} \equiv \boldsymbol{\Omega}_{lin}(\boldsymbol{\theta}) = \boldsymbol{\Lambda}_0{}^{T} \boldsymbol{\theta}_{,s} \end{array}\right\} \tag{2.276}$$

where $\boldsymbol{\Lambda}_0 = \boldsymbol{\Lambda}_0(s)$ denotes an initial orthogonal transformation matrix such that $\mathbf{j}_I(s) = \boldsymbol{\Lambda}_0(s)\mathbf{e}_I$ ($I = 1,2,3$), and $\mathbf{j}_I = \mathbf{j}_I(s)$ and $\mathbf{e}_I$ respectively denote the initial orthonormal and global Cartesian basis, and $\mathbf{j}_1$ is a unit tangent vector. $(\bullet)_{,s}$ represents the differentiation with respect to s. The virtual strains are $\bar{\boldsymbol{\Gamma}}_{lin} \equiv \boldsymbol{\Gamma}_{lin}(\bar{\mathbf{z}}, \bar{\boldsymbol{\theta}})$ and $\bar{\boldsymbol{\Omega}}_{lin} \equiv \boldsymbol{\Omega}_{lin}(\bar{\boldsymbol{\theta}})$.

A linear elastic constitutive relation is given by

$$\left.\begin{array}{c} \mathbf{N}_{lin} = \mathbf{C}_F \boldsymbol{\Gamma}_{lin} \\ \mathbf{M}_{lin} = \mathbf{C}_M \boldsymbol{\Omega}_{lin} \end{array}\right\}, \tag{2.277}$$

where $\mathbf{N}_{lin}$ and $\mathbf{M}_{lin}$ denote the linearized internal force and momentum resultants, respectively. The constitutive matrices $\mathbf{C}_F$ and $\mathbf{C}_M$ are defined by

$$\left.\begin{array}{c} \mathbf{C}_F = diag[EA, GA_1, GA_2] \\ \mathbf{C}_M = diag[GI_p, EI_1, EI_2] \end{array}\right\}, \tag{2.278}$$

where $diag[a,b,c]$ defines a diagonal matrix of components a, b, and c. E, G, and A are respectively the Young's modulus, shear modulus, and cross-sectional area, and $A_1 = k_1 A$, $A_2 = k_2 A$ where k_1 and k_2 are the shear correction factors. I_1 and I_2 are the second moments of inertia, and I_p denotes the polar moment of inertia.

In the IGA method, the displacement and rotation fields are discretized as

$$\mathbf{z}(s(\xi)) = \sum_{N=1}^{n} W_N(\xi) \mathbf{y}_N, \text{ and } \boldsymbol{\theta}(s(\xi)) = \sum_{N=1}^{n} W_N(\xi) \boldsymbol{\theta}_N, \tag{2.279}$$

where $W_N(\xi)$ represents the NURBS basis function, and ξ is the parametric coordinate.

Substituting Eq. (2.279) in to Eqs. (2.274) and (2.275) yield the following discretized form of a generalized eigenvalue problem.

$$(\mathbf{K} - \omega^2 \mathbf{M})\mathbf{u} = \mathbf{0}, \tag{2.280}$$

where $\mathbf{K}$ and $\mathbf{M}$ respectively denote the assembled global stiffness and mass matrices, and $\mathbf{u}$ is a global assembly of response coefficient vectors. From the Bloch periodic condition of Eq. (2.270), we have the following transformation.

$$\mathbf{u} = \mathbf{T}(\boldsymbol{\mu})\tilde{\mathbf{u}}, \tag{2.281}$$

where $\tilde{\mathbf{u}}$ denotes a global assembly of reduced response coefficients. Substituting Eq. (2.281) into Eq. (2.280) and premultiplying the resulting equation with $\mathbf{T}(\boldsymbol{\mu})^H$ yields the following generalized Hermitian eigenvalue problem within a unit cell [90]

$$\left\{\tilde{\mathbf{K}}(\boldsymbol{\mu}) - \zeta\tilde{\mathbf{M}}(\boldsymbol{\mu})\right\}\tilde{\mathbf{u}} = \mathbf{0}, \tag{2.282}$$

where $\tilde{\mathbf{K}}(\boldsymbol{\mu}) \equiv \mathbf{T}(\boldsymbol{\mu})^H\mathbf{K}\mathbf{T}(\boldsymbol{\mu})$ and $\tilde{\mathbf{M}}(\boldsymbol{\mu}) \equiv \mathbf{T}(\boldsymbol{\mu})^H\mathbf{M}\mathbf{T}(\boldsymbol{\mu})$ defines the reduced stiffness and mass matrices, and $(\bullet)^H$ denotes the conjugate transpose. Solving Eq. (2.282) gives eigenvalues $\zeta \equiv \omega^2$ for a given propagation constants $\boldsymbol{\mu}$.

2.6.2 Harmonic response analysis

To investigate wave transmissions of finite size models constructed by tessellating primitive cells, we perform harmonic response analyses. The responses are computed by solving Eq. (2.280) for a given harmonic excitation at different values of frequencies (ω). The excitation is enforced by prescribe a displacement on a boundary point of the lattice (input port), then collecting the magnitude of the response on the other side of the lattice (output port). The wave transmission coefficient (unit: dB) is calculated as

$$T = 20\log_{10}\left(\frac{U_{out}}{U_{in}}\right), \tag{2.283}$$

where U_{in} and U_{out}, respectively, denote magnitudes of displacement vectors at the input and output ports. This coefficient T quantifies wave transmission at a specified frequency such that very low values of T means the applied perturbation quickly decays near the excitation point. A significant drop of T is associated with a band gap.

Chapter 3

Isogeometric configuration DSA of geometrically exact nonlinear structures

3.1 Geometrically exact Kirchhoff beam structures

3.1.1 Concept of configuration design variation in curved structures

In configuration DSA formulation, the design variations of beam structures can be regarded as a deformation process. Therefore, it is possible to consistently utilize the kinematical description of the beam in section 2.3 to account for the design variations.

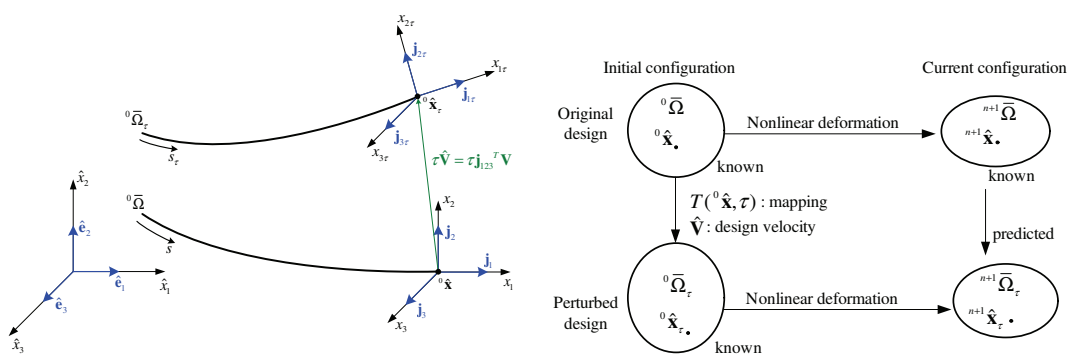

(a) Coordinate systems

(b) Overall DSA scheme

Figure 3.1: Design variation of curved beam

Figure 3.1a shows the design variation of a curved beam in three-dimensional space. $x_{1\tau}-x_{2\tau}-x_{3\tau}$ frame is a local orthogonal curvilinear coordinate system in the perturbed design ${}^0\bar{\Omega}_\tau$ and $x_{1\tau}$ axis represents the tangential direction. $\{\mathbf{j}_{1\tau}, \mathbf{j}_{2\tau}, \mathbf{j}_{3\tau}\}$ and s_τ are the orthonormal base vectors and the arc-length coordinate in the perturbed design, respectively. In this paper, along with the

deformation analysis, the design variation is considered in $\hat{x}_1 - \hat{x}_2$ plane, *i.e.*, $\mathbf{j}_{3\tau} = \mathbf{j}_3 = \hat{\mathbf{e}}_3$.

Assume that only one parameter τ defines a mapping $T : {}^0\hat{\mathbf{x}} \rightarrow {}^0\hat{\mathbf{x}}_\tau({}^0\hat{\mathbf{x}})$, ${}^0\hat{\mathbf{x}} \in {}^0\bar{\Omega}$ given by

$$\left.\begin{array}{l} {}^0\hat{\mathbf{x}}_\tau \equiv T({}^0\hat{\mathbf{x}}, \tau) \\ {}^0\bar{\Omega}_\tau \equiv T({}^0\bar{\Omega}, \tau) \end{array}\right\}. \tag{3.1}$$

Considering τ as time, a design velocity field $\hat{\mathbf{V}} = \hat{\mathbf{V}}(s)$ can be defined as

$$\hat{\mathbf{V}} \equiv \left.\frac{d^0\hat{\mathbf{x}}_\tau}{d\tau}\right|_{\tau=0}. \tag{3.2}$$

Then, we can express the perturbed position vector $\mathbf{r}_\tau$ at ${}^0\hat{\mathbf{x}}_\tau$ using the design velocity, as

$$\mathbf{r}_\tau = \mathbf{r} + \tau\hat{\mathbf{V}} = \mathbf{r} + \tau\mathbf{j}_{123}{}^T\mathbf{V}, \tag{3.3}$$

where $\mathbf{r}$ represents the corresponding original position vector at ${}^0\hat{\mathbf{x}}$, and $\mathbf{V} = \mathbf{V}(s)$ denotes a design velocity component vector that represents the design velocity measured in $x_1 - x_2 - x_3$ frame. Employing Eq. (2.53) with $\mathbf{z}$ replaced by $\tau\mathbf{V}$, the tangential derivative $\mathbf{r}_{\tau,s}$ is expressed by

$$\mathbf{r}_{\tau,s} = \mathbf{j}_{123}{}^T\mathbf{E}(s, \tau\mathbf{V}), \tag{3.4}$$

where the components of $\mathbf{E}(s, \tau\mathbf{V})$ are obtained by replacing $\mathbf{z}$ with $\tau\mathbf{V}$ in Eq. (2.65), as

$$\left.\begin{array}{l} E_1(s, \tau\mathbf{V}) = 1 + \tau(V_{1,s} - V_2 k) \\ E_2(s, \tau\mathbf{V}) = \tau(V_{2,s} + V_1 k) \\ E_3(s, \tau\mathbf{V}) = 0 \end{array}\right\}. \tag{3.5}$$

Shape variation

The expression for the relative length change of a domain, which is regarded as a shape variation of the domain, is derived by substituting $\tau\mathbf{V}$ into $\mathbf{z}$ in Eq. (2.55), as

$$\tilde{E} \equiv e(s, \tau\mathbf{V}) = \|\mathbf{E}(s, \tau\mathbf{V})\| - 1. \tag{3.6}$$

Also, like Eq. (2.56), an infinitesimal length of the perturbed domain (ds_τ) is expressed by that of the original domain (ds) as

$$ds_\tau = (1 + \tilde{E})ds. \tag{3.7}$$

Using the components of Eq. (3.5), the material derivative of Eq. (3.6) is derived as

$$\dot{\tilde{E}} \equiv \frac{d}{d\tau}\, e(s,\tau\mathbf{V})|_{\tau=0} = \left. \frac{\{1+\tau(V_{1,s}-kV_2)\}(V_{1,s}-kV_2)+\tau(V_{2,s}+kV_1)(V_{2,s}+kV_1)}{\sqrt{\{1+\tau(V_{1,s}-kV_2)\}^2+\tau^2(V_{2,s}+kV_1)^2}} \right|_{\tau=0}$$
$$= V_{1,s}-kV_2 = \nabla_s\cdot\hat{\mathbf{V}}, \tag{3.8}$$

where $\nabla_s\cdot(\bullet)\equiv(\bullet)_{,s}\cdot\mathbf{j}_1$, and for the last equality, the relation $\hat{\mathbf{V}}={\mathbf{j}_{123}}^T\mathbf{V}$ and Eqs. (2.51) and (2.64) are used.

Orientation variation

Since the sets of base vectors $\{\mathbf{j}_1,\mathbf{j}_2,\mathbf{j}_3\}$ and $\{\mathbf{j}_{1\tau},\mathbf{j}_{2\tau},\mathbf{j}_{3\tau}\}$ are orthonormal, there exists a proper orthogonal rotation tensor $\mathbf{\Lambda}_\tau\equiv\mathbf{T}(s,\tau\mathbf{V})$ such that

$$\mathbf{j}_{123\tau}=\mathbf{\Lambda}_\tau\mathbf{j}_{123}=\begin{bmatrix}\Lambda_{11\tau} & \Lambda_{12\tau} & 0\\ -\Lambda_{12\tau} & \Lambda_{11\tau} & 0\\ 0 & 0 & 1\end{bmatrix}\mathbf{j}_{123}, \tag{3.9}$$

where $\mathbf{j}_{123\tau}\equiv[\mathbf{j}_{1\tau},\mathbf{j}_{2\tau},\mathbf{j}_{3\tau}]^T$, and by replacing $\mathbf{z}$ with $\tau\mathbf{V}$ in Eq. (2.60), we have

$$\Lambda_{1i\tau}=\frac{E_i(s,\tau\mathbf{V})}{1+e(s,\tau\mathbf{V})}, i=1,2. \tag{3.10}$$

Then, taking the material derivative of Eq. (3.9) leads to

$$(\mathbf{j}_{123})^{\cdot}={\mathbf{V}_\Theta}^T\mathbf{j}_{123}, \tag{3.11}$$

where $(\bullet)^{\cdot}$ denotes the material derivative and

$$\mathbf{V}_\Theta\equiv\frac{d}{d\tau}\mathbf{\Lambda}_\tau^T\big|_{\tau=0}. \tag{3.12}$$

Note that $\mathbf{V}_\Theta$ is skew-symmetric since (i,j) component $(\mathbf{V}_\Theta)_{ij}=(\mathbf{j}_j)^{\cdot}\cdot\mathbf{j}_i=-\mathbf{j}_j\cdot(\mathbf{j}_i)^{\cdot}$ by Eq. (3.11). Using Eq. (3.12) and the expression of $\Lambda_{12\tau}$ in (3.10), we derive $(\mathbf{V}_\Theta)_{12}$ as

$$(\mathbf{V}_\Theta)_{12}\equiv-\frac{d}{d\tau}\left.\frac{E_2(s,\tau\mathbf{V})}{\{1+e(s,\tau\mathbf{V})\}}\right|_{\tau=0}=-\left.\frac{(V_{2,s}+kV_1)\{1+e(s,\tau\mathbf{V})\}-\tau(V_{2,s}+kV_1)\{1+e(s,\tau\mathbf{V})\}^{\cdot}}{\{1+e(s,\tau\mathbf{V})\}^2}\right|_{\tau=0}$$
$$=-(V_{2,s}+V_1k), \tag{3.13}$$

where $e(s,\tau\mathbf{V})=0$ at $\tau=0$ is used for the last equality. Finally, using Eqs. (3.12), (3.13) and the fact that $\mathbf{V}_\Theta$ is skew-symmetric, we have the following.

$$\mathbf{V}_\Theta=\begin{bmatrix}0 & -(V_{2,s}+kV_1) & 0\\ V_{2,s}+kV_1 & 0 & 0\\ 0 & 0 & 0\end{bmatrix}. \tag{3.14}$$

3.1.2 Direct differentiation method

A structural system in its final equilibrium configuration (n+1) with a given original design ${}^0\bar{\Omega}$ reaches another equilibrium configuration (n+1), as shown in Figure 3.1b, if the design is perturbed to ${}^0\bar{\Omega}_\tau$. The equilibrium equation for the perturbed design at the configuration (n+1) is written as

$$a_{0\bar{\Omega}_\tau}({}^{n+1}\mathbf{z}_\tau, \bar{\mathbf{z}}_\tau) = \ell_{0\bar{\Omega}_\tau}({}^{n+1}\mathbf{z}_\tau, \bar{\mathbf{z}}_\tau), \quad \forall \bar{\mathbf{z}}_\tau \in \bar{Z}_\tau, \tag{3.15}$$

where $\bar{Z}_\tau$ is the variational space for the perturbed design, and the subscript ${}^0\bar{\Omega}_\tau$ is used to denote the dependence on the design. The response ${}^{n+1}\mathbf{z}_\tau(s_\tau)$ depends on the parameter τ in two ways. First, ${}^{n+1}\mathbf{z}_\tau$ is the solution of the equilibrium equation (3.15) in ${}^0\bar{\Omega}_\tau$. Second, ${}^{n+1}\mathbf{z}_\tau(s_\tau)$ is evaluated at a point s_τ which moves with τ. Thus, the pointwise material derivative of ${}^{n+1}\mathbf{z}$ at s is defined as

$${}^{n+1}\dot{\mathbf{z}}(s) \equiv \frac{d}{d\tau}\,{}^{n+1}\mathbf{z}_\tau(s_\tau)\Big|_{\tau=0} = {}^{n+1}\mathbf{z}' + {}^{n+1}\mathbf{z}_{,s}\dot{s}, \tag{3.16}$$

where

$${}^{n+1}\mathbf{z}' \equiv \frac{d}{d\tau}\,{}^{n+1}\mathbf{z}_\tau(s)\Big|_{\tau=0} = \lim_{\tau\to 0}\frac{{}^{n+1}\mathbf{z}_\tau(s) - {}^{n+1}\mathbf{z}(s)}{\tau} \tag{3.17}$$

is the partial derivative of ${}^{n+1}\mathbf{z}$ with respect to τ. Using Eq. (3.7), s_τ can be expressed as

$$s_\tau = \int_0^{s_\tau} ds_\tau = \int_0^s (1+\tilde{E})ds. \tag{3.18}$$

Taking the material derivative of Eq. (3.18) gives

$$\dot{s} \equiv \left.\frac{ds_\tau}{d\tau}\right|_{\tau=0} = \int_0^s \dot{\tilde{E}}ds. \tag{3.19}$$

Then, Eq. (3.16) is rewritten as

$${}^{n+1}\dot{\mathbf{z}} = {}^{n+1}\mathbf{z}' + {}^{n+1}\mathbf{z}_{,s}\int_0^s \dot{\tilde{E}}ds. \tag{3.20}$$

Replacing ${}^{n+1}\mathbf{z}$ by ${}^{n+1}\mathbf{z}_{,s}$ in Eq. (3.20) and using the fact that the partial derivative commutes with the tangential derivative, followed by using Eq. (3.8), yield

$$\begin{aligned}({}^{n+1}\mathbf{z}_{,s})^{\cdot} &= {}^{n+1}\mathbf{z}'_{,s} + {}^{n+1}\mathbf{z}_{,ss}\int_0^s \dot{\tilde{E}}ds \\ &= ({}^{n+1}\dot{\mathbf{z}} - {}^{n+1}\mathbf{z}_{,s}\int_0^s \dot{\tilde{E}}ds)_{,s} + {}^{n+1}\mathbf{z}_{,ss}\int_0^s \dot{\tilde{E}}ds = {}^{n+1}\dot{\mathbf{z}}_{,s} - {}^{n+1}\mathbf{z}_{,s}\nabla_s\cdot\hat{\mathbf{V}}.\end{aligned} \tag{3.21}$$

Using the relation that ${}^{n+1}\hat{\mathbf{z}} = \mathbf{j}_{123}{}^T\,{}^{n+1}\mathbf{z}$ and Eq. (3.9), a physical displacement vector ${}^{n+1}\hat{\mathbf{z}}_\tau$ on the perturbed design can be expressed as

$${}^{n+1}\hat{\mathbf{z}}_\tau = \mathbf{j}_{123\tau}{}^T\,{}^{n+1}\mathbf{z}_\tau = \mathbf{j}_{123}{}^T(\mathbf{\Lambda}_\tau{}^T\,{}^{n+1}\mathbf{z}_\tau). \tag{3.22}$$

Taking the material derivative of Eq. (3.22) and using Eq. (3.12) give

$$ {}^{n+1}\dot{\hat{\mathbf{z}}} \equiv \frac{d}{d\tau}\,{}^{n+1}\hat{\mathbf{z}}_\tau\big|_{\tau=0} = \mathbf{j}_{123}{}^T\{{}^{n+1}\dot{\mathbf{z}} + \mathbf{V}_\Theta\,{}^{n+1}\mathbf{z}\}. \tag{3.23} $$

We derive the material derivative of $\mathbf{E} = \mathbf{E}({}^{n+1}\mathbf{z})$ of Eq. (2.53) using Eq. (3.21), for future use, as

$$ \dot{\mathbf{E}} = ({}^{n+1}\dot{\mathbf{z}}_{,s} - \boldsymbol{\Omega}_0\,{}^{n+1}\dot{\mathbf{z}}) + (-{}^{n+1}\mathbf{z}_{,s}\nabla_s\cdot\hat{\mathbf{V}} - \dot{\boldsymbol{\Omega}}_0\,{}^{n+1}\mathbf{z}) \equiv \widehat{\mathbf{E}}({}^{n+1}\dot{\mathbf{z}}) + \mathbf{E}_V({}^{n+1}\mathbf{z}), \tag{3.24} $$

where $\mathbf{E}_V({}^{n+1}\mathbf{z})$ represents the explicit dependence term on the design velocity. For future use, the material derivative of $\mathbf{T}_1$ by using Eq. (A.2) and substituting Eq. (3.24), is derived as

$$ \dot{\mathbf{T}}_1 = \boldsymbol{\Gamma}\dot{\mathbf{E}} = \boldsymbol{\Gamma}\left\{\widehat{\mathbf{E}}({}^{n+1}\dot{\mathbf{z}}) + \mathbf{E}_V({}^{n+1}\mathbf{z})\right\}. \tag{3.25} $$

Considering the design dependence of initial curvature, the material derivative of $\boldsymbol{\Omega}_0$ of Eq. (2.64) is derived as (A.4)

$$ \dot{\boldsymbol{\Omega}}_0 = \mathbf{V}_{\Theta,s}{}^T - \boldsymbol{\Omega}_0\nabla_s\cdot\hat{\mathbf{V}}. \tag{3.26} $$

Using Eq. (3.21) with ${}^{n+1}\mathbf{z}_{,s}$ replaced by $\mathbf{E}_{,s}$ and using Eq. (3.24), we obtain the following.

$$ (\mathbf{E}_{,s})^{\cdot} = \dot{\mathbf{E}}_{,s} - \mathbf{E}_{,s}\nabla_s\cdot\hat{\mathbf{V}} = \{\widehat{\mathbf{E}}({}^{n+1}\dot{\mathbf{z}})\}_{,s} + \{\mathbf{E}_V({}^{n+1}\mathbf{z})\}_{,s} - \mathbf{E}_{,s}\nabla_s\cdot\hat{\mathbf{V}}. \tag{3.27} $$

Consider a structural performance measure of the perturbed design that can be written in an integral form at the final equilibrium configuration $(n+1)$ having the initial reference configuration ${}^0\bar{\Omega}_\tau$.

$$ \psi_\tau = \int_{\Omega_\tau} f_\tau(s_\tau)\,ds_\tau, \tag{3.28} $$

where Ω_τ denotes the parametric domain of the arc-length coordinate s_τ in the perturbed design ${}^0\bar{\Omega}_\tau$. Taking the material derivative of Eq. (3.28) after converting the integral domain into the corresponding original one using Eq. (3.7), and using Eq. (3.8) yield

$$ \psi' \equiv \frac{d}{d\tau}\int_{\Omega_\tau} f_\tau(s_\tau)\,ds_\tau\bigg|_{\tau=0} = \frac{d}{d\tau}\int_\Omega f_\tau(s_\tau)(1+\tilde{E})\,ds\bigg|_{\tau=0} = \int_\Omega (\dot{f} + f\nabla_s\cdot\hat{\mathbf{V}})\,ds. \tag{3.29} $$

Taking the material derivative of both sides of Eq. (3.15) by the formula (3.29) and using the chain rule of differentiation, followed by using Eq. (3.21) with $\mathbf{z}$ replaced by $\bar{\mathbf{z}}$ give

$$ \begin{aligned} &\int_\Omega \left\{EA(\dot{\varepsilon}_m\bar{\varepsilon}_m + \varepsilon_m\dot{\bar{\varepsilon}}_m) + EI(\dot{\omega}_b\bar{\omega}_b + \omega_b\dot{\bar{\omega}}_b) + (EA\varepsilon_m\bar{\varepsilon}_m + EI\omega_b\bar{\omega}_b)\nabla_s\cdot\hat{\mathbf{V}}\right\} ds \\ &= \int_\Omega \left[\dot{\bar{\mathbf{z}}}^T(\mathbf{f}^c + \mathbf{f}^{nc} + \mathbf{f}_1^{eq}) + \dot{\bar{\mathbf{z}}}_{,s}^T\mathbf{f}_2^{eq} + \bar{\mathbf{z}}^T(\dot{\mathbf{f}}^c + \dot{\mathbf{f}}^{nc} + \dot{\mathbf{f}}_1^{eq}) + \bar{\mathbf{z}}_{,s}^T\dot{\mathbf{f}}_2^{eq} + \bar{\mathbf{z}}^T(\mathbf{f}^c + \mathbf{f}^{nc} + \mathbf{f}_1^{eq})\nabla_s\cdot\hat{\mathbf{V}}\right] ds. \end{aligned} \tag{3.30} $$

Using Eq. (3.24) and the differentiation process of Eq. (2.72), the material derivative of membrane strain of Eq. (2.55) is derived as

$$ \dot{\varepsilon}_m = \mathbf{T}_1{}^T\dot{\mathbf{E}} = \mathbf{T}_1{}^T\widehat{\mathbf{E}}({}^{n+1}\dot{\mathbf{z}}) + \mathbf{T}_1{}^T\mathbf{E}_V({}^{n+1}\mathbf{z}) \equiv \widehat{\varepsilon}_m({}^{n+1}\mathbf{z};{}^{n+1}\dot{\mathbf{z}}) + \varepsilon_m^V({}^{n+1}\mathbf{z}), \tag{3.31} $$

where $\varepsilon_m^V({}^{n+1}\mathbf{z})$ represents the explicit dependence term on the design velocity. Taking the material derivative of Eq. (2.72) and using the differentiation process of Eq. (A.2) for $\dot{\mathbf{T}}_1$ and Eq. (3.24), we have

$$\begin{aligned}
\dot{\bar{\varepsilon}}_m &= \{\widehat{\bar{\mathbf{E}}}(\bar{\mathbf{z}})^T\}^{\cdot}\mathbf{T}_1 + \widehat{\bar{\mathbf{E}}}(\bar{\mathbf{z}})^T\dot{\mathbf{T}}_1 \\
&= \{\widehat{\bar{\mathbf{E}}}(\dot{\bar{\mathbf{z}}}) + \mathbf{E}_V(\bar{\mathbf{z}})\}^T\mathbf{T}_1 + \widehat{\bar{\mathbf{E}}}(\bar{\mathbf{z}})^T\mathbf{\Gamma}\{\widehat{\bar{\mathbf{E}}}({}^{n+1}\dot{\mathbf{z}}) + \mathbf{E}_V({}^{n+1}\mathbf{z})\} \\
&= \left\{\widehat{\bar{\mathbf{E}}}(\dot{\bar{\mathbf{z}}})^T\mathbf{T}_1\right\} + \left\{\widehat{\bar{\mathbf{E}}}(\bar{\mathbf{z}})^T\mathbf{\Gamma}\widehat{\bar{\boldsymbol{E}}}({}^{n+1}\dot{\mathbf{z}})\right\} + \left\{\mathbf{E}_V(\bar{\mathbf{z}})^T\mathbf{T}_1 + \widehat{\bar{\mathbf{E}}}(\bar{\mathbf{z}})^T\mathbf{\Gamma}\mathbf{E}_V({}^{n+1}\mathbf{z})\right\} \\
&\equiv \widehat{\bar{\varepsilon}}_m({}^{n+1}\mathbf{z};{}^{n+1}\dot{\bar{\mathbf{z}}}) + \widehat{\bar{\eta}}_m({}^{n+1}\mathbf{z};{}^{n+1}\dot{\mathbf{z}},\bar{\mathbf{z}}) + \bar{\varepsilon}_m^V({}^{n+1}\mathbf{z};\bar{\mathbf{z}}),
\end{aligned} \tag{3.32}$$

where $\bar{\varepsilon}_m^V({}^{n+1}\mathbf{z};\bar{\mathbf{z}})$ represents the explicit dependence term on the design velocity. Similarly, the material derivative of the bending and virtual bending strains are derived as

$$\left.\begin{aligned}
\dot{\omega}_b &= \widehat{\omega}_b({}^{n+1}\mathbf{z};{}^{n+1}\dot{\mathbf{z}}) + \omega_b^V({}^{n+1}\mathbf{z}) \\
\dot{\bar{\omega}}_b &= \widehat{\bar{\omega}}_b({}^{n+1}\mathbf{z};\dot{\bar{\mathbf{z}}}) + \widehat{\bar{\eta}}_b({}^{n+1}\mathbf{z};{}^{n+1}\dot{\mathbf{z}},\bar{\mathbf{z}}) + \bar{\omega}_b^V({}^{n+1}\mathbf{z};\bar{\mathbf{z}})
\end{aligned}\right\}, \tag{3.33}$$

where $\omega_b^V({}^{n+1}\mathbf{z})$ and $\bar{\omega}_b^V({}^{n+1}\mathbf{z};\bar{\mathbf{z}})$ are the explicit dependence terms on design velocity (Appendix A.5).

$$\left.\begin{aligned}
\omega_b^V({}^{n+1}\mathbf{z}) &\equiv \mathbf{E}_{,s}{}^T\mathbf{D}_2\mathbf{E}_V({}^{n+1}\mathbf{z}) - \frac{1}{1+\varepsilon_m}\tilde{\mathbf{T}}_1{}^T\left\{\{\mathbf{E}_V({}^{n+1}\mathbf{z})\}_{,s} - \mathbf{E}_{,s}\nabla_s\cdot\hat{\mathbf{V}}\right\} \\
\bar{\omega}_b^V({}^{n+1}\mathbf{z};\bar{\mathbf{z}}) &\equiv \mathbf{E}_V(\bar{\mathbf{z}})^T\mathbf{D}_2\mathbf{E}_{,s} + \widehat{\bar{\mathbf{E}}}(\bar{\mathbf{z}})^T\mathbf{D}_1\mathbf{E}_V({}^{n+1}\mathbf{z}) + \widehat{\bar{\mathbf{E}}}(\bar{\mathbf{z}})^T\mathbf{D}_2\left\{\{\mathbf{E}_V({}^{n+1}\mathbf{z})\}_{,s} - \mathbf{E}_{,s}\nabla_s\cdot\hat{\mathbf{V}}\right\} \\
&\quad + \{\widehat{\bar{\mathbf{E}}}(\bar{\mathbf{z}})\}_{,s}^T\mathbf{D}_2\mathbf{E}_V({}^{n+1}\mathbf{z}) - \frac{1}{1+\varepsilon_m}\{\mathbf{E}_V(\bar{\mathbf{z}})\}_{,s}^T\tilde{\mathbf{T}}_1 + \frac{1}{1+\varepsilon_m}\{\widehat{\bar{\mathbf{E}}}(\bar{\mathbf{z}})\}_{,s}^T\nabla_s\cdot\hat{\mathbf{V}}\tilde{\mathbf{T}}_1
\end{aligned}\right\}. \tag{3.34}$$

Since the conservative force component vector $\mathbf{f}^c$ explicitly depends on design through the base vectors $\{\mathbf{j}_1,\mathbf{j}_2,\mathbf{j}_3\}$, $\dot{\mathbf{f}}^c$ includes only the explicitly expressed terms of design velocity. Using Eq. (3.11), under the assumption that the global force vector is independent of design, *i.e.* $\dot{\hat{\mathbf{f}}}_c = \mathbf{0}$, $\dot{\mathbf{f}}^c$ is derived as

$$\dot{\mathbf{f}}^c = (\mathbf{j}_{123})^{\cdot}\hat{\mathbf{f}}^c = \mathbf{V}_\Theta{}^T\mathbf{j}_{123}\hat{\mathbf{f}}^c = \mathbf{V}_\Theta{}^T\mathbf{f}^c \equiv \mathbf{f}_V^c. \tag{3.35}$$

The conservative force components in $x_1-x_2-x_3$ frame change only with the orientation design variation. Using Eq. (3.24), the relation $\dot{\mathbf{T}} = [\dot{\mathbf{T}}_1, -\dot{\tilde{\mathbf{T}}}_1, \mathbf{0}]^T$, and the differentiation process of Eqs. (A.2) and (A.4) for $\dot{\mathbf{T}}_1$ and $\dot{\tilde{\mathbf{T}}}_1$, respectively, the material derivative of the non-conservative force component vector $\mathbf{f}^{nc}$ is derived as

$$\begin{aligned}
\dot{\mathbf{f}}^{nc} &= \dot{\mathbf{T}}^T\tilde{\mathbf{f}} + \mathbf{T}^T\dot{\tilde{\mathbf{f}}} \\
&= \dot{\mathbf{T}}_1\tilde{f}_1 - \dot{\tilde{\mathbf{T}}}_1\tilde{f}_2 \\
&= \left\{(\tilde{f}_1\mathbf{I} - \tilde{f}_2\tilde{\mathbf{I}})\mathbf{\Gamma}\mathbf{E}({}^{n+1}\dot{\mathbf{z}})\right\} + \left\{(\tilde{f}_1\mathbf{I} - \tilde{f}_2\tilde{\mathbf{I}})\mathbf{\Gamma}\mathbf{E}_V({}^{n+1}\mathbf{z})\right\} \equiv \widehat{\mathbf{f}}^{nc}({}^{n+1}\mathbf{z};\dot{\mathbf{z}}) + \mathbf{f}_V^{nc}({}^{n+1}\mathbf{z}),
\end{aligned} \tag{3.36}$$

where the force components in $\tilde{x}_1-\tilde{x}_2-\tilde{x}_3$ frame are assumed independent of design, *i.e.* $\dot{\tilde{\mathbf{f}}} = \mathbf{0}$, and $\mathbf{f}_V^{nc} = \mathbf{f}_V^{nc}({}^{n+1}\mathbf{z})$ represents the explicit dependence term on design velocity. Also, using Eq. (3.24),

the differentiation process of Eqs. (A.8) and (A.7) for $\{\mathbf{T}_1/(1+\varepsilon_m)\}^{\cdot}$ and $\{\tilde{\mathbf{T}}_1/(1+\varepsilon_m)\}^{\cdot}$, respectively, the material derivatives of the equivalent load vectors $\mathbf{f}_1^{eq}$ and $\mathbf{f}_2^{eq}$ are derived as

$$\begin{aligned}\dot{\mathbf{f}}_1^{eq} &= \frac{m\dot{k}}{1+\varepsilon_m}\mathbf{T}_1 + mk\left(\frac{1}{1+\varepsilon_m}\mathbf{T}_1\right)^{\cdot} \\ &= \left\{mk\tilde{\mathbf{I}}\mathbf{D}_2\widehat{\mathbf{E}}({}^{n+1}\dot{\mathbf{z}})\right\} + \left\{\frac{m\dot{k}}{1+\varepsilon_m}\mathbf{T}_1 + mk\tilde{\mathbf{I}}\mathbf{D}_2\mathbf{E}_V({}^{n+1}\mathbf{z})\right\} \equiv \widehat{\mathbf{f}}_1^{eq}({}^{n+1}\mathbf{z};{}^{n+1}\dot{\mathbf{z}}) + \mathbf{f}_{1V}^{eq}({}^{n+1}\mathbf{z}),\end{aligned} \tag{3.37}$$

and

$$\begin{aligned}\dot{\mathbf{f}}_2^{eq} &= -m\left(\frac{1}{1+\varepsilon_m}\tilde{\mathbf{T}}_1\right)^{\cdot} \\ &= m\mathbf{D}_2\widehat{\mathbf{E}}({}^{n+1}\dot{\mathbf{z}}) + m\mathbf{D}_2\mathbf{E}_V({}^{n+1}\mathbf{z}) \equiv \widehat{\mathbf{f}}_2^{eq}({}^{n+1}\mathbf{z};{}^{n+1}\dot{\mathbf{z}}) + \mathbf{f}_{2V}^{eq}({}^{n+1}\mathbf{z}),\end{aligned} \tag{3.38}$$

where $\dot{k}$ is derived in Eq. (A.26), and the magnitude of the moment is assumed independent of design, *i.e.* $\dot{m}=0$. $\mathbf{f}_{1V}^{eq}({}^{n+1}\mathbf{z})$ and $\mathbf{f}_{2V}^{eq}({}^{n+1}\mathbf{z})$ represent the explicit dependence terms of the design velocity. Substituting Eqs. (3.31)-(3.33) and (3.35)-(3.38) into Eq. (3.30) and rearranging the terms yield

$$a^*({}^{n+1}\mathbf{z};{}^{n+1}\dot{\mathbf{z}},\bar{\mathbf{z}}) = \left\{\ell'_V({}^{n+1}\mathbf{z},\bar{\mathbf{z}}) - a'_V({}^{n+1}\mathbf{z},\bar{\mathbf{z}})\right\} + \left\{\ell({}^{n+1}\mathbf{z},\dot{\bar{\mathbf{z}}}) - a({}^{n+1}\mathbf{z},\dot{\bar{\mathbf{z}}})\right\}, \quad \forall\bar{\mathbf{z}}\in\bar{Z}, \tag{3.39}$$

where

$$a'_V({}^{n+1}\mathbf{z},\bar{\mathbf{z}}) \equiv \int_\Omega \left\{\begin{array}{l} EA\left(\bar{\varepsilon}_m^V({}^{n+1}\mathbf{z};\bar{\mathbf{z}})\varepsilon_m + \bar{\varepsilon}_m\varepsilon_m^V({}^{n+1}\mathbf{z})\right) \\ +EI\left(\bar{\omega}_b^V({}^{n+1}\mathbf{z};\bar{\mathbf{z}})\omega_b + \bar{\omega}_b\omega_b^V({}^{n+1}\mathbf{z})\right) \\ +(EA\bar{\varepsilon}_m\varepsilon_m + EI\bar{\omega}_b\omega_b)\nabla_s\cdot\hat{\mathbf{V}} \end{array}\right\} ds, \tag{3.40}$$

and

$$\ell'_V({}^{n+1}\mathbf{z},\bar{\mathbf{z}}) \equiv \int_\Omega \left\{\bar{\mathbf{z}}^T(\mathbf{f}_V^c + \mathbf{f}_V^{nc} + \mathbf{f}_{1V}^{eq}) + \bar{\mathbf{z}}_{,s}^T\mathbf{f}_{2V}^{eq} + \bar{\mathbf{z}}^T(\mathbf{f}^c + \mathbf{f}^{nc} + \mathbf{f}_1^{eq})\nabla_s\cdot\hat{\mathbf{V}}\right\} ds. \tag{3.41}$$

Then, using the fact that

$$a({}^{n+1}\mathbf{z},\dot{\bar{\mathbf{z}}}) = \ell({}^{n+1}\mathbf{z},\dot{\bar{\mathbf{z}}}), \quad \forall\dot{\bar{\mathbf{z}}}\in\bar{Z}, \tag{3.42}$$

the design sensitivity equation is stated as : For a given ${}^{n+1}\mathbf{z}$, find ${}^{n+1}\dot{\mathbf{z}}\in\bar{Z}$ such that

$$a^*({}^{n+1}\mathbf{z};{}^{n+1}\dot{\mathbf{z}},\bar{\mathbf{z}}) = \ell'_V({}^{n+1}\mathbf{z},\bar{\mathbf{z}}) - a'_V({}^{n+1}\mathbf{z},\bar{\mathbf{z}}), \quad \forall\bar{\mathbf{z}}\in\bar{Z}, \tag{3.43}$$

where the right-hand side is termed the fictitious load associated with the design velocity.

3.1.2.1 Isogeometric discretization

Here, only positions of control points are considered as the design variables. From Eqs. (2.7) and (3.2), we obtain the expression for the design velocity field by the perturbation of control points,

$$\hat{\mathbf{V}}(s(\xi)) \equiv \left.\frac{d^0\hat{\mathbf{x}}_\tau}{d\tau}\right|_{\tau=0} = \frac{d}{d\tau}\left\{\sum_{I=1}^{CP} W_I(\xi)\left(\mathbf{B}_I + \tau\delta\mathbf{B}_I\right)\right\} = \sum_{I=1}^{CP} W_I(\xi)\delta\mathbf{B}_I, \tag{3.44}$$

where $\delta\mathbf{B}_I$ represents the perturbation of I-th control point. $\mathbf{E}_V(\bar{\mathbf{z}})$, obtained by replacing ${}^{n+1}\mathbf{z}$ with $\bar{\mathbf{z}}$ in Eq. (3.24), is discretized as

$$\mathbf{E}_V(\bar{\mathbf{z}}) = \left\{-\mathbf{N}_{I,s}(\nabla_s\cdot\hat{\mathbf{V}}) - \dot{\mathbf{\Omega}}_0\mathbf{N}_I\right\}\bar{\mathbf{y}}_I \equiv \mathbf{B}_{1I}^V\bar{\mathbf{y}}_I. \tag{3.45}$$

Taking the tangential derivative of Eq. (3.45), $\{\mathbf{E}_V(\bar{\mathbf{z}})\}_{,s}$ is discretized as

$$\{\mathbf{E}_V(\bar{\mathbf{z}})\}_{,s} = \left\{-\mathbf{N}_{I,ss}(\nabla_s\cdot\hat{\mathbf{V}}) - \mathbf{N}_{I,s}(\nabla_s\cdot\hat{\mathbf{V}})_{,s} - \dot{\mathbf{\Omega}}_0\mathbf{N}_{I,s} - \dot{\mathbf{\Omega}}_{0,s}\mathbf{N}_I)\right\}\bar{\mathbf{y}}_I \equiv \mathbf{B}_{2I}^V\bar{\mathbf{y}}_I. \tag{3.46}$$

Then, using Eqs. (3.45) and (3.46), $\bar{\varepsilon}_m^V({}^{n+1}\mathbf{z};\bar{\mathbf{z}})$ and $\bar{\omega}_b^V({}^{n+1}\mathbf{z};\bar{\mathbf{z}})$ are discretized as

$$\bar{\varepsilon}_m^V({}^{n+1}\mathbf{z};\bar{\mathbf{z}}) = \bar{\mathbf{y}}_I^T\{{\mathbf{B}_{1I}^V}^T\mathbf{T}_1 + {\mathbf{B}_{1I}}^T\mathbf{\Gamma}\mathbf{E}_V({}^{n+1}\mathbf{z})\} \equiv \bar{\mathbf{y}}_I^T\mathbf{H}_I^m, \tag{3.47}$$

and

$$\begin{aligned}\bar{\omega}_b^V({}^{n+1}\mathbf{z};\bar{\mathbf{z}}) &= {\bar{\mathbf{y}}_I}^T\begin{bmatrix} {\mathbf{B}_{1I}^V}^T\mathbf{D}_2\mathbf{E}_{,s} + {\mathbf{B}_{1I}}^T\mathbf{D}_1\mathbf{E}_V({}^{n+1}\mathbf{z}) + {\mathbf{B}_{1I}}^T\mathbf{D}_2\left\{\{\mathbf{E}_V({}^{n+1}\mathbf{z})\}_{,s} - \mathbf{E}_{,s}\nabla_s\cdot\hat{\mathbf{V}}\right\} \\ +{\mathbf{B}_{2I}}^T\mathbf{D}_2\mathbf{E}_V({}^{n+1}\mathbf{z}) + \frac{1}{1+\varepsilon_m}(-{\mathbf{B}_{2I}^V}^T\tilde{\mathbf{T}}_1) + \frac{1}{1+\varepsilon_m}({\mathbf{B}_{2I}}^T\nabla_s\cdot\hat{\mathbf{V}}\tilde{\mathbf{T}}_1)\end{bmatrix} \\ &\equiv {\bar{\mathbf{y}}_I}^T\mathbf{H}_I^b\end{aligned} \tag{3.48}$$

Rewriting the explicitly design-dependent terms of Eqs. (3.40) and (3.41) in discrete form, we have

$$\begin{aligned}a'_V({}^{n+1}\mathbf{z},\bar{\mathbf{z}}) &= \bar{\mathbf{y}}^T\overset{CP}{\underset{I=1}{\mathbf{A}}}\int_\Omega\left\{\begin{array}{l} EA\left(\mathbf{H}_I^{mT}\varepsilon_m + \mathbf{G}_I^{mT}\varepsilon_m^V({}^{n+1}\mathbf{z})\right) + EI\left(\mathbf{H}_I^{bT}\omega_b + \mathbf{G}_I^{bT}\omega_b^V({}^{n+1}\mathbf{z})\right) \\ +\left(EA\mathbf{G}_I^{mT}\varepsilon_m + EI\mathbf{G}_I^{bT}\omega_b\right)\nabla_s\cdot\hat{\mathbf{V}}\end{array}\right\}ds \\ &\equiv \bar{\mathbf{y}}^T\mathbf{F}_{aV},\end{aligned} \tag{3.49}$$

and

$$\ell'_V({}^{n+1}\mathbf{z},\bar{\mathbf{z}}) = \bar{\mathbf{y}}^T\overset{CP}{\underset{I=1}{\mathbf{A}}}\int_\Omega\left\{\mathbf{N}_I^T\left(\mathbf{f}_V^c + \mathbf{f}_V^{nc} + \mathbf{f}_{1V}^{eq}\right) + \mathbf{N}_{I,s}^T\mathbf{f}_{2V}^{eq} + \mathbf{N}_I^T(\mathbf{f}_c + \mathbf{f}_{nc} + \mathbf{f}_1^{eq})\nabla_s\cdot\hat{\mathbf{V}}\right\}ds \equiv \bar{\mathbf{y}}^T\mathbf{F}_{lV}. \tag{3.50}$$

3.1.2.2 Cubic Hermite interpolation of FEA

In case Hermite basis functions are used for the discretization of design sensitivity equation, the element length parameters in the basis functions have explicit dependence on the design, which should be taken into account for the accurate DSA. Consequently, additional fictitious load terms are present in the design sensitivity equation. The initial geometry, displacement component vector at the final equilibrium configuration (n+1), and virtual displacement component vector for an element are approximated, using the Hermite interpolation, as

$${}^0\hat{\mathbf{x}}^h(\xi) = N_1^H(\xi)\hat{\mathbf{x}}^1 + N_2^H(\xi)\mathbf{t}^1 + N_3^H(\xi)\hat{\mathbf{x}}^2 + N_4^H(\xi)\mathbf{t}^2, \tag{3.51}$$

$${}^{n+1}\mathbf{z}^h(\xi) = N_1^H(\xi)\mathbf{u}^1 + N_2^H(\xi)\boldsymbol{\alpha}^1 + N_3^H(\xi)\mathbf{u}^2 + N_4^H(\xi)\boldsymbol{\alpha}^2, \tag{3.52}$$

and

$$\bar{\mathbf{z}}^h(\xi) = N_1^H(\xi)\bar{\mathbf{u}}^1 + N_2^H(\xi)\bar{\boldsymbol{\alpha}}^1 + N_3^H(\xi)\bar{\mathbf{u}}^2 + N_4^H(\xi)\bar{\boldsymbol{\alpha}}^2, \tag{3.53}$$

where $\hat{\mathbf{x}}^i$ and $\mathbf{t}^i$ denote i-th nodal position and tangential vectors, respectively. $\{\mathbf{u}^i, \boldsymbol{\alpha}^i\}$ and $\{\bar{\mathbf{u}}^i, \bar{\boldsymbol{\alpha}}^i\}$ are respectively i-th nodal and virtual responses where $\mathbf{u}_{,s} = \boldsymbol{\alpha}^i$ and $\bar{\mathbf{u}}_{,s} = \bar{\boldsymbol{\alpha}}^i$ at i-th nodal position.

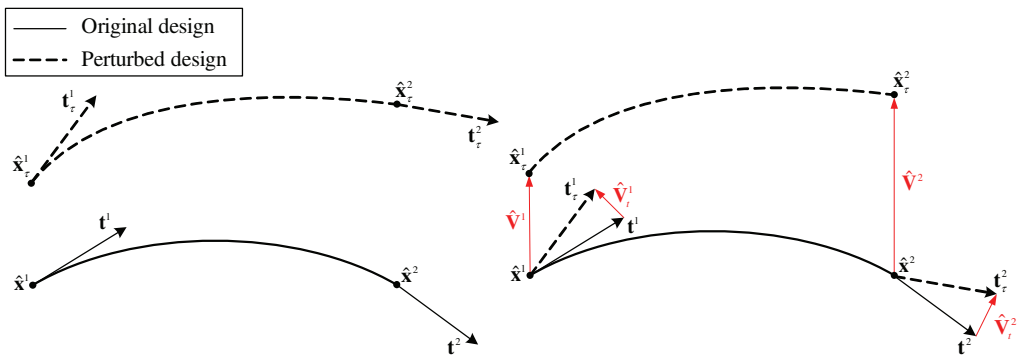

(a) Design variation of curved element (b) Nodal design velocity

Figure 3.2: Design variation of curved element using Hermite interpolation

Taking the material derivative of the approximated geometry of Eq. (3.51), the approximated design velocity field is obtained by

$$\hat{\mathbf{V}}^h(\xi) \equiv \left.\frac{d^0\hat{\mathbf{x}}_\tau^h}{d\tau}\right|_{\tau=0} = \left(N_1^H\hat{\mathbf{V}}^1 + N_2^H\hat{\mathbf{V}}_t^1 + N_3^H\hat{\mathbf{V}}^2 + N_4^H\hat{\mathbf{V}}_t^2\right) + \left(\dot{N}_2^H\mathbf{t}^1 + \dot{N}_4^H\mathbf{t}^2\right), \tag{3.54}$$

where $\hat{\mathbf{V}}^i$ and $\hat{\mathbf{V}}_t^i$ denote the design velocities of i-th nodal position and tangential vector, respectively, as shown in Figure 3.2. Note that the last two terms of Eq. (3.54) appear due to the design dependence of basis functions. The Hermite basis functions N_i^H and $\dot{N}_i^H$ are given in A.6. Taking the material derivatives of Eqs. (3.52) and (3.53) yield

$$^{n+1}\dot{\mathbf{z}}^h(\xi) = (N_1^H\dot{\mathbf{u}}^1 + N_2^H\dot{\boldsymbol{\alpha}}^1 + N_3^H\dot{\mathbf{u}}^2 + N_4^H\dot{\boldsymbol{\alpha}}^2) + (\dot{N}_2^H\boldsymbol{\alpha}^1 + \dot{N}_4^H\boldsymbol{\alpha}^2) \equiv \dot{\mathbf{v}}^h + \dot{\mathbf{v}}^h, \tag{3.55}$$

and

$$\dot{\bar{\mathbf{z}}}^h(\xi) = (N_1^H\dot{\bar{\mathbf{u}}}^1 + N_2^H\dot{\bar{\boldsymbol{\alpha}}}^1 + N_3^H\dot{\bar{\mathbf{u}}}^2 + N_4^H\dot{\bar{\boldsymbol{\alpha}}}^2) + (\dot{N}_2^H\bar{\boldsymbol{\alpha}}^1 + \dot{N}_4^H\bar{\boldsymbol{\alpha}}^2) \equiv \dot{\bar{\mathbf{v}}}^h + \dot{\bar{\mathbf{v}}}^h. \tag{3.56}$$

Since $\dot{\bar{\mathbf{z}}}^h \notin \bar{Z}^h$ and $\dot{\bar{\mathbf{v}}}^h \in \bar{Z}^h$ [26], the following, instead of Eq. (3.42), holds.

$$a(^{n+1}\mathbf{z}^h, \dot{\bar{\mathbf{v}}}^h) = \ell(^{n+1}\mathbf{z}^h, \dot{\bar{\mathbf{v}}}^h), \quad \forall\dot{\bar{\mathbf{v}}}^h \in \bar{Z}^h. \tag{3.57}$$

Then, substituting Eqs. (3.55) and (3.56) into Eq. (3.39), and using Eq. (3.57), we have the following design sensitivity equation: For a given ${}^{n+1}\mathbf{z}^h$, find $\dot{\mathbf{v}}^h \in \bar{Z}^h$ such that

$$
\begin{aligned}
&a^*({}^{n+1}\mathbf{z}^h; \dot{\mathbf{v}}^h, \bar{\mathbf{z}}^h) \\
&= \left\{ \ell'_V({}^{n+1}\mathbf{z}^h, \bar{\mathbf{z}}^h) - a'_V({}^{n+1}\mathbf{z}^h, \bar{\mathbf{z}}^h) \right\} + \left\{ \ell({}^{n+1}\mathbf{z}^h, \dot{\bar{\mathbf{v}}}^h) - a({}^{n+1}\mathbf{z}^h, \dot{\bar{\mathbf{v}}}^h) - a^*({}^{n+1}\mathbf{z}^h; \dot{\mathbf{v}}^h, \bar{\mathbf{z}}^h) \right\} \\
&= \left\{ \ell'_V({}^{n+1}\mathbf{z}^h, \bar{\mathbf{z}}^h) - a'_V({}^{n+1}\mathbf{z}^h, \bar{\mathbf{z}}^h) \right\} + \left\{ \ell^*({}^{n+1}\mathbf{z}^h, \dot{\bar{\mathbf{v}}}^h) - a^*({}^{n+1}\mathbf{z}^h; \dot{\mathbf{v}}^h, \bar{\mathbf{z}}^h) \right\}, \quad \forall \bar{\mathbf{z}}^h \in \bar{Z}^h.
\end{aligned} \tag{3.58}
$$

Note that the terms in the second parentheses in Eq. (3.58) are the additional fictitious load terms due to the design dependence of basis functions. The effect of these additional fictitious load terms on the accuracy of DSA is significant, which will be verified through several numerical examples in section 4.2.

3.1.2.3 DSA for the invariant formulation

Here we derive a configuration DSA expression for the invariant formulation presented in section 2.3.4. From Eq. (3.21), we have

$$
({}^{n+1}\mathbf{z}_{,s})^{\cdot} = {}^{n+1}\dot{\mathbf{z}}_{,s} - {}^{n+1}\mathbf{z}_{,s} \nabla_s \cdot \hat{\mathbf{V}}. \tag{3.59}
$$

Taking the material derivative of $\mathbf{E}({}^{n+1}\mathbf{z})$ in Eq. (2.112) and using Eq. (3.59) gives the following.

$$
\begin{aligned}
\left\{ \mathbf{E}({}^{n+1}\mathbf{z}) \right\}^{\cdot} &= \mathbf{j}_{123}\, {}^{n+1}\dot{\mathbf{z}}_{,s} + \left\{ \mathbf{V}_\Theta{}^T - (\nabla_s \cdot \hat{\mathbf{V}})\mathbf{I} \right\} \mathbf{j}_{123}\, {}^{n+1}\mathbf{z}_{,s} \\
&\equiv \widehat{\mathbf{E}}({}^{n+1}\dot{\mathbf{z}}) + \mathbf{E}_V({}^{n+1}\mathbf{z}),
\end{aligned} \tag{3.60}
$$

where $\mathbf{E}_V({}^{n+1}\mathbf{z})$ represents the explicit dependence term on the design variation. The sensitivity equation is presented as: For a given ${}^{n+1}\mathbf{z}$, find ${}^{n+1}\dot{\mathbf{z}} \in \bar{Z}$ such that

$$
a^*({}^{n+1}\mathbf{z}; {}^{n+1}\dot{\mathbf{z}}, \bar{\mathbf{z}}) = \ell'_V({}^{n+1}\mathbf{z}, \bar{\mathbf{z}}) - a'_V({}^{n+1}\mathbf{z}, \bar{\mathbf{z}}), \quad \forall \bar{\mathbf{z}} \in \bar{Z}, \tag{3.61}
$$

where the explicit dependence terms of the strain energy and load forms are defined as

$$
a'_V({}^{n+1}\mathbf{z}, \bar{\mathbf{z}}) \equiv \int_\Omega \left\{ \begin{array}{l} EA\left(\bar{\varepsilon}_m^V({}^{n+1}\mathbf{z}; \bar{\mathbf{z}}) \varepsilon_m + \bar{\varepsilon}_m \varepsilon_m^V({}^{n+1}\mathbf{z}) \right) \\ + EI\left(\bar{\omega}_b^V({}^{n+1}\mathbf{z}; \bar{\mathbf{z}}) \omega_b + \bar{\omega}_b \omega_b^V({}^{n+1}\mathbf{z}) \right) \\ + (EA\bar{\varepsilon}_m \varepsilon_m + EI\bar{\omega}_b \omega_b) \nabla_s \cdot \hat{\mathbf{V}} \end{array} \right\} ds, \tag{3.62}
$$

and

$$
\ell'_V({}^{n+1}\mathbf{z}, \bar{\mathbf{z}}) \equiv \int_\Omega \left\{ \bar{\mathbf{z}}^T \mathbf{f}_V^{nc} + \bar{\mathbf{z}}_{,s}^T \mathbf{f}_V^{eq} + \bar{\mathbf{z}}^T (\mathbf{f}^c + \mathbf{f}^{nc}) \nabla_s \cdot \hat{\mathbf{V}} \right\} ds. \tag{3.63}
$$

Taking the material derivative of Eq. (2.115) using the differentiation process of Eq. (A.7), and substituting Eqs. (3.11) and (3.60) yields

$$\begin{aligned}\dot{\mathbf{f}}^{eq} &= \left\{m\mathbf{j}_{123}{}^{T}\mathbf{D}_2\bar{\mathbf{E}}({}^{n+1}\dot{\mathbf{z}})\right\} + \left\{m\mathbf{j}_{123}{}^{T}\mathbf{D}_2\mathbf{E}_V({}^{n+1}\mathbf{z}) - \frac{m}{1+\varepsilon_m}\mathbf{j}_{123}{}^{T}\mathbf{V}_\Theta\tilde{\mathbf{T}}_1\right\} \\ &\equiv \bar{\mathbf{f}}^{eq}({}^{n+1}\mathbf{z};{}^{n+1}\dot{\mathbf{z}}) + \mathbf{f}_V^{eq}({}^{n+1}\mathbf{z}).\end{aligned} \tag{3.64}$$

Similarly, the explicit design dependence term of the non-conservative force vector can be derived by taking the material derivative of Eq. (2.114), as

$$\begin{aligned}\dot{\mathbf{f}}^{nc} &= \left\{(\tilde{f}_1\mathbf{I} - \tilde{f}_2\tilde{\mathbf{I}})\boldsymbol{\Gamma}\mathbf{E}({}^{n+1}\dot{\mathbf{z}})\right\} + \left\{(\tilde{f}_1\mathbf{I} - \tilde{f}_2\tilde{\mathbf{I}})\boldsymbol{\Gamma}\mathbf{E}_V({}^{n+1}\mathbf{z}) + \mathbf{j}_{123}{}^{T}\mathbf{V}_\Theta\mathbf{T}^T\tilde{\mathbf{f}}\right\} \\ &\equiv \bar{\mathbf{f}}^{nc}({}^{n+1}\mathbf{z};\dot{\mathbf{z}}) + \mathbf{f}_V^{nc}({}^{n+1}\mathbf{z}).\end{aligned} \tag{3.65}$$

3.1.3 Configuration DSA of multi-patch continuity constraints

3.1.3.1 DSA of displacement continuity constraint

We derive design sensitivity expressions for the inter-patch displacement continuity conditions in the local displacement discretization formulation, presented in section 2.3.5.1. In FEA-based DSA where only the case #1 is considered, the design dependence of Hermite basis function need not be considered, since its material derivative vanishes at the boundary of elements where the junction continuity conditions are imposed.

Case #1: continuous displacement

By taking the material derivative of the energy form of Eq. (2.127) and using Eq. (3.11), the following is obtained.

$$\begin{aligned}[b({}^{n+1}\mathbf{d},\bar{\mathbf{d}})]' &= \left\{\bar{\boldsymbol{\lambda}}^{*T}(\mathbf{j}_{123}{}^{*T}{}^{n+1}\dot{\mathbf{z}}^* - \underset{\sim}{\mathbf{j}}_{123}{}^{*T}{}^{n+1}\dot{\underset{\sim}{\mathbf{z}}}^*) + (\bar{\mathbf{z}}^{*T}\mathbf{j}_{123}{}^{*} - \underset{\sim}{\bar{\mathbf{z}}}^{*T}\underset{\sim}{\mathbf{j}}_{123}{}^{*})^{n+1}\dot{\boldsymbol{\lambda}}^*\right\} \\ &+ \left\{\dot{\bar{\boldsymbol{\lambda}}}^{*T}(\mathbf{j}_{123}{}^{*T}{}^{n+1}\mathbf{z}^* - \underset{\sim}{\mathbf{j}}_{123}{}^{*T}{}^{n+1}\underset{\sim}{\mathbf{z}}^*) + (\dot{\bar{\mathbf{z}}}^{*T}\mathbf{j}_{123}{}^{*} - \dot{\underset{\sim}{\bar{\mathbf{z}}}}^{*T}\underset{\sim}{\mathbf{j}}_{123}{}^{*})^{n+1}\boldsymbol{\lambda}^*\right\} \\ &+ \left\{\bar{\boldsymbol{\lambda}}^{*T}(\mathbf{j}_{123}{}^{*T}\mathbf{V}_\Theta^{*}{}^{n+1}\mathbf{z}^* - \underset{\sim}{\mathbf{j}}_{123}{}^{*T}\underset{\sim}{\mathbf{V}}_\Theta^{*}{}^{n+1}\underset{\sim}{\mathbf{z}}^*) + (\bar{\mathbf{z}}^{*T}\mathbf{V}_\Theta^{*T}\mathbf{j}_{123}{}^{*} - \underset{\sim}{\bar{\mathbf{z}}}^{*T}\underset{\sim}{\mathbf{V}}_\Theta^{*T}\underset{\sim}{\mathbf{j}}_{123}{}^{*})^{n+1}\boldsymbol{\lambda}^*\right\} \\ &\equiv b^*({}^{n+1}\dot{\mathbf{d}},\bar{\mathbf{d}}) + b({}^{n+1}\mathbf{d},\dot{\bar{\mathbf{d}}}) + b'_V({}^{n+1}\mathbf{d},\bar{\mathbf{d}}),\end{aligned} \tag{3.66}$$

where ${}^{n+1}\dot{\mathbf{d}} = ({}^{n+1}\dot{\mathbf{z}};{}^{n+1}\dot{\underset{\sim}{\mathbf{z}}};{}^{n+1}\dot{\boldsymbol{\lambda}}^*)$, $\dot{\bar{\mathbf{d}}} = (\dot{\bar{\mathbf{z}}};\dot{\underset{\sim}{\bar{\mathbf{z}}}};\dot{\bar{\boldsymbol{\lambda}}}^*)$. In the isogeometric discrete form, we have

$$\begin{aligned}b'_V({}^{n+1}\mathbf{d},\bar{\mathbf{d}}) &= \bar{\boldsymbol{\lambda}}^{*T}(\mathbf{j}_{123}{}^{*T}\mathbf{V}_\Theta^{*}{}^{n+1}\mathbf{z}^* - \underset{\sim}{\mathbf{j}}_{123}{}^{*T}\underset{\sim}{\mathbf{V}}_\Theta^{*}{}^{n+1}\underset{\sim}{\mathbf{z}}^*) \\ &+ \bar{\mathbf{y}}^T(\mathbf{N}^{*T}\mathbf{V}_\Theta^{*T}\mathbf{j}_{123}{}^{*n+1}\boldsymbol{\lambda}^*) + \bar{\mathbf{y}}^T(-\underset{\sim}{\mathbf{N}}^{*T}\underset{\sim}{\mathbf{V}}_\Theta^{*T}\underset{\sim}{\mathbf{j}}_{123}{}^{*n+1}\boldsymbol{\lambda}^*) \\ &\equiv \bar{\boldsymbol{\lambda}}^{*T}\mathbf{Q}_3^V + \bar{\mathbf{y}}^T\mathbf{Q}_1^V + \bar{\mathbf{y}}^T\mathbf{Q}_2^V.\end{aligned} \tag{3.67}$$

Case #2: continuous first order tangential derivative of local displacement

Taking the material derivative of Eq. (2.132) and using Eq. (3.21) yield

$$\begin{aligned}[b(^{n+1}\mathbf{d},\bar{\mathbf{d}})]' &= \left\{\bar{\boldsymbol{\lambda}}^{*T}(^{n+1}\dot{\mathbf{z}}^*_{,s} - {}^{n+1}\dot{\underset{\sim}{\mathbf{z}}}^*_{,\underset{\sim}{s}}) + (\bar{\mathbf{z}}^*_{,s} - \bar{\underset{\sim}{\mathbf{z}}}^*_{,\underset{\sim}{s}})^{T\,n+1}\dot{\boldsymbol{\lambda}}^*\right\} \\ &+ \left\{\dot{\bar{\boldsymbol{\lambda}}}^{*T}(^{n+1}\mathbf{z}^*_{,s} - {}^{n+1}\underset{\sim}{\mathbf{z}}^*_{,\underset{\sim}{s}}) + (\dot{\bar{\mathbf{z}}}^*_{,s} - \dot{\bar{\underset{\sim}{\mathbf{z}}}}^*_{,\underset{\sim}{s}})^{T\,n+1}\boldsymbol{\lambda}^*\right\} \\ &+ \left\{-\bar{\boldsymbol{\lambda}}^{*T}(^{n+1}\mathbf{z}^*_{,s}\nabla_s\cdot\hat{\mathbf{V}} - {}^{n+1}\underset{\sim}{\mathbf{z}}^*_{,\underset{\sim}{s}}\nabla_{\underset{\sim}{s}}\cdot\hat{\underset{\sim}{\mathbf{V}}}) - (\bar{\mathbf{z}}^*_{,s}\nabla_s\cdot\hat{\mathbf{V}} - \bar{\underset{\sim}{\mathbf{z}}}^*_{,\underset{\sim}{s}}\nabla_{\underset{\sim}{s}}\cdot\hat{\underset{\sim}{\mathbf{V}}})^{T\,n+1}\boldsymbol{\lambda}^*\right\} \\ &\equiv b^*(^{n+1}\dot{\mathbf{d}},\bar{\mathbf{d}}) + b(^{n+1}\mathbf{d},\dot{\bar{\mathbf{d}}}) + b'_V(^{n+1}\mathbf{d},\bar{\mathbf{d}}). \end{aligned} \tag{3.68}$$

In isogeometric discrete form,

$$\begin{aligned} b'_V(^{n+1}\mathbf{d},\bar{\mathbf{d}}) &= \bar{\boldsymbol{\lambda}}^{*T}(-{}^{n+1}\mathbf{z}^*_{,s}\nabla_s\cdot\hat{\mathbf{V}} + {}^{n+1}\underset{\sim}{\mathbf{z}}^*_{,\underset{\sim}{s}}\nabla_{\underset{\sim}{s}}\cdot\hat{\underset{\sim}{\mathbf{V}}}) + \bar{\mathbf{y}}^T(-\mathbf{N}^{*T}_{,s}{}^{n+1}\boldsymbol{\lambda}^*\nabla_s\cdot\hat{\mathbf{V}}) + \bar{\mathbf{y}}^T(\underset{\sim}{\mathbf{N}}^{*T}_{,\underset{\sim}{s}}{}^{n+1}\boldsymbol{\lambda}^*\nabla_{\underset{\sim}{s}}\cdot\hat{\underset{\sim}{\mathbf{V}}}) \\ &\equiv \bar{\boldsymbol{\lambda}}^{*T}\mathbf{Q}^V_3 + \bar{\mathbf{y}}^T\mathbf{Q}^V_1 + \bar{\mathbf{y}}^T\mathbf{Q}^V_2. \end{aligned} \tag{3.69}$$

Considering the case 1 or 2 of the junction continuity, the sensitivity equation (3.43) can be rewritten as follows: For a given ${}^{n+1}\mathbf{d} = ({}^{n+1}\mathbf{z}; {}^{n+1}\underset{\sim}{\mathbf{z}}; {}^{n+1}\boldsymbol{\lambda}^*)$, find ${}^{n+1}\dot{\mathbf{d}} = ({}^{n+1}\dot{\mathbf{z}}; {}^{n+1}\dot{\underset{\sim}{\mathbf{z}}}; {}^{n+1}\dot{\boldsymbol{\lambda}}^*) \in \bar{W}$ such that

$$\begin{aligned} &a^*(^{n+1}\mathbf{z}; {}^{n+1}\dot{\mathbf{z}}, \bar{\mathbf{z}}) + a^*(^{n+1}\underset{\sim}{\mathbf{z}}; {}^{n+1}\dot{\underset{\sim}{\mathbf{z}}}, \bar{\underset{\sim}{\mathbf{z}}}) + b^*(^{n+1}\dot{\mathbf{d}}, \bar{\mathbf{d}}) \\ &\equiv \left\{\ell'_V(^{n+1}\mathbf{z}, \bar{\mathbf{z}}) + \underset{\sim}{\ell}'_V(^{n+1}\underset{\sim}{\mathbf{z}}, \bar{\underset{\sim}{\mathbf{z}}})\right\} - \left\{a'_V(^{n+1}\mathbf{z}, \bar{\mathbf{z}}) + \underset{\sim}{a}'_V(^{n+1}\underset{\sim}{\mathbf{z}}, \bar{\underset{\sim}{\mathbf{z}}}) + b'_V(^{n+1}\mathbf{d}, \bar{\mathbf{d}})\right\}, \quad \forall\bar{\mathbf{d}} \in \bar{W}. \end{aligned} \tag{3.70}$$

Finally, we have the following matrix equation,

$$\left[\begin{array}{cc|c} \mathbf{K}^r & \mathbf{0} & \mathbf{C}_1{}^T \\ \mathbf{0} & \underset{\sim}{\mathbf{K}}^r & \mathbf{C}_2{}^T \\ \hline \mathbf{C}_1 & \mathbf{C}_2 & \mathbf{0} \end{array}\right]^f \left\{\begin{array}{c} \dot{\mathbf{y}} \\ \dot{\underset{\sim}{\mathbf{y}}} \\ \dot{\tilde{\boldsymbol{\lambda}}}^* \end{array}\right\} = \left\{\begin{array}{c} \mathbf{F}_{lV} - \mathbf{F}_{aV} \\ \underset{\sim}{\mathbf{F}}_{lV} - \underset{\sim}{\mathbf{F}}_{aV} \\ \mathbf{0} \end{array}\right\} - \left\{\begin{array}{c} \mathbf{Q}^V_1 \\ \mathbf{Q}^V_2 \\ \mathbf{Q}^V_3 \end{array}\right\}, \tag{3.71}$$

where the superscript f represents the LU-factorized tangent stiffness matrix at final equilibrium configuration. The design sensitivity equation (3.71) is linear and solved without iterations, which makes the sensitivity computation very efficient. The additional fictitious load terms in Eq. (3.58) should be considered in case the DSA is performed using the finite elements of Hermite interpolation.

3.1.3.2 DSA of rotation continuity constraint

We derive the design sensitivity expressions for the rotational continuity condition, presented in section 2.3.5.2.

Lagrange multiplier method

Taking the material derivative of Eq. (2.57) and using Eqs. (2.57) and (3.11) yields

$$(\mathbf{i}_{123})^{\cdot} = \dot{\mathbf{T}}\mathbf{j}_{123} + \mathbf{T}(\mathbf{j}_{123})^{\cdot} = \boldsymbol{\Theta}(\dot{\theta})\mathbf{i}_{123} + \mathbf{T}\mathbf{V}_{\Theta}{}^T\mathbf{j}_{123}. \tag{3.72}$$

Multiplying the matrix ${\mathbf{i}_{123}}^T$ to both sides of Eq. (3.72) and extracting the $(1,2)$ component of the matrix gives

$$\dot{\theta} = (\mathbf{i}_1)^{\cdot T}\mathbf{i}_2 + {\mathbf{T}_1}^T\mathbf{V}_\Theta{}^T\tilde{\mathbf{T}}_1. \tag{3.73}$$

Taking the material derivative of Eq. (2.58) and using Eqs. (3.11) and (3.25), the following expression can be obtained.

$$(\mathbf{i}_1)^{\cdot} = {\mathbf{j}_{123}}^T\left\{\mathbf{V}_\Theta\mathbf{T}_1 + \boldsymbol{\Gamma}\mathbf{E}_V({}^{n+1}\mathbf{z}) + \boldsymbol{\Gamma}\widehat{\mathbf{E}}({}^{n+1}\dot{\mathbf{z}})\right\}. \tag{3.74}$$

Substituting Eq. (3.74) and the relation $\mathbf{i}_2 = -{\mathbf{j}_{123}}^T\tilde{\mathbf{T}}_1$ into Eq. (3.73) yields the following.

$$\begin{aligned}\dot{\theta} &= \left\{-\frac{1}{1+\varepsilon_m}{\tilde{\mathbf{T}}_1}^T\widehat{\mathbf{E}}({}^{n+1}\dot{\mathbf{z}})\right\} + \left\{-\frac{1}{1+\varepsilon_m}{\tilde{\mathbf{T}}_1}^T\mathbf{E}_V({}^{n+1}\mathbf{z})\right\} \\ &\equiv \widehat{\theta}({}^{n+1}\mathbf{z};{}^{n+1}\dot{\mathbf{z}}) + \theta_V({}^{n+1}\mathbf{z}),\end{aligned} \tag{3.75}$$

where the orthogonality of $\mathbf{j}_{123}$ and the relation ${\tilde{\mathbf{T}}_1}^T\mathbf{T}_1 = 0$ are employed in the first and second equalities, respectively. Also, taking the material derivative of the virtual rotation angle of Eq. (2.82), and substituting the expression of $\dot{\varepsilon}_m$ in Eq. (3.31) and using Eqs. (3.60) and (3.25) leads to

$$\dot{\bar{\theta}} = \widehat{\theta}({}^{n+1}\mathbf{z};\dot{\bar{\mathbf{z}}}) + \widehat{\eta}_\theta({}^{n+1}\mathbf{z};{}^{n+1}\dot{\mathbf{z}},\bar{\mathbf{z}}) + \bar{\theta}_V({}^{n+1}\mathbf{z}), \tag{3.76}$$

where the explicit design dependence term is derived as

$$\begin{aligned}\bar{\theta}_V({}^{n+1}\mathbf{z}) \equiv{}& \frac{1}{(1+\varepsilon_m)^2}\widehat{\mathbf{E}}(\bar{\mathbf{z}})^T\tilde{\mathbf{T}}_1\varepsilon_m^V({}^{n+1}\mathbf{z}) - \frac{1}{1+\varepsilon_m}\mathbf{E}_V(\bar{\mathbf{z}})^T\tilde{\mathbf{T}}_1 \\ &- \frac{1}{1+\varepsilon_m}\widehat{\mathbf{E}}(\bar{\mathbf{z}})^T\tilde{\mathbf{I}}\boldsymbol{\Gamma}\mathbf{E}_V({}^{n+1}\mathbf{z}).\end{aligned} \tag{3.77}$$

Then, taking the material derivative of Eq. (2.140) and substituting Eqs. (3.75) and (3.77) yields

$$\left[b({}^{n+1}\mathbf{d},{}^{n+1}\bar{\mathbf{d}})\right]^{\cdot} = b({}^{n+1}\mathbf{d},{}^{n+1}\dot{\bar{\mathbf{d}}}) + b^*({}^{n+1}\mathbf{d};{}^{n+1}\dot{\mathbf{d}},{}^{n+1}\bar{\mathbf{d}}) + b^V({}^{n+1}\mathbf{d},{}^{n+1}\bar{\mathbf{d}}), \tag{3.78}$$

where ${}^{n+1}\dot{\mathbf{d}} \equiv ({}^{n+1}\dot{\mathbf{z}};{}^{n+1}\dot{\underline{\mathbf{z}}};{}^{n+1}\dot{\lambda}_L)$ and $\dot{\bar{\mathbf{d}}} \equiv (\dot{\bar{\mathbf{z}}};\dot{\underline{\bar{\mathbf{z}}}};\dot{\bar{\lambda}}_L)$, and the explicit design dependence term is derived as

$$\begin{aligned}b^V({}^{n+1}\mathbf{d},{}^{n+1}\bar{\mathbf{d}}) \equiv{}& \bar{\lambda}_L(\tilde{\mathbf{T}}_1+\mathbf{T}_1)^T\underline{\mathbf{T}}_1\left\{\theta_V(\mathbf{z}) - \underline{\theta}_V(\mathbf{z})\right\} + \lambda_L(\tilde{\mathbf{T}}_1+\mathbf{T}_1)^T\underline{\mathbf{T}}_1\left\{\bar{\theta}_V(\mathbf{z}) - \underline{\bar{\theta}}_V(\underline{\mathbf{z}})\right\} \\ &+ \lambda_L(\bar{\theta}-\underline{\bar{\theta}})(\mathbf{T}_1-\tilde{\mathbf{T}}_1)^T\underline{\mathbf{T}}_1\left\{\theta_V(\mathbf{z}) - \underline{\theta}_V(\underline{\mathbf{z}})\right\}.\end{aligned} \tag{3.79}$$

Penalty method

Taking the material derivative of both sides of Eq. (2.146), and using the relations of Eqs. (A.16) and (2.147) lead to

$$[b(^{n+1}\mathbf{d},\bar{\mathbf{d}})]^{\cdot} = b(^{n+1}\mathbf{d},\dot{\bar{\mathbf{d}}}) + b^*(^{n+1}\mathbf{d};^{n+1}\dot{\mathbf{d}},\bar{\mathbf{d}}) + b'_V(^{n+1}\mathbf{d},\bar{\mathbf{d}}), \tag{3.80}$$

where $^{n+1}\mathbf{d} \equiv (^{n+1}\dot{\mathbf{z}};^{n+1}\dot{\underset{\sim}{\mathbf{z}}})$, $\bar{\mathbf{d}} \equiv (\dot{\bar{\mathbf{z}}};\dot{\bar{\underset{\sim}{\mathbf{z}}}})$ and the explicit design dependence term is derived as

$$\begin{aligned} b'_V(^{n+1}\mathbf{d},\bar{\mathbf{d}}) \equiv\ & k_p\left\{\mathbf{E}_V(\bar{\mathbf{z}})^T\boldsymbol{\Gamma} - \underset{\sim}{\mathbf{E}}_V(\bar{\underset{\sim}{\mathbf{z}}})^T\underset{\sim}{\boldsymbol{\Gamma}}\right\}\mathbf{T}_1^d \\ & + k_p\left\{\widehat{\mathbf{E}}(\bar{\mathbf{z}})^T\boldsymbol{\Gamma} - \widehat{\underset{\sim}{\mathbf{E}}}(\bar{\underset{\sim}{\mathbf{z}}})^T\underset{\sim}{\boldsymbol{\Gamma}}\right\}\left\{\boldsymbol{\Gamma}\mathbf{E}_V(^{n+1}\mathbf{z}) - \underset{\sim}{\boldsymbol{\Gamma}}\underset{\sim}{\mathbf{E}}_V(^{n+1}\underset{\sim}{\mathbf{z}})\right\} \\ & - \frac{k_p}{1+\varepsilon_m}\widehat{\mathbf{E}}(\bar{\mathbf{z}})^T\left\{\boldsymbol{\Gamma}\mathbf{T}_1{}^T\mathbf{T}_1^d + sym\left(\boldsymbol{\Gamma}\mathbf{T}_1^d\mathbf{T}_1{}^T\right)\right\}\mathbf{E}_V(^{n+1}\mathbf{z}) \\ & + \frac{k_p}{1+\underset{\sim}{\varepsilon}_m}\widehat{\underset{\sim}{\mathbf{E}}}(\bar{\underset{\sim}{\mathbf{z}}})^T\left\{\underset{\sim}{\boldsymbol{\Gamma}}\underset{\sim}{\mathbf{T}}_1{}^T\mathbf{T}_1^d + sym\left(\underset{\sim}{\boldsymbol{\Gamma}}\mathbf{T}_1^d\underset{\sim}{\mathbf{T}}_1{}^T\right)\right\}\underset{\sim}{\mathbf{E}}_V(^{n+1}\underset{\sim}{\mathbf{z}}). \end{aligned} \tag{3.81}$$

Hence, considering the rotational continuity condition, the sensitivity equation (3.61) can be rewritten as follows: For a given $^{n+1}\mathbf{d}$, find $^{n+1}\dot{\mathbf{d}} \in \bar{W}$ such that

$$\begin{aligned} & a^*(^{n+1}\mathbf{z};^{n+1}\dot{\mathbf{z}},\bar{\mathbf{z}}) + \underset{\sim}{a}^*(^{n+1}\underset{\sim}{\mathbf{z}};^{n+1}\dot{\underset{\sim}{\mathbf{z}}},\bar{\underset{\sim}{\mathbf{z}}}) + b^*(^{n+1}\mathbf{d};^{n+1}\dot{\mathbf{d}},\bar{\mathbf{d}}) \\ & = \left\{\ell'_V(^{n+1}\mathbf{z},\bar{\mathbf{z}}) + \underset{\sim}{\ell}'_V(^{n+1}\underset{\sim}{\mathbf{z}},\bar{\underset{\sim}{\mathbf{z}}})\right\} - \left\{a'_V(^{n+1}\mathbf{z},\bar{\mathbf{z}}) + \underset{\sim}{a}'_V(^{n+1}\underset{\sim}{\mathbf{z}},\bar{\underset{\sim}{\mathbf{z}}}) + b'_V(^{n+1}\mathbf{d},\bar{\mathbf{d}})\right\},\ \forall\bar{\mathbf{d}} \in \bar{W}. \end{aligned} \tag{3.82}$$

It is noted that the linearized energy form $b^*(^{n+1}\mathbf{d};^{n+1}\dot{\mathbf{d}},\bar{\mathbf{d}})$ and the explicit design dependence term $b'_V(^{n+1}\mathbf{d},\bar{\mathbf{d}})$ are chosen as Eqs. (2.147) and (3.81) for the penalty method, and Eqs. (2.140) and (3.79) for the Lagrange multiplier method.

3.1.4 Adjoint variable method

We present configuration DSA and sizing DSA expressions in the following.

3.1.4.1 Configuration DSA

We consider two cases of performance measures; displacement and rotation angle at a specific position. *First,* consider the performance measure of displacement at a specific position. The displacement performance measure at a position $s = s^*$ can be expressed as

$$\psi_1 = \int_\Omega {}^{n+1}z_i(s)\delta(s-s^*)ds, \tag{3.83}$$

where $^{n+1}z_i$ denotes the i-th component of the displacement vector $^{n+1}\mathbf{z}$, and $\delta(\bullet)$ denotes the Dirac delta measure. The material derivative of the functional (3.83) is obtained as

$$\dot{\psi}_1 = \int_\Omega {}^{n+1}\dot{z}_i(s)\delta(s-s^*)ds. \tag{3.84}$$

Second, consider a rotation angle at a position $s = s^*$ as a performance measure.

$$\psi_2 = \int_\Omega \theta(s)\delta(s-s^*)ds. \tag{3.85}$$

The material derivative of the functional (3.85) is obtained, using Eq. (3.75), as

$$\dot{\psi}_2 = \int_\Omega \widehat{\theta}({}^{n+1}\mathbf{z}; {}^{n+1}\dot{\mathbf{z}})\delta(s-s^*)ds + \int_\Omega \theta_V({}^{n+1}\mathbf{z})\delta(s-s^*)ds. \tag{3.86}$$

In Eq. (3.81), changing variables, ${}^{n+1}\dot{\mathbf{z}} \to \bar{\boldsymbol{\lambda}}$ and $\bar{\mathbf{z}} \to \boldsymbol{\lambda}$ since each pair of them belongs to the same function space $\bar{Z}$, we have the following.

$$\begin{aligned} &a^*({}^{n+1}\mathbf{z}; \bar{\boldsymbol{\lambda}}, \boldsymbol{\lambda}) + \underset{\sim}{a}^*({}^{n+1}\underset{\sim}{\mathbf{z}}; \bar{\underset{\sim}{\boldsymbol{\lambda}}}, \underset{\sim}{\boldsymbol{\lambda}}) + b^*(\bar{\mathbf{d}}_\lambda, \mathbf{d}_\lambda) \\ &= \left\{ \ell'_V({}^{n+1}\mathbf{z}, \boldsymbol{\lambda}) + \underset{\sim}{\ell}'_V({}^{n+1}\underset{\sim}{\mathbf{z}}, \underset{\sim}{\boldsymbol{\lambda}}) \right\} - \left\{ \ a'_V({}^{n+1}\mathbf{z}, \boldsymbol{\lambda}) + \underset{\sim}{a}'_V({}^{n+1}\underset{\sim}{\mathbf{z}}, \underset{\sim}{\boldsymbol{\lambda}}) + b'_V({}^{n+1}\mathbf{d}, \mathbf{d}_\lambda) \ \right\}, \end{aligned} \tag{3.87}$$

where $\mathbf{d}_\lambda \equiv (\boldsymbol{\lambda}; \underset{\sim}{\boldsymbol{\lambda}})$ and $\bar{\mathbf{d}}_\lambda \equiv (\bar{\boldsymbol{\lambda}}; \bar{\underset{\sim}{\boldsymbol{\lambda}}})$ for the penalty method, and $\mathbf{d}_\lambda \equiv (\boldsymbol{\lambda}, \underset{\sim}{\boldsymbol{\lambda}}, \lambda_L^*)$ and $\bar{\boldsymbol{d}}_\lambda \equiv (\bar{\boldsymbol{\lambda}}, \bar{\underset{\sim}{\boldsymbol{\lambda}}}, \bar{\lambda}_L^*)$ for the Lagrange multiplier method, where $\lambda_L^* \in \mathbf{R}^1$ denotes a Lagrange multiplier for which $\bar{\lambda}_L^* \in \mathbf{R}^1$ is a virtual one. Consider first the displacement performance measure. Changing variables ${}^{n+1}\dot{z}_i \to \bar{\lambda}_i$ in the implicit dependence term of Eq. (3.84) since they belong to the same function space $\bar{Z}$, and equating to the energy form of Eq. (3.87), we have the following adjoint equation: For a given ${}^{n+1}\mathbf{d}$, find $\mathbf{d}_\lambda \in \bar{W}$, such that

$$a^*({}^{n+1}\mathbf{z}; \bar{\boldsymbol{\lambda}}, \boldsymbol{\lambda}) + \underset{\sim}{a}^*({}^{n+1}\underset{\sim}{\mathbf{z}}; \bar{\underset{\sim}{\boldsymbol{\lambda}}}, \underset{\sim}{\boldsymbol{\lambda}}) + b^*(\bar{\mathbf{d}}_\lambda, \mathbf{d}_\lambda) = \int_\Omega \bar{\lambda}_i(s)\delta(s-s^*)ds, \tag{3.88}$$

where $\boldsymbol{\lambda}$ and $\bar{\boldsymbol{\lambda}}$ respectively denote the adjoint response and virtual adjoint response. The right hand side means a unit force acted on the position $s = s^*$. In the same way, for the rotation angle performance measure, we obtain the following adjoint equation: For a given ${}^{n+1}\mathbf{d}$, find $\mathbf{d}_\lambda \in \bar{W}$, such that

$$a^*({}^{n+1}\mathbf{z}; \bar{\boldsymbol{\lambda}}, \boldsymbol{\lambda}) + \underset{\sim}{a}^*({}^{n+1}\underset{\sim}{\mathbf{z}}; \bar{\underset{\sim}{\boldsymbol{\lambda}}}, \underset{\sim}{\boldsymbol{\lambda}}) + b^*(\bar{\mathbf{d}}_\lambda, \mathbf{d}_\lambda) = \int_\Omega \widehat{\theta}({}^{n+1}\mathbf{d}; \bar{\mathbf{d}}_\lambda)\delta(s-s^*)ds. \tag{3.89}$$

The right hand side means a unit moment acted on the position $s = s^*$. After evaluating Eq. (3.88) at $\bar{\lambda}_i(s) = {}^{n+1}\dot{z}_i$ since they belong to the same space $\bar{Z}$, and using the equivalence of Eqs. (3.87) and (3.88), the implicit dependence term in Eq. (3.84) can be replaced by the explicit dependence one as

$$\begin{aligned} \dot{\psi}_1 &= {}^{n+1}\dot{z}_i(s^*) \\ &= \left\{ \ell'_V({}^{n+1}\mathbf{z}, \boldsymbol{\lambda}) + \underset{\sim}{\ell}'_V({}^{n+1}\underset{\sim}{\mathbf{z}}, \underset{\sim}{\boldsymbol{\lambda}}) \right\} - \left\{ a'_V({}^{n+1}\mathbf{z}, \boldsymbol{\lambda}) + \underset{\sim}{a}'_V({}^{n+1}\underset{\sim}{\mathbf{z}}, \underset{\sim}{\boldsymbol{\lambda}}) + b'_V({}^{n+1}\mathbf{d}, \mathbf{d}_\lambda) \right\}. \end{aligned} \tag{3.90}$$

Similarly, for the rotation angle performance measure, evaluating Eq. (3.89) at $\bar{\lambda}_i(s) = {}^{n+1}\dot{z}_i$ and using the equivalence of Eqs. (3.87) and (3.89), the implicit dependence term in Eq. (3.86) can be

replaced by the explicit dependence one as

$$\begin{aligned}\psi_2 &= \dot{\theta}(s^*) \\ &= \left\{\ell'_V({}^{n+1}\mathbf{z},\boldsymbol{\lambda}) + \underset{\sim}{\ell}'_V({}^{n+1}\underset{\sim}{\mathbf{z}},\underset{\sim}{\boldsymbol{\lambda}})\right\} - \left\{a'_V({}^{n+1}\mathbf{z},\boldsymbol{\lambda}) + \underset{\sim}{a}'_V({}^{n+1}\underset{\sim}{\mathbf{z}},\underset{\sim}{\boldsymbol{\lambda}}) + b'_V({}^{n+1}\mathbf{d},\mathbf{d}_\lambda)\right\} \\ &+ \int_\Omega \theta_V({}^{n+1}\mathbf{z})\delta(s-s^*)ds. \end{aligned} \tag{3.91}$$

It should be noted that, considering a non-conservative loading condition, the energy form $a^*({}^{n+1}\mathbf{z};\boldsymbol{\lambda},\bar{\boldsymbol{\lambda}})$ of Eqs. (3.88) and (3.89) is asymmetric for $\boldsymbol{\lambda}$ and $\bar{\boldsymbol{\lambda}}$, thus the tangent stiffness matrix at the final equilibrium configuration of Eq. (2.119) should be transposed before being used in solving the adjoint equations (3.88) and (3.89). If a conservative loading condition is considered only, then the energy form $a^*({}^{n+1}\mathbf{z};\boldsymbol{\lambda},\bar{\boldsymbol{\lambda}})$ can be replaced by $a^*({}^{n+1}\mathbf{z};\bar{\boldsymbol{\lambda}},\boldsymbol{\lambda})$ due to symmetry, and the original tangent stiffness matrix at the final equilibrium configuration of Eq. (2.119) can be utilized for the adjoint equations (3.88) and (3.89).

Isogeometric discretization

$\mathbf{E}_V(\bar{\mathbf{z}})$ in Eq. (3.81) can be obtained by replacing ${}^{n+1}\mathbf{z}$ with $\bar{\mathbf{z}}$ in Eq. (3.60), and then it is discretized using Eq. (2.126) as

$$\mathbf{E}_V(\bar{\mathbf{z}}) = \left\{\mathbf{V}_\Theta{}^T - (\nabla_s\cdot\hat{\mathbf{V}})\mathbf{I}\right\}\mathbf{j}_{123}\sum_{N=1}^{n} W_{N,s}\bar{\mathbf{y}}_N. \tag{3.92}$$

3.1.4.2 Sizing DSA

We consider the beam cross-section thickness as a sizing design. The cross-section thickness distributions along beam members can be continuously parameterized by combining thickness coefficients assigned to control points and the NURBS basis functions, as [80]

$$h \equiv h(\xi) = \sum_{N=1}^{n_{th}} h_I W_N(\xi), \tag{3.93}$$

where h_I denotes the I-th thickness control coefficient, and n_{th} denotes the number of thickness control coefficients in each patch. We define the first variation of displacement with respect to sizing design $\mathbf{u}$, as

$${}^{n+1}\mathbf{z}'(s) \equiv \frac{d}{d\tau}{}^{n+1}\mathbf{z}(s;\mathbf{u}+\tau\delta\mathbf{u})|_{\tau=0}, \tag{3.94}$$

where τ denotes the design time, and $(\bullet)'$ denotes the first variation or is sometimes called the partial derivative. Taking the first variation of the variational equation of Eq. (2.117), and using the fact that $\bar{\mathbf{z}}' \in \bar{Z}$, we have the following sizing design sensitivity equation: For a given ${}^{n+1}\mathbf{z}$, find ${}^{n+1}\mathbf{z}' \in \bar{Z}$ such that

$$a^*({}^{n+1}\mathbf{z};{}^{n+1}\mathbf{z}',\bar{\mathbf{z}}) = \ell'_{\delta\mathbf{u}}({}^{n+1}\mathbf{z},\bar{\mathbf{z}}) - a'_{\delta\mathbf{u}}({}^{n+1}\mathbf{z},\bar{\mathbf{z}}),\ \forall\bar{\mathbf{z}}\in\bar{Z}. \tag{3.95}$$

The explicit design dependence term of the strain energy form with respect to the K-th thickness coefficient is obtained as

$$a'_{\delta\mathbf{u}}(\mathbf{z},\bar{\mathbf{z}}) \equiv \int_\Omega \left\{ \begin{array}{l} E\,(\partial A/\partial h_K)\,\varepsilon_m(\mathbf{z})\widehat{\varepsilon}_m(\mathbf{z};\bar{\mathbf{z}}) \\ +E\,(\partial I/\partial h_K)\,\omega_b(\mathbf{z})\widehat{\omega}_b(\mathbf{z};\bar{\mathbf{z}}) \end{array} \right\} ds, \tag{3.96}$$

where $\partial A/\partial h_K$ and $\partial I/\partial h_K$, respectively, denote the partial derivatives of the cross-sectional area and second moment of inertia, with respect to h_K, which can be obtained by using the chain rule of differentiation and Eq. (3.93), as

$$\frac{\partial A(\xi)}{\partial h_K} = \frac{\partial A(\xi)}{\partial h}\frac{\partial h}{\partial h_K} = \frac{\partial A(\xi)}{\partial h}W_K(\xi), \text{ and } \frac{\partial \mathbf{I}_\rho(\xi)}{\partial h_K} = \frac{\partial I(\xi)}{\partial h}\frac{\partial h}{\partial h_K} = \frac{\partial \mathbf{I}_\rho(\xi)}{\partial h}W_K(\xi). \tag{3.97}$$

It is assumed that the load form does not have explicit dependence on the sizing design, that is, $\ell'_{\delta\mathbf{u}}({}^{n+1}\mathbf{z},\bar{\mathbf{z}}) = 0$. Using the similar procedure in the configuration DSA, the adjoint sizing design sensitivity of the displacement and rotation angle can be expressed by the same expression as

$$\psi'_1 = {}^{n+1}z'_i(s^*) = -\left\{a'_{\delta\mathbf{u}}({}^{n+1}\mathbf{z},\boldsymbol{\lambda}) + \underline{a}'_{\delta\mathbf{u}}({}^{n+1}\underline{\mathbf{z}},\underline{\boldsymbol{\lambda}})\right\}, \tag{3.98}$$

and

$$\psi'_2 = \theta'(s^*) = -\left\{a'_{\delta\mathbf{u}}({}^{n+1}\mathbf{z},\boldsymbol{\lambda}) + \underline{a}'_{\delta\mathbf{u}}({}^{n+1}\underline{\mathbf{z}},\underline{\boldsymbol{\lambda}})\right\}, \tag{3.99}$$

where the adjoint responses $\boldsymbol{\lambda}$ in Eqs. (3.98) and (3.99) can be obtained, respectively, from solving Eqs. (3.88) and (3.89).

3.1.5 Shape memory polymer material model

3.1.5.1 Evolution of stored strain sensitivity

We explain the expressions of the design sensitivity equation considering the design dependence of stored strains. Since we consider only prescribed displacement as a mechanical load as mentioned in section 3.5.2, the sensitivity equation of Eq. (3.82) is rewritten as: For a given ${}^{n+1}\mathbf{d} = ({}^{n+1}\mathbf{z};{}^{n+1}\underline{\mathbf{z}}) \in W$, find ${}^{n+1}\dot{\mathbf{d}} = ({}^{n+1}\dot{\mathbf{z}};{}^{n+1}\dot{\underline{\mathbf{z}}}) \in \bar{W}$ such that

$$\begin{aligned} &a^*({}^{n+1}\mathbf{z};{}^{n+1}\dot{\mathbf{z}},\bar{\mathbf{z}}) + \underline{a}^*({}^{n+1}\underline{\mathbf{z}};{}^{n+1}\dot{\underline{\mathbf{z}}},\bar{\underline{\mathbf{z}}}) + b^*({}^{n+1}\dot{\mathbf{d}},\bar{\mathbf{d}}) \\ &= -\left\{ \begin{array}{l} a'_V({}^{n+1}\mathbf{z},\bar{\mathbf{z}}) + \underline{a}'_V({}^{n+1}\underline{\mathbf{z}},\bar{\underline{\mathbf{z}}}) \\ +b'_V({}^{n+1}\mathbf{d},\bar{\mathbf{d}}) \end{array} \right\}, \ \forall \bar{\mathbf{d}} \in \bar{W}. \end{aligned} \tag{3.100}$$

Since the thermal strain is assumed to depend only on the temperature as expressed in Eq. (2.153), it does not have any dependence on the configuration design. Thus, among the three strain components, total and stored strains are considered to have design dependences. Then,

the explicit design dependence term of the strain energy form is derived as

$$
\begin{aligned}
a'_V({}^{n+1}\mathbf{z},\bar{\mathbf{z}}) \equiv & \int_\Omega \begin{bmatrix} E^t A\{\varepsilon_m^V({}^{n+1}\mathbf{z}) - k_3{}^n\dot{\varepsilon}_m^s\}\bar{\varepsilon}_m \\ +E^t I\{\omega_b^V({}^{n+1}\mathbf{z}) - k_3{}^n\dot{\omega}_b^s\}\bar{\omega}_b \end{bmatrix} ds \\
& + \int_\Omega \left[{}^{n+1}N\bar{\varepsilon}_m^V({}^{n+1}\mathbf{z},\bar{\mathbf{z}}) + {}^{n+1}M\bar{\omega}_b^V({}^{n+1}\mathbf{z},\bar{\mathbf{z}})\right] ds \\
& + \int_\Omega ({}^{n+1}N\bar{\varepsilon}_m + {}^{n+1}M\bar{\omega}_b)\nabla_s\cdot\hat{\mathbf{V}} ds,
\end{aligned} \tag{3.101}
$$

where $\nabla_s\cdot\hat{\mathbf{V}} = \hat{\mathbf{V}}_{,s}\cdot\mathbf{j}_1$. Comparing Eq. (3.101) with the explicit design dependence term presented in Eq. 3.40 for purely elastic materials, the only difference is that the stored strain sensitivity terms at previous configuration (n) appear. The stored membrane and bending strains in Eq. (3.101) can be determined from the following evolution equation obtained by taking the material derivative of Eq. (2.158),

$$
\left.\begin{aligned}
{}^{n+1}\dot{\varepsilon}_m^s &= k_3({}^n\dot{\varepsilon}_m^s + k_1{}^{n+1}\dot{\varepsilon}_m^a{}^{n+1}\phi_{f,T}\Delta T) \\
{}^{n+1}\dot{\omega}_b^s &= k_3({}^n\dot{\omega}_b^s + k_1{}^{n+1}\dot{\omega}_b^{a\,n+1}\phi_{f,T}\Delta T)
\end{aligned}\right\}, \tag{3.102}
$$

where the sensitivity of the active elastic strains can be obtained, by taking the material derivative of Eq. (2.163), as

$$
\left.\begin{aligned}
{}^{n+1}\dot{\varepsilon}_m^a &= C^a({}^{n+1}\dot{\varepsilon}_m - k_3{}^n\dot{\varepsilon}_m^s) \\
{}^{n+1}\dot{\omega}_b^a &= C^a({}^{n+1}\dot{\omega}_b - k_3{}^n\dot{\omega}_b^s)
\end{aligned}\right\}. \tag{3.103}
$$

Table 3.1 shows the overall procedure for updating the stored strain sensitivity. As noted in Table 3.1, in our implementation, the stored strain sensitivity at all the Gauss integration points at the previous temperature step are kept and utilized at the current temperature step to calculate the current stored strain sensitivity at each Gauss point. The overall procedure of deformation analysis and DSA during the four steps of thermomechanical process of SMP material is illustrated in Fig. 3.3.

Table 3.1: Update procedure of stored strain sensitivity

(i) Calculate the fictitious load of the sensitivity equation (3.100) using the stored strain sensitivity at previous configuration (n), and solve the sensitivity equation.
(ii) Calculate the total strain sensitivity $\dot{\varepsilon}_m$ and $\dot{\omega}_b$ using Eqs. (3.31),(3.33), and (3.34).
(iii) Calculate the active strain sensitivity by evaluating Eq. (3.103) using the stored strain sensitivity at configuration (n).
(iv) Update the stored strain sensitivities at configuration $(n+1)$ using Eq. (3.102), and keep the stored strain sensitivities at all the Gauss integration points.

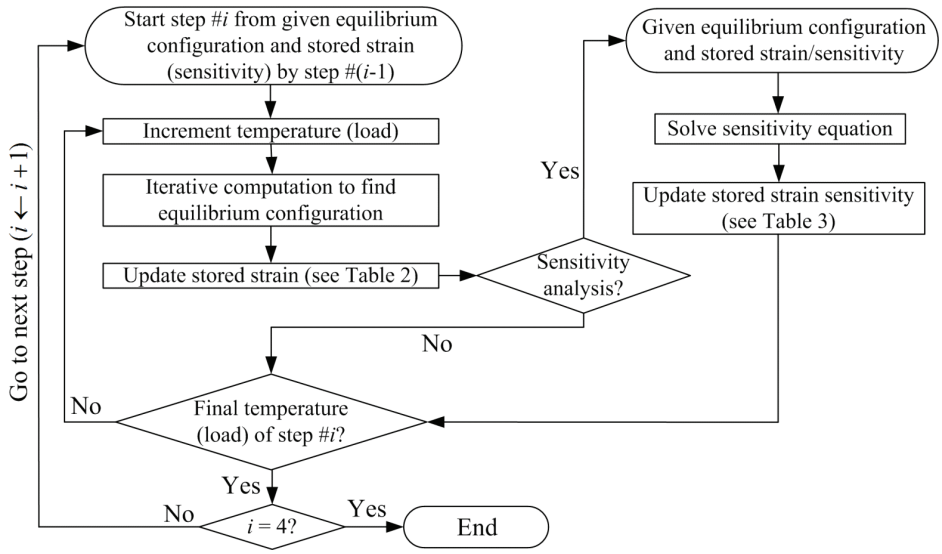

Figure 3.3: Overall procedure of deformation and design sensitivity analyses

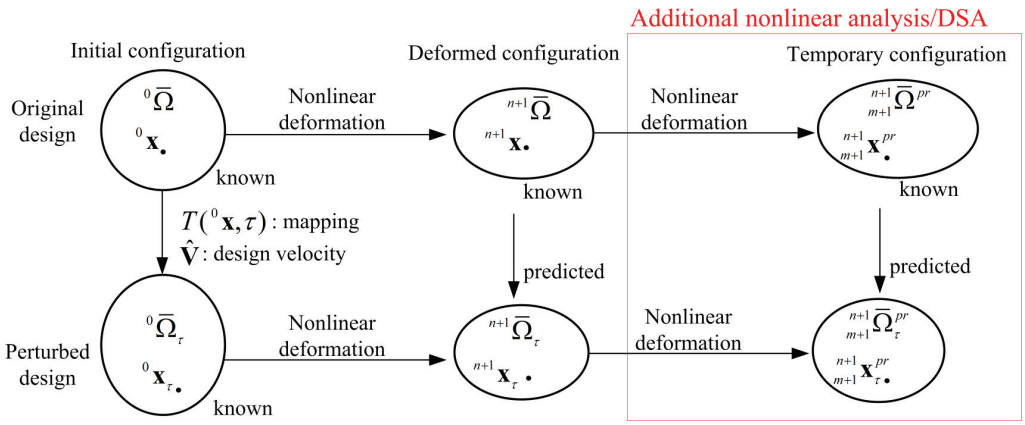

Figure 3.4: Overall DSA procedures of original and additional problems

3.1.5.2 Poisson's ratio sensitivity calculation during shape recovery

Fig. 3.4 illustrates the overall procedure of calculating the design sensitivity of Poisson's ratio during the shape recovery process (step #4). The term "*temporary configuration*" denotes an equilibrium configuration during the additional nonlinear analysis, and the Poisson's ratio is calculated using the displacement (${}^{m+1}\mathbf{y}^{pr}$) of the additional nonlinear analysis. After combining the material derivatives of Eqs. (2.174) and (2.175), and using the fact that ${}^{m+1}\dot{\mathbf{w}}^{pr} = \mathbf{0}$, the following expression can be obtained.

$$\overset{n+1}{\underset{m+1}{\dot{\mathbf{z}}}}{}^{tot} = {}^{n+1}\dot{\mathbf{z}} + {}^{m+1}\dot{\mathbf{y}}^{pr}. \tag{3.104}$$

In Eq. (3.100), after replacing ${}^{n+1}\mathbf{z}$ and ${}^{n+1}\dot{\mathbf{z}}$ respectively with $\overset{n+1}{\underset{m+1}{\mathbf{z}}}{}^{tot}$ and $\overset{n+1}{\underset{m+1}{\dot{\mathbf{z}}}}{}^{tot}$ of Eq. (3.104), rearranging terms gives the following DSA equation to determine ${}^{m+1}\dot{\mathbf{y}}^{pr}$: For given $\overset{n+1}{\underset{m+1}{\mathbf{d}}}{}^{tot}$ =

$({}^{n+1}_{m+1}\mathbf{z}^{tot}; {}^{n+1}_{m+1}\underset{\sim}{\mathbf{z}}^{tot}) \in W$ and ${}^{n+1}\dot{\mathbf{d}} = ({}^{n+1}\dot{\mathbf{z}}; {}^{n+1}\underset{\sim}{\dot{\mathbf{z}}}) \in \bar{W}$, find ${}^{m+1}\dot{\mathbf{d}}^{pr} = ({}^{m+1}\dot{\mathbf{y}}^{pr}; {}^{m+1}\underset{\sim}{\dot{\mathbf{y}}}^{pr}) \in \bar{W}$ such that

$$
\begin{aligned}
&a^*({}^{n+1}_{m+1}\mathbf{z}^{tot}; {}^{m+1}\dot{\mathbf{y}}^{pr}, \bar{\mathbf{z}}) + \underset{\sim}{a}^*({}^{n+1}_{m+1}\underset{\sim}{\mathbf{z}}^{tot}; {}^{m+1}\underset{\sim}{\dot{\mathbf{y}}}^{pr}, \underset{\sim}{\bar{\mathbf{z}}}) + b^*({}^{m+1}\dot{\mathbf{d}}^{pr}, \bar{\mathbf{d}}) \\
&= -a'_V({}^{n+1}_{m+1}\mathbf{z}^{tot}, \bar{\mathbf{z}}) - \underset{\sim}{a}'_V({}^{n+1}_{m+1}\underset{\sim}{\mathbf{z}}^{tot}, \underset{\sim}{\bar{\mathbf{z}}}) - b'_V({}^{n+1}_{m+1}\mathbf{d}^{tot}, \bar{\mathbf{d}}) - a^*({}^{n+1}_{m+1}\mathbf{z}^{tot}; {}^{n+1}\dot{\mathbf{z}}, \bar{\mathbf{z}}) \\
&- \underset{\sim}{a}^*({}^{n+1}_{m+1}\underset{\sim}{\mathbf{z}}^{tot}; {}^{n+1}\underset{\sim}{\dot{\mathbf{z}}}, \underset{\sim}{\bar{\mathbf{z}}}) - b^*({}^{n+1}\dot{\mathbf{d}}, \bar{\mathbf{d}}), \quad \forall \bar{\mathbf{d}} \in \bar{W},
\end{aligned}
\tag{3.105}
$$

where ${}^{n+1}\dot{\mathbf{d}}$ is previously determined by solving Eq. (3.100) in the DSA of original nonlinear analysis. The obtained sensitivity ${}^{m+1}\dot{\mathbf{y}}^{pr}$ is utilized to calculate the Poisson's ratio sensitivity, and the detailed procedure can be found in Appendix F.1.

3.2 Geometrically exact shear deformable beam structures

3.2.1 Configuration design velocity field

We present a continuum-based analytical DSA formulation for beam neutral axis configuration design. It is assumed that a cross-section is always orthogonal to neutral axis in initial (undeformed) state, and does not have a design degree-of-freedom of rotation about the neutral axis. Thus, in this paper, an initial cross-section orientation is determined by a neutral axis configuration design only. Let $\tau \geq 0$ denote a time-like parameter that controls a design variation, and hereafter, a subscript τ represents a quantity evaluated at a perturbed design. The perturbed neutral axis position can be expressed using a given design velocity field $\mathbf{V}(s)$ and a perturbation amount τ as

$$
\boldsymbol{\varphi}_{0\tau}(s_\tau) \equiv \boldsymbol{\varphi}_0(s) + \tau \mathbf{V}(s), \tag{3.106}
$$

where the design velocity field is defined as

$$
\mathbf{V}(s) \equiv \frac{d}{d\tau}\boldsymbol{\varphi}_{0\tau}(s_\tau)\big|_{\tau=0} = \dot{\boldsymbol{\varphi}}_0(s). \tag{3.107}
$$

Fig. 3.5 depicts a design variation and induced changes of a neutral axis configuration and orthonormal frame attached to a cross-section. Taking derivative of Eq. (2.182) and using Eq. (3.107), the material derivative of the current neutral axis position can be decomposed as

$$
{}^{n+1}\dot{\boldsymbol{\varphi}}(s) = \mathbf{V}(s) + {}^{n+1}\dot{\mathbf{z}}(s) \tag{3.108}
$$

where the pointwise material derivative of ${}^{n+1}\mathbf{z}(s)$ is defined as

$$
{}^{n+1}\dot{\mathbf{z}} \equiv \frac{d}{d\tau}\,{}^{n+1}\mathbf{z}_\tau(s_\tau)\big|_{\tau=0} = {}^{n+1}\mathbf{z}' + {}^{n+1}\mathbf{z}_{,s}\dot{s}, \tag{3.109}
$$

and the partial derivative of ${}^{n+1}\mathbf{z}$ is defined as

$$
{}^{n+1}\mathbf{z}' \equiv \frac{d}{d\tau}\,{}^{n+1}\mathbf{z}_\tau(s)\big|_{\tau=0} = \lim_{\tau\to 0}\frac{{}^{n+1}\mathbf{z}_\tau(s) - {}^{n+1}\mathbf{z}(s)}{\tau}. \tag{3.110}
$$

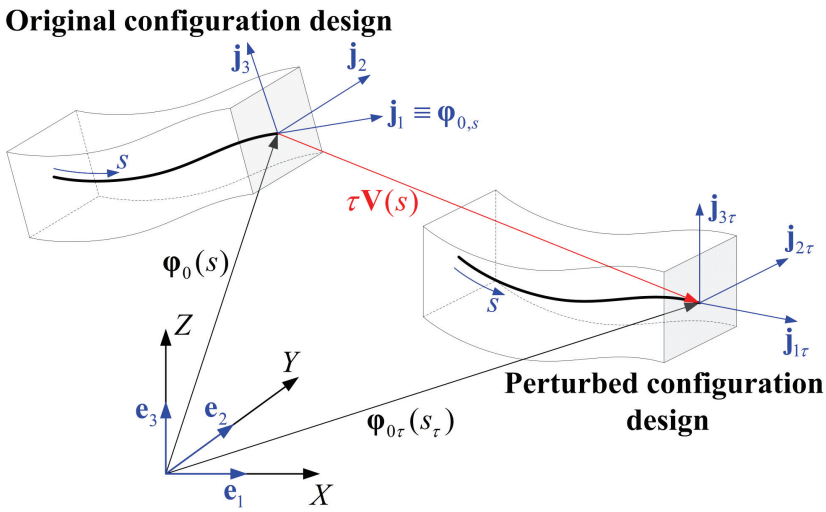

Figure 3.5: Configuration design variation of a spatial beam

Here and hereafter, we denote the material derivative of $(\bullet)$ by an upper dot $\dot{(\bullet)}$, or sometimes by a superscript dot $(\bullet)^{\bullet}$. The superscript $(n+1)$ represents quantities at final equilibrium configuration in deformation analysis. For future use, we have the formula of material derivative of tangential derivative from the Eq. 3.21) as

$$\left\{(\bullet)_{,s}\right\}^{\bullet} = \dot{(\bullet)}_{,s} - (\bullet)_{,s}\nabla_s \cdot \mathbf{V}, \tag{3.111}$$

where $\nabla_s \cdot \mathbf{V} \equiv \mathbf{V}_{,s} \cdot \mathbf{j}_1$. By using Eqs. (3.108) and (3.111), we have the following.

$$({}^{n+1}\boldsymbol{\varphi}_{,s})^{\bullet} = \mathbf{V}_{,s} + {}^{n+1}\dot{\mathbf{z}}_{,s} - {}^{n+1}\boldsymbol{\varphi}_{,s}\nabla_s \cdot \mathbf{V}. \tag{3.112}$$

Taking the material derivative of the orthogonality relation $\boldsymbol{\Lambda}_0 {\boldsymbol{\Lambda}_0}^T = \mathbf{I}$, we have

$$\dot{\boldsymbol{\Lambda}}_0(s) {\boldsymbol{\Lambda}_0(s)}^T \equiv \hat{\boldsymbol{\Theta}}_0^* \in so(3). \tag{3.113}$$

From Eq. (2.177), we have $\boldsymbol{\Lambda}_0(s) = \left[\mathbf{j}_1(s), \mathbf{j}_2(s), \mathbf{j}_3(s)\right]$; thus, $\hat{\boldsymbol{\Theta}}_0^*(s)$ can be calculated using Eq. (3.113) as

$$\hat{\boldsymbol{\Theta}}_0^* = \left[\mathbf{j}_1^{\bullet}(s), \mathbf{j}_2^{\bullet}(s), \mathbf{j}_3^{\bullet}(s)\right] {\boldsymbol{\Lambda}_0}^T, \tag{3.114}$$

and in the later section 3.6, we detail a procedure of determining the orthonormal base vectors $\mathbf{j}_1(s), \mathbf{j}_2(s), \mathbf{j}_3(s)$ and calculating their material derivatives $\mathbf{j}_1^{\bullet}(s), \mathbf{j}_2^{\bullet}(s), \mathbf{j}_3^{\bullet}(s)$ which are explicit in terms of a given design velocity field. Multiplying $\boldsymbol{\Lambda}_0$ to both sides of Eq. (3.113) yields

$$\dot{\boldsymbol{\Lambda}}_0(s) \equiv \frac{d}{d\tau}\boldsymbol{\Lambda}_{0\tau}(s_\tau)|_{\tau=0} = \hat{\boldsymbol{\Theta}}_0^*(s)\boldsymbol{\Lambda}_0(s). \tag{3.115}$$

In a similar way, from the orthogonality ${}^{n+1}\mathbf{\Lambda}\,{}^{n+1}\mathbf{\Lambda}^T = \mathbf{I}$, we obtain

$$ {}^{n+1}\dot{\mathbf{\Lambda}}(s)\,{}^{n+1}\mathbf{\Lambda}(s)^T \equiv \hat{\mathbf{\Theta}}^* \in so(3), \tag{3.116} $$

and multiplying ${}^{n+1}\mathbf{\Lambda}$ to both sides yields

$$ {}^{n+1}\dot{\mathbf{\Lambda}}(s) \equiv \frac{d}{d\tau}\,{}^{n+1}\mathbf{\Lambda}_\tau(s_\tau)\big|_{\tau=0} = \hat{\mathbf{\Theta}}^*(s)\,{}^{n+1}\mathbf{\Lambda}(s). \tag{3.117} $$

Taking the material derivative of ${}^{n+1}\mathbf{\Lambda}_L \equiv {}^{n+1}\mathbf{\Lambda}\mathbf{\Lambda}_0{}^T$ from Eq. (2.179) and substituting Eqs. (3.117) and (3.115), followed by multiplying ${}^{n+1}\mathbf{\Lambda}_L{}^T$ yields

$$ {}^{n+1}\dot{\mathbf{\Lambda}}_L\,{}^{n+1}\mathbf{\Lambda}_L{}^T = \hat{\mathbf{\Theta}}^* - {}^{n+1}\mathbf{\Lambda}_L\hat{\mathbf{\Theta}}_0^*\,{}^{n+1}\mathbf{\Lambda}_L{}^T \equiv \hat{\mathbf{\Theta}}_L^* \in so(3). \tag{3.118} $$

Using Eq. (3.118), Eq. (3.117) can be rewritten as

$$ {}^{n+1}\dot{\mathbf{\Lambda}}(s) = \left\{\hat{\mathbf{\Theta}}_L^*(s) + \hat{\boldsymbol{\theta}}_0^*(s)\right\}{}^{n+1}\mathbf{\Lambda}(s), \text{ where } \hat{\boldsymbol{\theta}}_0^* \equiv {}^{n+1}\mathbf{\Lambda}_L(s)\hat{\mathbf{\Theta}}_0^*(s)\,{}^{n+1}\mathbf{\Lambda}_L(s)^T \in so(3). \tag{3.119} $$

At a clamped boundary Γ_d, it is apparent that ${}^{n+1}\mathbf{z}(s) = {}^{n+1}\mathbf{z}_\tau(s_\tau) = \mathbf{0}$ and ${}^{n+1}\mathbf{\Lambda}_L(s) = {}^{n+1}\mathbf{\Lambda}_{L\tau}(s_\tau) = \mathbf{I}$ at $s \in \Gamma_d$ and $s_\tau \in \Gamma_{d\tau}$. Thus, it can be easily verified that ${}^{n+1}\dot{\mathbf{z}}(s) = \mathbf{0}$ and ${}^{n+1}\dot{\mathbf{\Lambda}}_L(s) = \mathbf{0}_{3\times3}$ followed by $\hat{\mathbf{\Theta}}_L^*(s) = \mathbf{0}_{3\times3}$ at $s \in \Gamma_d$. Therefore, we state that $\boldsymbol{\eta}^* \equiv \left({}^{n+1}\dot{\mathbf{z}}, \mathbf{\Theta}_L^*\right) \in \bar{Z}$.

3.2.1.1 Material derivatives of strain measures

Taking the material derivative of the strain measures in Eq. (2.195), and substituting Eqs. (3.112) and (3.119) gives

$$ \begin{aligned} {}^{n+1}\dot{\mathbf{\Gamma}} &= {}^{n+1}\mathbf{\Lambda}^T\left({}^{n+1}\dot{\mathbf{z}}_{,s} - \mathbf{\Theta}_L^* \times {}^{n+1}\boldsymbol{\varphi}_{,s}\right) + \left[{}^{n+1}\mathbf{\Lambda}^T\left\{\mathbf{V}_{,s} - \left(\hat{\boldsymbol{\theta}}_0^* + \nabla_s\cdot\mathbf{VI}\right){}^{n+1}\boldsymbol{\varphi}_{,s}\right\}\right] \\ &\equiv \widehat{\mathbf{\Gamma}}({}^{n+1}\boldsymbol{\eta}; {}^{n+1}\boldsymbol{\eta}^*) + \mathbf{\Gamma'}_V({}^{n+1}\boldsymbol{\eta}), \end{aligned} \tag{3.120} $$

and

$$ {}^{n+1}\dot{\hat{\mathbf{\Omega}}} = {}^{n+1}\mathbf{\Lambda}^T\hat{\mathbf{\Theta}}_{L,s}^*\,{}^{n+1}\mathbf{\Lambda} + {}^{n+1}\hat{\mathbf{\Omega}}\hat{\mathbf{\Theta}}_{0M}^* - \hat{\mathbf{\Theta}}_{0M}^*\,{}^{n+1}\hat{\mathbf{\Omega}} - {}^{n+1}\hat{\mathbf{\Omega}}\nabla_s\cdot\mathbf{V}, \tag{3.121} $$

where $\hat{\mathbf{\Theta}}_{0M}^* \equiv \mathbf{\Lambda}_0{}^T\hat{\mathbf{\Theta}}_0^*\mathbf{\Lambda}_0 \in so(3)$. A dual vector of ${}^{n+1}\dot{\hat{\mathbf{\Omega}}}$ can be obtained by using the relation ${}^{n+1}\mathbf{\Lambda}^T\hat{\mathbf{\Theta}}_{L,s}^*\,{}^{n+1}\mathbf{\Lambda} = \widehat{{}^{n+1}\mathbf{\Lambda}^T\mathbf{\Theta}_{L,s}^*}$ and recalling the Lie bracket such that $\left({}^{n+1}\hat{\mathbf{\Omega}}\hat{\mathbf{\Theta}}_{0M}^* - \hat{\mathbf{\Theta}}_{0M}^*\,{}^{n+1}\hat{\mathbf{\Omega}}\right)\mathbf{h} = \left({}^{n+1}\mathbf{\Omega} \times \mathbf{\Theta}_{0M}^*\right) \times \mathbf{h}$, $\forall \mathbf{h} \in \mathbf{R}^3$, as follows.

$$ {}^{n+1}\dot{\mathbf{\Omega}} = {}^{n+1}\mathbf{\Lambda}^T\mathbf{\Theta}_{L,s}^* + \left({}^{n+1}\mathbf{\Omega} \times \mathbf{\Theta}_{0M}^* - {}^{n+1}\mathbf{\Omega}\nabla_s\cdot\mathbf{V}\right) \equiv \widehat{\mathbf{\Omega}}({}^{n+1}\mathbf{\Lambda}; \mathbf{\Theta}_L^*) + \mathbf{\Omega'}_V({}^{n+1}\mathbf{\Lambda}). \tag{3.122} $$

In Eqs. (3.120) and (3.122), $\mathbf{\Gamma'}_V(^{n+1}\boldsymbol{\eta})$ and $\mathbf{\Omega'}_V(^{n+1}\boldsymbol{\Lambda})$ represents explicit expressions in terms of a given design velocity field. From the constitutive relation of Eq. (2.196), we obtain

$$\dot{\mathbf{R}} = \begin{Bmatrix} \dot{\mathbf{N}} \\ \dot{\mathbf{M}} \end{Bmatrix} = \mathbf{C} \begin{Bmatrix} \widehat{\dot{\mathbf{\Gamma}}}(^{n+1}\boldsymbol{\eta};\boldsymbol{\eta}^*) \\ \widehat{\dot{\mathbf{\Omega}}}(^{n+1}\boldsymbol{\Lambda};\dot{\boldsymbol{\Theta}}_L^*) \end{Bmatrix} + \mathbf{C} \begin{Bmatrix} \mathbf{\Gamma'}_V(^{n+1}\boldsymbol{\eta}) \\ \mathbf{\Omega'}_V(^{n+1}\boldsymbol{\Lambda}) \end{Bmatrix}. \tag{3.123}$$

Also, taking the material derivative of the virtual strains in Eq. (2.194), and substituting Eqs. (3.112) and (3.119) gives, after some algebraic manipulations, the following.

$$\begin{aligned} \begin{Bmatrix} \dot{\bar{\mathbf{\Gamma}}} \\ \dot{\bar{\mathbf{\Omega}}} \end{Bmatrix}^T \mathbf{R} = & \begin{Bmatrix} \bar{\mathbf{z}} \\ \bar{\boldsymbol{\Theta}} \end{Bmatrix}^T \mathbf{\Psi B \Psi}^T \begin{Bmatrix} {}^{n+1}\dot{\mathbf{z}} \\ \boldsymbol{\Theta}_L^* \end{Bmatrix} + \begin{Bmatrix} \widehat{\dot{\mathbf{\Gamma}}}(^{n+1}\boldsymbol{\eta};\dot{\tilde{\boldsymbol{\eta}}}) \\ \widehat{\dot{\mathbf{\Omega}}}(^{n+1}\boldsymbol{\Lambda};\dot{\tilde{\boldsymbol{\Theta}}}) \end{Bmatrix}^T \mathbf{R} \\ & + \begin{Bmatrix} \bar{\mathbf{z}} \\ \bar{\boldsymbol{\Theta}} \end{Bmatrix}^T \left\{ \begin{bmatrix} \mathbf{0}_{3\times3} & \mathbf{0}_{3\times3} \\ -[\mathbf{V}_{,s}\times] & \mathbf{0}_{3\times3} \end{bmatrix} + \mathbf{\Xi} \begin{bmatrix} \hat{\boldsymbol{\theta}}_0^* & \mathbf{0}_{3\times3} \\ \mathbf{0}_{3\times3} & \hat{\boldsymbol{\theta}}_0^* \end{bmatrix} - (\nabla_s \cdot \mathbf{V})\mathbf{\Xi} \right\} \mathbf{\Pi R}. \end{aligned} \tag{3.124}$$

3.2.2 Direct differentiation method

In this section, we present a direct differentiation method of DSA. We often use the following formula: for a unit vector $\mathbf{b} \equiv \mathbf{a}/\|\mathbf{a}\|$, $\mathbf{a}, \mathbf{b} \in \mathbf{R}^3$, we have

$$\dot{\mathbf{b}} = \frac{1}{\|\mathbf{a}\|} \mathbf{P}_{\mathbf{b}} \dot{\mathbf{a}}. \tag{3.125}$$

3.2.2.1 Material derivatives of pressure load vectors

In B.2, we derive material derivatives of base vectors $\mathbf{a}_I (I = 1,2,3)$. From Eq. (2.199), by assuming that the pressure load components $\tilde{n}_I^p (I = 1,2,3)$ does not have design dependence, we derive the material derivative of the pressure load vector, using Eqs. (B.5), (B.8) and (B.9), as

$$\begin{aligned} \dot{\mathbf{n}}_p = & \left\{ \left(\tilde{n}_2^p \mathbf{T}_{2\varphi}^p + \tilde{n}_3^p \mathbf{T}_{3\varphi}^p + \tilde{\mathbf{n}}_p \otimes \mathbf{a}_1 \right) \dot{\mathbf{z}}_{,s} + \left(\tilde{n}_2^p \mathbf{T}_{2\Theta}^p + \tilde{n}_3^p \mathbf{T}_{3\Theta}^p \right) \boldsymbol{\Theta}_L^* \right\} \\ & + \left\{ \left(\tilde{n}_2^p \mathbf{T}_{2\varphi}^p + \tilde{n}_3^p \mathbf{T}_{3\varphi}^p + \tilde{\mathbf{n}}_p \otimes \mathbf{a}_1 \right) \left(\mathbf{V}_{,s} - \boldsymbol{\varphi}_{,s} \nabla_s \cdot \mathbf{V} \right) + \left(\tilde{n}_2^p \mathbf{T}_{2\Theta}^p + \tilde{n}_3^p \mathbf{T}_{3\Theta}^p \right) \boldsymbol{\theta}_0^* \right\} \\ & \equiv \widehat{\dot{\mathbf{n}}}_p(^{n+1}\boldsymbol{\eta};\boldsymbol{\eta}^*) + \mathbf{n'}_{pV}(^{n+1}\boldsymbol{\eta}), \end{aligned} \tag{3.126}$$

where $\boldsymbol{\eta}^* \equiv \left({}^{n+1}\dot{\mathbf{z}}, \boldsymbol{\Theta}_L^* \right)$ we use

$$\tilde{\mathbf{n}}_p \left(\|\boldsymbol{\varphi}_{,s}\| \right)^\bullet = \left(\tilde{\mathbf{n}}_p \otimes \mathbf{a}_1 \right) \dot{\mathbf{z}}_{,s} + \left(\tilde{\mathbf{n}}_p \otimes \mathbf{a}_1 \right) \left(\mathbf{V}_{,s} - \boldsymbol{\varphi}_{,s} \nabla_s \cdot \mathbf{V} \right). \tag{3.127}$$

Finally, we have

$$\begin{aligned} \left[\ell_p(^{n+1}\boldsymbol{\eta};\bar{\mathbf{z}}) \right]^\bullet = & \int_\Omega \dot{\bar{\mathbf{z}}}^T \mathbf{n}_p ds + \int_\Omega \bar{\mathbf{z}}^T \widehat{\dot{\mathbf{n}}}_p(^{n+1}\boldsymbol{\eta};^{n+1}\dot{\boldsymbol{\eta}}) ds + \left\{ \int_\Omega \bar{\mathbf{z}}^T \mathbf{n'}_{pV}(^{n+1}\boldsymbol{\eta}) ds + \int_\Omega \bar{\mathbf{z}}^T \mathbf{n}_p \nabla_s \cdot \mathbf{V} ds \right\} \\ & \equiv \ell_p(^{n+1}\boldsymbol{\eta};\dot{\bar{\mathbf{z}}}) + \ell_p^*(^{n+1}\boldsymbol{\eta};^{n+1}\dot{\boldsymbol{\eta}},\bar{\mathbf{z}}) + \ell'_{pV}(^{n+1}\boldsymbol{\eta};\bar{\mathbf{z}}). \end{aligned} \tag{3.128}$$

From Eq. (2.201), the following identity holds.

$$a({}^{n+1}\boldsymbol{\eta};\dot{\bar{\boldsymbol{\eta}}}) = \ell(\dot{\bar{\boldsymbol{\eta}}}) + \ell_p({}^{n+1}\boldsymbol{\eta};\dot{\bar{\boldsymbol{\eta}}}),\ \ \forall \dot{\bar{\boldsymbol{\eta}}} \in \bar{Z}. \tag{3.129}$$

Taking the material derivatives of both sides of Eq. (2.201) and using Eq. (3.29) and substituting Eqs. (3.123), (3.124) and (3.128), followed by rearranging the terms, we obtain the following sensitivity equation: For a given ${}^{n+1}\boldsymbol{\eta} \equiv ({}^{n+1}\mathbf{z}, {}^{n+1}\boldsymbol{\Lambda})$, find $\boldsymbol{\eta}^* \equiv \left({}^{n+1}\dot{\mathbf{z}}, \boldsymbol{\Theta}_L^*\right) \in \bar{Z}$ such that

$$a^*({}^{n+1}\boldsymbol{\eta};\bar{\boldsymbol{\eta}},\boldsymbol{\eta}^*) = \ell'_V({}^{n+1}\boldsymbol{\eta};\bar{\boldsymbol{\eta}}) + \ell'_{pV}({}^{n+1}\boldsymbol{\eta};\bar{\boldsymbol{\eta}}) - a'_V({}^{n+1}\boldsymbol{\eta};\bar{\boldsymbol{\eta}}),\ \ \forall \bar{\boldsymbol{\eta}} \in \bar{Z}. \tag{3.130}$$

where the following explicit design dependence terms are defined.

$$\begin{aligned} a'_V({}^{n+1}\boldsymbol{\eta};\bar{\boldsymbol{\eta}}) \equiv & \int_\Omega \left\{ \begin{array}{c} \widehat{\boldsymbol{\Gamma}}({}^{n+1}\boldsymbol{\eta};\bar{\boldsymbol{\eta}}) \\ \widehat{\boldsymbol{\Omega}}({}^{n+1}\boldsymbol{\Lambda};\bar{\boldsymbol{\Theta}}) \end{array} \right\}^T \mathbf{C} \left\{ \begin{array}{c} \boldsymbol{\Gamma}'_V({}^{n+1}\boldsymbol{\eta}) \\ \boldsymbol{\Omega}'_V({}^{n+1}\boldsymbol{\Lambda}) \end{array} \right\} ds \\ & + \int_\Omega \bar{\boldsymbol{\eta}}^T \left\{ \left[\begin{array}{cc} \mathbf{0} & \mathbf{0} \\ -[\mathbf{V}_{,s}\times] & \mathbf{0} \end{array} \right] + \boldsymbol{\Xi} \left[\begin{array}{cc} \hat{\boldsymbol{\theta}}_0^* & \mathbf{0} \\ \mathbf{0} & \hat{\boldsymbol{\theta}}_0^* \end{array} \right] \right\} \boldsymbol{\Pi}\mathbf{R} ds, \end{aligned} \tag{3.131}$$

and

$$\ell'_V({}^{n+1}\boldsymbol{\eta};\bar{\boldsymbol{\eta}}) \equiv \int_\Omega \left(\left\{ \begin{array}{c} \bar{\mathbf{z}} \\ \bar{\boldsymbol{\Theta}} \end{array} \right\}^T \mathbf{n}_{\text{ext}} + \bar{\boldsymbol{\Theta}}^T \mathbf{m}_{\text{ext}} \right) \nabla_s \cdot \mathbf{V} ds. \tag{3.132}$$

Since Eq. (3.130) solves directly for $\boldsymbol{\eta}^* \equiv ({}^{n+1}\dot{\mathbf{z}}, \boldsymbol{\Theta}_L^*)$, it is called the *direct differentiation method*. It is noted that if $\boldsymbol{\Theta}_L^*$ is determined, then ${}^{n+1}\dot{\boldsymbol{\Lambda}}$ can be directly computed from Eq. (3.119). It is obvious that in Eq. (3.130), the same tangent stiffness operator as used in Eq. (2.204) is employed with different right-hand side. As this method solves this linear equation for each of design variables, it becomes much less efficient than an adjoint variable method which will be explained in the following section, if the number of design variables is much larger than the number of performance measures.

3.2.3 Adjoint variable method

We present an adjoint variable method of configuration DSA for two kinds of performance measures; first, displacement at a specific position, and second, total strain energy of a structure.

3.2.3.1 Displacement at a specific position

A displacement at a position $s = s^*$ on a neutral axis can be expressed as

$$\psi_1 = \int_\Omega {}^{n+1}z_i(s)\delta(s-s^*)ds, \tag{3.133}$$

where ${}^{n+1}z_i$ denotes the i-th component of the displacement vector ${}^{n+1}\mathbf{z}$, and $\delta(\bullet)$ denotes the Dirac delta measure. The material derivative of the functional (3.133) is obtained as

$$\dot{\psi}_1 = \int_\Omega {}^{n+1}\dot{z}_i(s)\delta(s-s^*)ds. \tag{3.134}$$

Let the adjoint response $\boldsymbol{\lambda} \equiv (\lambda_z, \lambda_\Theta) \in \bar{Z}$ and the virtual adjoint response $\bar{\boldsymbol{\lambda}} \equiv (\bar{\lambda}_z, \bar{\lambda}_\Theta) \in \bar{Z}$. In Eq. (3.130), changing variables $\boldsymbol{\eta}^* \to \bar{\boldsymbol{\lambda}}$ and $\bar{\boldsymbol{\eta}} \to \boldsymbol{\lambda}$, since each pair of them belongs to the same function space $\bar{Z}$, we have the following.

$$a^*({}^{n+1}\boldsymbol{\eta}; \bar{\boldsymbol{\lambda}}, \boldsymbol{\lambda}) = \ell'_V({}^{n+1}\boldsymbol{\eta}; \boldsymbol{\lambda}) + \ell'_{pV}({}^{n+1}\boldsymbol{\eta}; \boldsymbol{\lambda}) - a'_V({}^{n+1}\boldsymbol{\eta}; \boldsymbol{\lambda}),\ \forall \bar{\boldsymbol{\lambda}} \in \bar{Z}. \tag{3.135}$$

Changing variables ${}^{n+1}\dot{z}_i \to \bar{\lambda}_i$ in Eq. (3.134) since they belong to the same function space $\bar{Z}$, and equating to the linearized strain energy form of Eq. (3.135), we have the following adjoint equation: For a given ${}^{n+1}\boldsymbol{\eta} \equiv ({}^{n+1}\mathbf{z}, {}^{n+1}\boldsymbol{\Lambda})$, find $\boldsymbol{\lambda} \in \bar{Z}$, such that

$$a^*({}^{n+1}\boldsymbol{\eta}; \bar{\boldsymbol{\lambda}}, \boldsymbol{\lambda}) = \int_\Omega \bar{\lambda}_i(s)\delta(s-s^*)ds,\ \forall \bar{\boldsymbol{\lambda}} \in \bar{Z}, \tag{3.136}$$

where $\boldsymbol{\lambda}$ and $\bar{\boldsymbol{\lambda}}$, respectively, denote the adjoint and virtual adjoint responses. The right hand side of Eq. (3.136) is physically interpreted as a unit force acting on the position $s = s^*$. Evaluating Eq. (3.136) at $\bar{\boldsymbol{\lambda}} = \boldsymbol{\eta}^* \in \bar{Z}$, we have the following identity.

$$a^*({}^{n+1}\boldsymbol{\eta}; \boldsymbol{\eta}^*, \boldsymbol{\lambda}) = \int_\Omega {}^{n+1}\dot{z}_i(s)\delta(s-s^*)ds. \tag{3.137}$$

Similarly, Eq. (3.130) may be evaluated at $\bar{\boldsymbol{\eta}} = \boldsymbol{\lambda} \in \bar{Z}$ to obtain

$$a^*({}^{n+1}\boldsymbol{\eta}; \boldsymbol{\eta}^*, \boldsymbol{\lambda}) = \ell'_V({}^{n+1}\boldsymbol{\eta}; \boldsymbol{\lambda}) + \ell'_{pV}({}^{n+1}\boldsymbol{\eta}; \boldsymbol{\lambda}) - a'_V({}^{n+1}\boldsymbol{\eta}; \boldsymbol{\lambda}). \tag{3.138}$$

Using the equivalence of Eqs. (3.137) and (3.138), we can substitute the right-hand side of Eq. (3.134) with the explicit design dependence terms as

$$\dot{\psi}_1 = \ell'_V({}^{n+1}\boldsymbol{\eta}; \boldsymbol{\lambda}) + \ell'_{pV}({}^{n+1}\boldsymbol{\eta}; \boldsymbol{\lambda}) - a'_V({}^{n+1}\boldsymbol{\eta}; \boldsymbol{\lambda}). \tag{3.139}$$

3.2.3.2 Total strain energy

A total strain energy can be expressed as

$$\psi_2 \equiv \frac{1}{2}\int_\Omega \left(\boldsymbol{\Gamma}^T\mathbf{N} + \boldsymbol{\Omega}^T\mathbf{M}\right) ds. \tag{3.140}$$

Taking the material derivative of Eq. (3.140) using Eqs. (3.120), (3.122), (3.123), and (3.29) gives

$$\dot{\psi}_2 = \int_\Omega \left\{ \widehat{\mathbf{\Gamma}}({}^{n+1}\boldsymbol{\eta};\boldsymbol{\eta}^*)^T \mathbf{N} + \widehat{\mathbf{\Omega}}({}^{n+1}\boldsymbol{\eta};\boldsymbol{\eta}^*)^T \mathbf{M} \right\} ds + \int_\Omega \left\{ \mathbf{\Gamma}'_V({}^{n+1}\boldsymbol{\eta})^T \mathbf{N} + \mathbf{\Omega}'_V({}^{n+1}\boldsymbol{\eta})^T \mathbf{M} \right\} ds$$
$$+ \frac{1}{2}\int_\Omega \left(\mathbf{\Gamma}^T \mathbf{N} + \mathbf{\Omega}^T \mathbf{M} \right) \nabla_s \cdot \mathbf{V} ds, \tag{3.141}$$

where the first integral term represents the implicit dependence on design, and the second and third integral terms are explicitly expressed in terms of a given design velocity field. Changing variables $\boldsymbol{\eta}^* \to \bar{\boldsymbol{\lambda}}$ in the implicit design dependence terms since they belong to the same function space $\bar{Z}$, and equating to the linearized strain energy form of Eq. (3.135) gives the following adjoint equation: For a given ${}^{n+1}\boldsymbol{\eta} \equiv ({}^{n+1}\mathbf{z}, {}^{n+1}\mathbf{\Lambda})$, find $\boldsymbol{\lambda} \in \bar{Z}$, such that

$$a^*({}^{n+1}\boldsymbol{\eta}; \bar{\boldsymbol{\lambda}}, \boldsymbol{\lambda}) = \int_\Omega \left\{ \widehat{\mathbf{\Gamma}}({}^{n+1}\boldsymbol{\eta}; \bar{\boldsymbol{\lambda}})^T \mathbf{N} + \widehat{\mathbf{\Omega}}({}^{n+1}\boldsymbol{\eta}; \bar{\boldsymbol{\lambda}})^T \mathbf{M} \right\} ds, \ \forall \bar{\boldsymbol{\lambda}} \in \bar{Z}. \tag{3.142}$$

Evaluating Eq. (3.142) at $\bar{\boldsymbol{\lambda}} = \boldsymbol{\eta}^* \in \bar{Z}$, we have

$$a^*({}^{n+1}\boldsymbol{\eta}; \boldsymbol{\eta}^*, \boldsymbol{\lambda}) = \int_\Omega \left\{ \widehat{\mathbf{\Gamma}}({}^{n+1}\boldsymbol{\eta}; \boldsymbol{\eta}^*)^T \mathbf{N} + \widehat{\mathbf{\Omega}}({}^{n+1}\boldsymbol{\eta}; \boldsymbol{\eta}^*)^T \mathbf{M} \right\} ds. \tag{3.143}$$

Upon the identity of Eqs. (3.143) and (3.138), the first integral term of Eq. (3.141) can be replaced by explicit design dependence terms, then we finally have

$$\dot{\psi}_2 = \ell'_V({}^{n+1}\boldsymbol{\eta}; \boldsymbol{\lambda}) + \ell'_{pV}({}^{n+1}\boldsymbol{\eta}; \boldsymbol{\lambda}) - a'_V({}^{n+1}\boldsymbol{\eta}; \boldsymbol{\lambda}) + \int_\Omega \left\{ \mathbf{\Gamma}'_V({}^{n+1}\boldsymbol{\eta})^T \mathbf{N} + \mathbf{\Omega}'_V({}^{n+1}\mathbf{\Lambda})^T \mathbf{M} \right\} ds$$
$$+ \frac{1}{2}\int_\Omega \left(\mathbf{\Gamma}^T \mathbf{N} + \mathbf{\Omega}^T \mathbf{M} \right) \nabla_s \cdot \mathbf{V} ds. \tag{3.144}$$

3.2.3.3 Isogeometric discretization of adjoint equation

A virtual adjoint response and adjoint response are approximated by using the NURBS basis function as

$$\begin{Bmatrix} \lambda_z^h \\ \lambda_\Theta^h \end{Bmatrix} = \sum_{N=1}^{n} W_N(\xi) \bar{\boldsymbol{\lambda}}_N, \ \text{and} \ \begin{Bmatrix} \bar{\lambda}_z^h \\ \bar{\lambda}_\Theta^h \end{Bmatrix} = \sum_{N=1}^{n} W_N(\xi) \boldsymbol{\lambda}_N, \tag{3.145}$$

where $\bar{\boldsymbol{\lambda}}_N$ and $\boldsymbol{\lambda}_N$ denote coefficients assigned to N-th control point. Replacing the virtual response and incremental solution in Eq. (2.204) respectively with $\boldsymbol{\lambda}$ and $\bar{\boldsymbol{\lambda}}$, and substituting Eq. (3.145) leads to the following discretized expressions of the tangent operator in the adjoint equations of Eqs. (3.136) and (3.142).

$$a^*({}^{n+1}\boldsymbol{\eta}^h; \bar{\boldsymbol{\lambda}}^h, \boldsymbol{\lambda}^h) = \bar{\boldsymbol{d}}_\lambda^T \mathbf{K}_T({}^{n+1}\boldsymbol{\eta})^T \mathbf{d}_\lambda, \tag{3.146}$$

where $\mathbf{d}_\lambda$ and $\bar{\mathbf{d}}_\lambda$ respectively denotes the global assembly of adjoint response and virtual adjoint response coefficients. It should be noted that $\mathbf{K}_T({}^{n+1}\boldsymbol{\eta})$ has the same form of the tangent stiffness matrix in Eq. (2.215). This means the adjoint equations solve with transposed form of the tangent stiffness matrices at equilibrium in the deformation analysis. However, if $\mathbf{K}_T({}^{n+1}\boldsymbol{\eta})$ is symmetric,

the transpose operation is unnecessary, and the same tangent stiffness matrix at equilibrium during the deformation analysis can be utilized.

3.3 Geometrically exact shear-deformable shell structures

3.3.1 Configuration design velocity field

We present a continuum-based analytical DSA formulation for shell configuration design. It is assumed that the *director vector* is always normal to the neutral surface in the initial configuration. Thus, in this work, the initial director orientation is determined by a neutral surface configuration design. Let $\tau \geq 0$ denote a time-like parameter that controls a design variation, and hereafter, a subscript τ represents a quantity evaluated at a perturbed design. It is assumed that the parametric domain $\bar{A}$ and the parametric coordinates ξ^1 and ξ^2 of a material point does not have design dependence. The perturbed neutral surface position can be expressed using a design velocity vector $\mathbf{V}(\xi^1,\xi^2)$ and the parameter τ as

$$\boldsymbol{\varphi}_{0\tau}(\xi^1,\xi^2) = \boldsymbol{\varphi}_0(\xi^1,\xi^2) + \tau\mathbf{V}(\xi^1,\xi^2), \tag{3.147}$$

where the design velocity field is defined as

$$\mathbf{V}(\xi^1,\xi^2) \equiv \frac{d}{d\tau}\boldsymbol{\varphi}_{0\tau}(\xi^1,\xi^2)\big|_{\tau=0} = \dot{\boldsymbol{\varphi}}_0(\xi^1,\xi^2). \tag{3.148}$$

Taking the material derivative of Eq. (2.221) and using Eq. (3.147), the material derivative of the current neutral axis position can be decomposed into

$$^{n+1}\dot{\boldsymbol{\varphi}}(\xi^1,\xi^2) = \mathbf{V}(\xi^1,\xi^2) + {}^{n+1}\dot{\mathbf{z}}. \tag{3.149}$$

where the material derivative of $^{n+1}\mathbf{z}$ is defined as

$$^{n+1}\dot{\mathbf{z}} \equiv \frac{d}{d\tau}\,{}^{n+1}\mathbf{z}_\tau(\xi^1,\xi^2)\big|_{\tau=0}. \tag{3.150}$$

We denote the material derivative of $(\bullet)$ by an upper dot $(\dot{\bullet})$ or a superscript dot $(\bullet)^\bullet$. The superscript $(n+1)$ represents quantities at final equilibrium configuration in deformation analysis. Taking the material derivative of the orthogonality relation $\boldsymbol{\Lambda}_L\boldsymbol{\Lambda}_L{}^T = \mathbf{I}$, we have

$$\dot{\boldsymbol{\Lambda}}_L\boldsymbol{\Lambda}_L{}^T \equiv \hat{\boldsymbol{\Theta}}_L^* \in so(3), \tag{3.151}$$

followed by

$$\dot{\boldsymbol{\Lambda}}_L = \hat{\boldsymbol{\Theta}}_L^*\boldsymbol{\Lambda}_L. \tag{3.152}$$

At a clamped boundary, it is apparent that $^{n+1}\mathbf{z} = {}^{n+1}\mathbf{z}_\tau = \mathbf{0}$ and $^{n+1}\boldsymbol{\Lambda}_L = {}^{n+1}\boldsymbol{\Lambda}_{L\tau} = \mathbf{I}$. Thus, it can be easily verified that $^{n+1}\dot{\mathbf{z}} = \mathbf{0}$ and $^{n+1}\dot{\boldsymbol{\Lambda}}_L = \mathbf{0}_{3\times3}$ at the clamped boundary, which yields that $\boldsymbol{\Theta}_L^*$ satisfies the homogenous boundary condition. Therefore, we state that $^{n+1}\boldsymbol{\eta}^* \equiv (^{n+1}\dot{\mathbf{z}}, \boldsymbol{\Theta}_L^*) \in \bar{Z}$.

3.3.1.1 Material derivatives of strain measures

For the sake of taking material derivatives of strain measures including a differentiated quantity $(\bullet)_{,\alpha}$, we use the transformation of Eq. (2.224). By taking the material derivative of the orthogonality relation $\mathbf{J}\mathbf{J}^{-1} = \mathbf{I}$, we have

$$\left(\mathbf{J}^{-1}\right)^{\bullet} = -\mathbf{J}^{-1}\dot{\mathbf{J}}\mathbf{J}^{-1}, \tag{3.153}$$

which is rewritten in a component form by

$$\left(\mathbf{J}^{-1}\right)^{\bullet} = -\mathbf{J}^{-1}\dot{\mathbf{J}}\mathbf{J}^{-1}. \tag{3.154}$$

From Eqs. (2.225) and (3.154), we obtain

$$\left\{(\bullet)_{,\alpha}\right\}^{\bullet} = (\dot{\bullet})_{,\alpha} - J^{-1}_{\alpha\gamma}\dot{J}_{\gamma\delta}(\bullet)_{,\delta}. \tag{3.155}$$

The material derivatives of the strain measures are derived by applying Eq. (3.155) together with Eqs. (3.149) and (3.148) as

$$\begin{aligned} {}^{n+1}\dot{\mathbf{E}}_{\alpha} &= {}^{n+1}\mathbf{\Lambda}_L{}^{T}\left({}^{n+1}\dot{\mathbf{z}}_{,\alpha} + {}^{n+1}\boldsymbol{\varphi}_{,\alpha} \times \mathbf{\Theta}^{*}_{L}\right) + \left\{{}^{n+1}\mathbf{\Lambda}_L{}^{T}\left(\mathbf{V}_{,\alpha} - J^{-1}_{\alpha\gamma}\dot{J}_{\gamma\delta}{}^{n+1}\boldsymbol{\varphi}_{,\delta}\right) - (\mathbf{j}_{\alpha})^{\bullet}\right\} \\ &\equiv \widehat{\mathbf{E}}_{\alpha}({}^{n+1}\boldsymbol{\eta}; {}^{n+1}\boldsymbol{\eta}^{*}) + \mathbf{E}'_{\alpha V}({}^{n+1}\boldsymbol{\eta}), \end{aligned} \tag{3.156}$$

and

$${}^{n+1}\dot{\hat{\mathbf{K}}}_{\alpha} = {}^{n+1}\mathbf{\Lambda}_L{}^{T}\hat{\mathbf{\Theta}}^{*}_{L,\alpha}{}^{n+1}\mathbf{\Lambda}_L - J^{-1}_{\alpha\gamma}\dot{J}_{\gamma\delta}{}^{n+1}\hat{\mathbf{K}}_{\delta}. \tag{3.157}$$

Using the fact that $\mathbf{\Lambda}_L{}^{T}\hat{\mathbf{\Theta}}^{*}_{L,\alpha}\mathbf{\Lambda}_L = \widehat{\mathbf{\Lambda}_L{}^{T}\mathbf{\Theta}^{*}_{L,\alpha}}$, the dual vector $\dot{\hat{\mathbf{K}}}_{\alpha}$ can be obtained by

$$\dot{\mathbf{K}}_{\alpha} = \mathbf{\Lambda}_L{}^{T}\mathbf{\Theta}^{*}_{L,\alpha} - J^{-1}_{\alpha\gamma}\dot{J}_{\gamma\delta}\mathbf{K}_{\delta} \equiv \widehat{\mathbf{K}}_{\beta}(\boldsymbol{\eta}; \dot{\boldsymbol{\eta}}) + \mathbf{K}'_{\beta V}(\boldsymbol{\eta}). \tag{3.158}$$

From the constitutive relation of Eq. (2.246), we have

$$\begin{Bmatrix} \dot{\mathbf{N}}^{\alpha}_{\gamma} \\ \dot{\mathbf{M}}^{\alpha}_{Q} \end{Bmatrix} = \mathbf{C}^{\alpha\beta}\begin{Bmatrix} \widehat{\mathbf{E}}_{\beta}({}^{n+1}\boldsymbol{\eta}; {}^{n+1}\boldsymbol{\eta}^{*}) \\ \widehat{\mathbf{K}}_{\beta}(\eta; {}^{n+1}\boldsymbol{\eta}^{*}) \end{Bmatrix} + \mathbf{C}^{\alpha\beta}\begin{Bmatrix} \mathbf{E}'_{\beta V}({}^{n+1}\boldsymbol{\eta}) \\ \mathbf{K}'_{\beta V}({}^{n+1}\boldsymbol{\eta}) \end{Bmatrix}. \tag{3.159}$$

Taking the material derivative of the virtual strain in Eq. (2.235), and applying Eq. (3.155) with Eqs. (3.149) and (3.152) gives, after some algebraic manipulation, the following.

$$\begin{aligned} \begin{Bmatrix} \dot{\bar{\mathbf{E}}}_{\alpha} \\ \dot{\bar{\mathbf{K}}}_{\alpha} \end{Bmatrix}^{T}\mathbf{R}^{\alpha}_{\gamma} &= \begin{Bmatrix} \bar{\mathbf{z}} \\ \bar{\mathbf{\Theta}} \end{Bmatrix}^{T}\mathbf{\Psi}_{\alpha}\mathbf{B}_{\alpha}\mathbf{\Psi}_{\alpha}{}^{T}\begin{Bmatrix} {}^{n+1}\dot{\mathbf{z}} \\ \mathbf{\Theta}^{*}_{L} \end{Bmatrix} + \begin{Bmatrix} \widehat{\mathbf{E}}_{\alpha}({}^{n+1}\boldsymbol{\eta}; \bar{\boldsymbol{\eta}}) \\ \widehat{\mathbf{K}}_{\alpha}({}^{n+1}\boldsymbol{\eta}; \dot{\bar{\mathbf{\Theta}}}) \end{Bmatrix}^{T}\mathbf{R}^{\alpha}_{\gamma} \\ &\quad + \begin{Bmatrix} \bar{\mathbf{z}} \\ \bar{\mathbf{\Theta}} \end{Bmatrix}^{T}\left\{\begin{bmatrix} \mathbf{0} & \mathbf{0} \\ -[\mathbf{V}_{,\alpha}\times] & \mathbf{0} \end{bmatrix} - J^{-1}_{\alpha\gamma}\dot{J}_{\gamma\delta}\mathbf{\Xi}_{\delta}\right\}\mathbf{\Pi}\mathbf{R}^{\alpha}_{\gamma}. \end{aligned} \tag{3.160}$$

3.3.2 Direct differentiation method

The material derivative of the initial surface Jacobian of Eq. (2.260) is derived using Eq. (3.148) as

$$\dot{\tilde{J}} = \left(\mathbf{V}_{,\xi^1} \times \mathbf{G}_2 + \mathbf{G}_1 \times \mathbf{V}_{,\xi^2}\right) \cdot \mathbf{j}_3. \tag{3.161}$$

Since $\dot{\tilde{\boldsymbol{\eta}}} \in \bar{Z}$, the following identity from Eq. (2.248) holds.

$$a^{\gamma}({}^{n+1}\boldsymbol{\eta}, \dot{\tilde{\boldsymbol{\eta}}}) = \ell(\dot{\tilde{\boldsymbol{\eta}}}). \tag{3.162}$$

Taking the material derivatives of both sides of Eq. (2.248) and substituting Eqs. (3.159)-(3.161), and using Eq. (3.162), followed by some algebraic manipulations, we have the following sensitivity equation: For a given ${}^{n+1}\boldsymbol{\eta} \equiv ({}^{n+1}\mathbf{z}, {}^{n+1}\boldsymbol{\Lambda}_L)$, find ${}^{n+1}\boldsymbol{\eta}^* \equiv ({}^{n+1}\dot{\mathbf{z}}, \boldsymbol{\Theta}_L^*) \in \bar{Z}$ such that

$$a^{\gamma *}({}^{n+1}\boldsymbol{\eta}; \tilde{\boldsymbol{\eta}}, {}^{n+1}\boldsymbol{\eta}^*) = \ell'_V({}^{n+1}\boldsymbol{\eta}; \tilde{\boldsymbol{\eta}}) - a_V^{\gamma\,\prime}({}^{n+1}\boldsymbol{\eta}; \tilde{\boldsymbol{\eta}}),\ \forall \begin{Bmatrix} \bar{\mathbf{z}} \\ \bar{\boldsymbol{\Theta}} \end{Bmatrix}^T \in \bar{Z}, \tag{3.163}$$

where the explicit design dependence terms are defined as

$$\begin{aligned} a_V^{\gamma\,\prime}({}^{n+1}\boldsymbol{\eta}; \tilde{\boldsymbol{\eta}}) = & \int_{\Xi_A} \begin{Bmatrix} \bar{\mathbf{z}} \\ \bar{\boldsymbol{\Theta}} \end{Bmatrix}^T \boldsymbol{\Xi}_\alpha \mathbf{C}^{\alpha\beta} \begin{Bmatrix} \mathbf{E}'_{\beta V}({}^{n+1}\boldsymbol{\eta}) \\ \mathbf{K}'_{\beta V}({}^{n+1}\boldsymbol{\eta}) \end{Bmatrix} \tilde{J} d\xi^1 d\xi^2 \\ & + \int_{\Xi_A} \begin{Bmatrix} \bar{\mathbf{z}} \\ \bar{\boldsymbol{\Theta}} \end{Bmatrix}^T \left\{ \begin{bmatrix} \mathbf{0}_{3\times3} & \mathbf{0}_{3\times3} \\ -[\mathbf{V}_{,\alpha}\times] & \mathbf{0}_{3\times3} \end{bmatrix} - J^{-1}_{\alpha\gamma} \dot{J}_{\gamma\delta} \boldsymbol{\Xi}_\delta \right\} \boldsymbol{\Pi}\mathbf{R}^\alpha_\gamma \tilde{J} d\xi^1 d\xi^2 \\ & + \int_{\Xi_A} \begin{Bmatrix} \bar{\mathbf{z}} \\ \bar{\boldsymbol{\Theta}} \end{Bmatrix}^T \boldsymbol{\Xi}_\alpha \begin{Bmatrix} \mathbf{n}^\alpha \\ \mathbf{m}^\alpha \end{Bmatrix} \dot{\tilde{J}} d\xi^1 d\xi^2, \end{aligned} \tag{3.164}$$

and

$$\ell'_V(\tilde{\boldsymbol{\eta}}) = \int_{\Xi_A} \left(\bar{\mathbf{z}} \cdot \mathbf{n}_{ext} + \bar{\boldsymbol{\Theta}} \times \mathbf{m}_{ext}\right) \dot{\tilde{J}} d\xi^1 d\xi^2. \tag{3.165}$$

As Eq. (3.163) directly solves for ${}^{n+1}\boldsymbol{\eta}^* \equiv ({}^{n+1}\dot{\mathbf{z}}, \boldsymbol{\Theta}_L^*)$, it is called the *direct differentiation method*. It is noted that if $\boldsymbol{\Theta}_L^*$ is determined, then ${}^{n+1}\dot{\boldsymbol{\Lambda}}$ can be directly computed from Eq. (3.152). It is apparent that in the sensitivity equation of Eq. (3.163), the same tangent stiffness operator as used in Eq. (2.249) is utilized with different right hand side.

3.3.3 Adjoint variable method

3.3.3.1 Displacement at a specific position

For brevity we denote a parametric position of material point by $\boldsymbol{\xi} \equiv [\xi^1, \xi^2]^T \in \mathbf{R}^2$. A displacement at a position $\boldsymbol{\xi} = \boldsymbol{\xi}^*$ on a neutral surface can be expressed as

$$\psi_1 \equiv \int_{\Xi_A} {}^{n+1}z_i(\xi) \delta(\xi - \xi^*) d\xi^1 d\xi^2, \tag{3.166}$$

where ${}^{n+1}z_i$ denotes the i-th component of the displacement vector ${}^{n+1}\mathbf{z}$, and $\delta(\bullet)$ denotes the Dirac delta measure. The material derivative of the functional (3.166) is obtained as

$$\dot{\psi}_1 \equiv \int_{\Xi_A} {}^{n+1}\dot{z}_i(\boldsymbol{\xi})\delta(\boldsymbol{\xi}-\boldsymbol{\xi}^*)d\xi^1 d\xi^2. \tag{3.167}$$

In Eq. (3.162), substituting variables, $\boldsymbol{\eta}^* \rightarrow \bar{\boldsymbol{\lambda}}$ and $\bar{\boldsymbol{\eta}} \rightarrow \boldsymbol{\lambda}$ since each pair of them belongs to the same function space $\bar{Z}$, we have the following.

$$a^{\gamma *}({}^{n+1}\boldsymbol{\eta};\boldsymbol{\lambda},\bar{\boldsymbol{\lambda}}) = \ell'_V({}^{n+1}\boldsymbol{\eta};\boldsymbol{\lambda}) - a'_V({}^{n+1}\boldsymbol{\eta};\boldsymbol{\lambda}). \tag{3.168}$$

Changing variables ${}^{n+1}\dot{z}_i \rightarrow \bar{\lambda}_i$ in the implicit dependence term of Eq. (3.167) since they belong to the same function space, and equating to the energy form of Eq. (3.162), we have the following adjoint equation: For a given ${}^{n+1}\boldsymbol{\eta} \equiv ({}^{n+1}\mathbf{z}, {}^{n+1}\boldsymbol{\Lambda})$, find $\boldsymbol{\lambda} \in \bar{Z}$, such that

$$a^{\gamma *}(\boldsymbol{\eta};\bar{\boldsymbol{\lambda}},\boldsymbol{\lambda}) = \int_{\Xi_A} \bar{\lambda}_i(\boldsymbol{\xi})\delta(\boldsymbol{\xi}-\boldsymbol{\xi}^*)d\xi^1 d\xi^2, \ \forall \bar{\boldsymbol{\lambda}} \in \bar{Z}. \tag{3.169}$$

The right hand side of Eq. (3.169) is interpreted as a unit force acting on the position $\boldsymbol{\xi} = \boldsymbol{\xi}^*$. Evaluating Eq. (3.169) at $\bar{\boldsymbol{\lambda}} = \boldsymbol{\eta}^* \in \bar{Z}$ we have the following identity.

$$a^{\gamma *}({}^{n+1}\boldsymbol{\eta};\boldsymbol{\lambda},{}^{n+1}\boldsymbol{\eta}^*) = \int_{\Xi_A} {}^{n+1}\dot{z}_i(\boldsymbol{\xi})\delta(\boldsymbol{\xi}-\boldsymbol{\xi}^*)d\xi^1 d\xi^2. \tag{3.170}$$

Similarly, Eq. (3.163) may be evaluated at $\bar{\boldsymbol{\eta}} = \boldsymbol{\lambda} \in \bar{Z}$ to obtain

$$a^{\gamma *}({}^{n+1}\boldsymbol{\eta};\boldsymbol{\lambda},{}^{n+1}\boldsymbol{\eta}^*) = \ell'_V({}^{n+1}\boldsymbol{\eta};\boldsymbol{\lambda}) - a^{\gamma\,\prime}_V({}^{n+1}\boldsymbol{\eta};\boldsymbol{\lambda}). \tag{3.171}$$

Using the equivalence of Eqs. (3.170) and (3.171), we can substitute the right-hand side of Eq. (3.167) with the explicit design dependence terms as

$$\dot{\psi}_1 = \ell'_V({}^{n+1}\boldsymbol{\eta};\boldsymbol{\lambda}) - a^{\gamma\,\prime}_V({}^{n+1}\boldsymbol{\eta};\boldsymbol{\lambda}). \tag{3.172}$$

3.4 Adjoint DSA of elastic wave propagation in periodic structures

In this research, we perform a simple eigenvalue sensitivity analysis for a generalized Hermitian eigenvalue problem given in section 2.6.1.1.

3.4.1 Configuration DSA of simple eigenvalues

Eq. (2.273) can be rewritten for a response $\tilde{\boldsymbol{\eta}} \equiv \left(\tilde{\mathbf{z}}(s), \tilde{\boldsymbol{\theta}}(s)\right)$ within a unit cell satisfying the Bloch periodic boundary condition, as

$$a(\boldsymbol{\mu};\tilde{\boldsymbol{\eta}},\bar{\tilde{\boldsymbol{\eta}}}) = \zeta d(\boldsymbol{\mu};\tilde{\boldsymbol{\eta}},\bar{\tilde{\boldsymbol{\eta}}}), \ \ \forall \bar{\tilde{\boldsymbol{\eta}}} \in \bar{\mathbb{Z}}, \ \ \boldsymbol{\mu} \in \Gamma_{IBZ}, \tag{3.173}$$

where $\zeta \equiv \omega^2$ and $\bar{\mathbb{Z}}$ defines the complex space of kinematically admissible virtual responses. Γ_{IBZ} denotes a perimeter of irreducible Brillouin zone (IBZ). The following sesquilinear forms are defined

$$a(\boldsymbol{\mu};\tilde{\boldsymbol{\eta}},\bar{\tilde{\boldsymbol{\eta}}}) = \zeta\, d(\boldsymbol{\mu};\tilde{\boldsymbol{\eta}},\bar{\tilde{\boldsymbol{\eta}}}),\ \ \forall \bar{\tilde{\boldsymbol{\eta}}} \in \bar{\mathbb{Z}},\ \ \boldsymbol{\mu} \in \Gamma_{IBZ}, \tag{3.174}$$

and

$$d(\boldsymbol{\mu};\tilde{\boldsymbol{\eta}},\bar{\tilde{\boldsymbol{\eta}}}) \equiv \int_\Omega \left(\bar{\tilde{\mathbf{z}}}^H A_\rho \tilde{\mathbf{z}} + \bar{\tilde{\boldsymbol{\theta}}}^H \mathbf{I}_\rho \tilde{\boldsymbol{\theta}} \right) ds, \tag{3.175}$$

Assuming that the translational periodicity and unit cell dimension does not have design dependences, taking the material derivative of both sides of Eq. (3.173) and rearranging terms gives

$$\left\{ \begin{array}{c} a(\boldsymbol{\mu};\dot{\tilde{\boldsymbol{\eta}}},\bar{\tilde{\boldsymbol{\eta}}}) + a'_V(\boldsymbol{\mu};\tilde{\boldsymbol{\eta}},\bar{\tilde{\boldsymbol{\eta}}}) \\ = \zeta \left\{ d(\boldsymbol{\mu};\dot{\tilde{\boldsymbol{\eta}}},\bar{\tilde{\boldsymbol{\eta}}}) + d'_V(\boldsymbol{\mu};\tilde{\boldsymbol{\eta}},\bar{\tilde{\boldsymbol{\eta}}}) \right\} + \dot{\zeta}\, d(\boldsymbol{\mu};\tilde{\boldsymbol{\eta}},\bar{\tilde{\boldsymbol{\eta}}}) \end{array} \right. ,\ \forall \bar{\tilde{\boldsymbol{\eta}}} \in \bar{\mathbb{Z}}\ , \boldsymbol{\mu} \in \Gamma_{IBZ}. \tag{3.176}$$

Evaluating Eq. (3.176) at $\bar{\tilde{\boldsymbol{\eta}}} = \tilde{\boldsymbol{\eta}}$, as they belong to the same function space $\bar{\mathbb{Z}}$, and using the normalization condition of $d(\boldsymbol{\mu};\tilde{\boldsymbol{\eta}},\tilde{\boldsymbol{\eta}}) = 1$, we have

$$\dot{\zeta} = a'_V(\boldsymbol{\mu};\tilde{\boldsymbol{\eta}},\tilde{\boldsymbol{\eta}}) - \zeta\, d'_V(\boldsymbol{\mu};\tilde{\boldsymbol{\eta}},\tilde{\boldsymbol{\eta}}). \tag{3.177}$$

The explicit design dependence terms of the strain energy and kinetic energy forms are

$$a'_V(\boldsymbol{\mu};\tilde{\boldsymbol{\eta}},\tilde{\boldsymbol{\eta}}) \equiv \int_\Omega \left[\begin{array}{l} \boldsymbol{\Gamma}'_{linV}(\tilde{\boldsymbol{\eta}})^H \mathbf{C}_F \boldsymbol{\Gamma}_{lin}(\tilde{\boldsymbol{\eta}}) + \boldsymbol{\Omega}'_{linV}(\tilde{\boldsymbol{\eta}})^H \mathbf{C}_M \boldsymbol{\Omega}_{lin}(\tilde{\boldsymbol{\eta}}) \\ + \boldsymbol{\Gamma}_{lin}(\tilde{\boldsymbol{\eta}})^H \mathbf{C}_F \boldsymbol{\Gamma}'_{linV}(\tilde{\boldsymbol{\eta}}) + \boldsymbol{\Omega}_{lin}(\tilde{\boldsymbol{\eta}})^H \mathbf{C}_M \boldsymbol{\Omega}'_{linV}(\tilde{\boldsymbol{\eta}}) \\ + \left\{ \boldsymbol{\Gamma}_{lin}(\tilde{\boldsymbol{\eta}})^H \mathbf{C}_F \boldsymbol{\Gamma}_{lin}(\tilde{\boldsymbol{\eta}}) + \boldsymbol{\Omega}_{lin}(\tilde{\boldsymbol{\eta}})^H \mathbf{C}_M \boldsymbol{\Omega}_{lin}(\tilde{\boldsymbol{\eta}}) \right\} \nabla_s \cdot \mathbf{V} \end{array} \right] ds. \tag{3.178}$$

and

$$d'_V(\boldsymbol{\mu};\tilde{\boldsymbol{\eta}},\tilde{\boldsymbol{\eta}}) \equiv \int_\Omega \left(\tilde{\mathbf{z}}^H A_\rho \tilde{\mathbf{z}} + \tilde{\boldsymbol{\theta}}^H \mathbf{I}_\rho \tilde{\boldsymbol{\theta}} \right) \nabla_s \cdot \mathbf{V} ds, \tag{3.179}$$

where $\nabla_s \cdot \mathbf{V} \equiv \mathbf{V}_{,s} \cdot \mathbf{j}_1$, and the following is used.

$$\begin{aligned} \left\{ \boldsymbol{\Gamma}_{lin}(\tilde{\boldsymbol{\eta}}) \right\}^\bullet &= \boldsymbol{\Lambda}_0^T (\dot{\tilde{\mathbf{z}}}_{,s} - \dot{\tilde{\boldsymbol{\theta}}} \times \mathbf{j}_1) + \left\{ \boldsymbol{\Lambda}_0^T (-\tilde{\mathbf{z}}_{,s} \nabla_s \cdot \mathbf{V} - \tilde{\boldsymbol{\theta}} \times \mathbf{j}_1^\bullet) + \mathbf{e}_J \mathbf{j}_J^{\bullet T} \boldsymbol{\Lambda}_0 \boldsymbol{\Gamma}_{lin} \right\} \\ &\equiv \boldsymbol{\Gamma}_{lin}(\dot{\tilde{\boldsymbol{\eta}}}) + \boldsymbol{\Gamma}'_{linV}(\tilde{\boldsymbol{\eta}}), \end{aligned} \tag{3.180}$$

and

$$\left\{ \boldsymbol{\Omega}_{lin}(\tilde{\boldsymbol{\eta}}) \right\}^\bullet = \boldsymbol{\Lambda}_0{}^T \dot{\tilde{\boldsymbol{\theta}}}_{,s} + \left\{ \boldsymbol{\Lambda}_0{}^T (-\tilde{\boldsymbol{\theta}}_{,s} \nabla_s \cdot \mathbf{V}) + \mathbf{e}_J \mathbf{j}_J^{\bullet T} \boldsymbol{\Lambda}_0 \boldsymbol{\Omega}_{lin} \right\} \equiv \boldsymbol{\Omega}_{lin}(\dot{\tilde{\boldsymbol{\eta}}}) + \boldsymbol{\Omega}'_{linV}(\boldsymbol{\eta}). \tag{3.181}$$

3.4.2 Sizing DSA of simple eigenvalues

A beam cross-section thickness distribution is continuously paramterized using Eq. (3.93). Similar to Eq. (3.177), the sizing design sensitivity of eigenvalue can be evaluated by

$$\zeta' = a'_{\delta\mathbf{u}}(\boldsymbol{\mu};\tilde{\boldsymbol{\eta}},\tilde{\boldsymbol{\eta}}) - \zeta\, d'_{\delta\mathbf{u}}(\boldsymbol{\mu};\tilde{\boldsymbol{\eta}},\tilde{\boldsymbol{\eta}}). \tag{3.182}$$

The explicit design dependence terms of the strain and kinetic energy forms are

$$a'_{\delta\mathbf{u}}(\boldsymbol{\mu};\tilde{\boldsymbol{\eta}},\tilde{\boldsymbol{\eta}}) \equiv \int_\Omega \left(\bar{\tilde{\boldsymbol{\Gamma}}}_{lin}{}^{H} \mathbf{C}_F{}' \tilde{\boldsymbol{\Gamma}}_{lin} + \bar{\tilde{\boldsymbol{\Omega}}}_{lin}{}^{H} \mathbf{C}_M{}' \tilde{\boldsymbol{\Omega}}_{lin} \right) ds, \tag{3.183}$$

and

$$d'_{\delta\mathbf{u}}(\boldsymbol{\mu};\tilde{\boldsymbol{\eta}},\tilde{\boldsymbol{\eta}}) \equiv \int_\Omega \left(\bar{\tilde{\mathbf{z}}}^{H} A_\rho{}' \tilde{\mathbf{z}} + \bar{\tilde{\boldsymbol{\theta}}}^{H} \mathbf{I}_\rho{}' \tilde{\boldsymbol{\theta}} \right) ds, \tag{3.184}$$

where the partial derivatives of the constitutive matrices and the cross-section properties can be evaluated using $\partial A/\partial h_K$ and $\partial I/\partial h_K$ in Eq. (3.97).

3.5 Computation of design velocity on curved domain

The basic concept of free-form deformation (FFD) states that an object which we wish to deform is imagined to be embedded in a pliable solid, and then deformations of the surrounding solid get through to the embedded object. In this paper, the surrounding solid before and after deformations are designated as *initial* and *target* parent domains, respectively. There are four main steps in the FFD method [60]. *First*, we construct an initial parent domain where objects to be deformed are embedded. *Second*, we determine the parametric coordinates of the embedded object points. For the initial parent domain of generally curved shape or non-uniform parametrization, a point inversion problem needs to be solved using Newton-Raphson method to find the parametric coordinates [60]. However, for the initial parent domain of parallelepiped region with uniform parametrization, the parametric coordinates can be easily determined by a simple algebra [98]. *Third*, the initial parent domain is deformed into a target parent one by substituting the initial control points with the control points of target parent domain. The original FFD formulation proposed by Sederberg and Parry [98] employed Bernstein polynomials in the parameterization of parent domain. Lamousin and Waggenspack [60] presented a NURBS-based FFD (NFFD). In the NFFD, the variation of basis function order, non-uniform parametrization, rational formulation, and control point weighting are exploited, which yields the enhanced control of deformation. *Fourth*, the effect of deformation on the embedded object is evaluated. Basis functions are evaluated at the parametric positions determined in the second step using the given basis function order and a set of knots. The obtained basis functions are combined with the given control net of the target parent domain to compute the new positions of embedded object points. Even though this processe of FFD provides a geometry of lattice structure exactly on the target parent domain, the FFD has a substantial limitation of no analytical expression [60]. To determine the corresponding control net describing the geometry, an additional process is

required.

A problem of finding a change of control net position to result in a desired geometry change can be treated as an inverse problem, expressed by a system of linear equations where the unknown is the control net position [44]. This equation could have multiple solutions or no solution. The pseudoinverse of the system matrix enables to find the best solution, in the least square sense, to the equations [44]. However, the singular value decomposition to find the pseudoinverse matrix requires large computational costs. Also, if a patch-wise manner to find the least square solution is used, inter-patch C^0-continuity is not able to be assured without any special treatment. Thus, in this paper, we employ the global curve interpolation method [91] to determine the control point positions that satisfy a given system of linear equations. The FFD method enables to obtain the desired positions of the lattice structure embedded in the target parent domain at discrete points, which can be used to construct a system of linear equations with unknown control point positions. The system matrix is composed of basis function values at the selected discrete points. Then, by solving the system of linear equations the positions of control points can be determined. However, it should be clear that the determined control net does not guarantee to represent geometry exactly on the target domain, but to enforce the geometry pass through the selected discrete points. In other words, there might be a deviation from the target domain, in modeling of lattice structures. This deviation is called as *modeling error* and can be effectively reduced by increasing the geometry degrees of freedom, *i.e.*, increasing the number of control points (h-refinement) or increasing the basis function order (p-refinement). *Our main idea of the design velocity computation comes from the fact that the global curve interpolation gives us an analytical expression of the control net position of the lattice structure embedded in target parent domain. By taking the material derivative of this analytical expression, we can identify the design velocity coefficients at control points, and significantly, it should be clear that this design velocity field is an exact differentiation of the constructed analysis model, regardless of the modeling error mentioned before. In this paper, the developed design velocity field computation scheme is verified by comparison with finite differences.*

3.5.1 Free-form deformation and global curve interpolation

We explain the procedure to obtain the geometric information of lattice structures in a target domain. *First*, through the four steps of the aforementioned FFD procedure, the position of discrete points in the lattice structure can be obtained in the target parent domain (Fig. 3.6: middle), which is utilized to construct a system of linear equations to determine the corresponding control net. *Second*, the position of control net is determined by solving the system of linear equations, which is a global curve interpolation (Fig. 3.6: right). Noting that $\widetilde{(\bullet)}$ and $(\bullet)^0$ are respectively used for the quantities in the parent and the initial domains, the geometry of a given initial parent domain $\tilde{\Omega}^0$ is expressed as

$$\tilde{\mathbf{X}}^0(\tilde{\xi},\tilde{\eta}) = \sum_{I=1}^{m} \tilde{W}_I(\tilde{\xi},\tilde{\eta})\tilde{\mathbf{B}}_I^0, \tag{3.185}$$

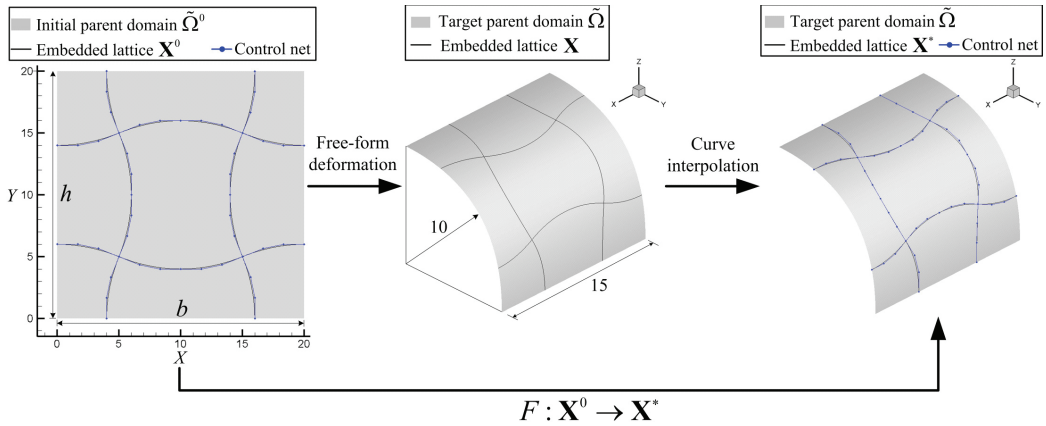

Figure 3.6: Geometric information of embedded lattice structure

where $\tilde{W}_I(\tilde{\xi},\tilde{\eta})$ is the I^{th} NURBS basis function, and $\tilde{\xi}$ and $\tilde{\eta}$ are parametric coordinates. $\tilde{\mathbf{B}}_I^0$ is the I^{th} control point position. m denotes the number of control points. Also, the geometry of the given initial embedded lattice is expressed as

$$\mathbf{X}^0(\xi) = \sum_{J=1}^{n} W_J(\xi)\mathbf{B}_J^0, \tag{3.186}$$

where $\mathbf{X}^0$ denotes a point of the embedded object. W_J and $\mathbf{B}_J^0$ are the corresponding NURBS basis function and control point, respectively. n and ξ denote the number of control points, and the parametric coordinate, respectively. It should be noted that, as illustrated in Fig. 3.6, this embedded object always belongs to the initial parent domain, *i.e.*, $\mathbf{X}^0 \in \tilde{\Omega}^0$. By substituting $\tilde{\mathbf{B}}_I^0$ with $\tilde{\mathbf{B}}_I$ in Eq. (3.185), the geometry of the given target parent domain $\tilde{\Omega}$ is expressed as

$$\tilde{\mathbf{X}}(\tilde{\xi},\tilde{\eta}) = \sum_{I=1}^{m} \tilde{W}_I(\tilde{\xi},\tilde{\eta})\tilde{\mathbf{B}}_I \tag{3.187}$$

where $\tilde{\mathbf{X}} \in \tilde{\Omega} \subset \mathbf{R}^2$ denote a point in the target parent domain. As the initial parent domain is considered to have always a rectangular shape and uniform parametrization, the parametric position $(\tilde{\xi},\tilde{\eta})$ corresponding to the parametric position ξ can be easily determined as

$$\left.\begin{aligned} \tilde{\xi}(\xi) &= X_1^0(\xi)/b \\ \tilde{\eta}(\xi) &= X_2^0(\xi)/h \end{aligned}\right\}, \tag{3.188}$$

where $\mathbf{X}^0 = [X_1^0, X_2^0, 0]^T$, and b and h are the width and the height of the initial parent domain, respectively, as shown in Fig. 3.6. Then, the geometry of the embedded lattice in the target domain, by the FFD process, is obtained as

$$\mathbf{X}(\xi) \equiv \tilde{\mathbf{X}}(\tilde{\xi}(\xi),\tilde{\eta}(\xi)). \tag{3.189}$$

The parametric position $(\tilde{\xi}_L, \tilde{\eta}_L)$ corresponding to the L-th discrete point at parametric position $\xi = \xi_L^c$ can be determined, from Eq. (3.188), as

$$\left.\begin{array}{l} \tilde{\xi}_L = X_1^0(\xi_L^c)/b \\ \tilde{\eta}_L = X_2^0(\xi_L^c)/h \end{array}\right\}, L = 1 \sim n. \tag{3.190}$$

The position ξ_L^c is determined by using the Greville abscissae which is a moving average of the knots [38]. Then, by evaluating Eq. (3.187) at the parametric position $(\tilde{\xi}_L, \tilde{\eta}_L)$ of Eq. (3.190), the discrete point position in the target domain can be expressed as

$$\tilde{\mathbf{X}}(\tilde{\xi}_L, \tilde{\eta}_L) = \sum_{I=1}^{m} \tilde{W}_I(\tilde{\xi}_L, \tilde{\eta}_L)\tilde{\mathbf{B}}_I = \mathbf{X}(\xi_L^c) \tag{3.191}$$

where $L = 1 \sim n$. In order to determine the control net of lattice in the target domain, we construct the following system of linear equations, by combining Eq. (3.191) and the expression of lattice geometry using the same basis function with Eq. (3.186) and unknown control points, as

$$\sum_{I=1}^{n} W_I(\xi_L^c)\mathbf{B}_I = \mathbf{X}(\xi_L^c), L = 1 \sim n. \tag{3.192}$$

In matrix form,

$$\begin{bmatrix} W_1(\xi_1^c)\mathbf{I} & \cdots & W_n(\xi_1^c)\mathbf{I} \\ \vdots & \ddots & \vdots \\ W_1(\xi_n^c)\mathbf{I} & \cdots & W_n(\xi_n^c)\mathbf{I} \end{bmatrix} \begin{Bmatrix} \mathbf{B}_1 \\ \vdots \\ \mathbf{B}_n \end{Bmatrix} = \begin{Bmatrix} \mathbf{X}(\xi_1^c) \\ \vdots \\ \mathbf{X}(\xi_n^c) \end{Bmatrix}, \tag{3.193}$$

where $\mathbf{I}$ denotes the identity matrix. Eq. (3.193) can be constructed for each patch of the NURBS curve. Through the typical assembly process, a global equation can be constructed as

$$\mathbf{N}_g\mathbf{B}_g = \mathbf{X}_g. \tag{3.194}$$

The matrix $\mathbf{B}_g$ of Eq. (3.194) represents the global assembly of the control point positions of the whole NURBS patches, which is determined by solving Eq. (3.194). As the NURBS basis function is not affected by the optimization process, the factorized system matrix of Eq. (3.194) can be saved and utilized again during the whole optimization process. The geometry of each patch, by denoting $\mathbf{B}_I$ as a control point position of the patch extracted from $\mathbf{B}_g$, is expressed as

$$\mathbf{X}^*(\xi) \equiv \sum_{I=1}^{n} W_I(\xi)\bar{\mathbf{B}}_I. \tag{3.195}$$

We note that the reconstructed lattice structure geometry $\mathbf{X}^*$ could have a deviation from the target one $\mathbf{X}(\xi)$ of Eq. (3.189), and a measure of the deviation is defined as follows.

$$\varepsilon(\xi) \equiv \left\| \mathbf{X}^*(\xi) - \mathbf{X}(\xi) \right\|, \tag{3.196}$$

which is designated as "*modeling error*". In section 4.5, through a suitable numerical example, we verify that this modeling error can be significantly reduced by increasing the modeling degree of freedom of the lattice structure through *h*- or *p*-refinement. Also, it should be noted that the C^0 inter-patch continuity of the given lattice structure in the initial parent domain is inherited by the reconstructed geometry of the lattice structure in the target parent domain. Hereafter, we designate the mapping F of the initial lattice $\mathbf{X}^0$ to the one $\mathbf{X}^*$ in the target parent domain, *i.e.*, $F : \mathbf{X}^0 \rightarrow \mathbf{X}^*$, as indicated in Fig. 3.6.

3.5.2 Computation of design velocity field

Lattice structures embedded in a curved domain inherently have a nonlinear constraint in their configuration design space. As shown in Fig. 3.7, there is an admissible design space illustrated as a hypersurface C in 3-D space. Each point on the hypersurface C represents an admissible design that satisfies the nonlinear constraint. For n design step and the corresponding design D^n, a tangent space $T_{D_n}C$ is spanned by the design velocity field. A design change vector (blue arrow) in Fig. 3.7 always lies on the tangent space $T_{D_n}C$. It should be noted that the design velocity field should be updated after a design change, since the nonlinear constraint of configuration design has different tangent with respect to design. Once a design change vector is determined, the additional mapping $F : \mathbf{X}^0 \rightarrow \mathbf{X}^*$ yields the updated design that satisfies the configuration design constraint.

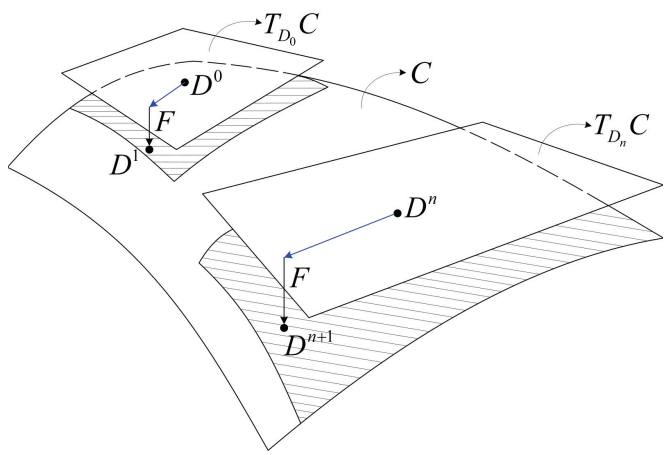

Figure 3.7: Geometric interpretation of admissible design space

The given design velocity of lattice embedded in the initial parent domain is expressed as

$$\mathbf{V}^0 \equiv \frac{d}{d\tau}\mathbf{X}^0_\tau\big|_{\tau=0} = \sum_{I=1}^{n} W_I(\xi)\dot{\mathbf{B}}^0_I = \sum_{I=1}^{n} W_I(\xi)\mathbf{V}^0_I, \tag{3.197}$$

where τ denotes a design parameter and $\mathbf{V}^0_I \equiv \dot{\mathbf{B}}^0_I$ is the given design velocity coefficient. The upper dot ($\bullet$) denotes the material derivative. As we consider the initial parent domain as planar one, $V^0_3 = 0$ where $\mathbf{V}^0 = [V^0_1, V^0_2, V^0_3]^T$. Then, using Eq. (3.197), the material derivative of discrete point

at parametric position $\xi = \xi_L^c$ of Eq. (3.190) can be obtained as

$$\left.\begin{array}{l} \dot{\tilde{\xi}}_L = V_1^0(\xi_L^c)/b \\ \dot{\tilde{\eta}}_L = V_2^0(\xi_L^c)/h \end{array}\right\}, L = 1 \sim n. \tag{3.198}$$

In this paper, as a position of control points is considered as a design variable, a NURBS basis function does not have any design dependence. Taking the material derivative of Eq. (3.194) gives the following expression.

$$\mathbf{N}_g \dot{\mathbf{B}}_g = \dot{\mathbf{X}}_g. \tag{3.199}$$

$\dot{\mathbf{X}}_g$ is obtained through a typical assembly procedure of $\dot{\mathbf{X}}(\tilde{\xi}_L)$ $(L = 1 \sim n)$ for each patch calculated by taking the material derivative of Eq. (3.191), considering the fact that the specified target parent domain is independent of the design, *i.e.*, $\dot{\tilde{\mathbf{B}}}_{I,J} = \mathbf{0}$.

$$\dot{\mathbf{X}}(\tilde{\xi}_L) = \sum_{I=1}^{m} \left(\tilde{W}_{I,\tilde{\xi}} \dot{\tilde{\xi}}_L + \tilde{W}_{I,\tilde{\eta}} \dot{\tilde{\eta}}_L \right) \tilde{\mathbf{B}}_I \tag{3.200}$$

where $\tilde{W}_I \equiv \tilde{W}_I(\tilde{\xi}, \tilde{\eta})$, and $L = 1 \sim n$. $(\bullet)_{,\tilde{\xi}}$ and $(\bullet)_{,\tilde{\eta}}$ denote the differentiation with respect to the parametric coordinates $\tilde{\xi}$ and $\tilde{\eta}$, respectively. Eqs. (3.194) and (3.199) have the same system matrix, thus, the factorized system matrix in the solution process of Eq. (3.194) can be utilized again in solving Eq. (3.199). Finally, by taking the material derivative of Eq. (3.195), the design velocity of lattice embedded in the target parent domain is expressed as

$$\mathbf{V} \equiv \frac{d}{d\tau} \mathbf{X}_\tau^* \big|_{\tau=0} = \sum_{I=1}^{n} W_I(\xi) \dot{\tilde{\mathbf{B}}}_I = \sum_{I=1}^{n} W_I(\xi) \mathbf{V}_I, \tag{3.201}$$

where $\mathbf{V}_I \equiv \dot{\tilde{\mathbf{B}}}_I$ denotes the design velocity coefficient at each control point. The overall procedure of design update and design velocity computation is summarized in Table 3.2.

Table 3.2: Procedure of design update and design velocity computation

(a) Update the design of lattice structure embedded in the initial parent domain, using the given design velocity field $\mathbf{V}^0$.
(b) Calculate the parametric position $(\tilde{\xi}_L, \tilde{\eta}_L)$ of discrete points of the embedded lattice structure by using Eq. (3.188).
(c) Construct a system of linear equations of Eq. (3.194), and determine the control point positions of the lattice structure embedded in target parent domain by solving Eq. (3.194).
(d) If DSA is required, calculate design velocity coefficients by solving Eq. (3.199) using Eqs. (3.198), and (3.200), and then evaluate the velocity using Eq. (3.201).

3.6 Explicit parameterization of initial orthonormal frame

We describe the SR method of explicit parameterization of initial orthonormal frame for a circular cross-section model using a unit tangent vector and a reference orthonormal basis. This method was employed by Meier et al. [78] to construct orthonormal frames of Kirchhoff rods in the FEA context. In this paper, within the IGA context, we detail procedures of determining reference orthonormal basis for two cases; first, a general spatial curve model, and second, an embedded curve on a smooth surface. It is noted that a notation $\mathbf{j}_i(\xi)$ $(i = 1,2,3)$ is often used instead of $\mathbf{j}_i(s(\xi))$ for brief expressions.

3.6.1 Smallest rotation (SR) method

For a C^1-continuous curve, a unit tangent vector $\mathbf{j}_1(\xi)$ is uniquely defined at a given parametric position. For a given vector $\mathbf{j}_1(\xi)$ and reference orthonormal basis $\mathbf{j}_{123}^{ref} \equiv \left\{\mathbf{j}_1^{ref}, \mathbf{j}_2^{ref}, \mathbf{j}_3^{ref}\right\}$, the other two base vectors of orthonormal frame can be determined by

$$\mathbf{j}_k(\xi) = \mathbf{j}_k^{ref} - \frac{\mathbf{j}_k^{ref\,T}\mathbf{j}_1(\xi)}{1+\mathbf{j}_1^{ref\,T}\mathbf{j}_1(\xi)}\left\{\mathbf{j}_1(\xi)+\mathbf{j}_1^{ref}\right\} \equiv \mathbf{s}_k\left(\mathbf{j}_1(\xi), \mathbf{j}_{123}^{ref}\right), k = 2,3, \tag{3.202}$$

where $\mathbf{s}_k(\bullet, *)$ denotes a smallest rotation operation, which can be interpreted as a rotation of a given reference basis (*) such that the first reference vector ($\mathbf{j}_1^{ref}$) is rotated to a given vector ($\bullet$) with rotation angle minimized [78]. This operation is termed "SR mapping". We define a reference basis for each knot span, from which an initial orthonormal basis at an arbitrary point within the knot span is determined as: for a given i-th knot span $\Xi_i \equiv \left[{}^{(i)}\xi, {}^{(i+1)}\xi\right]$, we have

$$\mathbf{j}_k(\xi) = \mathbf{s}_k\left(\mathbf{j}_1(\xi), {}^{(i)}\mathbf{j}_{123}^{ref}\right), k = 2,3, \text{ for } \xi \in \Xi_i, \tag{3.203}$$

where ${}^{(i)}\mathbf{j}_{123}^{ref} \equiv \left\{{}^{(i)}\mathbf{j}_1^{ref}, {}^{(i)}\mathbf{j}_2^{ref}, {}^{(i)}\mathbf{j}_3^{ref}\right\}$ denotes a set of reference basis for the i-th knot span. For the whole ne knot spans of a given NURBS patch, reference basis ${}^{(i)}\mathbf{j}_{123}^{ref}$ are defined at the parametric position ${}^{(i)}\xi$ of each knot span Ξ_i following a sequential procedure as

$${}^{(i)}\mathbf{j}_1^{ref} \equiv \mathbf{j}_1({}^{(i)}\xi), \text{ and } {}^{(i)}\mathbf{j}_k^{ref}(\xi) = \mathbf{s}_k\left(\mathbf{j}_1({}^{(i)}\xi), {}^{(i-1)}\mathbf{j}_{123}^{ref}\right), k = 2,3, \tag{3.204}$$

where $i = 1 \sim ne$, and ${}^{(0)}\mathbf{j}_{123}^{ref} \equiv \left\{{}^{(0)}\mathbf{j}_1^{ref}, {}^{(0)}\mathbf{j}_2^{ref}, {}^{(0)}\mathbf{j}_3^{ref}\right\}$ can be determined by ${}^{(0)}\mathbf{j}_1^{ref} \equiv \mathbf{j}_1({}^{(1)}\xi)$ and

$$\begin{cases} {}^{(0)}\mathbf{j}_2^{ref} = {}^{(0)}\mathbf{j}_1^{ref} \times \mathbf{e}_1 / \left\| {}^{(0)}\mathbf{j}_1^{ref} \times \mathbf{e}_1 \right\| , \text{ if } \left\| {}^{(0)}\mathbf{j}_1^{\text{ref}} \times \mathbf{e}_1 \right\| \neq 0 \\ {}^{(0)}\mathbf{j}_2^{ref} = {}^{(0)}\mathbf{j}_1^{ref} \times \mathbf{e}_2 / \left\| {}^{(0)}\mathbf{j}_1^{ref} \times \mathbf{e}_2 \right\| , \text{ otherwise} \end{cases}, \tag{3.205}$$

and

$${}^{(0)}\mathbf{j}_3^{ref} = {}^{(0)}\mathbf{j}_1^{ref} \times {}^{(0)}\mathbf{j}_2^{ref}. \tag{3.206}$$

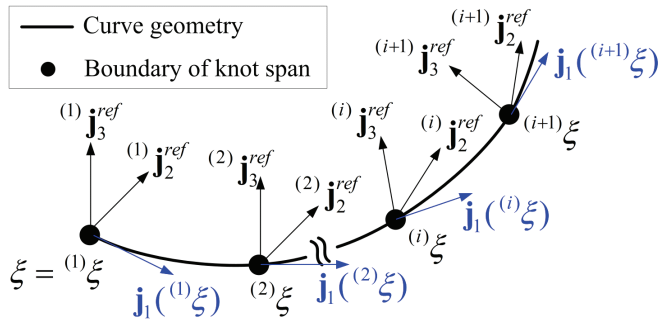

Figure 3.8: Determination of reference orthonormal basis for each knot span

Fig. 3.8 schematically illustrates the reference basis of each knot span, and Table 3.3 summarizes the overall procedure of constructing initial orthonormal frames. It is observed that $\mathbf{j}_2(\xi)$ and $\mathbf{j}_3(\xi)$

Table 3.3: A procedure of determining initial orthonormal frame by the SR method

1. Determine ${}^{(0)}\mathbf{j}_{123}^{ref}$ by ${}^{(0)}\mathbf{j}_1^{ref} \equiv \mathbf{j}_1({}^{(1)}\xi)$ and Eqs. (3.205) and (3.206).
2. Sequentially determine a reference orthonormal basis of each knot span by Eq. (3.204).
3. Calculate $\mathbf{j}_2(\xi)$ and $\mathbf{j}_3(\xi)$ at an arbitrary point using Eq. (3.203).

are not defined by Eq. (3.202) if $\mathbf{j}_1^{ref}$ and $\mathbf{j}_1(\xi)$ are antiparallel to each other. This singularity may arise from two sources; first, in the second or third step of the procedure of Table 3.3, if a knot span has a large curvature so that a tangent vector within the knot span becomes antiparallel to the reference tangent vector. Meier et al. [78] discussed that this case of singularity poses a restriction on the level of spatial discretization, and the maximal segment of a single element is limited by a semi-circle; however, in a practical level of spatial discretization, such a large curvature of single element will not be encountered. Second, since ${}^{(0)}\mathbf{j}_2^{ref}$ and ${}^{(0)}\mathbf{j}_3^{ref}$ may not be continuous at a specific configuration satisfying $\left\| {}^{(0)}\mathbf{j}_1^{ref} \times \mathbf{e}_1 \right\| = 0$, we determine ${}^{(0)}\mathbf{j}_{123}^{ref}$ prior to the optimization and fix it; in other words, it is assumed that ${}^{(0)}\mathbf{j}_{123}^{ref}$ does not have a design dependence during optimization in order to avoid non-differentiability in DSA process. Thus, if a large design change occurs such that $\mathbf{j}_1({}^{(1)}\xi)$ rotates with angle π or its odd multiples, ${}^{(0)}\mathbf{j}_1^{ref}$ and $\mathbf{j}_{1\tau}({}^{(1)}\xi)$ can become to be antiparallel. This case of singularity poses a restriction on the amount of design change such that rotation angle π and its odd multiples should be avoided at a starting parametric position of NURBS patch (${}^{(1)}\xi$). In order to circumvent this restriction, it is required to suitably update the reference basis ${}^{(0)}\mathbf{j}_{123}^{ref}$ during the optimization process. However, in this paper, we assume that such a large design change does not occur, and proceed with ${}^{(0)}\mathbf{j}_{123}^{ref}$ without design dependence during optimizations. We term this approach as the curve framing "*method* #1" for convenience. Assuming that a perturbed design also has C^1-regularity, $\mathbf{j}_1^{(}\xi)$ can be expressed in terms of given design velocity field by taking the material derivative of $\mathbf{j}_1 \equiv \boldsymbol{\varphi}_{0,s}$ using Eqs. (3.111) and (3.107) as

$$\mathbf{j}_1^{\bullet}(\xi) = \mathbf{V}_{,s} - \boldsymbol{\varphi}_{0,s}\nabla_s \cdot \mathbf{V}. \tag{3.207}$$

The material derivative of Eq. (3.202) is derived as

$$\mathbf{j}_k^{\bullet}(\xi) = \mathbf{j}_k^{ref\bullet} - \frac{1}{1+\mathbf{j}_1^{ref\,T}\mathbf{j}_1(\xi)} \left[\begin{array}{l} \left\{\mathbf{j}_k^{ref\bullet\,T}\mathbf{j}_1(\xi) + \mathbf{j}_k^{ref\,T}\mathbf{j}_1^{\bullet}(\xi)\right\}\left\{\mathbf{j}_1(\xi) + \mathbf{j}_1^{ref}\right\} \\ -\left\{\mathbf{j}_1^{ref\bullet\,T}\mathbf{j}_1(\xi) + \mathbf{j}_1^{ref\,T}\mathbf{j}_1^{\bullet}(\xi)\right\}\left\{\mathbf{j}_k^{ref} - \mathbf{j}_k(\xi)\right\} \\ +\mathbf{j}_k^{ref\,T}\mathbf{j}_1(\xi)\left\{\mathbf{j}_1^{\bullet}(\xi) + \mathbf{j}_1^{ref\bullet}\right\} \end{array} \right]$$
$$\equiv \mathbf{s}_k^{\bullet}\left(\mathbf{j}_1(\xi), \mathbf{j}_{123}^{ref}; \mathbf{j}_1^{\bullet}(\xi), \mathbf{j}_{123}^{ref\bullet}\right), k = 2,3. \tag{3.208}$$

Then, we obtain the material derivative of initial orthonormal basis at an arbitrary point as

$$\mathbf{j}_k^{\bullet}(\xi) = \mathbf{s}_k^{\bullet}\left(\mathbf{j}_1(\xi), {}^{(i)}\mathbf{j}_{123}^{ref}; \mathbf{j}_1^{\bullet}(\xi), {}^{(i)}\mathbf{j}_{123}^{ref\bullet}\right), k = 2,3, \text{ for } \xi \in \Xi_i, \tag{3.209}$$

where ${}^{(i)}\mathbf{j}_{123}^{ref\bullet} \equiv \left\{{}^{(i)}\mathbf{j}_1^{ref\bullet}, {}^{(i)}\mathbf{j}_2^{ref\bullet}, {}^{(i)}\mathbf{j}_3^{ref\bullet}\right\}$ denotes a set of material derivatives of SR reference orthonormal base vectors for the i-th knot span. We have the following sequential calculation for each knot span as

$${}^{(i)}\mathbf{j}_1^{ref\bullet} \equiv \mathbf{j}_1^{\bullet}({}^{(i)}\xi), \text{ and } {}^{(i)}\mathbf{j}_k^{ref\bullet}(\xi) = \mathbf{s}_k^{\bullet}\left(\mathbf{j}_1({}^{(i)}\xi), {}^{(i-1)}\mathbf{j}_{123}^{ref}; \mathbf{j}_1^{\bullet}({}^{(i)}\xi), {}^{(i-1)}\mathbf{j}_{123}^{ref\bullet}\right), k = 2,3, \tag{3.210}$$

where $i = 1 \sim ne$, and it is noted that ${}^{(0)}\mathbf{j}_1^{ref\bullet} = {}^{(0)}\mathbf{j}_2^{ref\bullet} = {}^{(0)}\mathbf{j}_3^{ref\bullet} = \mathbf{0}$, as we assume ${}^{(0)}\mathbf{j}_{123}^{ref}$ is calculated at an original design and has no design dependence during optimizations. Table 3.4 summarizes the overall procedure of calculating material derivatives of initial orthonormal frames.

Table 3.4: A procedure of calculating material derivatives of initial orthonormal frames

1. Sequentially calculate the material derivative of each reference orthonormal basis by Eq. (3.210), where $\mathbf{j}_1^{\bullet}({}^{(i)}\xi)$ is calculated by Eq. (3.207), and ${}^{(0)}\mathbf{j}_1^{ref\bullet} = {}^{(0)}\mathbf{j}_2^{ref\bullet} = {}^{(0)}\mathbf{j}_3^{ref\bullet} = \mathbf{0}$ is assumed.
2. Calculate the material derivatives $\mathbf{j}_2(\xi)$ and $\mathbf{j}_3(\xi)$ at an arbitrary point by using Eq. (3.209).

3.6.2 Reference orthonormal frame by surface convected basis

We present a method of using a surface convected basis to obtain a reference orthonormal frame for surface embedded curves. A reference orthonormal basis $\mathbf{j}_{123}^{ref}(\xi) \equiv \left\{\mathbf{j}_1^{ref}(\xi), \mathbf{j}_2^{ref}(\xi), \mathbf{j}_3^{ref}(\xi)\right\}$ is defined at an arbitrary point of curve, in contrast to the previous case (*method* #1) where it was defined for each knot span. By taking partial differentiations of a surface geometry $\tilde{\mathbf{X}} \equiv \tilde{\mathbf{X}}(\tilde{\xi}, \tilde{\eta})$ of Eq. (3.187) with respect to parametric coordinates $\tilde{\xi}$ and $\tilde{\eta}$, we obtain surface convected basis $\tilde{\mathbf{X}}_{,\tilde{\xi}}$ and $\tilde{\mathbf{X}}_{,\tilde{\eta}}$. Then, we define the third reference vector $\mathbf{j}_3^{ref}(\xi)$ by the cross-product of two convected base vectors as

$$\mathbf{j}_3^{ref}(\xi) \equiv \frac{\tilde{\mathbf{X}}_{,\tilde{\xi}} \times \tilde{\mathbf{X}}_{,\tilde{\eta}}}{\left\|\tilde{\mathbf{X}}_{,\tilde{\xi}} \times \tilde{\mathbf{X}}_{,\tilde{\eta}}\right\|}. \tag{3.211}$$

The first reference base vector is defined as a unit tangent to the target parent domain along the direction of parametric coordinate ξ of an embedded curve

$$\mathbf{j}_1^{ref}(\xi) \equiv \frac{\partial\tilde{\mathbf{X}}/\partial\xi}{\left\|\partial\tilde{\mathbf{X}}/\partial\xi\right\|}, \tag{3.212}$$

where $\partial\tilde{\mathbf{X}}/\partial\xi$ is calculated by using the chain rule of differentiation and Eq. (3.188) as

$$\frac{\partial\tilde{\mathbf{X}}}{\partial\xi} = \frac{1}{b}\frac{\partial X_1^0}{\partial\xi}\tilde{\mathbf{X}}_{,\tilde{\xi}} + \frac{1}{h}\frac{\partial X_2^0}{\partial\xi}\tilde{\mathbf{X}}_{,\tilde{\eta}}. \tag{3.213}$$

The second reference base vector can be simply determined as

$$\mathbf{j}_2^{ref}(\xi) \equiv \mathbf{j}_3^{ref}(\xi) \times \mathbf{j}_1^{ref}(\xi). \tag{3.214}$$

Then, after calculating $\mathbf{j}_1(\xi)$, we finally calculate the other two base vectors using the SR mapping of Eq. (3.202) as

$$\mathbf{j}_k(\xi) = \mathbf{s}_k\left(\mathbf{j}_1(\xi), \mathbf{j}_{123}^{ref}(\xi)\right), k = 2,3. \tag{3.215}$$

We term this approach of selecting reference orthonormal basis as the curve framing "*method* #2" for convenience. Applying the material derivative to Eq. (3.212) by the formula of Eq. (3.125) gives

$$\mathbf{j}_1^{ref\bullet}(\xi) = \frac{1}{\left\|\partial\tilde{\mathbf{X}}/\partial\xi\right\|}\mathbf{P}_{\mathbf{j}_1^{ref}}\frac{\partial\dot{\tilde{\mathbf{X}}}}{\partial\xi}, \tag{3.216}$$

and $\partial\dot{\tilde{\mathbf{X}}}/\partial\xi$ can be explicitly expressed in terms of the given design velocity field $\mathbf{V}^0 = \mathbf{V}^0(\xi)$ of Eq. (3.197) using Eqs. (3.213) and (3.198) as

$$\begin{aligned}\frac{\partial}{\partial\xi}\dot{\tilde{\mathbf{X}}}(\tilde{\xi},\tilde{\eta}) = &\frac{1}{b}\left\{V_{1,\xi}^0\tilde{\mathbf{X}}_{,\tilde{\xi}} + X_{1,\xi}^0\left(\frac{V_1^0}{b}\tilde{\mathbf{X}}_{,\tilde{\xi}\tilde{\xi}} + \frac{V_2^0}{h}\tilde{\mathbf{X}}_{,\tilde{\xi}\tilde{\eta}}\right)\right\}\\ &+\frac{1}{h}\left\{V_{2,\xi}^0\tilde{\mathbf{X}}_{,\tilde{\eta}} + X_{2,\xi}^0\left(\frac{V_1^0}{b}\tilde{\mathbf{X}}_{,\tilde{\eta}\tilde{\xi}} + \frac{V_2^0}{h}\tilde{\mathbf{X}}_{,\tilde{\eta}\tilde{\eta}}\right)\right\},\end{aligned} \tag{3.217}$$

Also, we obtain the following using the formula of Eq. (3.125).

$$\mathbf{j}_3^{ref\bullet}(\xi) = \frac{1}{\left\|\tilde{\mathbf{X}}_{,\tilde{\xi}}\times\tilde{\mathbf{X}}_{,\tilde{\eta}}\right\|}\mathbf{P}_{\mathbf{j}_3^{ref}}\left\{\left(\frac{V_1^0}{b}\tilde{\mathbf{X}}_{,\tilde{\xi}\tilde{\xi}} + \frac{V_2^0}{h}\tilde{\mathbf{X}}_{,\tilde{\xi}\tilde{\eta}}\right)\times\tilde{\mathbf{X}}_{,\tilde{\eta}} + \tilde{\mathbf{X}}_{,\tilde{\xi}}\times\left(\frac{V_1^0}{b}\tilde{\mathbf{X}}_{,\tilde{\eta}\tilde{\xi}} + \frac{V_2^0}{h}\tilde{\mathbf{X}}_{,\tilde{\eta}\tilde{\eta}}\right)\right\}. \tag{3.218}$$

The material derivative of the second reference vector is

$$\mathbf{j}_2^{ref\bullet}(\xi) \equiv \mathbf{j}_3^{ref\bullet}(\xi)\times\mathbf{j}_1^{ref}(\xi) + \mathbf{j}_3^{ref}(\xi)\times\mathbf{j}_1^{ref\bullet}(\xi). \tag{3.219}$$

Finally, after calculating $\mathbf{j}_1^{\bullet}(\xi)$ using Eq. (3.207), the material derivatives of the other two base vectors are determined by using Eq. (3.208) as

$$\mathbf{j}_k^{\bullet}(\xi) = \mathbf{s}_k^{\bullet}\left(\mathbf{j}_1(\xi), \mathbf{j}_{123}^{ref}(\xi); \mathbf{j}_1^{\bullet}(\xi), \mathbf{j}_{123}^{ref\bullet}(\xi)\right), k = 2,3. \tag{3.220}$$

Chapter 4

Numerical examples

4.1 Investigation of invariant locking-free formulations

4.1.1 Self-straining in curved beam models

We demonstrate self-straining phenomenon and its elimination by employing the invariant formulation presented in section 2.2.

We consider two curved beam models; model #1 and model #2. The geometry of model #1 is described by cubic B-spline basis functions and four control points, as shown in Figure 4.1a. The vertical coordinates (H) of control points B and C are altered to investigate the dependence of non-invariance on the initial geometry. Figure 4.1b shows the norm of vector $\mathbf{a}$ in Eq. (2.30) for two cases; H=0.125 and H=1 over the half of the parametric domain ($0 \leq \xi < 0.5$) due to the symmetry of the curve about the mid-point ($\xi = 0.5$), where $\mathbf{a} = \mathbf{0}$ due to the point symmetry. It shows that $\mathbf{a}$ does not vanish in the domain. In other words, the membrane and shear strains are generated during rigid body motions. Figure 4.1c shows that the L_2 norm of $\mathbf{a}$ increases as we increase H, which indicates that self-straining gets worse as the initial curvature variation of domain increases.
Model #2 is constructed as a straight geometry with quadratic B-spline basis functions and uniform knot distribution. Then, 6 control points in the middle of the beam are vertically moved to the positions A(0.0025), B(0.0075), C(0.05), D(0.05), E(0.0075), and F(0.0025), where the numbers in the parentheses represent Y-coordinates as shown in Figure 4.2a.

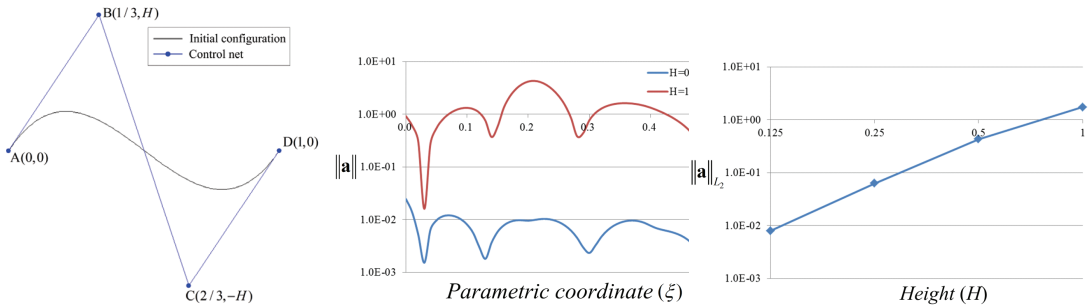

(a) Model description (b) Distribution of $\|\mathbf{a}\|$ (c) $\|\mathbf{a}\|_{L_2}$ for increasing H

Figure 4.1: Non-invariance of model #1

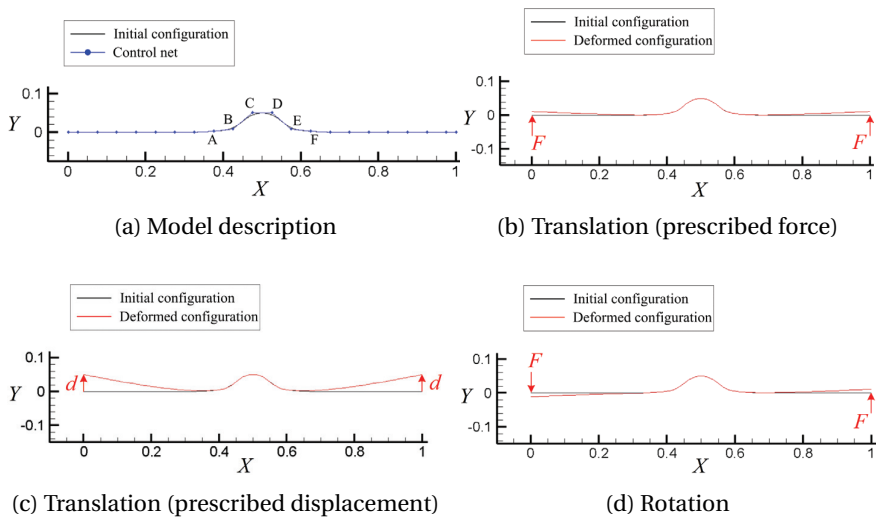

(a) Model description (b) Translation (prescribed force)

(c) Translation (prescribed displacement) (d) Rotation

Figure 4.2: Inability of model #2 to represent rigid body motions due to self-straining

To verify self-straining of model #2 using the formulation D#1, three loading conditions (concentrated force F=100, displacement d=0.05) are imposed for rigid body translation (Figure 4.2b and 4.2c) and the infinitesimal rigid body rotation (Figure 4.2d). Three Gauss integration points (full integration) are used for each element. Even though no essential boundary conditions are imposed, spurious constraints restrict rigid body motions due to self-straining in the middle region of large curvature. For the same problems, the formulation D#2 results in singular stiffness matrices properly. In the following section, it is shown that these self-straining phenomena have significant influence on the accuracy of response analysis.

4.1.2 Errors in displacement field due to self-straining

For both of the models #1 and #2, pure bending problems are considered with a clamped boundary condition and a sinusoidal loading of distributed moment as follows:

$$m(s) = EI\left(\frac{\pi}{2L}\right)^2 \sin\left(\frac{\pi}{2L}s\right), \tag{4.1}$$

where s and L are the arc-length coordinate and the length of the beam, respectively. E=210GPa and $I = bh^3/12$ are the Young's modulus and the second moment of inertia, respectively. b=0.01 and h are respectively the width and thickness of beam, and Poisson's ratio is set to be zero. In this paper, two locking-free formulations are considered; the selective reduced integration (SRI) [1] and the $\bar{B}$ projection method [15]. Also, the effect of replacing the strain field discretization with D#2 is investigated. The exact solution of rotation angle for this problem is derived in Adam *et al.* [1] as Eq. (D.1), which involves the arc-length coordinate s. We further extend the exact solution to the exact solution of the first order derivatives of global displacements, which is followed by retrieving the global displacement field through numerical integration of Eq. (D.5). As the arc-length coordinate s is also calculated by the numerical integration, the obtained reference solutions for both of displacement and rotation are not exact. However, we calculate these numerical integrations using enough number of elements and Gauss integration points, so that the solutions are denominated as precise solutions. Detailed expressions for the reference solutions can be found in Appendix.

Consider the model #1 of cantilever with the vertical coordinate H=1 and thickness h=0.01 as shown in Figure 4.3a. Figure 4.3b illustrates the deformed configurations of the 5 elements cantilever beam under two different formulations D#1 and D#2, combined with the SRI.

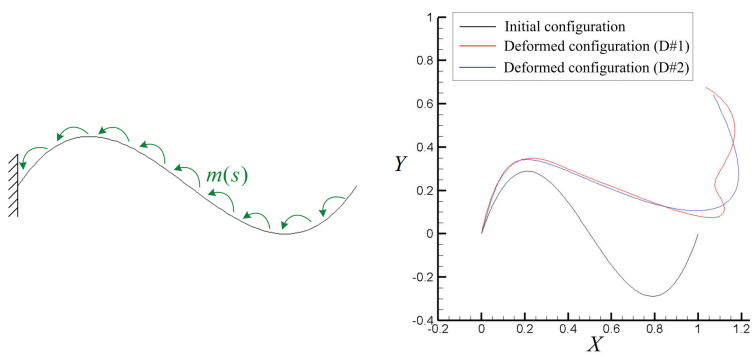

(a) Problem description (b) Deformation (SRI)

Figure 4.3: Response analysis of model #1 (H=1)

The result of formulation D#1 is significantly deteriorated, compared with that of formulation D#2. Figure 4.4 shows the dependence of L_2 error of responses on the vertical coordinate H. As increasing the H, the error of displacement obtained by the formulation D#1 significantly increases, which is mainly due to the numerical instability caused by self-straining. It is noted that, since the approximated bending strain measure is invariant, the rotation angle is not affected by self-straining and shows good agreement with the precise solution even if the formulation D#1 is used.

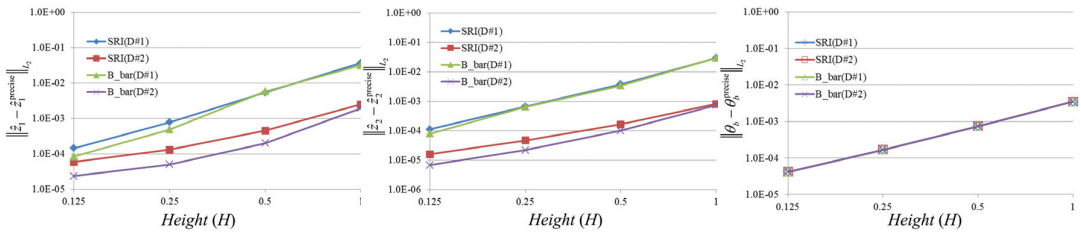

(a) X-directional displacement (b) Y-directional displacement (c) Rotation

Figure 4.4: Dependence on vertical coordinate H

Figure 4.5a shows that the L_2 norm of vector $\mathbf{a}$ reduces according to h-refinement, as mentioned in Observation 2. The spurious strain energy generated in the rigid body motions reduces as the mesh is refined. However, the non-invariance still persists and consequently yields overall poor accuracy of the displacement field. Figures 4.5b and 4.5c present the convergence of displacements. The invariant formulation D#2 gives much more accurate results than D#1 for both SRI and $\bar{B}$ projection method.

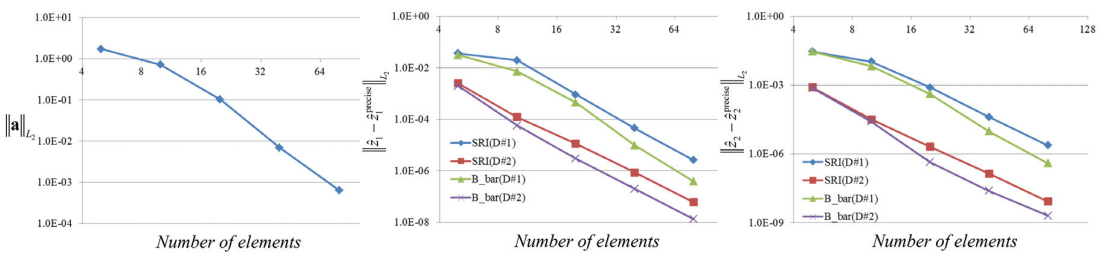

(a) Self-straining (b) X-directional displacement (c) Y-directional displacement

Figure 4.5: Displacement comparison in discretization methods (D#1 and D#2)

To investigate the effect of higher-order discretization on self-straining, we consider the single element cantilever of model #1 with the vertical coordinate H=1 and thickness h=0.01 as shown in Figure 4.3a. For three different orders of basis function, Figure 4.6a shows the norm of the vector $\mathbf{a}$ in Eq. (2.30) over the half of the parametric domain ($0 \leq \xi < 0.5$) due to the point symmetry of the curve about the mid-point ($\xi = 0.5$) where $\mathbf{a} = \mathbf{0}$. As shown in Figure 4.7a, the self-straining is still persisting in the higher order discretization, which implies that the p-refinement does not effectively reduce the numerical instability. Consequently, compared with the results of D#2 using cubic basis function (Light blue) in Figures 4.7b and 4.7c, the displacement field obtained by D#1 is significantly deteriorated with oscillations, even employing quartic (Green) and quintic (Orange) basis functions.

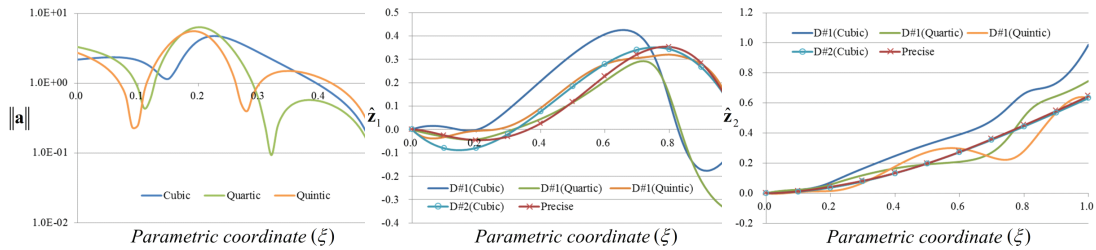

(a) Self-straining (b) X-directional displacement (c) Y-directional displacement

Figure 4.6: Comparison of displacement fields

Consider the model #2 of cantilever model with the number of elements NE and thickness h=0.01, as shown in Figure 4.7a. Figures 4.7b and 4.7c illustrate the deformed configurations obtained by the formulations D#1 and D#2, combined with the SRI. The displacement field obtained by the D#1 undergoes severe oscillations from the position where the abrupt change of curvature occurs, as shown in Figure 4.7b. As the mesh is refined, the amplitude of oscillations is significantly reduced. This can be explained by the reduction of self-straining due to the h-refinement (Observation 2). However, compared with the results of D#2 using coarse mesh shown in Figure 4.7c, it is apparent that the persisting oscillations in the refined model significantly deteriorate the quality of responses.

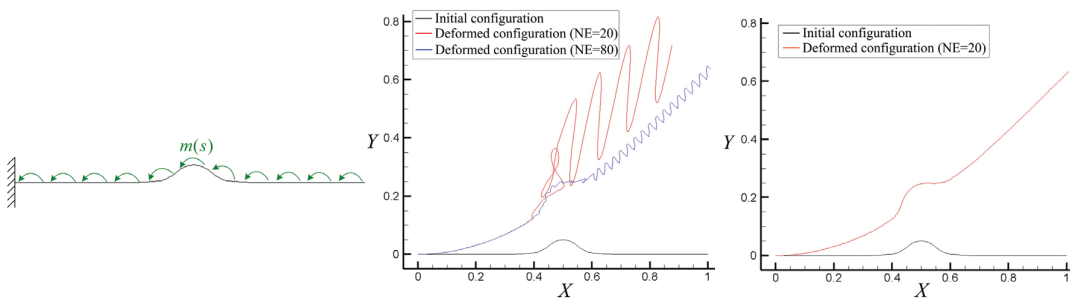

(a) Problem description (b) Deformation (SRI, D#1) (c) Deformation (SRI, D#2)

Figure 4.7: Comparison of configuration

Figure 4.8 shows the global displacement fields using the SRI combined with the formulations D#1 and D#2. The displacement fields using the D#1 exhibit serious oscillations persisting even in the refined model, even though the overall accuracy is improved. The rotation angle is always accurate regardless of discretization method, due to the invariance of the approximated bending strain measure.

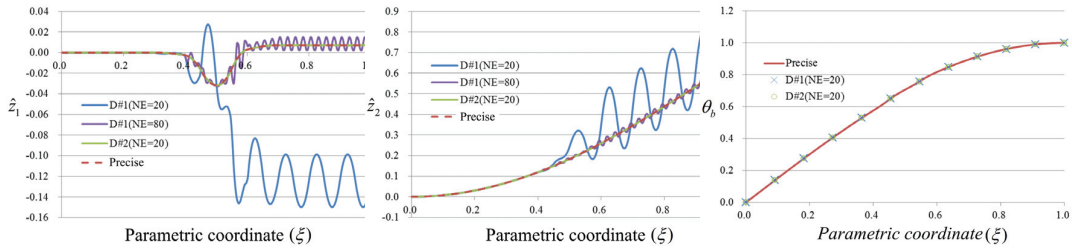

(a) X-direction (b) Y-direction (c) Rotation

Figure 4.8: Comparison of displacement and rotation fields

Figure 4.9 shows the comparison of strain fields, where the vertical dotted lines represent the element boundaries. We notice that several discontinuities appear in the strain fields using the D#1, due to the discontinuity of initial curvature. In both formulations of D#1 and D#2, the vanishing points of membrane and shear strains coincide with the position of integration points in the SRI [1]. However, it is obvious that the amplitude of strains in the D#1 is much larger than that of the D#2. This is mainly due to the numerical instability triggered by self-straining around the region of large curvature and its propagation due to the higher order continuity of displacement field. The bending strain is accurate, regardless of discretization method, due to its invariance property.

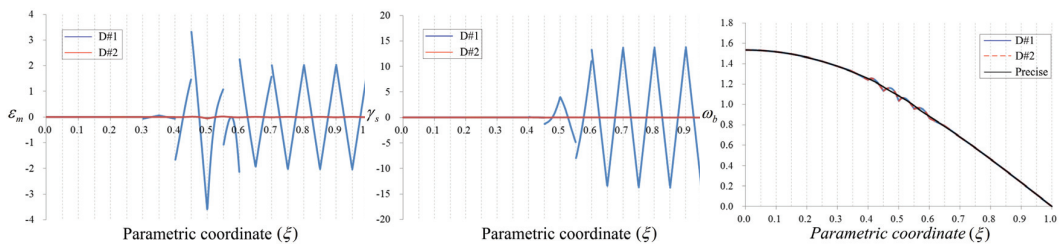

(a) Membrane (b) Shear (c) Bending

Figure 4.9: Comparison of strain fields

4.1.3 Comparison with the conventional locking-free formulations

We compare the accuracy of results obtained from the conventional (D#1) and invariant (D#2) locking-free formulations (SRI and $\bar{B}$ projection method). Consider again the model #2 whose initial length is L=1.02, with the distributed moment loading and clamped boundary condition, as described in Figure 4.7a. 20 elements with uniform knot distribution are used. Figure 10 shows the change of the relative L_2 error of responses as we increase the slenderness ratio (L/h). If the full integration (3 integration points for each element) is used in the formulation D#1, the deformation (Green) vanishes even for small slenderness ratio. This is due to self-straining of the membrane and shear strains which absorb the major part of the strain energy, especially in the region of large curvature. If the invariant formulation D#2 is employed, the accuracy of responses (Orange) in small slenderness ratio is significantly improved but deteriorated due to membrane

and shear locking troubles as the slenderness ratio increases. To alleviate these locking troubles, the SRI [1] and the $\bar{B}$ projection method [15] are employed.

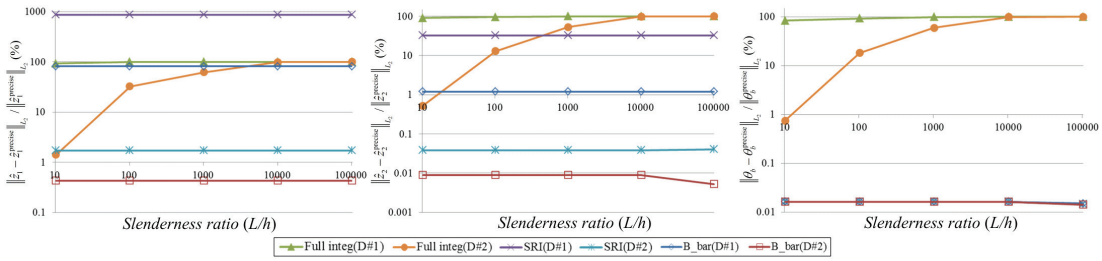

(a) X-displacement (b) Y-displacement (c) Rotation

Figure 4.10: Comparison of relative L_2 errors in model #2

As shown in Figure 4.10, although locking-free formulations combined with D#1 eliminate the dependence of solution on the slenderness ratio, the accuracy (Purple, Blue) is still not satisfactory. This inaccuracy stems from the severe numerical instability triggered by self-straining, as illustrated in Figures 7 and 8. As the invariant formulation D#2 is employed, the self-straining problem is resolved and the accuracy of responses is significantly improved in all the slenderness ratios (Light blue, Red).

Figure 4.11 illustrates the deformed configurations obtained from D#1 and D#2 using the full integration, for the case of slenderness ratio L/h=10.2. As shown in the curved region of Figure 4.11a, the beam seems to be constrained by the spurious constraint that restricts the deformation of beam to be very small.

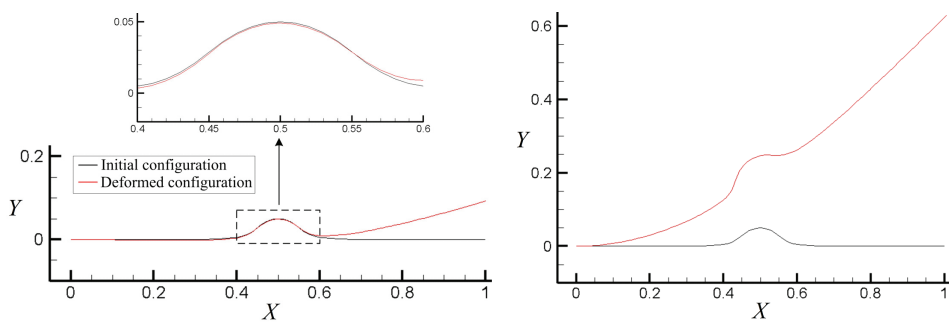

(a) Formulation D#1 (b) Invariant formulation D#2

Figure 4.11: Comparison of deformed configurations

Table 4.1 presents the strain energy of each deformation mode and its ratio to the total strain energy in the curved region ($0.4 \leq X \leq 0.6$). In the result of D#1, the membrane and shear strain energy constitutes a half of total strain energy, which is mainly due to the spurious membrane and shear strains generated by self-straining that appears as a serious spurious constraint in the curved region. This trouble is fully resolved through the invariant formulation D#2, as shown in Figure 4.11b. Table 4.1 shows that the beam model nearly recovers the pure bending nature.

Table 4.1: Comparison of contribution in total strain energy

	Formulation D#1			
	E_{total}	$E_{membrane}$	E_{shear}	$E_{bending}$
	1.93E+04	2.83E+03	7.17E+03	9.29E+03
Ratio (%)	100	14.65	37.17	48.17
	Invariant formulation D#2			
	E_{total}	$E_{membrane}$	E_{shear}	$E_{bending}$
	4.48E+04	1.03E+03	4.59E+02	4.33E+04
Ratio (%)	100	2.31	1.03	96.67

4.2 Configuration DSA of Kirchhoff beam structures

Through numerical examples, we verify the superiority of isogeometric analysis in terms of per-degree-of-freedom (DOF) accuracy of deformation analysis and DSA in comparison with cubic FEA results. In the cubic FEA, C^1-continuous Hermite polynomial is employed as basis functions. The element length parameter in the Hermite polynomial is calculated using a closed form expression presented in [3]. The nodal position and tangential vectors are constructed from CAD model. To ensure the C^1-continuity of responses, the cubic FEA based on Hermite interpolation employs the additional DOFs, $\boldsymbol{\alpha}^1$ and $\boldsymbol{\alpha}^2$ in Eq. (3.52), associated with rotations. This increases the size of stiffness matrix and consequently makes the computation inefficient. On the contrary, the IGA uses only the displacement DOFs. Along with the inherent advantages of exact geometry and higher order continuity, the IGA yields superior per-DOF accuracy to the FEA results in both deformation analysis and the DSA.

The design velocity field can be expressed by the perturbation of control points for the IGA whereas it should be generated from the mesh data of original and perturbed designs for the FEA. In the displacement-based formulation, a clamped boundary condition is implemented by fixing first two control points from the clamped ends so that the slopes at the ends are fixed. For the purpose of convergence tests, uniform h-refinements are carried out for the IGA and the FEA. In the case of IGA, through k-refinement, it turns out that the increase of the order of basis function and the degrees of smoothness significantly improves the accuracy.

4.2.1 Pure bending of clamped beam

This example handles the shape design variation that undergoes no change in the local coordinate system. We consider the pure bending of clamped beams with two different initial configurations; straight and semi-circular models, whose exact solutions are available. The exact rotation angle of neutral axis at end and its exact sensitivity with respect to initial length change δL are respectively

$$\Psi_{exact} = \frac{ML}{EI} \tag{4.2}$$

and

$$\dot{\Psi}_{exact} = \frac{M}{EI}\delta L, \tag{4.3}$$

where M is an applied end moment and L is the initial length of the beam. In both of the initially straight and the curved beam models, the bending rigidity is EI=175. For the numerical integration of each element, four Gauss integration points are used for both of cubic IGA and FEA, and five Gauss integration points for quartic IGA.

Straight beam

A straight beam of unit length (L=1) is subjected to a concentrated end moment M. An applied moment, M=$2n\pi EI$, will force the rod to wind around itself n-times. For example, the exact deformed configurations are a semi-circle and a fully closed circle for n=0.5 and n=1, respectively. Cross section has squared shape and thickness is h=0.01. Figure 4.12a shows the deformed configurations at various load steps, obtained using quartic NURBS basis functions and 148 DOFs. Figure 4.12b shows the shape design variation of initial beam length, and the perturbation amount is $\delta L = 10^{-3}$.

Figure 4.13 shows the convergence test results of deformation analysis and DSA. The cubic IGA shows much more accurate and fast convergent result than the cubic FEA. Furthermore, when the order of basis function is increased to quartic through k-refinement in the isogeometric methods, the convergence rate becomes significantly improved in both deformation and design sensitivity analyses.

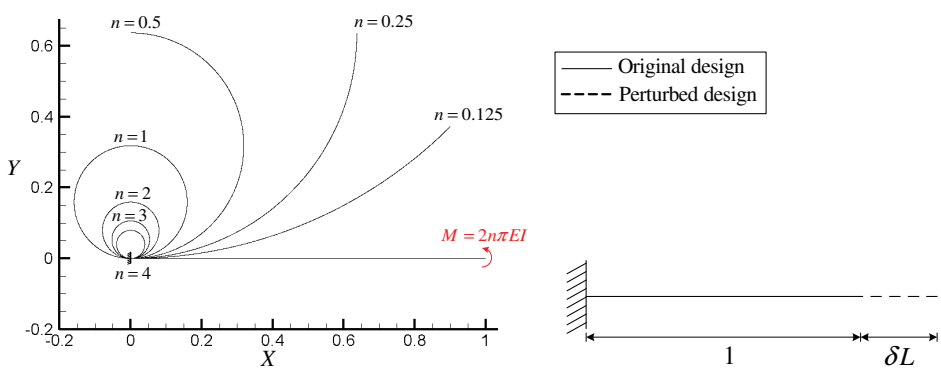

(a) Deformed configurations (b) Shape design variation

Figure 4.12: Design variation of straight beam

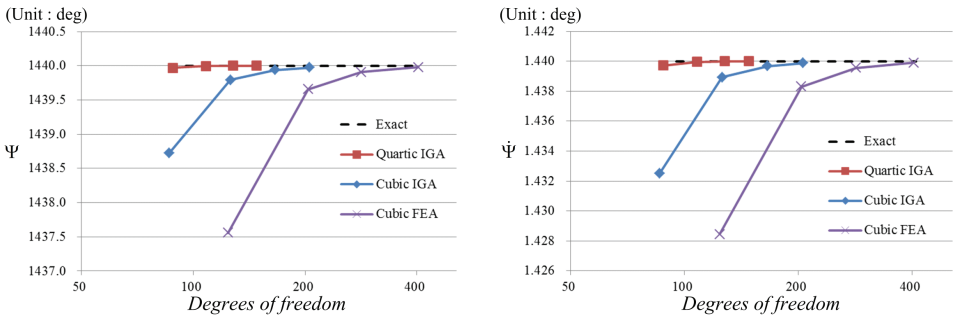

(a) Deformation analysis (b) Design sensitivity analysis

Figure 4.13: Convergence tests for straight beam model

Initially curved beam

A curved beam of semi-circular arc is subjected to a concentrated end moment M. An applied moment (M=-0.4nEI) enforces the beam to be wound around itself n-times. For n = 0.5, 1, and 1.5, the exact solutions are a straight line, a semi-circle, and a fully closed circle, respectively. As shown in Figure 4.14a, the semi-circular arc model is constructed using two NURBS patches. Γ^* is the junction between the patches, where C^1-continuity (junction case 2) condition is weakly imposed. In the other region except the junction, the continuity is C^2 for cubic IGA and C^3 for quartic IGA. Figure 4.14a shows deformed configurations at various load steps, obtained using quartic NURBS basis functions and 156 DOFs. Figure 4.14b shows the design variation by changing the position of center and the radius of circle ($\delta = 2 \times 10^{-3}$) such that the circular shape is maintained in the perturbed design.

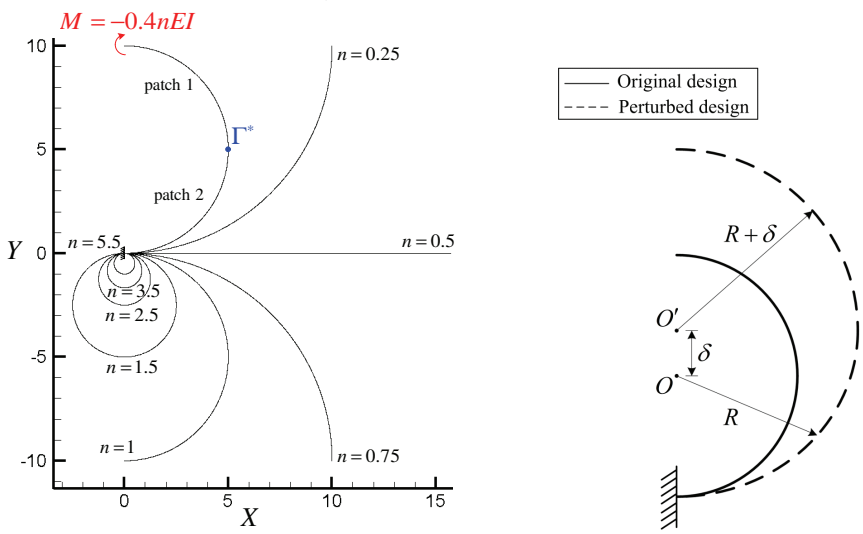

(a) Deformed configurations (b) Shape design variation

Figure 4.14: Semi-circular beam model

Figure 4.15 shows the results of deformation analysis and DSA. Even though the continuity

of isogeometric method is reduced due to the presence of the multi-patch junction, the isogeometric method shows much more accurate and fast convergent solutions than the FEA. Furthermore, when the order of basis function in the isogeometric methods is increased to quartic, the convergence rate becomes significantly improved as shown in Figure 4.15. This example of rod winding many times illustrates the capability of GEBT-based Jaumann strain formulation to handle both large displacements and finite strains. Similar numerical results are found in Marino [73] employing the GEBT.

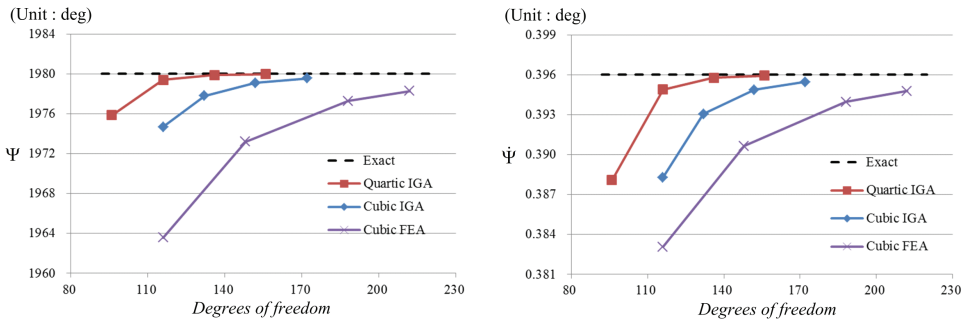

(a) Deformation analysis (b) Design sensitivity analysis

Figure 4.15: Convergence tests for curved beam model

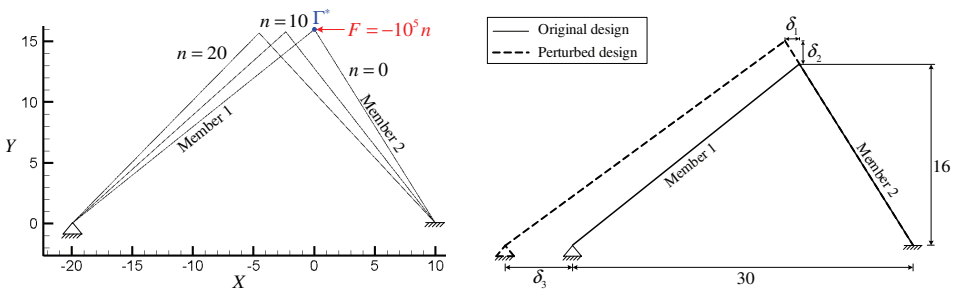

(a) Deformed configurations (b) Configuration design variation

Figure 4.16: Two-bar frame structure

4.2.2 Two-bar frame: conservative loading

This example includes both shape and orientation design variations. Since the initial and perturbed design components have linear geometry, the design variation can be easily decomposed into shape and orientation variations. We consider a two-bar frame structure consisting of members 1 and 2, as shown in Figure 4.16a, subjected to a concentrated conservative load at the junction Γ^*. The base vectors are not continuous at the junction Γ^* so that C^0-continuity (junction case 1) condition is imposed at the junction Γ^* in both FEA and IGA models. Figure 4.16a shows deformed configurations for various load steps, obtained using quartic IGA with 402 DOFs. Figure 4.16b shows the design variation of two-bar frame structure such that the member 1 changes in its shape and orientation whereas the member 2 in its shape only. The amounts of design perturbation are $\delta_1 = 0.1, \delta_2 = 0.16, \delta_3 = 0.2$ and the straight geometry

is maintained after the variations.

Since a conservative load is considered and the local coordinates of member 1 changes due to the orientation design variation, the force vector component of member 1 has design dependence. For the member 2 subjected to only shape design variation, the force vector component is independent of the design. In this problem, the design velocity field can be exactly expressed even for the FEA-based DSA. Figure 4.17 shows the results of deformation analysis and DSA for vertical displacement at the junction Γ^*. The cubic IGA (deformation analysis and DSA) shows better accuracy than the cubic FEA. Also, in case the order of basis function in the IGA methods is increased to quartic, the convergence rate is improved.

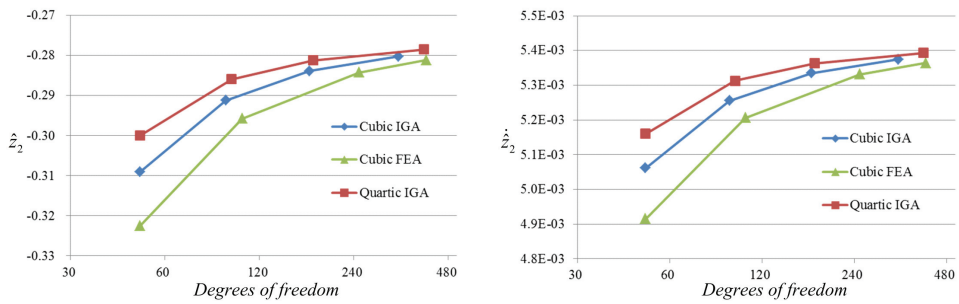

(a) Deformation analysis (b) Design sensitivity analysis

Figure 4.17: Convergence tests for displacement at junction

Table 4.2: Verification of design sensitivity

Cubic IGA				
DOFs	$\hat{z}_2$	$\dot{\hat{z}}_2$(a)	$\hat{z}_{2\tau} - \hat{z}_2$(b)	(a)/(b)
50	-0.3091	5.0613E-03	5.0246E-03	1.0073
94	-0.2913	5.2553E-03	5.2183E-03	1.0071
174	-0.2840	5.3348E-03	5.2977E-03	1.0070
334	-0.2803	5.3745E-03	5.3374E-03	1.0070
Quartic IGA				
DOFs	$\hat{z}_2$	$\dot{\hat{z}}_2$(c)	$\hat{z}_{2\tau} - \hat{z}_2$(d)	(c)/(d)
50	-0.3000	5.1233E-03	5.1602E-03	1.0072
98	-0.2860	5.2755E-03	5.3126E-03	1.0070
178	-0.2813	5.3263E-03	5.3635E-03	1.0070
402	-0.2786	5.3559E-03	5.3930E-03	1.0069

For the vertical displacement in the IGA, Table 4.2 compares the analytical design sensitivity obtained by the direct differentiation method (DDM) with the finite difference sensitivity. The agreements are excellent for all the selected DOFs. On the other hand, for the sensitivity of vertical displacement in the FEA, there are significant errors without considering the design dependence of basis functions as shown in Table 4.3, where the column (a*) denotes the analytical sensitivity with no dependence of basis functions on design.

Table 4.3: Effect of design dependence in Hermite basis function

DOFs	$\hat{z}_2$	$\dot{\hat{z}}_2$(a)	$\dot{\hat{z}}_2$(a*)	$\hat{z}_{2\tau} - \hat{z}_2$(b)	(a)/(b)	(a*)/(b)
50	-0.3226	4.9153E-03	5.6113E-03	4.8787E-03	1.0075	1.1502
106	-0.2958	5.2059E-03	5.4977E-03	5.1690E-03	1.0071	1.0636
250	-0.2843	5.3309E-03	5.4479E-03	5.2938E-03	1.0070	1.0291
410	-0.2812	5.3643E-03	5.4346E-03	5.3271E-03	1.0070	1.0202

4.2.3 Curved beam: non-conservative load

This example includes a curved geometry and the configuration design, *i.e.* coupled shape and orientation variations. The whole domain consists of parts 1 and 2. Pressure loading ($p = 1000n$) is applied only in part 1. Figure 4.18a shows the analysis results obtained by quartic IGA with 96 DOFs. In the IGA model, two patches are used to apply the pressure loading only in part 1. C^1-continuity (junction case 2) condition is imposed at the junction Γ^*. Figure 4.18b shows the design variations, keeping G^2-continuity. The perturbation amount of control points is $\delta = 1 \times 10^{-2}\alpha$ and a set of parametric studies is performed by varying the α value.

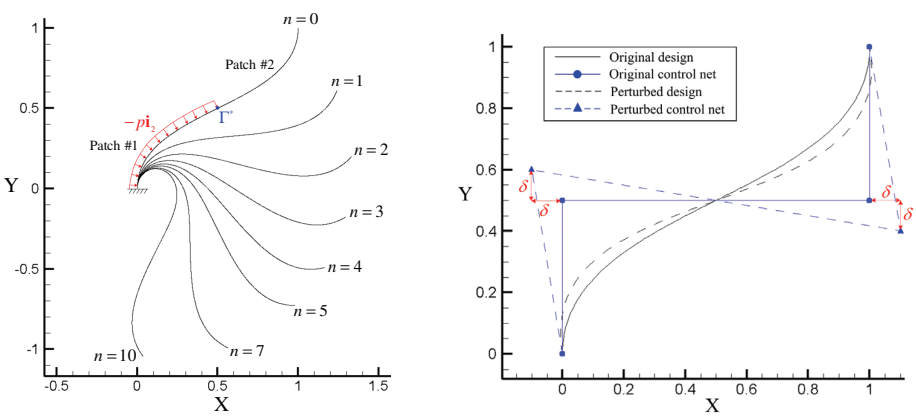

(a) Deformed configurations (b) Configuration design variation

Figure 4.18: Curved beam under non-conservative load

For the curved beam model (IGA: 100 DOFs, FEA: 404 DOFs) in Figure 4.19, the accuracy of analytical sensitivity for the vertical displacement is verified with finite difference sensitivity (FDM), as increasing the perturbation amount (α). As shown in Figure 4.19b, the sensitivity using the cubic FEA is nonlinear with respect to the design perturbation. This is due to the fact that the design velocity field in the FEA model is approximated by the design velocity of nodal tangential vector. Also, the perturbation amount in the FEA should be small to obtain accurate sensitivity.

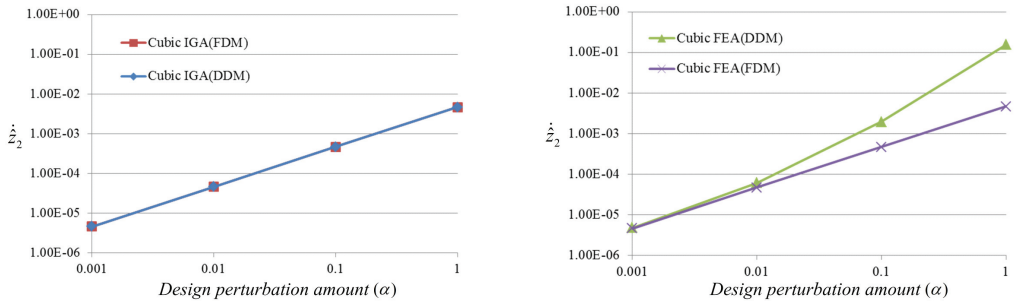

(a) Cubic IGA (b) Cubic FEA

Figure 4.19: Agreement of DDM and FDM sensitivities

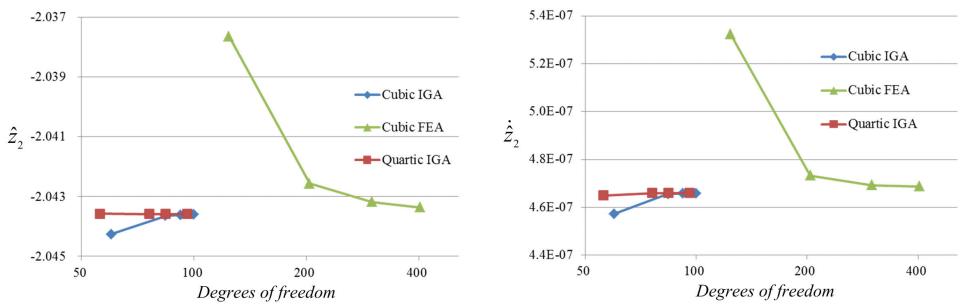

(a) Deformation analysis (b) Design sensitivity analysis

Figure 4.20: Convergence tests for curved beam model

Table 4.4: Effect of design dependence in Hermite basis functions

DOFs	$\hat{z}_2$	$\dot{\hat{z}}_2$(a)	$\dot{\hat{z}}_2$(a*)	$\hat{z}_{2\tau} - \hat{z}_2$(b)	(a)/(b)	(a*)/(b)
124	-2.0376	5.3233E-07	1.3101E-06	5.3221E-07	1.0002	2.4616
204	-2.0426	4.7335E-07	8.8579E-07	4.7301E-07	1.0007	1.8727
300	-2.0432	4.6932E-07	8.5970E-07	4.6853E-07	1.0017	1.8349
404	-2.0434	4.6879E-07	8.5632E-07	4.6732E-07	1.0031	1.8324

In Figure 4.20, using the FEA and the IGA, the accuracy in the deformation analysis and the DSA are compared as increasing the DOFs. As aforementioned, the perturbation amount is set to be very small, $\alpha = 10^{-4}$ to obtain sufficiently accurate results in the FEA. Figure 4.20a shows the convergence test for the vertical displacement at the tip and Figure 4.20b does for the sensitivity of vertical displacement. The results of IGA are much better than those of FEA even though less number of DOFs are used in the IGA methods, which implies that the IGA-based methods are more appropriate for the models of curved geometry in both deformation and design sensitivity analyses. The quartic NURBS model obtained from k-refinement shows significantly improved convergence rate.

Next, the design dependence of basis function in the FEA is investigated. For the case of very small perturbation ($\alpha = 10^{-4}$), we compare two cases of design dependence and no dependence

of basis function as shown in Table 4.4. The column (a*) denotes the analytical sensitivity with no dependence of basis functions on design. The effect of design dependence in basis functions is much more significant in the curved beam than the linear beam in section 4.2.2. The reason is that the effect of additional fictitious load term becomes bigger due to the initial curvature and the deformation-dependent loading condition.

4.2.4 Shape memory polymer-based self-unwinding beam

Simulation

A straight beam of length $L = 10$ and square cross-section with thickness $h = 0.2$ is subjected to a concentrated end moment M. 10 uniform knot spans of cubic B-spline are used for the discretization, and the temperature step size is selected as $\Delta T = 0.1(K)$. As illustrated in Fig. 4.21a, an applied end moment, $M = 0.01n\pi E^a I$, will enforce the rod to be wound around itself into a full circle at the final equilibrium configuration (n=20). n denotes the load step number. Fig. 4.21b shows that a cooling process with the applied moment fixed results in a slight further deformation (blue), and subsequent unloading process results in a spring-back (pink). It should be noted that the "unloading" means removal of the applied moment loading not the clamped boundary condition which is maintained during whole shape memory and recovery process. Then, increasing temperature yields unwinding of the beam due to shape recovery, as depicted in Fig. 4.21c. It is notable that the shape recovery drastically occurs around the glass transition temperature $T_g = 343K$ of the SMP material.

Design sensitivity analysis

To verify the developed DSA method considering the stored strain sensitivity, the sensitivity of displacement from initial configuration is calculated during the shape recovery process and compared with finite difference sensitivity. The displacement sensitivity is calculated at the tip indicated in Fig. 4.21a at several specified temperatures. A shape design variation, illustrated in Fig. 4.22, is considered. δ represents a perturbation amount of initial beam length.
Tables 4.5 and 4.6 show the results of design sensitivity verification. In the calculation of finite difference sensitivity, the perturbation amount is selected as $\delta = 10^{-3}$. The analytic sensitivity agrees very well with the finite difference sensitivity. The displacements at $T = 358K$ are almost equal to zero, which implies that the shape of beam is recovered to the original shape.

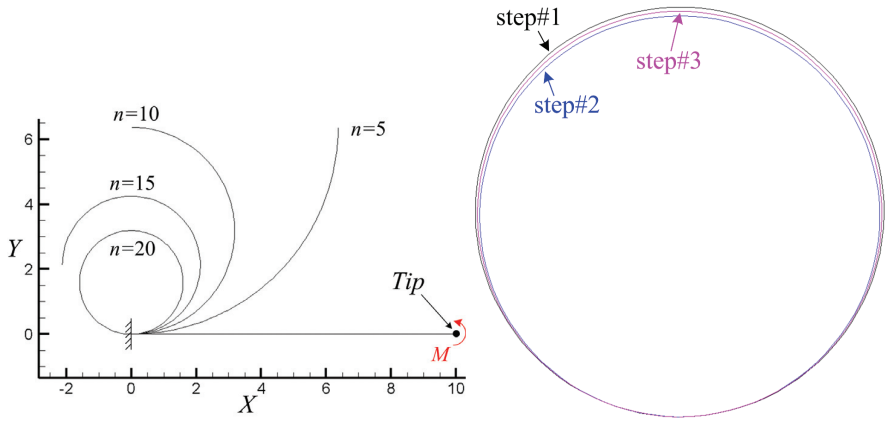

(a) Pre-deformation

(b) Cooling and spring-back

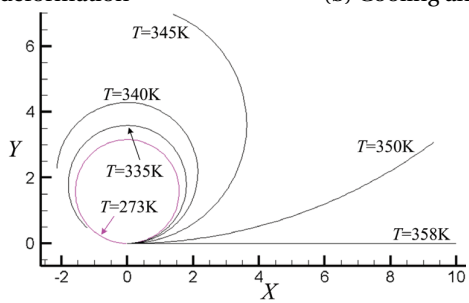

(c) Shape recovery by heating

Figure 4.21: Simulation of shape memory and recovery

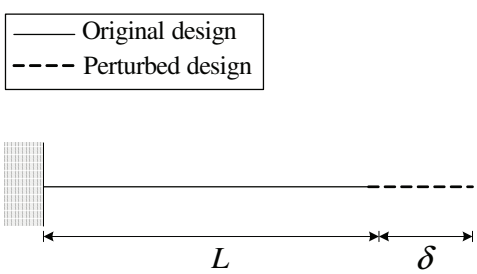

Figure 4.22: Shape design variation

Table 4.5: Verification of displacement sensitivity

Temp. (K)	Original displacement z_1	Finite difference z_1 (a)	Analytic sensitivity $\dot{z}_1$ (b)	Agreement(%) (b)/(a)
320	-1.0191E+01	-2.3304E-02	-2.3336E-02	100.14
325	-1.0321E+01	-3.4744E-02	-3.4800E-02	100.16
330	-1.0595E+01	-7.8394E-02	-7.8493E-02	100.13
335	-1.1203E+01	-2.6781E-01	-2.6799E-01	100.07
340	-1.2140E+01	-1.0609E+00	-1.0612E+00	100.02
345	-8.6202E+00	-1.9131E+00	-1.9131E+00	100.00
350	-6.8159E-01	-1.9749E-01	-1.9747E-01	99.99
358	-4.0320E-13	-2.3893E-13	-2.1251E-13	88.94

Table 4.6: Verification of displacement sensitivity

Temp. (K)	Original displacement z_1	Finite difference z_1 (a)	Analytic sensitivity $\dot{z}_1$ (b)	Agreement(%) (b)/(a)
320	1.1192E-02	-1.1547E-01	-1.1577E-01	100.26
325	3.1617E-02	-1.9253E-01	-1.9282E-01	100.15
330	1.0837E-01	-3.4805E-01	-3.4832E-01	100.08
335	4.6137E-01	-6.6048E-01	-6.6068E-01	100.03
340	2.2692E+00	-9.8496E-01	-9.8495E-01	100.00
345	6.9811E+00	3.8363E-01	3.8375E-01	100.03
350	3.0863E+00	5.9329E-01	5.9326E-01	100.00
358	1.9199E-06	3.8210E-07	3.8208E-07	100.00

4.3 Configuration DSA of shear-deformable beam structures

4.3.1 Twisting of a circular ring by prescribed rotation

This is a benchmark example undergoing very large displacements and rotations. Fig. 4.23a shows the problem description. Consider a circular ring with radius $R = 20$ is exposed to the two prescribed rotation angles $\boldsymbol{\theta}_1 = [\theta, 0, 0]^T$ at the material point with initial coordinate $[R, 0, 0]^T$ and Y- and Z-displacements constrained, and $\boldsymbol{\theta}_2 = [-\theta, 0, 0]^T$ at the immovable material point with initial coordinate $[-R, 0, 0]^T$. A rectangular cross-section has width $b = 1/3$ and height $h = 1$ ($I_2 \approx 3.086 \times 10^{-3}$ and $I_3 \approx 2.778 \times 10^{-2}$), and a polar moment of inertia $I_p = 9.753 \times 10^{-3}$. Young's modulus of $E = 21 \times 10^6$ and Poisson's ratio of $\nu = 0.3$. The prescribed rotation angle is increased from $\theta = 0°$ to $\theta = 180°$ in 180 load steps with uniform increments. Two, three, and four Gauss integration points are respectively used for numerical integrations in quadratic, cubic, and quartic IGA. Fig. 4.23b shows the deformed configurations at selected four load steps. It was addressed that the analytical solution for this problem is a planar circular ring with radius $R/3$ in [78], and we perform a convergence test using a L_2 error norm of deformed radius, as shown in

Fig. 4.24. At all degrees of basis functions we obtain monotonic convergences.
A design variable is selected as the radius of circle R. Table 4.7 shows the verification of the adjoint sensitivity of X- and Y-displacements at the point A indicated in Fig. 4.23a. It is shown that the finite difference sensitivity approaches to the analytical ones as the perturbation amount decreases.

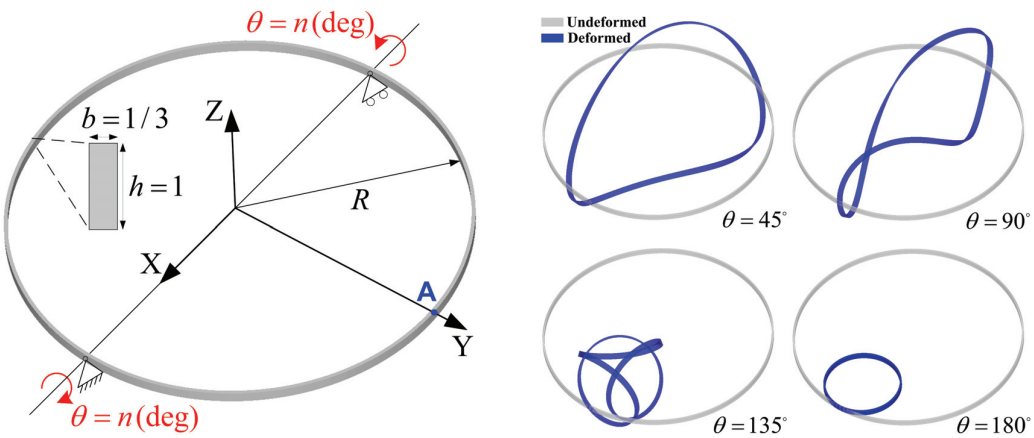

(a) Problem description (b) Deformations

Figure 4.23: Twist of a circular ring model

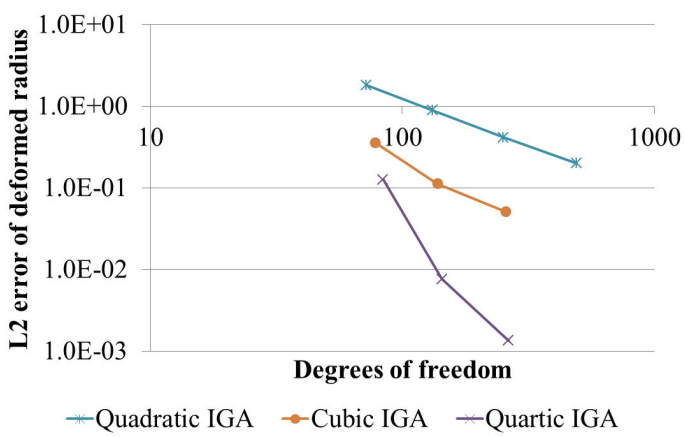

Figure 4.24: Twist of a circular ring model

Table 4.7: Verification of adjoint DSA of displacement at the point A

	Perturbation amount(%)	Displacement	Finite difference sensitivity(a)	Adjoint sensitivity(b)	Agreement(%) (b)/(a)
	1		-1.4371E+02		92.77
Y-disp.	0.1	-1.3328E+01	-1.3355E+02	-1.3331E+02	99.82
	0.01		-1.3334E+02		99.98
	1		1.3516E+02		98.63
X-disp.	0.1	1.3332E+01	1.3330E+02	1.3331E+02	100.00
	0.01		1.3331E+02		100.00

4.3.2 Twisted tower model

We verify the developed adjoint DSA method in a non-conservative loading condition. For the purpose of investigation of symmetry property of tangent operator exploited in solving the adjoint equation, we additionally implement a displacement loading condition. We consider a twisted tower model initially constructed by a rhombic lattice structure of Fig. 4.25a and is mapped to a smooth cylindrical surface of Fig. 4.25b. A rectangular domain with width $b = 4$ and height $h = 10$ shown in Fig. 4.25a is selected as an initial parent domain. A target parent domain shown in Fig. 4.25b consists of four cubic B-spline surfaces. Through the aforementioned FFD and global curve interpolation procedure, a lattice structure shown in Fig. 4.25c is obtained, and it has a circular cross-section of radius 0.1. We compare initial orthonormal frames by the SR method

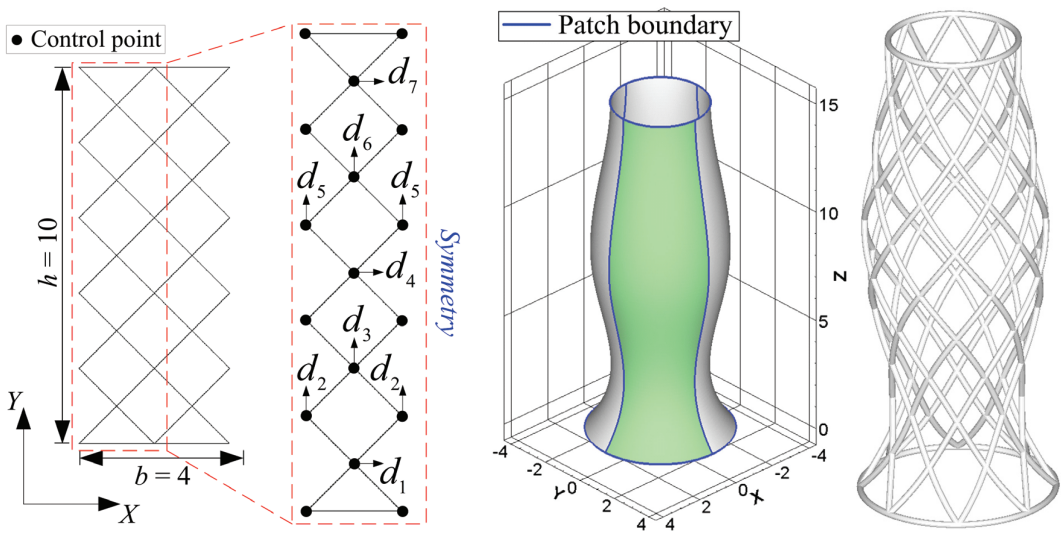

(a) Design variables (b) Target parent domain (c) Twisted tower

Figure 4.25: Geometric modeling of a twisted tower model

with two different kinds of reference orthonormal basis respectively by the *method* #1 and #2. Fig. 4.26a and 4.26b(R) illustrate the initial orthonormal frames at several selected points by the *method* #1 and #2, respectively. The *method* #1 leads to abrupt changes of directions of vectors $\mathbf{j}_2$

and $\mathbf{j}_3$ at the top members, due to the determination of ${}^{(0)}\mathbf{j}_2^{ref}$ by a cross-product of global base vectors in Eq. (3.205). On the contrary, the *method* #2 employing the reference basis from surface convected basis illustrated in Fig. 4.26b(L) shows a smooth parameterization.

Two kinds of loadings on the top members are considered; a prescribed displacement in vertical direction and a pressure load. Figs. 4.27a and 4.27b show the problem description and deformed configurations, where a prescribed Z-displacement $d = -0.6n$ and a pressure load with magnitude $p = 0.16n$ are applied, respectively, and n denotes the load increment number. Total ten and five uniform load increments are used for the former and latter loading cases, respectively. A pressure load vector of Eq. (2.199) on the top members are defined as $\tilde{\mathbf{n}}^p \equiv -p\mathbf{a}_2$, and the vector $\mathbf{a}_2$ is, in the undeformed configuration, the same with $\mathbf{j}_2$ which is directed to Z-direction. Through a k-refinement process, quartic B-spline basis functions with uniform 20 knot spans are used for spatial discretization, and four Gauss integration points are utilized to numerical integration.

Table 4.8 shows the verification of the design sensitivity of total strain energy for the prescribed displacement loading condition, where the tangent operator is symmetric at equilibrium configuration; hence, the same tangent stiffness matrix at the equilibrium configuration can be utilized to solve the adjoint equation. However, in case of the pressure load, due to the load stiffness, the tangent operator is asymmetric at equilibrium. Thus, the tangent stiffness matrix needs to be transposed in adjoint equation, which is verified by the result of Table 4.9. In both loading cases, selected design perturbation amount for each design variable is 10^{-4} for finite difference sensitivity calculation.

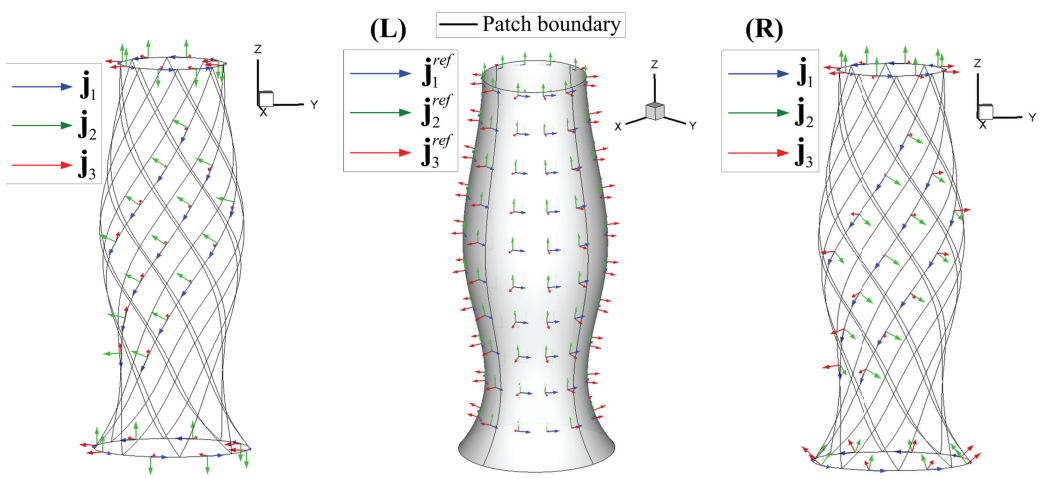

(a) Curve framing *method*#1 (b) Curve framing *method*#2

Figure 4.26: Comparison of constructed initial orthonormal basis by *method*#1 and #2

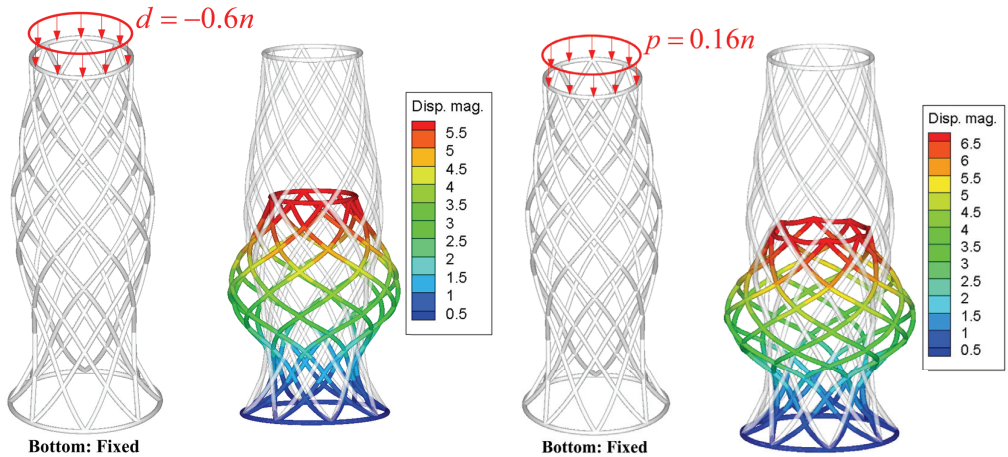

(a) Prescribed displacement at the top (b) Pressure load at the top

Figure 4.27: Deformations of twisted tower model

Table 4.8: Design sensitivity verification for the case of prescribed displacement

Design variable#(i)	Strain energy	Adjoint (w/o transpose)(a)	Finite difference(b)	Agreement(%) (b)/(a)
1		3.4037E-02	3.3992E-02	100.13
2		-9.6681E-03	-9.6970E-03	99.70
3		6.0073E-02	6.0047E-02	100.04
4	2.6947E+01	-1.1335E-02	-1.1400E-02	99.43
5		8.0050E-02	8.0033E-02	100.02
6		-1.6919E-01	-1.6921E-01	99.99
7		2.5360E-02	2.5308E-02	100.20

Table 4.9: Design sensitivity verification for the case of pressure load

Design variable# (i)	Strain energy	Adjoint (w/o trans.) (a)	Adjoint (w/ trans.) (b)	Finite difference (c)	Agreement (a)/(c) (%)	Agreement (b)/(c) (%)
1		-5.7720E-02	-7.1227E-02	-7.1150E-02	81.12	100.11
2		1.2411E-02	7.7970E-02	7.7995E-02	15.91	99.97
3		-7.7287E-01	-1.4689E-01	-1.4686E-01	526.26	100.02
4	3.5035E+01	1.6266E-02	6.6668E-03	6.7869E-03	239.66	98.23
5		-6.0638E-01	-1.6401E+00	-1.6401E+00	36.97	100.00
6		1.0123E+00	4.9473E-02	4.9446E-02	2047.35	100.05
7		-4.8892E-02	2.9988E-02	3.0036E-02	-162.78	99.84

4.3.3 Hexagonal honeycomb lattice structure under pressure load

Here we consider a hexagonal honeycomb structure embedded in a planar circular domain on the XY-plane, where only a quarter model is considered by exploiting a symmetric boundary condition. Fig. 4.28a shows a hexagonal honeycomb structure modeled by linear B-spline curves in a rectangular domain with width $b = 240$ and height $h = 80$, where the red-colored one indicates a selected unit cell due to a translational periodicity. We define 9 design variables of changes of control point positions in the unit cell as depicted in Fig. 4.28b.

A target parent domain is selected as a quarter circular domain with inner radius $R_i = 20$ and outer radius $R_o = 40$ as depicted by a gray region in Fig. 4.29a, and through the FFD and global curve interpolation procedure, a constrained lattice structure is modeled, as shown in Fig. 4.29a, where the indicated unit cell corresponds to the one in the initial parent domain, and is the minimal repeating unit by a rotational periodicity. We employ two kinds of loading directions of pressure on the inner circular boundary; first, an in-plane direction with magnitude $p = 400n$ ($\tilde{\mathbf{n}}^p \equiv p\mathbf{a}_2$) and second, the out-of-plane direction with magnitude $p = 4n$ ($\tilde{\mathbf{n}}^p \equiv p\mathbf{a}_3$), where n denotes the load increment number, and total 15 and 100 load steps are used respectively for the first and second load cases. For the second case, we fix outer circular boundary, and for both cases, symmetric boundary conditions are enforced at the lateral boundary points. Fig. 4.29b and 4.29c show the deformations and plots of displacement magnitudes, obtained by using quartic B-spline basis functions with 20 uniform knot spans per patch. Fig. 4.33 shows the results of strain energy convergence tests for both load cases, where monotonic convergences are observed.

We verify adjoint configuration design sensitivities of the total strain energy for selected three design variables d_1, d_2, and d_3, by comparison with finite difference ones in Table 4.10. An excellent agreement is obtained. We also perform a configuration design optimization for the in-plane pressure load case for maximizing structural stiffness through minimizing total strain energy under volume constraint, which can be stated as: Find a set of design variables $\mathbf{d} \equiv \{d_i\}$ such that

$$\text{Minimize } \psi({}^{n+1}\boldsymbol{\eta};\mathbf{d}) \equiv \frac{1}{2}\int_\Omega \left(\boldsymbol{\Gamma}^T\mathbf{N} + \boldsymbol{\Omega}^T\mathbf{M}\right) ds, \tag{4.4}$$

$$\text{subject to } V(\mathbf{d}) \equiv \int_\Omega A ds \le V_f V_0, \tag{4.5}$$

$$d_i^{lower} \le d_i \le d_i^{upper}, \tag{4.6}$$

where V_0 and V_f respectively denotes the initial volume and the allowable volume fraction selected as $V_f = 0.9999$, and the side constraints of design variables are $d_i^{lower} = -3$ and $d_i^{upper} = 3$. Fig. 4.31a shows the optimal configuration design of the unit cell in the initial parent domain and corresponding lattice structure in the target parent domain. Fig. 4.31b shows that the overall deformation significantly decreases, compared with that of the original design in Fig. 4.29b. Fig. 4.32a and 4.32b show the optimization history of total strain energy and volume ratio to initial one. The total strain energy shows monotonic decreases and convergence within a few iterations,

and the volume of optimal design is almost the same as the initial one, and to be more concretely, the optimal design volume is 1.3718×10^2, slightly smaller than the original one 1.3719×10^2.

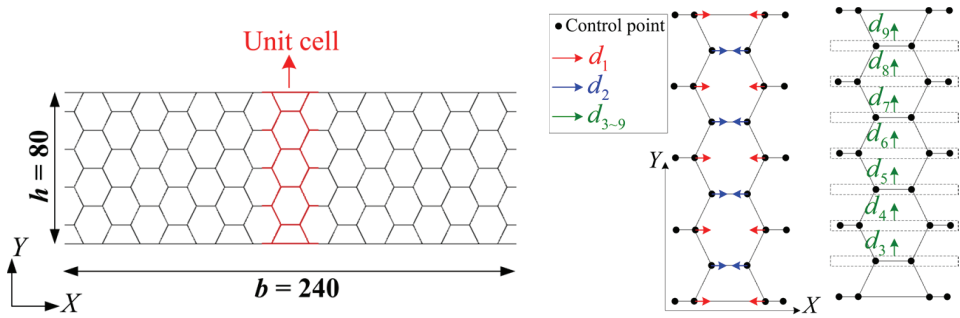

(a) Initial parent domain (b) Design variables of the unit cell

Figure 4.28: Geometric modeling and design variables in initial parent domain

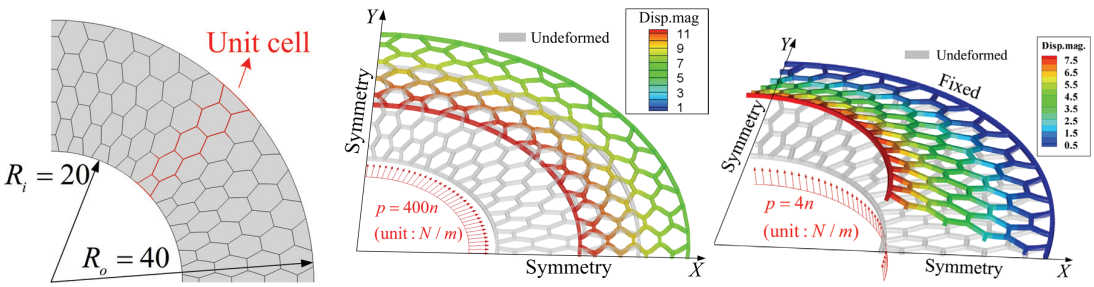

(a) Target parent domain (b) In-plane deformation (c) Out-of-plane deformation

Figure 4.29: Deformation of hexagonal honeycomb structure

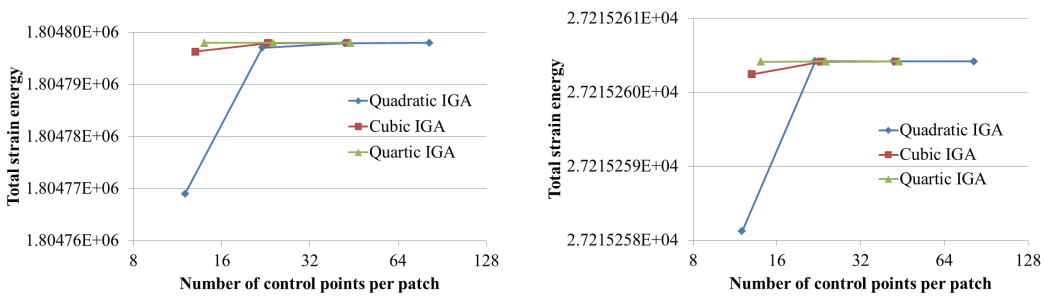

(a) In-plane pressure load (b) Out-of-plane pressure load

Figure 4.30: Deformation of hexagonal honeycomb structure in circular domain

Table 4.10: Verification of adjoint DSA of total strain energy

Load type	Design variable#	Strain energy	Adjoint sensitivity(a)	Finite difference(b)	Agreement(%) (b)/(a)
In-plane pressure	1	1.8048E+06	8.7113E+04	8.7111E+04	100.00
	2		-8.3792E+04	-8.3793E+04	100.00
	3		-1.5312E+04	-1.5318E+04	99.96
Out-of-plane pressure	1	2.7215E+04	-2.4427E+02	-2.4425E+02	100.00
	2		1.9715E+02	1.9716E+02	99.99
	3		-1.2586E+01	-1.2598E+01	99.91

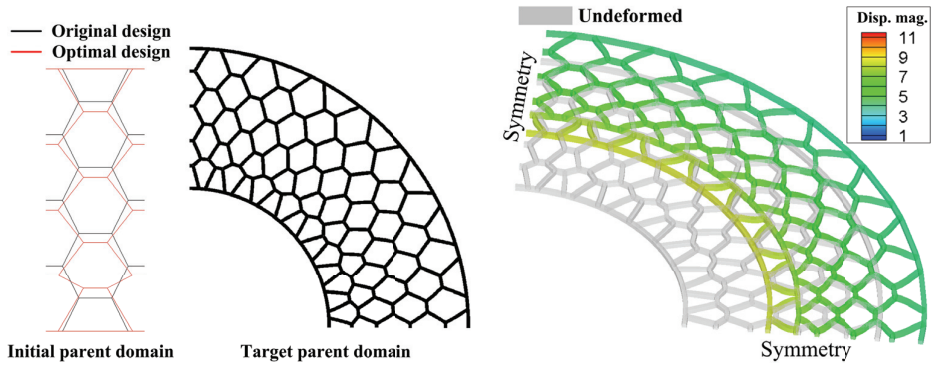

(a) Optimal design (b) Deformation

Figure 4.31: Deformation of optimal design

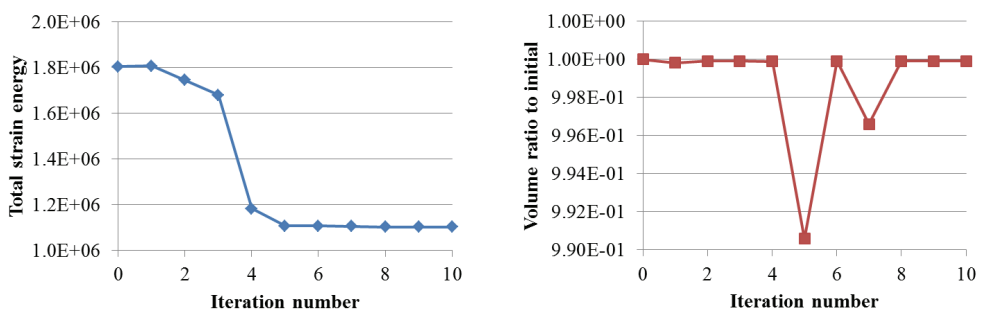

(a) Objective function (b) Volume ratio

Figure 4.32: Optimization history

4.3.4 Auxetic lattice structure

We architect a three-dimensional auxetic structures having nearly constant negative Poisson's ratio during large tensile deformations. Fig. 4.33a shows an original design of a unit cell of a periodic structure with translational periodicity. A circular cross-section with diameter 0.8 is considered, and the unit cell is inscribed by a cube whose boundary faces are indicated in Fig. 4.33a by green-, blue-, and red-colored planes respectively perpendicular to X-, Y-, and Z-axes, and overall dimension is $20 \times 20 \times 20$ as illustrated in 4.33b. It is noted that we often replace

the notations X, Y, and Z with X_1, X_2, and X_3 for brief expression, and we term each set of boundary faces facing to each other as $X_i(+)$ and $X_i(-)$ which are respectively located at positive and negative X_i-axis ($i = 1,2,3$). Young's modulus and Poisson's ratio of bulk material are chosen as $E = 848.3$ and $\nu = 0.3458$.

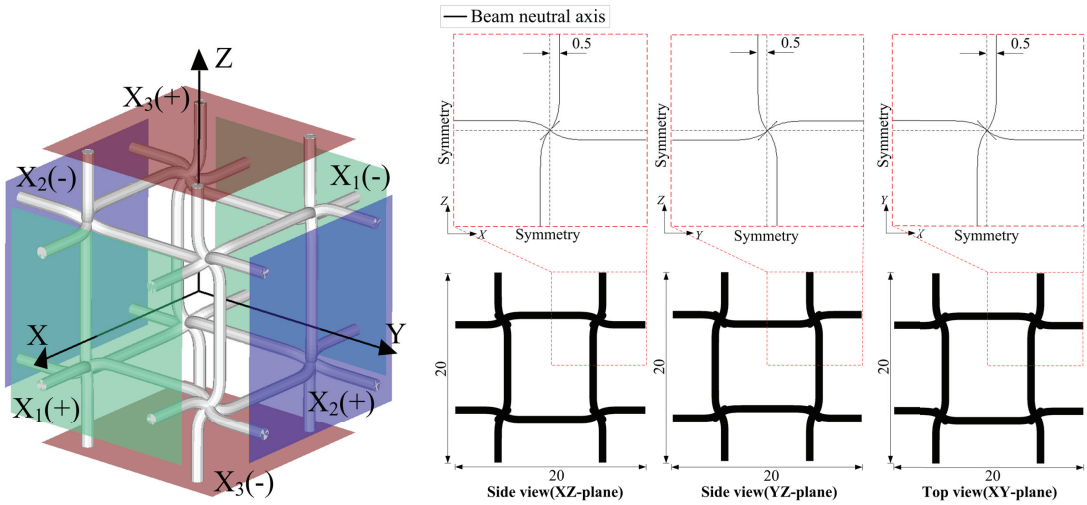

(a) Original design (b) Plane view

Figure 4.33: Original design description

We employ a periodic boundary condition to model an infinitely periodic lattice structure, following the method presented in Wang et al. [107]. We introduce notations (u_i, v_i, w_i) and (u_{0i}, v_{0i}, w_{0i}) for the X_i-directional displacement components of material points on the $X_i(+)$ and $X_i(-)$ faces ($i = 1,2,3$), respectively. In order to depict the translational periodicity, for the three pairs of $X_i(+)$ and $X_i(-)$ faces ($i = 1,2,3$), the following kinematic boundary conditions are imposed.

$$u_3 = u_{03},\ \ v_3 = v_{03},\ \ w_{03} = 0,\ \text{and}\ \ w_3\ \ \text{is prescribed}, \tag{4.7}$$

$$u_{01} = 0,\ \ v_1 = v_{01},\ \ w_1 = w_{01},\ \text{and}\ \ u_1\ \ \text{is free}, \tag{4.8}$$

and

$$u_2 = u_{02},\ \ v_{02} = 0,\ \ w_2 = w_{02},\ \text{and}\ \ v_2\ \ \text{is free}, \tag{4.9}$$

and the rotations at the material points on the whole boundary faces are constrained. An effective (secant) Poisson's ratio due to lateral X_k-displacement ($k = 1,2$) under the Z-directional loading can be calculated as

$$\nu_{31} \equiv -\frac{\varepsilon_1}{\varepsilon_3} = -\frac{u_1^c/L_0^1}{u_3^c/L_0^3},\ \text{and}\ \ \nu_{32} \equiv -\frac{\varepsilon_2}{\varepsilon_3} = -\frac{u_2^c/L_0^2}{u_3^c/L_0^3}, \tag{4.10}$$

where u_i^c denotes the X_i-displacement at the center of unit cell, obtained by averaging X_i-displacements at the eight junctions, and $\varepsilon_i \equiv u_i^c/L_0^i$ defines the X_i-directional nominal strain.

L_0^i $(i = 1,2,3)$ denotes the initial overall dimension of unit cell in X_i-direction, and our model has $L_0^1 = L_0^2 = L_0^3 = 20$. We select total 8 configuration design variables described in detail in appendix F.2.1. An optimization problem to achieve a target effective Poisson's ratio $\nu^* = -0.4$ within a given applied strain range can be stated as: find a set of design variables $\mathbf{d} \equiv \{d_i\}$ such that

$$\text{Minimize } \psi(^{n+1}\boldsymbol{\eta}; \mathbf{d}) \equiv \sum_i \left\{ \left| \nu_{31}(\varepsilon_i^0) - \nu^* \right|^2 + \left| \nu_{32}(\varepsilon_i^0) - \nu^* \right|^2 \right\}, \tag{4.11}$$

$$\text{subject to } g_j(\mathbf{d}) \equiv \frac{1}{L_j(\mathbf{d})} \int_{\Xi_j} \left[\left\{ \kappa^f(\xi) / \kappa_U^f \right\}^2 - 1 \right] J_c(\xi) d\xi, \; j = 1 \sim ne, \tag{4.12}$$

and

$$d_i^{lower} \le d_i \le d_i^{upper}, \tag{4.13}$$

where ε_i^0 represents the applied nominal strain level, and we divide total 10% applied strain into 10 uniform increments, *i.e.*, $i = 1 \sim 10$. The side constraints are selected as $d_i^{lower} = -4$ and $d_i^{upper} = 4$. Eq. (4.12) represents curvature constraints, introduced to avoid self-intersection of ligaments, and $k^f(\xi)$ represents the Frenet curvature calculated as

$$\begin{cases} \mathbf{n} \equiv \mathbf{j}_{1,s} / \left\| \mathbf{j}_{1,s} \right\| \text{ and } \kappa^f = \mathbf{j}_{1,s} \cdot \mathbf{n}, & \text{if } \left\| \mathbf{j}_{1,s} \right\| \neq 0 \\ \kappa^f = 0, & \text{otherwise} \end{cases}, \tag{4.14}$$

where $\mathbf{n}$ denotes a Frenet normal vector. Ξ_i denotes the i-th knot span among total ne knot spans for a given patch. L_i denotes a length of a curve segment (Ω_i) corresponding to i-th knot span, calculated by a numerical integration as

$$L_i \equiv \int_{\Omega_i} ds = \int_{\Xi_i} J_c(\xi) d\xi. \tag{4.15}$$

Due to the rotational symmetry of design parameterization explained in F.2.1 we impose curvature constraints to one of the six ligaments attached to a junction in the one-eight model of unit cell. We select an upper bound value $\kappa_U^f = 1$. We note that Nagy et al. [80] presented a similar form of finite set of curvature constraints for a planar beam model, where each constraint was assigned to a control point through a corresponding basis function. Eq. (4.12) differs from their expression in terms of knot span-wise evaluation, normalization by an element length, and generalization to spatial curves. We present a design sensitivity expression of the curvature constraint of Eq. (4.12) in E.1. Fig. 4.34 shows the optimal design, where more rounded shape around junctions is obtained. Fig. 4.35a compares changes of Poisson's ratios during deformations, and the optimal design shows nearly constant negative Poisson's ratio, in contrast to the result of original design having significant decrease in magnitude of Poisson's ratio. Fig. 4.35b shows the history of the objective function during the optimization processes. It is noticeable that the objective function monotonically decreases and converges within a few iterations.

For verifying auxetic behaviors of the optimal design, we perform an uniaxial tension simulation

for the $3 \times 3 \times 3$ assemblies of architected unit cell shown in Fig. 4.36a where top and bottom surfaces are depicted to explain the kinematic boundary conditions. On the top surface, Z-displacement is prescribed and all rotational DOFs are constrained. On the bottom surface, Z-displacement and all rotational DOFs are constrained. Lateral displacements, *i.e.*, X- and Y-displacements are free on both of the top and bottom surfaces. Figs. 4.36b and 4.36c illustrate deformed configurations with X- and Y-displacement plots, respectively. An auxetic behavior that the structure expands in lateral directions due to Z-directional tension is apparent.

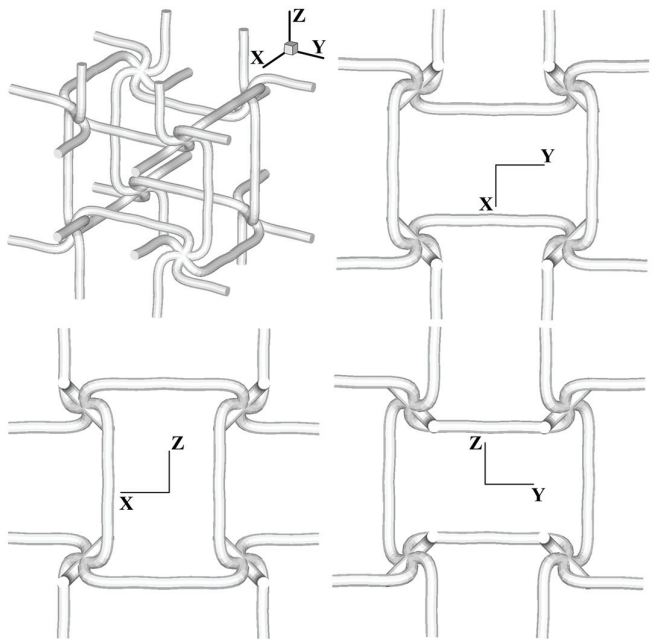

Figure 4.34: Plot of optimal design in four different views

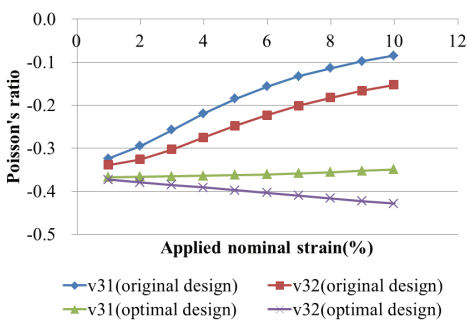

(a) Change of Poisson's ratio

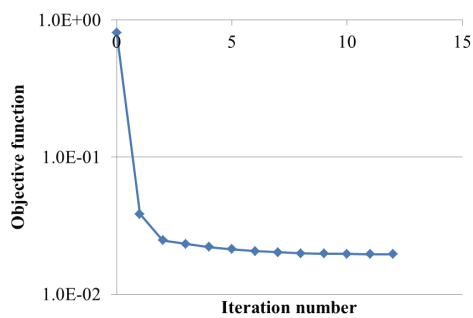

(b) Optimization history

Figure 4.35: Design optimization result

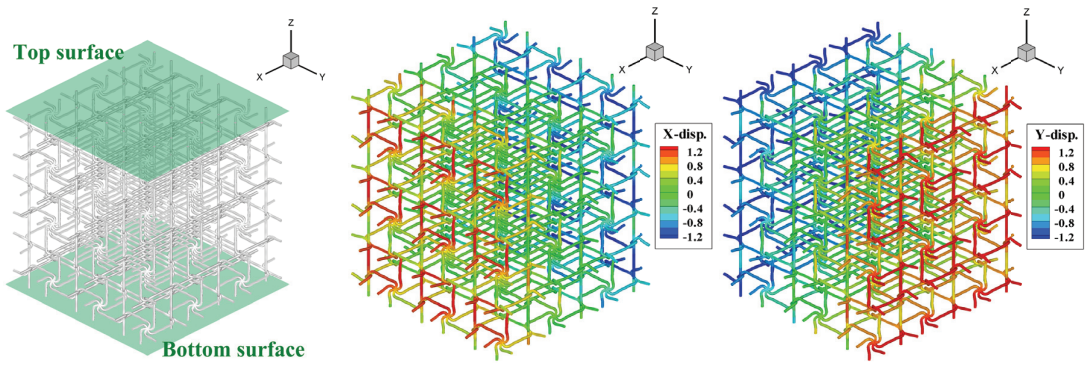

(a) $3 \times 3 \times 3$ array of unit cells (b) X-displacement plot (c) Y-displacement plot

Figure 4.36: Tensile deformation analysis of $3 \times 3 \times 3$ array of unit cells

4.4 Configuration DSA of shear-deformable shell structures

4.4.1 Cantilever plate under end moment

Fig. 4.37 illustrates a plate clamped at one end and subjected to two kinds of loading condition at the other end; moment about Y-axis and Z-directional shear force. In this problem, the material properties are chosen as $E = 1.2 \times 10^6$ and $\nu = 0$. We select the initial length $L = 12$, width $w = 1$ and thickness $h = 0.1$. Under the moment load, the cantilever becomes circular arc with radius R

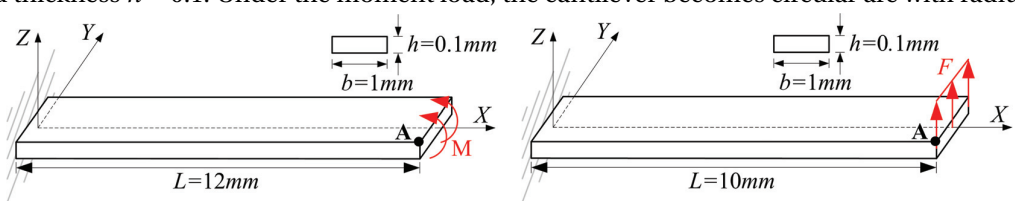

(a) Bending moment (b) Shear force

Figure 4.37: Cantilever plate under end load

given by the formula $R = EI/M$ from which the exact solution of X- and Z-displacements at the end (point A) are respectively derived to be [103]

$$U_A = \frac{EI}{M}\sin\frac{ML}{EI} - L \text{ and } W_A = \frac{EI}{M}\left(1 - \cos\frac{ML}{EI}\right). \tag{4.16}$$

We apply the end moment $M = \pi EI/3$ at which the beam will wind twice itself, and total 40 uniform load steps are utilized, *i.e.*, $M = n\pi/120$ for n^{th} load step. We use an isogeometric discretization using cubic B-spline basis functions with 20 uniform knot spans in longitudinal direction and single knot span in transversal direction with a full integration of 4×4 Gauss integration points for each knot span. Figs. 4.38a and 4.38b respectively show the beam winding due to end moment and comparison of calculated displacement components with the exact solution of Eq. (4.17) where an excellent agreement is found. Fig. 4.38a shows a vertical large deflection due to end shear force and Fig. 4.38b compares the computed tip displacement

components with the reference solution given by Sze et al. [103].

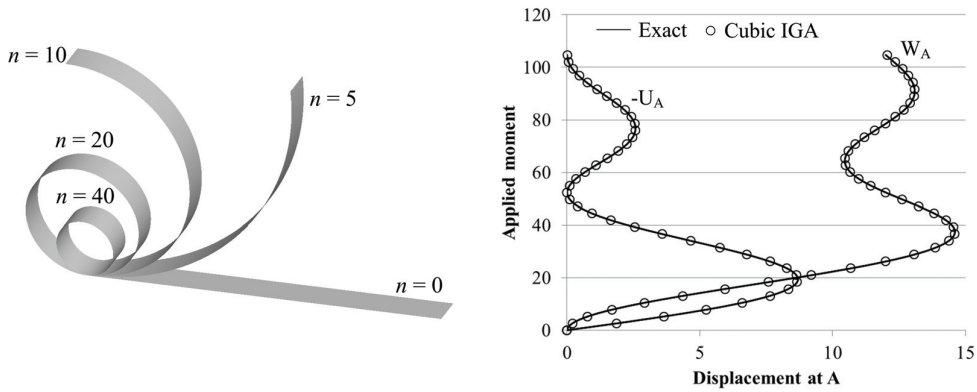

(a) Deformation (b) Comparison with exact solution

Figure 4.38: Deformation due to end moment load

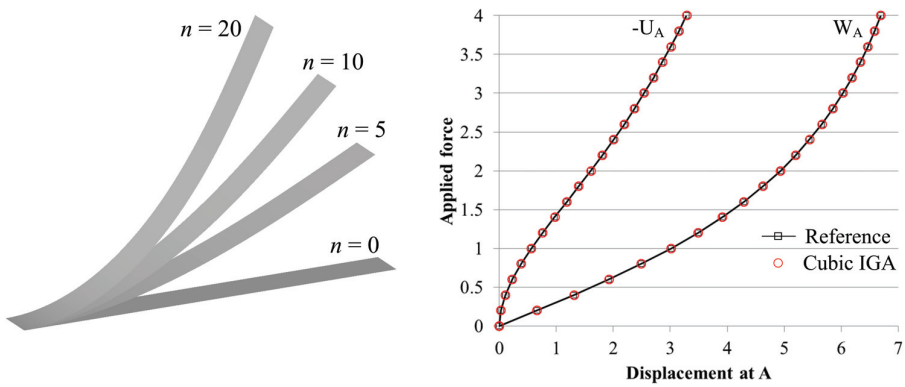

(a) Deformation (b) Comparison with exact solution

Figure 4.39: Deformation due to end shear force

The initial length of the plate (L) is selected as a shape design variable. Table 4.11 compares the design sensitivity of displacement components using the adjoint method with the finite difference sensitivity by a perturbation amount 0.1% of the original length. In all the comparisons, excellent agreements are found. In the moment load case, the exact sensitivity of displacement components with respect to initial length change δL are respectively

$$\dot{U}_A = \left(\cos\frac{ML}{EI} - 1\right)\delta L \text{ and } \dot{W}_A = \left(\sin\frac{ML}{EI}\right)\delta L. \tag{4.17}$$

Thus, the exact sensitivity is $\dot{U}_A = \dot{W}_A = 0$. In Fig. 4.40, we observe the convergence of calculated displacement components and their design sensitivity to the exact solutions as increasing discretization level.

Table 4.11: Cantilever plate under end moment: DSA verification

Load type	Performance measure	Original	Adjoint sensitivity(a)	Finite difference(b)	Agreement (a)/(b)(%)
Moment	X-disp.	-1.2058E+01	-3.1811E-03	-3.1789E-03	100.07
	Z-disp.	1.6011E-03	-5.6160E-03	-5.5669E-03	100.88
Shear force	X-disp.	-3.2895E+00	-1.0269E-01	-1.0270E-01	100.00
	Z-disp.	6.7000E+00	1.3130E-01	1.3130E-01	100.00

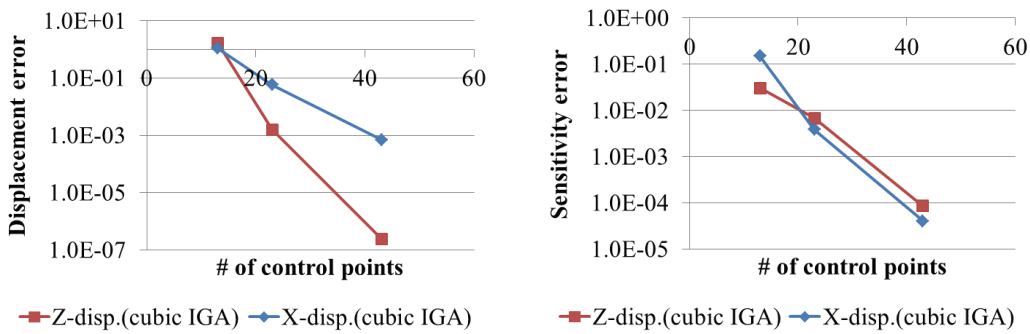

(a) Displacement components

(b) Design sensitivity

Figure 4.40: Convergence of displacement components and their design sensitivity

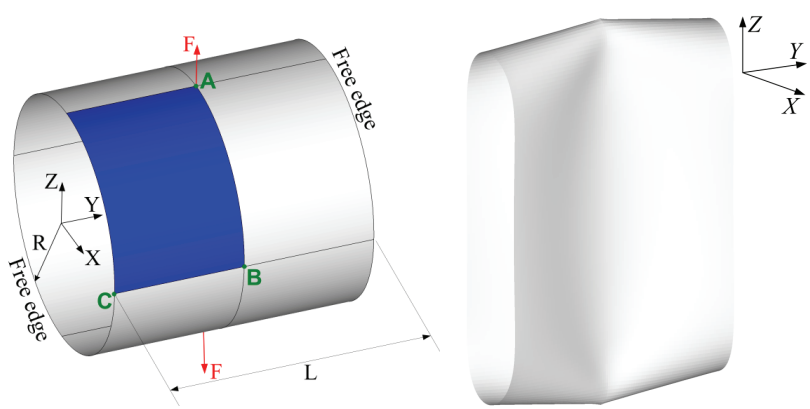

(a) Problem description

(b) Deformation

Figure 4.41: Pullout of an open-ended cylindrical shell

4.4.2 Pullout of an open-ended cylindrical shell

Fig. 4.41a shows an open-ended cylinder being pulled by a pair of radial forces. The cylindrical shell has a radius $R = 4.953$, and a length $L = 10.35$, and thickness $h = 0.094$. Material properties are Poisson's ratio $\nu = 0.3125$ and Young's modulus $E = 10.5 \times 10^6$. Force magnitude $F = 4 \times 10^4$ is applied in 80 uniform load increments. Owing to symmetry condition, we perform DSA using a one-eighth model depicted by blue-color in Fig. 4.41a. Fig. 4.41b shows a deformation of the full

model calculated by IGA using cubic B-spline basis function with 10×10 uniform knot elements and 5×5 Gauss points for numerical integrations. Fig. 4.42 compares displacements at several selected points A, B, and C indicated in Fig. 4.41a with those presented in [103]. Fig. 4.42 compares the solution by quartic IGA with 10 × 10 uniform knot elements with the reference solution. The circle and solid line in Fig. 4.42 indicate solutions by the reference and quartic IGA, respectively. Quartic IGA result agrees very well with the reference solution in the large deformation range.

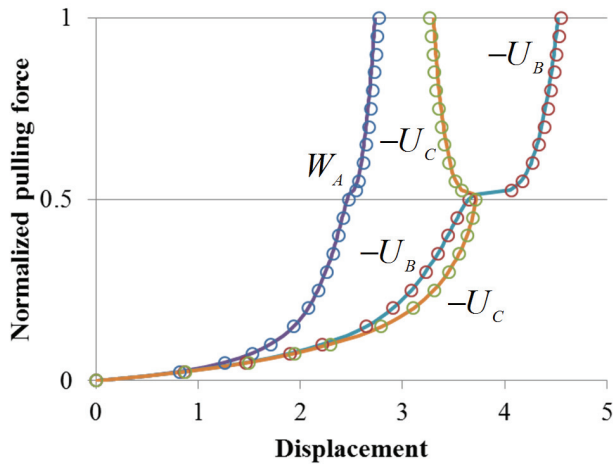

Figure 4.42: Pullout of cylindrical shell: verification by the reference solution

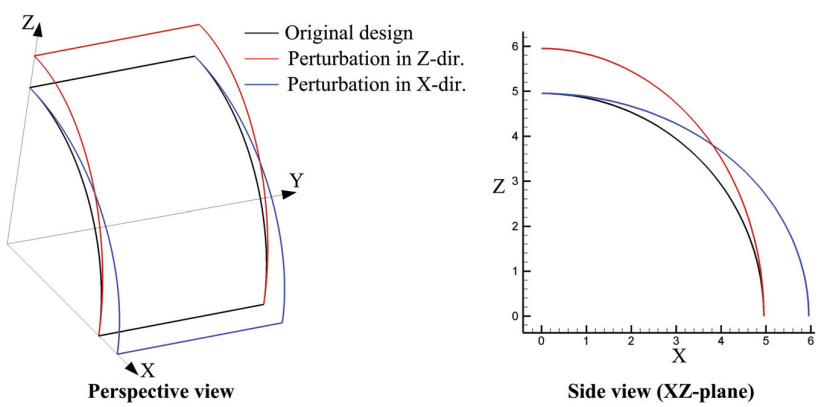

Figure 4.43: Pullout of cylindrical shell: two design perturbations

Fig. 4.43 shows two kinds of configuration design perturbations. Table 4.12 shows the excellent agreement of the analytic sensitivities using the direct differentiation method (DDM) with the finite difference ones by 0.1% of the perturbation amount illustrated in Fig. 4.43.

Table 4.12: Pullout of cylindrical shell: Design sensitivity verification

Design perturbation	Total strain energy	DDM sensitivity (a)	Finite difference sensitivity (b)	Agreement (a)/(b) (%)
X-dir.	4.1201E+03	3.6963E+02	3.6954E+02	100.02
Z-dir.		-2.8826E+02	-2.8865E+02	99.87

4.4.3 Pinched semi-cylindrical shell

Fig. 4.44a shows the semi-cylindrical shell subjected to an end pinching force in radial direction at the middle of the free-end circumferential edge with the other edge clamped. Along the longitudinal edges, the vertical deflection and the rotation about the Y-axis are restricted. Material parameters are the Young's modulus $E = 2.0685 \times 10^3$ and Poisson's ratio $\nu = 0.3$. Thickness is $h = 3$, and cylinder has a length $L = 304.8$ and circumferential radius $R = 101.6$. Fig. 4.44b shows the deformed configuration calculated by using the quartic NURBSS basis function with uniform 20 knot elements in each of the parametric coordinate directions. We compare the deflection at the loaded point with that of the reference solution in [103]. An isogeometric discretization using the quartic NURBS basis function with uniform 20×20 knot elements is used, and Fig. 4.45a shows the load-deflection curves where excellent agreements with the reference solution is found. Fig. 5(4.45b) shows the monotonic convergence of the total strain energy.
For the verification of analytical DSA using the direct differentiation method (DDM), the same two design perturbations with the previous example (Fig. 4.43) are considered. Table 4.13 compares the analytic sensitivity with finite difference one by 0.1% perturbation, and both are calculated by quartic NURBS basis functions with 80 uniform knot spans along each of two parametric coordinate directions. The analytic sensitivities agree very well with the finite difference ones.

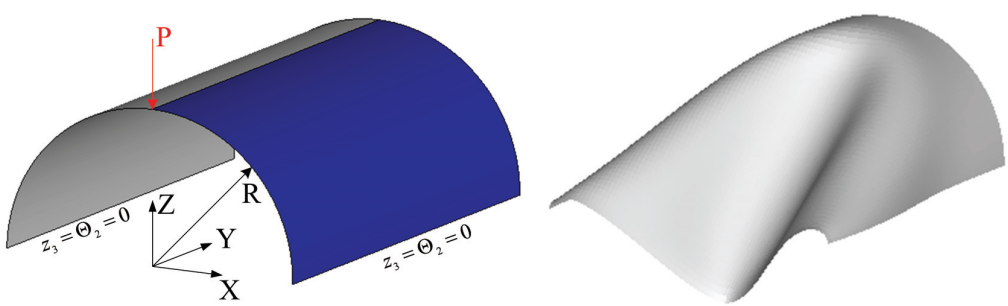

(a) Problem description (b) Deformation

Figure 4.44: Pinched semi-cylinder: problem description and deformation

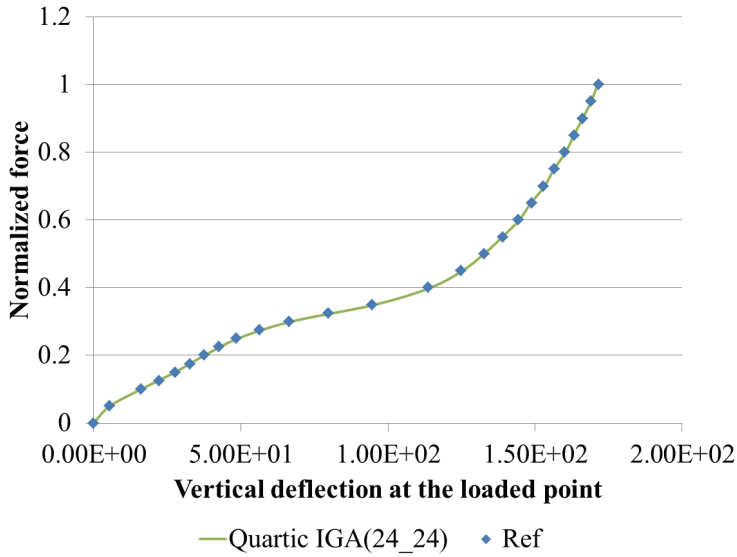

(a) Solution verification

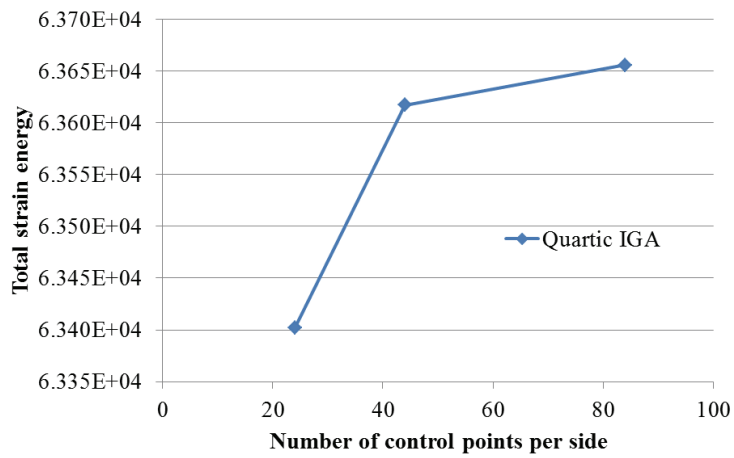

(b) Convergence test

Figure 4.45: Pinched semi-cylinder: verification of solution accuracy and convergence

Table 4.13: Pinched semi-cylinder: verification of total strain energy sensitivity

Design perturbation	Total strain energy	DDM sensitivity (a)	Finite difference sensitivity (b)	Agreement (a)/(b) (%)
X-dir.	6.3656E+04	-1.8720E+02	-1.8723E+02	99.98
Z-dir.		8.4340E+02	8.4320E+02	100.02

4.4.4 Hinged cylindrical isotropic roof with beam stiffeners

Fig. 4.46 shows the hinged semi-cylindrical roof subjected to a vertical force at center. The overall structural dimension parameters are selected as $R = 2{,}540$mm, $L = 254$mm, and $\theta = 0.1$rad. The shell thickness is $h = 12.7$mm. We consider a beam stiffener aligned as depicted by red-colored lines in Fig. 4.46, and the beam has a square cross-section with the thickness $h = 12.7mm$. Material properties are selected as Young's modulus $E = 3{,}102$(MPa) and Poisson's ratio $\nu = 0.3$. This problem has been shown to undergoes a snapping behavior, and it is solved in this work by using the arc-length method presented by [29, 37]. In order to prescribe a specific maximum force $P_{\max} = 3{,}000N$, we combine the arc-length method with a load control method in a way that the solution procedure by the arc-length method is changed to the load control if load level reaches within a specified range from the maximum force.

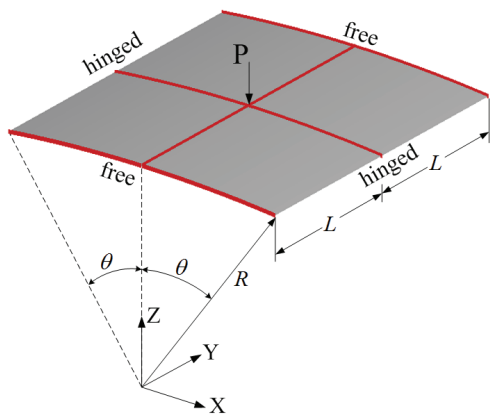

Figure 4.46: Hinged cylindrical roof under central force

We model the shell structure using four cubic NURBS patches with 5×5 knot elements for each patch and the stiffeners are located along edges of the patches. Fig. 4.47 compares the vertical deflections in the stiffened and unstiffened structures. As expected, the stiffened one has smaller deflection at central region than the unstiffened one. Fig. 4.48 shows load-displacement curves and the result of unstiffened structure is compared with the reference solution obtained in [103] where an excellent agreement is found. It is shown that the stiffened structure has higher load level for the same deflection amount due to higher stiffness compared with the unstiffened one. We consider two design variables; length L and radius of curvature R. Table 4.14 and 4.15 verify the adjoint sensitivity of vertical displacement at the loaded point for both of the stiffened and unstiffened structures. As decreasing the design perturbation amount finite difference sensitivities approaches to analytic ones.

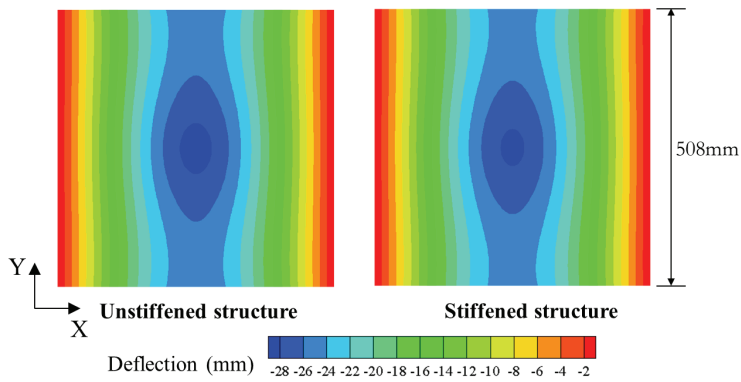

Figure 4.47: Comparison of vertical deflections in stiffened and unstiffened structures

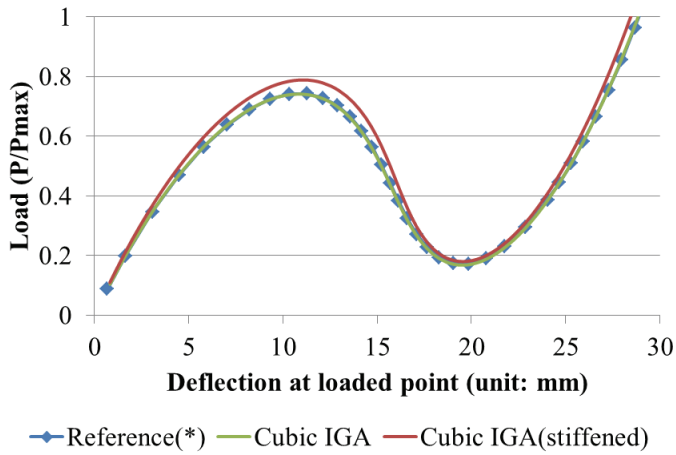

Figure 4.48: Comparison of load-displacement curves

Table 4.14: Stiffened shell structure: verification of design sensitivity

Design variable#	Perturbation amount	Vertical displacement	Adjoint sensitivity(a)	Finite difference sensitivity(b)	Agreement (a)/(b)(%)
1	10%	-2.8451E+01	8.4254E-01	7.0500E-01	119.51
	5%			7.6936E-01	109.51
	1%			8.2713E-01	101.86
2	10%		-3.4331E+01	-3.3827E+01	101.49
	5%			-3.4056E+01	100.81
	1%			-3.4272E+01	100.17

Table 4.15: Unstiffened shell structure: verification of design sensitivity

Design variable#	Perturbation amount	Vertical displacement	Adjoint sensitivity(a)	Finite difference sensitivity(b)	Agreement (a)/(b)(%)
1	10%	-2.8843E+01	1.0640E+00	8.9353E-01	119.07
	5%			9.7321E-01	109.32
	1%			1.0448E+00	101.83
2	10%		-3.4338E+01	-3.3871E+01	101.38
	5%			-3.4084E+01	100.74
	1%			-3.4283E+01	100.16

4.5 Configuration design of constrained structure on curved domains

In this section, the developed scheme of design velocity computation and the accuracy of configuration DSA are verified through numerical examples. Also, configuration design optimizations are performed. The material constants are chosen as $E = 210 \times 10^9$, $\nu = 0.3$, and $k_1 = k_2 = 5/6$. A circular cross-section with radius $r = 0.05$, $I_2 = I_3 = \pi r^4/4$, and $J = I_2 + I_3$ are considered.

4.5.1 Lattice structure on spherical surface

Fig. 4.49a shows an initial parent domain with $b = h = 3$ and embedded lattice structure which is represented by 24 linear B-spline patches. 3 design variables are defined considering symmetrical design variation about $X = 1.5$ axis.

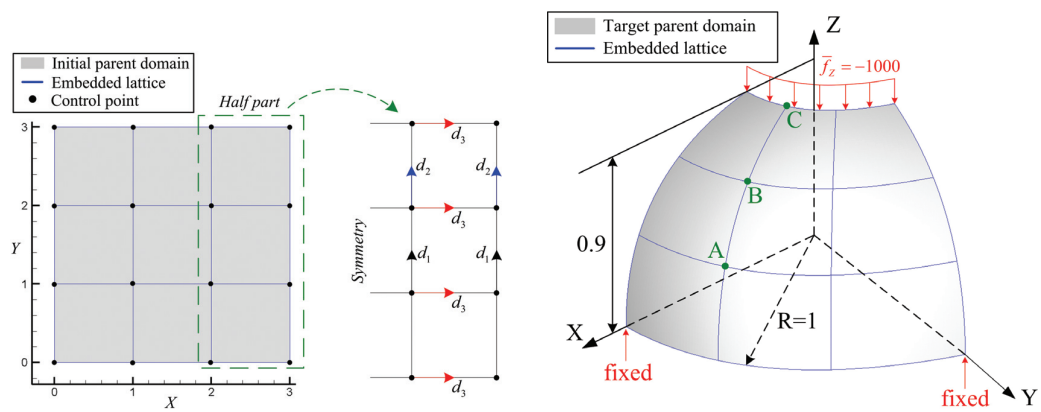

(a) Initial domain and design variables

(b) Target domain and problem description

Figure 4.49: Lattice structure on spherical surface

Using the k-refinement capability of the IGA method, we construct a refined model for the response and design sensitivity analyses, which consists of 10 uniform knot spans of cubic B-spline for each patch. This refined model in the initial parent domain is mapped into the target

domain which is a quarter of hemispherical surface, as shown in Fig. 4.49b. We note that the blue colored lines in Fig. 4.49b represent the lattice structures, modeled by the Timoshenko beams. Two points are fixed as kinematic boundary conditions, and the Z-directional distributed force of $\bar{f}_z = -1000N/m$ is applied at the top members ($Z = 0.9$) of the lattice structure.

Verification of design velocity field and sensitivity

For each of the three design variables, illustrated in Fig. 4.49a, design velocity fields in the initial parent domain are shown in Fig. 4.50.

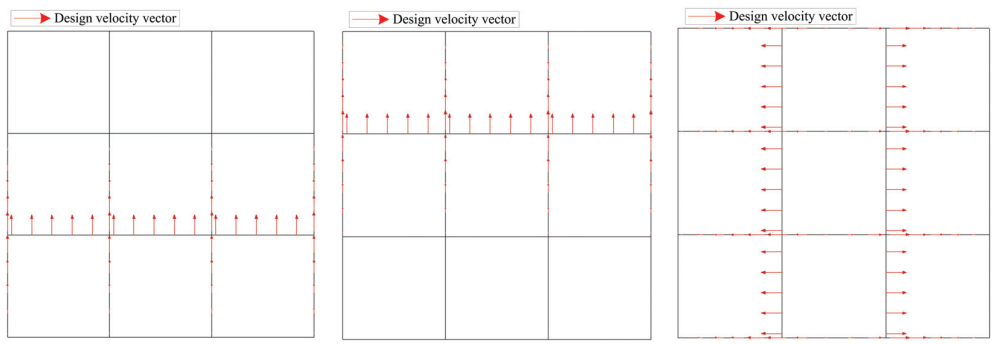

(a) Design variable#1(d_1) (b) Design variable#2(d_2) (c) Design variable#3(d_3)

Figure 4.50: Given design velocity field for each design variable

Using the developed computation scheme, the design velocity field for each design variable is calculated at the initial design, as shown in Fig. 4.51. As mentioned before, in the target parent domain, the design velocity field should be updated after the design change.

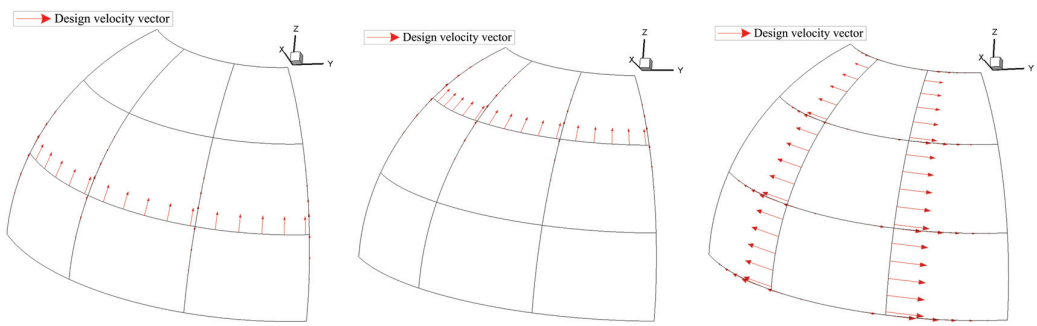

(a) Design variable#1(d_1) (b) Design variable#2(d_2) (c) Design variable#3(d_3)

Figure 4.51: Computed design velocity field for each design variable

At the points of A, B, and C in Fig. 4.49b, the design velocity vectors $\hat{\mathbf{V}} = [\hat{V}_1, \hat{V}_2, \hat{V}_3]^T$ for the design variables d_1, d_2, and d_3 are compared with finite difference ones, where perturbation amount is selected as $d_1 = d_2 = d_3 = 10^{-3}$. Table 4.16 shows the verification results. The computed design velocity agrees very well with the finite difference. As the third design variable d_3 does not change the Z-coordinate of point C, both the finite difference and the computed design velocity have zero values up to machine precision. Also, we verify the design sensitivity of the displacement

and rotation components for each of three design variables at point C by comparison with the finite differences. Table 4.17 shows that the analytic design sensitivity using the computed design velocity field agrees very well with the finite difference sensitivity.

Table 4.16: Verification of design velocity

	$x_{1\tau} - x_1$(a)	$x_{2\tau} - x_2$(b)	$x_{3\tau} - x_3$(b)	$\hat{V}_1$(d)	$\hat{V}_2$(e)	$\hat{V}_3$(f)	(d)/(a) (%)	(e)/(b) (%)	(f)/(c) (%)
A(d_1)	1.1950E-01	6.6999E-02	3.5427E-01	1.1944E-01	6.6965E-02	3.5429E-01	99.95	99.95	100.01
B(d_2)	2.2611E-01	1.2677E-01	2.7762E-01	2.2607E-01	1.2675E-01	2.7767E-01	99.98	99.98	100.02
C(d_3)	-1.1547E-01	2.0608E-01	0.0000E+00	-1.1553E-01	2.0606E-01	3.7007E-17	100.05	99.99	-

Table 4.17: Verification of design sensitivity at point C

	Original response	Analytic sensitivity			Finite difference sensitivity			Agreement(%)		
		d_1(a)	d_2(b)	d_3(c)	d_1(d)	d_2(e)	d_3(f)	(a)/(d)	(b)/(e)	(c)/(f)
z_1	1.477E-05	9.061E-07	-1.804E-07	-5.868E-06	9.058E-07	-1.796E-07	-5.870E-06	100.04	100.45	99.98
z_2	1.475E-05	9.139E-07	-1.866E-07	-5.847E-06	9.135E-07	-1.858E-07	-5.849E-06	100.04	100.42	99.98
z_3	-1.153E-05	-1.168E-07	6.281E-07	2.905E-06	-1.166E-07	6.271E-07	2.905E-06	100.21	100.15	100.00
θ_1	-2.008E-05	-1.973E-06	4.775E-07	1.423E-05	-1.971E-06	4.772E-07	1.423E-05	100.07	100.07	99.99
θ_2	2.568E-05	1.555E-06	-1.704E-06	-3.448E-06	1.553E-06	-1.703E-06	-3.451E-06	100.09	100.03	99.91
θ_3	8.208E-07	1.001E-07	3.547E-07	2.814E-06	1.001E-07	3.542E-07	2.814E-06	99.96	100.14	99.97

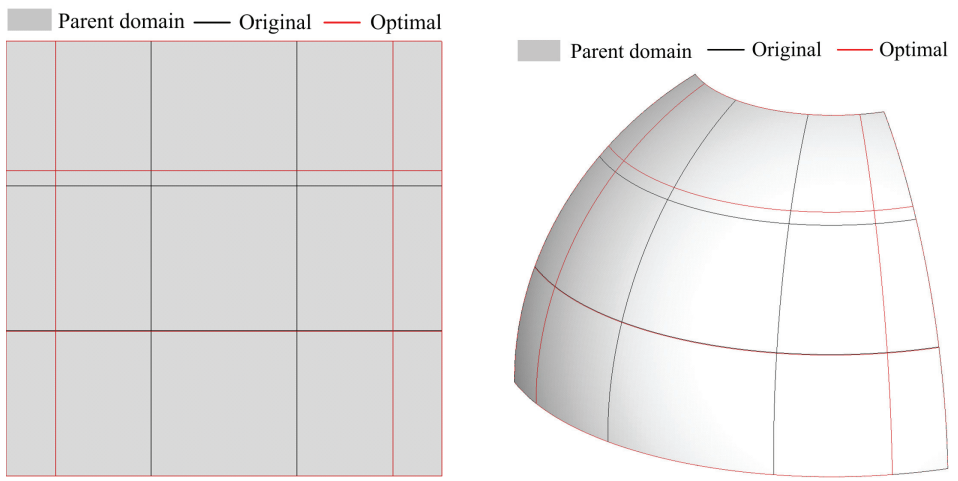

(a) Initial parent domain (b) Target parent domain

Figure 4.52: Optimal design

Design optimization

The developed design velocity computation scheme and DSA method are applied to solve a compliance minimization problem. The optimization problem can be stated as follows.

$$\text{Minimize } \psi \equiv \int_\Omega \mathbf{f}^T \mathbf{z} ds, \tag{4.18}$$

$$\text{subject to } V \equiv A \int_\Omega ds \leq V_f V_0, \tag{4.19}$$

and

$$d_i^{lower} \le d_i \le d_i^{upper}, \tag{4.20}$$

where V, V_0, and V_f are the current and initial volumes, and allowable volume fraction, respectively. The side constraints are selected as $d_i^{lower} = -0.8$ and $d_i^{upper} = 0.8$. In this example, the allowable volume fraction is selected as $V_f = 1$. Fig. 4.52 shows the optimal designs in initial and target parent domains. As shown in the optimization history of Fig. 4.53, the objective function monotonically decreases, and the volume is also decreased through the optimization. The volume constraint function plotted in Fig. 4.53b represents a normalized quantity of the volume constraint of Eq. (4.19), i.e., $V/V_f V_0 - 1$.

The determined design variable values are shown in Table 4.18, and all variables are within the feasible region of the side constraint. Fig. 4.54 compares the deformed configurations of the original and optimal designs where the deformation is 10^4 times exaggerated for visualization purpose and the contour represent Z-directional displacement. It is noticeable that the overall Z-directional deflection is significantly reduced after the optimization.

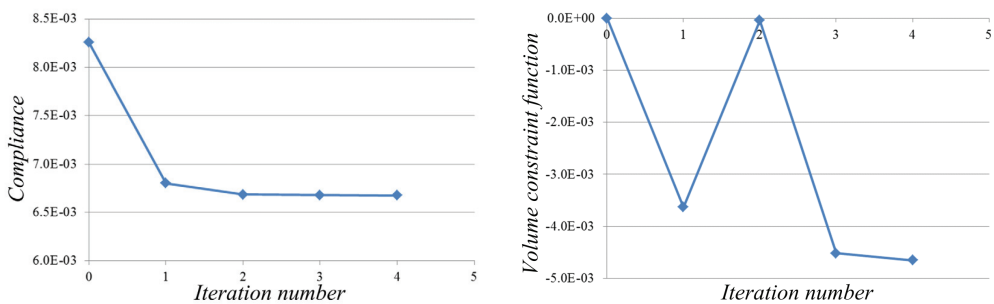

(a) Objective function (b) Volume constraint

Figure 4.53: Optimization history

Table 4.18: Design variables of optimum design

Design variable#	d_i
1	-4.6063E-03
2	1.0721E-01
3	6.6073E-01

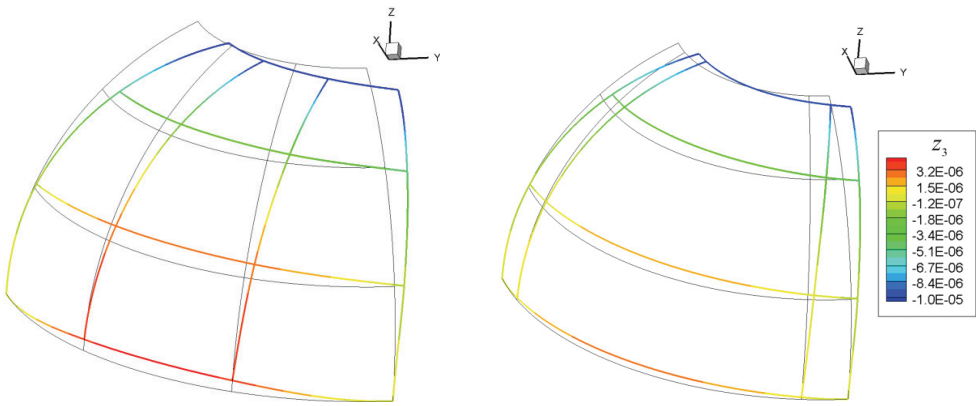

(a) Original design (b) Optimal design

Figure 4.54: Comparison of deformed configurations

4.5.2 Lattice structure on wavy surface

This example considers a target domain of more general shape than the previous one. Fig. 4.55a shows the initial parent domain and the embedded lattice structure which is modeled by 55 linear B-spline patches. Two cases of design parameterizations are considered; the first case in Fig. 4.55b includes 8 design variables of X- and Y-directional movement of the internal vertical and horizontal lines. The second case in Fig. 4.55c has 24 design variables with symmetric design variation about $Y = 1.5$ axis. Note that the design variables are defined in the initial parent domain.

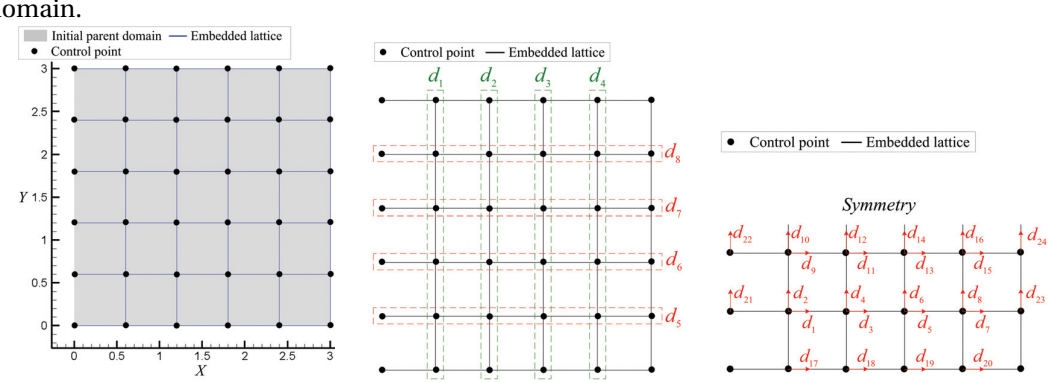

(a) Initial domain (b) Design variables (case#1) (c) Design variables (case#2)

Figure 4.55: Lattice structure in initial domain

Using the k-refinement, we construct a refined model of 10 uniform knot spans of cubic B-spline for each patch. The refined model is mapped into a target domain. The target parent domain is a wavy surface, as shown in Fig. 4.56a, which is constructed by the tensor product of four cubic B-spline boundary curves. Fig. 4.56b shows the embedded lattice structure obtained by the mapping F of the lattice structure in the initial domain of Fig. 4.55a, and depicts the kinematic boundary and force loading conditions. The blue-colored lines in Fig. 4.56b represents the embedded lattice

structure, and distributed force loading in Z-direction, $\bar{f}_z = -10N/m$, is applied at the free-end ($X = 6$) of the lattice structure.

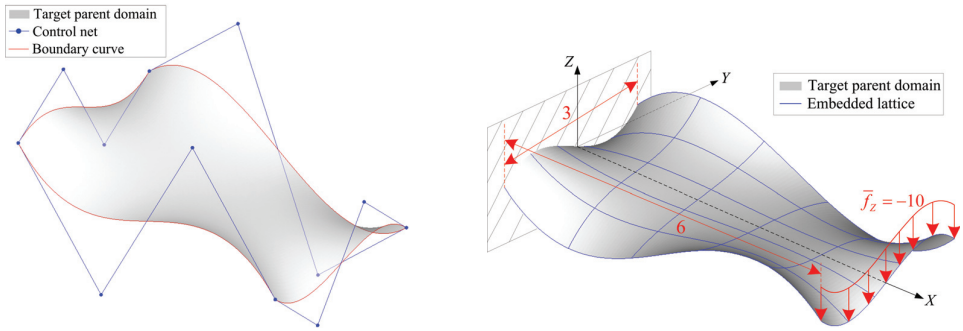

(a) Target parent domain (b) Problem description

Figure 4.56: Lattice structure on wavy domain

Verification of design sensitivity

The objective of this problem is to find the optimal configuration of lattice structure through compliance minimization. Prior to the design optimization, we verify the design sensitivity of compliance with respect to 8 design variables (case#1). Table 4.19 shows that the obtained analytical sensitivity agrees very well with finite differences. We can notice that as the perturbation amount decreases, the finite difference one approaches to the analytical one.

Table 4.19: Verification of design sensitivity of compliance

Design variable#(i)	Original response	Finite difference sensitivity $\delta = 10^{-3}$(a)	$\delta = 10^{-4}$(b)	Analytic sensitivity(c)	Agreement(%) (c)/(a)	(c)/(b)
1	7.7960E-03	-4.4523E-04	-4.4879E-04	-4.4919E-04	100.89	100.09
2		1.9328E-04	1.9151E-04	1.9132E-04	98.99	99.90
3		9.1262E-04	9.1293E-04	9.1297E-04	100.04	100.00
4		1.1686E-04	1.1697E-04	1.1700E-04	100.12	100.03
5		5.3626E-04	5.3585E-04	5.3579E-04	99.91	99.99
6		-2.9090E-04	-2.9166E-04	-2.9173E-04	100.29	100.03
7		2.9256E-04	2.9182E-04	2.9173E-04	99.72	99.97
8		-5.3532E-04	-5.3575E-04	-5.3579E-04	100.09	100.01

It is noticeable that the sensitivity for the design variables #5 and 6 have same magnitudes and opposite signs with those of design variables #8 and 7, respectively. It turns out that since the lattice structure in Fig. 4.56b has a point symmetry about X-axis, the symmetric design variation in each part of the symmetry results in the same change of responses.

Design optimization

The optimization problem formulation of Eqs. (4.18)-(4.20) is utilized. Side constraint is selected as $d_i^{lower} = -0.8$ and $d_i^{upper} = 0.8$. The allowable volume fraction is selected as $V_f = 1$. First, we

consider the design parametrization of case#1. Table 4.20 shows the determined design variables through the optimization, and all variables are within the side constraints. As previously observed in the design sensitivity values of Table 4.19, the determined design variable values have the same symmetry. The optimal designs of the initial and the target parent domains shown in Fig. 4.57 also have symmetry about $Y = 1.5$ and X axes, respectively. This comes from the fact that since the lattice structure in the target parent domain has a point symmetry about X axis with the opposite direction of force loading, each part of the symmetry has the same optimal design to minimize the structural compliance. In the design parametrization of case#2, to increase the degrees of freedom in design space, 24 design variables are selected as shown in Fig. 4.55c. Fig. 4.58 shows the optimal designs of the lattice structures in the initial and the target parent domains.

Table 4.20: Determined design variables (case#1)

i	Design variable(d_i)	i	Design variable(d_i)
1	-2.2309E-02	5	-1.0073E-01
2	-4.5068E-02	6	8.7217E-02
3	-4.9107E-01	7	-8.7217E-02
4	-9.7544E-02	8	1.0073E-01

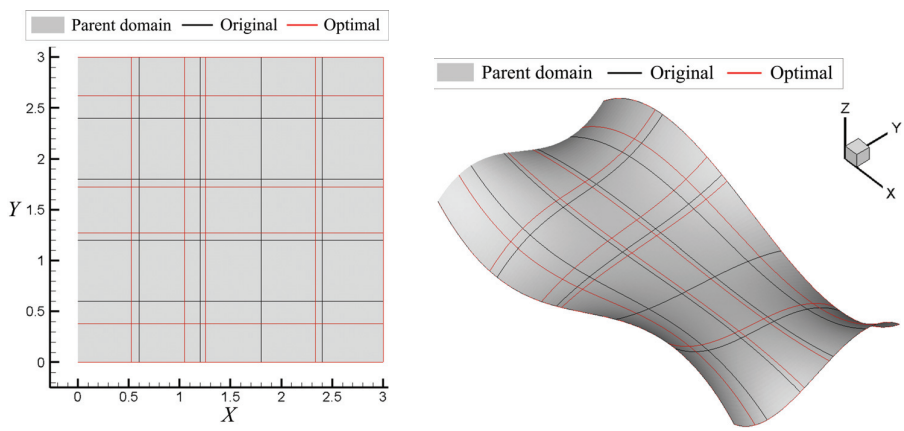

(a) Initial parent domain

(b) Target parent domain

Figure 4.57: Lattice on wavy surface: optimal design (case#1)

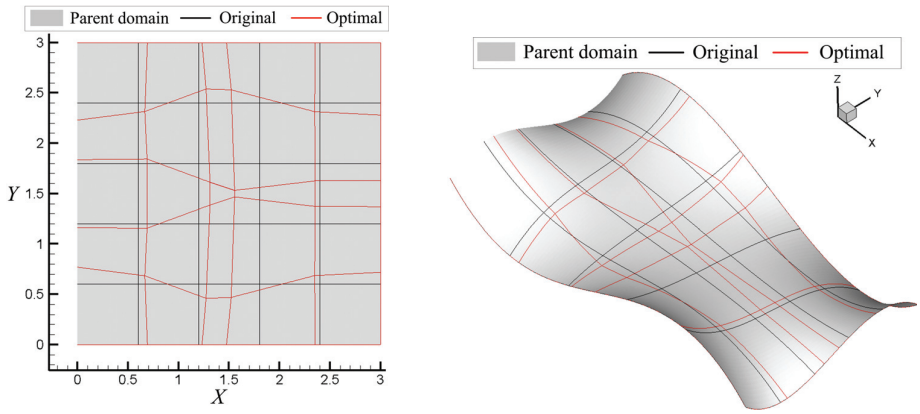

(a) Initial parent domain (b) Target parent domain

Figure 4.58: Lattice on wavy surface: optimal design (case#2)

Fig. 4.59 compares the deformed configurations for the original, and two optimal designs in case#1 and case#2. The deformation is 10^4 times exaggerated for visualization and the contour illustrates the Z-directional displacement. The improvement of overall stiffness as increasing the design degrees of freedom from case#1 to case#2 is apparent.

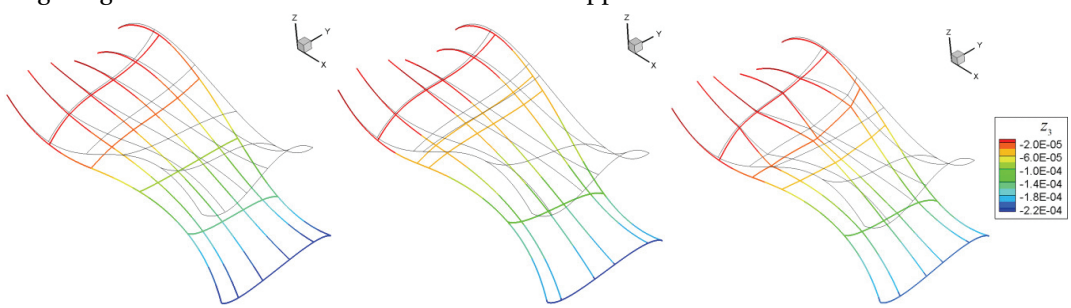

(a) Original design (b) Optimal design (case#1) (c) Optimal design (case#2)

Figure 4.59: Comparison of deformed configurations

Next, we investigate the modeling error in the analysis models constructed by the mapping F. As a spatially averaged value of the modeling error of Eq. (3.196), we define the following measure.

$$\varepsilon_{avg} = \frac{1}{L}\int_{\Omega} \varepsilon ds, \tag{4.21}$$

which is designated as "*average modeling error*", and L denotes the total length of the neutral axis of the beam structure. Fig. 4.60 shows the change of the average modeling error of Eq. (4.21) during the optimization process in the design parameterization case#1 and #2. p and N respectively denote the degree of basis function, and the total number of control point of beam structures. At the initial design, the lattice structure is well placed on the target domain. In the design parameterization of case#1, the modeling error of almost zero is maintained during the

optimization process. In the case#2, we test four different cases of mesh refinement level (p,N) to investigate that the modeling error can be effectively reduced by increasing the modeling degrees of freedom like the number of control points (h-refinement) or the degree of basis functions (p-refinement).

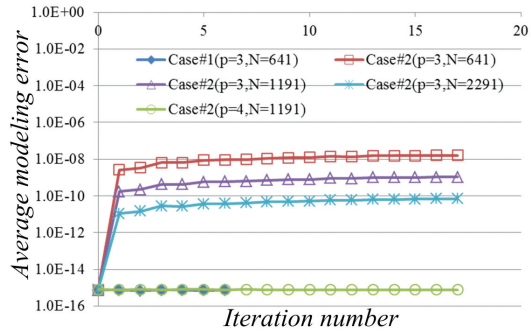

Figure 4.60: Comparison of average modeling errors

For the cubic B-spline models ($p = 3$) of the case#2, the modeling error drastically increases after design change occurs. However, the magnitude of error is still very low compared with the overall structural size, and it is noticeable that the h- and p-refinement reduces the average modeling error effectively. p-refinement is shown to be much more effective than the h-refinement. From these results, it is observed that the modeling error maintains at very low level during the optimization process, and importantly, this error can be significantly reduced by mesh refinement, especially by the p-refinement. Even though a small modeling error in the analysis model could persist during the optimization process, it is noted again that the design velocity field computed using the developed method is always consistent with the analysis model, *i.e.*, the design velocity field is always an exact differentiation of the analysis model configuration with respect to design variables.

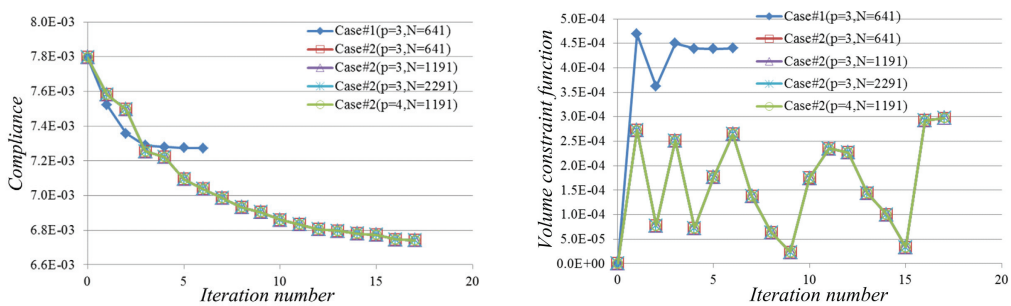

(a) Objective function

(b) Volume constraint

Figure 4.61: Comparison of optimization history

Fig. 4.61 shows the optimization history. In order to investigate the effect of modeling error on the optimization results, we perform design optimizations for the four cases of mesh refinement level (p,N) of the case#2. The reduction of compliance in case#2 is much bigger than that of case#1,

even though the case#2 optimal designs have less volume than that of case#1. Also, in the case #2, all the results of the mesh refinement levels (p,N) show almost same optimization histories. This indicates that the modeling error observed in Fig. 4.60 is too low to affect the design optimization results.

Table 4.21: Design variables in optimum design (case#2)

i	Design variable(d_i)		i	Design variable(d_i)	
	$p=3$, $n=641$	$p=4$, $n=1191$		$p=3$, $n=641$	$p=4$, $n=1191$
1	6.5100E-02	6.5079E-02	13	-2.4547E-01	-2.4549E-01
2	8.4605E-02	8.4608E-02	14	2.6758E-01	2.6758E-01
3	7.1816E-02	7.1810E-02	15	-4.9721E-02	-4.9723E-02
4	-1.3920E-01	-1.3920E-01	16	1.7342E-01	1.7342E-01
5	-2.7914E-01	-2.7915E-01	17	9.1081E-02	9.1051E-02
6	-1.3054E-01	-1.3055E-01	18	3.1596E-02	3.1592E-02
7	-5.1972E-02	-5.1975E-02	19	-3.2550E-01	-3.2552E-01
8	8.6402E-02	8.6402E-02	20	-5.0153E-02	-5.0156E-02
9	8.7742E-02	8.7722E-02	21	1.6985E-01	1.6985E-01
10	-4.3787E-02	-4.3790E-02	22	-3.7316E-02	-3.7313E-02
11	1.1097E-01	1.1097E-01	23	1.1942E-01	1.1942E-01
12	1.8683E-01	1.8683E-01	24	1.7050E-01	1.7050E-01

Table 4.21 shows the determined design variable values. All variables are within the side constraints. Comparing the two cases of mesh refinement (p,N)=(3,641) and (4,1191), the determined design variable values of the two cases are almost same, which confirms again that the effect of the modeling error, shown in Fig. 4.60, on the design optimization results is negligible.

4.5.3 Lattice structure on non-smooth surface

In this example, we consider a non-smooth target parent domain to discuss how to treat local non-smoothness of the lattice structure and study the effect of modeling error on the accuracy of optimal design. Fig. 4.62 explains the modeling of the considered non-smooth target surface. A cubic B-spline surface (middle) is constructed by using the boundary curves obtained by translating or rotating the green-colored cubic B-spline curve (left). The side and top views of the target surface are also illustrated (right). The red-colored lines indicated in Fig. 4.62 (middle and right) are the reference lines of the mirror symmetry within the target surface. Also, the surface is non-smooth (C^0-continuity) in the direction across the red-colored lines due to repeated knots, and in the other areas, it has C^2-continuity at the knots.

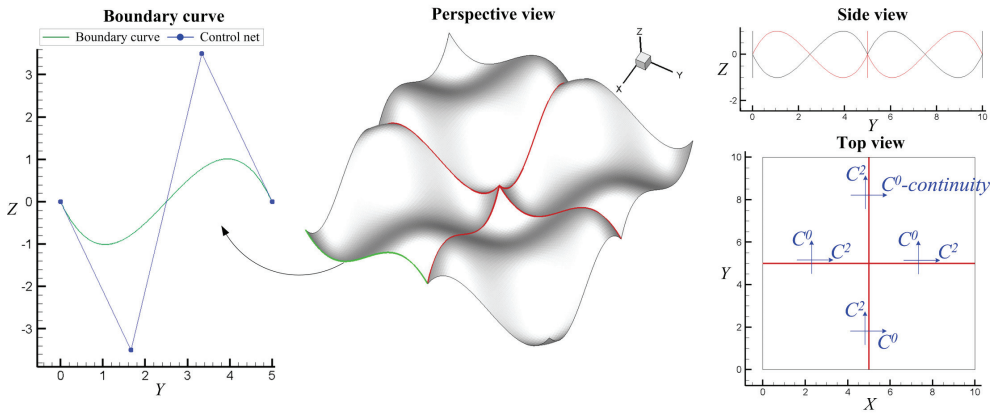

Figure 4.62: Modeling of a non-smooth target surface

Fig. 4.63a shows the embedded lattice structure in the initial parent domain, where the bold blue lines indicate lattice members lying across the non-smooth regions indicated in Fig. 4.62. To reduce the modeling error, it is desirable for the lattices to express the cusp points exactly. Thus, we compare two cases of modeling the lattice members across the non-smooth regions; *First*, a single patch modeling having C^2-continuity. *Second*, two patch modeling which incorporates the C^0-continuity at desired cusp point positions. Fig. 4.63b and 4.63c respectively show the modeling and design parameterization of the cases #1 and #2. In both cases, the design parameterizations are the same as 12 design variables of X- and Y-directional movement of the internal vertical and horizontal lines. We first construct the geometry using the linear B-spline, and each lattice member is modeled using a single element, so that it should be clear, from the illustration of the control points in Figs. 4.63b and 4.63c, that the lattice members across the non-smooth regions are modeled using single and two patches in the case #1 and #2, respectively.

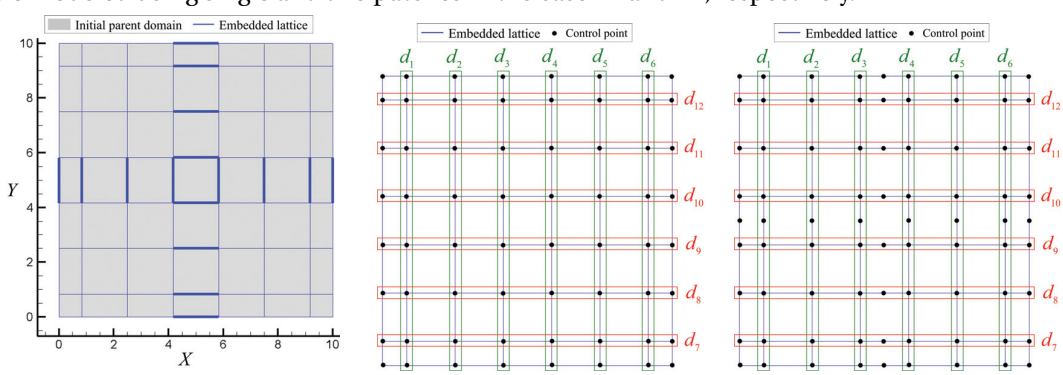

(a) Initial domain (b) Case#1 (c) Case#2

Figure 4.63: Two cases of modeling embedded lattice structure

In both cases, refined models of quartic B-spline are constructed using the k-refinement. In the refined model, each lattice member consists of 10 uniform knot spans of quartic B-spline. The refined models are mapped into the target domain of Fig. 4.62. Fig. 4.64 depicts the lattice

structure mapped into the target parent domain and the kinematic boundary conditions and force loading condition. The blue-colored line represents the lattice structure. Four vertices of the lattice structure are fixed, and all lattice members are loaded by the Z-directional distributed force, $\bar{f}_z = -1N/m$.

Fig. 4.64b and 4.64c plot the modeling error of Eq. (3.196), *i.e.*, the deviation of lattice structure position from the target parent domain. As the case #1 expresses the cusp points with smooth curves, large modeling error occurs in the vicinity of the non-smooth regions. On the contrary, the case #2 is able to exactly express the cusp points by the patch division, so that the modeling error is nearly zero.

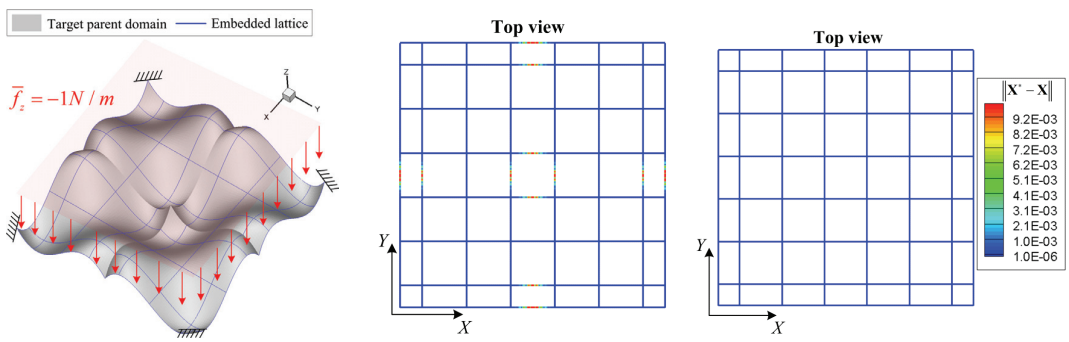

(a) Problem description (b) Modeling error (case#1) (c) Modeling error (case#2)

Figure 4.64: Two cases of modeling embedded lattice structure

Design optimization

The optimization problem formulation of Eqs. (4.18)-(4.20) is utilized. The allowable volume fraction is selected as $V_f = 0.95$, and the side constraint is selected as $d_i^{lower} = -2$ and $d_i^{upper} = 2$. Table 4.22 compares the modeling error, compliance, and volume of the lattice structure in original and optimal designs of using the modeling cases #1 and #2. In order to investigate the effect of modeling error on the optimal design solution, in the case #1, the lattice members across the non-smooth regions (bold lines in Fig. 4.63a) are locally h-refined. N denotes the total number of control points in the lattice structure. As shown in Table 4.22, large modeling error occurs in the case#1, compared with the case#2 which has nearly zero modeling error. However, it is noticeable that the compliance and volume of the case#1 monotonically approaches to that of the case#2 as the modeling error decreases by the local h-refinement.

Table 4.22: Comparison of two cases of modeling non-smooth parts

	N	Modeling error		Compliance		Volume	
		Original	Optimal	Original	Optimal	Original	Optimal
Case#1	1408	7.8197E-04	4.9062E-03	9.3687E-03	6.5398E-03	1.4992E+00	1.4246E+00
	1568	2.1051E-04	1.3183E-03	9.4362E-03	6.9556E-03	1.5035E+00	1.4285E+00
	1888	5.4376E-05	3.5047E-04	9.4708E-03	7.1885E-03	1.5057E+00	1.4306E+00
	2528	1.3825E-05	9.0661E-05	9.4879E-03	7.3160E-03	1.5068E+00	1.4316E+00
	3808	3.4860E-06	2.3138E-05	9.4964E-03	7.3647E-03	1.5073E+00	1.4324E+00
Case#2	1616	2.0283E-15	1.9812E-15	9.5048E-03	7.4325E-03	1.5079E+00	1.4327E+00

Figs. 4.65a and 4.65b compare the original and optimal designs of case#2 at initial and target parent domains, respectively. The optimal design has the same symmetry with the original design, due to the symmetry of the target parent domain.

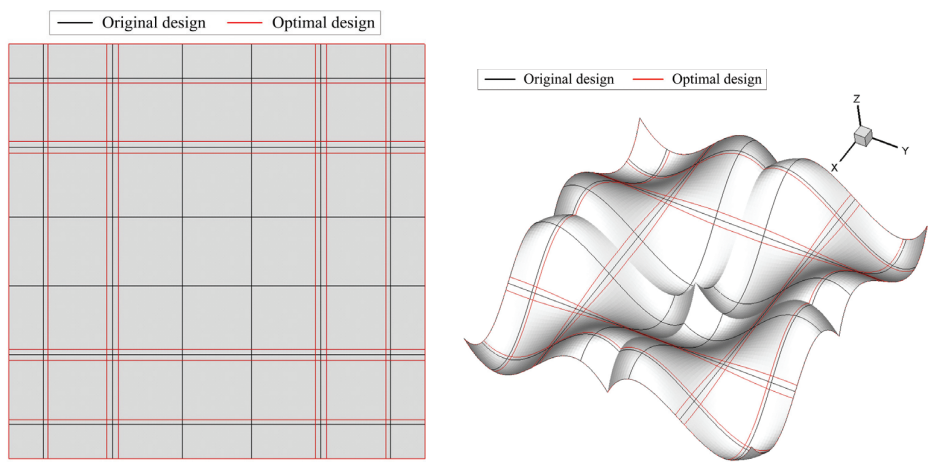

(a) Initial domain (b) Target domain

Figure 4.65: Optimal design

Fig. 4.66 shows the optimization history in the case #2. As the allowable volume fraction is selected as $V_f = 0.95$, the original design is located at infeasible region of the volume constraint, and the design change occurs in the direction to feasible region of the volume constraint at the first iteration. Meanwhile, the objective function (compliance) slightly increases. Then, as the optimization proceeds, the objective function monotonically decreases, and the volume constraint becomes to be active.

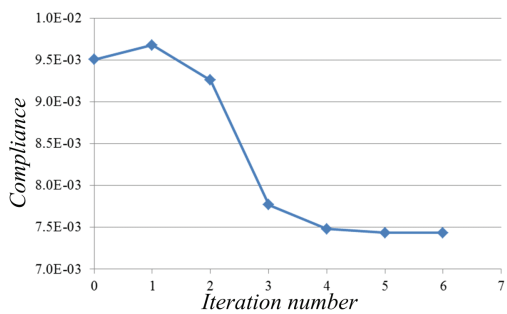

(a) Objective function

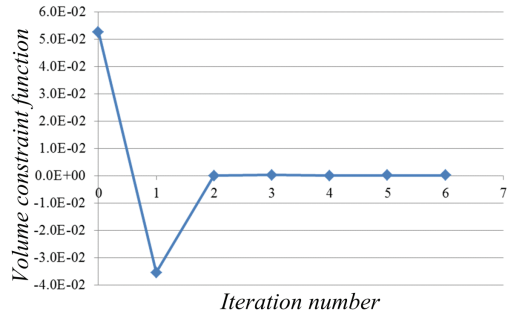

(b) Volume constraint

Figure 4.66: Optimization history

Table 4.23 shows the determined design variable values through the optimization (case#2). Due to the symmetry of the target parent domain and the original design of the lattice structure, the design variable values are also determined symmetrically, that is, the optimal design also has the same symmetry with the original design and the target parent domain.

Table 4.23: Determined design variables (case#2)

i	Design variable(d_i)	i	Design variable(d_i)
1	1.0247E-01	7	1.0247E-01
2	-1.4514E-01	8	-1.4514E-01
3	-1.5345E+00	9	-1.5345E+00
4	1.5345E+00	10	1.5345E+00
5	1.4514E-01	11	1.4514E-01
6	-1.0247E-01	12	-1.0247E-01

4.6 Lattice structures having extremal negative Poisson's ratio

We present systematic synthesis of lattice structures using a gradient-based mathematical optimization method to achieve constant negative Poisson's ratio lower than -1 in both of large tensile and compressive deformations. A proposed design achieves negative Poisson's ratio -2 nearly constant within 10% of the applied tensile strain range and about 4% of applied compressive strain range, which are successfully verified by experiments. The first case optimal design having internal rotational symmetry within the unit cell cannot exceed the stability limit of isotropic material -1; however, the other two designs successfully attain the target Poisson's ratio -1.5 and -2 in large deformation ranges. Our experimental verification employs 3-D printing technology to fabricate the optima designs, and optical deformation measurements to obtain displacement fields of lateral expansion or contraction, which is shown to quantitatively agrees significantly well with the simulation results. This work paves the way to systematically design lattice structures with extremal negative Poisson's ratios using the mathematical optimization method. Our future extension includes to architect three-dimensional lattice structures and their

experimental verifications.

4.6.1 Two-dimensional structures with experimental verifications

We consider two-dimensional structures undergoing in-plane deformations. Two kinds of design parameterizations are used: first, rotational symmetry of 90° within the unit cell, and second, no such a rotational symmetry. In order to obtain optimal design in both of uniaxial tension and compression, a multi-step design optimization with loading direction altered step by step is performed. Detailed model description of the original design and design parameterization are explained in section 3.1. Figure 4.67 shows the optimal design for the target negative Poisson's ratio $\nu_{21}^{*} = -1.2$. Compared with the original design of Figure 4.76, more rounded shape than the original one is obtained, and the ligaments near the junctions become thicker, which enables almost rigid-like rotational deformation near the junctions. Also, the other ligament region becomes thinner, so that it reduces stiffness and makes deformation large to ehance the rotation of ligaments around the junction. However, even though the unit cell design is desired to have target Poisson's ratio -1.2, the optimal design does not exceed the value $\nu_{21} = -1$ in both of tension and compression due to the stability limit induced by the rotational symmetry. It will be shown that if we reduce the internal symmetry, the Poisson's ratio can be lower than -1 in a specific direction. Figure 4.68a and 4.68b respectively show the optimal designs that successfully attained the target Poisson's ratio $\nu_{21}^{*} = -1.5$ and $\nu_{21}^{*} = -2$.
For convenience, the three optimal designs are designated as "case #1" for the design of $\nu_{21}^{*} = -1.2$ (Figure 4.67), "case #2" for the design of $\nu_{21}^{*} = -1.5$, and "case #3" for the design of $\nu_{21}^{*} = -2$. Optimal design models are fabricated by using the 3-D printing technology, and experimental verifications are performed through uniaxial tension and compression tests. Figure 4.69 shows the change of Poisson's ratio during tensile deformations by applied nominal strain 10%, and Figure 4.69a and 4.69b respectively plot secant and tangent Poisson's ratios. In the simulations, we measure the Poisson's ratio at every load step in total 10 load increments. In experiments, we acquire total 400 and 160 deformation images with uniform frame rate, respectively, for uniaxial tension and compression. From these result, the following two novel points are verified. First, the optimal designs of anisotropic structures obtained by mathematical optimization successfully attained target Poisson's ratio lower than -1 during large deformations, and also, the case #1 design attains the Poisson's ratio -1. Second, numerically predicted performances of these simulation-based designs show significantly well agreements with the experimental results. In the experimental results, the secant Poisson's ratio graph shows much less oscillations than that of tangent Poisson's ratio, since it uses the undeformed state as a reference configuration. Although the tangent Poisson's ratio inevitably contains moderate level of measurement noises, the overall structural behaviors have well agreement with those of simulation results. For each of three design cases, we perform five uniaxial tension experiments with a single specimen. In Figure 4.71a and Figure 4.72a, the solid line indicates the average value of the five experiments and the error bar indicates the standard deviation. It is noticeable that the standard deviation is significantly small in the secant Poisson's ratio, which means that a specimen shows a nearly elastic behavior

within the considered deformation range. The tangent Poisson's ratio shows larger oscillations than the secant cases due to measurement noise.

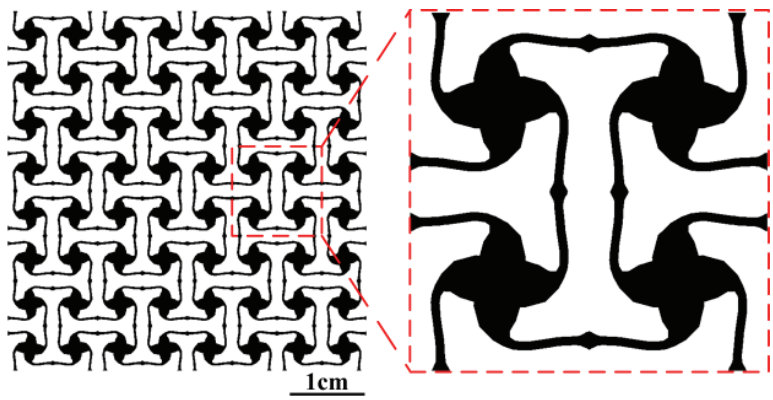

Figure 4.67: A two-dimensional structure with Poisson's ratio $\nu_{21} = -1$ (case #1)

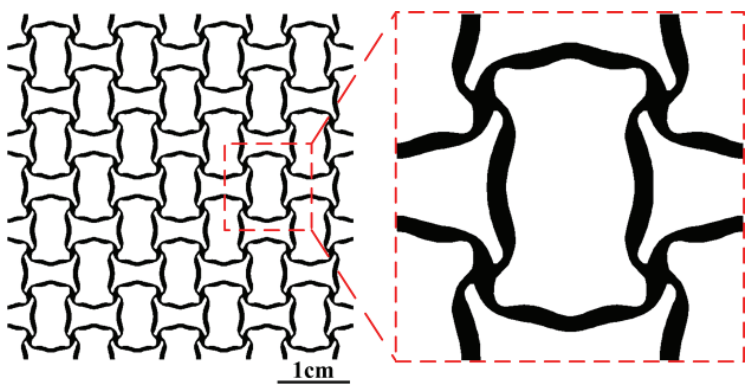

(a) $\nu_{21} = -1.5$ (case #2)

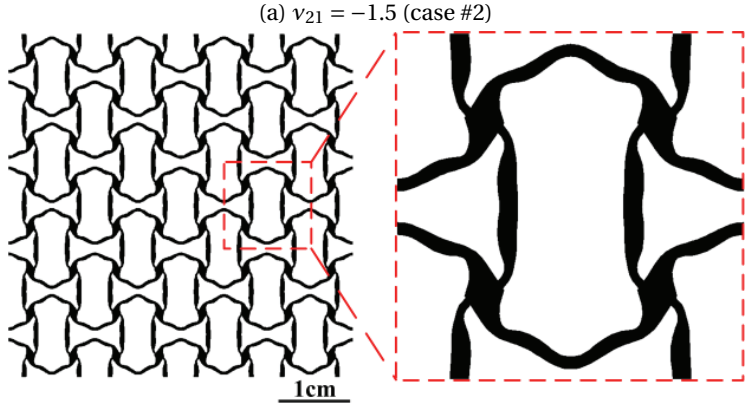

(b) $\nu_{21} = -2$ (case #3)

Figure 4.68: Two-dimensional structures with Poisson's ratio

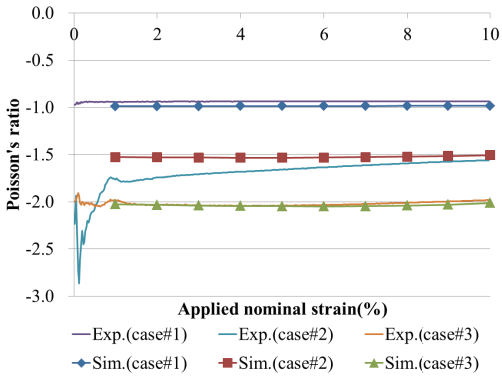

(a) Secant Poisson's ratio

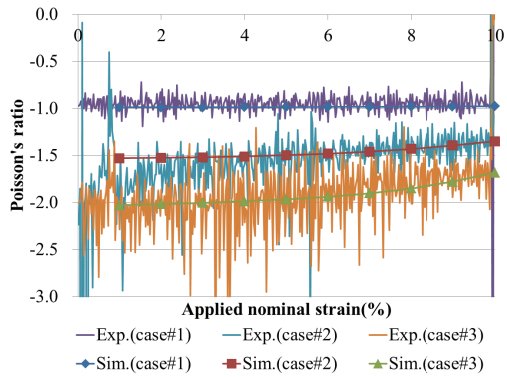

(b) Tangent Poisson's ratio

Figure 4.69: Comparison of simulation and experimental results in tension

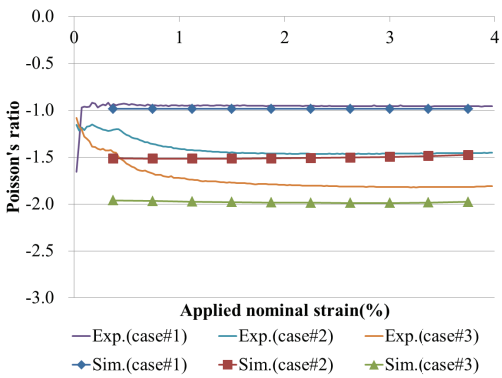

(a) Secant Poisson's ratio

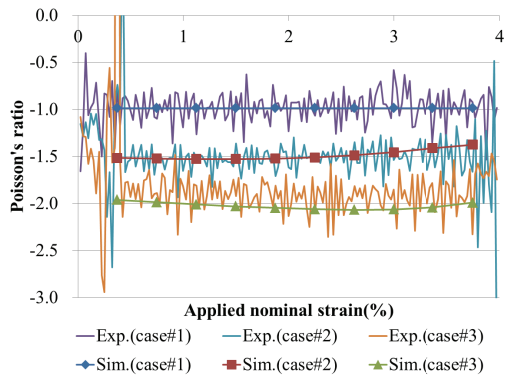

(b) Tangent Poisson's ratio

Figure 4.70: Comparison of simulation and experimental results in compression

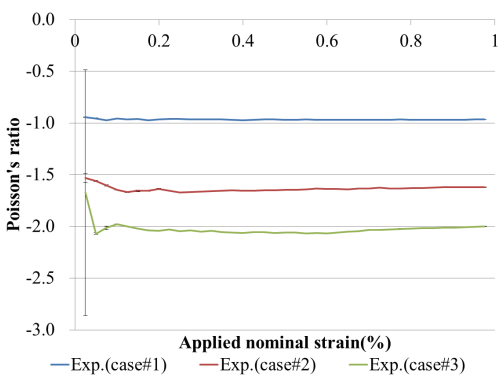

(a) Secant Poisson's ratio

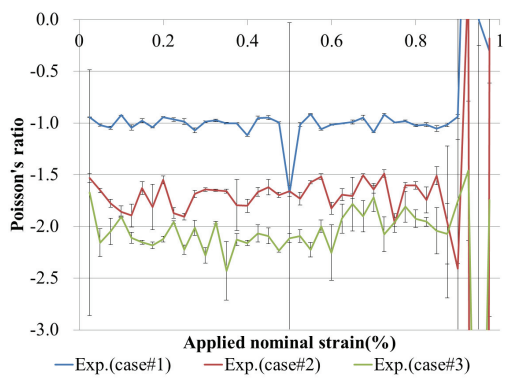

(b) Tangent Poisson's ratio

Figure 4.71: Experimental results in tension due to 1% strain

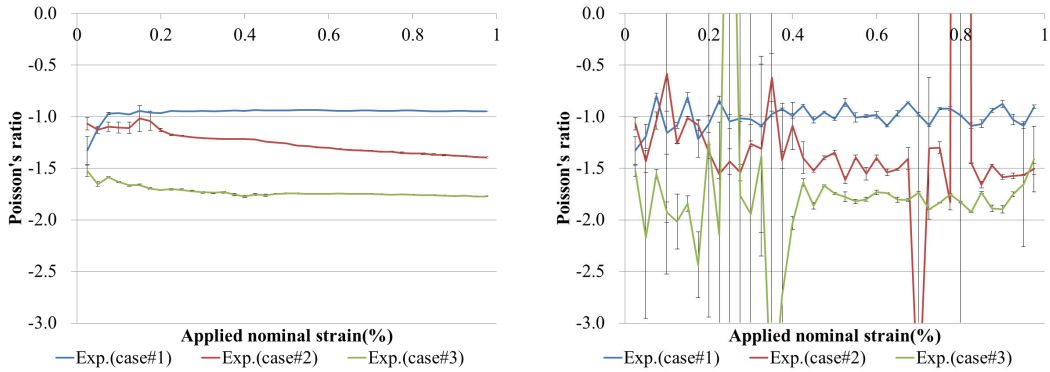

(a) Secant Poisson's ratio

(b) Tangent Poisson's ratio

Figure 4.72: Experimental results in compression due to 1% strain

Optimization problem

An optimization problem to attain target Poisson's ratio can be stated as: find the design variable $\mathbf{d} = \{d_i\}$ such that

$$\text{Maximize } \psi \equiv \sum_{i=1}^{NL} \left| \nu_{21}^{\tan}(\mathbf{d}; \varepsilon_i) - \nu_{21}^{*} \right|^2, \tag{4.22}$$

$$\text{subjectto } g_k(\mathbf{d}) = \frac{1}{L_k} \int_{\Omega_k} \left(\kappa^2 / {\kappa_U}^2 - 1 \right) ds < 0, \; k = 1 \sim ne, \tag{4.23}$$

$$D_{mn} \equiv \left\| \mathbf{X}_i^m - \mathbf{X}_j^n \right\| > D_{mn}^0, \;\; i, j = 1 \sim n_d, \tag{4.24}$$

and

$$d_i^{lower} \le d_i \le d_i^{upper}. \tag{4.25}$$

where the constraint of Eq. (4.23) limits maximum curvature of ligaments to avoid self-intersections, and ne denotes the total number of knot spans, and Ω_k and L_k denotes a curve segment corresponding to the k-th knot span and its initial length. κ_U denotes a given maximum curvature value. The constraint of Eq. (4.24) imposes minimum distance between selected n_d pairs of discrete points to avoid overlapped design, and D_{mn} defines the set of distance magnitudes of all possible discrete point pairs. D_{mn}^0 denotes a given minimum distance value.

Model description

We consider a square honeycomb structure as an original design in which a slight perturbation, as illustrated in Fig. 4.73a, is introduced to implement eccentric load on the ligaments around junctions. A square cross-section with uniform thickness 1mm is selected, and two different cross-section widths are employed as 3mm and 30mm for the tensile and compressive

load cases, where the compression model has 10 times larger width to avoid out-of-plane deformations during experiments. A periodic boundary condition is employed to describe an infinite arrangement of unit cell structure, following the work of Wang et al. [107]. On the left and right sides, periodic boundary conditions are imposed to the vertical displacements as $v_1 = v_{01}$, and a constant horizontal displacement difference, u, is assumed as $u_1 - u_{01} = u$. Similarly, on the lower and upper sides, periodic boundary conditions are imposed to the horizontal displacements as $u_2 = u_{02}$, and a constant vertical displacement difference, v, is assumed as $v_2 - v_{02} = v$. As we focus on the Poisson's ratio ν_{21} by a horizontal displacement due to a vertical load, the following boundary conditions are used.

$$u_{01} = 0, \;\; v_1 = v_{01}, \text{ and } \mathrm{u}_1 \text{ is free}, \tag{4.26}$$

and

$$u_2 = u_{02}, \;\; v_{02} = 0, \text{ and } \mathrm{v}_2 \text{ is prescribed}. \tag{4.27}$$

For two-dimensional structures, the tangent Poisson's ratio is calculated by using the previous equilibrium configuration as a reference configuration as

$$\nu_{21}^{\tan} \equiv -\frac{\varepsilon_X}{\varepsilon_Y} = -\frac{(u^c - u_0^c)/X_0^c}{(v^c - v_0^c)/Y_0^c}. \tag{4.28}$$

where u^c and v^c respectively denote the current X- and Y-displacements at the center of unit cell, obtained by averaging X- and Y-displacements at the four junctions, and u_0^c and v_0^c denote the displacements at the reference configuration. X_0^c and Y_0^c respectively denote the X- and Y-coordinates of unit cell center at the reference configuration. ε_X and ε_Y defines the X- and Y-directional nominal strains. For a secant Poisson's ratio, the reference unit cell is selected as undeformed one where $X_0^c = Y_0^c = 6mm$ and $u_0^c = v_0^c = 0$; therefore, we have

$$\nu_{21}^{\sec} \equiv -\frac{u^c}{v^c}. \tag{4.29}$$

In our optimization, we pursue to atttain target tangent Poissons ratio, and the design sensitivity of the tangent Poisson's ratio is derived as

$$\dot{\nu}_{21} = -\left\{\frac{\dot{u}^c}{v^c - v_0^c}\left(\frac{Y_0^c}{X_0^c}\right) + \nu_{21}\frac{\dot{v}^c}{v^c - v_0^c}\right\} + \left\{\frac{\dot{u}_0^c}{v^c - v_0^c}\left(\frac{Y_0^c}{X_0^c}\right) + \nu_{21}\frac{\dot{v}_0^c}{v^c - v_0^c}\right\} + \nu_{21}\left(\frac{\dot{v}_0^c}{Y_0^c} - \frac{\dot{u}_0^c}{X_0^c}\right), \tag{4.30}$$

where it is assumed that the initial unit cell center position does not has design dependence due to symmetric design variations, so that $\dot{X}_0^c = \dot{u}_0^c$ and $\dot{Y}_0^c = \dot{v}_0^c$. The displacement sensitivities $\dot{u}^c$ and $\dot{v}^c$ are calculated by the adjoint DSA method presented in section 3.2, and the previous (reference) center displacement sensitivities $\dot{u}_0^c$, $\dot{v}_0^c$ are kept and utilized at the next equilibrium configuration.

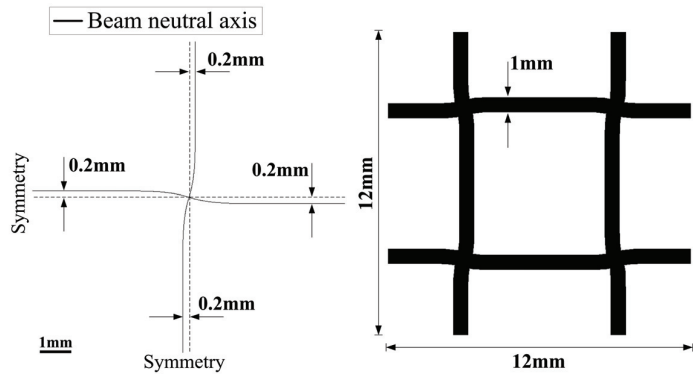

(a) Neutral axis (b) Unit cell dimension

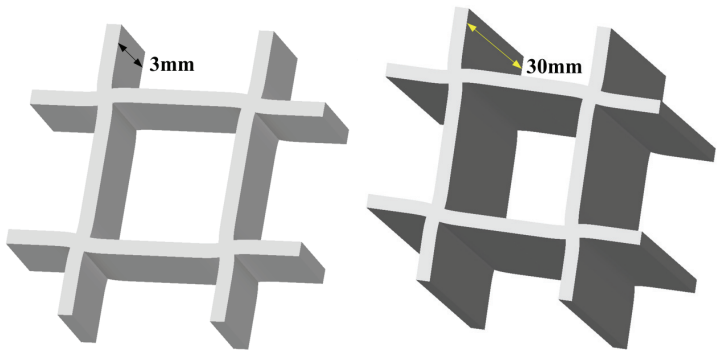

(c) Unit cell(tension case) (d) Unit cell(compression case)

Figure 4.73: Model description

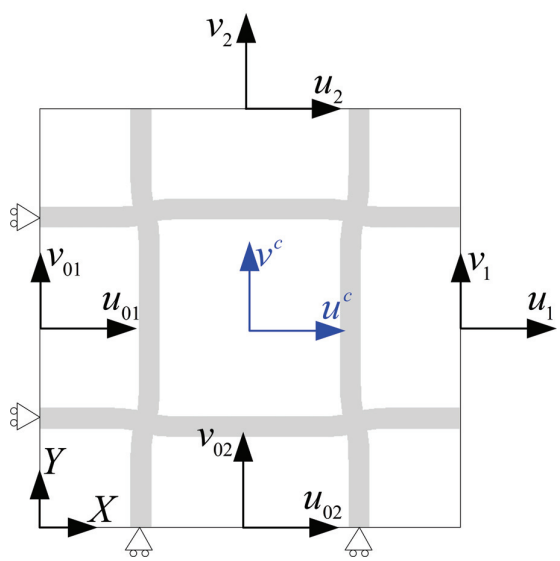

Figure 4.74: Illustration of boundary conditions for the two-dimensional structure

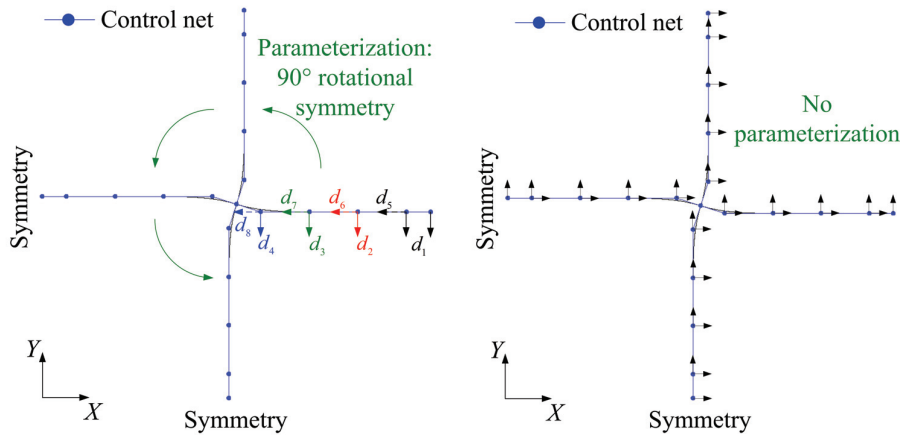

(a) 8 configuration design variables (b) 32 configuration design variables

Figure 4.75: Parameterization of configuration design

Design parameterization

Design variables are selected in the quarter part of the unit cell, and the other parts are symmetrically determined. Two cases of design parameterizations are considered. The first case has 8 configuration design variables selected as shown in Figure 4.75a and 20 thickness control coefficients in a single ligament, and the designs of other three ligaments are determined by the rotational symmetry. The second case has no rotational symmetry, and 32 configuration design variables are employed, and 20 thickness control coefficients in each of the four ligaments. X- and Y-directional movements of control points are selected as configuration design variables. In both cases of parameterizations, normal directional design perturbations of the last and second last control points are parameterized to preserve G^1-continuity at junctions. It is noted that, the optimization "case #1" uses the first design parameterization having rotational symmetry and 8 configuration design variables, and the optimizations "case #2" and "case #3" use the second case of design parameterization having 32 configuration design variables.

Experiments

Fabrication and material test Objet 260 connex3 3-D multi-material printer is utilized to fabricate the structures. This machine is based on the PolyJet printing technology and has a resolution of 600dpi (dots per inch), 600dpi, and 1600dpi in X-, Y-, and Z-directions, respectively. The material composition of VeroWhite and TangoBlack using the grey60 mode is selected. Uniaxial tensile and compression tests are performed using the universal testing machine (Instron 5800) in order to measure the bulk material properties. The Young's modulus is measured as 848.3MPa, an average value of the 6 uniaxial tension tests of the dog-bone specimens with the strain rate 10^{-2}s^{-1} whose results are plotted in Figure 4.76b. Poisson's ratio is calculated from the

lateral contraction (ΔW) due to tension (ΔH) as

$$\nu = -\frac{\Delta W / W_0}{\Delta H / H_0}. \tag{4.31}$$

where the initial dimension of the specimen is H_0 = 80mm and W_0 = 16mm. The specimens are sprayed with randomly distributed marks, and the lateral contraction is measured by the optical deformation measuring system (ARAMIS) in a way that the movements of the black dots are traced within a specified region, and then the deformation can be obtained by comparing the photo taken at any moment with the photo taken at the beginning of the tensile test. We performed 6 uniaxial tension experiments whose result is plotted in Figure 4.76c where the solid line indicates the average Poisson's ratio, and error bar represents standard deviation. At the initial stage of experiment, measurement noise deteriorates experimental results, so that we take an average within a section having nearly constant Poisson's ratio, and finally we determine the bulk material Poisson's ratio as 0.3458.

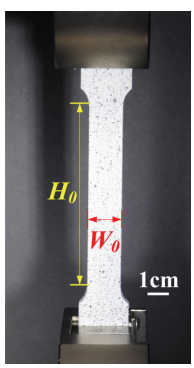

(a) Experiments

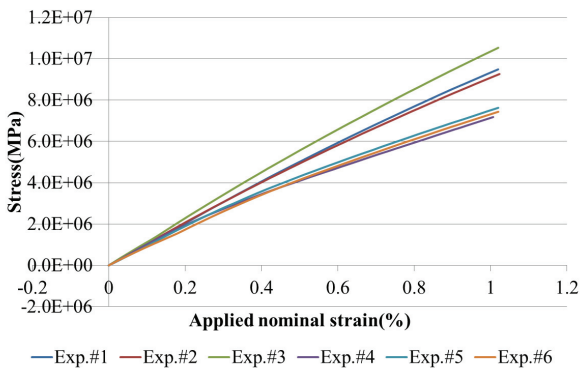

(b) Measured strain-stress relation

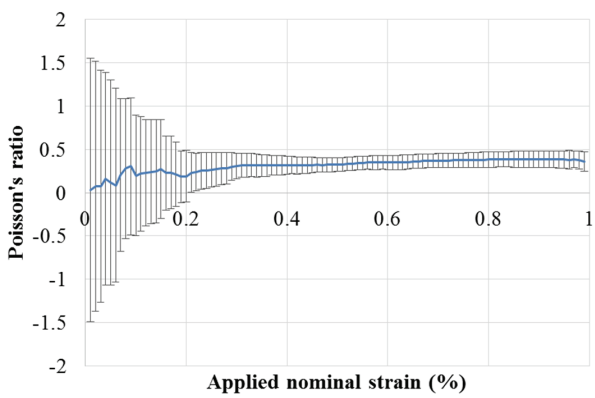

(c) Measured Poisson's ratio

Figure 4.76: Uniaxial tension test of bulk material

Optical deformation measurements Figures 4.77a and 4.77b shows the uniaxial tension and compression experiments. In order to avoid the boundary effects, we focus on the behavior of eight unit cells in the central part of the specimens, as indicated by block dots in Figure 4.77c. The quasi-static uniaxial tension and compression tests are performed, in which the applied nominal strain rate is respectively $2.5 \times 10^{-3}\text{s}^{-1}$ and $6.25 \times 10^{-3}\text{s}^{-1}$. An optical deformation measuring system (ARAMIS) enables a non-contact and material independent measurement by using a digital high resolution OCD camera (5mega pixel). For optical measurements, the specimens are marked by black dots whose coordinates are traced, and then used to calculate the displacement field by the internal Digital Image Correlation (DIC) program. Detailed expression of the Poisson's ratio calculation from the hole center displacement can be found in Appendix F.1.

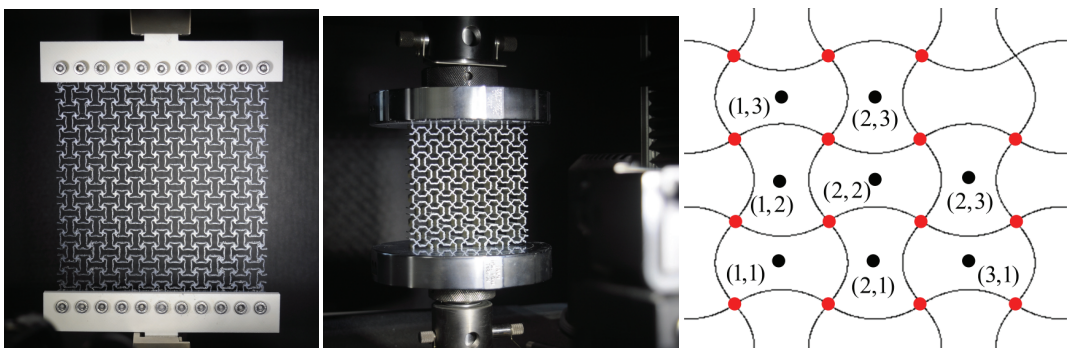

(a) Uniaxial tension (b) Uniaxial compression (c) Selected eight holes

Figure 4.77: Experimental verifications

Figure 4.78 and Figure 4.79 respectively compare the X-displacement fields obtained by simulations and experiments. In the tensile and compressive load cases, 9×18 and 8×8 arrays of unit cells are respectively used, and rectangular plates with identical material composition are attached. The lateral expansion and contraction due to loadings are apparent in tensile and compressive loadings, respectively. Above all, the agreement of X-displacement plots between the simulation and experiment results is noticeable. In tensile load cases, 10% nominal strain is applied. In compressive load case, the structures undergo elastic instability, *i.e.*, buckling, so that we apply smaller loads. In the case #1 and #3, we verify the X-displacement field at the 3.75% applied nominal strain, and the case #2 design is verified at the 2.675% applied nominal strain.
Figure 4.80 shows the history of objective functions in the three cases of design optimization. As we alter loading conditions of tension and compression step by step, some abrupt changes between adjacent optimization steps are observed. Total four steps of design optimizations are performed in each design case. Monotonic convergences of objective function are observed within each optimization step except a slight increase in the step #1 of case #3 due to initial distance constraint violation at several points. The final optimal designs of all the design cases show sufficiently reduced deviations of Poisson's ratios from the target ones, as verified in Figure 4.69 and 4.70.

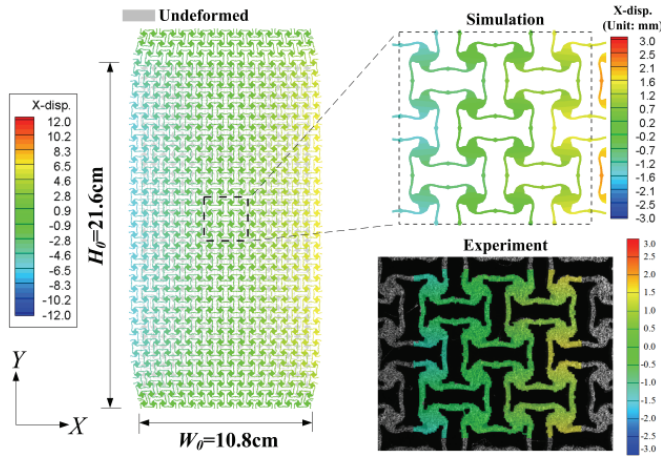

(a) case #1 model (10% tension)

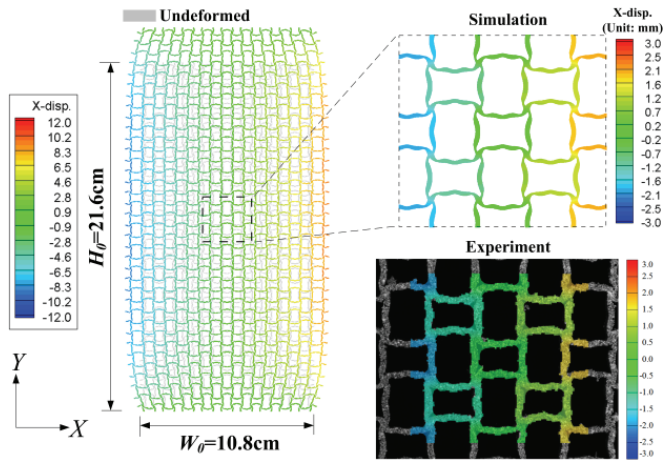

(b) case #2 model (10% tension)

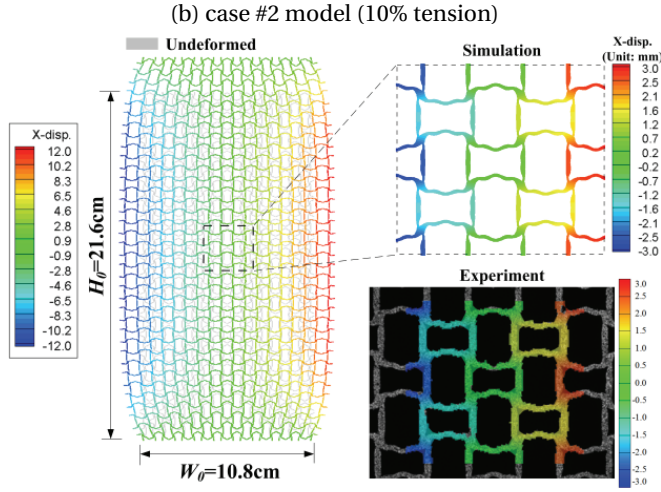

(c) case #3 model (10% tension)

Figure 4.78: Experimental verification of displacement field in tension

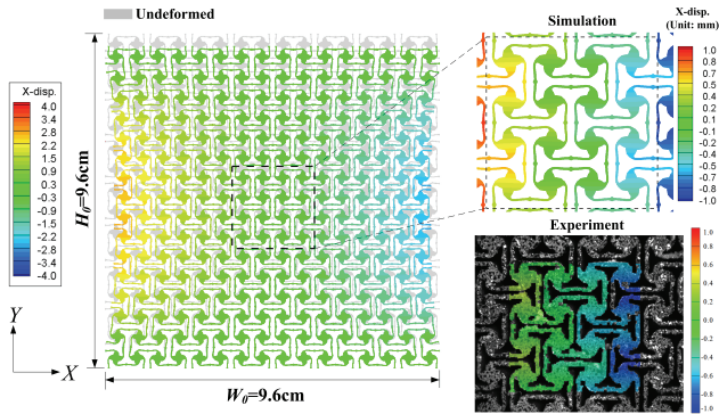

(a) case #1 model (3.75% compression)

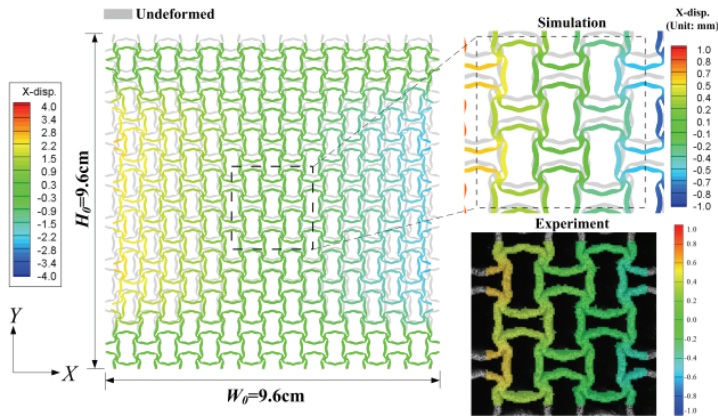

(b) case #2 model (2.625% compression)

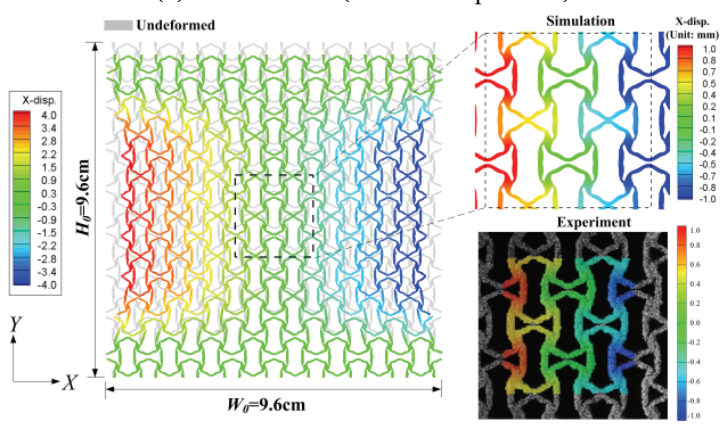

(c) case #3 model (3.75% compression)

Figure 4.79: Experimental verification of displacement field in compression

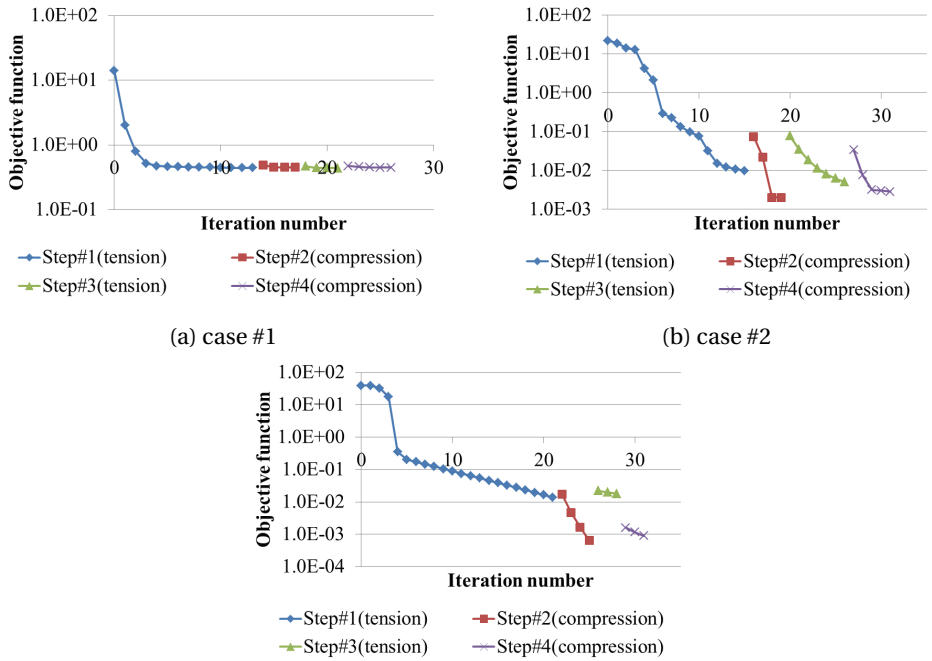

(a) case #1

(b) case #2

(c) case #3

Figure 4.80: History of objective function during multi-step optimization

4.6.2 Three-dimensional structures

We architect three-dimensional auxetic structures having extremal negative Poissn's ratio. We consider two cases of design paramterizations; case A and B. In both design cases, the same bulk material parameters are used as in the previous two-dimensional design case, and the same periodic boundary condition as employed in the example of section 4.3.4. is applied to unit cell of each cases.

Design case A

The case A design has the same 8 configuration design variables as in the example of section 4.3.4, which is detailed in Appendix F.2.1. 20 thickness design variables are additionally employed. Fig. 4.81 describes the case A original design, and it has a circular cross-section with diameter $1.5mm$ and overall dimension $20 \times 20 \times 20(mm)$. The same design optimization formulation is used as in the example of section 4.3.4, and the target Poisson's ratio is selected as $\nu_{31}^* = \nu_{32}^* = -0.5$, and tensile and compressive load conditions are separately considered. Figs. 4.82a and 4.82b show the optimal designs in the tensile and compressive load cases. Figs. 4.83a and 4.83b respectively compare the changes of Poisson's ratios during large deformations under 10% applied tensile and compressive nominal strains with those of the original design. Fig. 4.84 shows the optimization history, where it is shown that optimal designs are sought by only a few iterations.
In order to demonstrate the auxetic behaviors, we analyze $3 \times 3 \times 3$ array of unit cells in the tensile

and compressive load cases, whose undeformed configurations are depicted in Figs. 4.85 and 4.86. In both load cases, the Z-displacements are prescribed at top surfaces and restricted at bottom surfaces, and the rotations are restricted on both of the top and bottom surfaces. Lateral displacements , *i.e.*, are free at the top an bottom surfaces in both load cases. Figs. 4.85b and 4.85c illustrate the lateral displacement due to tension, and Figs. 4.86b and 4.86c show the lateral contraction due to compression, where auxetic behaviors are apparently shown.

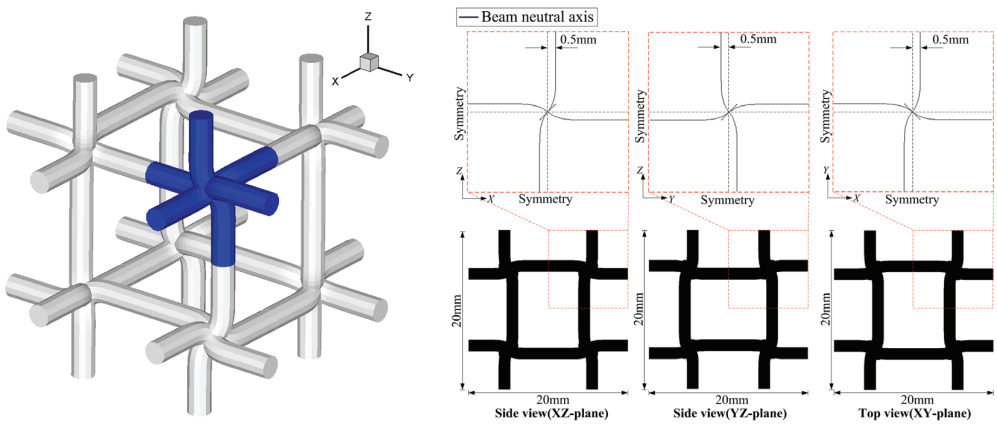

(a) Original design (b) Original design description in planar views

Figure 4.81: Original design of three-dimensional auxetic structure (case A)

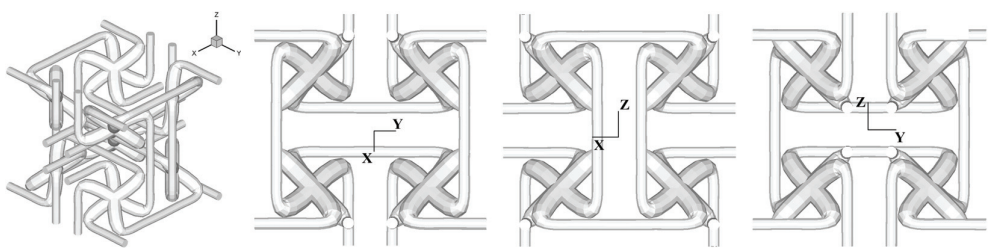

(a) Tensile load case

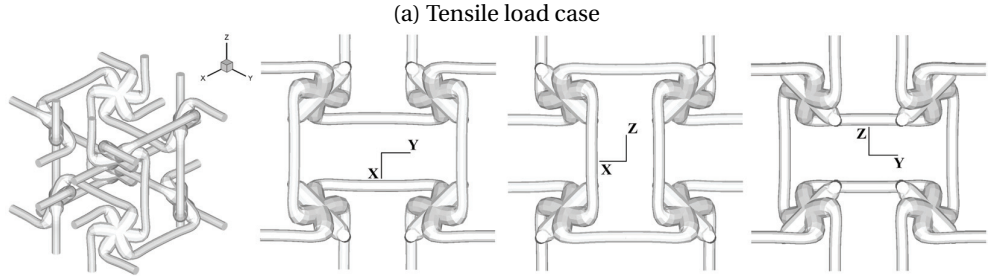

(b) Compressive load case

Figure 4.82: Optimal design of three-dimensional auxetic structure (case A)

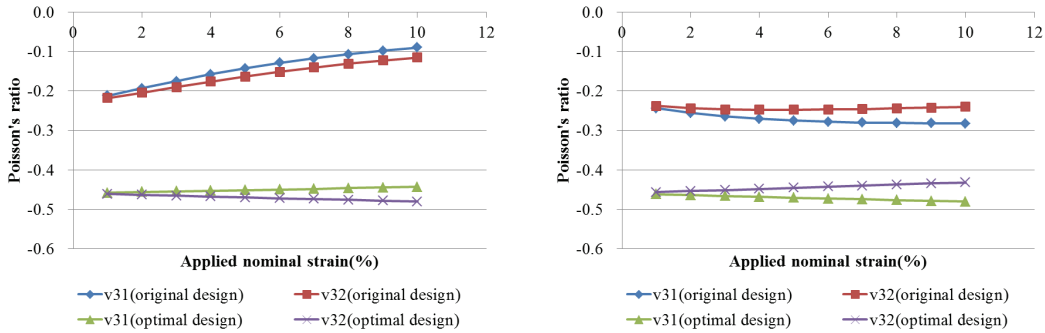

(a) Tensile load case

(b) Compressive load case

Figure 4.83: Change of Poisson's ratio during large deformations (case A)

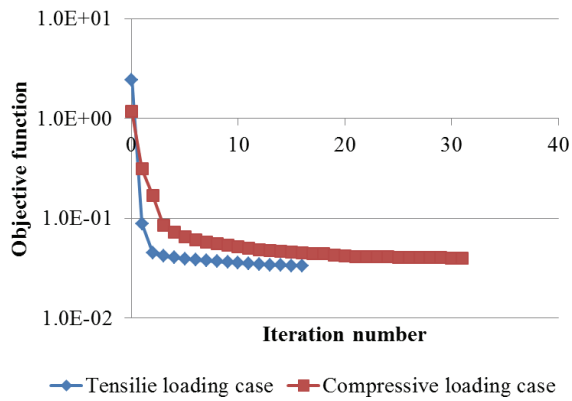

Figure 4.84: Optimization history (case A)

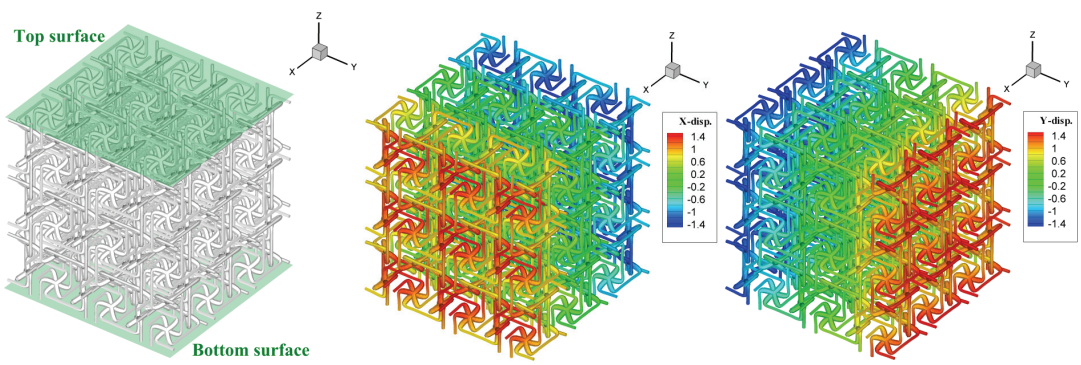

(a) $3 \times 3 \times 3$ array of unit cells

(b) X-displacement plot

(c) Y-displacement plot

Figure 4.85: Tensile deformation analysis of $3 \times 3 \times 3$ array of unit cells

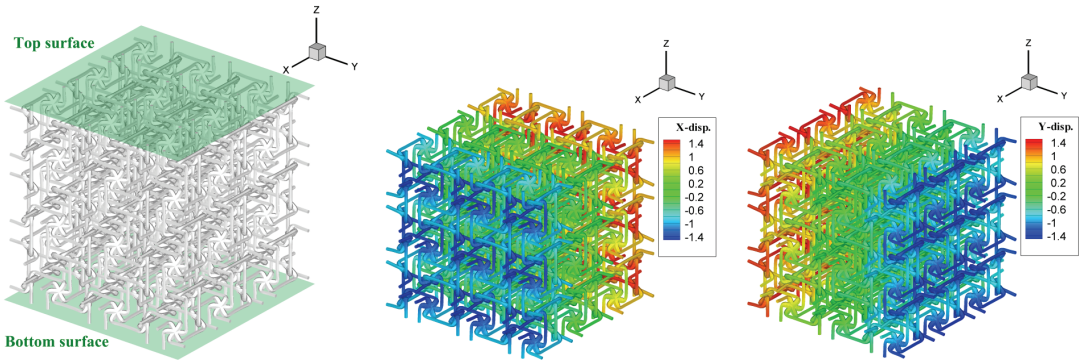

(a) $3 \times 3 \times 3$ array of unit cells (b) X-displacement plot (c) Y-displacement plot

Figure 4.86: Compressive deformation analysis of $3 \times 3 \times 3$ array of unit cells

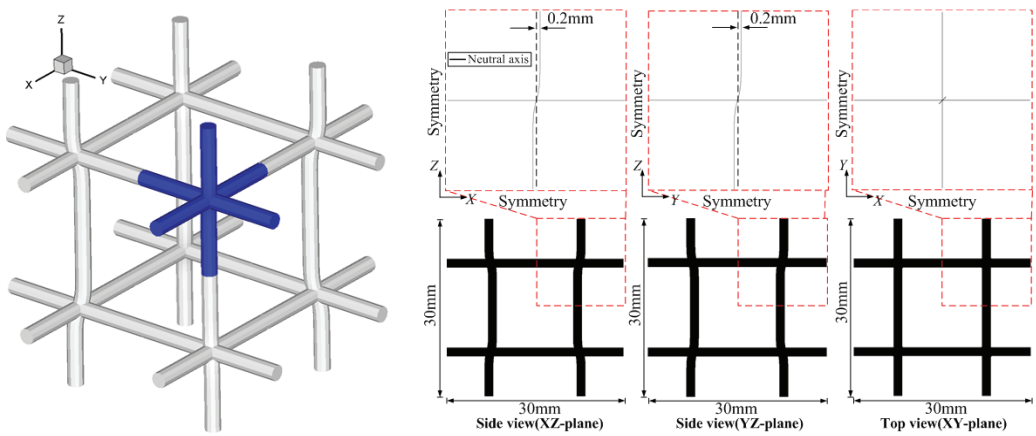

(a) Original design (b) Original design description in planar views

Figure 4.87: Original design of three-dimensional auxetic structure (case B)

Design case B

The case B design has 72 configuration and 120 thickness design variables, and the configuration design parameterization is explained in Appendix F.2.2. Fig.4.87 shows the case B original design, which has the same cross-section geometry material parameters with those of the previous case A and with different overall dimension as $30 \times 30 \times 30(mm)$. In this design case, we pursue to have two target tangent Poisson's ratio $\nu_{31}^* = \nu_{32}^* = -1.5$ (case #1) and $\nu_{31}^* = \nu_{32}^* = -2$ (case #2) during large tensile and compressive deformations. Fig. 4.87 shows and original deisgn of a unit cell where the blue color indicates the one-eighth part due to a mirror symmetry. Fig. 4.87b shows lateral views of the unit cell. The vertical members have a slight perturbation of $0.2mm$ from straight line to introduce a load eccentricity for auxetic behavior. The unit cell has overall dimension $30 \times 30 \times 30(mm)$, and a circular cross-section with diameter $1.5mm$ is considered. The effective (tangent) Poisson's ratio due to lateral X- and Y-displacements under the Z-directional

loading can be calculated as

$$\nu_{31}^{\tan} \equiv -\frac{\varepsilon_X}{\varepsilon_Z} = -\frac{(u^c - u_0^c)/X_0^c}{(w^c - w_0^c)/Z_0^c}, \tag{4.32}$$

and

$$\nu_{32}^{\tan} \equiv -\frac{\varepsilon_Y}{\varepsilon_Z} = -\frac{(v^c - v_0^c)/Y_0^c}{(w^c - w_0^c)/Z_0^c}, \tag{4.33}$$

where ε_X and ε_Y defines the X- and Y-directional nominal strain of a current configuration about the previous equilibrium configuration, and the superscript "c" indicates a center displacement component, and the lowerscript "0" indicates a quantity at the previous equilibrium configuration. The center hole displacement is calculated by averaging displacements at eight junctions. As we pursue to attain target tangent Poisson's ratio, and the design sensitivity of the tangent Poisson's ratio is derived as

$$\dot{\nu}_{31}^{\tan} = -\frac{\dot{u}^c}{w^c - w_0^c}\frac{Z_0^c}{X_0^c} - \nu_{31}^{\tan}\frac{\dot{w}^c}{w^c - w_0^c} + \frac{\dot{u}_0^c}{w^c - w_0^c}\frac{Z_0^c}{X_0^c} + \nu_{31}^{\tan}\frac{\dot{w}_0^c}{w^c - w_0^c} + \nu_{31}^{\tan}\left(\frac{\dot{w}_0^c}{Z_0^c} - \frac{\dot{u}_0^c}{X_0^c}\right), \tag{4.34}$$

and

$$\dot{\nu}_{32}^{\tan} = -\frac{\dot{v}^c}{w^c - w_0^c}\frac{Z_0^c}{Y_0^c} - \nu_{32}^{\tan}\frac{\dot{w}^c}{w^c - w_0^c} + \frac{\dot{v}_0^c}{w^c - w_0^c}\frac{Z_0^c}{Y_0^c} + \nu_{32}^{\tan}\frac{\dot{w}_0^c}{w^c - w_0^c} + \nu_{32}^{\tan}\left(\frac{\dot{w}_0^c}{Z_0^c} - \frac{\dot{v}_0^c}{Y_0^c}\right), \tag{4.35}$$

where it is assumed that the initial unit cell center position does not have design dependence due to mirror-symmetric design variations, so that $\dot{X}_0^c = \dot{u}_0^c$, $\dot{Y}_0^c = \dot{v}_0^c$, and $\dot{Z}_0^c = \dot{w}_0^c$. In the same manner with the case of two-dimensional structure, the displacement sensitivities $\dot{u}^c$, $\dot{v}^c$, and $\dot{w}^c$ are calculated by the adjoint DSA method, and the previous (reference) center displacement sensitivities $\dot{u}^c$, $\dot{v}^c$, and $\dot{w}^c$ are kept and utilized at the next equilibrium. Then, we utilize the optimization formulation of Eqs. (4.22)-(4.31) with the objective function replaced by

$$\psi({}^{n+1}\boldsymbol{\eta};\mathbf{d}) \equiv \sum_i \left\{ \left|\nu_{31}(\varepsilon_i^0) - \nu^*\right|^2 + \left|\nu_{32}(\varepsilon_i^0) - \nu^*\right|^2 \right\}. \tag{4.36}$$

Figs. 4.88a and 4.88b show the optimal designs for the target Poisson's ratios $\nu_{31}^* = \nu_{32}^* = -1.5$ and $\nu_{31}^* = \nu_{32}^* = -2$, respectively. In order to verify the auxetic behavior of the architected unit cell, we investigate large deformations of finite-sized structure having 3, 3, and 15 unit cells in each of X-, Y-, and Z-directions, respectively ($3 \times 3 \times 15$ array of unit cells). Fig. 4.89a illustrates the lateral expansion in X- and Y-directions due to Z-directional tensile loadings, where lateral expansions are apparently shown, and case #2 design shows larger expansion. Also, Fig. 4.91 shows the lateral contraction in X- and Y-directions due to Z-directional compressive loadings, where a compressive loading is applied to 2% nominal strain prior to undergo structural buckling. Figs. 4.90a and 4.90b respectively show the change of secant and tangent Poisson's ratio during large tensile deformations in 10% applied nominal strain. Also, Figs. 4.92a and 4.92b show the

change of secant and tangent Poisson's ratio during large compressive deformations in 2% applied nominal strain. We perform multi-step design optimizations with alternating load condition, and total four steps are used, as shown in Fig. 4.93.

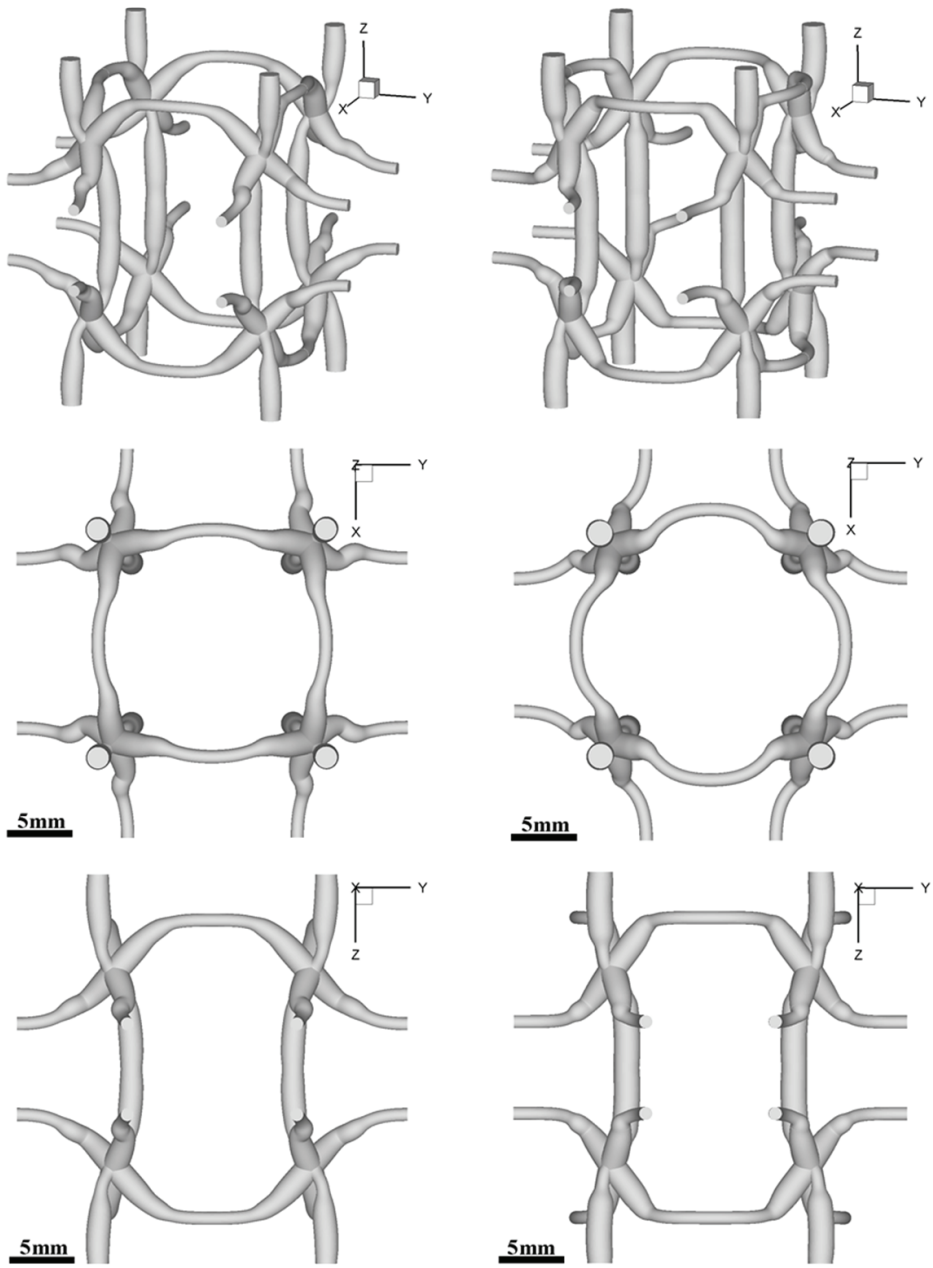

(a) $\nu_{31}^{*} = \nu_{32}^{*} = -1.5$ (b) $\nu_{31}^{*} = \nu_{32}^{*} = -2$

Figure 4.88: Optimal design of three-dimensional auxetic structure (case B)

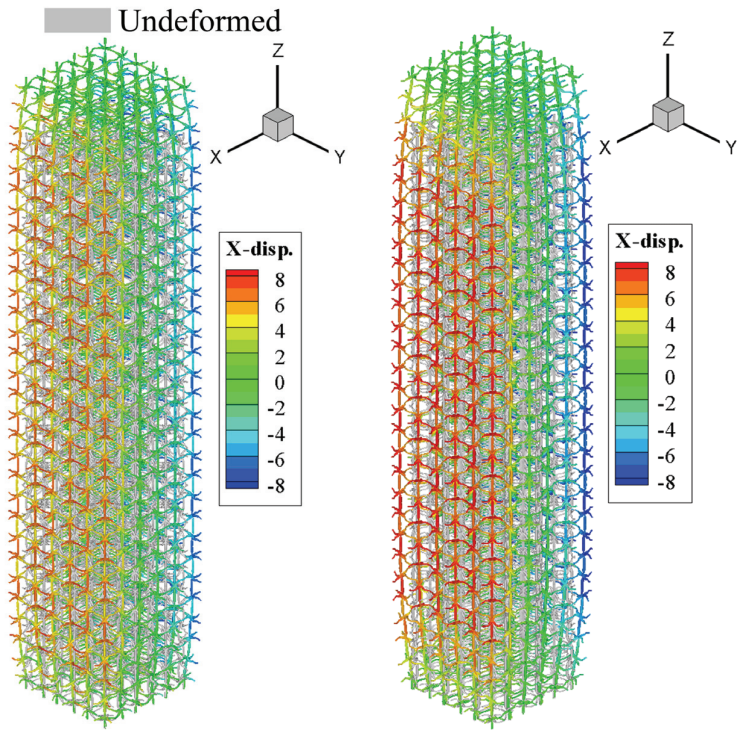

(a) $\nu_{31}^* = \nu_{32}^* = -1.5$ (b) $\nu_{31}^* = \nu_{32}^* = -2$

Figure 4.89: Uniaxial tension test of $3 \times 3 \times 15$ array of architeced unit cell (case B)

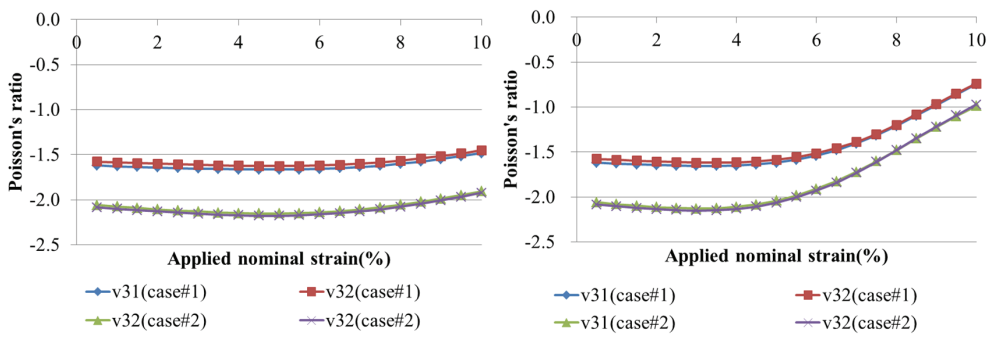

(a) $\nu_{31}^* = \nu_{32}^* = -1.5$ (b) $\nu_{31}^* = \nu_{32}^* = -2$

Figure 4.90: Optimal design of three-dimensional auxetic structure (case B)

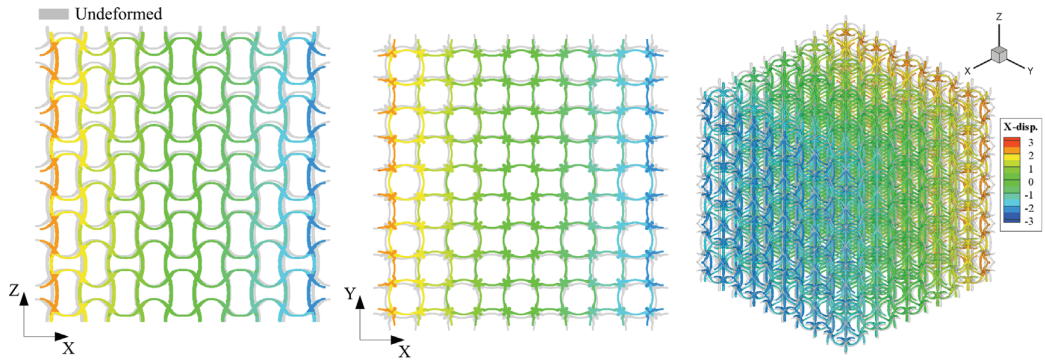

(a) $\nu_{31}^* = \nu_{32}^* = -1.5$

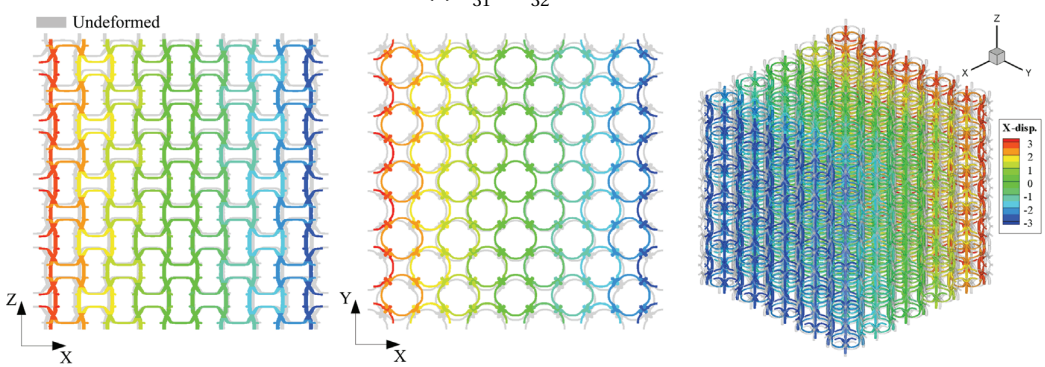

(b) $\nu_{31}^* = \nu_{32}^* = -2$

Figure 4.91: Uniaxial compression test of $5 \times 5 \times 5$ array of architeced unit cell (case B)

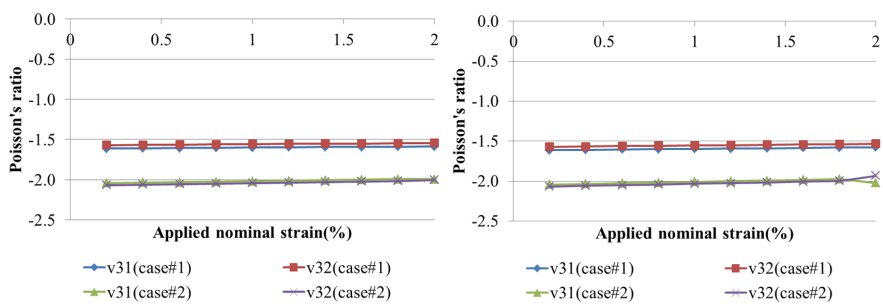

(a) $\nu_{31}^* = \nu_{32}^* = -1.5$ (b) $\nu_{31}^* = \nu_{32}^* = -2$

Figure 4.92: Optimal design of three-dimensional auxetic structure (case B)

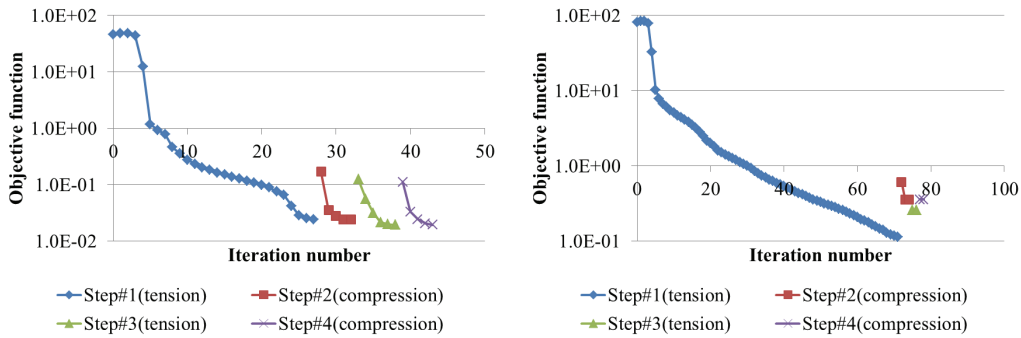

(a) $v_{31}^* = v_{32}^* = -1.5$ (b) $v_{31}^* = v_{32}^* = -2$

Figure 4.93: Optimization history (case B)

4.7 Phononic band gap structures

In this section, we architects single material two- and three-dimensional beam lattice structures having significantly enlarged band-gaps at low audible frequency range by using a gradient-based configuration and sizing design optimization method. For given various lattice topologies, beam neutral axis geometry and cross-section thickness are smoothly parameterized by higher order B-spline basis functions using the isogeometric analysis framework, and controlled by an optimization algorithm with the translational lattice periodicities and unit cell sizes maintained. Also, the enhanced band-gap properties are verified by comparison with wave transmissions in assemblies of finite number of unit cells obtained by using the harmonic response analysis.

The goal of the optimization is to maximize the relative band-gap size between the two adjacent $j-th$ and $(j+1)-th$ modes, that is, maximize the lowest frequency value of the overlying bands and minimize the maximum frequency value of the underlying bands; the following objective function can be defined [101].

$$f(\mathbf{d}) = 2\frac{\min_{\mathbf{k}}\zeta_{j+1}(\mathbf{k}^*,\mathbf{d}) - \max_{\mathbf{k}}\zeta_j(\mathbf{k}^*,\mathbf{d})}{\min_{\mathbf{k}}\zeta_{j+1}(\mathbf{k}^*,\mathbf{d}) + \max_{\mathbf{k}}\zeta_j(\mathbf{k}^*,\mathbf{d})}, \ \mathbf{k}^* \in \Gamma_{IBZ}, \tag{4.37}$$

where $\mathbf{d} \equiv \{d_i\}$ denotes a set of design variables. The optimization problem can be stated as: find $\mathbf{d}$ such that

$$\text{Maximize } f(\mathbf{d}), \tag{4.38}$$

subject to

$$\left\{\tilde{\mathbf{K}}(\mu) - \omega^2\tilde{\mathbf{M}}(\mu)\right\}\tilde{\mathbf{u}} = \mathbf{0}, \ \tilde{\mathbf{u}} \neq \mathbf{0}, \tag{4.39}$$

$$g_j(\mathbf{d}) \equiv \frac{1}{L_j(\mathbf{d})}\int_{\Omega_j}\left[\left\{\kappa^f(\xi)/\kappa_U^f\right\}^2 - 1\right]ds < 0, \ j = 1\sim ne, \tag{4.40}$$

and

$$d_i^{lower} \leq d_i \leq d_i^{upper}. \tag{4.41}$$

Eq. (4.40) represents geometric constraints to avoid self- intersecting ligaments due to abrupt design change, and Ω_j represents a curve segment corresponding to j-th knot span among total ne knot spans, whose length is denoted by L_j. Also, κ^f and κ_U^f respectively denote the Frenet curvature and its selected upper bound. Detailed expressions of calculating the curvature constraint and its design sensitivity is presented in Appendix E.1. In all the examples, the Modified Method of Feasible Directions (MMFD) algorithm is used in order to solve the nonlinear constrained optimization problems. Table 4.24 shows lattice base vectors and positions of vertices of the irreducible Brillouin zones (IBZs) for each of the lattice topologies. A set of wave vector components ($\boldsymbol{\mu}$) on the IBZ perimeter is required for the band structure calculation. In this paper, 80 uniformly-spaced discrete points on each edge of the IBZ are selected, at which the eigenvalue problem is solved to calculate band structures.

Table 4.24: List of direct and reciprocal lattice base vectors

	Direct	Reciprocal	IBZ(Im(μ_i))
Square	$\mathbf{b}_1 = 2L\mathbf{e}_1$ $\mathbf{b}_2 = 2L\mathbf{e}_2$	$\mathbf{b}_1^* = \frac{\pi}{L}\mathbf{e}_2$ $\mathbf{b}_2^* = \frac{\pi}{L}\mathbf{e}_2$	$O : [0,0]$ $A : [\pi,0]$ $B : [\pi,\pi]$
Triangular	$\mathbf{b}_1 = L\mathbf{e}_1$ $\mathbf{b}_2 = L\left(\frac{1}{2}\mathbf{e}_1 + \frac{\sqrt{3}}{2}\mathbf{e}_2\right)$	$\mathbf{b}_1^* = \frac{2\pi}{L}\left(\mathbf{e}_1 - \frac{1}{\sqrt{3}}\mathbf{e}_2\right)$ $\mathbf{b}_2^* = \frac{2\pi}{L}\left(\frac{2}{\sqrt{3}}\mathbf{e}_2\right)$	$O : [0,0]$ $A : [0,\pi]$ $B : [2\pi/3, 4\pi/3]$
Kagomé	$\mathbf{b}_1 = L\left(\mathbf{e}_1 + \sqrt{3}\mathbf{e}_2\right)$ $\mathbf{b}_2 = L\left(-\mathbf{e}_1 + \sqrt{3}\mathbf{e}_2\right)$	$\mathbf{b}_1^* = \frac{\pi}{L}\left(\mathbf{e}_1 + \frac{\sqrt{3}}{3}\mathbf{e}_2\right)$ $\mathbf{b}_2^* = \frac{\pi}{L}\left(-\mathbf{e}_1 + \frac{\sqrt{3}}{3}\mathbf{e}_2\right)$	$O : [0,0]^T$ $A : [\pi,\pi]^T$ $B : [4\pi/3, 2\pi/3]^T$
Hexagonal	$\mathbf{b}_1 = \sqrt{3}L\left(\frac{1}{2}\mathbf{e}_1 + \frac{\sqrt{3}}{2}\mathbf{e}_2\right)$ $\mathbf{b}_2 = \sqrt{3}L\left(-\frac{1}{2}\mathbf{e}_1 + \frac{\sqrt{3}}{2}\mathbf{e}_2\right)$	$\mathbf{b}_1^* = \frac{2\pi}{\sqrt{3}L}\left(\mathbf{e}_1 + \frac{1}{\sqrt{3}}\mathbf{e}_2\right)$ $\mathbf{b}_2^* = \frac{2\pi}{\sqrt{3}L}\left(-\mathbf{e}_1 + \frac{1}{\sqrt{3}}\mathbf{e}_2\right)$	$O : [0,0]^T$ $A : [\pi,\pi]^T$ $B : [4\pi/3, 2\pi/3]^T$
Simple cubic	$\mathbf{b}_1 = 2L\mathbf{e}_1$ $\mathbf{b}_2 = 2L\mathbf{e}_2$ $\mathbf{b}_3 = 2L\mathbf{e}_3$	$\mathbf{b}_1^* = \frac{\pi}{L}\mathbf{e}_1$ $\mathbf{b}_2^* = \frac{\pi}{L}\mathbf{e}_2$ $\mathbf{b}_3^* = \frac{\pi}{L}\mathbf{e}_3$	$O : [0,0,0]^T$ $A : [0,\pi,0]^T$ $B : [\pi,\pi,0]^T$ $C : [\pi,\pi,\pi]^T$

4.7.1 Two-dimensional triangular lattice structure

A planar triangular lattice structure composed of regular triangles 40mm on each side, as illustrated in Figure 4.94a. A unit cell can be defined by a translational periodicity along the directions of lattice base vectors $\mathbf{b}_1$ and $\mathbf{b}_2$. We select a square cross-section with uniform thickness b_0 = 2mm as shown in Figure 4.94b, and material properties of Young's modulus E = 1.14GPa, Poisson's ratio ν = 0.3, and density $\rho = 1050 kg/m^3$. The reciprocal lattice basis $\mathbf{b}_1^*$,

$\mathbf{b}_2^*$, and the boundary of irreducible first Brillouin zone ($O-A-B$) are depicted in Figure 4.94c.

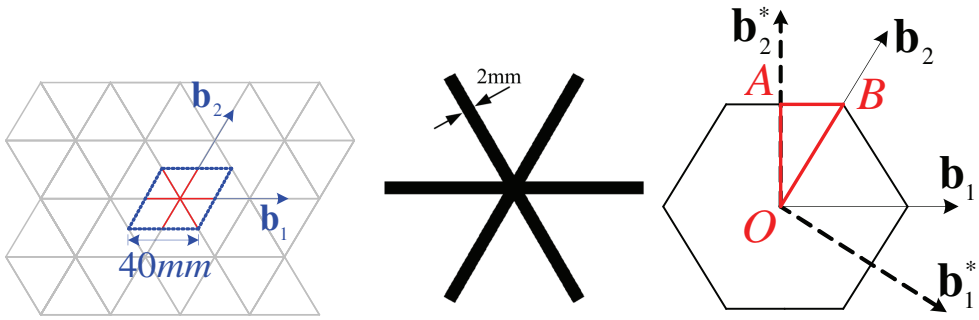

(a) Triangular lattice (b) Unit cell (c) Brillouin zone

Figure 4.94: Triangular lattice structure

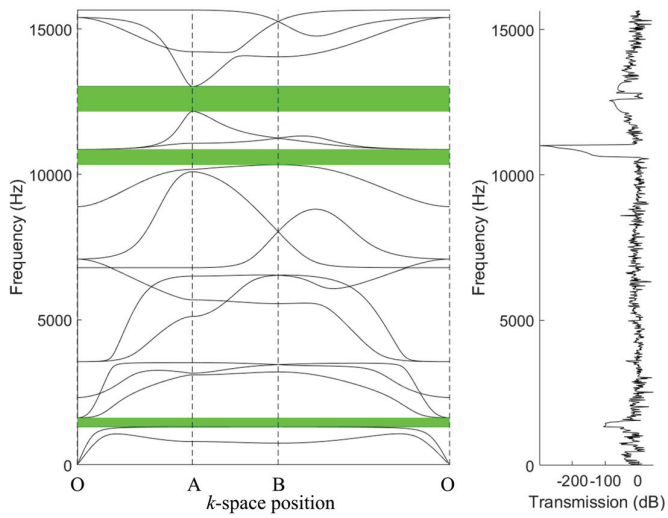

Figure 4.95: Band structure and frequency response of original straight design

Figure 4.95 shows that the triangular structure has three band gaps within the considered frequency range, and the low wave transmission are apparently shown at the band gap frequency regions. Figure 4.96 illustrates the design parameterization of configuration design in coarse level discretization by quartic B-spline basis function with 6 control points for each ligament. For a ligament indicated by red-colored box, the X- and Y-directional changes of 8 control point positions are selected as configuration design variables, and the end control point indicated by red-colored circle is fixed during optimization process in order to maintain the translational periodicity and unit cell size. The other five ligaments are designed by exploiting the rotational symmetry within the unit cell in the original design. Also, 20 thickness control coefficients corresponding to quartic B-spline basis functions are used as sizing design variables to parameterize cross-section thickness distribution within a ligament, *i.e.*, $n_{th} = 20$.

First, we start our optimization from the straight geometry of Figure 4.94b for maximizing the first band gap between 3^{rd}-4^{th} bands. We obtain the optimal design of Figure 4.97a where the neutral

axis geometry does not change, and cross-section becomes thinner around the junction and thicker on the other side. The target band gap between 3rd-4th modes is located at lower frequency region than that of the original design due to the decrease of stiffness near the junction; however, the band-gap size decreases. Interestingly, the other two band gaps generated in the original design are enlarged through the optimization, and wave transmission becomes much lower than those of original designs. The nearly flat two branches appear between the third and fourth band-gaps represent nearly zero group velocity in all the wave propagation directions, which represents an isolated wave. In the purpose of verifying the mechanism of band gap generation in the optimal design, we investigate the natural frequencies of a single ligament with clamped-clamped boundary conditions. Table 4.25 compares the band gap frequencies of the original and optimal designs. Table 4.26 lists the lowest five natural frequencies of a single ligament for the original straight and optimal design (case #1). It is noticeable that the first natural frequency coincides with the maximum frequency of underlying band of the first band-gap in the original straight design. This was discussed in Wang et al. [108] that this is an evidence for local resonance induced band-gap. Similarly, in the optimal design, the maximum frequency of the first band-gap is almost same with the first natural frequency, which means that the same local resonance mechanism generates the band-gap. As discussed in Wang et al. [108], another evidence of local resonance is the nearly flat underlying band which represents band-gap is generated at the same frequency for any direction of wave propagations. Thus, in this optimization, it is concluded that a local resonance band-gap is generated in lower frequency region than that of the original design, and we also obtain larger band-gaps in higher frequency ranges which is still within the audible frequency range (20~20,000Hz).

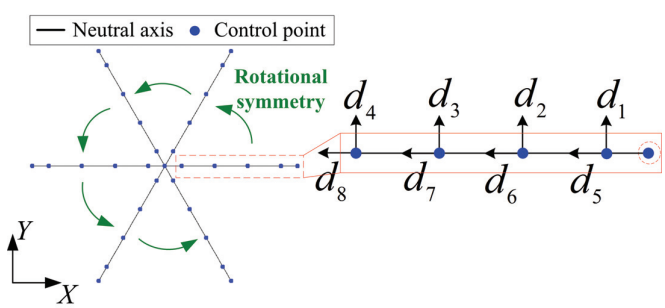

Figure 4.96: Illustration of 8 configuration design variables for the triangular lattice

For convenience, we call the above optimal design as “optimal design case #1”. As a next step, an undulated design of Figure 4.98a is generated by perturbing the first four design variables such that $d_1 = d_2 = -2.5$mm and $d_3 = d_4 = 2.5$mm, which turns out to have more band gaps, compared with the original straight design. We start design optimizations from this undulated design, which is hereafter called an “original undulated design”, for two cases of target band gaps; first, a band gap between 3rd and 4th modes (case #2), and second, a band gap between 6th and 7th modes (case #3).

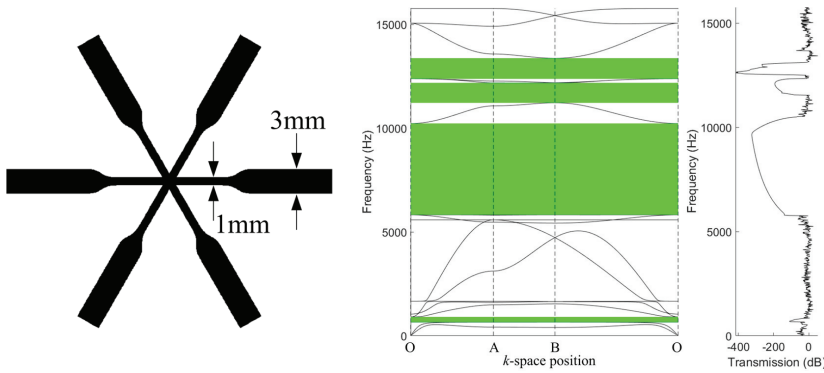

(a) Optimal design (b) Band structure and frequency response

Figure 4.97: Optimal design of triangular lattice structure

Table 4.25: Comparison of band gap sizes and frequency ranges

	Band gap#	Band gap size(Hz)	Underlying band	
			Mode#	Max.freq.(Hz)
Original design	1	307.0	3	1316.6
	2	532.9	12	10325.9
	3	862.0	14	12162.7
Optimal design	1	251.0	3	653.8
	2	4398.1	12	5827.1
	3	957.2	13	11224.0
	4	987.8	15	12381.8

Table 4.26: Natural frequencies of single ligament in triangular lattice

Mode#	Natural frequency (Hz)	
	Original design	Optimal design
1	1316.6	663.1
2	3553.4	1678.8
3	6781.6	5594.2
4	10858.9	5732.1
5	13024.7	12343.5

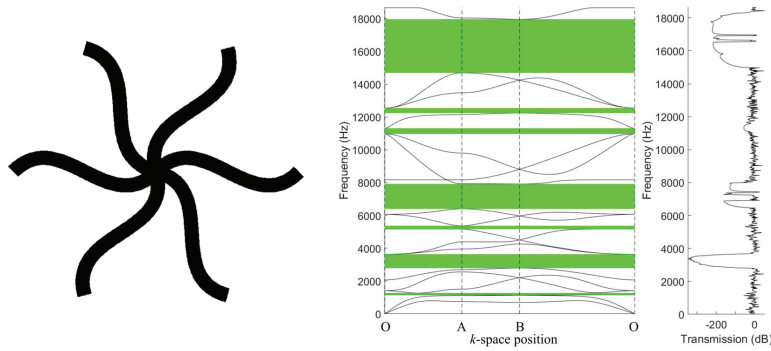

(a) Unit cell (b) Band structure and frequency response

Figure 4.98: Original undulated design

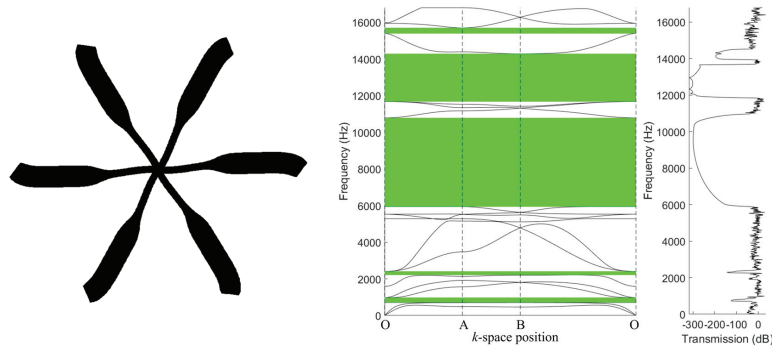

(a) Unit cell (b) Band structure and frequency response

Figure 4.99: Optimal undulated design (case#2)

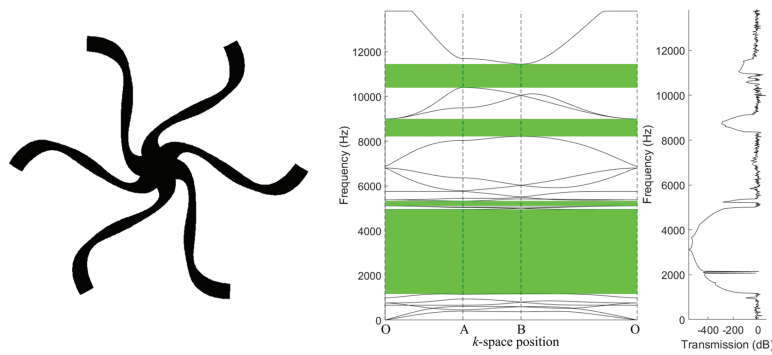

(a) Unit cell (b) Band structure and frequency response

Figure 4.100: Optimal undulated design (case#3)

Figures 4.99 and 4.100 illustrate the optimal designs and band diagrams for the cases #2 and #3, and Table 4.27 lists the sizes and frequency ranges of their band gaps. In the optimal design case #2, similar to the optimal design case #1, cross-section becomes thinner around the junction and thicker on the other sides, which decreases overall stiffness, and consequently the target first

band-gap has lower frequency range than that of the original undulated design. The band gap size slightly increases. Also, it is noticeable that the other higher modes of band gaps are significantly enlarged, and the wave transmissions become much lower at those frequency ranges. In the case #3 optimal design, the local resonance band gap between 3^{rd} and 4^{th} modes is suppressed; however, very large band-gap appears at the low frequency range $1,174 \sim 4,952$Hz.

For the above three cases of design optimizations, Figure 4.101 plots the history of the objective function of Eq. (4.37). In all the cases, the solutions converge within a few iterations. As mentioned above, even though the target relative band-gap size slightly increases in the cases #1 and #2, several other significantly large band gaps are generated in audible frequency ranges.

Table 4.27: Comparison of band-gaps in triangular lattices

	Band gap#	Band gap size(Hz)	Underlying band	
			Mode#	Max.freq.(Hz)
Original design	1	113.0	3	1156.0
	2	841.3	6	2789.4
	3	196.1	9	5168.1
	4	1513.9	11	6402.3
	5	337.4	14	10972.9
	6	301.1	15	12243.6
	7	3263.7	17	14693.8
Optimal design	1	269.6	3	707.0
	2	195.4	6	2211.5
	3	4845.1	12	5938.2
	4	2608.0	15	11673.4
	5	306.2	16	15389.5
Optimal design	1	3778.1	6	1174.1
	2	216.9	9	5108.8
	3	776.7	15	8219.3
	4	1049.0	17	10399.3

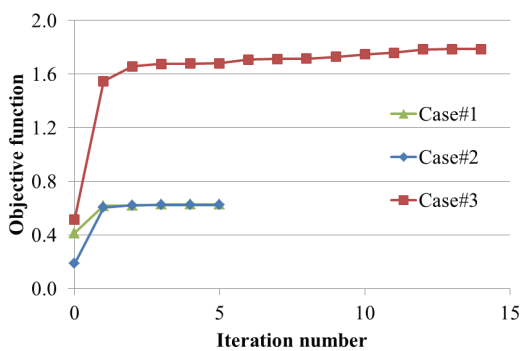

Figure 4.101: Optimization history for triangular lattice structure

4.7.2 Two-dimensional square lattice structure

We consider a planar square lattice structure composed of squares with 40mm on each side. Considering the translational periodicity in X- and Y-directions, the direct lattice base vectors $\mathbf{b}_1$, $\mathbf{b}_2$, and the unit cell is defined, as illustrated in Figure 4.102a. We select a square cross-section with uniform thickness $b_0 = 2$mm as shown in Figure 4.102b, and material properties of Young's modulus $E = 1.14GPa$, Poisson's ratio $\nu = 0.3$, and mass density $\rho = 1050kg/m^3$. Figure 4.102c shows the reciprocal lattice basis $\mathbf{b}_1^*$ and $\mathbf{b}_2^*$ whose detailed expressions can be found in Appendix A, from which we identify the irreducible Brillouin zone whose boundary $O-A-B$ is indicated by the red-colored lines. Figure 4.104 illustrates a parameterization of configuration design variables. Within a quarter part of the unit cell, configuration of one ligament is parameterized by 6 control point positions in a coarse level discretization using quartic B-spline basis functions, and the other 3 ligaments are parameterized by using the rotational symmetry. 20 thickness control coefficients are used for thickness design parameterization of each ligament, *i.e.*, $n_{th} = 20$. Figure 4.103 shows the band diagram and wave transmission plot, where no complete band gap appears.

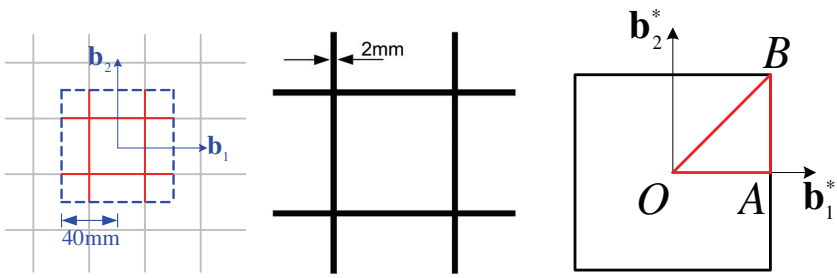

(a) Square lattice (b) Unit cell (c) Brillouin zone

Figure 4.102: Square lattice structure

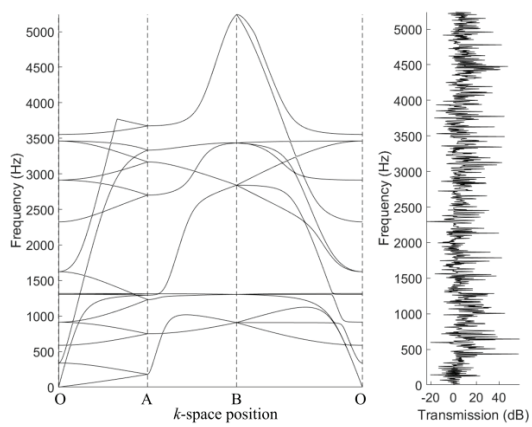

Figure 4.103: Band structure and frequency response of original straight design

We introduce an undulated geometry shown in Figure 4.105a by perturbing design variables such as d_i = 5mm (i = 1~4), which results in a couple of slight complete band gaps. The band gap between 8^{th} and 9^{th} modes is selected to be maximized by the optimization process.

Figure 4.106 shows the optimization results. The decrease of cross-section thickness around the junction is noticeable, and the other parts becomes thicker than those of the original design. Figure 4.106b shows that a very large band-gap is generated between the target 8^{th} and 9^{th} modes at the frequency range of 232 $2,132Hz$ where the wave transmission is shown to be significantly suppressed. Table 4.28 compares the band-gap sizes and frequency ranges of the original undulated and optimal designs. Figure 4.107 shows the history of objective function during the optimization, where the optimal design is sought through only a few iterations.

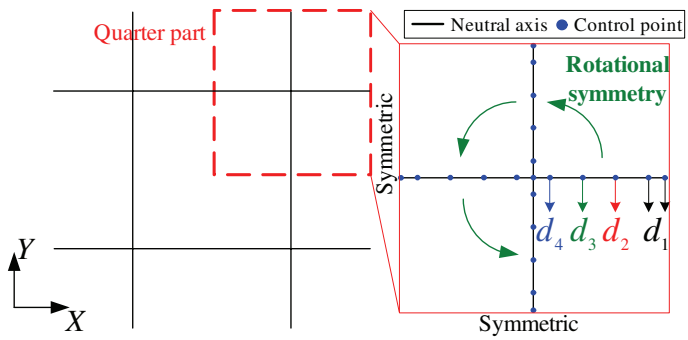

Figure 4.104: Illustration of 4 configuration design variables for the square lattice

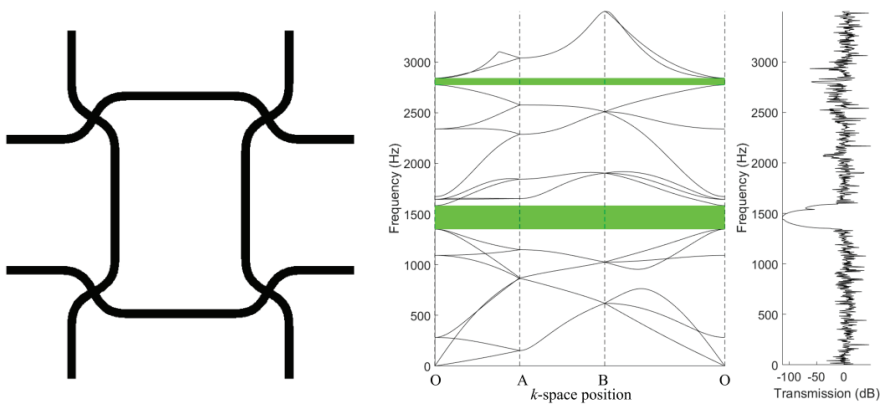

(a) Unit cell (b) Band structure and frequency response

Figure 4.105: Original undulated design of square lattice

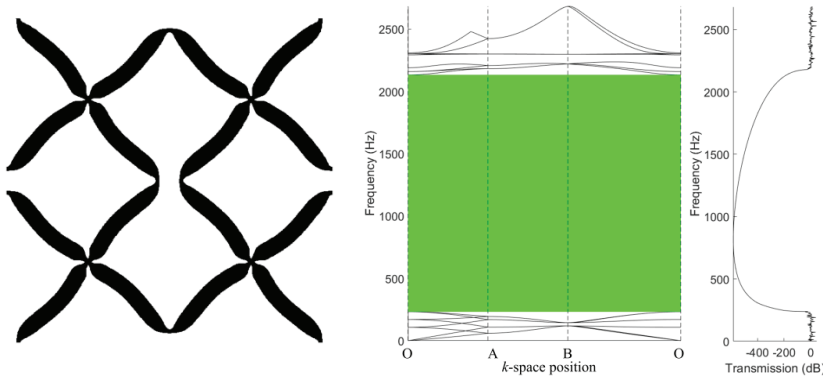

(a) Unit cell (b) Band structure and frequency response

Figure 4.106: Optimal undulated design of square lattice

Table 4.28: Comparison of band-gaps in square lattices

	Band gap#	Band gap size(Hz)	Underlying band	
			Mode#	Max.freq.(Hz)
Original	1	231.8	8	1350.9
design	2	65.7	16	2774.4
Optimal	1	1899.7	8	232.1
design	2	55.6	12	2236.7

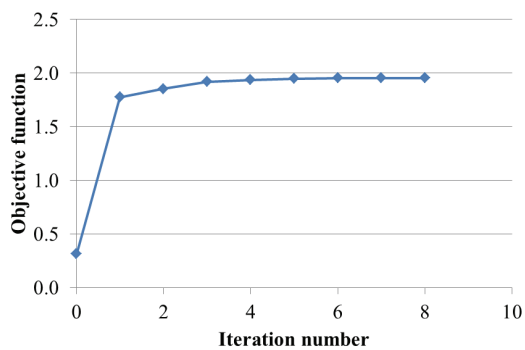

Figure 4.107: Optimization history for square lattice structure

4.7.3 Two-dimensional Kagomé lattice structure

We consider a planar Kagomé lattice structure composed of regular triangles with alternating orientations and 40mm on each side, as illustrated in Figure 4.108a. Due to the translational periodicity in the direction of base vectors $\mathbf{b}_1$ and $\mathbf{b}_2$, a unit cell indicated by red-colored lines is defined. We select a square cross-section with uniform thickness b_0 = 2mm, and material properties of Young's modulus $E = 1.14GPa$, Poisson's ratio $\nu = 0.3$, and mass density $\rho = 1050kg/m^3$. Figure 4.108c shows the reciprocal lattice basis $\mathbf{b}_1^*$ and $\mathbf{b}_2^*$ whose detailed expression

can be found in Appendix A, from which an irreducible Brillouin zone is determined whose boundary $O-A-B$ is indicated by the red-colored lines. Figure 4.109 shows that this structure has no complete band gap.

A single ligament configuration within the half part of the unit cell is parameterized by 8 configuration design variables in a coarse level discretization by quartic B-spline basis functions, and the other ligaments are parameterized by exploiting a rotational symmetry within the half part and the point symmetry within the unit cell, as illustrated in Figure 4.110. 20 cross-section thickness control coefficients are used in each ligament, *i.e.*, $n_{th} = 20$.

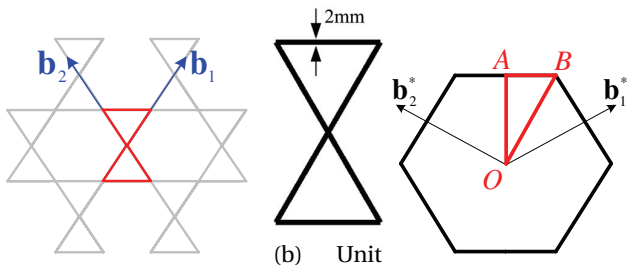

(a) Kagomé lattice (b) Unit cell (c) Brillouin zone

Figure 4.108: Kagomé lattice structure

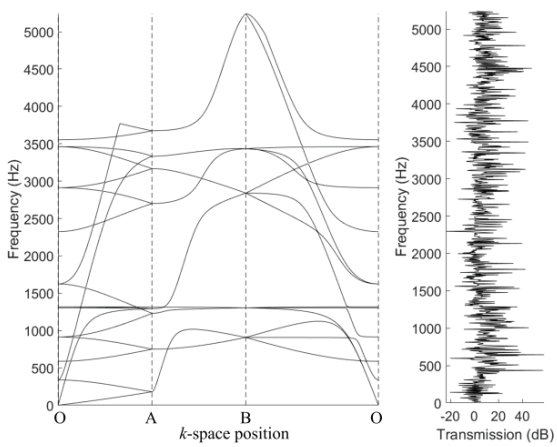

Figure 4.109: Band structure and frequency response of original straight design

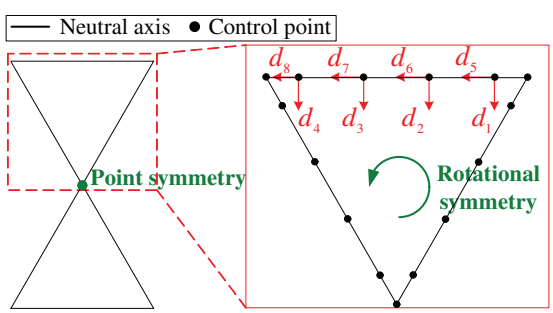

Figure 4.110: Illustration of 8 configuration design variables for the Kagomé lattice

We introduce an undulated design of Figure 4.111a by perturbing the design variables as $d_1 = d_2 = 2.5$mm and $d_1 = d_2 = -2.5$mm. As shown in Figure 4.111b, this undulated design show a couple of complete band gaps, and we perform design optimizations from this undulated design for maximizing two cases of target band gaps respectively between 9^{th}-10^{th} modes (case #1) and 3^{rd}-4^{th} modes (case #2). Figs. 4.112 and 4.113 show the optimization results, and significantly large band gaps at low frequency levels are noticeable, and the wave transmissions are also much lower at those frequency regions, compared with those of the original undulated design. Table 4.29 compares the band gap sizes and frequency ranges of the original undulated design and two cases of optimal designs. Both of the optimum solutions converge after about 10 iterations as show in Figure 4.114.

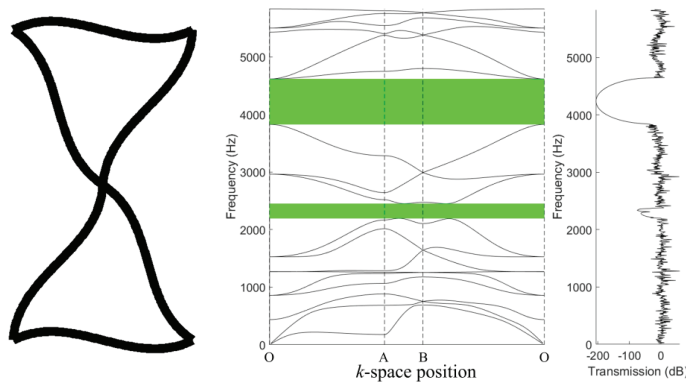

(a) Unit cell (b) Band structure and frequency response

Figure 4.111: Original undulated design of Kagomé lattice

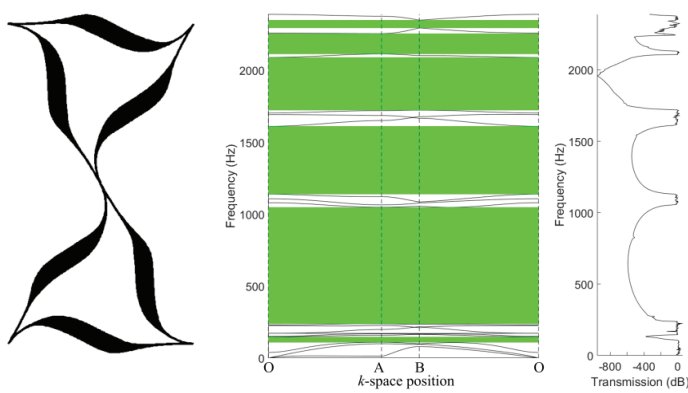

(a) Unit cell (b) Band structure and frequency response

Figure 4.112: Optimal undulated design of Kagomé lattice (case#1)

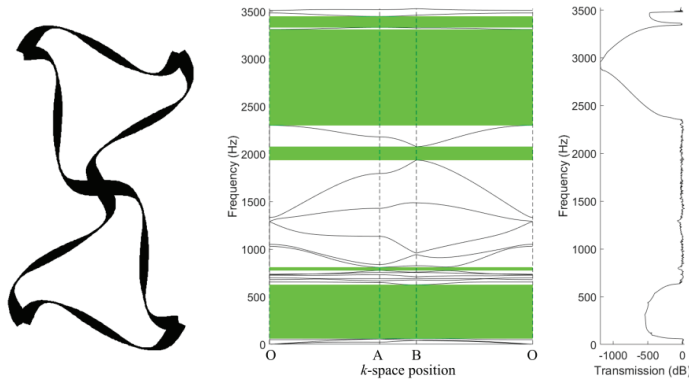

(a) Unit cell (b) Band structure and frequency response

Figure 4.113: Optimal undulated design of Kagomé lattice (case#2)

Table 4.29: Comparison of band-gaps in kagomé lattice

	Band gap#	Band gap size(Hz)	Underlying band	
			Mode#	Max.freq.(Hz)
Original undulated design	1	254.1	9	2196.5
	2	788.8	12	3829.5
Optimal design (case#1)	1	37.5	3	108.7
	2	810.3	9	237.4
	3	471.8	12	1139.5
	4	367.3	15	1723.1
	5	141.9	16	2113.9
	6	53.7	17	2295.3
Optimal design (case#2)	1	563.3	3	62.0
	2	31.8	9	777.5
	3	139.3	14	1937.7
	4	1007.4	15	2302.3
	5	115.4	16	3331.7

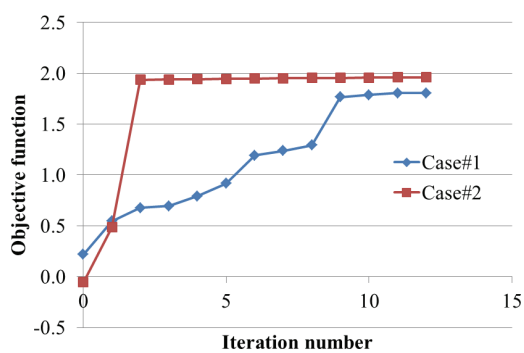

Figure 4.114: Optimization history for Kagomé lattice structure

4.7.4 Two-dimensional hexagonal honeycomb lattice structure

We consider a planar hexagonal honeycomb structure illustrated in Figure 4.115a. We select a minimal repeated unit, which is arranged in infinite lattice structures by translations in the directions of $\mathbf{b}_1$ and , $\mathbf{b}_2$ and it has a square cross-section with uniform thickness $b_0 = 2$mm. The corresponding reciprocal base vectors and irreducible Brillouin zone is obtained as shown in Figure 4.115c. Material properties of Young's modulus $E = 1.14GPa$, Poisson's ratio $\nu = 0.3$, and density $\rho = 1050kg/m^3$ are selected. Figure 4.116 shows a band diagram and wave transmission plot. Although there are a couple of slight complete band-gaps, wave transmissions at those frequencies are not distinctive. As illustrated in Figure. 4.117, a single ligament configuration

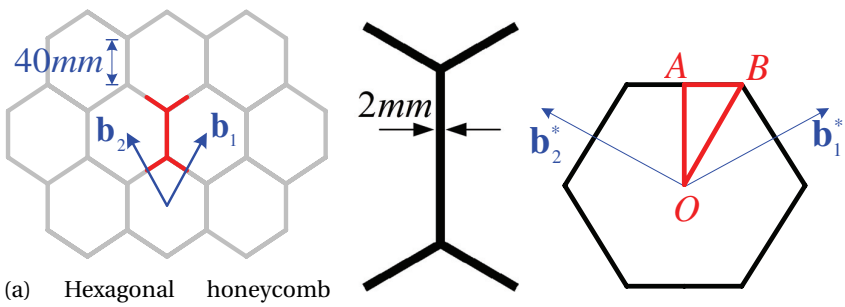

(a) Hexagonal honeycomb lattice (b) Unit cell (c) Brillouin zone

Figure 4.115: Hexabonal honeycomb lattice structure

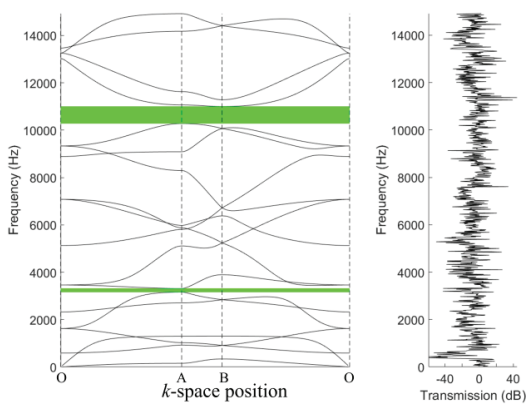

Figure 4.116: Band structure and frequency response of a hexagonal lattice

within the half part of the unit cell is parameterized by 8 configuration design variables as changes of control point positions in a coarse level discretization by quartic B-spline basis functions, and the other ligaments are parameterized by using a rotational symmetry within the half part and the point symmetry within the unit cell. 20 cross-section thickness control coefficients are used, *i.e.*, $n_{th} = 20$. An undulated design of Figure 4.118a is introduced by perturbing design variables as $d_1 = d_2 = 1.25$mm and $d_3 = d_4 = -1.25$mm, and it has four complete band gaps. We select two target band gaps; first, the band gap between 3$^{\text{rd}}$ and 4$^{\text{th}}$ modes (case #1) which is initially appear very slightly and the band gap between 9$^{\text{th}}$ and 10$^{\text{th}}$ modes (case#2).

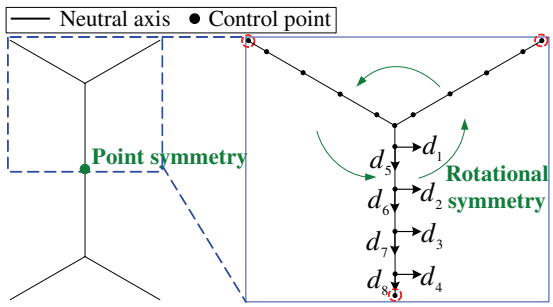

Figure 4.117: Design parameterization of hexagonal honeycomb lattice

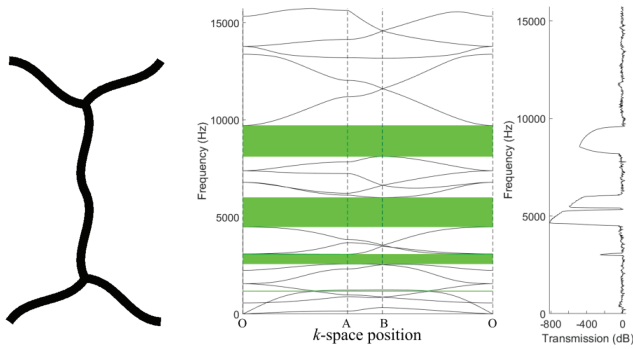

(a) Unit cell (b) Band structure and frequency response

Figure 4.118: Optimal undulated design of hexagonal honeycomb lattice

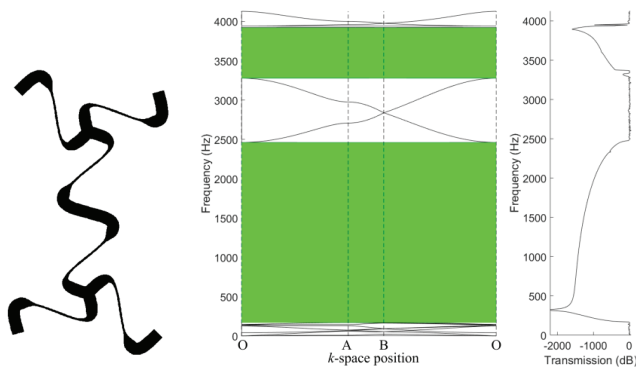

(a) Unit cell (b) Band structure and frequency response

Figure 4.119: Optimal undulated design (case #1)

In optimal design case #1, a large complete band gap is generated between 9th and 10th modes in the frequency region 170~2,461Hz , and the wave transmission is much lower than that of the original design. In the optimal design case #2, the target band-gap between 3th and 4th modes is significantly enlarged and located at lower frequency level of the region 13~160Hz, and several other band-gaps also show very low wave transmission. Table 4.30 compares the sizes and frequency regions of band gaps in the original undulated design and two optimal designs.

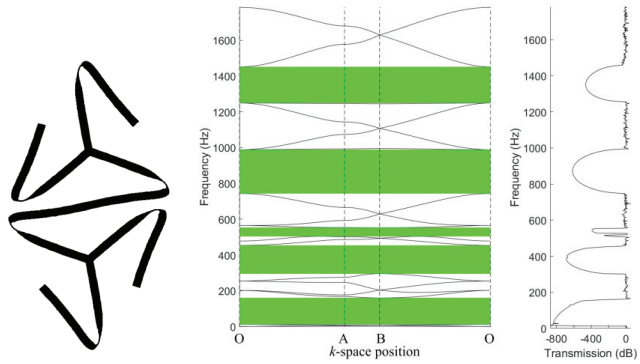

(a) Unit cell (b) Band structure and frequency response

Figure 4.120: Optimal undulated design (case #2)

Table 4.30: Comparison of band-gaps in hexagonal lattices

			Underlying band	
	Band gap#	Band gap size (Hz)	Mode#	Max.freq.(Hz)
Original undulated design	1	29.6	3	1165.9
	2	501.6	6	2582.4
	3	1513.7	9	4489.5
	4	1597.8	13	8114.7
Optimal design (case#1)	1	2291.6	9	169.8
	2	641.7	13	3278.5
Optimal design (case#2)	1	147.5	3	12.8
	2	158.2	7	295.5
	3	49.2	9	504.1
	4	244.5	12	743.7

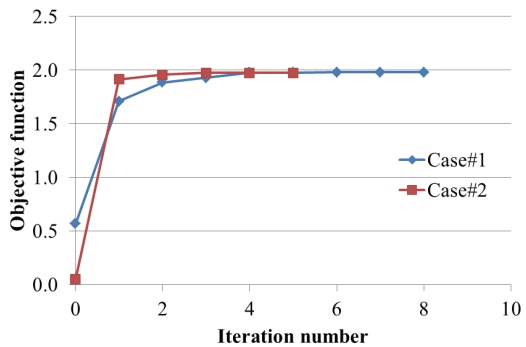

Figure 4.121: Optimization history for hexagonal honeycomb lattice structure

4.7.5 Three-dimensional simple cubic structure

We consider a three-dimensional simple cubic lattice structure as shown in Figure. 4.122a. Due to the translational periodicity in the direction of basis $\mathbf{b}_1$, $\mathbf{b}_2$, and $\mathbf{b}_3$, a unit cell indicated as a blue-colored one is defined. We select a circular cross-section with uniform diameter d_0 = 2mm

as shown in Figure 4.122b. Material properties of Young's modulus $E = 1.14GPa$, Poisson's ratio $\nu = 0.3$, and mass density $\rho = 1050kg/m^3$ are selected. Figure 4.122c shows the reciprocal lattice basis $\mathbf{b}_1^*$, $\mathbf{b}_2^*$, and $\mathbf{b}_3^*$ whose detailed expressions can be found in Appendix A. A boundary of irreducible Brillouin zone $O-A-B-C$ is indicated by the red-colored lines. Figure 4.123 shows the band diagram and wave transmission where no complete band-gap is generated. A single

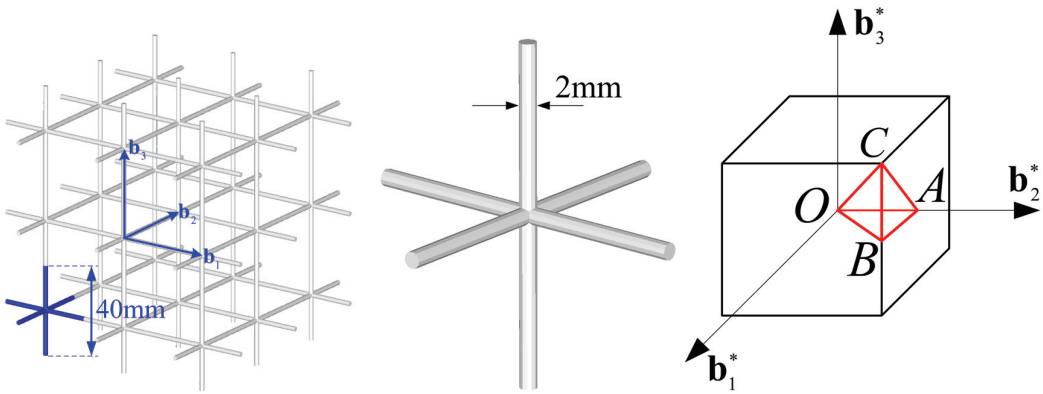

(a) Simple cubic lattice structure (b) Unit cell (c) Brillouin zone

Figure 4.122: Simple cubic honeycomb lattice

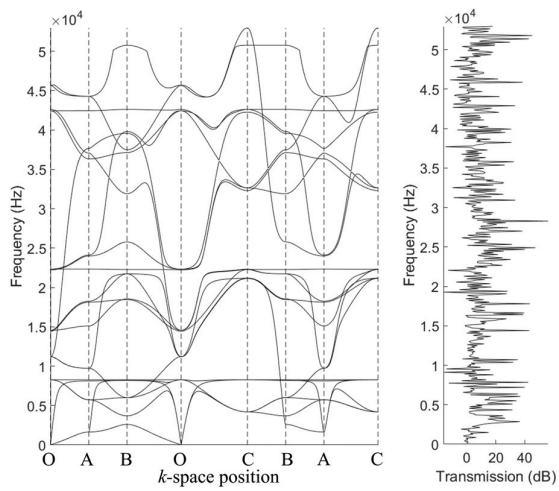

Figure 4.123: Band structure and frequency response of simple cubic lattice structure

ligament configuration is parameterized by 8 configuration design variables. 24 thickness control coefficients are used. We introduce a geometric undulation of ligaments as illustrated in Figure 4.124a, then the undulated design shows a couple of band gaps at high frequency level as shown in Figure 4.125a, and the first band-gap between 15^{th} and 16^{th} modes apparently shows low wave transmission. From this undulated design, we start design optimization to maximize the first band gap, and finally obtain the optimal design shown in Figure 4.124b. Figure 4.125b illustrates that the optimal design attained significantly larger band-gap in the frequency range of 2484 ~ 11539Hz with enhanced wave attenuation, compared with those of original undulated design. Table 4.31 compares the band gap sizes and frequency ranges of the original undulated

design and the optimal design. Figure 4.126 shows the monotonic convergence of the objective function during the optimization.

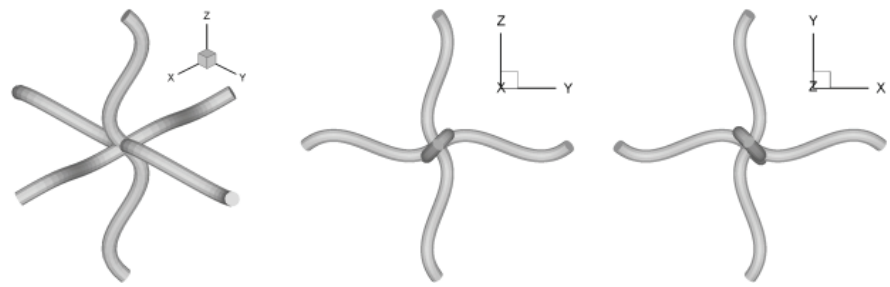

(a) Original undulated design

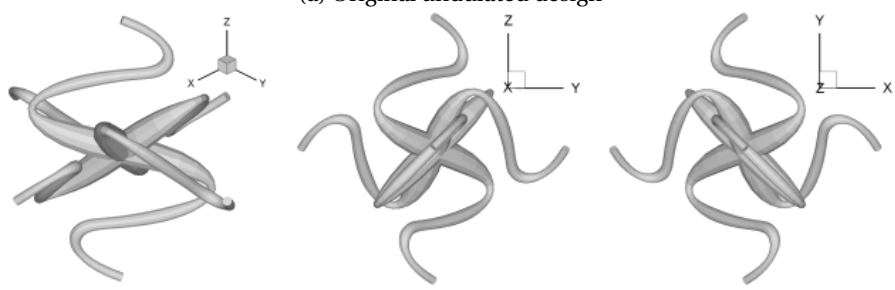

(b) Optimal design

Figure 4.124: Plot of unit cell in three different views

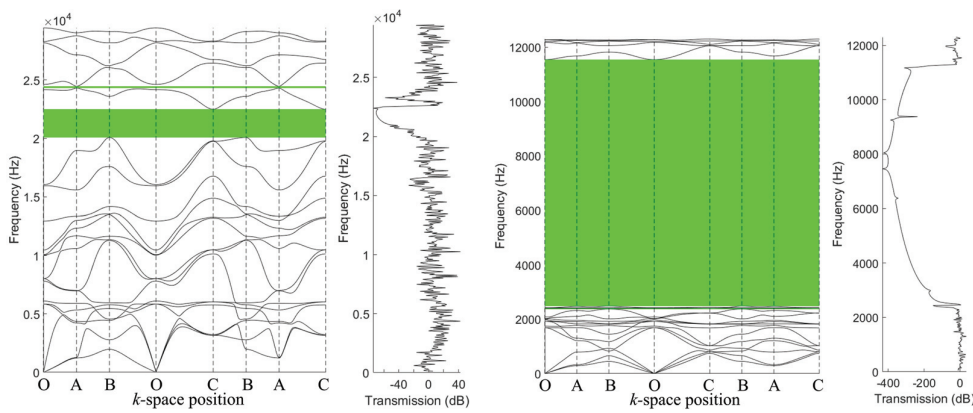

(a) Original undulated design

(b) Optimal design

Figure 4.125: Band gap in simple cubic lattice structure

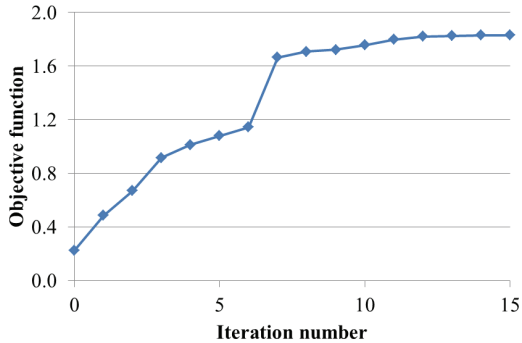

Figure 4.126: Optimization history for simple cubic lattice structure

Table 4.31: Comparison of band-gaps in cubic lattices

	Band gap#	Band gap size(Hz)	Underlying band	
			Mode#	Max.freq.(Hz)
Original undulated design	1	2416.9	15	20083.0
	2	145.0	16	24317.6
Optimal design	1	31.0	12	2371.3
	2	9054.7	15	2484.0

4.8 Compliant mechanism

4.8.1 Design optimization of compliant gripper

This example deals with the synthesis of micro-gripper model. The original coarse design is modeled using 19 quadratic B-spline patches shown in Fig. 4.127a, where a distributed force of $F_{in} = 5n$ is applied on the edge B, where n is the load increment number. Also, a spring of stiffness $k = 10$ is mounted on the tip (point A) to model the Y-directional resistance of the work-piece. The Young's modulus and thickness are respectively selected as $E = 210 \times 10^9$ and $h = 0.01$. To provide a kronecker-delta property at the middle of the edge B where the constraint of input displacement is to be imposed, the edge B is modeled using two B-spline patches so that a junction is located at the middle point. As shown in Fig. 4.127a, 25 design variables $d_1 \sim d_{25}$ are selected as the X- and Y-directional coordinate changes of control points. Symmetric design variations about the $Y = 0$ axis are performed. Using the k-refinement capability of isogeometric method, we construct a refined model for the response and design sensitivity analyses. In order to avoid irregular optimal design, it is necessary to reduce the number of design variables. Thus, the design velocity field is defined first in the coarse mesh model of Fig. 4.127a, and then it is mapped into a fine mesh model through the same k-refinement process. Since the knot insertion and degree-elevation preserve geometry of the CAD model, the design velocity field $\xi \in \Xi \rightarrow \mathbf{V}(\xi) \in \mathbf{R}^3$, where $\Xi \subset \mathbf{R}^1$ defines the NURBS parametric domain, is identical in the coarse and fine mesh model, so that the mapping of design velocity field from the coarse mesh model to fine one can be considered as a linear

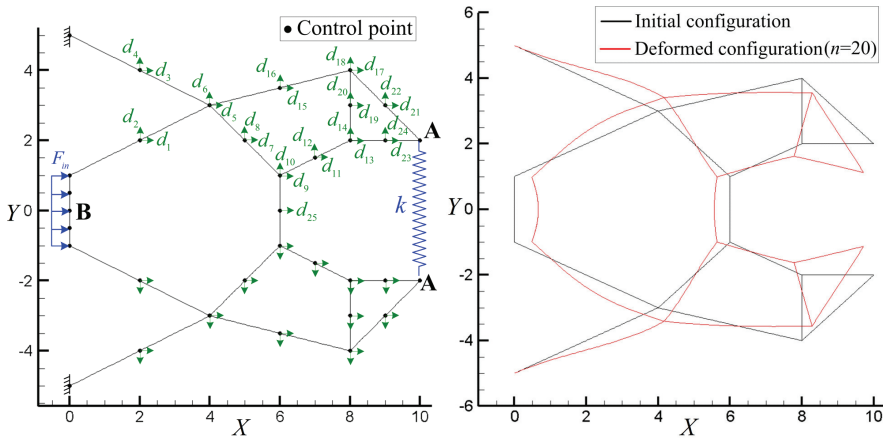

(a) Problem description (b) Deformation analysis

Figure 4.127: Design of micro-gripper

mapping. Fig. 4.127b shows the deformed shape of gripper model at the final load step $n = 20$. The objective of design optimization is to maximize the output force $F_{out} = k|v_{out}|$ where v_{out} denotes the output Y-displacement. Two cases are considered; constraint of X-directional output displacement (case#2) and no constraint on the output X-displacement (case#1). We restrict the input displacement at the middle point of the edge B to avoid structural instability, *i.e.*, snap-through behavior during the nonlinear analysis. Also, in [100], this constraint of maximum input displacement is shown to control the maximum stress level in the mechanism. The allowable volume is limited to the initial volume. Thus, a design optimization problem can be formulated as

$$\text{Maximize } F_{out} = k|v_{out}|, \tag{4.42}$$

$$\text{subject to } V = \int_{\Omega} A ds \le V_0, \tag{4.43}$$

$$u_{in} \le u_{in}^*, \tag{4.44}$$

$$|u_{out}| \le u_{out}^* \text{ (case\#2 only)}, \tag{4.45}$$

and

$$d_i^{lower} \le d_i \le d_i^{upper}, \tag{4.46}$$

where u_{out}^* is the allowable magnitude of the output X-displacement. It is noted again that the output X-displacement constraint of Eq. (4.45) is applied in case#2 only. In this example, the allowable input displacement is $u_{in}^* = 0.8$, and the lower and upper bounds of design variables are respectively $d_i^{lower} = -0.8$ and $d_i^{upper} = 0.8$. Also, the allowable magnitude of output X-displacement is $u_{out}^* = 0.05$. A SQP (Sequential Quadratic Programming) algorithm is utilized for the optimization process. Figs. 4.128a and 4.128b show the optimal designs for case#1 and case#2, respectively, which turn out to be noticeably different. Figs. 4.129a and 4.129b show the

deformed configurations of the optimal designs at the final load step n=20. Compared with the original design in Fig. 4.127b, the magnitude of Y-displacement at the tip significantly increases. Especially in case#2, the output X-displacement is shown to be constrained successfully.

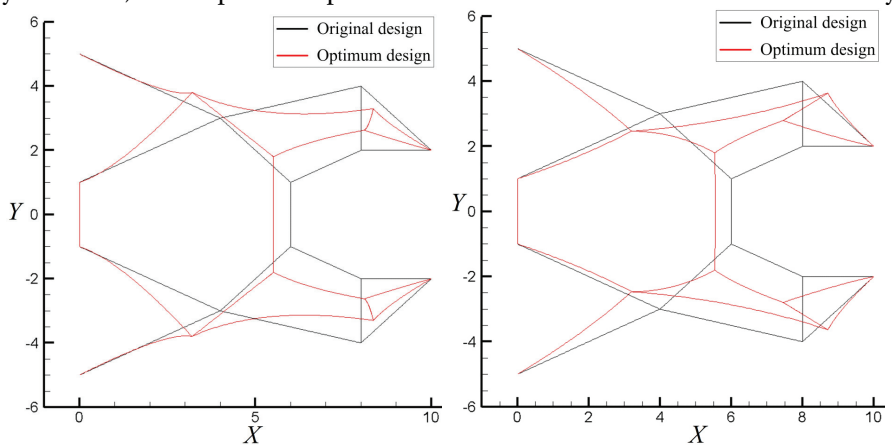

(a) Case#1 (b) Case#2

Figure 4.128: Comparison of optimal designs

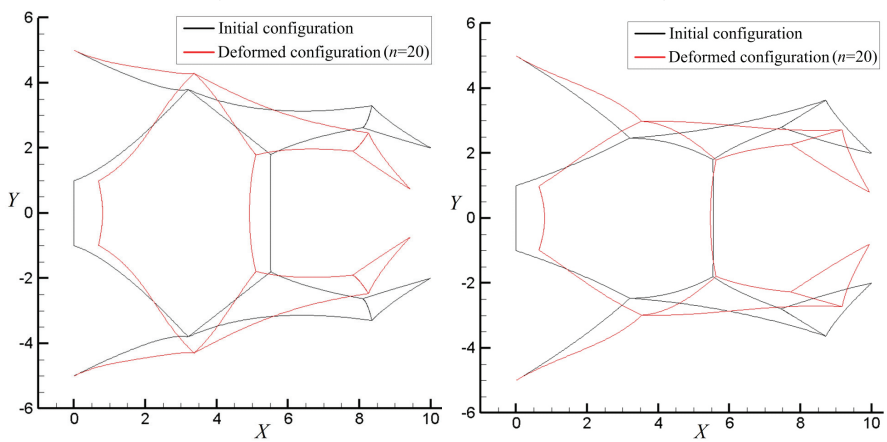

(a) Case#1 (b) Case#2

Figure 4.129: Comparison of deformed shapes

Fig. 4.130 shows the optimization history, which shows the volume constraint g_1 and the input X-displacement constraint g_2.

$$g_1 \equiv V/V_0 - 1 \leq 0, \tag{4.47}$$

$$g_2 \equiv u_{in}/u_{in}^* - 1 \leq 0. \tag{4.48}$$

Also, from the output X-displacement constraint of Eq. (4.45), the following constraint function g_3 is defined as

$$g_3 \equiv -u_{out}/u_{out}^* - 1 \leq 0. \tag{4.49}$$

Since the case#2 has one more constraint than the case#1, the objective function is slightly

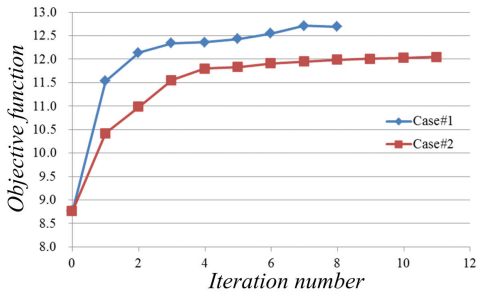

(a) Objective function

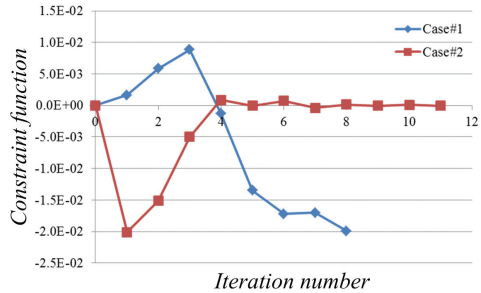

(b) Volume constraint

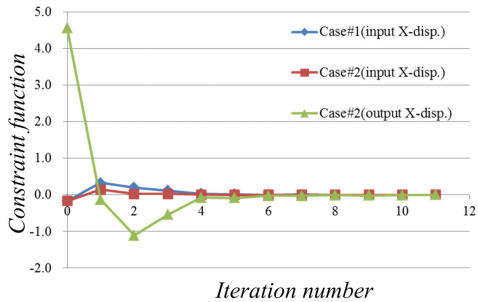

(c) Displacement constraint

Figure 4.130: History of design optimization

less than that of case#1, as shown in Fig. 4.130a. The optimization procedures of all the cases terminate with entire volume and displacement constraints active, as shown in Figs. 4.130b and 4.130c. Fig. 4.131a and 4.131b, respectively, show the convergence of calculated structural

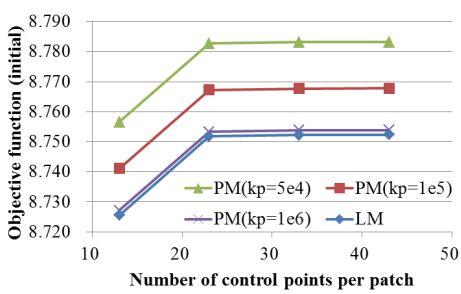

(a) Initial objective function

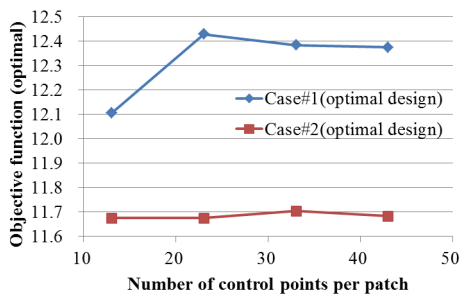

(b) Performance of optimal design

Figure 4.131: Convergence test

performance in the initial and optimal designs, as increasing the number of control points in each of the B-spline patch. Converged results are obtained by using 43 control points, *i.e.*, 40 B-spline element in each patch. In Fig. 4.131a, we observe that as increasing the penalization parameter in the case of using penalization method (PM) to enforce junction continuity, the objective function value in the initial design converges to that of the result from the Lagrange multiplier method (LM).

4.8.2 Design optimization of force inverter

This example deals with synthesis of a force inverter model. We investigate the effect of additional consideration of thickness design. Fig. 4.132a illustrates the original design of force inverter. A spring stiffness $k = 10$ is mounted to model the X-directional resistance of the work-piece. The design objective is to maximize the output force (F_{out}) for a given input force (F_{in}). A square cross-section with thickness $h = 1.2$ is selected, and Young' modulus is $E = 10^9$. The original design is modeled using 15 quadratic B-spline patches, as shown in Fig. 4.132b. Two cases of design parameterization are considered; first, configuration design is considered only (case#1). 14 configuration design variables are selected as the X- and Y-coordinate changes of control points with symmetric design change about $Y = 0$ axis. Second, in addition to the configuration design of case#1, cross-section thickness design is employed. As indicated in Fig. 4.132c, three thickness coefficients are assigned to each of the patches, *i.e.*, $n_{th} = 3$. Then, considering symmetric design variation, globally 15 thickness control coefficients are introduced, that is, 14 configuration design and 15 sizing design variables are simultaneously considered during the optimization process. The Lagrange multiplier method is used to enforce junction continuity. For the deformation and design sensitivity analysis, through k-refinement process, cubic B-spline model with 40 elements per each patch is constructed. The objective of the design

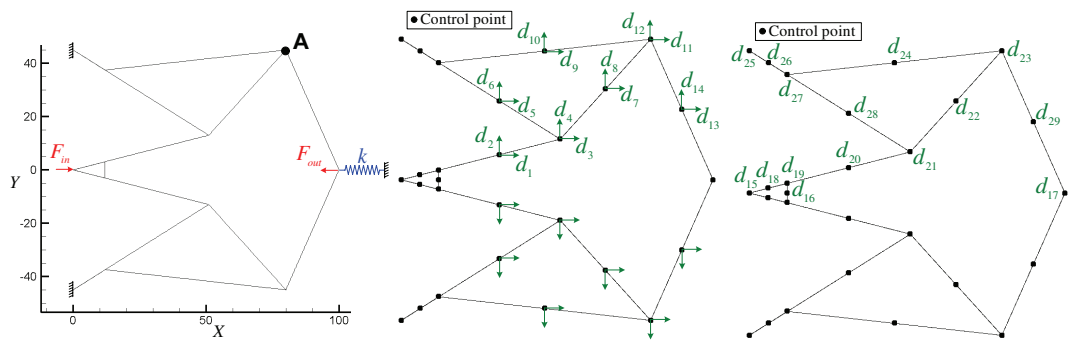

(a) Problem description (b) Configuration design (c) Thickness parameterization

Figure 4.132: Design of force inverting mechanism

optimization is to maximize the output force $F_{out} = k|u_{out}|$ where u_{out} denotes the output X-displacement. As in the previous compliant gripper example, a maximum input displacement constraint (u_{in}) is introduced to avoid snap-through behavior, and control the maximum stress level in the mechanism. Thus, the design optimization problem can be written as

$$\text{Maximize } F_{out} = k|u_{out}|, \tag{4.50}$$

$$\text{subject to } V = \int_{\Omega} A ds \leq V_f V_0, \tag{4.51}$$

$$u_{in} \leq u_{in}^*, \tag{4.52}$$

and

$$d_i^{lower} \leq d_i \leq d_i^{upper}, \tag{4.53}$$

where V_0 and u_{in}^* denote the initial volume, and the maximum input displacement, respectively. d_i (i = 1~29) are the i-th design variable, and d_i^{lower} and d_i^{upper} are the corresponding lower and upper bounds, respectively. The allowable input displacement is selected as u_{in}^* = 10. Also, for the configuration design variables, the lower and upper bounds of design variables are respectively $d_i^{lower} = -15$ and $d_i^{upper} = 15$. For the thickness design variables, $d_i^{lower} = -0.4$ and $d_i^{lower} = 0.4$ are chosen. The allowable volume fraction is selected as V_f = 1. For the optimization procedure, the sequential quadratic programming (SQP) algorithm is utilized. Fig. 4.133a show

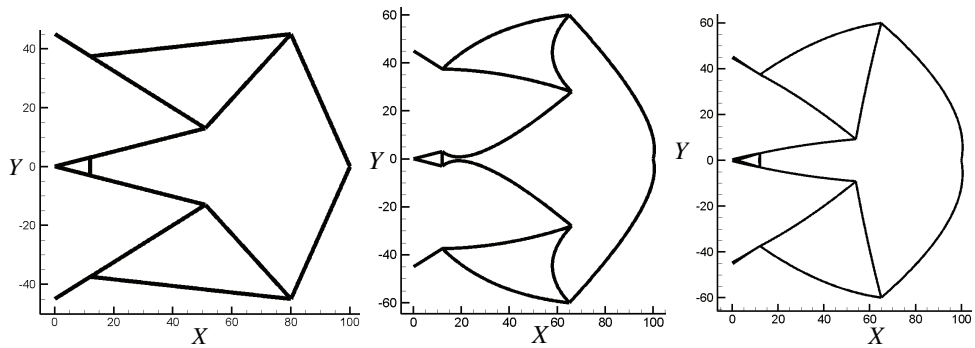

(a) Original design (b) Optimal design(case#1 (c) Optimal design(case#2

Figure 4.133: Optimum design comparison

the original design, and Fig. 4.133b and 4.133c show the optimum designs from the case#1 and #2, respectively. Overall thickness decrease in the optimal design of case#2 is apparent to make it more flexible to deform, except the regions of input port and clamped boundaries for effective load transfer. Fig. 4.134 compares deformations of optimal designs in case#1 and #2. It is obvious that the output displacement significantly increases through the optimizations, and case#2 optimal design shows better performance than that of case#1, and the input displacement is well constrained in both of the optimal designs. Fig. (4.135) shows the optimization history. As additional thickness design is considered (case#2), the objective function increases much larger than that of case #2. In the optimal design of case #1, the volume increases due to curved design, however, in the case #2, as a result, due to the thickness decrease in most parts, the total volume decreases as well. In both cases, input displacement constraints become active in optimal design.

4.8.3 Synthesis of path generating mechanism

The following examples demonstrate the capability of the proposed design algorithm to synthesize path-generating mechanisms for various output paths. The original configuration designs refer to the topologies obtained by using the genetic algorithm in Zhao and Schmiedeler [117]. In the following examples, as displacements at multiple target load steps are included in

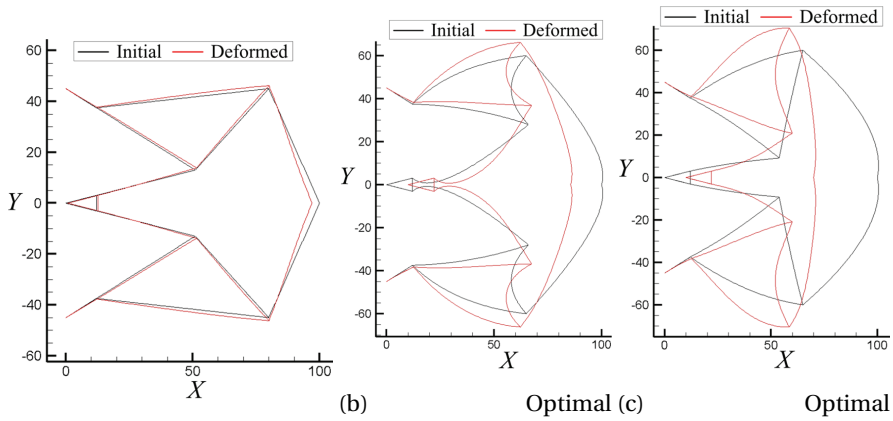

(a) Original design (b) Optimal design(case#1) (c) Optimal design(case#2)

Figure 4.134: Comparison of deformations

the performance measures, the adjoint equation (3.88) is solved at the end of every target load step and the displacement sensitivity (3.90) is evaluated using the adjoint response.

Path generator for straight line

The objective of this example is to design the mechanism that produces a horizontally straight path. The initial design consists of four beams as shown in Fig. 4.136a and the rotational continuity conditions are imposed at the junctions. Each member is represented by a single cubic B-spline patch. A moment loading of $M = -0.0125nEI$ is applied at the end position in Fig. 4.136a, where n is the load increment number. Fig. 4.136c shows the deformed configurations at every load step from n=0 to 20. The deformation path of the tip indicated in Fig. 4.136c is almost straight but our design objective is to produce a horizontally straight path and control the length of path. Three different target lengths of the deformation path are considered; $L^{tar} = 3$ (case#1), $L^{tar} = 4$ (case#2), $L^{tar} = 5$ (case#3). The corresponding target end points are shown in Fig. 4.136a. As shown in Fig. 4.136b, total 18 design variables of $d_1 \sim d_{18}$ are used, corresponding to the X- and Y-directional coordinate changes of the control points in the coarse mesh model. Using the h-refinement capability of isogeometric method, we construct a refined model for the response and design sensitivity analyses, which consists of 40 cubic B-spline elements for member #2~4, and member #1 undergoing rigid body motion during deformations is modeled using a single element. The design velocity field in the coarse model is linearly mapped into that in the refined model using the same h-refinement scheme. To make the deformation path horizontally straight, the objective function is chosen to minimize the magnitude of Y-displacement at the tip, for the selected N target load steps. In this example, every load step in total 20 load steps is selected as a target load step, *i.e.*, N=20. Also, the length of deformation path is controlled using an equality

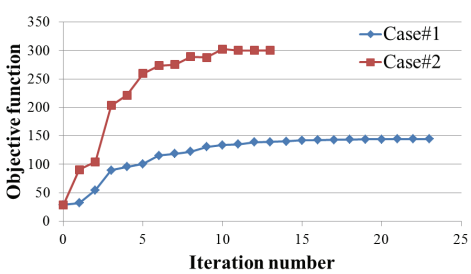

(a) Objective function

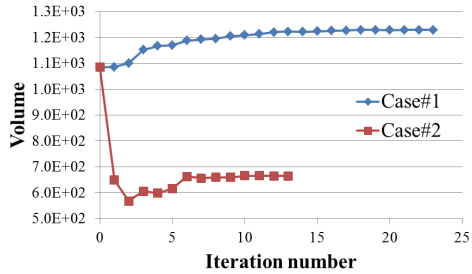

(b) Volume

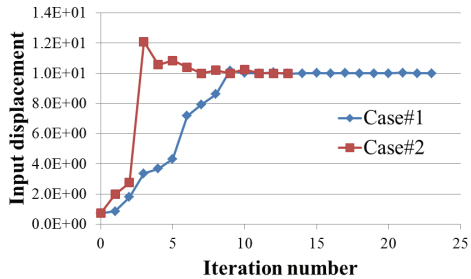

(c) Input displacement

Figure 4.135: Design optimization history

constraint on the X-displacement at the tip. Thus, an optimization problem can be stated as

$$\text{Minimize } \psi = \frac{1}{N}\sum_{I=1}^{N}(v_I^A)^2, \tag{4.54}$$

$$\text{subject to } u_A = L^{tar}, \tag{4.55}$$

and

$$d_i^{lower} \le d_i \le d_i^{upper}, \tag{4.56}$$

where v_I^A denotes the Y-displacement of tip at I-th target load step, and u_A denotes the X-displacement of tip at final deformed configuration, which is utilized to measure the length of deformation path since Y-displacement can be sufficiently suppressed by minimizing the objective function. The objective function ψ represents the average of squared deviation from the straight target path. The lower and upper bounds of design variables are respectively $d_i^{lower} = -4$ and $d_i^{upper} = 4$. A SQP algorithm is utilized for the optimization process. Fig. 4.137 shows the optimal designs for three cases. In each case, the design change at the loaded member is noticeable, which obviously contributes to make the deformation path horizontally straight. Fig. 4.138 shows the deformed configurations at every load step from n=0 to 20 of the optimal design for three cases. In all the cases, the deformation path successfully follows the target path and the length is also controlled sufficiently. Fig. 4.139a shows that the objective function sufficiently decreases for all the cases. Fig. 4.139b shows the X-displacement at the tip, satisfying the target

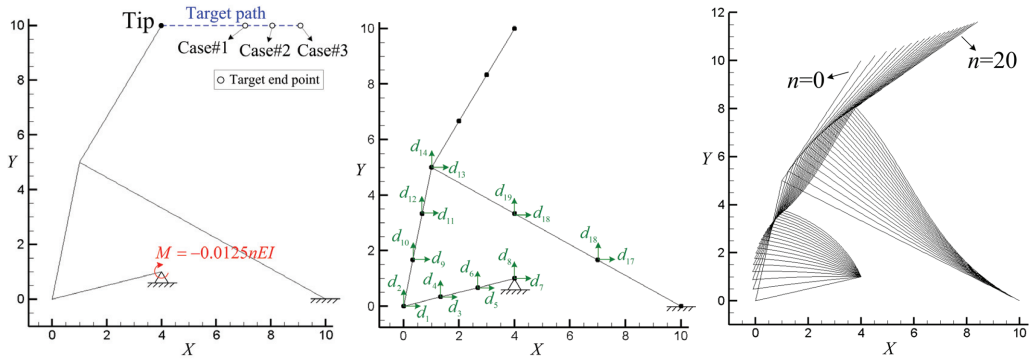

(a) Problem description (b) Design variables (c) Deformation analysis

Figure 4.136: Design of path generator for a straight line

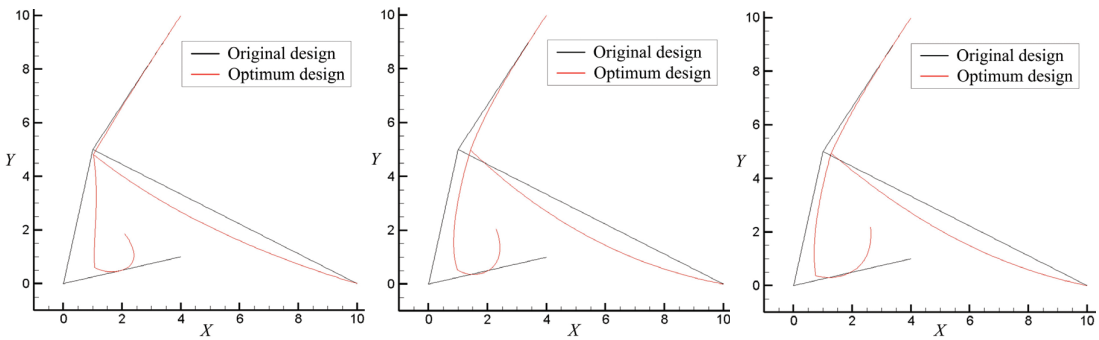

(a) Case#1 (b) Case#2 (c) Case#3

Figure 4.137: Comparison of optimal designs

value by imposing an equality constraint. This means that the target length of deformation path is successfully attained, as the Y-displacement at the tip is suppressed sufficiently through minimizing the objective function. Fig. 4.139c shows the deformation path of the tip for three cases. Although slight deviations from target paths may exist, the optimum configuration designs show remarkable improvement.

Path generator for curved line

Next example is to synthesize a mechanism with output path following a circular arc with center $\mathbf{C}^{tar}$ and radius r^{tar}. As shown in Fig. 4.140a, the original design consists of members #1 and #2, and the rotational continuity condition is imposed at the junction. The members #1 and #2 are modeled by a linear and a cubic B-spline patches, respectively. A follower force $F = 0.15n$ perpendicular to the member #2 at the junction is imposed, as shown in Fig. 4.140a, where n denotes the load increment number. Fig. 4.140c shows the deformed configuration at every load step from n=0 to 20. The deformation path follows the target circular path to some extent in the beginning of the deformation but the deviation gets significantly larger in the end of deformation. Three different target lengths L^{tar} of the deformation path are considered; L^*=4(case#1), L^*=5(case#2), L^*=6(case#3). As shown in Fig. 4.140b, total 14 design variables

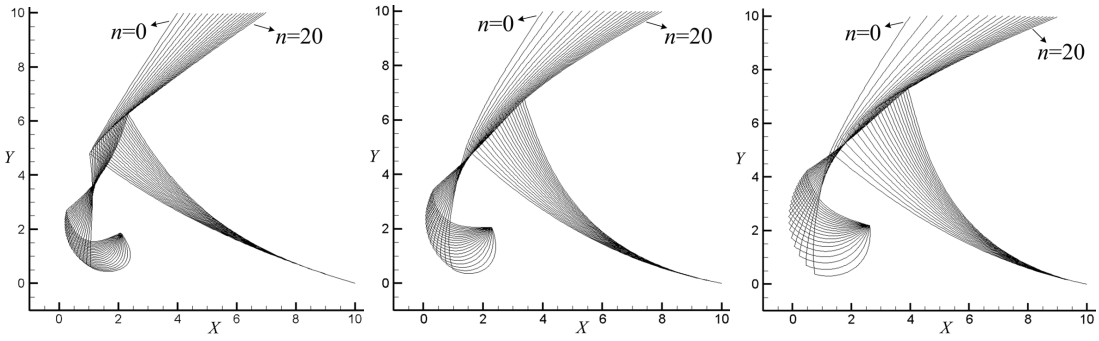

(a) Case#1 (b) Case#2 (c) Case#3

Figure 4.138: Comparison of deformed shapes

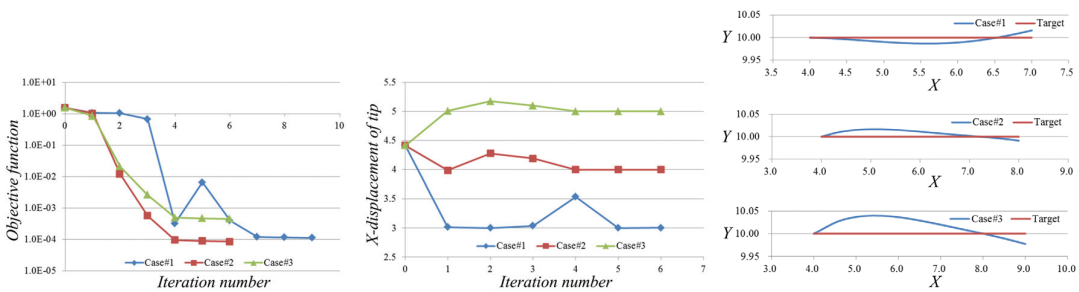

(a) Objective function (b) X-displacement of tip (c) Deformation path

Figure 4.139: Comparison of deformed shapes

$d_1 \sim d_{14}$ are selected as the X- and Y-directional coordinate changes of control points in the coarse model. Fine models of the member #2 having 40 cubic B-spline elements is constructed using the h-refinement schemes, and the member #1 undergoing rigid body motions during deformations is modeled using a single element. By using the same refinement scheme, the design velocity field constructed in the coarse model is linearly mapped into the fine model. In this path generator, the deformed path needs to follow the target circular path so that an objective function is constructed such that the distance between the deformed position of tip and the center of path $\mathbf{C}^{tar} = (3,5)$ is as close as the target radius $r^* = \sqrt{41}$. Also, the length of deformation path should be as close as the target length. The allowable volume is limited to the initial volume. Thus, a multi-objective optimization problem can be stated as

$$\text{Minimize } \psi_2 = \frac{1}{N}\sum_{I=1}^{N}\left(r^{(I)} - r^*\right)^2 + w(\tilde{L} - L^*)^2 \tag{4.57}$$

$$\text{subject to } V = \int_\Omega A ds \le V_0, \tag{4.58}$$

and

$$d_i^{lower} \le d_i \le d_i^{upper}, \tag{4.59}$$

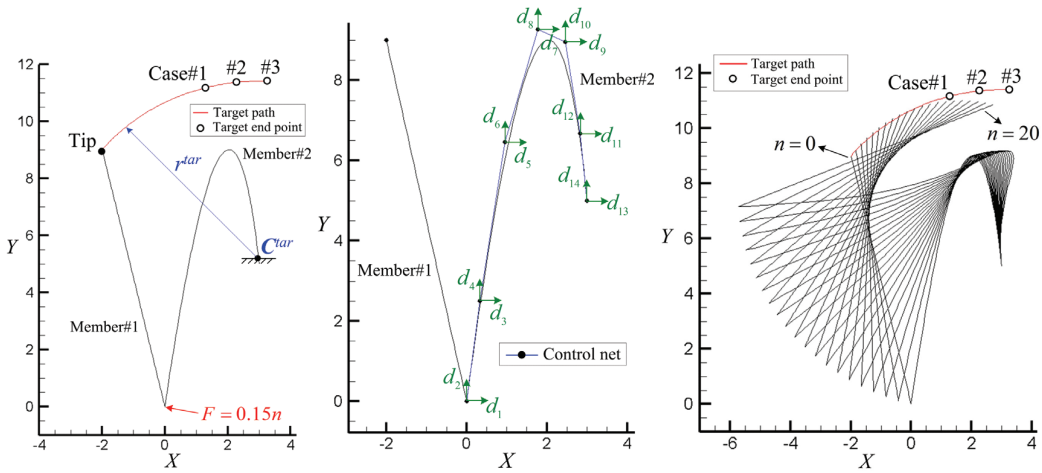

(a) Problem description (b) Design variables (c) Deformation of original design

Figure 4.140: Design of path generator for a curved line

where $r^{(I)} \equiv \left\| \mathbf{X}^{(I)} - \mathbf{C}^* \right\|$, and $\mathbf{X}^{(I)}$ denotes the deformed position of the tip at I-th target load step, and w is a weight. N denotes the number of target load steps. $\tilde{L}$ denotes the piecewise linear approximation of deformation path length, as

$$\tilde{L} = \sum_{I=0}^{N-1} \left\| \mathbf{X}^{(I+1)} - \mathbf{X}^{(I)} \right\|, \tag{4.60}$$

which obviously approaches to the actual length of the deformation path, as N increases. $\mathbf{X}^{(0)}$ denotes the initial position of the tip. The lower and upper bounds of design variables are respectively $d_i^{lower} = -5$ and $d_i^{upper} = 5$. A MMFD (modified method of feasible direction) algorithm is utilized for the optimization process. In all the cases, the weight of the objective function is selected as $w = 0.1$. Fig. 4.141 compares the optimal designs for three cases. In each case, the design change at the loaded member and the movement of clamped position are noticeable. Fig. 4.142 shows the deformed configurations at every load step from n=0 to 20 of the optimal design for three cases. In all the cases, the deformation path successfully follows the target path and the length is also controlled sufficiently. Fig. 4.143 shows the comparison of deformation paths in polar coordinate system whose origin is the center $\mathbf{C}^{tar}$ of target circular path. It turns out that, as shown in Fig. 4.143a, the path of original design is significantly deviated from the target ones which are horizontal straight lines in θ-r plane. The paths are vastly improved through the configuration design optimization processes of case#1~3 as shown in Figs. 4.143b, 4.143c, and 4.143d, respectively. Fig. 4.144a presents that the objective function sufficiently decreases for all the cases. The target length of deformation path is successfully attained for three cases as shown in Fig. 4.144b. Also, the volume decreases in all of the three cases, as shown in Fig. 4.144c.

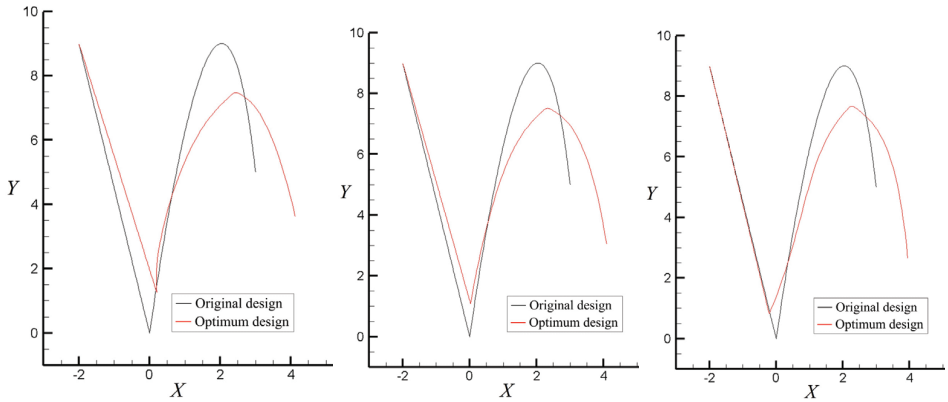

(a) Case#1 (b) Case#2 (c) Case#3

Figure 4.141: Comparison of optimal designs

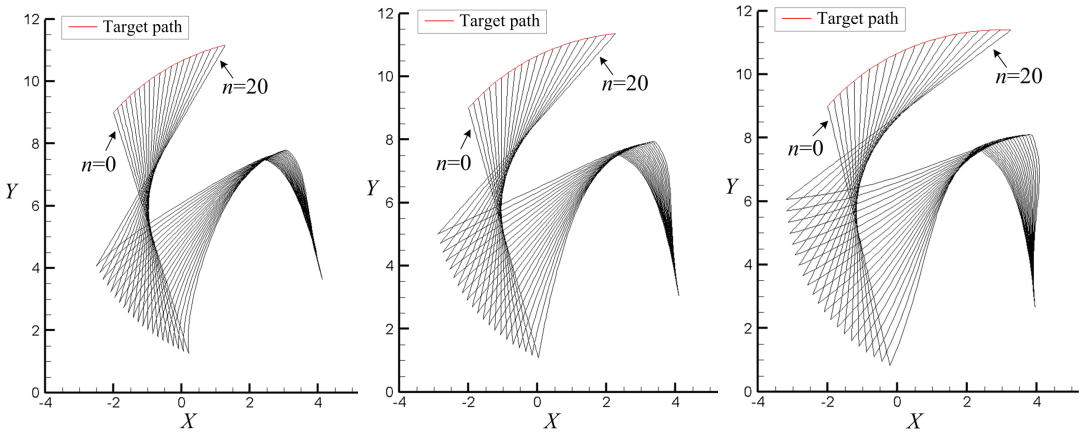

(a) Case#1 (b) Case#2 (c) Case#3

Figure 4.142: Comparison of deformed shapes

4.8.4 Synthesis of angular rotator with prescribed rotation angle

We design an angular rotator that transforms a uni-directional force into angular motion with a prescribed rotation angle. For this kind of angular rotator design, Lin and Shih [67] utilized the SIMP based topology optimization method, where the linear deformation analysis is employed. An original design of this example, shown in Fig. 4.145a refers to the second case optimal topology in [67], from which we perform design optimizations, using the developed adjoint DSA method, to attain target rotation angles. As depicted in Fig. 4.145a, the rotator model has 90° rotational symmetry. Thus, configuration and cross-section thickness design variables are defined in one of the four mechanism units connected to the central square ($d_2 \sim d_{26}$), and the other units are designed by a design parameterization in a way that the original rotational symmetry is maintained. In order to avoid wiggly shapes due to large number of design variables, we parameterize designs using the linear B-spline curve, therefore, straight designs are maintained during optimization procedures. Also, the central square has design dependence such that side

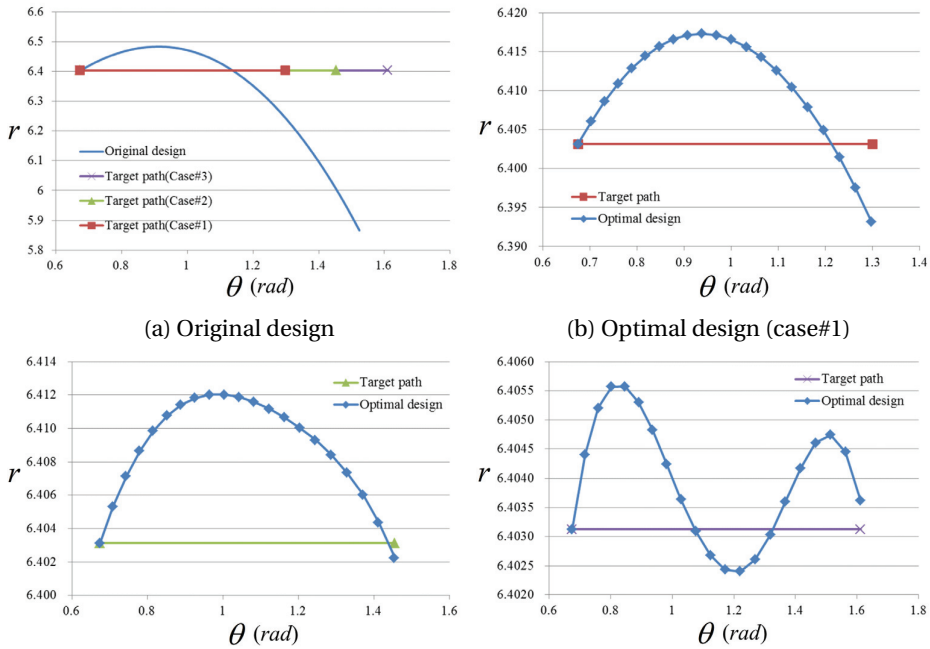

(a) Original design

(b) Optimal design (case#1)

(c) Optimal design (case#2)

(d) Optimal design (case#3)

Figure 4.143: Comparison of deformation paths in polar coordinate system

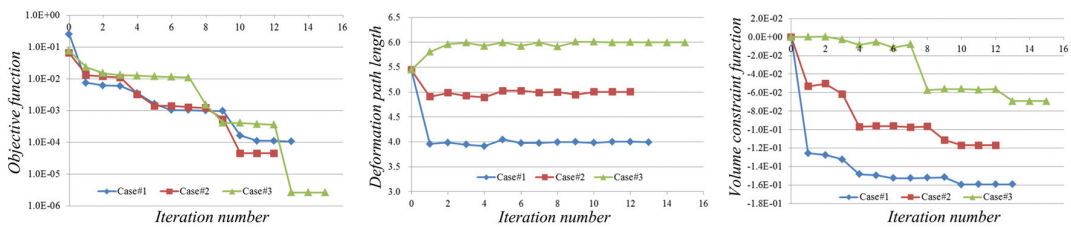

(a) Objective function

(b) Deformation path length

(c) Volume constraint

Figure 4.144: Optimization history

length of the square is controlled by the design variable d_1. It is noted that the positions of displacement and force boundary conditions also have design dependences. Furthermore, cross-section sizing design is also represented by the same control net of linear B-spline curves, that is, thickness distributions are linear interpolation within each of the straight beam members. Thickness of the center square is unchanged during optimizations. Thus, total 14 sizing design variables are utilized. The Young's modulus is $E = 10^9$ for 8 members of center square part and $E = 10^9$ for the others, and the square cross-section shape with uniform thickness $h = 0.5$ is considered in the original design. For the deformation and design sensitivity analysis, through k-refinement process, quartic B-spline model with 40 elements per each patch is constructed. Concentrated forces of magnitude $F = 20n$ are imposed at the four points indicated by red-colored arrows in Fig. 4.145a, which are called, in this example, as input ports. n denotes the load increment number, and $n = 10$ is selected. Each of the four mechanism units are fixed at the two

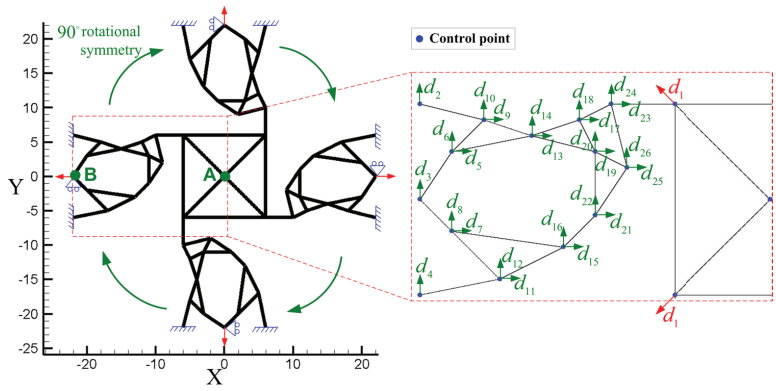

(a) Problem description and configuration design variables

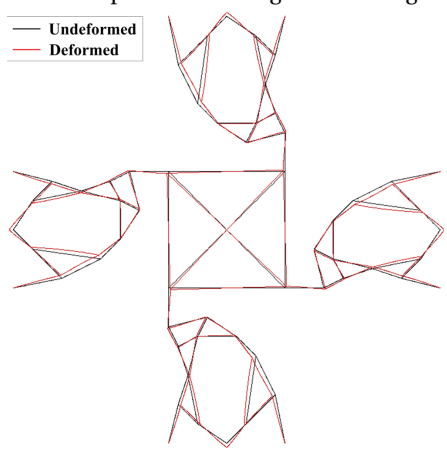

(b) Deformation

Figure 4.145: Design of angular rotator

boundary end points, and the displacements at the input ports are constrained in perpendicular directions of applied forces. Fig. 4.145b shows a deformation of neutral axis. Due to the rotational symmetry of the model geometry and boundary conditions, the deformed configuration also has the same symmetry. It is observed that the central square slightly rotates in the counter-clock wise, and the measured rotation angle at the point A, indicated in Fig. 4.145a, is $\theta_A = 1.4857°$. An optimization problem to attain target rotation angle θ_A^* can be stated as

$$\text{Minimize } \psi_3 = \left|\theta_A - \theta_A^*\right|^2 \tag{4.61}$$

$$\text{subject to } V \equiv \int_\Omega A ds \leq V_0, \tag{4.62}$$

$$u_{in} \leq u_{in}^*, \tag{4.63}$$

and

$$d_i^{lower} \leq d_i \leq d_i^{upper}, \tag{4.64}$$

where we select a target rotation angle $\theta_A^* = 10°$. By exploiting the symmetry, the input displacement constraint can be enforced to only one mechanism unit at the point B, indicated in Fig. 4.145a, and the displacementa at the input port is constrained by $u_{in}^* = -3$. For the side constraints of Eq. (4.64), we select $d_i^{lower} = -1$ and $d_i^{upper} = 1$ for the 26 configuration design variables, and $d_i^{lower} = -0.1$ and $d_i^{upper} = 0.1$ for the 14 sizing design variables. Fig. 4.146a and 4.146b, respectively, shows the neutral axis design change and cross-section thickness distribution. As noted before, the thickness of central square is fixed, and overall parts becomes thinner, which gives much more flexibility. Fig. 4.146c shows the deformation of neutral axis, and it is notable that the central square rotates much larger than that of original design. Fig. 4.147a

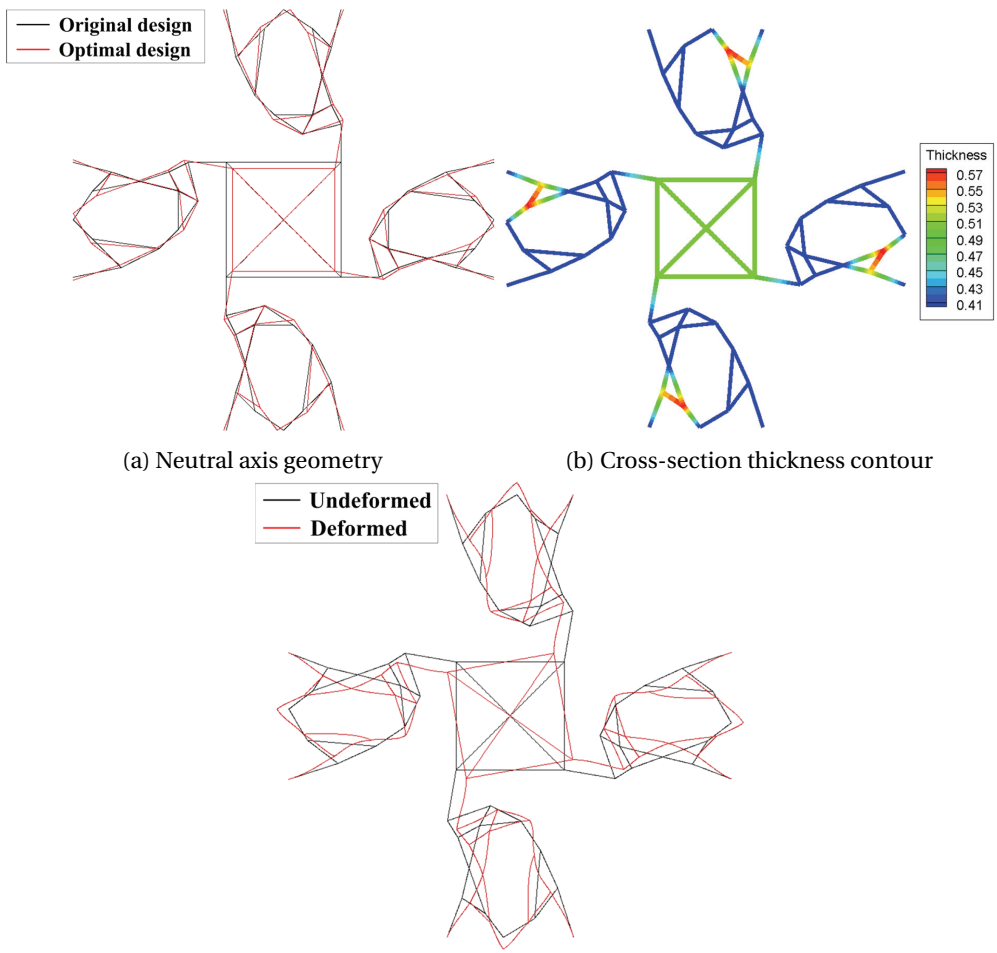

(a) Neutral axis geometry

(b) Cross-section thickness contour

(c) Deformation

Figure 4.146: Optimal design of angular rotator

presents that the target rotation angle $\theta_A^* = 10°$ is successfully attained through a few iterations. Fig. 4.147b and 4.147c show that the input displacement increases, and volume decreases during the optimization.

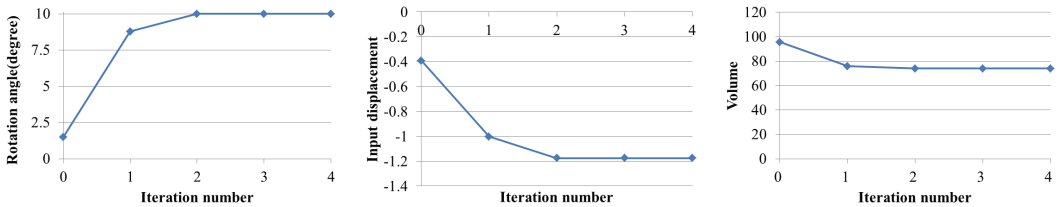

(a) Rotation angle (b) Input displacement (c) Volume

Figure 4.147: Design of angular rotator

4.9 Shape memory polymer-based structures

4.9.1 Design optimization for prescribed Poisson's ratio

Consider a planar lattice structure, in Fig. 4.148a, subjected to a compressive loading of prescribed displacement $d = -0.05n$ where n denotes the load step number. The Young's modulus and thickness are respectively selected as $E = E^f$ and $h = 0.2$, and a square-shaped cross-section is considered. Due to symmetry of analysis model, a quarter model is used as shown in Fig. 4.148b. To impose the symmetric boundary conditions, rotation DOFs are constrained using the penalty method. The rotations at the loading points (red-colored arrows in Figs. 4.148a and 4.148b) are also restrained for the stable imposition of displacement loading conditions. To avoid the influence of boundary conditions when the Poisson's ratio is computed, we investigate the behavior of the central voids indicated by black dots in Fig. 4.148b. Fig. 4.148c represents the overlay of initial configuration and the deformed one at $n = 100$. The auxetic behavior of lateral contraction due to compression is apparently present.

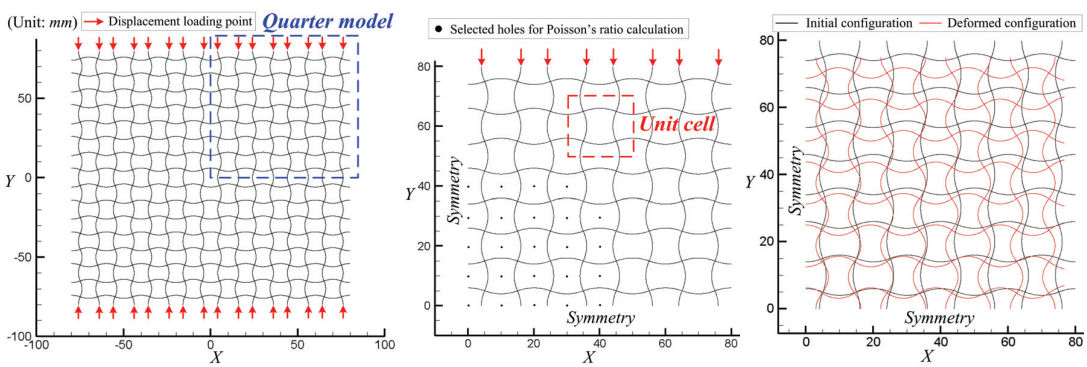

(a) Problem description (b) Quarter model (c) Deformation (n=100)

Figure 4.148: Planar lattice structure

For the design variations of the unit cell indicated in Fig. 4.148b, we consider only a quarter of the unit cell. Three cases of design parametrization are considered, as shown in Figs. 4.149a~4.149c. In case #1, the geometry is represented by a quadratic B-spline. Two design variables are employed; the position changes of control points d_1 and d_2. Using the k-refinement scheme, the refined analysis model composed of 10 uniform knot spans of cubic B-spline for each patch

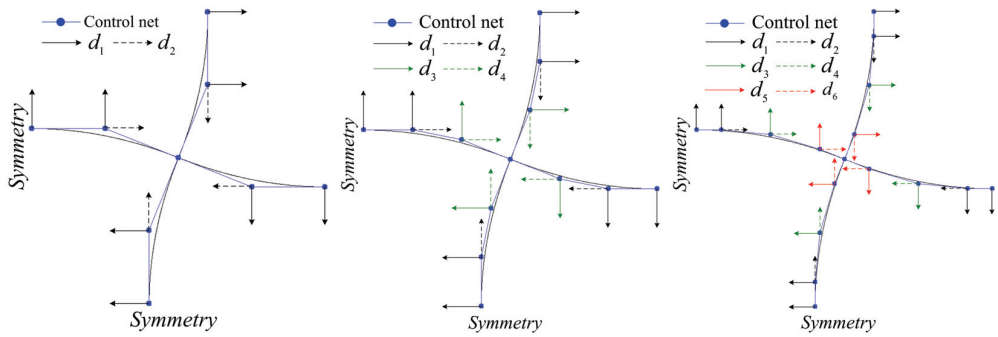

(a) Case #1 (b) Case #2 (c) Case #3

Figure 4.149: Three cases of design variable selections

is constructed. The design velocity field constructed from the coarse model is linearly mapped into the fine mesh model through the same k-refinement process. In each of the cases #2 and #3 in Figs. 4.149b and 4.149c, we utilize a single knot span and uniform two knot spans of cubic B-spline in each patch for geometric modeling, and take four and six design variables, respectively. Using the h-refinement scheme for both cases #2 and #3, we construct the refined analysis models composed of 10 uniform knot spans of cubic B-spline for each patch. Also, the design velocity field generated in the coarse model is linearly mapped into the refined model using the same h-refinement process. In all three cases, to enforce the G^1-continuity, the positions of two adjacent control points in the boundary of quarter part are parametrized. In all the optimization examples, a method of modified feasible direction (MMFD) algorithm is employed. We perform configuration design optimizations to achieve target Poisson's ratios during compressive deformations. Two target Poisson's ratios are selected, as $\nu^* = -0.7$ and $\nu^* = -0.8$. The prescribed displacement is $d = -0.05n$, and the total number of load steps is 100, thus the total prescribed displacement is $d = -5$.

Verification of Poisson's ratio sensitivity

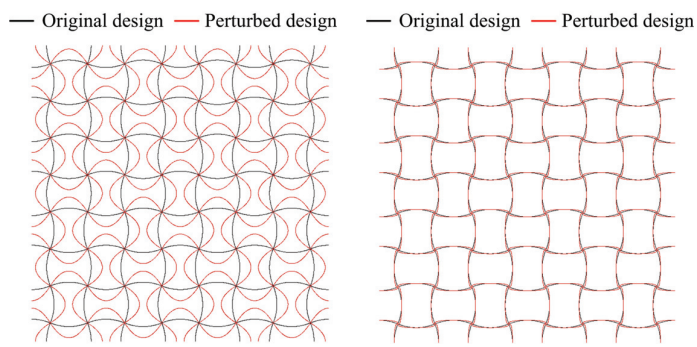

(a) Perturbation of $d_1 = 3$ (b) Perturbation of $d_2 = 3$

Figure 4.150: Design perturbation of lattice structure

Prior to perform the design optimizations, we verify the Poisson's ratio sensitivity by comparison with finite difference one. Figs. 4.150a and 4.150b, respectively, illustrate the design perturbations

of the lattice structure due to the perturbations of two design variables d_1 and d_2 of the case #1. Configuration designs of the lattice structure are parameterized so that the translational periodicity in the original design maintains in the perturbed ones. The Poisson's ratio sensitivity calculated for each of two design variables of the case #1 at every 20^{th} load step from n=20 to 100 is compared with finite difference one (Table 4.32). The analytical sensitivities agree very well with the finite difference ones.

Table 4.32: Verification of Poisson's ratio sensitivity

n	Original response(ν)	Analytic sensitivity d_1(a)	Analytic sensitivity d_2(b)	Finite difference sensitivity d_1(d)	Finite difference sensitivity d_2(e)	Agreement(%) (a)/(d)	Agreement(%) (b)/(e)
20	-0.6721	-3.8046E-02	-5.2370E-02	-3.8040E-02	-5.2370E-02	100.02	100.00
40	-0.6547	-5.5817E-02	-4.9234E-02	-5.5811E-02	-4.9235E-02	100.01	100.00
60	-0.6413	-6.5662E-02	-4.6509E-02	-6.5655E-02	-4.6510E-02	100.01	100.00
80	-0.6305	-7.1443E-02	-4.4137E-02	-7.1436E-02	-4.4138E-02	100.01	100.00
100	-0.6216	-7.4913E-02	-4.2052E-02	-7.4907E-02	-4.2052E-02	100.01	100.00

Configuration design optimization

To achieve the prescribed Poisson's ratio, an optimization problem can be formulated as minimizing the deviation from the prescribed Poisson's ratio at a given strain range: Find the design variable **d** such that

$$\text{Minimize } \psi \equiv \sum_{\mathrm{i}=1}^{\mathrm{NL}} \left|\nu(\mathbf{d};\varepsilon_{\mathrm{i}}) - \nu^*\right|^2, \tag{4.65}$$

$$\text{subject to } \mathrm{V}(\mathbf{d}) \le \mathrm{V_f V_0}, \tag{4.66}$$

and

$$d_i^{lower} \le d_i \le d_i^{upper}, \tag{4.67}$$

where ν denotes the Poisson's ratio. ε_i is the nominal strain at i-th load step and computed by dividing the prescribed displacement at i-th load step by the initial overall height of the quarter part (h = 80). NL denotes the total number of target load steps. We consider all 100 load steps as target ones, *i.e.* NL = 100. V_0 and V_f respectively denote the initial volume and the allowable volume fraction, and V_f = 1.2 is selected. The side constraints, which confine the range of design variable values to avoid excessive design changes, are selected as $d_i^{lower} = -3$ and $d_i^{upper} = 3$. We note that void center position from which the Poisson's ratio is calculated does not have explicit design dependence due to symmetric design variation, in all three cases of design parameterizations. Figs. 4.151a and 4.151b show the nominal strain-Poisson's ratio graphs for the target Poisson's ratios $\nu^* = -0.7$ and -0.8, respectively. In the original design, the Poisson's ratio is around -0.69 at the initial configuration and decreases in its magnitude as deformation proceeds. Through the optimizations, the Poisson's ratios are successfully attained around the target values in both cases $\nu^* = -0.7$ and -0.8 during the deformation processes. Fig. 4.152 and 4.153 respectively show the optimal designs for the two target values.

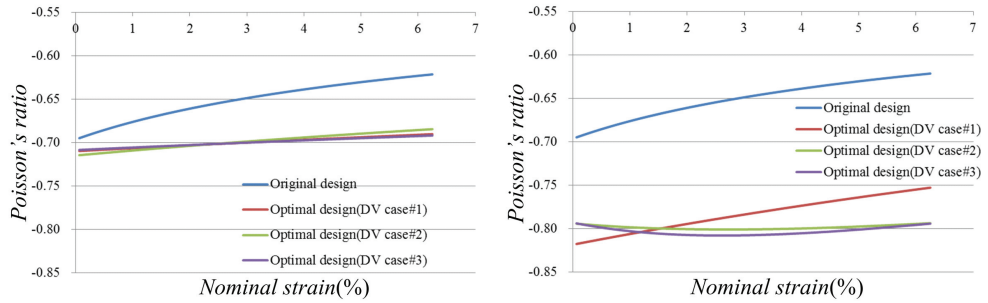

(a) $\nu^* = -0.7$ (b) $\nu^* = -0.8$

Figure 4.151: Poisson's ratio under finite compressive deformation

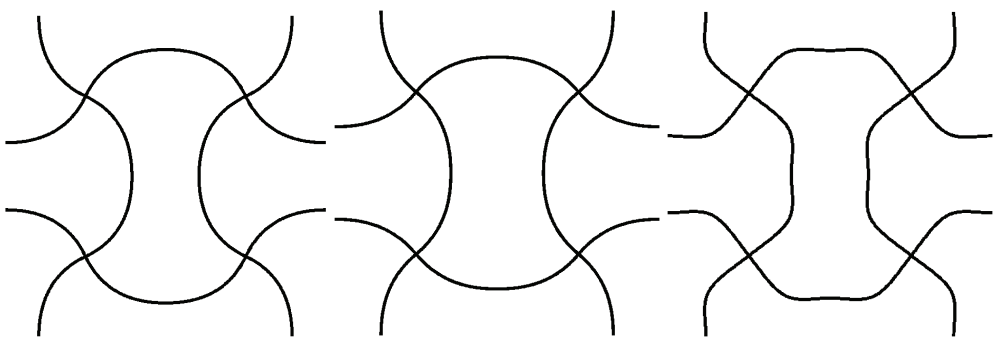

(a) Case#1 (b) Case#2 (c) Case#3

Figure 4.152: Comparison of optimal designs ($\nu^* = -0.7$)

Comparing with the original design of Fig. 4.148, the ligaments in the optimal designs are significantly rotated about the junction to exhibit the extreme auxetic behavior of lateral contraction. Fig. 4.154 and 4.155 show the history of the objective function and volume constraint function during the optimizations. The volume constraint function plotted in Fig. 4.154b and 4.155b represents a normalized quantity of the volume constraint of Eq. (4.66), *i.e.*, $V/V_f V_0 - 1$. As shown in Fig. 4.154a, in the case of $\nu^* = -0.7$, the case #1 (blue) gives a slightly better result than case #2 (red), although the case #2 has more design variables. Also, as shown in Fig. 4.155a, in the case of $\nu^* = -0.8$, the case #2 (red) yields a slightly better result than case #3 (green), even though the case #3 has more design variables. These can be interpreted as a nature of local minima found in the gradient-based optimization algorithm, due to the lack of convexity of the objective function. In the case of $\nu^* = -0.8$, the case #2 (red) and #3 (green) gives much more improvement in the objective function than case #1 (blue). This is due to more rounded shape of ligaments that makes the rotation of ligaments about the junction much easier. Table 4.33 lists the determined values of design variables. Fig. 4.156 compares the deformed configurations of the two cases of optimal designs. For the deformed shapes of optimal designs, the results of design variable case #3 are selected for both of the cases of $\nu^* = -0.7$ and -0.8. Compared with the result of original design in Fig. 4.148c, it is apparent that the lateral contraction due to the compressive loading increases through the optimizations, and also the optimal design of the case $\nu^* = -0.8$

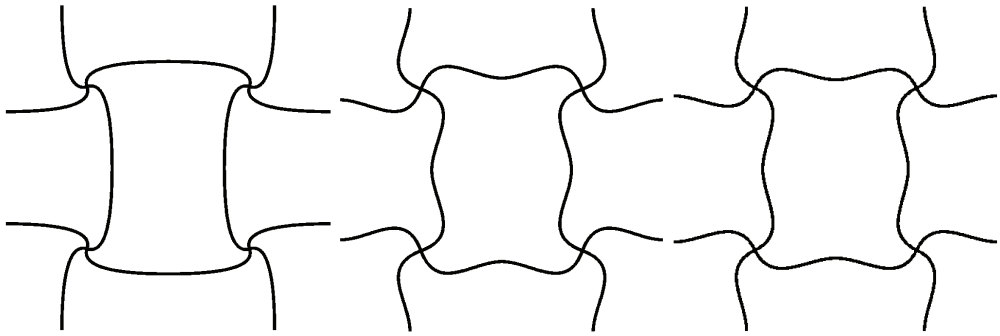

(a) Case#1 (b) Case#2 (c) Case#3

Figure 4.153: Comparison of optimal designs ($\nu^* = -0.8$)

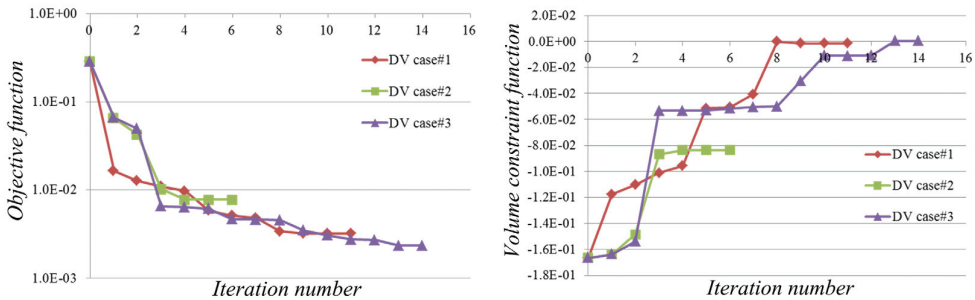

(a) Objective function (b) Volume constraint

Figure 4.154: Comparison of optimization history ($\nu^* = -0.7$)

Table 4.33: Design variables (d_i) in optimal design

Design variable#	$\nu^* = -0.7$			$\nu^* = -0.8$		
	Case #1	Case #2	Case #3	Case #1	Case #2	Case #3
1	1.9064	1.1487	1.6284	0.5455	-0.3260	-0.5005
2	1.1297	0.1474	0.1891	3.0000	0.2011	0.0144
3	-	1.0595	2.2901	-	2.0074	0.3934
4	-	0.2154	0.3747	-	0.6712	0.0903
5	-	-	0.7399	-	-	0.8951
6	-	-	0.0006	-	-	0.2261

shows bigger contraction than that of the case $\nu^* = -0.7$.

4.9.2 Design optimization for prescribed Poisson's ratio during shape recovery

While the shape recovery process of SMP progresses, the effective Poisson's ratio of the structure at each equilibrium configuration can vary due to the configuration change. In this example, two kinds of objectives are considered in the design optimizations. *First*, to attain a constant target Poisson's ratio in a specified temperature range is desired. *Second*, the target Poisson's ratio is set to be linearly proportional to temperature in another specified temperature range. The

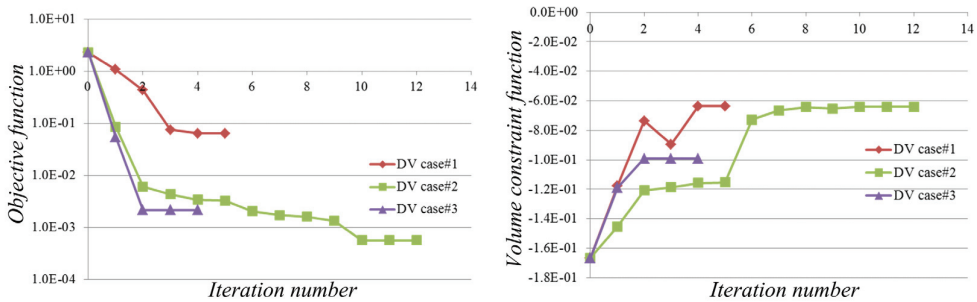

(a) Objective function (b) Volume constraint

Figure 4.155: Comparison of optimization history ($v^* = -0.8$)

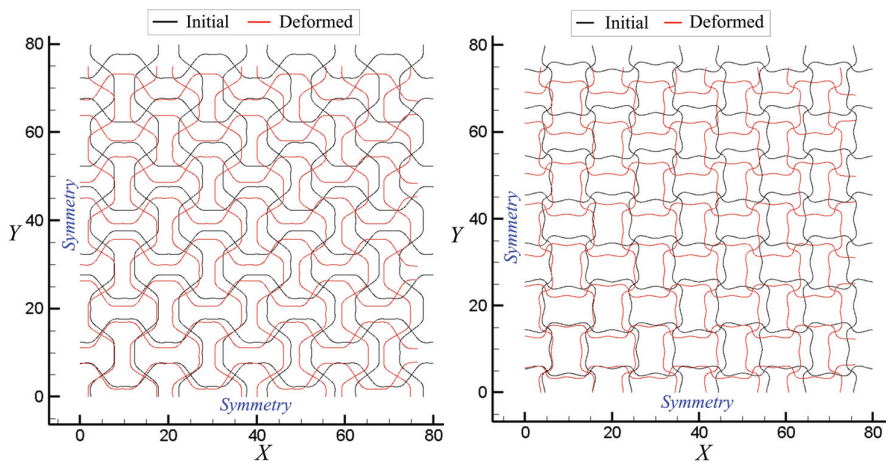

(a) Optimal design ($v^* = -0.7$, case #3) (b) Optimal design ($v^* = -0.8$, case #3)

Figure 4.156: Comparison of deformed configurations (n=100)

same model of Figs. 4.148a and 4.148b as used in the previous example is considered. Fig. 4.157 shows the shape memory and recovery processes. The temperature step size is initially selected as $\Delta T = 1$(K) and adaptively reduced if the iterative scheme has difficulty in convergence within the specified number of iterations. In pre-deformation process (step #1), the displacement loading ($d = -6$) is imposed. The deformed configuration at the high temperature of $T_h = 358K$ is the red-colored one in Fig. 4.157a. Subsequently, with the prescribed displacement fixed, a cooling down process to the low temperature of $T_\ell = 273K$ (step #2) results in a slight configuration change. Then, the displacement loading is removed and a spring-back occurs (step #3), which yields the deformed configuration of black-colored one in Fig. 4.157b. By increasing temperature to $T_h = 358K$, the original configuration can be recovered (step #4). To compute the Poisson's ratio of each equilibrium configuration during the shape recovery step, we need an additional nonlinear analysis, as mentioned before. We apply 10% of the prescribed displacement applied in the pre-deformation process, *i.e.* $d = -0.6$ in each additional nonlinear analysis at the target temperature steps.

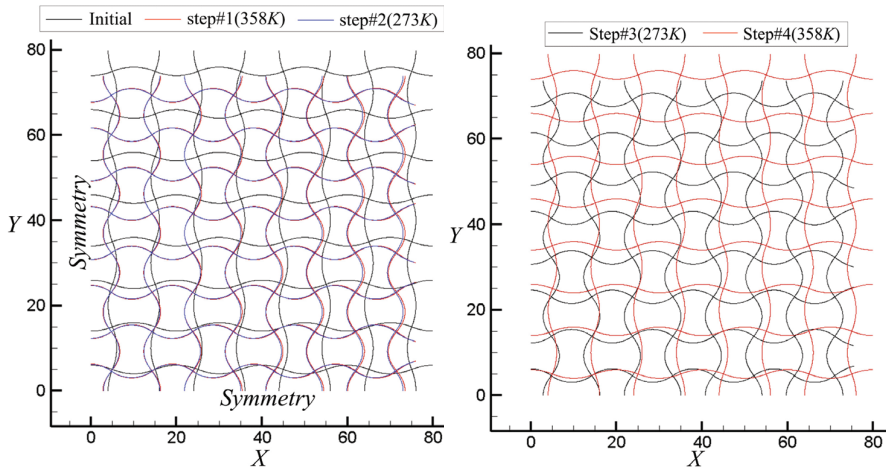

(a) Pre-deformation and cooling

(b) Shape recovery

Figure 4.157: Shape memory and recovery process of NPR structure

Verification of Poisson's ratio sensitivity

We verify the presented formulation to calculate the Poisson's ratio sensitivity by comparing with finite difference one. The design sensitivities for the two design variables in the case #1 in Fig. 4.149a are calculated using the developed method at some temperatures and compared with finite difference ones. For the finite difference sensitivity calculations for the two design variables, the perturbation amount is selected as $d_1 = d_2 = 10^{-4}$. Table 4.34 shows that the analytical sensitivities agree very well with the finite difference ones at all selected temperatures.

Table 4.34: Verification of Poisson's ratio sensitivity

$T(K)$	Original response(ν)	Analytic sensitivity		Finite difference sensitivity		Agreement(%)	
		d_1(a)	d_2(b)	d_1(d)	d_2(e)	(a)/(d)	(b)/(e)
300	-5.6922E-01	-8.7046E-02	-3.8255E-02	-8.7041E-02	-3.8255E-02	100.01	100.00
310	-5.6998E-01	-8.7061E-02	-3.8337E-02	-8.7056E-02	-3.8338E-02	100.01	100.00
320	-5.7150E-01	-8.7039E-02	-3.8521E-02	-8.7034E-02	-3.8521E-02	100.01	100.00
330.1	-5.7551E-01	-8.6726E-02	-3.9081E-02	-8.6721E-02	-3.9081E-02	100.01	100.00
340.1	-5.9487E-01	-8.3187E-02	-4.2014E-02	-8.3181E-02	-4.2014E-02	100.01	100.00
350.1	-6.7736E-01	-2.9846E-02	-5.3603E-02	-2.9841E-02	-5.3604E-02	100.02	100.00

Configuration design optimization

The optimization problem to achieve the target Poisson's ratio at each equilibrium configuration of a specified temperature range can be stated as: Find the design variable **d** such that

$$Minimize\ \psi \equiv \sum_{i=1}^{NT} \left|\nu(\mathbf{d};T_i) - \nu^*(T_i)\right|^2, \tag{4.68}$$

$$subject\ to\ V(\mathbf{d}) \le V_f V_0, \tag{4.69}$$

and

$$d_i^{lower} \le d_i \le d_i^{upper}, \tag{4.70}$$

where T_i denotes the i-th target temperature step, and NT is the total number of target temperature steps. The allowable volume fraction is $V_f = 1.2$. The side constraints are $d_i^{lower} = -3$ and $d_i^{upper} = 3$. As mentioned before, we consider two kinds of objectives. The first one is to select target Poisson's ratio $\nu^* = -0.8$ in the temperature range $T = 300\sim320K$ ($NT = 21$). The second one is to tune the Poisson's ratio by heating. During the shape recovery process, the configuration changes drastically occurs around the glass transition temperature $T_g = 343K$, which can be effectively utilized as a target temperature range to tune the Poisson's ratio, thus, we select two cases of target temperature ranges $T = 340\sim350K$ ($NT = 11$; case A) and $T = 330\sim350K$ ($NT = 21$; case B) where the Poisson's ratio is desired to linearly vary from -0.6 to -0.8. The case A and B respectively corresponds to set $\nu^*_{lin} \equiv \nu^*(T_i) = -0.02(i-1) - 0.6$ and $\nu^*_{lin} \equiv \nu^*(T_i) = -0.01(i-1) - 0.6$ in Eq. (4.68). We note that the glass transition temperature also can be effectively tailored by changing the polymer material parameters, as shown in [72]. The design variable case #3 in Fig. 4.149c is utilized in the optimization of $\nu^* = \nu^*_{lin}$. Fig. 4.158 shows the change of Poisson's ratio during the shape recovery process. The overall magnitude

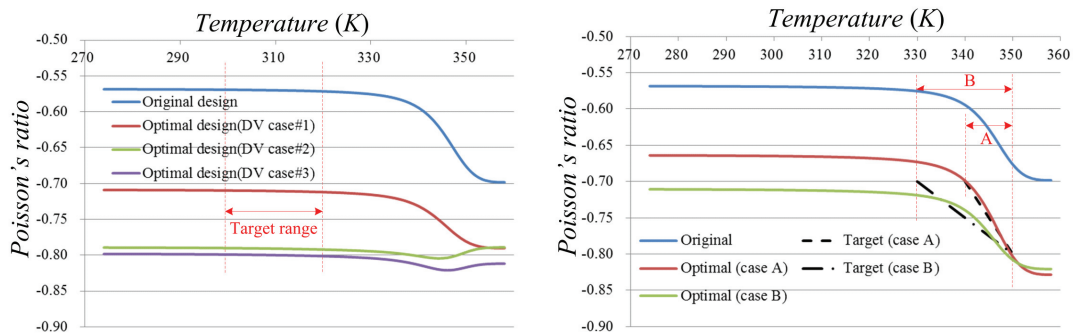

(a) $\nu^* = -0.7$ (b) $\nu^* = -0.8$

Figure 4.158: Comparison of Poisson's ratio change during shape recovery process

of the Poisson's ratio increases through the design optimization. In the case of $\nu^* = -0.8$, as increasing the design DOFs, the Poisson's ratio approaches to the target value more precisely. This also can be observed in the history of objective function, illustrated in Fig. 4.159a. Fig. 4.159b shows the history of volume constraint functions. As noted before, the volume constraint function represents a normalized quantity of the volume constraint of Eq. (4.69), *i.e.*, $V/V_0V_f - 1$. In the case of $\nu^* = -0.8$, the volume increase of the case #3 is less than the other cases, even though it shows the largest performance improvement. In the optimization of $\nu^* = \nu^*_{lin}$, in the target temperature range $T = 340\sim350K$ (case *A*), the Poisson's ratio variation approaches very well to the linear variation between $\nu^* = -0.6$ to -0.8, and shown in Fig. 4.158b and 4.160a. If a longer target temperature range $T = 330\sim350K$ is considered (case *B*), the Poisson's ratio more deviates from the target one than the case *A* as shown in Fig. 4.158b and 4.160a, however, the overall performance improvement is thought to be attained successfully. The determined design variable

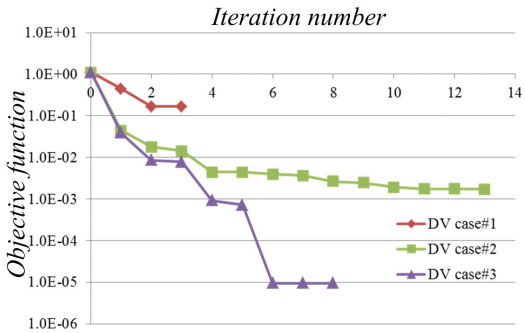

(a) Objective function

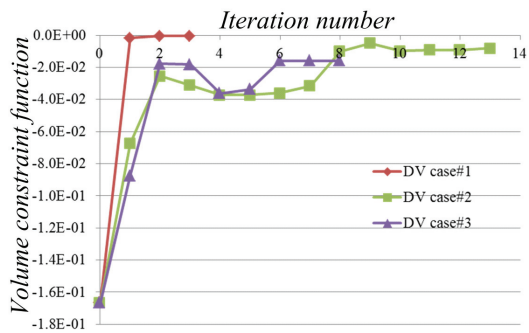

(b) Volume constraint

Figure 4.159: Optimization history ($v^* = -0.8$)

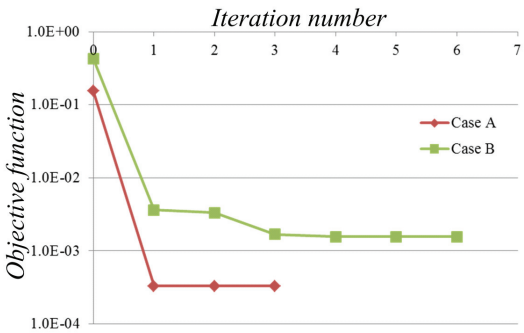

(a) Objective function

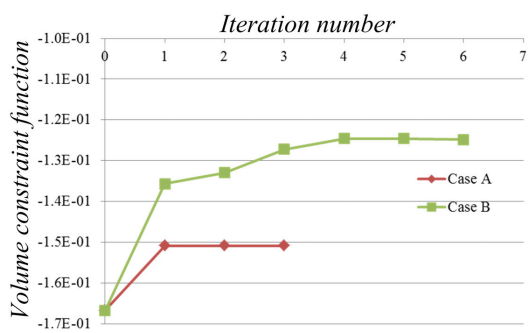

(b) Volume constraint

Figure 4.160: Optimization history ($v^* = v^*_{lin}$)

values are listed in Table 4.35. Fig. 4.161 and 4.162 compares the undeformed configurations of

Table 4.35: Design variables (d_i) in optimal design

Design variable#	$v^* = -0.7$ Case #1	Case #2	Case #3	$v^* = v^*_{lin}$ Target case A	Target case B
1	1.1475	-0.3906	-0.3002	-0.1515	-0.2410
2	3.0000	0.8059	0.1075	0.0030	0.0058
3	-	2.1371	0.1835	0.1472	0.5311
4	-	1.7103	0.3797	0.0446	0.0565
5	-	-	1.5595	0.3927	0.6354
6	-	-	0.7383	0.1237	0.0320

the optimal designs. As observed in the purely elastic material cases in the previous example, more rounded shape of ligaments, especially near the junctions, makes the rotation of ligaments about the junction much easier, and finally results in higher magnitude of the Poisson's ratio.

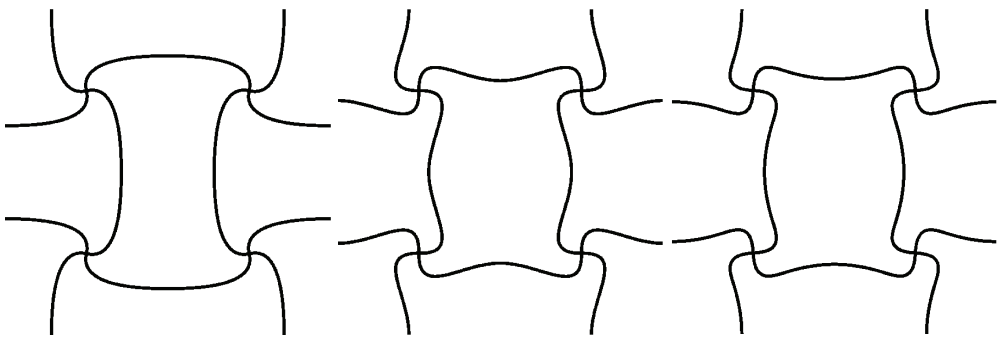

(a) Case#1 (b) Case#2 (c) Case#3

Figure 4.161: Comparison of optimal designs ($v^* = -0.8$)

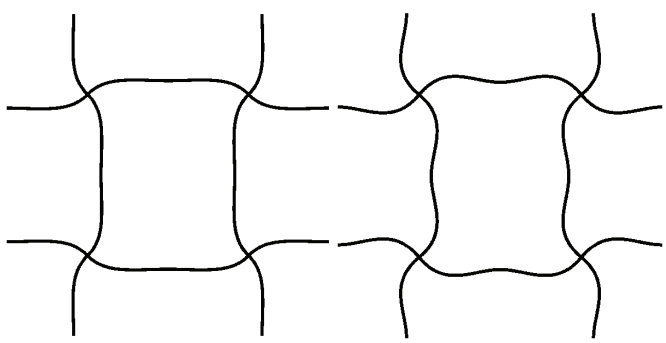

(a) Case A (b) Case B

Figure 4.162: Comparison of optimal designs ($v^* = v^*_{lin}$)

Chapter 5

Conculsions and future works

5.1 Conclusions

The present thesis work contributes to develop a continuum-based adjoint configuration design sensitivity analysis (DSA) method for curved built-up structures undergoing finite deformations. *In deformation analysis point of view*, we investigate basic invariance property of linearized strain measures of a planar shear-deformable beam model and combine the invariant spatial discretization with the selective reduced integration (SRI) and $\bar{B}$ projection method to circumvent shear and membrane locking troubles. Then, three different kinds of nonlinear structural models are considered. *First*, a planar Kirchhoff beam problem is solved using a rotation-free spatial discretization of isogeometric analysis (IGA) approach due to higher order continuity of NURBS basis function. A superiority of IGA in terms of per-DOF(degree-of-freedom) solution accuracy over conventional finite element analysis (FEA) using Hermite basis function is verified. Various inter-patch continuity condition including rotation continuity by Lagrange multiplier and penalization methods are presented. This formulation is combined with a phenomenological shape memory polymer constitutive model where the four steps of the thermomechanical process of SMP structures are simulated. *Second*, for a shear-deformable beam model, a multiplicative update procedure for finite rotation using an exponential map of a skew-symmetric matrix is used. An explicit parameterization method for initial orthonormal frame in spatial curve is presented using the smallest rotation (SR) method within the IGA framework. *Third*, in a shear-deformable shell problem, for a convenient modeling of built-up structures with sharp interface, a rotation field is parameterized by three rotational degrees-of-freedom and a regularized variational principle for drilling stabilization is used. *In the DSA point of view*, we apply the material derivative to the variational equations in order to derive configuration DSA expressions. For the shear-deformable structures, the material derivative of

the orthogonal transformation matrix can be evaluated at final equilibrium configuration, and this enables to calculate design sensitivity at the equilibrium without further iteration. Moreover, we develop a contrained optimization method for beam structures constrained on a curved surfaces, where free-form deformation and global curve interpolation methods are applied to have analytical expression of control point positions on the curved surface, whose material derivative yields precise design velocity field.

We apply the developed DSA and optimization methods in various engineering design problems. *First*, we architect various lattice structures having artificial mechanical properties like auxeticity and phononic band gap. We simultaneously tailor configuration and cross-sectional area to extremize those properties through mathematical optimization. Especially, we experimentally verify the two-dimensional auxetic structures using the 3-D printing technology and optical deformation measurement system, where excellent quantitative agreement of effective Poisson's ratio and displacement field are found. For phononic band gap structures, we basically use the Bloch periodic boundary condition to model an infinitely periodic structure, and the low wave transmission in low frequency region of architected unit cell designs are verified by harmonic response analysis of finite unit cell assemblies. Additionally, we synthesize various compliant mechanisms and shape memory polymer based structures to demonstrate the applicability of the developed method.

5.2 Future works

5.2.1 Design sensitivity analysis of geometrically exact nonlinear structures

We recommend several research directions to extend the current development in the DSA of beam and shell structures. In the current work, the Kirchhoff constraint is applied to planar beam model only, therefore, it would be possible to extend the DSA formulation to three-dimensional Kirchhoff beam and shell structures. A blended approach in Benson et al. [11] which selectively introduces rotational DOF would be effectively utilized for coupling of multiple patches, and this method would be combined with a transformed basis function method in Koo et al. [56] to introduce a rotational DOF at a desired position. We also need further investigations in three-dimensional shear-deformable nonlinear beam and shell models in terms of the additive update of finite rotation, mixed formulation to alleviate shear and membrane locking troubles, and objectivity of strain measures in discretized problem [30].

- **Configuration DSA of three-dimensional Kirchhoff beam and shell structures**
- **Selective introduction of rotational DOF for multipatch coupling**
- **Imposition of Kronecker-delta property using transformed basis function**
- **Additive rotation update and locking treatment**
- **Discussion on objectivity of strain measures in discretized problem**

In this thesis, for beam structures, we consider only square, retangular, and circular shaped cross-sections, and their cross-section areas are employed as design variables. However, cross-section orientation has a rotational design degree-of-freedom about a neutral axis tangent vector. Also, a distribution of material property like Young's modulus would be controlled during optimal design process. Furthermore, in many applications, the contact interactions between structural members may have significant effects on the structural performances, for examples, ligaments in energy-absorbing lattice strucures may undergo self-contact interactions where friction induced energy dissipation could be crucial. Thus, incorporation of contact constraint would be very interesting and give a possibility of increasing the applicability and practicality of the proposed designs. Thus, we suggest the following research subjects.

- **Consideration of more general beam cross-section geometries including T-, L-, and I-sections in deformation analysis,**
- **Sizing design variables could be a rotational design DOF of beam cross-section about tangent vector, and beam and shell material distribution parameters,**
- **Incorporation of a frictional self-contact model for nonlinear beam and shell structures.**

5.2.2 Applications in design of practical built-up structures

Auxetic lattice structures are versatile in many engineering applications including design of ship and offshore structures. For example, deck structure of car carrying ship requires low weight and enhanced impact resistance. Thus, we suggest the following future work.

- **Nonlinear transient dynamic analysis of plate structures with auxetic cores,**
- **Investigation of significances of auxeticity in practical engineering designs,**
- **Experimental validation of negative Poisson's ratio in three-dimensional auxetic lattice structures.**

Also, design of jacket support structure of offshore platform for maximum fundamental frequency would be a possible application candidate. We suggest

- **Design sensitivity analysis of post-buckled jacket structures,**
- **Maximization of fundamental frequency of pre-loaded structures,**
- **Optimal layout design of curved hull stiffeners.**

Appendix A

Supplements to the geometrically exact Kirchhoff beam model

A.1 Linearization of virtual bending strain

For future use, we derive the first variation of $1/(1+\varepsilon_m)$ using Eq. (2.72), as

$$\delta\left(\frac{1}{1+\varepsilon_m}\right) = -\frac{\delta\varepsilon_m}{(1+\varepsilon_m)^2} = -\frac{1}{(1+\varepsilon_m)^2}\widehat{\mathbf{E}}(\bar{\mathbf{z}})^T\mathbf{T}_1. \tag{A.1}$$

Taking the first variation of Eq. (2.60) and using the chain rule of differentiation, followed by using Eq. (A.1) and the fact that $\widehat{\mathbf{E}}(\bar{\mathbf{z}})^T\mathbf{T}_1$ is a scalar quantity such that $\widehat{\mathbf{E}}(\bar{\mathbf{z}})^T\mathbf{T}_1 = \mathbf{T}_1{}^T\widehat{\mathbf{E}}(\bar{\mathbf{z}})$, we have

$$\begin{aligned}
\delta\mathbf{T}_1 &= \delta\left(\frac{1}{1+\varepsilon_m}\right)\mathbf{E} + \frac{1}{1+\varepsilon_m}\delta\mathbf{E} \\
&= -\frac{1}{1+\varepsilon_m}\mathbf{T}_1\mathbf{T}_1{}^T\widehat{\mathbf{E}}(\bar{\mathbf{z}}) + \frac{1}{1+\varepsilon_m}\widehat{\mathbf{E}}(\bar{\mathbf{z}}) \\
&= \left\{\frac{1}{1+\varepsilon_m}(\mathbf{I}-\mathbf{T}_1\mathbf{T}_1{}^T)\right\}\widehat{\mathbf{E}}(\bar{\mathbf{z}}) \equiv \boldsymbol{\Gamma}\widehat{\boldsymbol{E}}(\bar{\mathbf{z}}),
\end{aligned} \tag{A.2}$$

where $\mathbf{I}$ is the identity matrix, and $\boldsymbol{\Gamma}$ is symmetric. Recalling the definition of $\mathbf{T}_1$ and $\tilde{\mathbf{T}}_1$,

$$\left.\begin{aligned}
\mathbf{T}_1 &\equiv [T_{11}, T_{12}, 0]^T \\
\tilde{\mathbf{T}}_1 &\equiv [T_{12}, -T_{11}, 0]^T
\end{aligned}\right\}$$

we can write the relation between $\mathbf{T}_1$ and $\tilde{\mathbf{T}}_1$ as

$$\tilde{\mathbf{T}}_1 = \begin{bmatrix} 0 & 1 & 0 \\ -1 & 0 & 0 \\ 0 & 0 & 0 \end{bmatrix} \mathbf{T}_1 \equiv \tilde{\mathbf{I}}\mathbf{T}_1. \tag{A.3}$$

Using Eqs. (A.2) and (A.3), the following is obtained.

$$\delta\tilde{\mathbf{T}}_1 = \tilde{\mathbf{I}}\delta\mathbf{T}_1 = \tilde{\mathbf{I}}\boldsymbol{\Gamma}\widehat{\mathbf{E}}(\bar{\mathbf{z}}). \tag{A.4}$$

Using the chain rule of differentiation, Eqs. (A.1) and (A.4), we have the following.

$$-\delta\left(\frac{1}{1+\varepsilon_m}\tilde{\mathbf{T}}_1{}^T\right) = -\delta\left(\frac{1}{1+\varepsilon_m}\right)\tilde{\mathbf{T}}_1{}^T - \frac{1}{1+\varepsilon_m}\delta\tilde{\mathbf{T}}_1{}^T = \frac{1}{(1+\varepsilon_m)^2}\widehat{\mathbf{E}}(\bar{\mathbf{z}})^T\mathbf{T}_1\tilde{\mathbf{T}}_1{}^T + \frac{1}{1+\varepsilon_m}\widehat{\mathbf{E}}(\bar{\mathbf{z}})^T\boldsymbol{\Gamma}\tilde{\mathbf{I}}. \tag{A.5}$$

$\mathbf{T}_1\tilde{\mathbf{T}}_1{}^T$ in Eq. (A.5) can be rewritten, using the fact that $\|\mathbf{T}_1\| = 1$ and the definition of $\boldsymbol{\Gamma}$ (A.2), as

$$\mathbf{T}_1\tilde{\mathbf{T}}_1{}^T = -\tilde{\mathbf{I}}(\mathbf{I} - \mathbf{T}_1\mathbf{T}_1{}^T) = -(1+\varepsilon_m)\tilde{\mathbf{I}}\boldsymbol{\Gamma}. \tag{A.6}$$

Then, substituting Eq. (A.6) into Eq. (A.5) yields

$$-\delta\left(\frac{1}{1+\varepsilon_m}\tilde{\mathbf{T}}_1{}^T\right) = \widehat{\mathbf{E}}(\bar{\mathbf{z}})^T\left\{\frac{1}{1+\varepsilon_m}(\boldsymbol{\Gamma}\tilde{\mathbf{I}} - \tilde{\mathbf{I}}\boldsymbol{\Gamma})\right\} \equiv \widehat{\mathbf{E}}(\bar{\mathbf{z}})^T\mathbf{D}_2, \tag{A.7}$$

where $\mathbf{D}_2$ is symmetric since $\boldsymbol{\Gamma}$ is symmetric and $\tilde{\mathbf{I}}$ is skew-symmetric. Using Eq. (A.7) and the relation of (A.3), we have the following.

$$\delta\left(\frac{1}{1+\varepsilon_m}\mathbf{T}_1{}^T\right) = -\widehat{\mathbf{E}}(\bar{\mathbf{z}})^T\mathbf{D}_2\tilde{\mathbf{I}}. \tag{A.8}$$

Using Eq. (A.6) and the fact that $\tilde{\mathbf{I}}$ is skew-symmetric, we have the following relation.

$$\boldsymbol{\Gamma}\tilde{\mathbf{I}} - \tilde{\mathbf{I}}\boldsymbol{\Gamma} = (\tilde{\mathbf{T}}_1\mathbf{T}_1{}^T + \mathbf{T}_1\tilde{\mathbf{T}}_1{}^T)/(1+\varepsilon_m). \tag{A.9}$$

We derive the expression for the incremental form of $\mathbf{D}_2$ of (A.7) multiplied by $\mathbf{E}_{,s}$, using the chain rule of differentiation and Eq. (A.9), as

$$\begin{aligned}
\Delta\mathbf{D}_2\mathbf{E}_{,s} &= \left\{\Delta\left(\frac{1}{1+\varepsilon_m}\right)(\boldsymbol{\Gamma}\tilde{\mathbf{I}} - \tilde{\mathbf{I}}\boldsymbol{\Gamma}) + \frac{1}{1+\varepsilon_m}\Delta(\boldsymbol{\Gamma}\tilde{\mathbf{I}} - \tilde{\mathbf{I}}\boldsymbol{\Gamma})\right\}\mathbf{E}_{,s} \\
&= \Delta\left(\frac{1}{1+\varepsilon_m}\right)(\boldsymbol{\Gamma}\tilde{\mathbf{I}} - \tilde{\mathbf{I}}\boldsymbol{\Gamma})\mathbf{E}_{,s} + \frac{1}{1+\varepsilon_m}\Delta\left\{\frac{1}{1+\varepsilon_m}(\tilde{\mathbf{T}}_1\mathbf{T}_1{}^T + \mathbf{T}_1\tilde{\mathbf{T}}_1{}^T)\right\}\mathbf{E}_{,s} \\
&= \Delta\left(\frac{1}{1+\varepsilon_m}\right)(\boldsymbol{\Gamma}\tilde{\mathbf{I}} - \tilde{\mathbf{I}}\boldsymbol{\Gamma})\mathbf{E}_{,s} + \Delta\left(\frac{1}{1+\varepsilon_m}\right)\left\{\frac{1}{1+\varepsilon_m}(\tilde{\mathbf{T}}_1\mathbf{T}_1{}^T + \mathbf{T}_1\tilde{\mathbf{T}}_1{}^T)\right\}\mathbf{E}_{,s} \\
&+ \frac{1}{(1+\varepsilon_m)^2}\Delta(\mathbf{T}_1\tilde{\mathbf{T}}_1{}^T + \tilde{\mathbf{T}}_1\mathbf{T}_1{}^T)\mathbf{E}_{,s}.
\end{aligned} \tag{A.10}$$

Using Eq. (A.9) again, and using Eq. (A.1) with $\bar{\mathbf{z}}$ replaced with $\Delta\mathbf{z}$, as following the same differentiation process, and using the chain rule of differentiation yield

$$\begin{aligned}\Delta\mathbf{D}_2\mathbf{E}_{,s} &= 2\Delta\left(\frac{1}{1+\varepsilon_m}\right)(\boldsymbol{\Gamma}\tilde{\mathbf{I}}-\tilde{\mathbf{I}}\boldsymbol{\Gamma})\mathbf{E}_{,s}+\frac{1}{(1+\varepsilon_m)^2}\Delta(\mathbf{T}_1\tilde{\mathbf{T}}_1{}^T+\tilde{\mathbf{T}}_1\mathbf{T}_1{}^T)\mathbf{E}_{,s}\\ &= \left(-\frac{2}{(1+\varepsilon_m)^2}\widehat{\mathbf{E}}(\Delta\mathbf{z})^T\mathbf{T}_1\right)(\boldsymbol{\Gamma}\tilde{\mathbf{I}}-\tilde{\mathbf{I}}\boldsymbol{\Gamma})\mathbf{E}_{,s}\\ &+\frac{1}{(1+\varepsilon_m)^2}(\Delta\mathbf{T}_1\tilde{\mathbf{T}}_1{}^T+\mathbf{T}_1\Delta\tilde{\mathbf{T}}_1{}^T+\Delta\tilde{\mathbf{T}}_1\mathbf{T}_1{}^T+\tilde{\mathbf{T}}_1\Delta\mathbf{T}_1{}^T)\mathbf{E}_{,s}. \end{aligned}\tag{A.11}$$

Using the definition of $\mathbf{D}_2$ (A.7) and following the same differentiation process of Eqs. (A.2) and (A.4) for $\Delta\mathbf{T}_1$ and $\Delta\tilde{\mathbf{T}}_1$, respectively, we have the following.

$$\begin{aligned}\Delta\mathbf{D}_2\mathbf{E}_{,s} &= \left[\left\{-\frac{2}{1+\varepsilon_m}\mathbf{D}_2\mathbf{E}_{,s}\mathbf{T}_1{}^T\right\}+\left\{\frac{1}{(1+\varepsilon_m)^2}(\tilde{\mathbf{T}}_1{}^T\mathbf{E}_{,s}\boldsymbol{\Gamma}+\mathbf{T}_1\mathbf{E}_{,s}{}^T\boldsymbol{\Gamma}\tilde{\mathbf{I}}+\mathbf{T}_1{}^T\mathbf{E}_{,s}\tilde{\mathbf{I}}\boldsymbol{\Gamma}+\tilde{\mathbf{T}}_1\mathbf{E}_{,s}{}^T\boldsymbol{\Gamma})\right\}\right]\widehat{\mathbf{E}}(\Delta\mathbf{z})\\ &\equiv \mathbf{D}_1\widehat{\mathbf{E}}(\Delta\mathbf{z}).\end{aligned}\tag{A.12}$$

Using the chain rule of differentiation and the fact that the Δ operation commutes with the tangential derivative, the incremental form of the virtual bending strain (2.74) is expressed as

$$\Delta\widehat{\omega}_b(\mathbf{z};\bar{\mathbf{z}}) = \widehat{\mathbf{E}}(\bar{\mathbf{z}})^T\Delta\mathbf{D}_2\mathbf{E}_{,s}+\widehat{\mathbf{E}}(\bar{\mathbf{z}})^T\mathbf{D}_2\{\widehat{\mathbf{E}}(\Delta\mathbf{z})\}_{,s}-\{\widehat{\mathbf{E}}(\bar{\mathbf{z}})\}_{,s}^T\Delta\{\tilde{\mathbf{T}}_1/(1+\varepsilon_m)\}.\tag{A.13}$$

Finally, substituting Eq. (A.12) into (A.13) and following the same differentiation process of Eq. (A.7) for $\Delta\{\tilde{\mathbf{T}}_1/(1+\varepsilon_m)\}$, we have

$$\Delta\widehat{\omega}_b(\mathbf{z};\bar{\mathbf{z}}) = \widehat{\mathbf{E}}(\bar{\mathbf{z}})^T\mathbf{D}_1\widehat{\mathbf{E}}(\Delta\mathbf{z})+\widehat{\mathbf{E}}(\bar{\mathbf{z}})^T\mathbf{D}_2\{\widehat{\mathbf{E}}(\Delta\mathbf{z})\}_{,s}+\{\widehat{\mathbf{E}}(\bar{\mathbf{z}})\}_{,s}^T\mathbf{D}_2\widehat{\mathbf{E}}(\Delta\mathbf{z})\equiv\widehat{\eta}_b({}^n\mathbf{z};\Delta\mathbf{z},\bar{\mathbf{z}}).\tag{A.14}$$

A.2 Penalty method for rotation continuity constraint

We derive the expression of the increment of $\boldsymbol{\Gamma}$, as follows. By taking derivative of $\boldsymbol{\Gamma}$ in Eq. (A.2), and using Eq. (A.2) again, we have the following.

$$\Delta\boldsymbol{\Gamma} = -\frac{1}{1+\varepsilon_m}\left\{\ \boldsymbol{\Gamma}\mathbf{T}_1{}^T\widehat{\mathbf{E}}(\Delta\mathbf{z})+\boldsymbol{\Gamma}\widehat{\mathbf{E}}(\Delta\mathbf{z})\mathbf{T}_1{}^T+\mathbf{T}_1\widehat{\mathbf{E}}(\Delta\mathbf{z})^T\boldsymbol{\Gamma}\ \right\}.\tag{A.15}$$

Then, by multiplying $\mathbf{T}_1^d$ to both sides of Eq. (A.15), and using the fact that $\mathbf{T}_1{}^T\widehat{\mathbf{E}}(\Delta\mathbf{z})$, $\mathbf{T}_1{}^T\mathbf{T}_1^d$ and $\widehat{\mathbf{E}}(\Delta\mathbf{z})^T\boldsymbol{\Gamma}\boldsymbol{T}_1^d$ are scalar quantities, we have the following expression.

$$\Delta\boldsymbol{\Gamma}\boldsymbol{T}_1^d = -\frac{1}{1+\varepsilon_m}\left\{\mathrm{sym}(\boldsymbol{\Gamma}\mathbf{T}_1^{\mathrm{d}}\mathbf{T}_1{}^{\mathrm{T}})+\boldsymbol{\Gamma}\mathbf{T}_1{}^{\mathrm{T}}\mathbf{T}_1^{\mathrm{d}}\right\}\widehat{\mathbf{E}}(\Delta\mathbf{z}),\tag{A.16}$$

where $\mathrm{sym}(\bullet)\equiv(\bullet)+(\bullet)^{\mathrm{T}}$.

A.3 A proof of membrane strain and rotation continuity

Proposition. *For initially G^2-continuous model with C^0-continuous displacement field, a condition of C^1-continuous displacement component vector is sufficient and necessary for continuous membrane strain and rigid body rotation.*

Proof. If rigid body rotation ($\mathbf{T} = \underset{\sim}{\mathbf{T}}$) and membrane strain ($\varepsilon_m = \underset{\sim}{\varepsilon}_m$) are continuous, by the relation of (2.60),

$$\mathbf{E} = \underset{\sim}{\mathbf{E}}. \tag{A.17}$$

Using G^2-continuity ($k = \underset{\sim}{k}$) and C^0-continuity ($\mathbf{z} = \underset{\sim}{\mathbf{z}}$) conditions, combining Eqs. (A.17) and (2.65) yield

$$\mathbf{z}_{,s} = \underset{\sim}{\mathbf{z}}_{,\underset{\sim}{s}}, \tag{A.18}$$

which represents that the displacement component vector is C^1-continuous. Conversely, if the displacement component vector is C^1-continuous ($\mathbf{z}_{,s} = \underset{\sim}{\mathbf{z}}_{,\underset{\sim}{s}}$), using Eq. (2.65), the G^2-continuity ($k = \underset{\sim}{k}$) and C^0-continuity ($\mathbf{z} = \underset{\sim}{\mathbf{z}}$) conditions give

$$\mathbf{E} = \underset{\sim}{\mathbf{E}}. \tag{A.19}$$

Combining Eqs. (A.19) and (2.55) leads to the condition of continuous membrane strain

$$\varepsilon_m = \underset{\sim}{\varepsilon}_m. \tag{A.20}$$

Also, combining Eqs. (A.19), (A.20), (2.60), and (2.66) gives the condition of continuous rigid body rotation

$$\mathbf{T} = \underset{\sim}{\mathbf{T}}. \tag{A.21}$$

A.4 Material derivative of initial curvature

Using Eq. (3.21) with ${}^{n+1}\mathbf{z}_{,s}$ replaced by $\mathbf{j}_{123,s}$, we have

$$(\mathbf{j}_{123,s})^{\cdot} = \{(\mathbf{j}_{123})^{\cdot}\}_{,s} - \mathbf{j}_{123,s}\nabla_s \cdot \hat{\mathbf{V}}. \tag{A.22}$$

Substituting Eqs. (2.51) and (3.11) into Eq. (A.22) yields

$$(\dot{\mathbf{\Omega}}_0 + \mathbf{\Omega}_0 \mathbf{V}_\Theta{}^T)\mathbf{j}_{123} = (\mathbf{V}_{\Theta,s}{}^T + \mathbf{V}_\Theta{}^T \mathbf{\Omega}_0 - \mathbf{\Omega}_0 \nabla_s \cdot \hat{\mathbf{V}})\mathbf{j}_{123}. \tag{A.23}$$

Using Eqs. (2.52) and (3.14), the following relation can be derived.

$$\mathbf{V}_\Theta{}^T \mathbf{\Omega}_0 = \mathbf{\Omega}_0 \mathbf{V}_\Theta{}^T. \tag{A.24}$$

Therefore, multiplying $\mathbf{j}_{123}{}^{-1}$ to both sides of Eq. (A.23), and using the relation of (A.24) give

$$\dot{\mathbf{\Omega}}_0 = \mathbf{V}_{\Theta,s}{}^T - \mathbf{\Omega}_0 \nabla_s \cdot \hat{\mathbf{V}}. \tag{A.25}$$

Also, by substituting Eq. (2.64) into Eq. (A.25) and using the fact that $\mathbf{V}_\Theta$ is skew-symmetric, we have

$$\dot{k} = -(\mathbf{V}_\Theta)_{12,s} - k\nabla_s \cdot \hat{\mathbf{V}}. \tag{A.26}$$

A.5 Material derivative of bending strain

By taking the material derivative of Eq. (2.71) and following the same differentiation process of Eq. (A.7) for $\{\tilde{\mathbf{T}}_1/(1+\varepsilon_m)\}^\cdot$, and using Eqs. (3.24) , (3.27), we have

$$\begin{aligned}
\dot{\omega}_b &= -\left(\frac{1}{1+\varepsilon_m}\tilde{\mathbf{T}}_1{}^T\right)^\cdot \mathbf{E}_{,s} - \frac{1}{1+\varepsilon_m}\tilde{\mathbf{T}}_1{}^T(\mathbf{E}_{,s})^\cdot \\
&= \mathbf{E}_{,s}{}^T\mathbf{D}_2\dot{\mathbf{E}} - \frac{1}{1+\varepsilon_m}\tilde{\mathbf{T}}_1{}^T\left\{\{\widehat{\mathbf{E}}({}^{n+1}\dot{\mathbf{z}})\}_{,s} + \{\mathbf{E}_V({}^{n+1}\mathbf{z})\}_{,s} - \mathbf{E}_{,s}\nabla_s\cdot\hat{\mathbf{V}}\right\} \\
&= \left[\mathbf{E}_{,s}{}^T\mathbf{D}_2\widehat{\mathbf{E}}({}^{n+1}\dot{\mathbf{z}}) - \frac{1}{1+\varepsilon_m}\tilde{\mathbf{T}}_1{}^T\{\widehat{\mathbf{E}}({}^{n+1}\dot{\mathbf{z}})\}_{,s}\right] + \left[\mathbf{E}_{,s}{}^T\mathbf{D}_2\mathbf{E}_V({}^{n+1}\mathbf{z}) - \frac{1}{1+\varepsilon_m}\tilde{\mathbf{T}}_1{}^T\left\{\{\mathbf{E}_V({}^{n+1}\mathbf{z})\}_{,s} - \mathbf{E}_{,s}\nabla_s\cdot\hat{\mathbf{V}}\right\}\right] \\
&\equiv \widehat{\omega}_b({}^{n+1}\dot{\mathbf{z}}) + \omega_b^V({}^{n+1}\mathbf{z}).
\end{aligned} \tag{A.27}$$

Taking the material derivative of Eq. (2.74) and following the same differentiation process of Eqs. (A.12) and (A.7) for $\dot{\mathbf{D}}_2\mathbf{E}_{,s}$ and $\{\tilde{\mathbf{T}}_1/(1+\varepsilon_m)\}^\cdot$, respectively, yield

$$\begin{aligned}
\dot{\hat{\omega}}_b &= \{\widehat{\mathbf{E}}(\bar{\mathbf{z}})^T\}^\cdot\mathbf{D}_2\mathbf{E}_{,s} + \widehat{\mathbf{E}}(\bar{\mathbf{z}})^T\dot{\mathbf{D}}_2\mathbf{E}_{,s} + \widehat{\mathbf{E}}(\bar{\mathbf{z}})^T\mathbf{D}_2(\mathbf{E}_{,s})^\cdot - \left(\frac{1}{1+\varepsilon_m}\tilde{\mathbf{T}}_1{}^T\right)^\cdot\{\widehat{\mathbf{E}}(\bar{\mathbf{z}})\}_{,s} - \frac{1}{1+\varepsilon_m}[\{\widehat{\mathbf{E}}(\bar{\mathbf{z}})\}_{,s}^T]^\cdot\tilde{\mathbf{T}}_1 \\
&= \{\widehat{\mathbf{E}}(\bar{\mathbf{z}})^T\}^\cdot\mathbf{D}_2\mathbf{E}_{,s} + \widehat{\mathbf{E}}(\bar{\mathbf{z}})^T\mathbf{D}_1\dot{\mathbf{E}} + \widehat{\mathbf{E}}(\bar{\mathbf{z}})^T\mathbf{D}_2(\mathbf{E}_{,s})^\cdot + \dot{\mathbf{E}}^T\mathbf{D}_2\{\widehat{\mathbf{E}}(\bar{\mathbf{z}})\}_{,s} - \frac{1}{1+\varepsilon_m}[\{\widehat{\mathbf{E}}(\bar{\mathbf{z}})\}_{,s}^T]^\cdot\tilde{\mathbf{T}}_1.
\end{aligned} \tag{A.28}$$

Finally, substituting Eqs. (3.24) and (3.27) with ${}^{n+1}\mathbf{z}$ replaced by $\bar{\mathbf{z}}$ gives

$$\begin{aligned}
\dot{\hat{\omega}}_b &= \left[\{\widehat{\mathbf{E}}(\dot{\bar{\mathbf{z}}})\}^T\mathbf{D}_2\mathbf{E}_{,s} - \frac{1}{1+\varepsilon_m}\{\widehat{\mathbf{E}}(\dot{\bar{\mathbf{z}}})\}_{,s}^T\tilde{\mathbf{T}}_1\right] + \left[\widehat{\mathbf{E}}(\bar{\mathbf{z}})^T\mathbf{D}_1\widehat{\mathbf{E}}({}^{n+1}\dot{\mathbf{z}}) + \widehat{\mathbf{E}}(\bar{\mathbf{z}})^T\mathbf{D}_2\{\widehat{\mathbf{E}}({}^{n+1}\dot{\mathbf{z}})\}_{,s} + \{\widehat{\mathbf{E}}(\bar{\mathbf{z}})\}_{,s}^T\mathbf{D}_2\widehat{\mathbf{E}}({}^{n+1}\dot{\mathbf{z}})\right] \\
&\quad + \left[\begin{array}{l} \mathbf{E}_V(\bar{\mathbf{z}})^T\mathbf{D}_2\mathbf{E}_{,s} + \widehat{\mathbf{E}}(\bar{\mathbf{z}})^T\mathbf{D}_1\mathbf{E}_V({}^{n+1}\mathbf{z}) + \widehat{\mathbf{E}}(\bar{\mathbf{z}})^T\mathbf{D}_2\left\{\{\mathbf{E}_V({}^{n+1}\mathbf{z})\}_{,s} - \mathbf{E}_{,s}\nabla_s\cdot\hat{\mathbf{V}}\right\} \\ \quad + \{\widehat{\mathbf{E}}(\bar{\mathbf{z}})\}_{,s}^T\mathbf{D}_2\mathbf{E}_V({}^{n+1}\mathbf{z}) - \frac{1}{1+\varepsilon_m}\{\mathbf{E}_V(\bar{\mathbf{z}})\}_{,s}^T\tilde{\mathbf{T}}_1 + \frac{1}{1+\varepsilon_m}\{\widehat{\mathbf{E}}(\bar{\mathbf{z}})\}_{,s}^T\nabla_s\cdot\hat{\mathbf{V}}\tilde{\mathbf{T}}_1 \end{array}\right] \\
&\equiv \widehat{\omega}_b({}^{n+1}\mathbf{z},\dot{\bar{\mathbf{z}}}) + \widehat{\eta}_b({}^{n+1}\mathbf{z};{}^{n+1}\dot{\mathbf{z}},\bar{\mathbf{z}}) + \bar{\omega}_b^V({}^{n+1}\mathbf{z};\bar{\mathbf{z}}).
\end{aligned} \tag{A.29}$$

A.6 Design dependence of Hermite basis functions

Cubic Hermite basis functions are given by

$$\left.\begin{array}{ll} N_1^H = \frac{1}{4}(\xi^3 - 3\xi + 2), & N_2^H = \frac{1}{4}\left(\frac{h_e}{2}\right)(\xi^3 - \xi^2 - \xi + 1) \\ N_3^H = \frac{1}{4}(-\xi^3 + 3\xi + 2), & N_4^H = \frac{1}{4}\left(\frac{h_e}{2}\right)(\xi^3 + \xi^2 - \xi - 1) \end{array}\right\}, \tag{A.30}$$

where h_e is the element length parameter. Taking material derivative of Eq. (A.30) gives

$$\left.\begin{array}{ll} \dot{N}_1^H = 0, & \dot{N}_2^H = \frac{1}{4}\left(\frac{\dot{h}_e}{2}\right)(\xi^3 - \xi^2 - \xi + 1) \\ \dot{N}_3^H = 0, & \dot{N}_4^H = \frac{1}{4}\left(\frac{\dot{h}_e}{2}\right)(\xi^3 + \xi^2 - \xi - 1) \end{array}\right\}. \tag{A.31}$$

We derive the material derivative of element length parameter in Hermite basis functions, using the analytical expression of element length parameter in [3].

$$h_e = \sqrt{\frac{c^2 - 12a}{b - 12}}, \tag{A.32}$$

and

$$\left.\begin{array}{l} a \equiv \left\| \mathbf{r}^2 - \mathbf{r}^1 \right\|^2 \\ b \equiv \left\| \mathbf{t}^2 - \mathbf{t}^1 \right\|^2 \\ c \equiv (\mathbf{r}^2 - \mathbf{r}^1) \cdot (\mathbf{t}^2 - \mathbf{t}^1) \end{array}\right\}, \tag{A.33}$$

where $\mathbf{r}^i$ and $\mathbf{t}^i$ are the i-th nodal position and tangential vectors, respectively. Taking the material derivatives of Eqs. (A.32) and (A.33), we have the following.

$$\dot{h}_e = \frac{2c\dot{c} - 12\dot{a} - {h_e}^2 \dot{b}}{2h_e(b - 12)}, \tag{A.34}$$

and

$$\left.\begin{array}{l} \dot{a} = 2(\hat{\mathbf{V}}^2 - \hat{\mathbf{V}}^1) \cdot (\mathbf{r}^2 - \mathbf{r}^1) \\ \dot{b} = 2(\hat{\mathbf{V}}_t^2 - \hat{\mathbf{V}}_t^1) \cdot (\mathbf{t}^2 - \mathbf{t}^1) \\ \dot{c} = (\hat{\mathbf{V}}^2 - \hat{\mathbf{V}}^1) \cdot (\mathbf{t}^2 - \mathbf{t}^1) + (\mathbf{r}^2 - \mathbf{r}^1) \cdot (\hat{\mathbf{V}}_t^2 - \hat{\mathbf{V}}_t^1) \end{array}\right\}, \tag{A.35}$$

where $\hat{\mathbf{V}}^i$ and $\hat{\mathbf{V}}_t^i$ denote the design velocity of i-th nodal position and tangential vectors, respectively.

Appendix B

Supplements to the geometrically exact shear-deformable beam model

B.1 Directional derivative of pressure load vector

We derive directional derivatives of base vectors $\mathbf{a_1}$, $\mathbf{a_2}$, and $\mathbf{a_3}$. The directional derivative of $\mathbf{a_1}$ gives

$$D\mathbf{a}_1 \cdot \Delta\mathbf{z} = \frac{1}{\left\|\boldsymbol{\varphi}_{,s}\right\|}\mathbf{P}_{\mathbf{a}_1}\Delta\mathbf{z}_{,s}. \tag{B.1}$$

For the directional derivative of $\mathbf{a}_2$, we derive, using Eq. (B.1), the following.

$$(D\mathbf{P}_{\mathbf{a}_1} \cdot \Delta\mathbf{z})\mathbf{i}_2 = -\frac{1}{\left\|\boldsymbol{\varphi}_{,s}\right\|}\left\{(\mathbf{a}_1 \cdot \mathbf{i}_2)\mathbf{I} + \mathbf{a}_1 \otimes \mathbf{i}_2\right\}\mathbf{P}_{\mathbf{a}_1}\Delta\mathbf{z}_{,s}. \tag{B.2}$$

Using the relation $D\mathbf{i}_2 \cdot \Delta\hat{\boldsymbol{\Theta}} = -\left[\mathbf{i}_2\times\right]\Delta\boldsymbol{\Theta}$ from $\mathbf{i}_2 = \boldsymbol{\Lambda}\mathbf{e}_2$ and Eqs. (B.2), we derive

$$\begin{aligned} D\mathbf{a}_2 \cdot \Delta\boldsymbol{\eta} &= \frac{1}{\left\|\boldsymbol{\varphi}_{,s}\right\|}\left[-\frac{1}{\left\|\mathbf{P}_{\mathbf{a}_1}\mathbf{i}_2\right\|}\mathbf{P}_{\mathbf{a}_2}\left\{(\mathbf{a}_1 \cdot \mathbf{i}_2)\,\mathbf{I} + \mathbf{a}_1 \otimes \mathbf{i}_2\right\}\mathbf{P}_{\mathbf{a}_1}\right]\Delta\mathbf{z}_{,s} \\ &\quad + \frac{1}{\left\|\boldsymbol{\varphi}_{,s}\right\|}\left(-\frac{\left\|\boldsymbol{\varphi}_{,s}\right\|}{\left\|\mathbf{P}_{\mathbf{a}_1}\mathbf{i}_2\right\|}\mathbf{P}_{\mathbf{a}_2}\mathbf{P}_{\mathbf{a}_1}\left[\mathbf{i}_2\times\right]\right)\Delta\boldsymbol{\Theta} \\ &\equiv \frac{1}{\left\|\boldsymbol{\varphi}_{,s}\right\|}\mathbf{T}^p_{2\varphi}\Delta\mathbf{z}_{,s} + \frac{1}{\left\|\boldsymbol{\varphi}_{,s}\right\|}\mathbf{T}^p_{2\Theta}\Delta\boldsymbol{\Theta}. \end{aligned} \tag{B.3}$$

The directional derivative of $\mathbf{a_3}$ is obtained by using Eqs. (B.1) and (B.3), as

$$
\begin{aligned}
D\mathbf{a}_3 \cdot \Delta\boldsymbol{\eta} &= \left[\frac{1}{\left\|\boldsymbol{\varphi}_{,s}\right\|} \left\{ \left(-\left[\mathbf{a}_2 \times\right] \mathbf{P}_{\mathbf{a}_1} + \left[\mathbf{a}_1 \times\right] \mathbf{T}^p_{2\varphi} \right) \right\} \right] \Delta\mathbf{z}_{,s} + \left[\frac{1}{\left\|\boldsymbol{\varphi}_{,s}\right\|} \left(\left[\mathbf{a}_1 \times\right] \right) \mathbf{T}^p_{2\Theta} \right] \Delta\boldsymbol{\Theta} \\
&\equiv \mathbf{T}^p_{3\varphi} \Delta\mathbf{z}_{,s} + \mathbf{T}^p_{3\Theta} \Delta\boldsymbol{\Theta}.
\end{aligned} \tag{B.4}
$$

B.2 Material derivative of pressure load vector

We derive material derivatives of base vectors $\mathbf{a}_I (I = 1,2,3)$. Taking the material derivative of $\mathbf{a_1}$ by using the formula of Eq. (3.125) and substituting Eq. (3.108) gives

$$
\dot{\mathbf{a}}_1 = \frac{1}{\left\|\boldsymbol{\varphi}_{,s}\right\|} \mathbf{P}_{\mathbf{a}_1} \dot{\mathbf{z}}_{,s} + \frac{1}{\left\|\boldsymbol{\varphi}_{,s}\right\|} \mathbf{P}_{\mathbf{a}_1} \left(\mathbf{V}_{,s} - \boldsymbol{\varphi}_{,s} \nabla_s \cdot \mathbf{V} \right). \tag{B.5}
$$

For the derivation of material derivative of $\mathbf{a}_2$, we derive the following by using Eq. (B.5).

$$
\dot{\mathbf{P}}_{\mathbf{a}_1} \mathbf{i}_2 = -\frac{1}{\left\|\boldsymbol{\varphi}_{,s}\right\|} \left\{ \left(\mathbf{a}_1 \cdot \mathbf{i}_2\right) \mathbf{I} + \mathbf{a}_1 \otimes \mathbf{i}_2 \right\} \mathbf{P}_{\mathbf{a}_1} \dot{\mathbf{z}}_{,s} - \frac{1}{\left\|\boldsymbol{\varphi}_{,s}\right\|} \left\{ \left(\mathbf{a}_1 \cdot \mathbf{i}_2\right) \mathbf{I} + \mathbf{a}_1 \otimes \mathbf{i}_2 \right\} \mathbf{P}_{\mathbf{a}_1} \left(\mathbf{V}_{,s} - \boldsymbol{\varphi}_{,s} \nabla_s \cdot \mathbf{V} \right). \tag{B.6}
$$

From the relation $\mathbf{i}_2 = \boldsymbol{\Lambda} \mathbf{e}_2$, we derive the following by using Eq. (3.119).

$$
\mathbf{i}_2^{\bullet} = -\left[\mathbf{i}_2 \times\right] \boldsymbol{\Theta}^*_L - \left[\mathbf{i}_2 \times\right] \boldsymbol{\theta}^*_0. \tag{B.7}
$$

Using Eqs. (B.6) and (B.7)

$$
\begin{aligned}
\dot{\mathbf{a}}_2 &= \frac{1}{\left\|\boldsymbol{\varphi}_{,s}\right\|} \left[-\frac{1}{\left\|\mathbf{P}_{\mathbf{a}_1} \mathbf{i}_2\right\|} \mathbf{P}_{\mathbf{a}_2} \left\{ \left(\mathbf{a}_1 \cdot \mathbf{i}_2\right) \mathbf{I} + \mathbf{a}_1 \otimes \mathbf{i}_2 \right\} \mathbf{P}_{\mathbf{a}_1} \right] \dot{\mathbf{z}}_{,s} + \frac{1}{\left\|\boldsymbol{\varphi}_{,s}\right\|} \left(-\frac{\left\|\boldsymbol{\varphi}_{,s}\right\|}{\left\|\mathbf{P}_{\mathbf{a}_1} \mathbf{i}_2\right\|} \mathbf{P}_{\mathbf{a}_2} \mathbf{P}_{\mathbf{a}_1} \left[\mathbf{i}_2 \times\right] \right) \boldsymbol{\Theta}^*_L \\
&\quad + \frac{1}{\left\|\boldsymbol{\varphi}_{,s}\right\|} \left[-\frac{1}{\left\|\mathbf{P}_{\mathbf{a}_1} \mathbf{i}_2\right\|} \mathbf{P}_{\mathbf{a}_2} \left\{ \left(\mathbf{a}_1 \cdot \mathbf{i}_2\right) \mathbf{I} + \mathbf{a}_1 \otimes \mathbf{i}_2 \right\} \mathbf{P}_{\mathbf{a}_1} \right] \left(\mathbf{V}_{,s} - \boldsymbol{\varphi}_{,s} \nabla_s \cdot \mathbf{V} \right) \\
&\quad + \frac{1}{\left\|\boldsymbol{\varphi}_{,s}\right\|} \left(-\frac{\left\|\boldsymbol{\varphi}_{,s}\right\|}{\left\|\mathbf{P}_{\mathbf{a}_1} \mathbf{i}_2\right\|} \mathbf{P}_{\mathbf{a}_2} \mathbf{P}_{\mathbf{a}_1} \left[\mathbf{i}_2 \times\right] \right) \boldsymbol{\theta}^*_0 \\
&\equiv \frac{1}{\left\|\boldsymbol{\varphi}_{,s}\right\|} \mathbf{T}^p_{2\varphi} \dot{\mathbf{z}}_{,s} + \frac{1}{\left\|\boldsymbol{\varphi}_{,s}\right\|} \mathbf{T}^p_{2\Theta} \boldsymbol{\Theta}^*_L + \frac{1}{\left\|\boldsymbol{\varphi}_{,s}\right\|} \mathbf{T}^p_{2\varphi} \left(\mathbf{V}_{,s} - \boldsymbol{\varphi}_{,s} \nabla_s \cdot \mathbf{V} \right) + \frac{1}{\left\|\boldsymbol{\varphi}_{,s}\right\|} \mathbf{T}^p_{2\Theta} \boldsymbol{\theta}^*_0.
\end{aligned} \tag{B.8}
$$

The material derivative of $\mathbf{a_3}$ is derived using Eqs. (B.5) and (B.8) as

$$
\begin{aligned}
\dot{\mathbf{a}}_3 &= \frac{1}{\left\|\boldsymbol{\varphi}_{,s}\right\|} \left(-\left[\mathbf{a}_2 \times\right] \mathbf{P}_{\mathbf{a}_1} + \left[\mathbf{a}_1 \times\right] \mathbf{T}^p_{2\varphi} \right) \left(\dot{\mathbf{z}}_{,s} + \mathbf{V}_{,s} - \boldsymbol{\varphi}_{,s} \nabla_s \cdot \mathbf{V} \right) + \frac{1}{\left\|\boldsymbol{\varphi}_{,s}\right\|} \left[\mathbf{a}_1 \times\right] \mathbf{T}^p_{2\Theta} \left(\boldsymbol{\Theta}^*_L + \boldsymbol{\theta}^*_0 \right) \\
&\equiv \frac{1}{\left\|\boldsymbol{\varphi}_{,s}\right\|} \left\{ \mathbf{T}^p_{3\varphi} \left(\dot{\mathbf{z}}_{,s} + \mathbf{V}_{,s} - \boldsymbol{\varphi}_{,s} \nabla_s \cdot \mathbf{V} \right) + \mathbf{T}^p_{3\Theta} \left(\boldsymbol{\Theta}^*_L + \boldsymbol{\theta}^*_0 \right) \right\}.
\end{aligned} \tag{B.9}
$$

Appendix C

Supplements to the geometrically exact shear-deformable shell model

C.1 Local cartesian basis

The local Cartesian base vectors are determined by [45]

$$\mathbf{j}_1 = \frac{\sqrt{2}}{2}\left(\tilde{\mathbf{j}}_{\xi^1} - \tilde{\mathbf{j}}_{\xi^2}\right),\ \mathbf{j}_2 = \frac{\sqrt{2}}{2}\left(\tilde{\mathbf{j}}_{\xi^1} + \tilde{\mathbf{j}}_{\xi^2}\right),\ \text{and}\ \mathbf{j}_3 \equiv \mathbf{G}_3 \tag{C.1}$$

where $\mathbf{j}_{\xi^\alpha} \equiv \mathbf{G}_\alpha / \|\mathbf{G}_\alpha\|$ $(\alpha = 1,2)$ followed by

$$\tilde{\mathbf{j}}_{\xi^1} = \frac{1}{2}\left(\mathbf{j}_{\xi^1} + \mathbf{j}_{\xi^2}\right) / \left\|\frac{1}{2}\left(\mathbf{j}_{\xi^1} + \mathbf{j}_{\xi^2}\right)\right\|,\ \text{and}\ \tilde{\mathbf{j}}_{\xi^2} = \left(\mathbf{G}_3 \times \tilde{\mathbf{j}}_{\xi^1}\right) / \left\|\mathbf{G}_3 \times \tilde{\mathbf{j}}_{\xi^1}\right\| \tag{C.2}$$

C.2 Material derivative of local Cartesian basis

Taking the material derivative of $\mathbf{G}_3$ in Eq. (2.217) gives

$$\dot{\mathbf{G}}_3 = \frac{1}{\|\mathbf{G}_1 \times \mathbf{G}_2\|}\mathbf{P}_{\mathbf{G}_3}\left(\dot{\mathbf{G}}_1 \times \mathbf{G}_2 + \mathbf{G}_1 \times \dot{\mathbf{G}}_2\right) \tag{C.3}$$

Also, we have

$$\dot{\mathbf{G}}_\alpha = \dot{\boldsymbol{\varphi}}_{0,\xi^\alpha} = \mathbf{V}_{,\xi^\alpha}. \tag{C.4}$$

Using Eqs. (3.125) and (C.4), the material derivative of $\mathbf{j}_{\xi^\alpha}$ $(\alpha = 1,2)$ gives

$$\left(\mathbf{j}_{\xi^\alpha}\right)^\bullet = \frac{1}{\|\mathbf{G}_\alpha\|}\mathbf{P}_{\mathbf{j}_{\xi^\alpha}}\dot{\mathbf{G}}_\alpha. \tag{C.5}$$

Similarly, using Eq. (3.125), the material derivative of $\tilde{\mathbf{j}}_{\xi^\alpha}$ $(\alpha = 1,2)$ gives

$$\left(\tilde{\mathbf{j}}_{\xi^1}\right)^\bullet = \frac{1}{\left\|\mathbf{j}_{\xi^1} + \mathbf{j}_{\xi^2}\right\|}\mathbf{P}_{\tilde{\mathbf{j}}_{\xi^1}}\left\{\left(\mathbf{j}_{\xi^1}\right)^\bullet + \left(\mathbf{j}_{\xi^2}\right)^\bullet\right\}, \tag{C.6}$$

and

$$\left(\tilde{\mathbf{j}}_{\xi^2}\right)^\bullet = \frac{1}{\left\|\mathbf{G}_3 \times \tilde{\mathbf{j}}_{\xi^1}\right\|}\mathbf{P}_{\tilde{\mathbf{j}}_{\xi^2}}\left\{\dot{\mathbf{G}}_3 \times \tilde{\mathbf{j}}_{\xi^1} + \mathbf{G}_3 \times \left(\tilde{\mathbf{j}}_{\xi^1}\right)^\bullet\right\}. \tag{C.7}$$

Thus, we have

$$(\mathbf{j}_2)^\bullet = \frac{\sqrt{2}}{2}\left\{\left(\tilde{\mathbf{j}}_{\xi^1}\right)^\bullet + \left(\tilde{\mathbf{j}}_{\xi^2}\right)^\bullet\right\}, \tag{C.8}$$

$$(\mathbf{j}_2)^\bullet = \frac{\sqrt{2}}{2}\left\{\left(\tilde{\mathbf{j}}_{\xi^1}\right)^\bullet + \left(\tilde{\mathbf{j}}_{\xi^2}\right)^\bullet\right\}, \tag{C.9}$$

and $(\mathbf{j}_3)^\bullet = \dot{\mathbf{G}}_3$. $\dot{\mathbf{J}}$ is derived, from Eq. (2.224), as

$$\dot{\mathbf{J}} = \begin{bmatrix} \mathbf{V}_{,\xi^1}\cdot\mathbf{j}_1 + \mathbf{G}_1\cdot\left(\mathbf{j}_1\right)^\bullet & \mathbf{V}_{,\xi^1}\cdot\mathbf{j}_2 + \mathbf{G}_1\cdot\left(\mathbf{j}_2\right)^\bullet \\ \mathbf{V}_{,\xi^2}\cdot\mathbf{j}_1 + \mathbf{G}_2\cdot\left(\mathbf{j}_1\right)^\bullet & \mathbf{V}_{,\xi^2}\cdot\mathbf{j}_2 + \mathbf{G}_2\cdot\left(\mathbf{j}_2\right)^\bullet \end{bmatrix}. \tag{C.10}$$

C.3 Constitutive matrix

The following constitutive matrix is constructured [48]

$$\mathbf{C}^{\alpha\beta} \equiv \begin{bmatrix} \left(\mathbf{C}_N^{\alpha\beta} + \mathbf{C}_\gamma^{\alpha\beta} + \mathbf{C}_Q^{\alpha\beta}\right) & \mathbf{0}_{3\times3} \\ \mathbf{0}_{3\times3} & \mathbf{C}_M^{\alpha\beta} \end{bmatrix}, \tag{C.11}$$

from

$$\begin{bmatrix} \mathbf{C}_N^{11} & \mathbf{C}_N^{12} \\ \mathbf{C}_N^{21} & \mathbf{C}_N^{22} \end{bmatrix} = \begin{bmatrix} \mathbf{j}_1 & \mathbf{0} & \mathbf{j}_2 \\ \mathbf{0} & \mathbf{j}_2 & \mathbf{j}_1 \end{bmatrix} \frac{Eh}{1-\nu^2}\mathbf{D} \begin{bmatrix} \mathbf{j}_1{}^T & \mathbf{0}^T \\ \mathbf{0}^T & \mathbf{j}_2{}^T \\ \mathbf{j}_2{}^T & \mathbf{j}_1{}^T \end{bmatrix}, \tag{C.12}$$

$$\begin{bmatrix} \mathbf{C}_\gamma^{11} & \mathbf{C}_\gamma^{12} \\ \mathbf{C}_\gamma^{21} & \mathbf{C}_\gamma^{22} \end{bmatrix} = \begin{bmatrix} \mathbf{j}_2 \\ -\mathbf{j}_1 \end{bmatrix} \frac{Eh}{1-\nu^2}\gamma \begin{bmatrix} \mathbf{j}_2{}^T & -\mathbf{j}_1{}^T \end{bmatrix}, \tag{C.13}$$

$$\begin{bmatrix} \mathbf{C}_Q^{11} & \mathbf{C}_Q^{12} \\ \mathbf{C}_Q^{21} & \mathbf{C}_Q^{22} \end{bmatrix} = \begin{bmatrix} \mathbf{j}_3 & \mathbf{0} \\ \mathbf{0} & \mathbf{j}_3 \end{bmatrix} \frac{Eh}{2(1+\nu)} \begin{bmatrix} \mathbf{j}_3{}^T & \mathbf{0}^T \\ \mathbf{0}^T & \mathbf{j}_3{}^T \end{bmatrix}, \tag{C.14}$$

and

$$\begin{bmatrix} \mathbf{C}_M^{11} & \mathbf{C}_M^{12} \\ \mathbf{C}_M^{21} & \mathbf{C}_M^{22} \end{bmatrix} = \begin{bmatrix} -\mathbf{j}_2 & \mathbf{0} & \mathbf{j}_1 \\ \mathbf{0} & \mathbf{j}_1 & -\mathbf{j}_2 \end{bmatrix} \frac{Eh^3}{12(1-\nu^2)}\mathbf{D} \begin{bmatrix} -\mathbf{j}_2{}^T & \mathbf{0}^T \\ \mathbf{0}^T & \mathbf{j}_1{}^T \\ \mathbf{j}_1{}^T & -\mathbf{j}_2{}^T \end{bmatrix}, \tag{C.15}$$

where

$$\mathbf{D} \equiv \begin{bmatrix} 1 & \nu & 0 \\ \nu & 1 & 0 \\ 0 & 0 & (1-\nu)/2 \end{bmatrix}. \tag{C.16}$$

Appendix D

Supplements to the invariant formulations

D.1 Analytic solution of pure bending problems

For the sinusoidal moment loading condition of Eq. (4.1), Adam *et al.* [1] derived the exact solution of the rotation angle as

$$\theta_b(s) = \sin\left(\frac{\pi}{2L}s\right). \tag{D.1}$$

Since the membrane and shear strains vanish due to the pure bending nature, using Eq. (2.15), for a given θ_b and $\forall\, s \in [0, L]$, we have two differential equations for the global displacement vector $\hat{\mathbf{z}}$ as

$$\left.\begin{aligned} \hat{\mathbf{z}}_{,s} \cdot \mathbf{j}_1 &= 0 \\ \hat{\mathbf{z}}_{,s} \cdot \mathbf{j}_2 &= \theta_b \end{aligned}\right\}. \tag{D.2}$$

Eq. (D.2) can be rewritten as

$$\begin{bmatrix} (\mathbf{j}_1)_1 & (\mathbf{j}_1)_2 \\ (\mathbf{j}_2)_1 & (\mathbf{j}_2)_2 \end{bmatrix} \hat{\mathbf{z}}_{,s} = \begin{Bmatrix} 0 \\ \theta_b \end{Bmatrix}, \forall\, s \in [0, L]. \tag{D.3}$$

Therefore, the exact solution of $\hat{\mathbf{z}}_{,s}$ is obtained as

$$\hat{\mathbf{z}}_{,s} = \frac{1}{(\mathbf{j}_1)_1(\mathbf{j}_2)_2 - (\mathbf{j}_1)_2(\mathbf{j}_2)_1} \begin{bmatrix} (\mathbf{j}_2)_2 & -(\mathbf{j}_1)_2 \\ -(\mathbf{j}_2)_1 & (\mathbf{j}_1)_1 \end{bmatrix} \begin{Bmatrix} 0 \\ \theta_b \end{Bmatrix} = \begin{Bmatrix} -(\mathbf{j}_1)_2 \\ (\mathbf{j}_1)_1 \end{Bmatrix} \theta_b, \tag{D.4}$$

since $(\mathbf{j}_1)_1(\mathbf{j}_2)_2 - (\mathbf{j}_1)_2(\mathbf{j}_2)_1 = \left\|\mathbf{j}_1 \times \mathbf{j}_2\right\| = 1$. Considering the clamped boundary condition, we have the final expression of the global displacement field as

$$\hat{\mathbf{z}}(s) = \int_0^s \begin{Bmatrix} -(\mathbf{j}_1)_2(\tilde{s}) \\ (\mathbf{j}_1)_1(\tilde{s}) \end{Bmatrix} \theta_b(\tilde{s})\, d\tilde{s}. \tag{D.5}$$

Appendix E

Supplements to the geometric constraints in design optimization

E.1 Design sensitivity of curvature constraint

We present a design sensitivity expression of the curvature constraint of Eq. (4.12). For convenience, the constraint function is rewritten as

$$g_i \equiv \frac{1}{L_i}\int_{\Xi_i} g^{\kappa}(\xi) J_c(\xi) d\xi, \text{ where } g^{\kappa}(\xi) \equiv \left\{\kappa^f(\xi)/\kappa_U^f\right\}^2 - 1. \tag{E.1}$$

The constraint function g_i is explicitly dependent to design, and its material derivative gives

$$\dot{g}_i = \frac{-\dot{L}_i}{L_i} g_i + \frac{1}{L_i}\int_{\Xi_i} \left\{\dot{g}^{\kappa}(\xi) + g^{\kappa}(\xi)\nabla_s \cdot \mathbf{V}\right\} J_c(\xi) d\xi, \tag{E.2}$$

where

$$\dot{g}^{\kappa}(\xi) = 2\kappa^f(\xi)\dot{\kappa}^f(\xi)/{\kappa_U^f}^2. \tag{E.3}$$

We derive the material derivative of the Frenet curvature of Eq. (4.15) as

$$\dot{\kappa}^f = \mathbf{j}_{1,s}^{\bullet} \cdot \mathbf{n} - \kappa^f \nabla_s \cdot \mathbf{V} + \mathbf{j}_{1,s} \cdot \dot{\mathbf{n}}. \tag{E.4}$$

where $\dot{\mathbf{n}}$ is derived, using Eqs. (3.125) and (3.111) as

$$\dot{\mathbf{n}} = \frac{1}{\left\|\mathbf{j}_{1,s}\right\|} \mathbf{P}_{\mathbf{n}}\left(\mathbf{j}_{1,s}^{-} \mathbf{j}_{1,s} \nabla_s \cdot \mathbf{V}\right), \tag{E.5}$$

and

$$\mathbf{j}_{1,s}^{\bullet} = \mathbf{P}_{\mathbf{j}_1}\mathbf{V}_{,ss} - \mathbf{j}_{1,s}\nabla_s \cdot \mathbf{V} - \mathbf{j}_1\left(\mathbf{V}_{,s} \cdot \mathbf{j}_{1,s}\right). \tag{E.6}$$

We also derive the material derivative of the length of a curve segment Ω_{0i}, using Eqs. (3.7) and (3.8), as

$$\dot{L}_i = \int_{\Omega_{0i}} (\nabla_s \cdot \mathbf{V})\, ds = \int_{\Xi_i} (\nabla_s \cdot \mathbf{V})\, J_c(\xi)\, d\xi. \tag{E.7}$$

Appendix F

Supplements to the design of auxetic structures

F.1 Calculation of Poisson's ratio of finite assembly of unit cells

We consider two types of materials; purely elastic and SMP. For both cases, if the displacement from a suitable reference configuration is determined, the position changes of selected void centers can be calculated. The reference configuration is selected as the undeformed configuration and the original equilibrium configuration at each temperature step for purely elastic and SMP material cases, respectively. Also, the term "*deformed configuration*" used in this appendix indicates the current configuration at each target load step and the temporary equilibrium configuration for the purely elastic and SMP material cases, respectively. The overall procedure of the Poisson's ratio calculation refers to Bertoldi *et al.* [13], and our contribution is made in the application to the SMP material case and the derivation of material derivative expressions.

Poisson's ratio is calculated using the differences of void center positions between reference and deformed configurations. Fig. F.1 illustrates the selected voids for the Poisson's ratio calculation and the corresponding indices (i, j).
$(X^0_{i,j}, Y^0_{i,j})$ and $(X_{i,j}, Y_{i,j})$ represent the positions of void (i, j) in reference and deformed configurations, respectively. The following expressions of the center-to-center distances are utilized.

$$\left.\begin{aligned} \Delta X_{i,j} &\equiv X_{i+1,j} - X_{i,j}, \Delta Y_{i,j} \equiv Y_{i,j+1} - Y_{i,j} \\ \Delta X^0_{i,j} &\equiv X^0_{i+1,j} - X^0_{i,j}, \Delta Y^0_{i,j} \equiv Y^0_{i,j+1} - Y^0_{i,j} \end{aligned}\right\}. \tag{F.1}$$

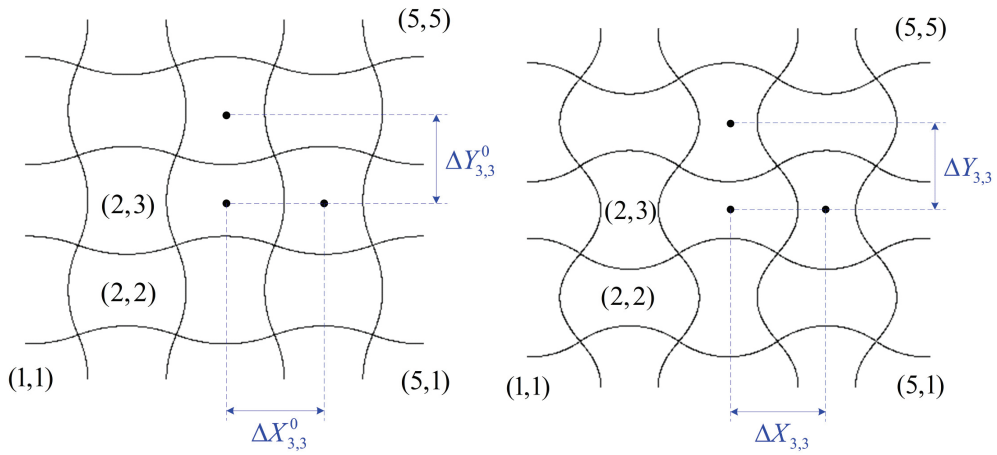

(a) Reference configuration (b) Deformed configuration

Figure F.1: Selected holes in reference and deformed configurations

The Poisson's ratio is calculated as follows.

$$\nu = \frac{1}{N_\nu} \sum_{i,j} \nu_{i,j}, \tag{F.2}$$

where

$$\begin{aligned} \nu_{i,j} &\equiv -\frac{(\Delta X_{i,j} - \Delta X^0_{i,j})/\Delta X^0_{i,j}}{(\Delta Y_{i,j} - \Delta Y^0_{i,j})/\Delta Y^0_{i,j}} \\ &= -\frac{(U_{i+1,j} - U_{i,j})/\Delta X^0_{i,j}}{(V_{i,j+1} - V_{i,j})/\Delta Y^0_{i,j}}, \end{aligned} \tag{F.3}$$

and N_ν is the number of values of $\nu_{i,j}$ used in the averaging. For example, in the case of Poisson's ratio calculation illustrated in Fig. 4.148, total 16 values of $\nu_{i,j}$ are utilized, *i.e.*, $N_\nu = 16$. In the second equality of Eq. (F.3), the following relation is utilized.

$$\begin{aligned} \Delta X_{i,j} - \Delta X^0_{i,j} &= \left(X_{i+1,j} - X^0_{i+1,j}\right) - \left(X_{i,j} - X^0_{i,j}\right) \\ &\equiv U_{i+1,j} - U_{i,j}, \end{aligned} \tag{F.4}$$

and

$$\begin{aligned} \Delta Y_{i,j} - \Delta Y^0_{i,j} &= \left(Y_{i,j+1} - Y^0_{i,j+1}\right) - \left(Y_{i,j} - Y^0_{i,j}\right) \\ &\equiv V_{i,j+1} - V_{i,j}, \end{aligned} \tag{F.5}$$

where $U_{i,j}$ and $V_{i,j}$ represent the horizontal and vertical displacements of the void (i,j) at the deformed configuration from the reference configuration. Next, we derive the sensitivity of the Poisson's ratio. Due to the symmetric design variations in the unit cell, the initial void center

position in the undeformed configuration does not have any design dependence. Thus, taking the material derivative of Eqs. (F.4) and (F.5) yields

$$\left.\begin{aligned}\Delta\dot{X}^0_{i,j} &= \dot{X}^0_{i+1,j} - \dot{X}^0_{i,j} \equiv \dot{U}^0_{i+1,j} - \dot{U}^0_{i,j}\\ \Delta\dot{Y}^0_{i,j} &= \dot{Y}^0_{i,j+1} - \dot{Y}^0_{i,j} \equiv \dot{V}^0_{i,j+1} - \dot{V}^0_{i,j}\end{aligned}\right\}, \tag{F.6}$$

where $U^0_{i,j}$ and $V^0_{i,j}$ represent the horizontal and vertical displacements of the void (i,j) at the reference configuration from the undeformed one. In the purely elastic material case considered in this paper, the reference configuration is selected as the undeformed configuration, thus, $\Delta\dot{X}^0_{i,j} = \Delta\dot{Y}^0_{i,j} = 0$. Taking the material derivative of Eq. (F.3) and using Eq. (F.6) gives

$$\dot{\nu}_{i,j} = \nu_{i,j}\left(\frac{\dot{U}_{i+1,j}-\dot{U}_{i,j}}{U_{i+1,j}-U_{i,j}} - \frac{\dot{V}_{i,j+1}-\dot{V}_{i,j}}{V_{i,j+1}-V_{i,j}} + \frac{\dot{V}^0_{i,j+1}-\dot{V}^0_{i,j}}{\Delta Y^0_{i,j}} - \frac{\dot{U}^0_{i+1,j}-\dot{U}^0_{i,j}}{\Delta X^0_{i,j}}\right). \tag{F.7}$$

Finally, from Eq. (F.2), the sensitivity of the Poisson's ratio can be obtained as

$$\dot{\nu} = \frac{1}{N_\nu}\sum_{i,j}\dot{\nu}_{i,j}. \tag{F.8}$$

F.2 Design parameterizations of three-dimensional lattice structures

F.2.1 A case of 8 configuration design variables

We explain the design parameterization of the auxetic structure presented in section 4.3.4. Design variables are selected in the one-eighth part of the unit cell due to the mirror symmetry. Total eight configuration design variables are selected as shown in Fig. F.2 in one of six ligaments attached to a junction, and control points of the other five ligaments are located by a rotational symmetry which is described in each of three plane views. In order to preserve G^1-continuity of ligament at junctions, normal directional design perturbations of the last and second last control points are parameterized by a single design variable

F.2.2 A case of 72 configuration design variables

Fig. F.3 shows the design parameterization with maximal design degree-of-freedom under the given discretization level, where no rotational symmetry is introduced within the one-eighth part of the unit cell. Normal and tangential directional movements of control points are selected as configuration design variables, whose linear combination with the corresponding design velocity fields yield design variation. In order to preserve the G^1 continuity between adjacent unit cells, the normal directional movements of two control end control points are parameterized.

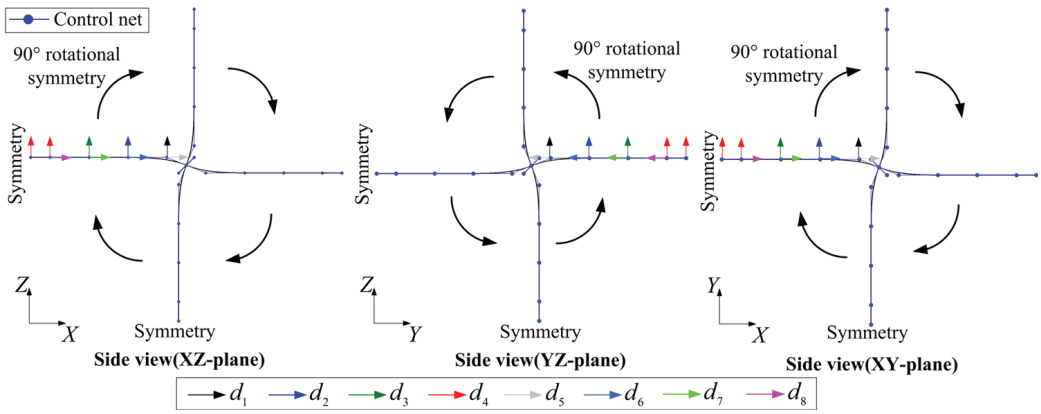

Figure F.2: Parameterization of configuration design with 8 variables

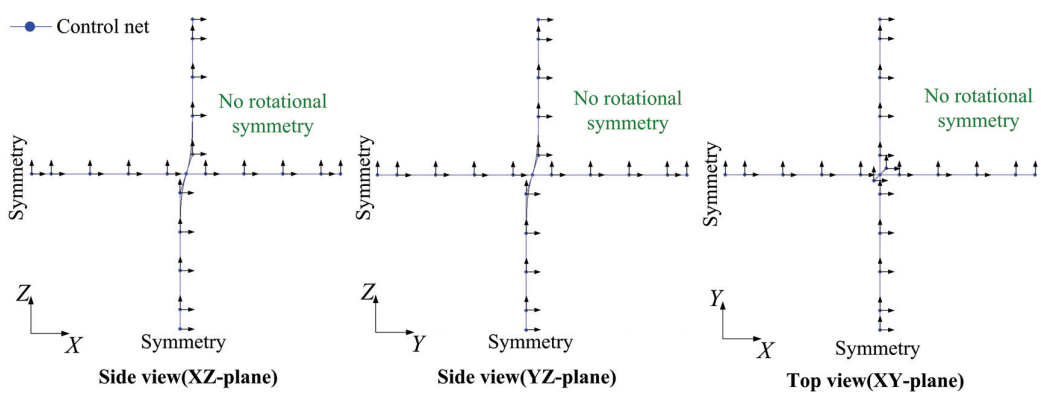

Figure F.3: Parameterization of configuration design with 72 variables

초 록

본 연구에서는 대변형을 고려한 휘어진 조립 구조물의 연속체 기반 해석적 애조인 형상 설계 민감도 해석 기법을 개발하였다. 평면 Timoshenko 빔의 선형화된 변형률의 invariance 특성을 고찰하였고 invariant 정식화를 선택적 축소적분(selective reduced integration) 기법 및 $\bar{B}$ projection 기법과 결합하여 shear 및 membrane 잠김 현상을 해소하였다. 비선형 구조 모델로서 기하학적으로 정밀한 빔 및 쉘 모델을 활용하였다. 평면 Kirchhoff 빔 모델을 NURBS 기저함수의 고차 연속성에 따른 아이소-지오메트릭 해석 기반 rotation-free 이산화를 활용하여 다루었으며, 기존의 Hermite 기저함수 기반의 유한요소법에 비해 자유도당 해의 정확도가 높음을 검증하였다. 라그랑지 승수법 및 벌칙 기법을 도입하여 회전의 연속성을 포함한 다양한 다중패치간 연속 조건을 고려하였다. 이러한 기법을 현상학적 (phenomenological) 형상기억 폴리머 (SMP) 재료 구성방정식과 결합하여 형상의 프로그래밍과 회복 과정을 시뮬레이션하였다. 전단변형을 겪는 (shear-deformable) 구조 모델에 대하여 대회전의 갱신을 교대 행렬의 exponential map에 의한 곱의 형태로 수행하였다. C^1의 연속성을 갖는 곡선 모델에서 최소회전 (smallest rotation) 기법을 통해 국소 정규직교좌표계의 명시적 매개화를 수행하였다. 형상 설계 민감도 해석을 위하여 전미분을 변분 방정식에 적용하였으며 휘어진 구조물의 배향 설계 변화는 국소 정규직교좌표계의 회전에 의하여 기술된다. 최종 변형 형상에서 직교 변환 행렬의 전미분을 계산함으로써 대회전 문제에서 추가적인 반복 계산없이 변형 해석에서의 접선강성행렬에 의해 해석적 설계 민감도를 계산할 수 있다. 쉘 구조물의 경우 면내 회전 자유도 및 안정화된 변분 방정식을 활용하여 보강재(stiffener)의 모델링을 용이하게 하였다. 또한 본 연구에서는 휘어진 영역에 구속되어있는 구조물에 대한 설계 속도장 계산 및 최적 설계 기법을 제안하며 특히 곡면에 구속된 빔 구조물의 설계를 집중적으로 다룬다. 자유형상변형 (Free-form deformation) 기법과 전역 곡선 보간기법을 활용하여 직사각 평면에서 형상 및 설계 변수를 정의하고 곡면상의 곡선 형상을 나타내는 조정점 위치를 해석적으로 표현할 수 있으며 이의 전미분을 통해 정확한 설계속도장을 계산한다. 이를 통해 설계 변수의 개수를 줄일 수 있고 설계의 매개화가 간편해진다. 개발된 방법론은 다양한 하중 및 운동학적 경계조건을 갖는 빔과 쉘의 대변형 문제를 통해 검증되며 여러가지 휘어진 조립 구조물의 최적 설계에 적용된다. 대표적으로, 전단 강성 및 충격 흡수 특성과 같은 기계적 물성치의 개선을 위해 활용되는 오그제틱 (auxetic) 특성이 극대화된 격자 구조를 설계하며 인장 및 압축 대변형 모두에서 일정한 음의 포아송비를 나타냄을 3차원 프린팅과 광학적 변형 측정 기술을 이용하여 실험적으로 검증한다. 또한 우리는 소음의 저감을 위해 활용되는 가청 저주파수 영역대에서의 밴드갭이 극대화된 격자 구조를 제시한다.

주요어: 아이소-지오메트릭 해석; 기하학적으로 정밀한 빔 및 쉘 모델; 대변형; 애조인 설계민감도; 조립구조물; 형상 최적설계; 설계 속도장
학 번: 2012-21076

Bibliography

[1] Cédric Adam, Salim Bouabdallah, Malek Zarroug, and Habibou Maitournam. Improved numerical integration for locking treatment in isogeometric structural elements, part i: Beams. *Computer Methods in Applied Mechanics and Engineering*, 279:1–28, 2014.

[2] Seung-Ho Ahn, Myung-Jin Choi, and Seonho Cho. Isogeometric shape design optimization of nanoscale structures using continuum-based shell theory considering surface effects. *International Journal of Mechanical Sciences*, 141:9–20, 2018.

[3] F Armero and J Valverde. Invariant hermitian finite elements for thin kirchhoff rods. i: The linear plane case. *Computer Methods in Applied Mechanics and Engineering*, 213:427–457, 2012.

[4] F Auricchio, L Beirao da Veiga, J Kiendl, C Lovadina, and A Reali. Locking-free isogeometric collocation methods for spatial timoshenko rods. *Computer Methods in Applied Mechanics and Engineering*, 263:113–126, 2013.

[5] Andrea Bacigalupo, Giorgio Gnecco, Marco Lepidi, and Luigi Gambarotta. Optimal design of low-frequency band gaps in anti-tetrachiral lattice meta-materials. *Composites Part B: Engineering*, 115:341–359, 2017.

[6] M Baghani, R Naghdabadi, J Arghavani, and S Sohrabpour. A thermodynamically-consistent 3d constitutive model for shape memory polymers. *International Journal of Plasticity*, 35:13–30, 2012.

[7] AM Bauer, M Breitenberger, B Philipp, R Wüchner, and K-U Bletzinger. Nonlinear isogeometric spatial bernoulli beam. *Computer Methods in Applied Mechanics and Engineering*, 303:101–127, 2016.

[8] AM Bauer, M Breitenberger, B Philipp, R Wüchner, and K-U Bletzinger. Embedded structural entities in nurbs-based isogeometric analysis. *Computer Methods in Applied Mechanics and Engineering*, 325:198–218, 2017.

[9] Alireza Bayat and Stavros Gaitanaros. Wave directionality in three-dimensional periodic lattices. *Journal of Applied Mechanics*, 85(1):011004, 2018.

[10] DJ Benson, Y Bazilevs, Ming-Chen Hsu, and TJR Hughes. Isogeometric shell analysis: the reissner–mindlin shell. *Computer Methods in Applied Mechanics and Engineering*, 199(5-8):276–289, 2010.

[11] DJ Benson, S Hartmann, Y Bazilevs, M-C Hsu, and TJR Hughes. Blended isogeometric shells. *Computer Methods in Applied Mechanics and Engineering*, 255:133–146, 2013.

[12] D Bergman and B Yang. A finite element model of shape memory polymer composite beams for space applications. *International Journal for Numerical Methods in Engineering*, 103(9):671–702, 2015.

[13] Katia Bertoldi, Pedro M Reis, Stephen Willshaw, and Tom Mullin. Negative poisson's ratio behavior induced by an elastic instability. *Advanced Materials*, 22(3):361–366, 2010.

[14] Richard L Bishop. There is more than one way to frame a curve. *The American Mathematical Monthly*, 82(3):246–251, 1975.

[15] Robin Bouclier, Thomas Elguedj, and Alain Combescure. Locking free isogeometric formulations of curved thick beams. *Computer Methods in Applied Mechanics and Engineering*, 245:144–162, 2012.

[16] Vincent Braibant and Claude Fleury. Shape optimal design using b-splines. *Computer Methods in Applied Mechanics and Engineering*, 44(3):247–267, 1984.

[17] Luigi Cabras and Michele Brun. Auxetic two-dimensional lattices with poisson's ratio arbitrarily close to- 1. In *Proceedings of the Royal Society of London A: Mathematical, Physical and Engineering Sciences*, volume 470, page 20140538. The Royal Society, 2014.

[18] Luigi Cabras and Michele Brun. A class of auxetic three-dimensional lattices. *Journal of the Mechanics and Physics of Solids*, 91:56–72, 2016.

[19] CP Chen and RS Lakes. Micromechanical analysis of dynamic behavior of conventional and negative poisson's ratio foams. *Journal of Engineering Materials and Technology*, 118(3):285–288, 1996.

[20] Yanyu Chen, Tiantian Li, Fabrizio Scarpa, and Lifeng Wang. Lattice metamaterials with mechanically tunable poisson's ratio for vibration control. *Physical Review Applied*, 7(2):024012, 2017.

[21] Seonho Cho and KK Choi. Design sensitivity analysis and optimization of non-linear transient dynamics. part ii:configuration design. *International Journal for Numerical Methods in Engineering*, 48(3):375–399, 2000.

[22] Seonho Cho and Seung-Hyun Ha. Isogeometric shape design optimization: exact geometry

and enhanced sensitivity. *Structural and Multidisciplinary Optimization*, 38(1):53–70, 2009.

[23] Seonho Cho and Hyun-Seung Jung. Design sensitivity analysis and topology optimization of displacement–loaded non-linear structures. *Computer Methods in Applied Mechanics and Engineering*, 192(22):2539–2553, 2003.

[24] Kyung K Choi and Kuang-Hua Chang. A study of design velocity field computation for shape optimal design. *Finite Elements in Analysis and Design*, 15(4):317–341, 1994.

[25] Kyung K Choi and Nam-Ho Kim. *Structural sensitivity analysis and optimization 1: linear systems*. Springer Science & Business Media, 2006.

[26] Myung-Jin Choi and Seonho Cho. Isogeometric shape design sensitivity analysis of stress intensity factors for curved crack problems. *Computer Methods in Applied Mechanics and Engineering*, 279:469–496, 2014.

[27] Anders Clausen, Fengwen Wang, Jakob S Jensen, Ole Sigmund, and Jennifer A Lewis. Topology optimized architectures with programmable poisson's ratio over large deformations. *Advanced Materials*, 27(37):5523–5527, 2015.

[28] VL Coenen and KL Alderson. Mechanisms of failure in the static indentation resistance of auxetic carbon fibre laminates. *physica status solidi (b)*, 248(1):66–72, 2011.

[29] MiA Crisfield. A fast incremental/iterative solution procedure that handles "snap-through". In *Computational Methods in Nonlinear Structural and Solid Mechanics*, pages 55–62. Elsevier, 1981.

[30] Michael A Crisfield and Gordan Jelenić. Objectivity of strain measures in the geometrically exact three-dimensional beam theory and its finite-element implementation. In *Proceedings of the Royal Society of London A: Mathematical, Physical and Engineering Sciences*, volume 455, pages 1125–1147. The Royal Society, 1999.

[31] L Beirao da Veiga, C Lovadina, and A Reali. Avoiding shear locking for the timoshenko beam problem via isogeometric collocation methods. *Computer Methods in Applied Mechanics and Engineering*, 241:38–51, 2012.

[32] AR Diaz, AG Haddow, and L Ma. Design of band-gap grid structures. *Structural and Multidisciplinary Optimization*, 29(6):418–431, 2005.

[33] W Dornisch, R Müller, and S Klinkel. An efficient and robust rotational formulation for isogeometric reissner–mindlin shell elements. *Computer Methods in Applied Mechanics and Engineering*, 303:1–34, 2016.

[34] Wolfgang Dornisch and Sven Klinkel. Treatment of reissner–mindlin shells with kinks without the need for drilling rotation stabilization in an isogeometric framework. *Computer Methods in Applied Mechanics and Engineering*, 276:35–66, 2014.

[35] Wolfgang Dornisch, Sven Klinkel, and Bernd Simeon. Isogeometric reissner–mindlin shell analysis with exactly calculated director vectors. *Computer Methods in Applied Mechanics and Engineering*, 253:491–504, 2013.

[36] Thang X Duong, Farshad Roohbakhshan, and Roger A Sauer. A new rotation-free isogeometric thin shell formulation and a corresponding continuity constraint for patch boundaries. *Computer Methods in Applied Mechanics and Engineering*, 316:43–83, 2017.

[37] M Fafard and B Massicotte. Geometrical interpretation of the arc-length method. *Computers & Structures*, 46(4):603–615, 1993.

[38] Gerald E Farin and Dianne Hansford. *The essentials of CAGD*. AK Peters Natick, MA, 2000.

[39] Ming-Hui Fu, Bin-Bin Zheng, and Wei-Hua Li. A novel chiral three-dimensional material with negative poisson's ratio and the equivalent elastic parameters. *Composite Structures*, 176:442–448, 2017.

[40] Leopoldo Greco and Massimo Cuomo. An implicit g1 multi patch b-spline interpolation for kirchhoff–love space rod. *Computer Methods in Applied Mechanics and Engineering*, 269:173–197, 2014.

[41] Youn Doh Ha. Generalized isogeometric shape sensitivity analysis in curvilinear coordinate system and shape optimization of shell structures. *Structural and Multidisciplinary Optimization*, 52(6):1069–1088, 2015.

[42] Thibaut Hirschler, Robin Bouclier, Arnaud Duval, Thomas Elguedj, and Joseph Morlier. Isogeometric sizing and shape optimization of thin structures with a solid-shell approach. *Structural and Multidisciplinary Optimization*, pages 1–19, 2018.

[43] Saman Hosseini, Joris JC Remmers, Clemens V Verhoosel, and René De Borst. An isogeometric continuum shell element for non-linear analysis. *Computer Methods in Applied Mechanics and Engineering*, 271:1–22, 2014.

[44] William M Hsu, John F Hughes, and Henry Kaufman. Direct manipulation of free-form deformations. In *ACM Siggraph Computer Graphics*, volume 26, pages 177–184. ACM, 1992.

[45] Thomas JR Hughes. *The finite element method: linear static and dynamic finite element analysis*. Courier Corporation, 2012.

[46] Thomas JR Hughes, John A Cottrell, and Yuri Bazilevs. Isogeometric analysis: Cad, finite elements, nurbs, exact geometry and mesh refinement. *Computer methods in applied mechanics and engineering*, 194(39):4135–4195, 2005.

[47] Adnan Ibrahimbegović. Stress resultant geometrically nonlinear shell theory with drilling rotations-part i. a consistent formulation. *Computer Methods in Applied Mechanics and Engineering*, 118(3-4):265–284, 1994.

[48] Adnan Ibrahimbegović and François Frey. Stress resultant geometrically nonlinear shell theory with drilling rotations-part ii. computational aspects. *Computer Methods in applied mechanics and Engineering*, 118(3-4):285–308, 1994.

[49] Hans Irschik and Johannes Gerstmayr. A continuum mechanics based derivation of reissner's large-displacement finite-strain beam theory: the case of plane deformations of originally straight bernoulli–euler beams. *Acta mechanica*, 206(1-2):1–21, 2009.

[50] Jakob Søndergaard Jensen. Phononic band gaps and vibrations in one-and two-dimensional mass–spring structures. *Journal of Sound and Vibration*, 266(5):1053–1078, 2003.

[51] Nicholas Karnessis and Gaetano Burriesci. Uniaxial and buckling mechanical response of auxetic cellular tubes. *Smart Materials and Structures*, 22(8):084008, 2013.

[52] J Kiendl, Y Bazilevs, M-C Hsu, R Wüchner, and K-U Bletzinger. The bending strip method for isogeometric analysis of kirchhoff–love shell structures comprised of multiple patches. *Computer Methods in Applied Mechanics and Engineering*, 199(37):2403–2416, 2010.

[53] J Kiendl, R Schmidt, R Wüchner, and K-U Bletzinger. Isogeometric shape optimization of shells using semi-analytical sensitivity analysis and sensitivity weighting. *Computer Methods in Applied Mechanics and Engineering*, 274:148–167, 2014.

[54] Josef Kiendl, K-U Bletzinger, J Linhard, and Roland Wüchner. Isogeometric shell analysis with kirchhoff–love elements. *Computer Methods in Applied Mechanics and Engineering*, 198(49-52):3902–3914, 2009.

[55] Nam Ho Kim, Kyung Kook Choi, Jiun-Shyan Chen, and Mark E Botkin. Meshfree analysis and design sensitivity analysis for shell structures. *International Journal for Numerical Methods in Engineering*, 53(9):2087–2116, 2002.

[56] Bonyong Koo, Seung-Hyun Ha, Hyun-Seok Kim, and Seonho Cho. Isogeometric shape design optimization of geometrically nonlinear structures#. *Mechanics Based Design of Structures and Machines*, 41(3):337–358, 2013.

[57] Sebastian Krödel, Tommaso Delpero, Andrea Bergamini, Paolo Ermanni, and Dennis M Kochmann. 3 d auxetic microlattices with independently controllable acoustic band gaps and quasi-s tatic elastic moduli. *Advanced Engineering Materials*, 16(4):357–363, 2014.

[58] Erin Kuci, François Henrotte, Pierre Duysinx, and Christophe Geuzaine. Design sensitivity analysis for shape optimization based on the lie derivative. *Computer Methods in Applied Mechanics and Engineering*, 317:702–722, 2017.

[59] Roderic Lakes. Foam structures with a negative poisson's ratio. *Science*, 235:1038–1041, 1987.

[60] Henry J Lamousin and NN Waggenspack. Nurbs-based free-form deformations. *IEEE Computer Graphics and Applications*, 14(6):59–65, 1994.

[61] M Langelaar, GH Yoon, YY Kim, and F Van Keulen. Topology optimization of planar shape memory alloy thermal actuators using element connectivity parameterization. *International Journal for Numerical Methods in Engineering*, 88(9):817–840, 2011.

[62] Matthijs Langelaar and Fred van Keulen. Modeling of shape memory alloy shells for design optimization. *Computers & Structures*, 86(9):955–963, 2008.

[63] Seung-Wook Lee and Seonho Cho. Isogeometric configuration design optimization of built-up structures. *Structural and Multidisciplinary Optimization*, 51(2):319–331, 2015.

[64] Zoe AD Lethbridge, Richard I Walton, Arnaud SH Marmier, Christopher W Smith, and Kenneth E Evans. Elastic anisotropy and extreme poisson's ratios in single crystals. *Acta Materialia*, 58(19):6444–6451, 2010.

[65] Dong Li, Jie Ma, Liang Dong, and Roderic S Lakes. A bi-material structure with poisson's ratio tunable from positive to negative via temperature control. *Materials Letters*, 181:285–288, 2016.

[66] Qi Jian Lim, Pai Wang, Soo Jin Adrian Koh, Eng Huat Khoo, and Katia Bertoldi. Wave propagation in fractal-inspired self-similar beam lattices. *Applied Physics Letters*, 107(22):221911, 2015.

[67] CF Lin and CJ Shih. Topological optimum design of a compliant mechanism for planar optical modulator. *Journal of Applied Science and Engineering*, 5(3):151–158, 2002.

[68] Scott Lipton, John A Evans, Yuri Bazilevs, Thomas Elguedj, and Thomas JR Hughes. Robustness of isogeometric structural discretizations under severe mesh distortion. *Computer Methods in Applied Mechanics and Engineering*, 199(5-8):357–373, 2010.

[69] Yiping Liu, Ken Gall, Martin L Dunn, Alan R Greenberg, and Julie Diani. Thermomechanics of shape memory polymers: uniaxial experiments and constitutive modeling. *International Journal of Plasticity*, 22(2):279–313, 2006.

[70] Zhengyou Liu, Xixiang Zhang, Yiwei Mao, YY Zhu, Zhiyu Yang, Che Ting Chan, and Ping Sheng. Locally resonant sonic materials. *science*, 289(5485):1734–1736, 2000.

[71] Yan Lu, Yang Yang, James K Guest, and Ankit Srivastava. 3-d phononic crystals with ultra-wide band gaps. *Scientific reports*, 7:43407, 2017.

[72] Yiqi Mao, Kai Yu, Michael S Isakov, Jiangtao Wu, Martin L Dunn, and H Jerry Qi. Sequential self-folding structures by 3d printed digital shape memory polymers. *Scientific reports*, 5:13616, 2015.

[73] Enzo Marino. Isogeometric collocation for three-dimensional geometrically exact shear-deformable beams. *Computer Methods in Applied Mechanics and Engineering*, 2016.

[74] Enzo Marino. Locking-free isogeometric collocation formulation for three-dimensional geometrically exact shear-deformable beams with arbitrary initial curvature. *Computer Methods in Applied Mechanics and Engineering*, 324:546–572, 2017.

[75] Kathryn H Matlack, Anton Bauhofer, Sebastian Krödel, Antonio Palermo, and Chiara Daraio. Composite 3d-printed metastructures for low-frequency and broadband vibration absorption. *Proceedings of the National Academy of Sciences*, 113(30):8386–8390, 2016.

[76] Florian Maurin, Luca Dedè, and Alessandro Spadoni. Isogeometric rotation-free analysis of planar extensible-elastica for static and dynamic applications. *Nonlinear Dynamics*, pages 1–20, 2015.

[77] J Michael McCarthy. 21st century kinematics: synthesis, compliance, and tensegrity. *Journal of Mechanisms and Robotics*, 3(2):020201, 2011.

[78] Christoph Meier, Alexander Popp, and Wolfgang A Wall. An objective 3d large deformation finite element formulation for geometrically exact curved kirchhoff rods. *Computer Methods in Applied Mechanics and Engineering*, 278:445–478, 2014.

[79] J Meng, Z Deng, K Zhang, X Xu, and F Wen. Band gap analysis of star-shaped honeycombs with varied poisson's ratio. *Smart Materials and Structures*, 24(9):095011, 2015.

[80] Attila P Nagy, Mostafa M Abdalla, and Zafer Gürdal. Isogeometric sizing and shape optimisation of beam structures. *Computer Methods in Applied Mechanics and Engineering*, 199(17):1216–1230, 2010.

[81] Attila P Nagy, Samuel T IJsselmuiden, and Mostafa M Abdalla. Isogeometric design of anisotropic shells: optimal form and material distribution. *Computer Methods in Applied Mechanics and Engineering*, 264:145–162, 2013.

[82] Bastian Oesterle, Renate Sachse, Ekkehard Ramm, and Manfred Bischoff. Hierarchic isogeometric large rotation shell elements including linearized transverse shear parametrization. *Computer Methods in Applied Mechanics and Engineering*, 321:383–405, 2017.

[83] Niels Olhoff, John Rasmussen, and Erik Lund. A method of exact numerical differentiation for error elimination in finite-element-based semi-analytical shape sensitivity analyses. *Mechanics of Structures and Machines*, 21(1):1–66, 1993.

[84] P Frank Pai. *Highly flexible structures: modeling, computation, and experimentation*. AIAA (American Institute of Aeronautics & Ast, 2007.

[85] P Frank Pai. Three kinematic representations for modeling of highly flexible beams and their applications. *International Journal of Solids and Structures*, 48(19):2764–2777, 2011.

[86] P Frank Pai, Tony J Anderson, and Eric A Wheater. Large-deformation tests and total-

lagrangian finite-element analyses of flexible beams. *International Journal of Solids and Structures*, 37(21):2951–2980, 2000.

[87] Perngjin F Pai and Anthony N Palazotto. Polar decomposition theory in nonlinear analyses of solids and structures. *Journal of engineering mechanics*, 121(4):568–581, 1995.

[88] Claus BW Pedersen, Thomas Buhl, and Ole Sigmund. Topology synthesis of large-displacement compliant mechanisms. *International Journal for numerical methods in engineering*, 50(12):2683–2705, 2001.

[89] Edwin A Peraza-Hernandez, Darren J Hartl, and Richard J Malak Jr. Design and numerical analysis of an sma mesh-based self-folding sheet. *Smart Materials and Structures*, 22(9):094008, 2013.

[90] A Srikantha Phani, J Woodhouse, and NA Fleck. Wave propagation in two-dimensional periodic lattices. *The Journal of the Acoustical Society of America*, 119(4):1995–2005, 2006.

[91] Les Piegl and Wayne Tiller. *The NURBS book*. Springer Science & Business Media, 2012.

[92] D Prall and RS Lakes. Properties of a chiral honeycomb with a poisson's ratio of -1. *International Journal of Mechanical Sciences*, 39(3):305–314, 1997.

[93] SB Raknes, X Deng, Y Bazilevs, DJ Benson, KM Mathisen, and T Kvamsdal. Isogeometric rotation-free bending-stabilized cables: statics, dynamics, bending strips and coupling with shells. *Computer Methods in Applied Mechanics and Engineering*, 263:127–143, 2013.

[94] M Salehi, M Hamedi, H Salmani Nohouji, and J Arghavani. Mechanical properties identification and design optimization of nitinol shape memory alloy microactuators. *Smart Materials and Structures*, 23(2):025001, 2013.

[95] F Scarpa and PJ Tomlin. On the transverse shear modulus of negative poisson's ratio honeycomb structures. *Fatigue & Fracture of Engineering Materials & Structures*, 23(8):717–720, 2000.

[96] F Scarpa, JR Yates, LG Ciffo, and S Patsias. Dynamic crushing of auxetic open-cell polyurethane foam. *Proceedings of the Institution of Mechanical Engineers, Part C: Journal of Mechanical Engineering Science*, 216(12):1153–1156, 2002.

[97] J Schwerdtfeger, F Wein, G Leugering, RF Singer, C Körner, M Stingl, and F Schury. Design of auxetic structures via mathematical optimization. *Advanced materials*, 23(22-23):2650–2654, 2011.

[98] Thomas W Sederberg and Scott R Parry. Free-form deformation of solid geometric models. *ACM SIGGRAPH computer graphics*, 20(4):151–160, 1986.

[99] Ole Sigmund. Tailoring materials with prescribed elastic properties. *Mechanics of Materials*, 20(4):351–368, 1995.

[100] Ole Sigmund. On the design of compliant mechanisms using topology optimization. *Journal of Structural Mechanics*, 25(4):493–524, 1997.

[101] Ole Sigmund and Jakob Søndergaard Jensen. Systematic design of phononic band–gap materials and structures by topology optimization. *Philosophical Transactions of the Royal Society of London A: Mathematical, Physical and Engineering Sciences*, 361(1806):1001–1019, 2003.

[102] Juan C Simo and Loc Vu-Quoc. A three-dimensional finite-strain rod model. part ii: Computational aspects. *Computer methods in applied mechanics and engineering*, 58(1):79–116, 1986.

[103] KY Sze, XH Liu, and SH Lo. Popular benchmark problems for geometric nonlinear analysis of shells. *Finite elements in analysis and design*, 40(11):1551–1569, 2004.

[104] TCT Ting and Tungyang Chen. Poisson's ratio for anisotropic elastic materials can have no bounds. *The quarterly journal of mechanics and applied mathematics*, 58(1):73–82, 2005.

[105] Giuseppe Trainiti, Julian J Rimoli, and Massimo Ruzzene. Wave propagation in undulated structural lattices. *International Journal of Solids and Structures*, 97:431–444, 2016.

[106] Sung-Ling Twu and Kyung K Choi. Configuration design sensitivity analysis of built-up structures part i: Theory. *International Journal for numerical methods in engineering*, 35(5):1127–1150, 1992.

[107] Fengwen Wang, Ole Sigmund, and Jakob Søndergaard Jensen. Design of materials with prescribed nonlinear properties. *Journal of the Mechanics and Physics of Solids*, 69:156–174, 2014.

[108] Pai Wang, Filippo Casadei, Sung Hoon Kang, and Katia Bertoldi. Locally resonant band gaps in periodic beam lattices by tuning connectivity. *Physical Review B*, 91(2):020103, 2015.

[109] Shuang Wang and John C Brigham. A computational framework for the optimal design of morphing processes in locally activated smart material structures. *Smart Materials and Structures*, 21(10):105016, 2012.

[110] Zhen-Pei Wang, Leong Hien Poh, Justin Dirrenberger, Yilin Zhu, and Samuel Forest. Isogeometric shape optimization of smoothed petal auxetic structures via computational periodic homogenization. *Computer Methods in Applied Mechanics and Engineering*, 323:250–271, 2017.

[111] Franziska Warmuth, Maximilian Wormser, and Carolin Körner. Single phase 3d phononic band gap material. *Scientific reports*, 7(1):3843, 2017.

[112] Oliver Weeger, Bharath Narayanan, and Martin L Dunn. Isogeometric shape optimization of nonlinear, curved 3d beams and beam structures. *Computer Methods in Applied Mechanics and Engineering*, 345:26–51, 2019.

[113] Oliver Weeger, Sai-Kit Yeung, and Martin L Dunn. Fully isogeometric modeling and analysis of nonlinear 3d beams with spatially varying geometric and material parameters. *Computer Methods in Applied Mechanics and Engineering*, 342:95–115, 2018.

[114] Maximilian Wormser, Fabian Wein, Michael Stingl, and Carolin Körner. Design and additive manufacturing of 3d phononic band gap structures based on gradient based optimization. *Materials*, 10(10):1125, 2017.

[115] Cheng-Lin Yang, Sheng-Dong Zhao, and Yue-Sheng Wang. Experimental evidence of large complete bandgaps in zig-zag lattice structures. *Ultrasonics*, 74:99–105, 2017.

[116] S Zhang and AD Belegundu. A systematic approach for generating velocity fields in shape optimization. *Structural and Multidisciplinary Optimization*, 5(1):84–94, 1992.

[117] Kai Zhao and James P Schmiedeler. Using rigid-body mechanism topologies to design path generating compliant mechanisms. *Journal of Mechanisms and Robotics*, 8(1):014506, 2016.

[118] R Zhu, XN Liu, GK Hu, CT Sun, and GL Huang. A chiral elastic metamaterial beam for broadband vibration suppression. *Journal of Sound and Vibration*, 333(10):2759–2773, 2014.